frontiers | Research Topics

Tropical cyclone intensity and structure changes: Theories, observations, numerical modeling and forecasting

Edited by
Eric Hendricks, Liguang Wu, Chun-Chieh Wu,
Anthony Didlake and Yuqing Wang

Published in
Frontiers in Earth Science

ISSN 1664-8714
ISBN 978-2-8325-3455-7
DOI 10.3389/978-2-8325-3455-7

About Frontiers

Frontiers is more than just an open access publisher of scholarly articles: it is a pioneering approach to the world of academia, radically improving the way scholarly research is managed. The grand vision of Frontiers is a world where all people have an equal opportunity to seek, share and generate knowledge. Frontiers provides immediate and permanent online open access to all its publications, but this alone is not enough to realize our grand goals.

Frontiers journal series

The Frontiers journal series is a multi-tier and interdisciplinary set of open-access, online journals, promising a paradigm shift from the current review, selection and dissemination processes in academic publishing. All Frontiers journals are driven by researchers for researchers; therefore, they constitute a service to the scholarly community. At the same time, the *Frontiers journal series* operates on a revolutionary invention, the tiered publishing system, initially addressing specific communities of scholars, and gradually climbing up to broader public understanding, thus serving the interests of the lay society, too.

Dedication to quality

Each Frontiers article is a landmark of the highest quality, thanks to genuinely collaborative interactions between authors and review editors, who include some of the world's best academicians. Research must be certified by peers before entering a stream of knowledge that may eventually reach the public - and shape society; therefore, Frontiers only applies the most rigorous and unbiased reviews. Frontiers revolutionizes research publishing by freely delivering the most outstanding research, evaluated with no bias from both the academic and social point of view. By applying the most advanced information technologies, Frontiers is catapulting scholarly publishing into a new generation.

What are Frontiers Research Topics?

Frontiers Research Topics are very popular trademarks of the *Frontiers journals series*: they are collections of at least ten articles, all centered on a particular subject. With their unique mix of varied contributions from Original Research to Review Articles, Frontiers Research Topics unify the most influential researchers, the latest key findings and historical advances in a hot research area.

Find out more on how to host your own Frontiers Research Topic or contribute to one as an author by contacting the Frontiers editorial office: frontiersin.org/about/contact

Tropical cyclone intensity and structure changes: Theories, observations, numerical modeling and forecasting

Topic editors
Eric Hendricks — National Center for Atmospheric Research (UCAR), United States
Liguang Wu — Fudan University, China
Chun-Chieh Wu — National Taiwan University, Taiwan
Anthony Didlake — The Pennsylvania State University (PSU), United States
Yuqing Wang — University of Hawaii at Manoa, United States

Citation
Hendricks, E., Wu, L., Wu, C.-C., Didlake, A., Wang, Y., eds. (2023). *Tropical cyclone intensity and structure changes: Theories, observations, numerical modeling and forecasting*. Lausanne: Frontiers Media SA.
doi: 10.3389/978-2-8325-3455-7

Table of contents

frontiers | Frontiers in Earth Science

TYPE Editorial
PUBLISHED 28 August 2023
DOI 10.3389/feart.2023.1275804

Editorial: Tropical cyclone intensity and structure changes: theories, observations, numerical modeling and forecasting

Eric A. Hendricks[1]*, Yuqing Wang[2], Liguang Wu[3], Anthony C. Didlake[4] and Chun-Chieh Wu[5]

[1]National Center for Atmospheric Research, Boulder, CO, United States, [2]Department of Atmospheric Sciences and International Pacific Research Center, University of Hawaii at Manoa, Honolulu, HI, United States, [3]Department of Atmospheric Sciences, Fudan University, Shanghai, China, [4]Department of Meteorology, Pennsylvania State University, University Park, State College, PA, United States, [5]Department of Atmospheric Sciences, National Taiwan University, Taipei, Taiwan

OPEN ACCESS

EDITED AND REVIEWED BY
Valerio Acocella,
Roma Tre University, Italy

*CORRESPONDENCE
Eric A. Hendricks,
erichend@ucar.edu

RECEIVED 10 August 2023
ACCEPTED 17 August 2023
PUBLISHED 28 August 2023

CITATION
Hendricks EA, Wang Y, Wu L, Didlake AC and Wu C-C (2023), Editorial: Tropical cyclone intensity and structure changes: theories, observations, numerical modeling and forecasting.
Front. Earth Sci. 11:1275804.
doi: 10.3389/feart.2023.1275804

KEYWORDS

tropical cyclone, intensity, structure, numerical modeling, observations, forecasting

Editorial on the Research Topic
Tropical cyclone intensity and structure changes: theories, observations, numerical modeling and forecasting

Tropical cyclones (TCs) have caused billions of dollars in damage and thousands of lives lost globally over the past 50 years. Mitigating this massive socioeconomic impact requires accurate forecasts of TC evolution. Substantial progress has been made in recent years in forecasting TC position. However, progress in forecasting TC intensity and structure has been more slowly incremental. Many challenges remain in forecasting intensity and structure changes, such as rapid intensification, eyewall replacement cycles, and impacts of complex vertical wind shear. It is imperative to advance our knowledge of intensity and structure changes on theoretical, observational, and numerical modeling grounds so that TC forecasts become more accurate in the future.

The goal of this Research Topic was to collect the latest advances on theories, observations, numerical modeling, and forecasting of TC intensity and structure changes. These include intensity and structure changes resulting from environmental influences (such as ocean interactions, vertical wind shear, trough interactions, upper-level outflow, and dry/dusty air intrusions); internal influences (such as inner-core dynamic instabilities and mixing processes, eyewall replacement cycles, spiral rainband dynamics, and air-sea interactions); the mutual interaction of the internal and external processes; the role of physical processes associated with the boundary layer, clouds, and radiation; advances on quantifying intensification rate theories and intensification mechanisms; and new development of forecasting techniques for TC intensity and structure. Eighteen research articles were published in this Research Topic and a summary of these articles is provided below.

First, we describe the theoretical studies. Schubert and Taft used a theoretical framework to examine rapid intensification (RI) through internal TC dynamical processes. In particular, they found that when the potential vorticity (PV) core evolves rapidly enough, inertia-gravity waves were excited at the edges of the PV structure. If the PV core evolved slower, inertia-gravity wave activity was more negligible. An interesting finding of their work was that the intensification rate was sensitive the amount of mass removed in a time period from an absolute angular momentum surface. Schubert et al. examined baroclinic effects on the distribution of TC eye subsidence through semi-analytic solutions to the Sawyer-Eliassen balanced vortex equation. They found conditions under which large values of the radial and vertical advection of potential temperature were located at the outer edge of the eye, producing the warm ring structure.

The next set of studies investigated TC structure, intensity, and associated variability from numerical modeling and observational perspectives. Liu B. et al. used ground-based Doppler radar to investigate the rapid intensification of sheared tropical cyclone Meranti (2010). They found two periods of RI, an asymmetric period and an axisymmetric period. Vertical shear favored deep convection in the downshear-left quadrant which favored development of low-level vortices that were ingested cyclonically inward during the asymmetric episode. This study highlighted the critical importance of asymmetric convective processes in RI. Patra et al. examined the role of random initial conditions, forcing, and parameters in the intensity variability of real TCs in numerical prediction models. Random forcing produced the largest variability in intensity and fastest intensity error growth during rapid intensification. The random initial condition was most important early in the development. Jin et al. examined the role of the upper-level outflow on the RI on Typhoon Roke (2011). Roke's outflow evolved from equatorward to poleward during the RI event. The RI was likely influenced by the outflow since the outflow was enhanced prior to the RI. Finally, Liu and Tang observationally investigated the impacts of volcanic eruption on Tropical Cyclone Cody (2022), through aerosol-cloud interactions using Moderate Resolution Imaging Spectroradiometer (MODIS) satellite and fifth generation European Center for Medium Range Weather Forecasting (ERA5) atmospheric data. They found that the precipitation and intensity of Cody were enhanced after the volcanic eruption. Even though volcanic eruptions near TCs are rare, this study points to the important implications of such events on TC evolution. Ito and Yamamoto used the multitude of Aircraft Communications, Addressing, and Reporting System/Aircraft Meteorological Data Relay (ACARS/AMDAR) observations to construct the composite mean structure of TCs. They found interesting characteristics of the TC warm core structure such as the dependence of the anomaly on intensity and that the anomalies can extend very far radially outward to 1,000 km.

An emerging area of research in TC science is the application of artificial intelligence and machine learning methods to understanding and forecasting TC structure and intensity. Zhu et al. used a machine learning method, the Gradient Boosted Regression Tree (GBRT), to predict intensity variability in the western North Pacific basin at lead times from 12–72 h. The predictors of the model were synoptic and environmental and persistence variables from reanalysis data. They showed that the GBRT was better at intensity forecasting than traditional multiple linear regression models. Yuan et al. used a machine learning method of physics-incorporated networks to estimate TC wind structure (both wind radii and intensity). The physics-incorporated network used satellite imagery and predictors from the Statistical Hurricane Intensity Prediction Scheme (SHIPS), and a neural network to generate the wind radii and intensity. The model was demonstrated to have skill in an operational environment.

Advances in understanding and modeling the TC boundary layer are welcome considering the complexity and societal importance of this region especially when TCs make landfall. Liu et al. used large-eddy simulations to show that tornado-scale vortices exist in the TC boundary layer and were important contributors to extreme wind gusts there. They showed that in the eyewall the peak gust factors associated with these vortices were near 1.8. This reenforced the importance of considering gusts in addition to the maximum sustained wind and on further understanding the coherent structures in the boundary that cause extreme winds. Li et al. used lidar data and computational fluid dynamics experiments to understand the vertical structure of the typhoon winds at landfall. Since most towers are below 100 m, the lidar data provided valuable data from 100–300 m above ground level. A local low-level jet was found in the mean wind profile between 100–300 m suggesting power laws may not always be valid. Finally, Han et al. performed a statistical study on the relationship between pre-landfall intensity change and post-landfall weakening of TCs over East and South China. Over East China, TCs often experienced pre-landfall weakening followed by post-landfall rapid decay. On the other hand, over South China, TCs typically intensified prior to landfall and weakened slowly after landfall.

The final set of studies focused on numerical modeling and forecasting of TCs. Li et al. examined the prediction skill of the Dynamical-Statistical-Analog Ensemble Forecast model for Landfalling Typhoon Gale (DSAEF_LTG model) in comparison to other numerical weather prediction (NWP) models in the South China Sea. They generally found that it was more skillful than the other models. Xie et al. applied the potential vorticity tendency (PVT) approach to very high-resolution numerical simulations (~1 km). While the PVT method has been widely used and successful in coarser numerical simulations, the utility of it in high resolution simulations was not as well known, since the PV structure is resolved to be more heterogeneous and complex, and can even be annular. The authors suggested that either smoothing of the PV field or increasing the temporal output helped to make the PVT method perform better using high-resolution output. Duan et al. examined the sensitivity of the boundary-layer schemes on reproducing the asymmetric rainfall pattern of landfalling Typhoon Lekima (2019). Broadly, they found significant sensitivity of the track, intensity, and structure to the PBL scheme. Su et al. studied the forecasting performance of Dynamical–Statistical–Analog Ensemble Forecast (DSAEF) model for Landfalling Typhoon Precipitation (DSAEF_LTP) over the Fujian Province using new values of two parameters: similarity region and ensemble method. They showed that DSEAF_LTP performed best with regard to precipitation threat scores in comparison to other NWP models. Wang et al. examined the role of a midlatitude upper-level trough on the unusual track and intensity of Typhoon Bavi (2020). Complex trough dynamics, such as the formation of the cutoff low at its base, impacted the track forecast of Bavi. The trough also contributed to its intensification through the upper-level eddy angular momentum flux convergence. Gao et al. examined an extreme rain event in Shandong Province from Typhoon Lekima (2019) using observations and numerical simulations. After landfall, Lekima moved northward along the coast producing the highest precipitation in recorded history in

Shandong Province. In numerical simulations, the intense rain was shown to be a result of the interaction of the typhoon rainbands with a mid-latitude synoptic system. The results show the multiscale characteristics and complexity of rainfall hazards resulting from TCs after landfall.

In summary, articles in this Research Topic advanced our understanding of TC structural and intensity variability using theoretical, observational, numerical-simulation, and forecasting approaches. Considering the societal implications of having accurate TC intensity and structure forecasts, future research is recommended along similar lines.

Author contributions

EH: Writing–original draft, Writing–review and editing. YW: Writing–review and editing. LW: Writing–review and editing. AD: Writing–review and editing. C-CW: Writing–review and editing.

Funding

The author(s) declare financial support was received for the research, authorship, and/or publication of this article. This material is based upon work supported by the National Center for Atmospheric Research (NCAR), which is a major facility sponsored by the National Science Foundation under Cooperative Agreement 1852977.

Conflict of interest

The authors declare that the research was conducted in the absence of any commercial or financial relationships that could be construed as a potential conflict of interest.

The author(s) declared that they were an editorial board member of Frontiers, at the time of submission. This had no impact on the peer review process and the final decision.

Publisher's note

frontiers | Frontiers in Earth Science

ORIGINAL RESEARCH
published: 26 April 2022
doi: 10.3389/feart.2022.871540

Asymmetric Inner-Core Structure and its Impact on Rapid Intensification of a Sheared Tropical Cyclone

Bojun Liu[1]*, **Mingjun Wang**[2] **and Kun Zhao**[3,4]

[1]Chongqing Meteorological Observation, Chongqing, China, [2]Nanjing Joint Institute for Atmospheric Sciences, Nanjing, China, [3]Key Laboratory of Mesoscale Severe Weather/MOE, School of Atmospheric Sciences, Nanjing University, Nanjing, China, [4]State Key Laboratory of Severe Weather and Joint Center for Atmospheric Radar Research of CMA/NJU, Beijing, China

Based on ground-based Doppler radar data with high spatial and temporal resolution, our study focuses on rapid intensification (RI) of a sheared tropical cyclone (TC). The asymmetric inner-core structure and its impact on RI are presented using the Advanced Regional Prediction System-3DVAR. The time evolution of the TC inner-core characteristics shows that Meranti experiences two stages of RI: the asymmetric dominant period and the axisymmetric dominant period. The comparison between the two RI stages shows that the vortex intensified more in the asymmetric stage than the axisymmetric stage. The wavenumber-1 component introduced by the vertical wind shear dominates the asymmetric structure. In the moderate-to-strong shear environment, deep convection occurs mainly in the downshear-left quadrant, generating substantial diabatic heating in the downshear region. Under a suitable inner-core structure configuration, the downshear vortices are entrained cyclonically inward, resulting in RI. It is the interaction between the axisymmetric inner-core structure of the TC and the mesoscale vortex that controls the intensification process, which can be replicated by the nondivergent barotropic model with a similar initial field. This infrequent case provided observation of RI during a strong shear period, which suggests that the inner core structure is vital for TC RI.

Keywords: rapid intensification, ARPS-3DVAR, vertical wind shear, barotropic model, asymmetric structure

Edited by:
Yuqing Wang,
University of Hawaii at Manoa,
United States

Reviewed by:
Eric Hendricks,
National Center for Atmospheric Research (UCAR), United States
Guanghua Chen,
Institute of Atmospheric Physics (CAS), China

***Correspondence:**
Bojun Liu
5inklbj@163.com

Specialty section:
This article was submitted to Atmospheric Science, a section of the journal Frontiers in Earth Science

Received: *08 February 2022*
Accepted: *04 April 2022*
Published: *26 April 2022*

Citation:
Liu B, Wang M and Zhao K (2022) Asymmetric Inner-Core Structure and its Impact on Rapid Intensification of a Sheared Tropical Cyclone.
Front. Earth Sci. 10:871540.
doi: 10.3389/feart.2022.871540

INTRODUCTION

Rapid intensification (RI) is defined as a maximum sustained surface wind speed increase of 15 m s^{-1} (30 kt) over a 24-h period (Kaplan and DeMaria 2003). Forecasting tropical cyclone (TC) intensity is one of the most difficult problems in atmospheric science. Although the intensity guidance of TCs has achieved statistically significant improvements in the past few decades, forecasting RI of TCs remains problematic (Brown 2017). The RI of typhoons often causes significant economic losses, which also makes research on RI a popular and challenging topic at present. Houze (2010) noted that the evolution of small-scale structures in typhoon cores is closely related to RI. From the perspective of the influence of the typhoon core structure on strength, previous studies can be divided into those focused on axisymmetric and asymmetric TC structures.

In axisymmetric structures, eyewall contraction and diabatic heating near the radius of maximum wind (RMW) are important manifestations of RI of TCs. According to the literature, depending on the model, Li et al. (2021) indicated that diabatic heating inside the RMW and radial inflow near the RMW increase, leading to a substantial increase in radial absolute vorticity flux near the RMW and thus rapid TC intensification. Nolan and Grasso (2003) and Nolan et al. (2007) found that even if diabatic heating shows a significant asymmetric distribution, its projection in the axisymmetric direction can still determine the strengthening intensity of TC. It is not simply the presence or even the amount of diabatic heating, but the radial location and the symmetry of precipitation that are more important to RI onset (Chen et al., 2018). In recent years, with the continuous improvement and enrichment of radar, satellite, drop sounding, and other observation technologies, the understanding of the TC inner core structure and its influence on intensity change has been constantly improving. In particular, ground-based radar is the only high spatial-temporal resolution remote sensing platform that can continuously observe the three-dimensional structure of offshore TCs. Since the establishment of the WSR-88D radar network in the United States and the CINRAD WSR-98D ground-based radar network in China, many radar observation data of offshore RI of TCs have been collected. Statistical analysis of the best-track data for the North Atlantic between 2000 and 2017 indicates that convective heating associated with deep convective clouds appearing toward the storm center is important for RMW contraction, and sufficient amounts of convective heating are important for intensification (Wu and Ruan 2021). Case studies of hurricanes (e.g., Blackwell 2000; Lee and Bell 2007; Zhao et al., 2008) also revealed the process and related mechanism of axisymmetric RI. In addition to ground-based radar, studies using satellite observations (Lin and Qian 2019) and airborne radar (Black et al., 1996; Rogers et al., 2013) have discussed the structural characteristics of RI of TCs.

The asymmetric structure also has an important influence on the TC strength. Generally, the main factors causing the asymmetric structure include environmental vertical wind shear (VWS), movement, sea and land impact, and vortex Rossby waves. Under a strong VWS, the large value area of wavenumber-1 energy mainly appears in the downshear-left quadrant (Corbosiero and Molinari 2002; 2003). Further studies indicate that the lightning active area in the TC core narrowed if VWS increased (Abarca et al., 2011). When the VWS is small, the effect of the TC movement on the energy distribution of wavenumber-1 becomes significant (Corbosiero and Molinari 2003; Lonfat et al., 2004; Chen et al., 2006). Generally, VWS is the main factor that determines the convection asymmetry in the eyewall, and factors such as movement velocity only adjust the convection distribution (Hence and Houze 2011; 2012). Some studies have shown that moderate to strong shear can contribute to intensification through the occurrence of vigorous deep convection, called convective bursts, inside the RMW on the downshear side (Reasor et al., 2009; Molinari and Vollaro 2010; Nguyen and Molinari 2012; Shimada and Horinouchi 2018). Sitkowski and Barnes (2009) further found that when RI occurred, convection to the left of the downwind quadrant was repeatedly entrained into the vortex center. Such asymmetric junctions have been observed in many rapidly intensifying TC observations (e.g., Corbosiero and Molinari 2003; Chen et al., 2006; Ryglicki et al., 2021) and model literature (e.g., Frank and Ritchie 2001; Xu and Wu 2005; Riemer et al., 2010). The contribution of these strong convective bursts to RI is mainly reflected in two aspects: 1) The adiabatic warming of the upper descending branch is conducive to the formation of the upper warm center. According to the static equation, the upper warm center will more effectively reduce the pressure in the typhoon center, and the gradient force of the lower pressure increases, forcing the inflow strength, facilitating angular momentum convergence to the typhoon center, and accelerating the main circulation (Guimond et al., 2010). 2) The vertical stretching of the vortex tube caused by diabatic heating of the convective position and the subsequent axial symmetry of the horizontal vorticity accelerate the main circulation.

Although previous studies have discussed several asymmetric mechanisms that may lead to RI, such as vortical hot towers (Hendricks et al., 2004; Montgomery et al., 2006; Reasor et al., 2009) and the transition from asymmetric structure to axisymmetric structure (Schubert et al., 1999; Kossin and Schubert 2001; Persing and Montgomery 2003; Cram et al., 2007), these enhancement mechanisms are mainly based on model simulation results or airborne radar data analysis. In the past, due to the lack of observational data, a numerical simulation method was used to discuss the case study of RI of TCs in the coastal areas of China, which lacked high spatial and temporal structure observations and quantitative analysis of RI typhoon inner cores. With the recent deployment of the Chinese next generation Weather Surveillance Radar 1998 Doppler (CINRAD WSR-98D) network and the Taiwan operational radar network, effective assimilation of high-resolution data from these radar systems into numerical weather prediction models for improving landfall of TC structure analysis provides foundational support for the study of mesoscale structural characteristics of the rapidly intensifying TC inner cores in the northwest Pacific Ocean. Meanwhile, the continuous development of Doppler radar wind field inversion technology and numerical models also provides a reliable analysis method for quantitative study of the inner core structure and evolution characteristics of offshore rapidly intensifying TCs. For example, Zhao et al. (2012) used Advanced Regional Prediction System (ARPS)-3DVAR to assimilate multiple radar data, significantly improved the analysis and forecast field of TC Meranti (2010) through cyclic assimilation analysis, and accurately reproduced the RI process of Meranti. The establishment of an observation network and the improvement in model analysis methods are helpful in studying the time evolution of inner core characteristics and the RI mechanism of offshore RI typhoons, and compensates for the shortcomings of research on offshore RI typhoons in China. TC Meranti was mainly located in the Taiwan Strait, and the Ken-Ting radar (RCKT), Chi-Gu radar (RCCG), and Xiamen radar (XMRD) were able to observe its internal structure at a relatively close distance. Observation data with high spatial and temporal resolution can provide 3D wind field inversion by dual Doppler radar in the early RI period, providing vital support for the ARPS-3DVAR cycle assimilation.

In this study, we show the asymmetric inner-core structure and evolution of TC Meranti (2010) during its RI stage based on observational analysis. A nondivergent barotropic model and

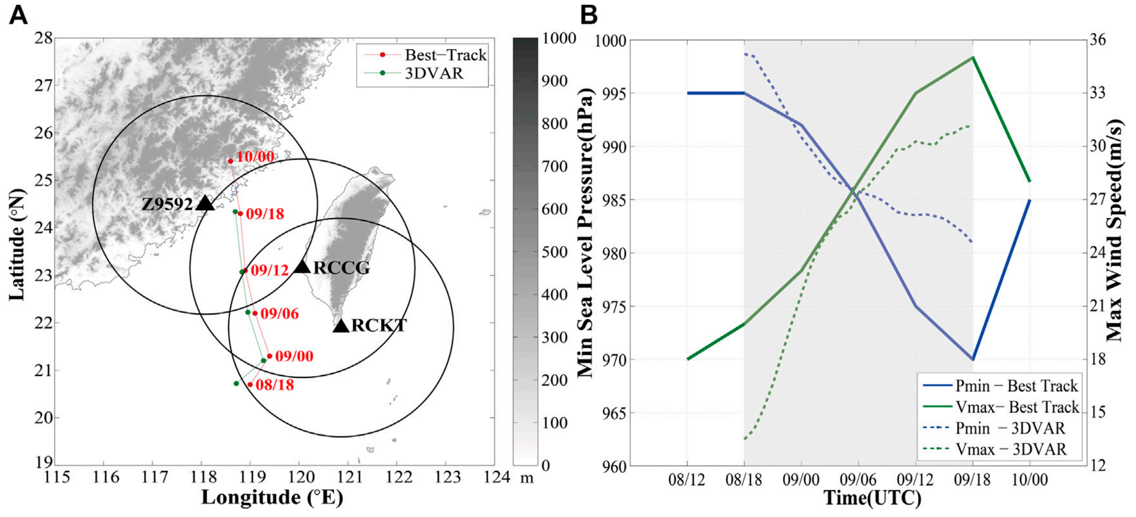

FIGURE 1 | Path and intensity information of Meranti. **(A)** The analysis domain at 3 km horizontal grid spacing, with the CMA best track (red) and APRS-3DVAR locations (green) of Meranti marked at 6 h intervals from 18:00 UTC September 8, to 0:00 UTC 10 September 2010. **(B)** The intensity evolution of TC Meranti, the green (blue) line represents wind speed (sea level pressure), and the solid lines and dotted lines are based on CMA and ARPS-3DVAR, respectively.

sensitivity test are used to discuss the effect of the asymmetric structure on the TC RI. The data and analysis methods used are described in the Data and Methods section. The TC Meranti section provides a brief overview of the path and intensity evolution of Meranti (2010). The characteristics of the asymmetric inner-core structure evolution section identifies the inner-core structure of TC Meranti and reasonable underlying mechanism. A possible mechanism of RI introduced by the asymmetric inner-core structure is discussed in the nondivergent barotropic model and sensitivity test section, followed by a summary.

DATA AND METHODS

Data

In this study, radar data from three S-band coastal Doppler radars were used, including one CINRAD WSR-98D radar (XMRD) along the southeast coast of mainland China and two Gematronik 1500S Doppler radars (RCCG & RCKT) on Taiwan Island (**Figure 1A**). All operated with the same volume coverage pattern 21 (VCP21) scanning mode of the WSR-88D in the United States, which can perform a 6-min volume scan and provide radar reflectivity and radial velocity data with observation ranges of 230 km, and radial resolutions of 1 and 0.25 km, respectively. The data were examined and edited manually using the National Center for Atmospheric Research software “SOLOII” (Oye et al., 1995). Subsequently, radar data were interpolated from polar coordinates to Cartesian coordinates using the bilinear interpolation method.

Typhoon center data come from the Typhoon Best Track dataset compiled by the Shanghai Typhoon Research Institute of the China Meteorological Administration (CMA), which can provide historical data such as longitude and latitude of the typhoon center every 6 h. The environmental VWS is based on the National Centers for Environmental Prediction (NCEP) Climate Forecast System Reanalysis (CFSR) data (Saha et al., 2010), which are available at 37 vertical levels from 1,000 hPa to one hPa with a grid spacing of 0.5° latitude × 0.5° longitude at 6-h intervals. The 200–850 hPa VWS is calculated using the averaged azimuthal mean Cartesian wind components between 300 and 800 km radii from TC center. The choice of the area average for environmental VWS is optimal for TCs over South China Sea (Chen et al., 2015). The formula for the environmental average wind after considering the area weight is as follows:

$$\langle \mathbf{U} \rangle = \frac{1}{\mathbf{A}}\sum_{\mathbf{i}=3}^{8}\left(\frac{\mathbf{U}_{\mathbf{i}-1}+\mathbf{U}_{\mathbf{i}}}{2}\right)\mathbf{A}_{\mathbf{i}}$$

$$\langle \mathbf{V} \rangle = \frac{1}{\mathbf{A}}\sum_{\mathbf{i}=3}^{8}\left(\frac{\mathbf{V}_{\mathbf{i}-1}+\mathbf{V}_{\mathbf{i}}}{2}\right)\mathbf{A}_{\mathbf{i}}$$

where **U** and **V** are the wind field grid data in a large-scale environmental field, **A** represents the total area, **i** is the distance coefficient, the bandwidth of each distance ring is 100 km, $\mathbf{A_i}$ is the area of the *i*th distance ring, and n is the value range of the large-scale environment (e.g., when calculating 500 km, **i** is 5). ⟨⟩ represents the average area. Then, the strong echo moves counterclockwise in the tangential direction and approaches the TC radially and can be calculated by subtracting the average wind at the upper level (200 hPa) from the average wind at the lower level (850 hPa). In subsequent analysis, VWS was linearly interpolated into 1 h resolution when required.

Methods

The nonhydrostatic ARPS with full physics was used for the analysis of “real” wind fields with radar data assimilation. A domain of 1830 × 1830 × 25 km was used, consisting of 611 ×

TABLE 1 | Main parameters in barotropic model.

Parameters	Value	unit	Description
Xlen	501	—	Grid number in the *x* direction
Ylen	501	—	Grid number in the *y* direction
dL	1	km	Step size of grid point
dt	10	Second	Time step
lat	22.7	°N	Latitude

611 × 53 grid points with a 3 km horizontal grid spacing and varying vertical resolutions ranging from 50 m at the surface to 770 m at the top of the model. The initial analysis background and lateral boundary conditions (LBCs) were from the NCEP CFSR data. The physics options, e.g., Lin ice microphysics, Goddard longwave and shortwave radiation, a 2-layer soil model, and the turbulent kinetic energy (TKE)-based subgrid-scale turbulence and planetary boundary layer (PBL) parameterizations, were used in this study (Xue et al., 2001). Detailed parameters and configuration of the ARPS can be found in Zhao et al. (2012). The model started at 18:00 UTC on 8 September 2010, and radar data were cyclically assimilated every hour until 18:00 UTC 9 September 2010. The analysis time selected in this study covers the main life stage of TC Meranti from initial generation to near landfall. From 1:00 UTC 9 September 2010, Meranti entered the observation range of the dual Doppler radar, which provided excellent observation data for studying the RI of typhoons with strong asymmetric structures in a sheared environment. Thus, analysis before 1:00 UTC focused on radar echo data, and physical quantities such as velocity and vorticity were used after 1:00 UTC.

A high-resolution quasi-geostrophic barotropic model was used to reveal the interaction between typhoon axisymmetric circulation and asymmetric disturbance. For Meranti, the wind field provided analysis by the ARPS-3DVAR helped to approach a more realistic initial field, thus exploring the main mechanism of asymmetric vorticity entrained and acceleration of the main circulation. The two-dimensional non-divergent quasi-geostrophic vorticity equation on the f-plane is expressed as follows (Luo 2003):

$$\frac{\partial}{\partial \mathbf{t}}\nabla^2\Psi + \mathbf{J}(\Psi, \nabla^2\Psi) = -\boldsymbol{\gamma}\nabla^2\Psi$$

where $\boldsymbol{\Psi}$ represents the geostrophic steam function, $\boldsymbol{J}$ represents the Jacobi operator, and $\boldsymbol{\gamma}$ is the dissipation coefficient. This formula is similar to that of Kossin and Schubert (2001). Detail of the main parameters of barotropic model are available in **Table 1**.

OVERVIEW OF TC MERANTI

Meranti formed a tropical depression east of Taiwan on 7 September 2010 and moved southwest immediately afterward. It intensified into a tropical storm by 6:00 UTC on September 8, then turned and moved northward. It underwent RI from 18:00 UTC September 8 to 18:00 UTC September 9, with the maximum surface wind speed increasing from 20 m s^{-1} to 35 m s^{-1} when approaching landfall according to the official best-track data from CMA. The TC weakened rapidly after the landfall at 19:30 UTC (**Figure 1A**). The intensity evolution of Meranti is shown in **Figure 1B**, where the solid and dotted lines represent the maximum wind speed (green) and minimum sea level pressure (blue) from the CMA optimal path dataset and APRS-3DVAR analysis, respectively. Due to the small scale of the TC and far distance from radar, ARPS-3DVAR analysis begins at 18:00 UTC September 8, and represents an underestimation of 7 m s^{-1} compared with CMA. After the ARPS-3DVAR analysis, the maximum tangential wind speed approached the CMA best-track data set. After 0:00 UTC, the analysis field was consistent with the CMA results. After 12:00 UTC September 9, the intensity of CMA was 3 m s^{-1} stronger than that of ARPS-3DVAR. Zhao et al. (2012) indicated that the CMA best-track dataset overestimated typhoon intensity to a certain extent, which may be the reason for the difference between the CMA and the analysis field. Although there are some differences between the CMA and 3DVAR analysis fields, some basic characteristics of evolution over time are shown. The analysis maximum wind speed from APRS-3DVAR increased from 13 m s^{-1} to 31 m s^{-1}, and the wind speed increased by 18 m s^{-1} within 24 h (CMA was 15 m s^{-1}), which approximates the definition of Kaplan and DeMaria (2003) on TC RI. The CMA and 3DVAR analysis field also indicated that the strengthening rate of Meranti was not the same throughout the RI period. The wind speed increased from 13 m s^{-1} (20 m s^{-1}, according to CMA) to 28 m s^{-1} (same for ARPS-3DVAR and CMA) within 12 h before 6:00 UTC September 9. Later, the strength increased from 28 m s^{-1} to 32 m s^{-1} (35 m s^{-1}, according to CMA) at a slower rate than before.

CHARACTERISTICS OF ASYMMETRIC INNER-CORE STRUCTURE EVOLUTION

RI of Meranti lasted from 18:00 UTC 8 September 2010, to 18:00 UTC 9 September 2010, and the entire RI process was observed by radar (**Figure 1A**). **Figure 2** shows the radar reflectivity factor detected by radar observations at an elevation of 0.5°. At 18:00 UTC September 8, the radar reflectivity factor was crescent, mainly distributed in the southeast semicircle of the TC center, and the echo intensity in the south was obviously weaker than that in the east. Meanwhile, the VWS of 200 hPa–850 hPa was 11.2 m s^{-1}. The strongest echo appeared on the left side of the downwind quadrant. At 21:00 UTC September 8, the echo near the circulation center still showed an obvious asymmetric structure, and the strong echo in the east was further expanded and enhanced. The strong echo moved tangentially counterclockwise, approaching the TC center in the radial direction. The VWS weakened significantly at 0:00 UTC September 9, with a magnitude of 7 m s^{-1}. Meanwhile, the Meranti echo still demonstrated an asymmetric structure, accompanied by a weakening of the radar echo and a movement to the north side of the TC center. At 3:00 UTC,

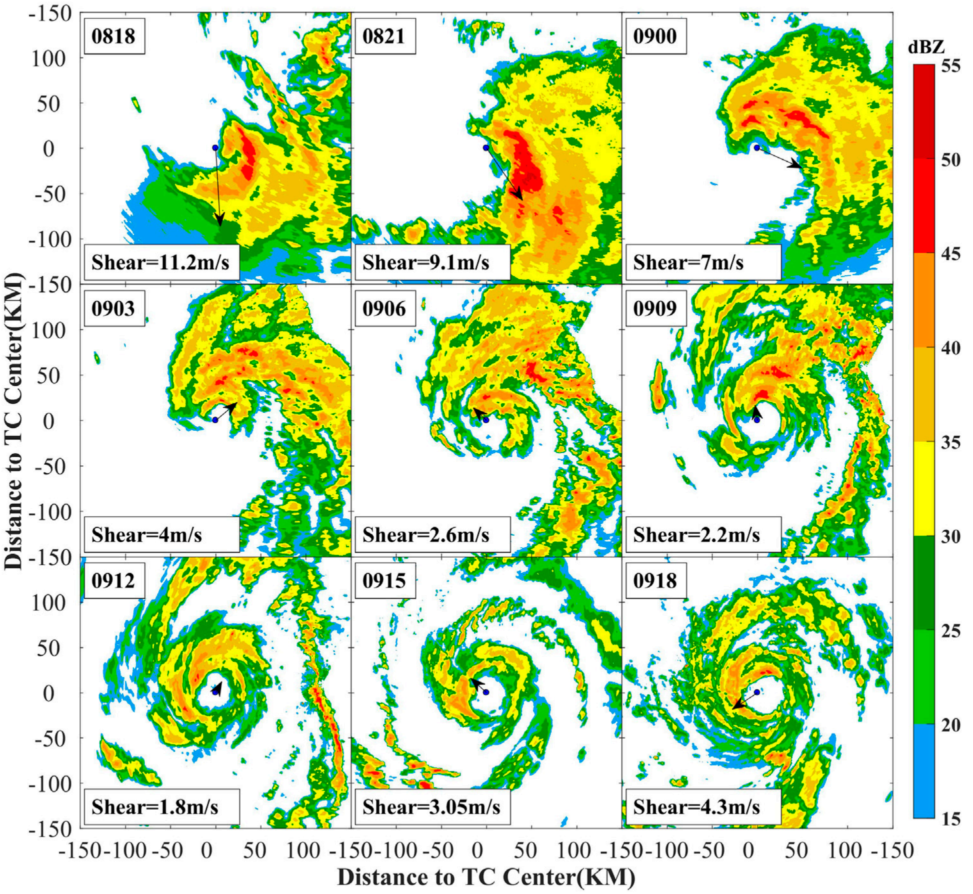

FIGURE 2 | Time evolution of radar reflectivity factor observed at 0.5° elevation during the RI period every 3 h. The black point in the center for each figure represents the TC center. Wind shear is superimposed on TC center in form of an arrow and indicated in the lower left corner.

the TC eyewall was obviously axisymmetric compared with before, although the pattern was not completely demonstrated. After 3 h, the rain belt developed southwest of the TC center, and the VWS was reduced to 2.6 m s^{-1}. From 9:00 to 12:00 UTC on September 9, the eyewall of Meranti was basically linked. At 12:00 UTC, VWS was only 1.8 m s^{-1}. At this point, Meranti essentially completed the axial symmetry, and the outer rain band weakened immediately. From 15:00 to 18:00 UTC, the inner-core echo structure generally remained stable and axisymmetric, and its intensity increased slightly.

Figure 2 qualitatively demonstrates the characteristics of Meranti's inner-core structure: strong asymmetry in the early stage and then becoming axisymmetric. To quantitatively describe the difference between the two stages, **Figure 3** shows the time evolution characteristics of each wave number energy (**Figure 3A**) of the echo near the RMW, the area percentage of strong convection in the core area, and VWS (**Figure 3B**) during the RI period. Here, "near RMW" denotes the radial range within ±10 km of the RMW which is a radius that varies with time. Strong convection is defined as a radar reflectivity factor of ≥40 dBZ at 5 km. To obtain the energy distribution of each wave number for TC Meranti, the echo on the contour plane at a height of 3 km uses Fourier decomposition with the typhoon center as the origin. When calculating the Fourier decomposition, referring to the method of Lonfat et al. (2004), the Fourier series expansion is carried out for the echo along the azimuth for the radar reflectivity factor on each radius of the core area on each distance circle:

$$\mathbf{R}(\boldsymbol{\theta}_\mathbf{n}) = \mathbf{a}_0 + \sum_{\mathbf{n}=1}^{\infty}\left(\mathbf{a}_\mathbf{n}\, cos\left(\mathbf{n}\boldsymbol{\theta}_\mathbf{n}\right) + \mathbf{b}_\mathbf{n}\, sin\left(\mathbf{n}\boldsymbol{\theta}_\mathbf{n}\right)\right)$$

where $\boldsymbol{R}$ is the reflectivity factor on the CAPPI plane; $\boldsymbol{\theta_n}$ represents the azimuth; $\boldsymbol{n}$ represents the wave number; $\boldsymbol{a_n}$ and $\boldsymbol{b_n}$ represent the Fourier number, which can be used to calculate the amplitude and phase of each periodic fluctuation $\boldsymbol{\theta_n}$. **Figure 3A** indicates that the asymmetric component was dominated by wavenumber-1 during the RI period, and the energy of wavenumber-2 (or more) was very weak (wavenumbers above two waves are omitted in **Figure 3A**). Before 6:00 UTC, the asymmetric energy exceeded the axisymmetric energy and occupied a dominant position. After 6:00 UTC, the energy in the Meranti inner core was symmetrical,

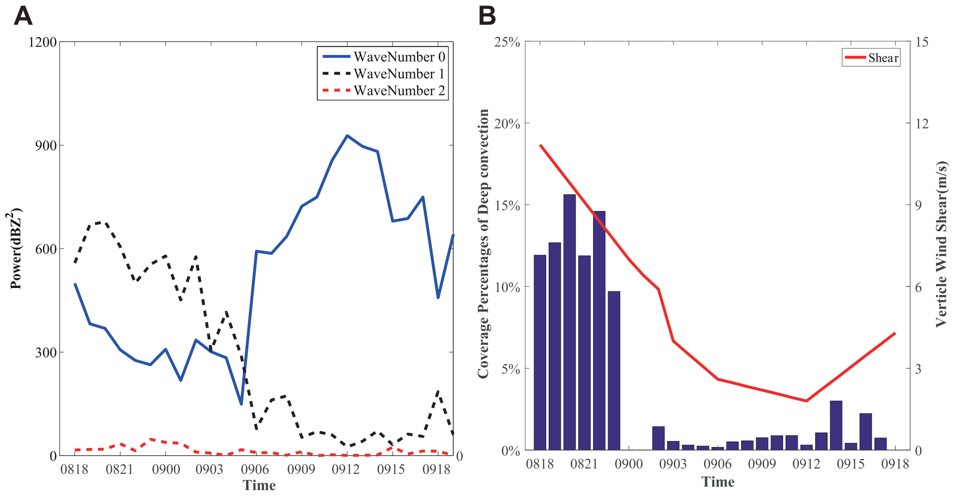

FIGURE 3 | Time evolution characteristics of wave number energy **(A)** of the echo near the maximum wind speed radius, and area percentage of strong convection in the core area overlying with vertical wind shear **(B)**.

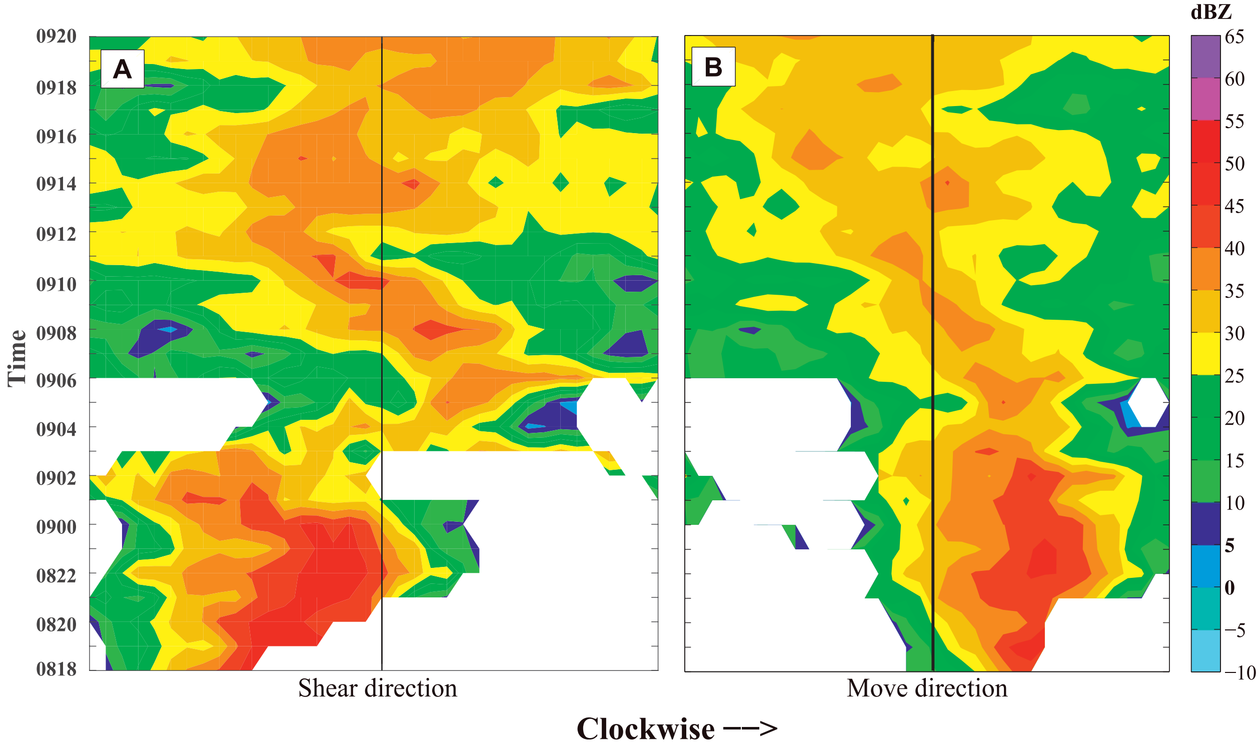

FIGURE 4 | Corresponding relationship between location of radar echo near eyewall and wind shear direction **(A)** or movement direction **(B)**.

which also corresponds to **Figure 2**. Therefore, the enhancement process before 6:00 UTC September 9 was the asymmetric dominant stage (hereinafter referred to as the asymmetric stage), followed by the axisymmetric dominant stage (hereinafter referred to as the axisymmetric stage). Interestingly, the change in the energy of wavenumber-1 is strongly consistent with the magnitude of the VWS and strong convection area in **Figure 3B**. In the initial asymmetric stage, the environmental VWS was generally large at 18:00 UTC September 9 and 0:00 UTC September 9 ($11.2\ \mathrm{m\,s^{-1}}$ and $7\ \mathrm{m\,s^{-1}}$, respectively). Previous studies have shown that a strong VWS is associated with abundant asymmetric strong convection in the downshear-left quadrant, although it is not conducive to TC enhancement. Due to the enhancement of the downshear-left

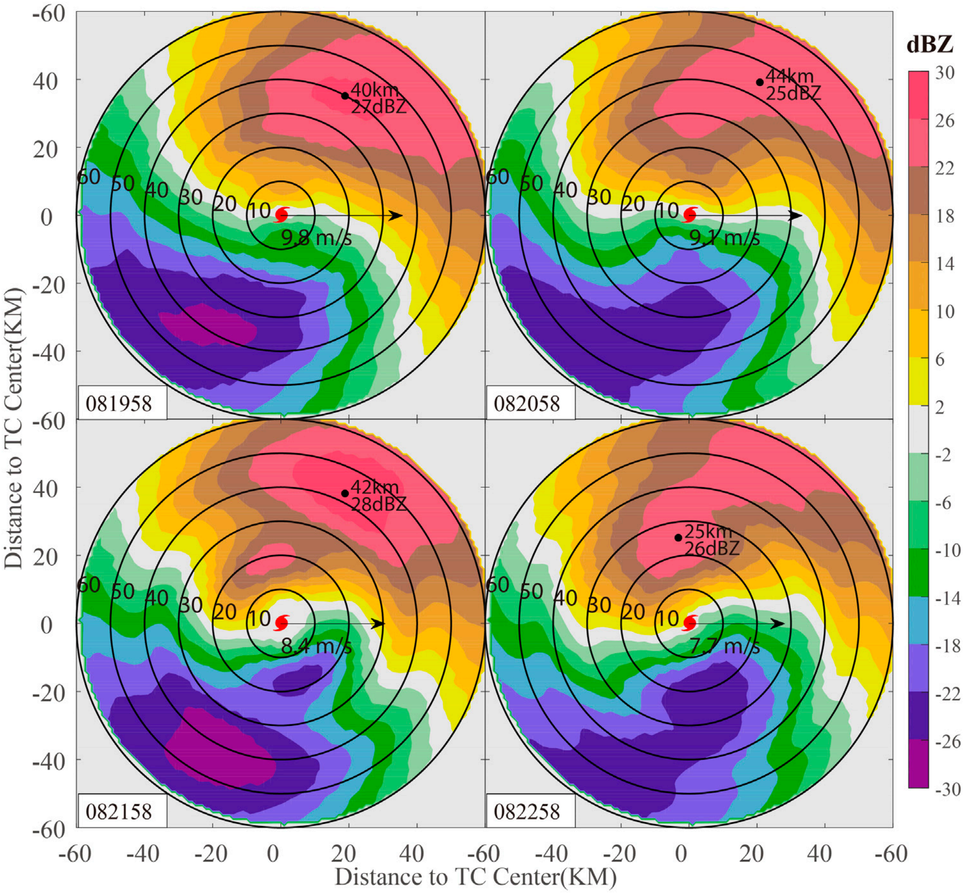

FIGURE 5 | Wavenumber-1 component of the radar echo according to Fourier decomposition at 3 km during 20:00 to 23:00 UTC. The VWS direction is uniformly adjusted to the right, and the arrow length indicates the size of the VWS. The black dot indicates the position of the maximum amplitude of wavenumber-1, with the label of intensity and distance from TC center. The dotted circle represents the distance to the TC center, marking from 10 to 60 km at intervals of 10 km.

quadrant and limitation of the upshear-right quadrant, abundant convection significantly increased the asymmetric wavenumber-1 energy of Meranti. With the decrease in wind shear, the area of strong convection in Meranti gradually decreased. Meanwhile, the asymmetric wave energy decreased, and the axisymmetry increased, which finally resulted in a TC RI.

To reveal the source of strong asymmetric energy in the early stage of Meranti RI, the wind shear direction and movement direction corresponded to the radar echo at 3 km near the eyewall. **Figure 4** indicates that the tendency of the radar echo gradually becomes axisymmetric during the RI period. Before 6:00 UTC, the echo near the eyewall was very strong. Subsequently, it was largely symmetrical. This is the exactly asymmetric stage and axisymmetric stage mentioned in the previous analysis. In the asymmetric stage, Meranti experienced a strong VWS, and the echo showed an obvious wavenumber-1 distribution. Strong convection was located on the left side of the downwind shear and on the right side of the TC movement. The motion effect arises from asymmetric frictional forcing in the boundary layer. Slab boundary layer model showed that the convergence concentrated in the right-front quadrant accompanied by the increase of moving speed (Shapiro, 1983). Corbosiero and Molinari (2002) indicated a strong vertical wind shear influence on convective asymmetries, with downshear to downshear left maxima in the core. Both effects exist only because storm motion is closely coupled to vertical wind shear. Furthermore, the well-documented effect of storm motion on convective asymmetries is largely a reflection of the much stronger vertical shear effect, which means wavenumber-1 is mainly introduced by VWS (Corbosiero and Molinari, 2002; 2003). In the axisymmetric stage, this relationship became insignificant with a decrease in the wind shear. This shows that the abundant asymmetric energy in the early stage of RI was associated with asymmetric convection induced by VWS and movement.

As shown in **Figure 3**, wavenumber-1 dominated the asymmetric stage. The motion of radar echo wavenumber-1 at 3 km from 20:00 to 23:00 UTC is shown in **Figure 5**. For convenience, the VWS direction is uniformly adjusted to the right, and the arrow length indicates the magnitude of the VWS. The black dot indicates the position of the maximum amplitude of wavenumber-1, with the label of intensity and

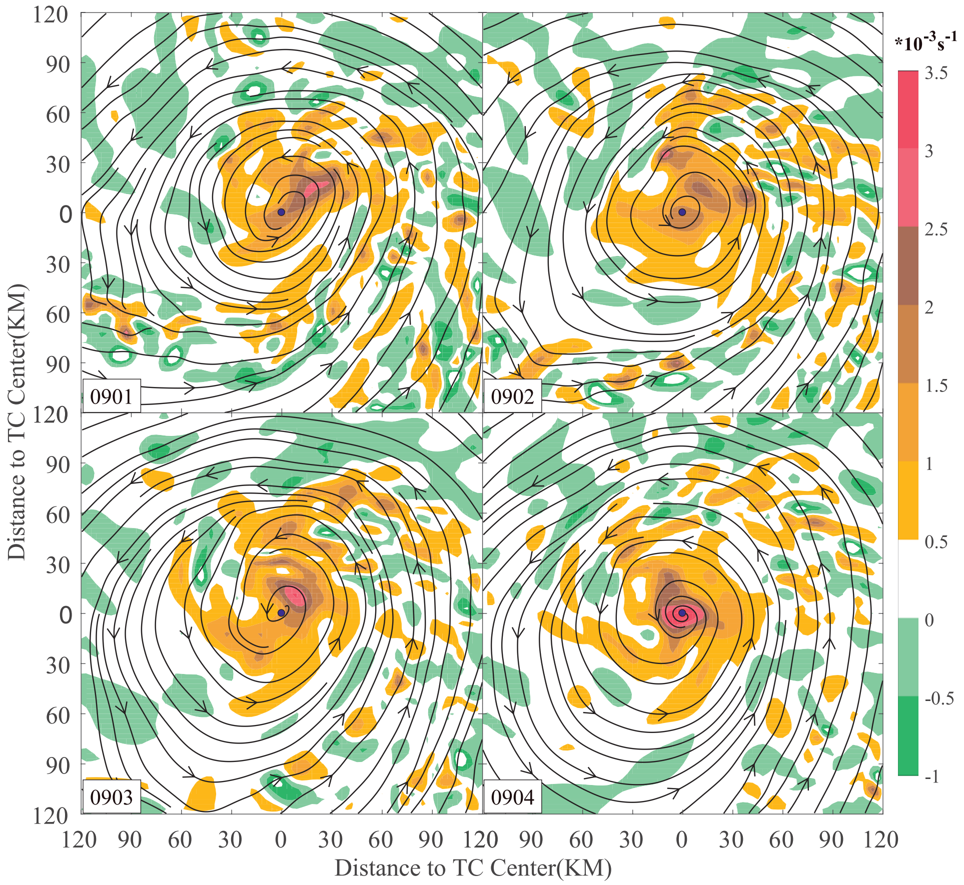

FIGURE 6 | Streamlines at 3 km and vorticity field (color scale) of Meranti core region from 1:00 to 4:00 UTC September 9. The solid blue point represents the approximate center of Meranti.

distance from the TC center. The dotted circle represents the distance to the TC center, marking from 10 to 60 km with an interval of 10 km. It can be seen from the figure that the moderate VWS ensured that the amplitude of the wavenumber-1 component of the reflectivity factor always maintained a high level from 20:00 to 23:00 UTC. At 20:00 UTC, the maximum amplitude of wavenumber-1 appeared 40 km from the TC center in the downshear-left quadrant, with an amplitude of 27 dBZ. After 1 hour, the position of maximum wavenumber-1 amplitude was generally stable, with a small amount of counterclockwise displacement in the tangential direction (relative to the circulation center, the same below). Subsequently, the tangential counterclockwise movement was maintained, and radial centripetal motion was enhanced at 22:00 UTC. Finally, at 23:00 UTC, the maximum amplitude of wavenumber-1 was entrained counterclockwise inward to only 25 km from the TC center. Although the maximum amplitude moved to the upper right quadrant, outside it, the large value area of wavenumber-1 was still located in the downshear-left quadrant, which indicates that moderate VWS continuously promoted new convection and released latent heat to provide energy for asymmetric wavenumber-1. Despite the decrease in VWS from 9.8 m s^{-1} to 7.7 m s^{-1}, the location of the high-value area of wavenumber-1 energy was locked on the downshear-left quadrant, combined with a slight decrease in strength. In general, the maximum amplitude of wavenumber-1 showed a trend of tangential cyclonic rotation with radial inward motion, which is very similar to the characteristics of tropical storm Gabrielle (2001), in which RI under a strong VWS was observed (Molinari and Vollaro, 2010).

Because the radar echo movement cannot completely represent the real wind field, the wind field analysis obtained by APRS-3DVAR is also needed to analyze the inner core dynamics and RI mechanism in the asymmetric stage. The core area entered the dual radar observation area after 1:00 UTC on September 9. According to the retrieval wind field, **Figure 6** shows the streamline and vorticity field (color scale) at a height of 3 km from 1:00 to 4:00 UTC on September 9. The solid blue point in the figure represents the approximate center of Meranti. At 0:00 UTC September 9, the maximum vorticity appeared on the northeast side of the circulation center, presenting a long elliptical distribution, approximately 30 km away from the TC center, with an intensity of 2.9 × 10^{-3} s^{-1}. After 1 hour, the strongest vorticity moved northwest of the circulation center. At this

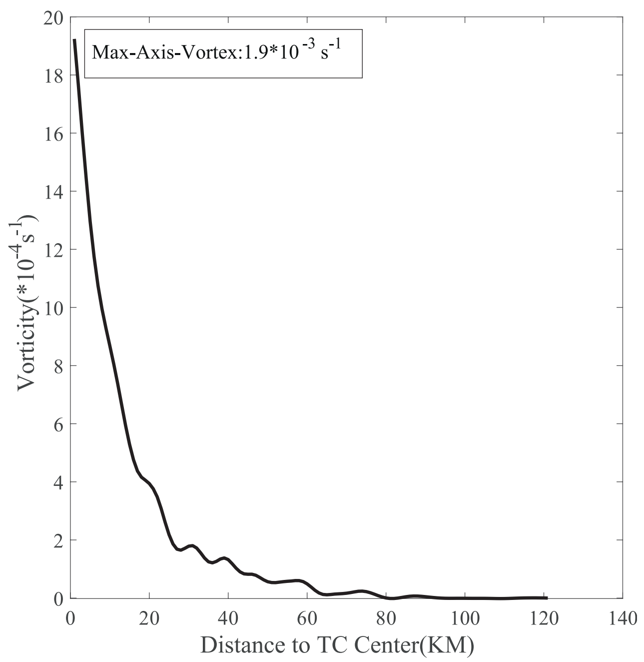

FIGURE 7 | Vorticity profile of axisymmetric circulation (wave component 0) at 1:00 UTC 9 September 2010.

time, new vorticity values were continuously generated on the northeast side. At 3:00 UTC, the maximum vorticity at the previous moment was absorbed by the base flow, while the vorticity northeast of the TC center was strengthened and appeared at a closer distance to the TC center (approximately 20 km). Finally, the axisymmetric vorticity was completed at 4: 00 UTC, which indicated that the maximum vorticity center coincided with the circulation center. Several strong mesoscale vorticities interacted with the TC circulation vorticity and finally merged. The phenomenon of mutual rotation is counterclockwise and cyclonic in the tangential direction. In the radial direction, mesoscale vorticities approached the TC circulation vorticity, and eventually merged in. This motion is consistent with the tangential cyclonic rotation with radial inward motion shown in **Figure 5**.

Xu and Wu (2005) used model and vorticity equation diagnostic method to explain the relationship between the asymmetric flow pattern and main circulation intensity. If wavenumber-1 is cyclonic inflow or anticyclonic outflow, the exchange of the asymmetric to symmetric accelerate the main circulation. In order to verify the correctness of the above conclusion in RI of Meranti, a nondivergent barotropic model and sensitivity test are used in the following section.

NONDIVERGENT BAROTROPIC MODEL AND SENSITIVITY TEST

Although boundary layer and moist processes certainly play an essential role in the evolutions of TCs, it is nevertheless meaningful to consider the role of conservative processes in the absence of additional physics. Such additional, and possibly extraneous, physics can obscure fundamental mechanisms, introduce parameterizations, compromise numerical resolution and dynamical accuracy (Kossin and Schubert, 2001). Meranti's wind field is mainly captured by dual-Doppler radar, which minimum observed altitude is about 3 km according to radar altimetry equation. It is over the height of boundary layer. The lack of reliable data of divergent processes limits the discussion of boundary layer. Thus, a nondivergent barotropic model was used to reveal the interaction between the typhoon axisymmetric vorticity and asymmetric mesoscale vorticity. On the premise that similar results can be roughly simulated, the simpler the model is, the more critical process of RI is grasped. The initial field steam function was composed of the background field steam function $\boldsymbol{\Psi_T}$ and mesoscale eddy steam function $\boldsymbol{\Psi_M}$. $\boldsymbol{\Psi_T}$ was calculated by a 3-km height axisymmetric vorticity field around the TC center at 1:00 UTC on 9 September 2010, through Poisson iteration. The wind field was extracted, and Fourier decomposition was performed using the polar coordinates of the TC center. The TC basic vorticity and strongest mesoscale vorticity in the northwest were obtained. The wavenumber-0 component represents the axisymmetric basic circulation of the typhoon $\boldsymbol{\Psi_T}$, as shown in **Figure 7**. The TC basic vorticity was mainly concentrated within 60 km from the TC center, presenting a unipolar distribution. The maximum axisymmetric vorticity appeared around the TC center, with a strength of $1.9 \times 10^{-3}\ s^{-1}$. Wave component 1 represents the mesoscale vortex $\boldsymbol{\Psi_M}$ caused by the strong convection excited by the VWS in Meranti. According to the retrieved wind field, the radius of the mesoscale vortex was approximately 50 km, with a distance of 40 km and an

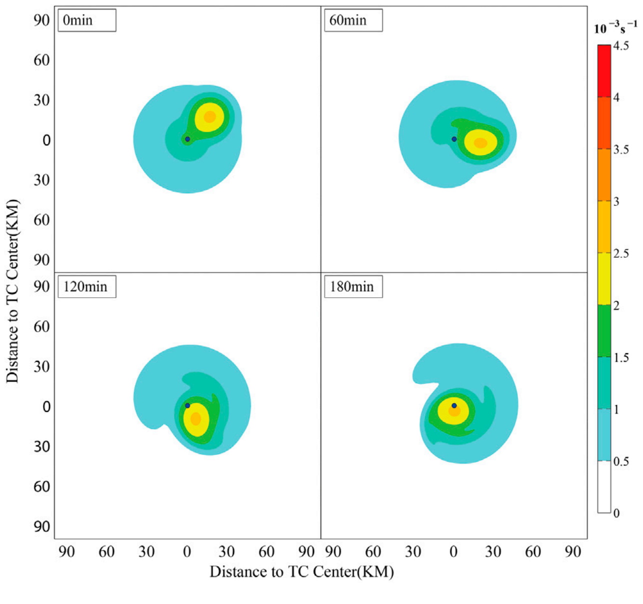

FIGURE 8 | Evolution of vorticity produced by nondivergence barotropic model within 3 h (corresponding with 1:00 to 4:00 UTC in **Figure 6**).

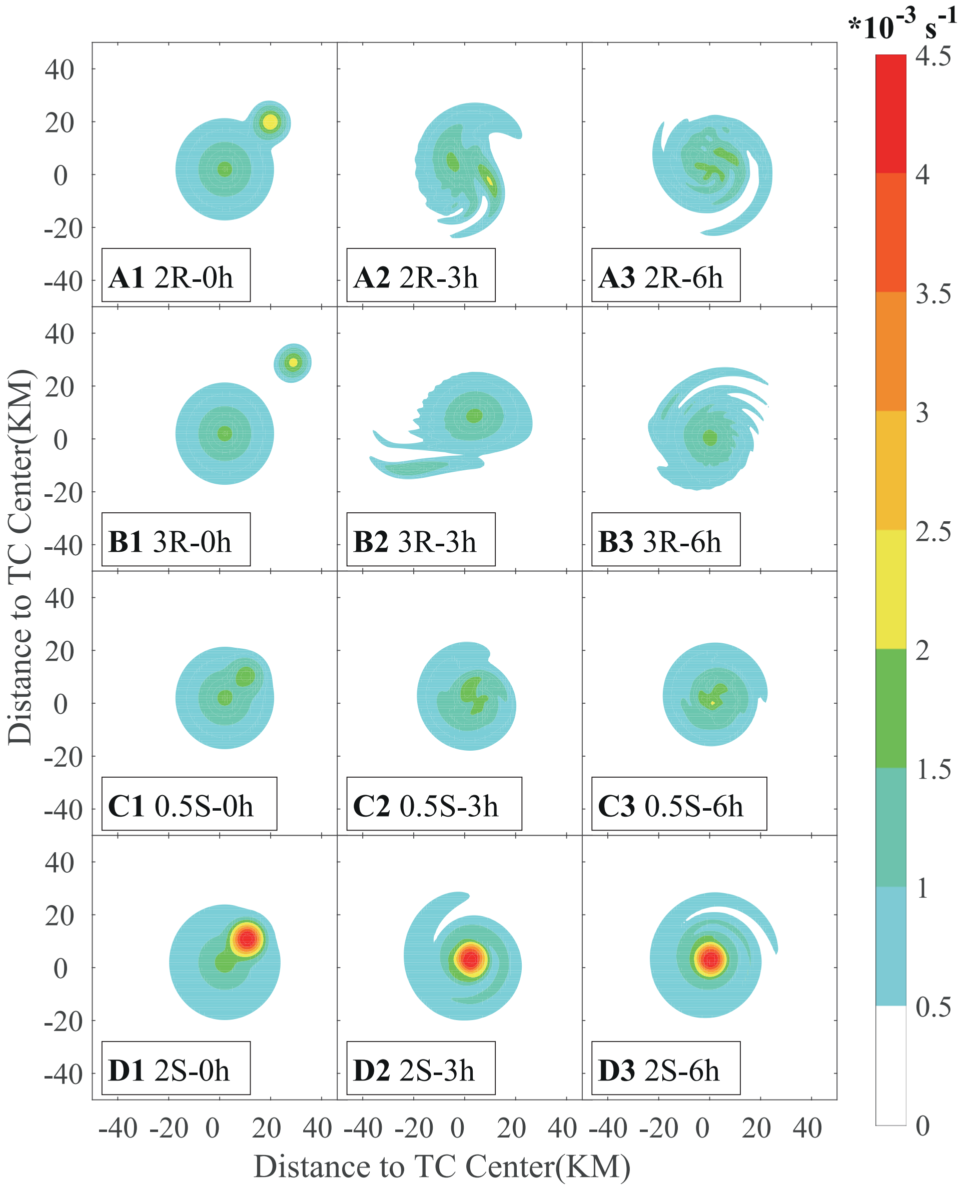

FIGURE 9 | Simulation results of nondivergent barotropic model sensitivity tests. The first, second, and third columns represent the integration times of 0, 3, and 6 h, respectively. Rows **(A–D)** represent the four situations in which the distance doubles, triples, the mesoscale vortex strength is halved, and the mesoscale vortex is doubled in strength, respectively.

intensity of 2.9 × $10^{-3}\,s^{-1}$. In the initial field of the nondivergent barotropic model, the mathematical expression of the mesoscale vorticity in the Cartesian coordinate system is expressed as follows:

$$vor_M(x,y)=\begin{cases}2\times10^{-3}\times\left(1-(s/R)^2\right)^2, & s\le R\\ 0, & s>R\end{cases}$$

where $s=\sqrt{(x-x_M)^2+(y-y_M)^2}$, (x_M, y_M) is the coordinate of the mesoscale vortex center, and R is the initial radius of the mesoscale vortex.

The simulation results of the nondivergent barotropic model are shown in **Figure 8**, where the vorticity field is colored and the black dot in the center represents the TC center at the initial moment (1:00 UTC 9 September 2010). Comparing the simulation results and the ARPS-3DVAR analysis field hourly, it can be found that: 1) The positions of large vorticity values basically correspond. 2) The nondivergent barotropic model can recreate the vorticity enhancement of the TC axisymmetric circulation to a certain extent. 3) The tangential cyclonic rotating and radial approaching processes between the TC vortex and mesoscale vortex can be reproduced distinctly. This means that the dynamic interaction between the TC vortex and mesoscale vortex is a reasonable explanation for their tangential cyclonic rotation with radial inward motion, which is associated with the RI of Meranti. Obviously, the real

RI process is more complex than that shown by the simulation results. For example, the mesoscale vorticity gradually weakened after 1:00 UTC, and new vorticity was excited in the downshear-left quadrant, forming a new strong asymmetric structure and interacting with the typhoon vortex again. During this process, the location of the typhoon circulation center and mesoscale vortex kept approaching, which was caused by the interaction of the two vortices.

Sensitivity tests were used to further demonstrate the dynamic interaction between the mesoscale vortex and typhoon axisymmetric circulation. The typhoon circulation vorticity in the experiment was consistent with that in the original experiment, and only the intensity and distance of the mesoscale vortex were adjusted. In **Figure 9**, rows A and B indicate that the distance between the mesoscale vortex and TC center is increased by two or three times that of the original, respectively. As shown in the figure, although the mesoscale vortex is tangential cyclonic rotated with a radial inward motioning to TC center, the strength of the axisymmetric TC vortex does not increase significantly and is manifested as a thready distribution of peripheral vorticity. Rows C and D mainly adjust the strength of the mesoscale vortex. The results show that both of the mesoscale vortexes merge into TC center, combined with the enhancement of axisymmetric vorticity. Stronger mesoscale vortices are associated with a more significant enhancement effect. The sensitivity tests indicate that in the same typhoon circulation, the distance and intensity of the mesoscale vortex play a key role in the occurrence of RI.

A preliminary summary of Meranti's asymmetric strengthening process is as follows. Although the deviation of the warm core caused by strong VWS is not conducive to TC enhancement, VWS can also provide a favorable environment for the development of convection in the downshear-left quadrant. The emergence of this convection is accompanied by substantial diabatic heating, so that sheared TCs are often rich in abundant energy in the wavenumber-1 structure (similarly, asymmetric vorticity is also strong at this time). The dynamic structure of the TC inner core is one of the key factors affecting the axisymmetrization of the asymmetric energy (vorticity). If there is a suitable initial field (reasonable distance from the TC center and sufficient asymmetric vortex strength), tangential cyclonic rotation with radial inward movement will introduce the energy in wavenumber-1 converted into axisymmetric energy through wave–flow interaction, which is associated with RI in the asymmetric stage.

SUMMARY

Few rapidly intensifying TCs with obvious asymmetric structures are captured in the northwest Pacific Ocean by ground-based radar, which provides high spatial-temporal resolution data. TC Meranti in 2010 provides a good opportunity to reveal the effect of inner-core dynamic structure on RI. Radar echo data indicate that the RI process can be divided into two stages due to the reduction in VWS: an asymmetric dominant stage and an axisymmetric dominant stage, and the vortex intensified more in the asymmetric stage than the axisymmetric stage.

This study focuses on the asymmetric inner-core structure evolution and notes that the asymmetry is dominated by wavenumber-1, which is associated with VWS and TC motion. During the asymmetric stage, strong asymmetric vortices are continuously excited in the downshear-left quadrant, and cyclonic vortices merge into TC center. This phenomenon was confirmed with both the radar echo and vorticity field data retrieved using ARPS-3DVAR. An increase in the wavenumber-0 vorticity indicates an increase in TC intensity. Observations show that the wavenumber-0 vorticity in TC Meranti increased significantly after the axisymmetrization of strong asymmetric vorticity. To explore this mechanism, a nondivergent barotropic model was used, and the process of asymmetric vortex cyclonic inward movement and axisymmetric vorticity enhancement modeled. Sensitivity tests further showed that the intensity and position of the asymmetric vortex are the key factors in determining whether the vorticity of wavenumber-0 is strengthened. Absolutely, besides the influence of asymmetric vortex, Meranti's RI also involves other mechanisms including internal and external dynamics which can not be ignored.

In this study, an idealization of the retrieved vorticity was used to drive a nondivergent barotropic model. It is shown that the dynamic interaction between asymmetric vorticity and TC axisymmetric vorticity was vital for RI in the early stage of Meranti, which provides a possible explanation for the RI of typhoons with strong asymmetric structures.

DATA AVAILABILITY STATEMENT

Publicly available datasets were analyzed in this study. This data can be found here: http://tcdata.typhoon.org.cn/en/ https://data.ucar.edu/dataset/ncep-climate-forecast-system-reanalysis-cfsr-6-hourly-products-january-1979-to-december-2010.

AUTHOR CONTRIBUTIONS

KZ designed the research. BL performed data analyses and prepared the figures. BL and MW wrote the manuscript. KZ discussed the results and commented on the manuscript.

FUNDING

This work was jointly supported by the Technology Innovation and Application Development Key Project of Chongqing (cstc2019jscx-tjsbX0007), the Natural Science Foundation of Chongqing (cstc2021jcyj-msxmX1007), the National Natural Science Foundation of China (41975123), the Chongqing Science and Technology Commission technology innovation and application demonstration project (cstc2019jscx-msxmX0297), and the Innovation team project of Chongqing Meteorological Bureau (ZHCXTD-202003; ZHCXTD-202023).

ACKNOWLEDGMENTS

We would like to express our gratitude to CMA Shanghai Typhoon Institute and U.S. NCAR to provide the reanalysis data. Thanks also go to Chen Xiaomin for improving the presentation of our results.

REFERENCES

Abarca, S. F., Corbosiero, K. L., and Vollaro, D. (2011). The World Wide Lightning Location Network and Convective Activity in Tropical Cyclones. *Monthly Weather Rev.* 139 (1), 175–191. doi:10.1175/2010MWR3383.1

Black, M. L., Burpee, R. W., and Marks, F. D. (1996). Vertical Motion Characteristics of Tropical Cyclones Determined with Airborne Doppler Radial Velocities. *J. Atmos. Sci.* 53 (13), 1887–1909. doi:10.1175/1520-0469(1996)053<1887:vmcotc>2.0.co;2

Blackwell, K. G. (2000). The Evolution of Hurricane Danny (1997) at Landfall: Doppler-Observed Eyewall Replacement, Vortex Contraction/Intensification, and Low-Level Wind Maxima. *Mon. Wea. Rev.* 128 (12), 4002–4016. doi:10.1175/1520-0493(2000)129<4002:teohda>2.0.co;2

Brown, D. (2017). Tropical Cyclone Intensity Forecasting: Still a Challenging Proposition. *Natl. Hurricane Cent. Presentation*. Available at: https://www.nhc.noaa.gov/outreach/presentations/NHC2017_IntensityChallenges.pdf.

Chen, S. S., Knaff, J. A., and Marks, F. D. (2006). Effects of Vertical Wind Shear and Storm Motion on Tropical Cyclone Rainfall Asymmetries Deduced from TRMM. *Monthly Weather Rev.* 134 (11), 3190–3208. doi:10.1175/MWR3245.1

Chen, X., Wang, Y., and Zhao, K. (2015). Synoptic Flow Patterns and Large-Scale Characteristics Associated with Rapidly Intensifying Tropical Cyclones in the South China Sea. *Monthly Weather Rev.* 143 (1), 64–87. doi:10.1175/MWR-D-13-00338.1

Chen, X., Xue, M., and Fang, J. (2018). Rapid Intensification of Typhoon Mujigae (2015) under Different Sea Surface Temperatures: Structural Changes Leading to Rapid Intensification. *J. Atmos. Sci.* 75 (12), 4313–4335. doi:10.1175/JAS-D-18-0017.1

Corbosiero, K. L., and Molinari, J. (2002). The Effects of Vertical Wind Shear on the Distribution of Convection in Tropical Cyclones. *Mon. Wea. Rev.* 130 (8), 2110–2123. doi:10.1175/1520-0493(2002)130<2110:teovws>2.0.co;2

Corbosiero, K. L., and Molinari, J. (2003). The Relationship between Storm Motion, Vertical Wind Shear, and Convective Asymmetries in Tropical Cyclones. *J. Atmos. Sci.* 60 (2), 366–376. doi:10.1175/1520-0469(2003)060<0366:trbsmv>2.0.co;2

Cram, T. A., Persing, J., Montgomery, M. T., and Braun, S. A. (2007). A Lagrangian Trajectory View on Transport and Mixing Processes between the Eye, Eyewall, and Environment Using a High-Resolution Simulation of Hurricane Bonnie (1998). *J. Atmos. Sci.* 64 (6), 1835–1856. doi:10.1175/JAS3921.1

Frank, W. M., and Ritchie, E. A. (2001). Effects of Vertical Wind Shear on the Intensity and Structure of Numerically Simulated Hurricanes. *Mon. Wea. Rev.* 129 (9), 2249–2269. doi:10.1175/1520-0493(2001)129<2249:eovwso>2.0.co;2

Guimond, S. R., Heymsfield, G. M., and Turk, F. J. (2010). Multiscale Observations of Hurricane Dennis (2005): The Effects of Hot Towers on Rapid Intensification. *J. Atmos. Sci.* 67 (3), 633–654. doi:10.1175/2009JAS3119.1

Hence, D. A., and Houze, R. A. (2011). Vertical Structure of Hurricane Eyewalls as Seen by the TRMM Precipitation Radar. *J. Atmos. Sci.* 68 (8), 1637–1652. doi:10.1175/2011JAS3578.1

Hence, D. A., and Houze, R. A. (2012). Vertical Structure of Tropical Cyclone Rainbands as Seen by the TRMM Precipitation Radar. *J. Atmos. Sci.* 69 (9), 2644–2661. doi:10.1175/JAS-D-11-0323.1

Hendricks, E. A., Montgomery, M. T., and Davis, C. A. (2004). The Role of "Vortical" Hot Towers in the Formation of Tropical Cyclone Diana (1984). *J. Atmos. Sci.* 61 (11), 1209–1232. doi:10.1175/1520-0469(2004)061<1209:trovht>2.0.co;2

Houze, R. A. (2010). Clouds in Tropical Cyclones. *Monthly Weather Rev.* 138 (2), 293–344. doi:10.1175/2009MWR2989.1

Kaplan, J., and DeMaria, M. (2003). Large-Scale Characteristics of Rapidly Intensifying Tropical Cyclones in the North Atlantic Basin. *Wea. Forecast.* 18 (6), 1093–1108. doi:10.1175/1520-0434(2003)018<1093:lcorit>2.0.co;2

Kossin, J. P., and Schubert, W. H. (2001). Mesovortices, Polygonal Flow Patterns, and Rapid Pressure Falls in Hurricane-Like Vortices. *J. Atmos. Sci.* 58 (15), 2196–2209. doi:10.1175/1520-0469(2001)058<2196:mpfpar>2.0.co;2

Lee, W.-C., and Bell, M. M. (2007). Rapid Intensification, Eyewall Contraction, and Breakdown of Hurricane Charley (2004) Near Landfall. *Geophys. Res. Lett.* 34 (2). doi:10.1029/2006GL027889

Li, Y., Wang, Y., Lin, Y., and Wang, X. (2021). Why Does Rapid Contraction of the Radius of Maximum Wind Precede Rapid Intensification in Tropical Cyclones? *J. Atmos. Sci.* 78 (11), 3441–3453. doi:10.1175/JAS-D-21-0129.1

Lin, J., and Qian, T. (2019). Rapid Intensification of Tropical Cyclones Observed by AMSU Satellites. *Geophys. Res. Lett.* 46 (12), 7054–7062. doi:10.1029/2019GL083488

Lonfat, M., Marks, F. D., and Chen, S. S. (2004). Precipitation Distribution in Tropical Cyclones Using the Tropical Rainfall Measuring Mission (TRMM) Microwave Imager: A Global Perspective. *Mon. Wea. Rev.* 132 (7), 1645–1660. doi:10.1175/1520-0493(2004)132<1645:pditcu>2.0.co;2

Luo, Z. (2003). Nonlinear Interaction between Axisymmetric Circulation and Asymmetric Turbulence of Typhoon. *Sci. China (Series D)* 33, 686–694. (in Chinese).

Molinari, J., and Vollaro, D. (2010). Rapid Intensification of a Sheared Tropical Storm. *Monthly Weather Rev.* 138 (10), 3869–3885. doi:10.1175/2010MWR3378.1

Montgomery, M. T., Nicholls, M. E., Cram, T. A., and Saunders, A. B. (2006). A Vortical Hot Tower Route to Tropical Cyclogenesis. *J. Atmos. Sci.* 63 (1), 355–386. doi:10.1175/JAS3604.1

Nguyen, L. T., and Molinari, J. (2012). Rapid Intensification of a Sheared, Fast-Moving Hurricane over the Gulf Stream. *Monthly Weather Rev.* 140 (10), 3361–3378. doi:10.1175/MWR-D-11-00293.1

Nolan, D. S., and Grasso, L. D. (2003). Nonhydrostatic, Three-Dimensional Perturbations to Balanced, Hurricane-Like Vortices. Part II: Symmetric Response and Nonlinear Simulations. *J. Atmos. Sci.* 60 (22), 2717–2745. doi:10.1175/1520-0469(2003)060<2717:ntptbh>2.0.co;2

Nolan, D. S., Moon, Y., and Stern, D. P. (2007). Tropical Cyclone Intensification from Asymmetric Convection: Energetics and Efficiency. *J. Atmos. Sci.* 64 (10), 3377–3405. doi:10.1175/JAS3988.1

Oye, R., Mueller, C., and Smith, S. (1995). "Software for Radar Translation, Visualization, Editing, and Interpolation," in Preprints, 27th Conf on Radar Meteorology, Vail, CO, Amer. Meteor. Soc., 359–361.

Persing, J., and Montgomery, M. T. (2003). Hurricane Superintensity. *J. Atmos. Sci.* 60 (19), 2349–2371. doi:10.1175/1520-0469(2003)060<2349:hs>2.0.co;2

Reasor, P. D., Eastin, M. D., and Gamache, J. F. (2009). Rapidly Intensifying Hurricane Guillermo (1997). Part I: Low-Wavenumber Structure and Evolution. *Monthly Weather Rev.* 137 (2), 603–631. doi:10.1175/2008MWR2487.1

Riemer, M., Montgomery, M. T., and Nicholls, M. E. (2010). A New Paradigm for Intensity Modification of Tropical Cyclones: Thermodynamic Impact of Vertical Wind Shear on the Inflow Layer. *Atmos. Chem. Phys.* 10 (7), 3163–3188. doi:10.5194/acp-10-3163-2010

Rogers, R., Reasor, P., and Lorsolo, S. (2013). Airborne Doppler Observations of the Inner-Core Structural Differences between Intensifying and Steady-State Tropical Cyclones. *Monthly Weather Rev.* 141 (9), 2970–2991. doi:10.1175/MWR-D-12-00357.1

Ryglicki, D. R., Velden, C. S., Reasor, P. D., Hodyss, D., and Doyle, J. D. (2021). Observations of Atypical Rapid Intensification Characteristics in Hurricane Dorian (2019). *Monthly Weather Rev.* 149 (7), 2131–2150. doi:10.1175/MWR-D-20-0413.1

Saha, S., Moorthi, S., Pan, H.-L., Wu, X., Wang, J., Nadiga, S., et al. (2010). The NCEP Climate Forecast System Reanalysis. *Bull. Amer. Meteorol. Soc.* 91 (8), 1015–1058. doi:10.1175/2010bams3001.1

Schubert, W. H., Montgomery, M. T., Taft, R. K., Guinn, T. A., Fulton, S. R., Kossin, J. P., et al. (1999). Polygonal Eyewalls, Asymmetric Eye Contraction, and Potential Vorticity Mixing in Hurricanes. *J. Atmos. Sci.* 56 (9), 1197–1223. doi:10.1175/1520-0469(1999)056<1197:peaeca>2.0.co;2

Shapiro, L. J. (1983). The Asymmetric Boundary Layer Flow under a Translating Hurricaneflow under a Translating hurricane. *J. Atmos. Sci.* 40, 1984–1998. doi:10.1175/1520-0469(1983)040<1984:tablfu>2.0.co;2

Shimada, U., and Horinouchi, T. (2018). Reintensification and Eyewall Formation in Strong Shear: A Case Study of Typhoon Noul (2015). *Monthly Weather Rev.* 146 (9), 2799–2817. doi:10.1175/MWR-D-18-0035.1

Sitkowski, M., and Barnes, G. M. (2009). Low-Level Thermodynamic, Kinematic, and Reflectivity Fields of Hurricane Guillermo (1997) during Rapid Intensification. *Monthly Weather Rev.* 137 (2), 645–663. doi:10.1175/2008MWR2531.1

Wu, Q., and Ruan, Z. (2021). Rapid Contraction of the Radius of Maximum Tangential Wind and Rapid Intensification of a Tropical Cyclone. *Geophys. Res. Atmos.* 126 (3), e2020JD033681. doi:10.1029/2020JD033681

Xu, Y., and Wu, R. (2005). The Numerical Simulation of the Genesis of Tropical Cyclone Bilis (2000): The Evolution and Transformation of Asymmetric Momentum. *Chin. J. Atmos. Sci.* 29, 79–90. (in Chinese).

Xue, M., Droegemeier, K. K., Wong, V., Shapiro, A., Brewster, K., Carr, F., et al. (2001). The Advanced Regional Prediction System (ARPS) - A Multi-Scale Nonhydrostatic Atmospheric Simulation and Prediction Tool. Part II: Model Physics and Applications. *Meteorology Atmos. Phys.* 76 (3), 143–165. doi:10.1007/s007030170027

Zhao, K., Lee, W.-C., and Jou, B. J.-D. (2008). Single Doppler Radar Observation of the Concentric Eyewall in Typhoon Saomai, 2006, Near Landfall. *Geophys. Res. Lett.* 35 (7), a–n. doi:10.1029/2007GL032773

Zhao, K., Li, X., Xue, M., Jou, B. J.-D., and Lee, W.-C. (2012). Short-term Forecasting through Intermittent Assimilation of Data from Taiwan and mainland China Coastal Radars for Typhoon Meranti (2010) at Landfall. *J. Geophys. Res.* 117 (D6), a–n. doi:10.1029/2011JD017109

Conflict of Interest: The authors declare that the research was conducted in the absence of any commercial or financial relationships that could be construed as a potential conflict of interest.

frontiers | Frontiers in Earth Science

ORIGINAL RESEARCH
published: 19 May 2022
doi: 10.3389/feart.2022.904128

Tongan Volcanic Eruption Intensifies Tropical Cyclone Cody (2022)

*Haiyang Liu and Xiaodong Tang**

Key Laboratory of Mesoscale Severe Weather, Ministry of Education and School of Atmospheric Sciences, Nanjing University, Nanjing, China

The aerosol–cloud impacts of the Tongan volcanic eruptions on the nearby tropical cyclone (TC) Cody on January 14~15, 2022 are investigated by the MODIS satellite and ERA5 reanalysis data. Both the precipitation and intensity of Cody were obviously enhanced after the main blast of the Tongan volcanic eruption on January 15, although the sea surface temperature and vertical wind shear of the environmental wind did not change much according to ERA5 data. The vision that a large amount of volcanic aerosol flowed from the Tongan eruption into the inflow of Cody was captured by the MODIS observations on January 15. The cloud top temperature dropped, and the cloud particle effective radius decreased in Cody from then on, which indicated the occurrence of deep convection. The analyzed results of ERA5 show that convection was strengthened in the periphery of Cody at the beginning of the volcanic eruption at 03:00 UTC on January 15 and later in Cody's inner core after the main blast at 06:00 UTC on January 15. This could be because of the microphysical process of aerosol–cloud interactions, which inhibited stratiform precipitation, increased vertical velocity and enhanced convective precipitation further. Since the deep convection in the inner core was conducive to the development of Cody, both the total precipitation and intensity of Cody increased after the main blast of the volcanic eruption. The result also suggests that major volcanic eruptions could increase the convective intensity and induce heavy precipitation in a nearby organized convective system (e.g., TC or mesoscale convective systems).

Keywords: Tongan volcanic eruption, tropical cyclone Cody, aerosol–cloud interaction, convection, MODIS observation

Edited by:
Yuqing Wang,
University of Hawaii at Manoa,
United States

Reviewed by:
Yanluan Lin,
Tsinghua University, China
Xuyang Ge,
Nanjing University of Information Science and Technology, China

Correspondence:
Xiaodong Tang
xdtang@nju.edu.cn

Specialty section:
This article was submitted to Atmospheric Science, a section of the journal Frontiers in Earth Science

Received: *25 March 2022*
Accepted: *08 April 2022*
Published: *19 May 2022*

Citation:
Liu H and Tang X (2022) Tongan Volcanic Eruption Intensifies Tropical Cyclone Cody (2022). Front. Earth Sci. 10:904128. doi: 10.3389/feart.2022.904128

INTRODUCTION

The eruption of Hunga Tonga–Hunga Ha'apai that devastated Tonga on January 15, 2022 lasting for 11 h sent a plume of ash soaring into the upper atmosphere for nearly 30 km (Witze, 2022). Researchers have been scrambling to understand what long-term impact it might have and even compared it to the Pinatubo eruption in the Philippines in the last century (1991), which temporarily cooled the planet by nearly 0.5 ℃ in 1992–1993 (Reynolds and Smith, 1994; McCormick et al., 1995). However, recent research shows that the Tonga volcanic eruption only lowered the global temperature by 0.004 ℃ and did not have a significant impact on the global climate (Zuo et al., 2022).

In addition to climate effects, a volcanic eruption also changes the regional atmospheric composition quickly. Observations have shown that volcanic aerosols could convert into cloud condensation nuclei (CCNs) to participate in cloud microphysical processes, which significantly reduce the effective radius of liquid cloud droplets and precipitation efficiency in addition to

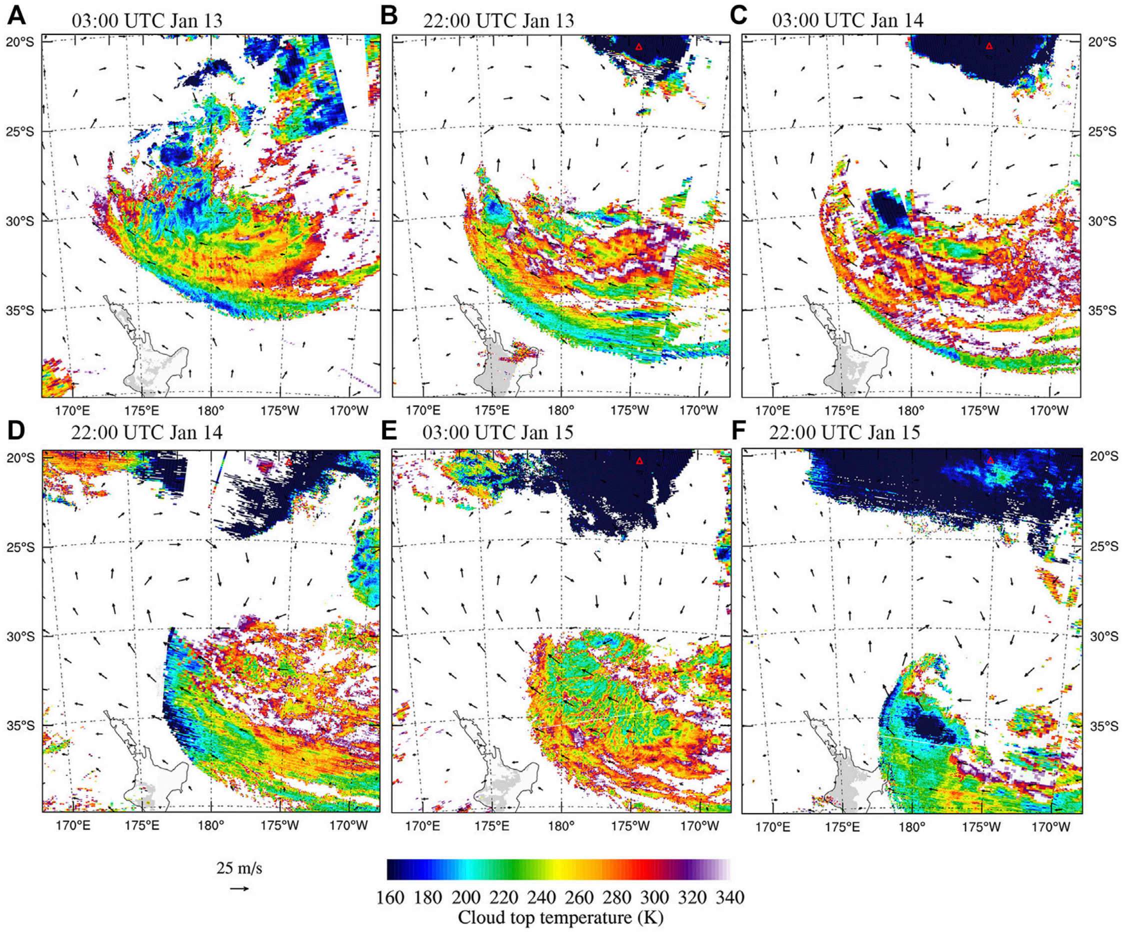

FIGURE 1 | Cloud top temperature from the MODIS and wind field at 10 m of ERA5. Red triangles indicate the location of the Tonga volcano. The UTC time and date is on each panel from **(A–F)**.

increasing cloud top height (e.g., Gasso, 2008; Yuan et al., 2011; Malavelle et al., 2017). As it happens, there is a tropical cyclone (TC) Cody on the ocean about 500 km away from the Tonga volcano during the eruption. What are the effects of aerosols from Tonga volcanic eruptions on cloud microphysical processes in Cody?

The simulation studies reveal that aerosol–cloud effects in TC depend on the region where it worked. The impact of aerosol–cloud interactions on the inner core of tropical cyclones can strengthen the convection there, thus maintaining the warm core structure and enhancing the intensity of the TC (Liang et al., 2021). However, it is also found in other studies that the aerosol–cloud effect in the periphery could invigorate the peripheral convection. The enhancement of peripheral clouds draws more ascending air at the periphery of the storm, thereby bleeding the low-level inflow toward the eyewall, which is not conducive to TC development (Khain et al., 2010; Rosenfeld et al., 2012; Lynn et al., 2016). This phenomenon was also captured by satellite observation (Rosenfeld et al., 2012). On the contrary, a few observations show the enhancement process of convection induced by the effects of aerosol–cloud interaction in the inner core of TCs, so far.

Could the people verify and understand these opposed effects of the aerosol–cloud interaction in the TC? The MODIS satellite and ERA5 reanalysis data are used to study the effect of volcanic aerosols on the evolution of the TC Cody (2022), which provides a rare chance to verify the previously simulated results of aerosol–cloud effects on TC. The data and method are described in *Data and Method*. The results are presented and discussed in *Results*, followed by a summary in *Conclusion and Discussion*.

Data and Method

MODIS

The Moderate Resolution Imaging Spectroradiometer (MODIS) is one of the five instruments aboard the Terra Earth Observing System (EOS) platform launched into a sun-synchronous polar orbit in December 1999. The instrument is also being flown on the Aqua spacecraft, launched in May 2002. The MODIS provides one daytime and one nighttime image in a 24-h period. A

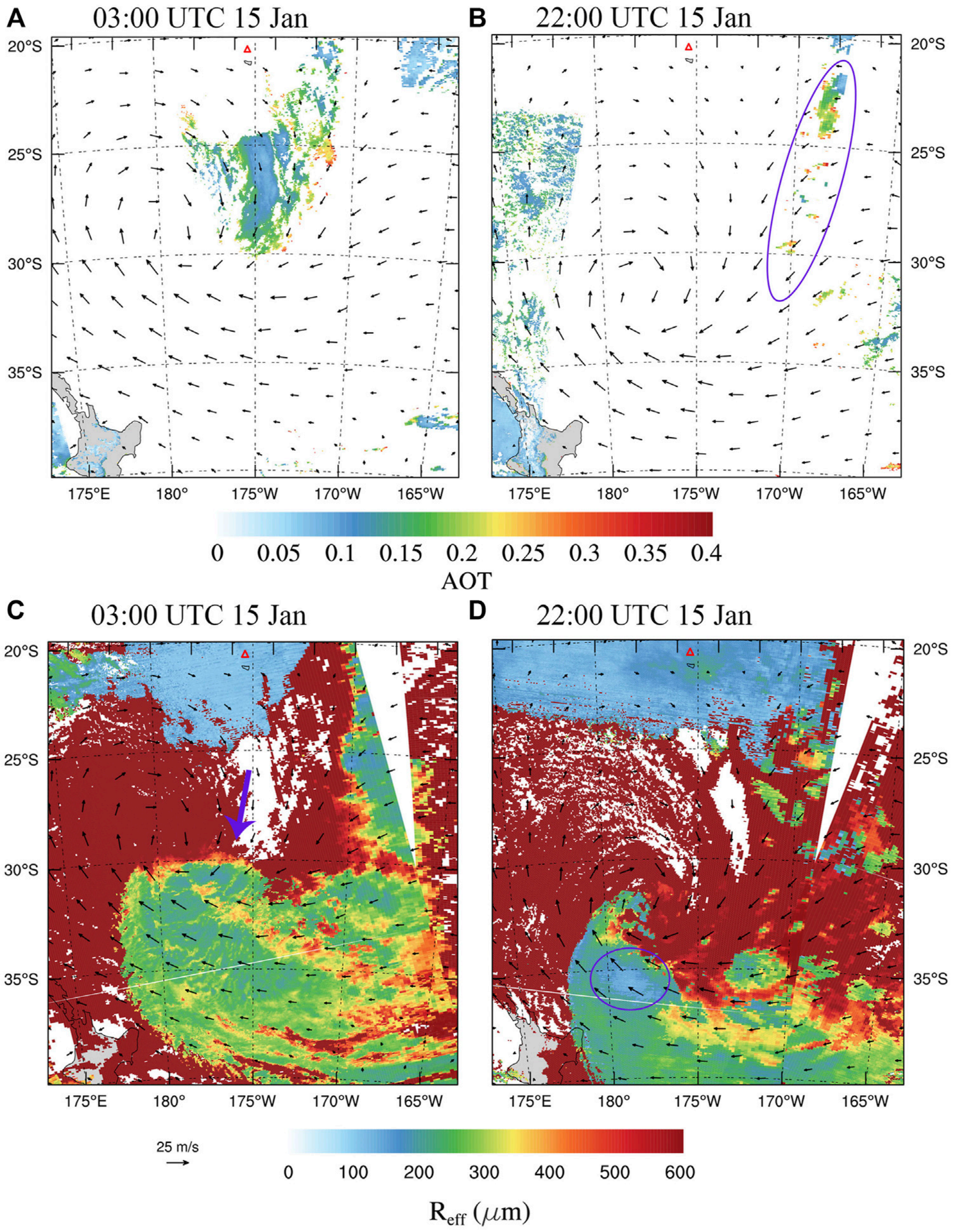

FIGURE 2 | MODIS observation with the wind field at 10 m of EAR5 on January 15, 2022. **(A,B)** Aerosol optical thickness (AOT); **(C,D)** cloud particle effective radius. Red triangles indicate the location of the Tonga volcano, the purple circle in **(B)** shows high-concentration aerosol and that in **(D)** shows deep convection, and the purple arrow in **(C)** denoted the inflow with high-concentration aerosol.

comprehensive set of remote sensing algorithms for cloud detection and the retrieval of cloud physical and optical properties have been developed by the members of the MODIS atmosphere science team. The archived products from these algorithms have applications in climate change studies, climate modeling, numerical weather prediction, and fundamental atmospheric research (Platnick et al., 2003). The aerosol optical thickness (AOT) product from the MODIS provides the observation of global aerosol distribution (Remer et al., 2005). The data retrieved by the MODIS have been widely used in Earth science, including volcanic eruption monitoring, air quality detection, tsunami, and atmospheric activity detection. Here, we use the cloud and AOT product of 1-km and 3-km spatial resolutions to analyze the interaction of volcanic aerosol

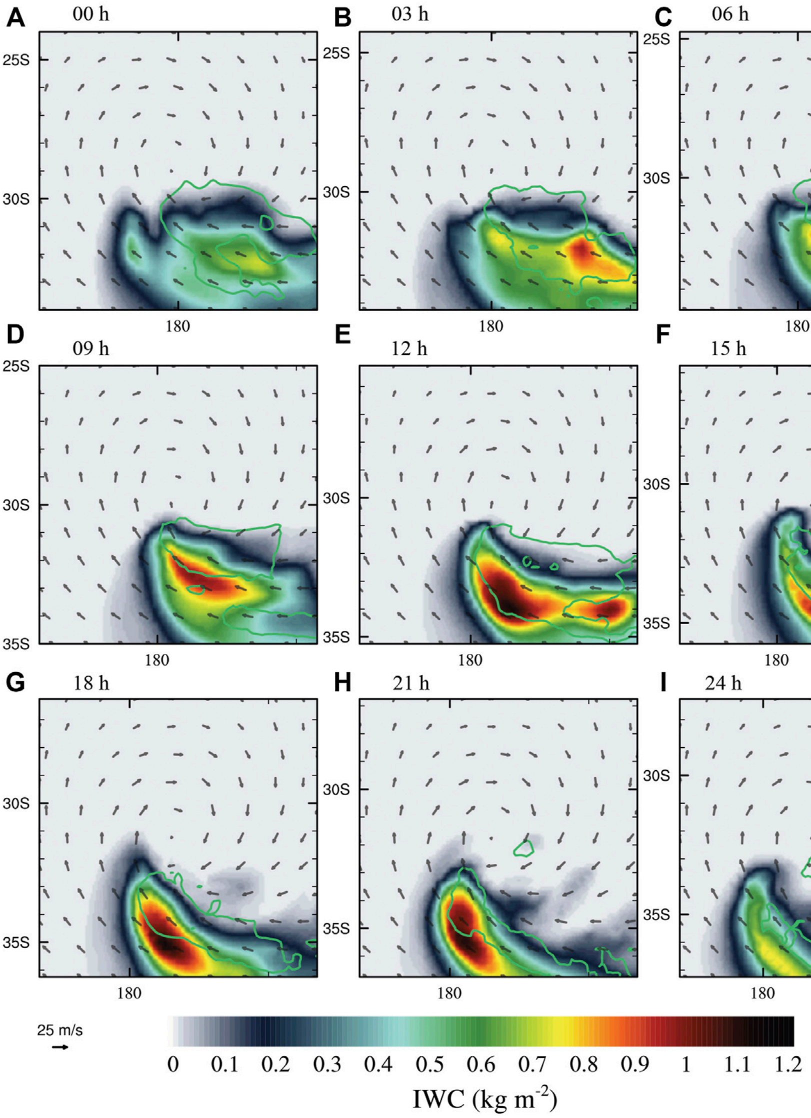

FIGURE 3 | Total column liquid (green lines at 0.4 $kg\,m^{-2}$) and ice water content (shading) of ERA5 on January 15, 2022. The UTC time is on each panel from **A–I**. The TC center is at the center of each panel.

with the TC. The scanning time of Terra was about 22:00 (UTC) and Aqua 03:00 when the satellite cross the area of Tonga volcano.

ERA5 Reanalysis Data

ERA5, produced by ECMWF, is one of the most advanced reanalysis data with a 31-km horizontal resolution and hourly output of atmosphere, land surface, and ocean. ERA5 is based on the Integrated Forecasting System (IFS) Cy41r2, which was operational in 2016. ERA5 thus benefits from a decade of developments in model physics, core dynamics, and data assimilation (Hersbach et al., 2020). The wind field, cloud ice content, cloud water content, precipitation, and sea surface temperature are used to analyze the convective activities and the intensity of the TC during the Tongan volcanic eruption. To estimate the effects of the Tonga volcanic eruption on the convection in the inner core of Cody, the precipitation is partitioned as convective and stratiform following the methods mentioned by Tao et al. (1993), Braun et al. (2010), and Wang et al. (2010). First, grid points with rain rates, twice as large as the average of their nearest four neighbors, are identified as convective cell cores. Second, all grid points with a surface precipitation rate greater than 10 $mm\,h^{-1}$, or a maximum vertical velocity greater than 5 $m\,s^{-1}$, are categorized as convection. All remaining grid columns with a surface

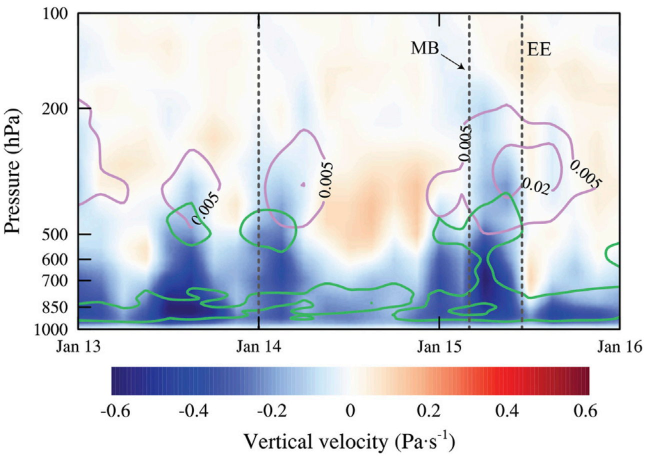

FIGURE 4 | Time series of averaged vertical velocity (shading), cloud ice water content (purple contours at 0.005, 0.02 $g\,kg^{-1}$), and cloud liquid water (green contours at 0.035 g kg^{-1}) content within a radius of 150 km of Cody every 3 h from 0000 UTC on January 13 to 0000 UTC January 16. The three dashed vertical lines denote the three moments: the weak eruption of the Tonga volcano on January 14, the main blast (MB), and the end of eruption (EE).

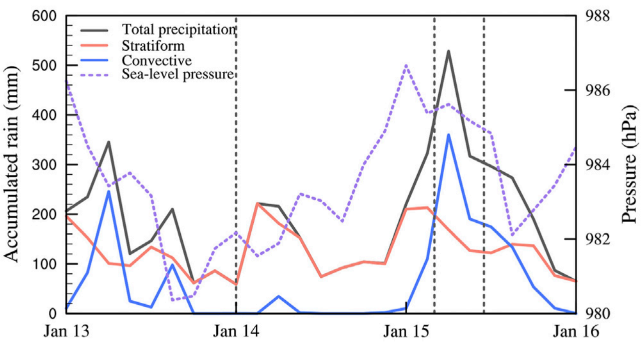

FIGURE 5 | Time series of minimum sea-level pressure (purple dashed, hPa), total (black curve), convective (blue), and stratiform (red) precipitation within a radius of 150 km of Cody every 3 h from 0000 UTC January 13 to 0000 UTC January 16 The three dashed lines are the same as in **Figure 4**.

precipitation greater than 0.1 $mm\,h^{-1}$ are categorized as stratiform, and all the other grid columns are considered nonprecipitating.

FNL Analysis Data

FNL analysis data are the output from NECP's Global Data Assimilation System, which uses the same forecast model as GFS. The difference is that the FNL assimilates as many observations as possible in the start-up stage to obtain more real atmospheric analysis fields and thus provide more accurate atmospheric states. This study uses the FNL to double-check the results of ERA5.

RESULTS

Satellite Observation of Aerosols From Tongan Volcanic Eruptions and Cody's Cloud Development

An observation suggests that the intensity of the convection in the inner core implies TC intensification (Rodgers et al., 1991; Guimond et al., 2010; Lin and Qian, 2019). It is characterized by a deep convection outbreak in the inner core of TCs. The cloud top temperature could be seen as a representation of the convective intensity as the cloud top temperature below 200 K can be considered a deep convection (Guimond et al., 2010; Mote and Frey, 2006). As shown in **Figure 1**, there was still a lot of deep convective activity in Cody at 03:00 UTC on January 13 before the volcano erupted, indicating that the TC was still developing and slowly moving southward (**Figure 1A**). After 19 h, the strong convection in the TC weakened and the rain band dissipated greatly, indicating that Cody began to weaken (**Figure 1B**). But at 03:00 UTC on January 14, a strong convection was invigorated in the TC inner core again. At the same time, there was a large area of low cloud top temperature over the Tonga volcano, which could be because of some weak eruptions in the Tonga volcano (**Figure 1C**) [see also the picture in Witze (2022)]. Although the convection in the inner core of Cody was strengthened at this time (**Figure 1C**), the weakening trend remains unchanged (**Figures 1C–E**). After 24 h, there is almost no strong convection in the inner core of Cody. However, at 00:00 UTC on January 15, the formidable eruption began, which expelled an estimated 400,000 tons ofSO_2 and lasted for about 11 h, with the main blast at 04:00 UTC on January 15 (Witze, 2022). Although there was a lack of continuous observation from the MODIS during the entire eruption, we find that the eruption sent a lot of ash clouds into the upper troposphere as the area of low cloud top temperature extended almost twice at 22:00 than At 03:00 UTC On January 15 (**Figures 1E,F**). Meanwhile, the convective activity in Cody was strengthened again. The area of low cloud top temperature in Cody is even close to that on January 13. It seems that Cody intensified after the eruption. Therefore, we suspect that a large amount of aerosol from the major eruption of the Tonga volcano transformed into Cody, converted into CCNs, and strengthened the convection in Cody's inner core.

An AOT observation from the MODIS manifested a large amount of volcanic aerosol into Cody's inner core after about 3 hours of the volcanic eruption, as shown in **Figure 2A**. The MODIS has no ability for aerosol observation in the high-albedo region (e.g., cloud cluster). Therefore, the volcanic aerosols could not be observed in the cloud cluster of Cody directly. However, a large amount of aerosol in the inflow direction (purple arrow in **Figure 2C**) around the cloud (**Figure 2A**) indicates that volcanic aerosols were entrained into the convection of Cody's inner core (**Figure 2C**). It is reasonable to speculate that more aerosol will enter the inner core of Cody after the main blast at about 04:00 UTC on January 15, thus affecting the convective activity tremendously. The results for 22:00 UTC January 15 confirmed it further. There were still a lot of volcanic aerosols in the circulation of Cody even 11 h after the volcanic eruption ended (**Figure 2B**). In addition, the average wind field indicates

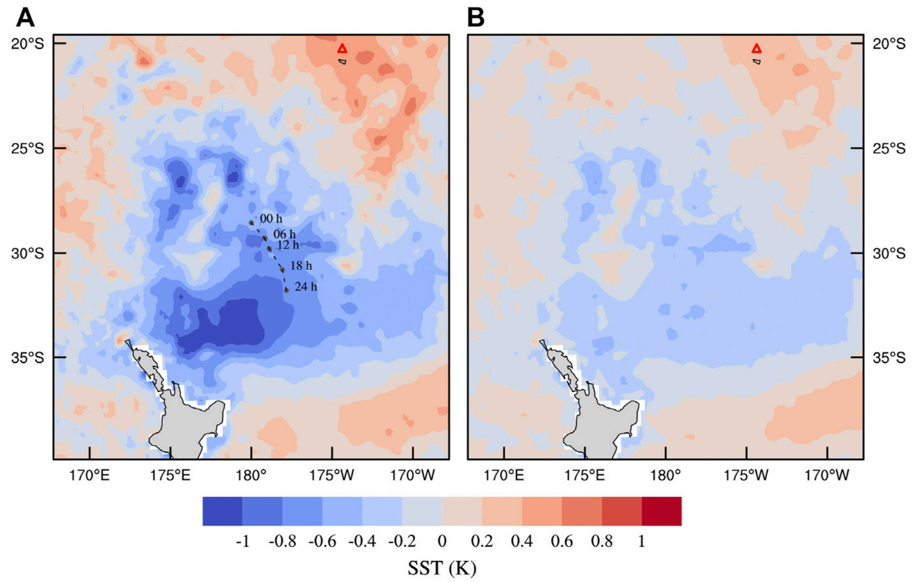

FIGURE 6 | Difference of averaged sea surface temperature. **(A)**: January 15 minus January 13, and **(B)** January 15 minus 3-day average of January 13 to January 15. Gray points denote the locations of Cody on January 15, with the UTC time at the right.

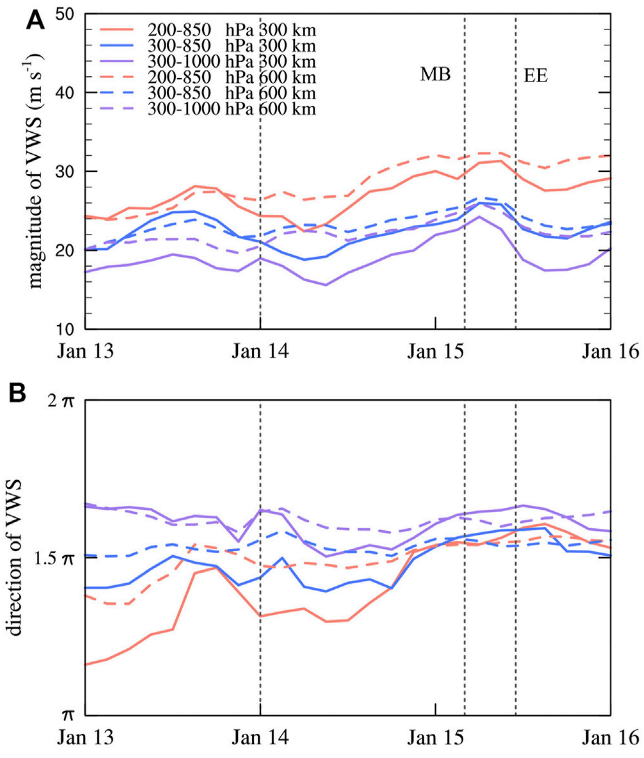

FIGURE 7 | Time series of average deep layer vertical wind shear over a circular area within the radii of 300 and 600 km (dashed) every 3 h from 0000 UTC on January 13 to 0000 UTC on January 16. **(A)** Magnitude of vertical wind shear and **(B)** direction of vertical wind shear (π for south, 1.5π for west, 2π for north). The three dashed lines are the same as in **Figure 4**.

that the volcanic aerosol could enter Cody's circulation by the low-level inflow during the eruption (**Supplementary Figure S1**). However, plenty of moisture in the boundary layer of Cody is beneficial to aerosols converting into CCN. Meanwhile, the effective cloud droplet radius in the inner core decreased (**Figure 2D**), which means that the convection there was enhanced greatly by the aerosol–cloud effect and is consistent with the result shown in **Figure 1F**.

In summary, a large amount of aerosol from the Tongan volcanic eruption entered the tropical cyclone Cody, which enhanced the convection and reduced the effective radius of cloud droplets in the inner core of Cody. The effects of volcanic aerosols on the precipitation and intensity of Cody will be analyzed in the following sections.

Effects of the Tongan Volcanic Aerosols on the Precipitation and Intensity of Cody

The column-integrated ice and liquid water content of ERA5 largely manifested the convective evolution in Cody on January 15 because the hydrometeor content can well represent the convective activity, especially ice water. After the Tongan volcano began erupting on January 15, volcanic aerosols with the in-draft of Cody's circulation strengthened the convection in the periphery of Cody first (**Figures 3A,B**), which was unfavorable to the TC's intensification (Rosenfeld et al., 2012; Khain et al., 2010; Lynn et al., 2016). However, the precipitation on the periphery could not deposit such a large amount of aerosol after the main blast of the eruption. Then, more volcanic aerosols entered the inner core of Cody, which invigorated the inner core convection (**Figure 3C**). With the enhancement of the inner convection, Cody appeared to separate the inner and outer rain bands, and the TC structure became more organized (**Figure 3D**), which indicated that Cody was intensified. Then, the intensity of convection in the inner core of Cody began to weaken, and the inner rain band expanded outward with the cessation of volcanic eruption (**Figures 3E–I**). **Figure 4** shows the evolution of the convective activity in the inner core clearly. As **Figure 4** shows, the mass of hydrometeor in Cody's inner core increases rapidly after the main blast. The increase in cloud liquid water at the beginning corresponds to the increase in precipitation (**Figure 5**). However, with the increase in the aerosol concentration in the inner core, more small droplets are produced, which began to inhibit rain (**Figure 5**). Then, many droplets were transported to the upper layers to form ice crystals (corresponding to a smaller effective radius of cloud droplets as shown in **Figure 2D**). More latent heating releases and upward vertical velocity also increased in the aforementioned process, which means intense deep convection (**Figure 4**). Deep convection even attached to the top of the troposphere. The increase in cloud ice water coincided with the falling of the minimum sea-level pressure (MSLP), suggesting that the process of convection enhancement in the inner core corresponds to the intensification of Cody (**Figures 4**, **5**). It is also consistent with that of previous studies which have confirmed that the deep convection in the inner core is conducive to the TC's intensification (Shapiro and Willoughby, 1982; Rogers et al., 2013; Tang & Zhang, 2016; Tang et al., 2019; Wu and Ruan, 2021). Therefore, the intensity of Cody increased after the explosive deep convection in the inner core. But the TC did not intensify further, because of the end of the eruption and the unfavorable environment (**Figures 6**, **7**). Meanwhile, the results of FNL show the same trend that the intensity and precipitation of Cody increased during the Tongan volcanic eruption (**Supplementary Figure S2**).

In addition to volcanic aerosol, the Tongan volcanic eruption also heated and evaporated a large area of sea surface water as the volcanic vent that erupted at Hunga Tonga–Hunga Ha'apai on January 15 was underwater about several tens to 250 m depth (Witze, 2022). Therefore, the low-level warm and humid air from the volcano flowing into Cody could also contribute to its intensification (**Supplementary Figure S3**).

Effects of Sea Surface Temperature and Deep Layer Vertical Wind Shear

The development of the TC is also often affected by large-scale environments, especially sea surface temperature (SST) and deep-layer vertical wind shear (VWS) (Wang et al., 2015; Emanuel, 2000; Holland, 1997). Therefore, it is necessary to analyze whether the implicit impacts of these factors on Cody's intensification could be excluded. The change of the SST between January 15 and January 13 (**Figure 6A**) or the 3-day average (**Figure 6B**) shows that the SST could not contribute to the intensification of Cody on January 15 as the SST was cooled at the positions of Cody, which usually implied a weaker surface heat flux from the ocean to the TC. Wang et al. (2015) suggest that the weak deep-layer wind shear is beneficial for intensifying the TC. Their results also indicate that the shear between 300 and 1,000 hPa ($VWS_{300-1000}$) exhibits the highest correlations with the 24-h TC intensity change. Here, we calculate the deep-layer vertical wind shear averaged over a circular area within the radii of 300 and 600 km (**Figure 7**). The deep-layer wind shear was about 20~30 m/s (**Figure 7A**) in the direction of west to the northwest (**Figure 7B**), especially $VWS_{300-1000}$. Such a strong VWS could already weaken Cody on January 14 (**Figures 5**, **7**). But Cody was intensified again on January 15 when the VWS remained almost unchanged compared with that on January 14. In addition, the size of Cody changed little on January 14–15 (**Supplementary Figure S4**). The area of over 17 m/s wind speed increased only after the eruption (**Supplementary Figure S4**). The outer size of Cody was so large at that time that Cody could resist the VWS more easily than other TCs of small size (Demaria, 1996). It means that the increase in the precipitation and intensity of Cody was not dominated by the dynamical force of the environment. The aerosol−cloud effects could mainly stimulate and contribute to intensifying the tropical cyclone Cody.

CONCLUSION AND DISCUSSION

In this study, we investigated the aerosol−cloud effects of the Tongan volcanic eruption on the development of the tropical cyclone Cody (2022) using the MODIS satellite observation and ERA5 reanalysis data. Although the model system of ERA5 doesn't explicitly include the volcanic aerosol-cloud interaction, it has assimilated lots of satellite observations of cloud and precipitation. Therefore, the effects of volcanic aerosol on Cody were already manifested in the reliable evolution of Cody' convection and precipitation provided by ERA5 data to a large extent. The results show that the aerosols from the Tonga volcano eruption in the TC inner core significantly intensified the convection in the TC. This could be because a large amount of volcanic aerosol caused extra droplet condensation on small droplets and freezing of the supercooled water. It releases extra latent heat at the mid- to high-level troposphere, causing an increase in updraft velocities. The strong updrafts transferred more moisture to the upper atmosphere and inhibited the stratiform rain, thus intensifying the convection further. Finally, the enhancement of deep convection in the inner core increased convective precipitation and intensified the TC later.

Our results here are consistent with those of the simulation studies of Liang et al. (2021), which suggest that the aerosol−cloud effect could invigorate the convection in the inner core and intensify the TC. On the other hand, our results are not consistent with those of some other studies that the aerosol−cloud effect would weaken the TC as aerosol ingested by the TC circulation invigorates the convection at a TC's periphery, limiting low-level inflow toward the eyewall and TC development (Khain et al., 2010; Rosenfeld et al., 2012; Lynn et al., 2016). A likely physical explanation is that the aerosol concentration in Cody was too high to deposit mostly by peripheral cloud activity, and a large amount of aerosol flowed into the inner core because the Tongan eruption expelled an estimated 400,000 tons of SO_2 (Witze, 2022), and the distance between the TC and the volcano was very small. The evolution of the convective available potential energy in the inner core and periphery of Cody on January 15 indicated that the outer-core convection was first enhanced at the beginning of the eruption, but the inner-core convection was obviously strengthened after the main blast (**Supplementary Figure S5A**), which was dominated by the cloud microphysical process within the TC (**Supplementary Figures S5B–D**). Rosenfeld et al. (2008) also suggest that a large amount of aerosol could increase the intensity and precipitation of deep convection, which is consistent with our deduction of the impacts of volcanic aerosols on Cody's evolution. It is suggested that the effect of the aerosol–cloud interaction on TC development could depend on the aerosol concentration, TC intensity, and atmospheric circulation. This requires further extensive numerical and statistical studies to elucidate the relationship between these factors.

The effect of volcanic aerosols from the Tongan eruption into Cody is similar to that of anthropogenic aerosols on landfalling TCs as the aerosol concentration on shores with large human activity is very high (e.g., East Asia and North America). Zhao et al. (2018) found the enlarging rainfall area of TCs over the western North Pacific by atmospheric aerosols. In addition, the simulation study of Jiang et al. (2016) suggested that the pollution increased the convective precipitation of landfalling TCs. In summary, our results provide evidence for the effects of volcanic aerosols on the evolution of a TC's intensity and precipitation. These further imply that an accurate description of the interaction between aerosol and the TC might improve the forecast of TC precipitation and intensity change.

DATA AVAILABILITY STATEMENT

MODIS data were downloaded at https://ladsweb.modaps.eosdis.nasa.gov/search/. ERA5 data were downloaded at https://cds.climate.copernicus.eu/cdsapp#!/dataset/reanalysis-era5-pressure-levels?tab=overview. FNL data were downloaded at http://rda.ucar.edu/datasets/ds083.2/.

AUTHOR CONTRIBUTIONS

XT conceptualized this study. HL and XT contributed to the figures included in the manuscript. HL and XT wrote the manuscript. All authors contributed to the article and approved the submitted version of the manuscript.

FUNDING

This work was supported by the National Key R&D Program of China (Grant 2017YFC1501601), the National Natural Science Foundation of China (Grant 42192555 and 41675054), and the Fundamental Research Funds for the Central Universities (Grant XJ2021001601).

ACKNOWLEDGMENTS

The authors thank Prof. Zhe-Min Tan for helpful discussions.

SUPPLEMENTARY MATERIAL

The Supplementary Material for this article can be found online at: https://www.frontiersin.org/articles/10.3389/feart.2022.904128/full#supplementary-material

REFERENCES

Braun, S. A., Montgomery, M. T., Mallen, K. J., and Reasor, P. D. (2010). Simulation and Interpretation of the Genesis of Tropical Storm Gert (2005) as Part of the NASA Tropical Cloud Systems and Processes Experiment. *J. Atmos. Sci.* 67 (4), 999–1025. doi:10.1175/2009jas3140.1

Demaria, M. (1996). The Effect of Vertical Shear on Tropical Cyclone Intensity Change. *J. Atmos. Sci.* 53, 2076–2088. doi:10.1175/1520-0469(1996)053<2076:teovso>2.0.co;2

Emanuel, K. (2000). A Statistical Analysis of Tropical Cyclone Intensity. *Mon. Wea. Rev.* 128, 1139–1152. doi:10.1175/1520-0493(2000)128<1139:asaotc>2.0.co;2

Gassó, S. (2008). Satellite Observations of the Impact of Weak Volcanic Activity on Marine Clouds. *J. Geophys. Res.* 113 (D14), 14. doi:10.1029/2007jd009106

Guimond, S. R., Heymsfield, G. M., and Turk, F. J. (2010). Multiscale Observations of Hurricane Dennis (2005): The Effects of Hot Towers on Rapid Intensification. *J. Atmos. Sci.* 67 (3), 633–654. doi:10.1175/2009jas3119.1

Hersbach, H., Bell, B., Berrisford, P., Hirahara, S., Horányi, A., Muñoz-Sabater, J., et al. (2020). The ERA5 Global Reanalysis. *Q.J.R. Meteorol. Soc.* 146 (730), 1999–2049. doi:10.1002/qj.3803

Holland, G. J. (1997). The Maximum Potential Intensity of Tropical Cyclones. *J. Atmos. Sci.* 54, 2519–2541. doi:10.1175/1520-0469(1997)054<2519:tmpiot>2.0.co;2

Jiang, B., Huang, B., Lin, W., and Xu, S. (2016). Investigation of the Effects of Anthropogenic Pollution on Typhoon Precipitation and Microphysical Processes Using WRF-Chem. *J. Atmos. Sci.* 73 (4), 1593–1610. doi:10.1175/jas-d-15-0202.1

Khain, A., Lynn, B., and Dudhia, J. (2010). Aerosol Effects on Intensity of Landfalling Hurricanes as Seen from Simulations with the WRF Model with Spectral Bin Microphysics. *J. Atmos. Sci.* 67 (2), 365–384. doi:10.1175/2009jas3210.1

Liang, Z., Ding, J., Fei, J., Cheng, X., and Huang, X. (20212009). Direct/indirect Effects of Aerosols and Their Separate Contributions to Typhoon Lupit (2009): Eyewall versus Peripheral rainbandsEyewall versus Peripheral Rainbands. *Sci. China Earth Sci.* 64, 2113–2128. doi:10.1007/s11430-020-9816-7

Lin, J., and Qian, T. (2019). Rapid Intensification of Tropical Cyclones Observed by AMSU Satellites. *Geophys. Res. Lett.* 46 (12), 7054–7062. doi:10.1029/2019gl083488

Lynn, B. H., Khain, A. P., Bao, J. W., Michelson, S. A., Yuan, T., Kelman, G., et al. (2016). The Sensitivity of Hurricane Irene to Aerosols and Ocean Coupling: Simulations with WRF Spectral Bin Microphysics. *J. Atmos. Sci.* 73 (2), 467–486. doi:10.1175/jas-d-14-0150.1

Malavelle, F. F., Haywood, J. M., Jones, A., Gettelman, A., Clarisse, L., Bauduin, S., et al. (2017). Strong Constraints on Aerosol-Cloud Interactions from Volcanic Eruptions. *Nature* 546 (7659), 485–491. doi:10.1038/nature22974

McCormick, M. P., Thomason, L. W., and Trepte, C. R. (1995). Atmospheric Effects of the Mt Pinatubo Eruption. *Nature* 373 (6513), 399–404. doi:10.1038/373399a0

Mote, P. W., and Frey, R. (2006). Variability of Clouds and Water Vapor in Low Latitudes: View from Moderate Resolution Imaging Spectroradiometer (MODIS). *J. Geophys. Res.* 111 (D16). doi:10.1029/2005jd006791

Platnick, S., King, M. D., Ackerman, S. A., Menzel, W. P., Baum, B. A., Riedi, J. C., et al. (2003). The MODIS Cloud Products: Algorithms and Examples from Terra. *IEEE Trans. Geosci. Remote Sensing* 41 (2), 459–473. doi:10.1109/tgrs.2002.808301

Remer, L. A., Kaufman, Y. J., Tanré, D., Mattoo, S., Chu, D. A., Martins, J. V., et al. (2005). The MODIS Aerosol Algorithm, Products, and Validation. *J. Atmos. Sci.* 62 (4), 947–973. doi:10.1175/jas3385.1

Reynolds, R. W., and Smith, T. M. (1994). Improved Global Sea Surface Temperature Analyses Using Optimum Interpolation. *J. Clim.* 7 (6), 929–948. doi:10.1175/1520-0442(1994)007<0929:igssta>2.0.co;2

Rodgers, E. B., Chang, S. W., Stout, J., Steranka, J., and Shi, J.-J. (1991). Satellite Observations of Variations in Tropical Cyclone Convection Caused by Upper-Tropospheric Troughs. *J. Appl. Meteorol.* 30 (8), 1163–1184. doi:10.1175/1520-0450(1991)030<1163:soovit>2.0.co;2

Rogers, R., Reasor, P., and Lorsolo, S. (2013). Airborne Doppler Observations of the Inner-Core Structural Differences between Intensifying and Steady-State Tropical Cyclones. *Mon. Weather Rev.* 141 (9), 2970–2991. doi:10.1175/mwr-d-12-00357.1

Rosenfeld, D., Lohmann, U., Raga, G. B., O'Dowd, C. D., Kulmala, M., Fuzzi, S., et al. (2008). Flood or Drought: How Do Aerosols Affect Precipitation? *Science* 321 (5894), 1309–1313. doi:10.1126/science.1160606

Rosenfeld, D., Woodley, W. L., Khain, A., Cotton, W. R., Carrió, G., Ginis, I., et al. (2012). Aerosol Effects on Microstructure and Intensity of Tropical Cyclones. *Bull. Amer. Meteorol. Soc.* 93 (7), 987–1001. doi:10.1175/bams-d-11-00147.1

Shapiro, L. J., and Willoughby, H. E. (1982). The Response of Balanced Hurricanes to Local Sources of Heat and Momentum. *J. Atmos. Sci.* 39 (2), 378–394. doi:10.1175/1520-0469(1982)039<0378:trobht>2.0.co;2

Tang, X., Tan, Z.-M., Fang, J., Munsell, E. B., and Zhang, F. (2019). Impact of the Diurnal Radiation Contrast on the Contraction of Radius of Maximum Wind during Intensification of Hurricane Edouard (2014). *J. Atmos. Sci.* 76 (2), 421–432. doi:10.1175/jas-d-18-0131.1

Tang, X., and Zhang, F. (2016). Impacts of the Diurnal Radiation Cycle on the Formation, Intensity, and Structure of Hurricane Edouard (2014). *J. Atmos. Sci.* 73 (7), 2871–2892. doi:10.1175/jas-d-15-0283.1

Tao, W.-K., Simpson, J., Sui, C. H., Ferrier, B., Lang, S., Scala, J., et al. (1993). Heating, Moisture, and Water Budgets of Tropical and Midlatitude Squall Lines: Comparisons and Sensitivity to Longwave Radiation. *J. Atmos. Sci.* 50 (5), 673–690. doi:10.1175/1520-0469(1993)050<0673:hmawbo>2.0.co;2

Wang, Y., Rao, Y., Tan, Z.-M., and Schönemann, D. (2015). A Statistical Analysis of the Effects of Vertical Wind Shear on Tropical Cyclone Intensity Change over the Western North Pacific. *Mon. Weather Rev.* 143 (9), 3434–3453. doi:10.1175/mwr-d-15-0049.1

Wang, Z., Montgomery, M. T., and Dunkerton, T. J. (2010). Genesis of Pre-Hurricane Felix (2007). Part II: Warm Core Formation, Precipitation Evolution, and Predictability. *J. Atmos. Sci.* 67 (6), 1730–1744. doi:10.1175/2010jas3435.1

Witze, A. (2022). Why the Tongan Eruption Will Go Down in the History of Volcanology. *Nature* 602 (7897), 376–378. doi:10.1038/d41586-022-00394-y

Wu, Q., and Ruan, Z. (2021). Rapid Contraction of the Radius of Maximum Tangential Wind and Rapid Intensification of a Tropical Cyclone. *Geophys. Res. Atmos.* 126 (3), e2020JD033681. doi:10.1029/2020JD033681

Yuan, T., Remer, L. A., and Yu, H. (2011). Microphysical, Macrophysical and Radiative Signatures of Volcanic Aerosols in Trade Wind Cumulus Observed by the A-Train. *Atmos. Chem. Phys.* 11 (14), 7119–7132. doi:10.5194/acp-11-7119-2011

Zhao, C., Lin, Y., Wu, F., Wang, Y., Li, Z., Rosenfeld, D., et al. (2018). Enlarging Rainfall Area of Tropical Cyclones by Atmospheric Aerosols. *Geophys. Res. Lett.* 45 (16), 8604–8611. doi:10.1029/2018gl079427

Zuo, M., Zhou, T., Man, W., Chen, X., Liu, J., Liu, F., et al. (2022). Volcanoes and Climate: Sizing up the Impact of the Recent Hunga Tonga-Hunga Ha'apai Volcanic Eruption from a Historical Perspective. *Adv. Atmos. Sci.* doi:10.1007/s00376-022-2034-1

Conflict of Interest: The authors declare that the research was conducted in the absence of any commercial or financial relationships that could be construed as a potential conflict of interest.

frontiers | Frontiers in Earth Science

ORIGINAL RESEARCH
published: 17 June 2022
doi: 10.3389/feart.2022.893781

Sensitivity of Tropical Cyclone Intensity Variability to Different Stochastic Parameterization Methods

Mahashweta Patra*[1], *Wai-Tong Fan*[2,3] *and Chanh Kieu*[1]

[1]Department of Earth and Atmospheric Sciences, Indiana University, Bloomington, IN, United States, [2]Department of Mathematics, Indiana University, Bloomington, IN, United States, [3]Center of Mathematical Sciences and Applications, Harvard University, Cambridge, MA, United States

Proper representations of stochastic processes in tropical cyclone (TC) models are critical for capturing TC intensity variability in real-time applications. In this study, three different stochastic parameterization methods, namely, random initial conditions, random parameters, and random forcing, are used to examine TC intensity variation and uncertainties. It is shown that random forcing produces the largest variability of TC intensity at the maximum intensity equilibrium and the fastest intensity error growth during TC rapid intensification using a fidelity-reduced dynamical model and a cloud-resolving model (CM1). In contrast, the random initial condition tends to be more effective during the early stage of TC development but becomes less significant at the mature stage. For the random parameter method, it is found that this approach depends sensitively on how the model parameters are randomized. Specifically, randomizing model parameters at the initial time appears to produce much larger effects on TC intensity variability and error growth compared to randomizing model parameters every model time step, regardless of how large the random noise amplitude is. These results highlight the importance of choosing a random representation scheme to capture proper TC intensity variability in practical applications.

Keywords: tropical cyclone development, stochastic parameterization, intensity error growth, intensity error saturation, random representation

Edited by:
Yuqing Wang,
University of Hawaii at Manoa,
United States

Reviewed by:
Eric Hendricks,
National Center for Atmospheric Research (UCAR), United States
Qingqing Li,
Nanjing University of Information Science and Technology, China

****Correspondence:***
Chanh Kieu
ckieu@indiana.edu

Specialty section:
This article was submitted to Atmospheric Science, a section of the journal Frontiers in Earth Science

Received: *10 March 2022*
Accepted: *29 April 2022*
Published: *17 June 2022*

Citation:
Patra M, Fan W-T and Kieu C (2022) Sensitivity of Tropical Cyclone Intensity Variability to Different Stochastic Parameterization Methods. Front. Earth Sci. 10:893781. doi: 10.3389/feart.2022.893781

1 INTRODUCTION

The application of stochastic physics parameterizations to weather and climate models is a rapidly advancing and important topic in current modeling systems (Palmer, 2001; Christensen et al., 2015; Dorrestijn et al., 2015). Palmer (2012) argued from the theoretical and practical bases that all comprehensive weather and climate models, no matter how complex they are, should be stochastic in nature. From this perspective, although the governing equations are formally deterministic, the best predictions should be based on models that could capture the uncertainty of the atmosphere, whether for climate on long time scales or weather on time scales of days to weeks. Developing practical tools for estimating such uncertainty of model forecasts would require the knowledge of random error effects, which then allows us to investigate the relative impacts of different types of uncertainties in models.

In general, TC intensity forecast errors in any numerical model are caused by several factors, including model errors, vortex initial uncertainties, global boundary guidance errors, random environmental forcings, and/or the intrinsic nature of TC intensity variability (Gopalakrishnan et al., 2011; Tallapragada et al., 2012; Kieu et al., 2018; Halperin and Torn, 2018; Trabing and Bell, 2020; Kieu et al., 2021, NKF). While these factors are technically non-separable in practice due to the nonlinear nature of TC dynamics and thermodynamics, it is possible to examine their relative roles under some specific conditions. For example, real-time verification of TC intensity forecast shows that model errors tend to be more important at a longer lead time compared to vortex initial condition errors (Du et al., 2013; Kieu et al., 2021). Likewise, uncertainties in global lateral boundary conditions could result in a wrong track forecast, which can lead to large intensity errors for incorrect landfalling storms or TCs under rapidly changing environments, even in perfect regional models with perfect initial conditions as discussed in Kieu et al. (2021).

Among those sources of intensity errors, the impacts of different random types on TC intensity variability appear to be the least examined. Even under the most idealized conditions with no other sources of model or initial condition errors, the atmospheric random fluctuation always exists and introduces uncontrollable uncertainties into TC development. While these random fluctuations are often small and probably less important than other types, such as model or initial condition errors, the nonlinearity of TC dynamics could amplify random fluctuations during TC development and eventually lead to noticeable variability in TC intensity that is currently not fully understood.

Despite such an inherent random nature of the atmosphere, examining how it affects TC intensity, especially the relative importance of different stochastic representations during TC intensification, is still an open question due to how random noise is parameterized in TC models. Using a low-order TC model (Nguyen et al., 2020, hereinafter NKF), recently examined the effects of random noise in terms of the Wiener process at the maximum intensity equilibrium. By analyzing the invariant intensity distribution at the mature stage, they showed that the stochastic forcing associated with tangential wind and warm-core anomaly has the largest contribution to TC intensity variability. This theoretical result is consistent with previous modeling studies, which captured strong sensitivity of TC intensity to vortex initialization schemes and warm-core retrieval in TC models (Kurihara et al., 1995; Liu et al., 2000; Van Nguyen and Chen, 2011; Rappin et al., 2013; Zou and Tian, 2018). How the effects of stochastic forcing are compared to those caused by random parameters or the vortex initial condition have not been addressed.

In this study, we wish to examine how different methods of representing atmospheric random noise will affect the variability of TC intensity and the intensity error growth during TC rapid intensification. Understanding the relative roles of stochastic parameterization approaches in TC intensity variability will help quantify an intensity error limit that one can achieve with numerical models in the future. Likewise, examining the error growth during the intensifying stage will help evaluate how the accuracy of the TC intensity forecast evolves during TC development for operational applications. For this purpose, we will use both a fidelity-reduced TC model (Kieu, 2015; Kieu and Wang, 2017, hereinafter KW17) and the cloud-resolving (CM1 Bryan and Fritsch, (2002)) model to study the effectiveness of different stochastic representation methods in capturing TC intensity fluctuations.

The structure of the article is organized as follows: **Section 2.1** presents a brief introduction of the TC-scale dynamical model, its extension for a stochastic system, and different types of random representations. **Section 2.2** discusses the application of stochastic parameterization for the CM1 model. A detailed algorithm to calculate the error growth during the rapid intensification is provided in **Section 2.3**. The results from the fidelity-reduced model are presented in **Section 3**, while error saturation at the mature stage and error growth for the CM1 model are discussed in **Section 4**. Finally, some concluding remarks are given in **Section 5**.

2 METHODOLOGY

2.1 Fidelity-Reduced TC Model

Given the complex nature of TC dynamics, a complete investigation of different stochastic mechanisms in full-physics TC models is generally not feasible. This is because full-physics models are highly nonlinear with various parameterization schemes that not only require a large computational resource to conduct stochastic simulations but also introduce insurmountable difficulty in analyzing nonlinear interactions among different physical components.

As a first step to examine the effects of different stochastic parameterizations on TC intensity, a simple model for TC development is needed. Among several existing low-order TC models, the TC-scale model proposed by Kieu (2015) and modified further by KW17 (hereinafter referred to as the modified TC-scale dynamics, or MSD, model) is of specific interest. Using TC scales as dynamical variables in the axisymmetric framework, the scale analyses of the governing equation can be reduced to a set of ordinary differential equations that contain only a few TC basic scales, including the maximum tangential wind (v), the maximum radial wind at the surface (u), and the warm anomaly in the TC central region (b). With the wind-induced surface heat exchange feedback closure, these non-dimensional scale equations are given as follows:

$$\dot{u} = pv^2 - (p+1)b - C_d u|v|, \tag{1}$$

$$\dot{v} = -uv - C_d v|v|, \tag{2}$$

$$\dot{b} = bu + su + T_s|v| - rb. \tag{3}$$

This MSD model includes several parameters (p, s, r, C_d, T_s) that characterize the TC dynamics, where p is a constant proportional to the squared ratio of the depth of the troposphere to the depth of the boundary layer, s denotes the effective tropospheric static stability, r represents the Newtonian cooling, and C_d and T_s are non-dimensional parameters representing the surface drag coefficient and sea surface temperature (SST). Note that, unlike the original MSD system in KW17, for which C_d and T_s are scaled to have a value of 1, we retain their explicit role in this study such that the sensitivity of

TC intensity and the error growth to these parameters can be explored.

While the MSD model is simple, it has some properties that are attractive for our investigation of random representations in this study. First, this system is explicitly time-dependent, which is required to examine the evolution of TC intensity and related error growth during TC intensification. Second, the model contains the maximum potential intensity (MPI) limit as its unique stable point in the phase space of (u, v, b), as discussed in KW17. The existence of such a stable point is vital because it allows us to quantify how the variability of TC intensity at the mature stage depends on different random parameterization methods, as discussed in NKF.

While the MSD system could describe both cyclonic and anticyclonic flows as discussed in Kieu and Wang (2018), we will limit our consideration hereinafter to cyclonic TCs in the Northern Hemisphere such that the absolute signs in **Eqs 1**–**3** can be removed. In the next sections, we will describe three different random mechanisms and how to implement them for the MSD system. These mechanisms include 1) random forcing, 2) random initial condition, and 3) random parameters, which are the most commonly used methods in the current numerical weather prediction models.

2.1.1 Random Forcing (RF) Representation

We first examine a type of random representation in which the model forcing is augmented by stochastic processes, often known also as physical stochastic parameterization (Palmer, 2001; Christensen et al., 2015; Dorrestijn et al., 2015). According to this method, random noise is added to prognostic variable tendencies or model states with different spatial and temporal scales (Palmer, 2001; Weisheimer et al., 2011; Zhang et al., 2015; Christensen, 2020). This approach is equivalent to adding random noise to model forcing (NKF, Fan et al., 2021a), which will be hereinafter referred to as the random forcing (RF) method.

Following NKF, we introduce additive driving noise in terms of the Wiener process to the MSD system (1–3) and obtain the following stochastic differential equations:

$$dU_t = \left(pV_t^2 - (p+1)B_t - C_d U_t V_t\right)dt + \sigma_u dW_t^{(u)}, \quad (4)$$

$$dV_t = \left(-U_t V_t - C_d V_t V_t\right)dt + \sigma_v dW_t^{(v)}, \quad (5)$$

$$dB_t = \left(B_t U_t + sU_t + T_s V_t - rB_t\right)dt + \sigma_b dW_t^{(b)}, \quad (6)$$

where $\{W^{(u)}, W^{(v)}, W^{(b)}\}$ are independent Wiener processes and $(\sigma_u, \sigma_v, \sigma_b)$ are the corresponding noise amplitude. While parameterizing stochastic forcings by the Wiener process appears to be reasonable, we note that the assumption of stochastic forcings as state-independent noise requires some justification because real stochastic forcings may be functions of atmospheric states instead of having a constant variance. Because our focus here is on the relative roles of different stochastic parameterization methods in TC intensity rather than the physical nature of each forcing term, we will choose this constant-variance stochastic forcing as a protocol for the RF method to compare with the other random methods. More detailed discussion of this assumption can be found in (NKF) Fan et al. (2021b).

With the RF representation in terms of the Wiener process, the numerical solution of **Eqs (4–6)** can be easily obtained using Monte Carlo simulations. In this study particularly, the Runge–Kutta fourth-order scheme is applied to the deterministic part of **Eqs (4–6)** with a discretized time-step Δt, identical to that used in NKF. The stochastic part is then added to the model forcing at each time step, using a Gaussian random variable with variance $(\Delta t)\sigma_i^2$ for each state variable $i \in \{u, v, b\}$. Because of the constant variance for the stochastic forcings, this approach is essentially equivalent to the Euler–Maruyama first-order scheme. So long as the time step Δt is sufficiently small, this first-order accuracy suffices for representing the random processes as expected.

2.1.2 Random Parameter (RP) Representation

The second common method for parameterizing stochastic processes in numerical models is to randomize model parameters based on a prior probability distribution of the parameters. A rationale behind this approach is that model parameters cannot be known accurately due to measurement uncertainties, incomplete understanding of physical processes, or the stochastic nature of phase transitions. For example, Zhang et al. (2015) implemented a mechanism that allows random fluctuation in the convective triggering function in an operational ensemble system, which is simply a numerical flag in the convection parameterization of the Hurricane Weather Research and Forecasting (HWRF) model. Similarly, other studies have applied the RP approach to, for example, the boundary parameterization to reflect the unknown variations in the land surface and/or boundary processes (Song et al., 2007; Plant and Craig, 2008; Doblas-Reyes, 2009; Breil and Schädler, 2017). This RP scheme has been shown to improve the model overall ensemble spread, thus capturing better the uncertainties of model physics than deterministic ensembles.

Given these inherent uncertainties of model parameters, we implement a scheme for the MSD model in which three key model parameters, including the tropospheric static stability (s), the sea surface temperature T_s, and the surface drag coefficient (C_d), are randomized around a given mean value. Generally, such model parameter randomization can be carried out in two different ways. In the first approach, random noise is introduced to model parameters at the beginning of the model integration and kept unchanged during the entire integration (hereinafter referred to as the initial RP approach). In the second approach, random noise is added to model parameters every time step during the integration to reflect the variability of these model parameters with time (hereinafter referred to as the time-varying RP approach).

While both the initial and time-varying RP approaches are practical and can be compared with each other, their mathematical and physical interpretations are quite different and require detailed examinations. For the initial RP approach, the uncertainties in the model parameters enter the system only as measurement errors, which prevent one from determining the model parameters accurately. Thus, model parameters take random values at the initial time but are fixed during the course of the model integration. In contrast, the time-varying RP method accounts for the fact that model parameters are itself a random function of time that must have a statistical distribution. An example of this is the convective triggering function in cumulus parameterization, which determines if deep convective plumes can occur or not (Arakawa and Schubert, 1974; Kain and Fritsch, 1990; Song et al., 2007; Suhas and Zhang, 2014; Zhang et al., 2015). This triggering function often depends on vertical motion, CAPE, or some other ambient variables, so it is inherently a random function of time. In this regard, the outcome from the initial RP and time-varying RP representation could bring different insights into the variability of TC intensity that we wish to explore herein.

To be specific for our implementation in this study, the three model parameters (s, T_s, C_d) are assumed to be Gaussian random variables with known means and standard deviations. In non-dimensional units, the mean and standard deviation values are $\bar{s} = 0.1$ and $\sigma_s = 0.01$ for the static stability s, $\bar{T}_s = 1$ and $\sigma_{T_s} = 0.1$ for SST T_s, and $\bar{C}_d = 1$ and $\sigma_{C_d} = 0.1$ for the surface drag coefficient C_d. These mean values are based on their observed magnitude in real TC-force wind environment (Kieu, 2015; Zhang, 2010), while the standard deviations are assumed to be 10% of the mean values based on the typical observational errors for TCs (Zhang, 2010; Richter et al., 2021). Because we wish to examine the relative importance of RF and RP approaches, no random noise is added to the model forcings in both the initial and time-varying RP implementations.

2.1.3 Random Initial Condition (RIC) Representation

The last approach to consider stochastic processes is to randomize model initial conditions, which is by far the most common method to account for uncertainties in operational models (Hamill et al., 2011; Aksoy et al., 2013; Aberson et al., 2015; Zhang and Weng, 2015; Tong et al., 2018). Often known as ensemble forecasting, the RIC approach introduces noise with a given probability distribution to reflect the initial condition uncertainties. This probability distribution comes from various pathways such as a prior background covariance matrix (cold-start), ensemble cycling (breeding), or an analysis covariance matrix (data assimilation), which are generally given at all model grid points.

Following the common practice of implementing random initial uncertainties in previous studies, our RIC method adds white noise to the MSD model initial conditions, using a Gaussian distribution with a given variance and zero mean. In the non-dimensional unit, the white noise for the RIC method with the MSD model has a standard deviation of 0.01 for all (u, v, b) components. In full physical dimension, this standard deviation respectively corresponds to ~ 1 $m\,s^{-1}$ for wind and ~ 0.5 K for temperature, which are reasonable for the random wind and temperature noise in real atmospheric conditions (Zhang, 2010; Zhang et al., 2010). Note that, unlike the RF or time-varying RP method for which the randomness is realized at every time step, the RIC representation introduces random noise only at the initial time, similar to the initial RP method. Therefore, conditioned on the realization of the random initial condition, the MSD model is deterministic at all time for the RIC method.

Given the above approaches to represent stochastic processes in the MSD model, Monte Carlo simulations of 1,000 members are then carried out to examine the variability of TC intensity and the error growth rate for each random representation method. In our range of Monte Carlo experiments, we observe that an ensemble of > 100 realizations is generally sufficient for a stable statistical distribution and significance. Given the cheap computational cost of the MSD model, a fixed number of 1,000 realizations is therefore used for all the RIC, RP, and RF methods in this study such that the ensemble-size sensitivity analyses are not necessary.

2.2 CM1 Model Experiments

While the MSD system could allow detailed examinations of the relative impacts of different random representations due to its efficient computation and low order, real TCs are much more complex, with various nonlinear feedback between different dynamics and thermodynamics components that are not accounted for in the MSD model. In addition, TC dynamics may contain chaotic behaviors at the MPI equilibrium, which can mask the stochastic effects that the MSD model could not capture (Kieu et al., 2018; Keshavamurthy and Kieu, 2021, NKF).

To further evaluate the relative effects of random representations on TC intensity, the cloud model (CM1, Bryan and Fritsch (2002)) is therefore employed in this study. By implementing different random mechanisms in the CM1 model, one can verify what results obtained from the MSD system are valid in a more complete full-physics model and thus applicable to real TCs. For our herein study, the axisymmetric setting of the CM1 model was used such that the results from the CM1 model can be used to verify those obtained from the MSD model under the same axisymmetric framework. Comparing analyses from the low-order MSD model and the full-physics CM1 model can therefore provide more understanding of the impacts of random noise on the variability and the error growth of TC intensity.

Because of the large computational requirement and the numerical stability of the CM1 model, it is noted that our implementation of the RF method for the CM1 model is slightly different from that for the MSD model. Specifically, we apply additive white noise to the momentum and temperature equations with a constant standard deviation of $[0.1–0.5]m\ s^{-1}\,\mathrm{min}^{-1}$ for wind and $[10^{-3} - 10^{-2}]K\ \mathrm{min}^{-1}$ for temperature, respectively (Zhang, 2010; Zhang et al., 2010). The constant variance design is to ensure the closest possible resemblance to the RF implementation for the MSD system described in the previous section. It also helps maintain the same order of the finite difference accuracy for the deterministic part, which is based on the Runge–Kutta scheme in the CM1 model. However, no random noise is added to the model moisture state variable due to unknown probability distributions of moist variables/graupel species. Our attempt to add random noise to moist variables did not show any significant difference in terms of model intensity output. However, the noise decreases the stability of the CM1 model and prevents examining a range of noise amplitude dependence. Thus, no random

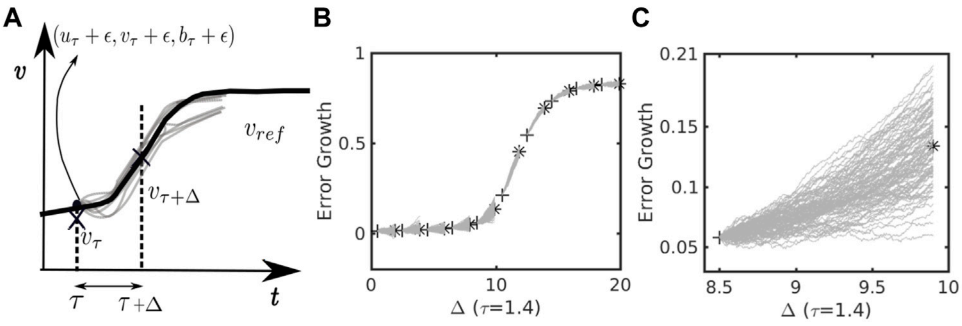

FIGURE 1 | A schematic diagram illustrating the algorithm for calculating TC intensity error growth at different stages of TC development for **(A)** a reference orbit (solid black) and an ensemble of perturbed stages at the beginning time τ and the end of the perturbation integration $\tau + \Delta$ (crosses); **(B)** time series for a range of stages starting from τ and ending at $\tau + \Delta$ for $N = 1{,}000$ realization; and **(C)** a magnified version of **(B)** for one specific stage. Note that pluses and asterisks in **(B,C)** show the points on the deterministic orbit at time τ when perturbations are added and at time $\tau + \Delta$ where the error growth rate is computed, respectively.

perturbations are applied to the moist equations in all of our CM1 experiments herein.

Regarding the RIC method, our approach for the CM1 model is identical to that for the MSD model. In other words, white noise with a range of standard deviations from 0.01 to 0.1 ms^{-1} is added to the CM1 model's initial conditions. Likewise, the implementation of the RP method for the CM1 model is also identical to that used in the MSD model. Nonetheless, it should be noted that CM1 has many model parameters that can be randomized. For comparison with the MSD model, two specific parameters that are directly relevant to the TC intensity in CM1, including the sea surface temperature (T_s) and the surface drag (C_d), are chosen in our RP experiments with the CM1 model. These parameters are assumed to be random variables with a standard derivation of 1 K for T_s and 10^{-4} for C_d, respectively. The mean values for these parameters are then varied in the range of [298–305 K] for T_s and [$10^{-3} - 3 \times 10^{-3}$] for C_d such that the dependence of TC intensity variability on different mean values of model parameters can also be studied. Note that tropospheric stratification is a parameter in the MSD model, but it is a diagnostic variable in CM1. Therefore, its random parameterization cannot be implemented in the CM1 model.

Due to the computational limit and a large number of model output, a fixed number of 100 realizations are conducted for each random noise amplitude in the CM1 experiments, regardless of the random representation method. Our *ad hoc* sensitivity analyses for ensemble members ranging from 100 to 200 show again insignificant differences in terms of statistics when the number of realizations changes. Thus, no ensemble size sensitivity experiment for CM1 will be provided.

2.3 An Error Growth Algorithm

To evaluate the effects of random noise on TC intensity error growth, we follow the approach of Kieu et al. (2018) and introduce small noise along a reference state at different stages of TC development. This type of state-dependent error growth rate mimics the real-time forecast cycles by which the TC intensity forecasts are re-initialized every 6 or 12 h. As TCs evolve, their intensity changes and TC intensity errors may therefore evolve differently, even with the same initial error. Examining how such an intensity error growth rate changes with time will allow forecasters to estimate how the accuracy of their intensity forecast varies during TC development.

In quantifying the dependence of intensity error growth on the stage of TC development, it is important to note that all environmental conditions must be fixed so that such dependence can be well-defined because any change in environmental conditions would cause not only changes in TC intensity along the trajectory but also a shift in the MPI equilibrium, which produces an unexpected intensity error variability. This is a subtle point in studying TC intensity errors, yet it has not been sufficiently emphasized in previous studies that we wish to emphasize again here.

With this approach, our algorithm for computing TC intensity error growth in the MSD model includes the following steps.

1) Select any initial state $x_0 = (u_0, v_0, b_0)$, where $v_0 > 0$ and generate a reference orbit $x_f(t) = (u_f(t), v_f(t), b_f(t))$ during a given interval $t \in [0, T]$, based on the deterministic MSD system (1–3) (see the thick black line in **Figure 1A**);
2) Choose a given time τ and its corresponding reference state $x_f(\tau)$ at the time τ to add a random perturbation vector ξ to x_τ, where $\xi = (\xi_u, \xi_v, \xi_b)$ are independent Gaussian variables with zero mean and standard deviations $\{\sigma_u, \sigma_v, \sigma_b\}$, respectively. This process gives us an initially perturbed state $x_f(\tau) + \xi$ at time τ (see the crosses in **Figure 1A**);
3) Denote the components of the perturbed state at τ as $(u'(\tau), v'(\tau), b'(\tau)) \equiv x_f(\tau) + \xi$; we then choose a lead time Δ and integrate $(u'(\tau), v'(\tau), b'(\tau))$ from 0 to Δ, using the same MSD model as for the reference integration;
4) For each pair (τ, Δ), repeat steps 2–3 several times (e.g., $N = 1{,}000$ times) to generate an ensemble of integration from the initially perturbed state $(u'(\tau), v'(\tau), b'(\tau))$. Note that different realizations of the Gaussian distribution will give different ξ, even with the same values of mean and standard deviation. Store all of these integrated states and denote their

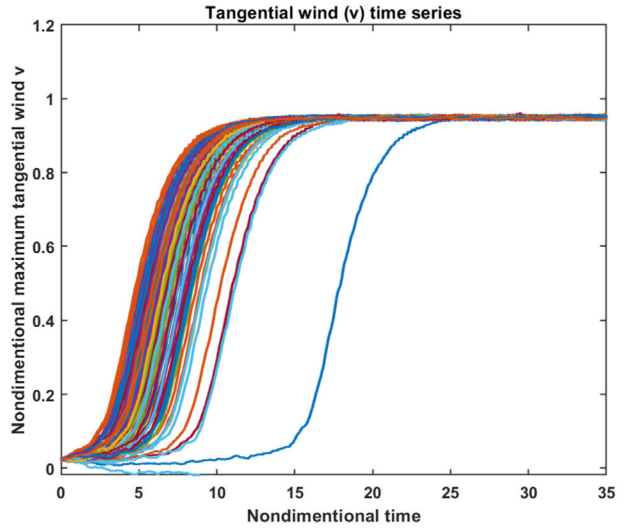

FIGURE 2 | Time series of the tangential wind component *v* as obtained from 1,000 Monte Carlo simulations of the MSD system, using the random forcing representation with noise amplitude $\sigma = 0.01$. Model initial condition is set as (−0.01, 0.01, 0.01), and other model parameters are $p = 200$, $s = 0.1$, $r = 0.25$, $C_d = 1.0$, $T_s = 1.0$.

corresponding states at $t = \tau + \Delta$ as $(u_i(\tau + \Delta), v_i(\tau + \Delta), b_i(\tau + \Delta))$, $i = 1..N$ (see the triangles in **Figure 1B**);

5) Compute the root mean square error $err(\tau, \Delta)$ for the $v_i(\tau + \Delta)$ component with respect to the reference component $v_f(\tau + \Delta)$ for each time τ and lead time Δ as follows:

$$err(\tau, \Delta) = \sqrt{\frac{1}{N}\sum_{i=1}^{N}\left(\frac{v_i(\tau + \Delta) - v_f(\tau + \Delta)}{\Delta}\right)^2}, \qquad (7)$$

which is defined hereafter as the intensity error growth rate corresponding to the lead time Δ at the forecast cycle τ.

6) Repeat steps 1–5 for different values of τ and Δ to obtain the distribution of the error growth rate as a function of (τ, Δ).

By varying τ, the error growth calculation as outlined above can capture the characteristics of TC intensity error at different stages of TC development. Likewise, varying Δ will allow us to examine how TC intensity error growth changes with forecast lead times similar to what is carried out in real-time intensity verification. Note that our definition of the intensity error growth in **Eq. 7** is relative to a given reference state $v_f(\tau + \Delta)$. If one replaces this reference state with the corresponding ensemble mean, **Eq. 7** would give us an ensemble spread instead of the absolute intensity errors. As our focus here is on the growth of the absolute error rather than the ensemble mean, definition (7) is therefore adopted here.

Although the same steps are carried out for all three random representation methods, we should mention that different realizations of ξ are added to the initial state only for the RIC method because the MSD system (1)–(3) is deterministic. For the RF method, stochastic forcing varies every time step, so there is no need to randomize the initial state. For the RP method, whether one applies different realizations of the initial perturbation ξ would depend on what RP scheme (i.e., the initial or time-varying) is used, as discussed in the previous section.

3 FIDELITY-REDUCED MODEL RESULTS

In this section, we present first the analyses of different random representation methods for TC intensity in the MSD model, using two key measures, including 1) TC intensity variability at the maximum equilibrium and 2) intensity error growth. The first measure provides insights into TC intensity error saturation at long forecast lead times, which plays a key role in estimating TC intensity predictability, as discussed by Kieu and Moon (2016) and Kieu et al. (2018). The second measure focuses on how the characteristics of TC intensity error growth change during TC development, relevant to the reliability of the operational forecast. These two aspects of TC intensity can be thoroughly examined within the low-order MSD model and compose the main results of this section.

3.1 Intensity Variability at the Mature Stage

To have a broad picture of TC intensity in our stochastic MSD model, **Figure 2** shows the time series of the v-component in the MSD system as obtained from the Monte Carlo simulations with the RF method. These simulations have the same numerical procedure and settings as in NKF, which are summarized in **Table 1**. Note that the v component represents the maximum tangential wind near the surface in the TC-scale dynamics. Thus, it can be used as a proxy to examine TC intensity and related variability in all following analyses.

As shown in **Figure 2**, the Monte Carlo simulations of **Eqs 4–6** overall capture expected TC development, with three distinct phases in all realizations, including a pre-condition (genesis) period, rapid intensification, and finally, the maximum intensity equilibrium stage. While the exact onset moment of rapid intensification highly varies among realizations (Fan W.-T. et al. 2021), these three stages are well displayed and reflect the inherent TC development in the MSD model under an idealized environment, even in the presence of random noise. Despite a similar intensification rate among all realizations, the stochastic nature of the MSD model is manifested in **Figure 2** as non-smooth fluctuations of TC intensity every time step along any trajectory. So long as the model parameters are fixed, the random forcing affects only fluctuations around the main trajectory but not the averaged state of TC development. As the RF amplitude increases, TC mean state is no longer maintained and the intensification rate or MPI will differ. In this regard, these Monte Carlo simulations confirm not only the main characteristics of TC development but also the stochastic property of the MSD system (4)–(6) with the RF representation as expected.

However, of more interest for our analyses is the variability of TC intensity at the maximum intensity equilibrium due to stochastic forcing, which dictates the limit in our ability to reduce TC intensity forecast errors. To examine how this variability depends on the amplitude of each RF in **Eqs 4–6**, **Figure 3** shows the standard deviation of v (denoted hereinafter

TABLE 1 | Configuration of Monte Carlo simulations for the stochastic MSD model (4)–(6). Details of physical interpretations and scaling analyses of these parameters can be found in KW17.

Parameter	Value	Remark
Δt	0.01	Non-dimensional time step
T	50	Non-dimensional duration of the Monte Carlo simulation
p	200	Non-dimensional square ratio of the PBL depth over the radius of the maximum wind
r	0.1	Non-dimensional parameter representing the radiative cooling
s	0.1	Non-dimensional parameter representing the tropospheric stratification
C_d	1	Non-dimensional parameter representing the surface drag coefficient
T_s	1	Non-dimensional parameter representing the surface temperature
σ_u	0.01	Non-dimensional variance of the *u*-wind stochastic forcing component
σ_v	0.01	Non-dimensional variance of the *v*-wind stochastic forcing component
σ_b	0.01	Non-dimensional variance of the buoyancy stochastic forcing component

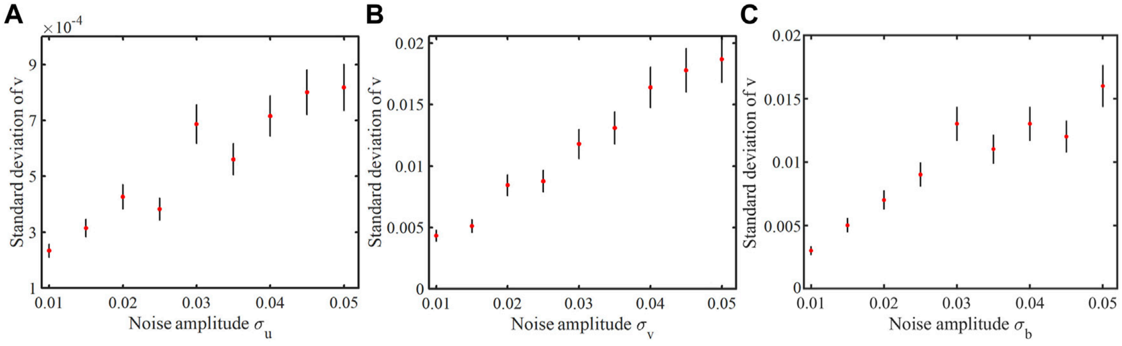

FIGURE 3 | The standard deviation of the *v* component for the RF representation method as a function of the stochastic forcing standard deviation added to **(A)** the *u* forcing, **(B)** the *v* forcing, **(C)** and the *b* forcing in the MSD system.

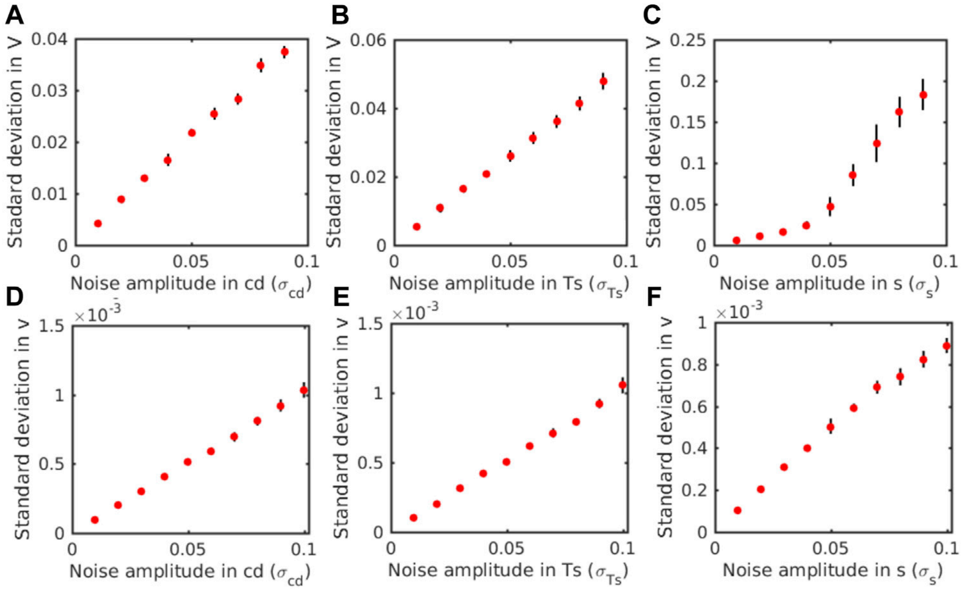

FIGURE 4 | Similar to **Figure 3** but for the RP representation as a function of the random standard deviation for **(A–C)** initial RP and **(D–F)** time-varying RP method.

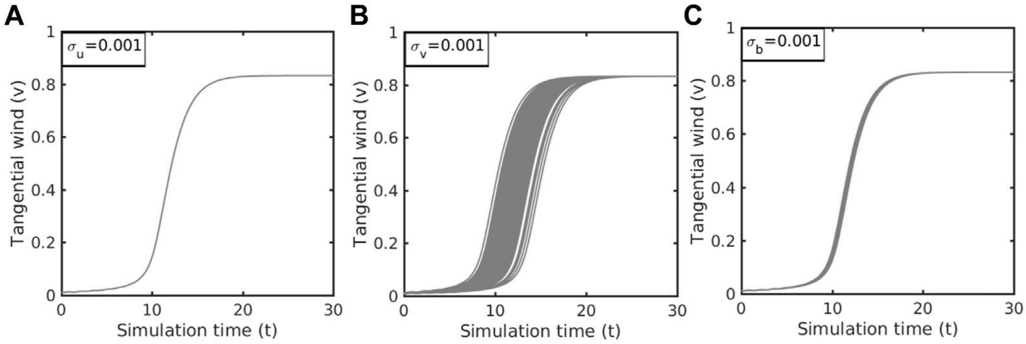

FIGURE 5 | Time series of tangential wind v for a fixed noise amplitude $\sigma_{u,v,b} = 0.001$ that is added to initial condition **(A)** u_0, **(B)** v_0, **(C)** b_0, respectively, where the initial condition $(u_0, v_0, b_0) = (-0.01, 0.01, 0.01)$, and other model parameters are $p = 200$, $s = 0.1$, $r = 0.25$, $C_d = 1.0$, $T_s = 1.0$.

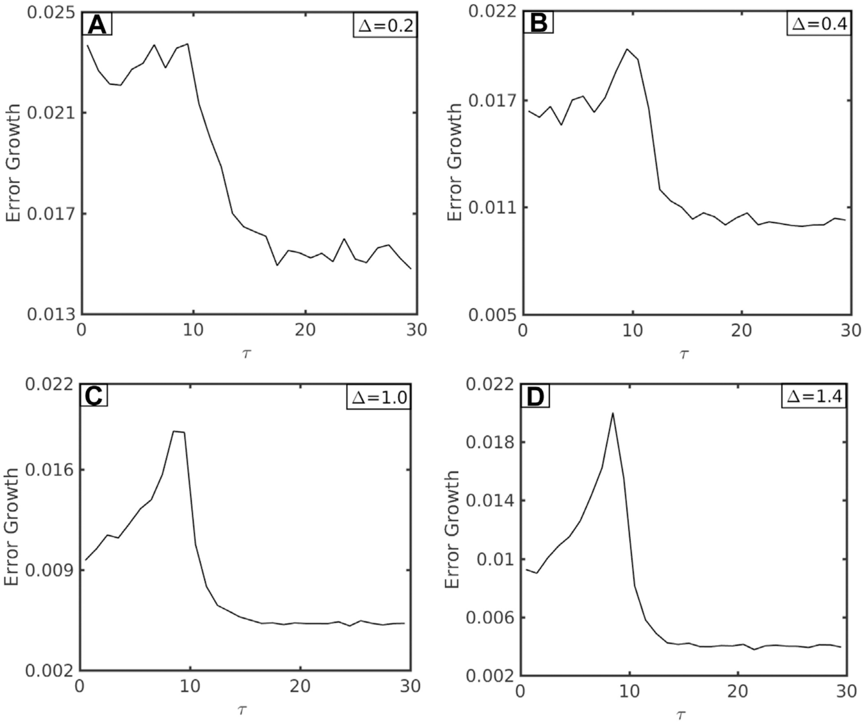

FIGURE 6 | The intensity error growth rate $err(\tau, \Delta)$ for different values of the forecast lead time Δ and the stage of development (τ) as obtained from the RF method, using the same set of model parameters as in **Figure 3** with $\sigma_u = \sigma_v = \sigma_b = 0.01$. For **(A)** $\Delta = 0.2$, **(B)** $\Delta = 0.4$, **(C)** $\Delta = 1.0$, and **(D)** $\Delta = 1.4$. Here, fixed perturbation amplitude $\epsilon = 0.001$ and $N = 1{,}000$ realizations are used for all error growth integration.

as Γ) as a function of (σ_u, σ_v, σ_b) during the equilibrium stage (i.e., t = 25–50 in **Figure 2**). Consistent with the results of Nguyen et al. (2020) (**Figure 4**), TC intensity fluctuations increase almost linearly with σ_u and σ_v, so long as these RF amplitudes are sufficiently small (<0.05 in non-dimensional unit). Such an asymptotically linear increase of Γ for the small noise can be proven rigorously based on the stationary distribution, as shown in NKF.

For the stochastic forcing component σ_b, we note that Γ differs somewhat from a linear function because it is possible that TC intensity deviates far away from the equilibrium when σ_b is sufficiently large, and the underlying stability assumption for the MSD system is thus no longer valid. Consistent with the finding in NKF, we also notice that the stochastic forcing for tangential wind or warm-core anomaly has the most impact on overall TC intensity variability (**Figures 3B,C**), which produces intensity fluctuation one order of magnitude larger than that caused by the radial wind stochastic forcing (**Figure 3A**).

Relative to the RF method, **Figure 4** shows a similar dependence of Γ on each model parameter at the MPI equilibrium obtained from the initial and time-varying RP methods. Overall, intensity

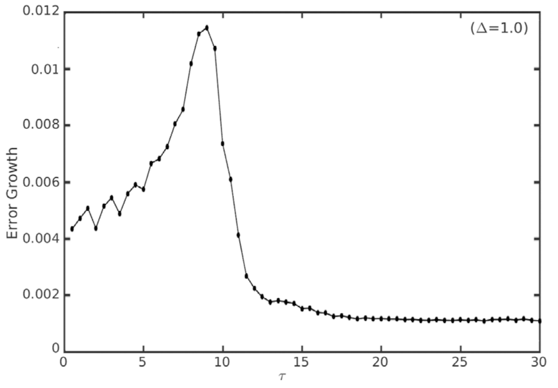

FIGURE 7 | Similar to **Figure 6** but for the RIC method, assuming the same set of model parameters as in **Figure 6** and a fixed lead time Δ = 1.0.

fluctuation increases with the magnitude of the parameter variance for both the RP implementations, similar to that with the RF method. However, one notices a fundamental difference between the RP and RF methods in terms of the magnitude of Γ. Particularly in the initial RP method (**Figures 4A–C**), Γ is of the same order of magnitude as in the RF method. In contrast, the time-varying RP method (**Figures 4E,F**) captures almost one order of magnitude smaller regardless of model parameters. This is a noteworthy point because it suggests that the randomness of the model parameters during TC development plays a less important role in TC intensity variability than the initial uncertainty in these model parameters. From a practical standpoint, this non-trivial result implies that our efforts in improving model parameters at the initial time will have more effects on TC intensity variability than randomly sampling model parameters during the course of model integration.

From the mathematical standpoint, such different behaviors of intensity variation between the initial and the time-varying RP approaches can be understood if one analyzes the intensity probability distribution at the equilibrium as in NKF. Indeed, sensitivity analyses of the intensity variance for the initial RP method at the MPI limit (**Supplementary Appendix S1**) show that the tropospheric static stability parameter s plays a smaller role in the overall variability of TC intensity when s is small. As s becomes sufficiently large (> 0.04), the MSD system becomes bifurcated Kieu and Wang (2018) and the deviation around the MPI equilibrium becomes much larger, thus resulting in larger Γ as seen in **Figure 4C**. On the contrary, the SST and surface drag coefficient parameters do not possess any bifurcation point. Therefore, Γ increases almost linearly with the random noise amplitude for the initial RP representation [1]. This result highlights the critical role of the tropospheric static stability in determining TC intensity variability compared to C_d or *SST* (KW17, Kieu et al., 2021).

Unlike the initial RP method, for which the MPI may settle down to different equilibria for different parameters, the time-varying RP method has a much more intriguing behavior. Herein, we study an important property of a linear stochastic system with time-varying random parameters, for which the fluctuation of the system around its stable point approaches zero as the numerical time step becomes finer (see **Supplementary Appendix S2**). This counter-intuitive behavior in the presence of pure random parameters is because a finer time step prevents the model state from deviating too far from its equilibrium at each iteration, leading to an overall smaller fluctuation with time when the time step decreases. While the MSD system is far from linear, the MSD system, under random forcing, captures smaller Γ for a smaller time step in our series of experiments, much like a linear system (not shown). This particular property of the time-varying RP indicates the subtle dependence of TC intensity variability on the way one implements the RP representation in TC models, as shown in **Figure 4**.

Although the initial and time-varying RP methods result in a different response of TC intensity to random parameters, it is of interest to note that Γ is somewhat the same among the three model parameters for each method in terms of magnitude. This indicates that the random fluctuation of each parameter could equally induce TC intensity variability that one has to consider. Of course, these relative roles among these parameters, as shown in **Figure 4**, are very specific to the MSD model. Therefore, it is necessary to further verify these properties in full physics models, as shown in **Section 4**.

Unlike the RF or RP approach, for which the stochasticity can take place at every time step, the RIC method is different due to the deterministic nature of the underlying model. We note again that the MSD model contains a single stable point that corresponds to the MPI equilibrium, as shown in KW17. Thus, regardless of initial conditions, all trajectories will eventually converge to a single MPI point after a sufficiently long time. In the absence of stochastic forcing or random parameters, the intensity variability at the MPI equilibrium in the MSD model must therefore approach zero irrespective of the initial random components, as confirmed in **Figure 5**. Apparently, this deterministic characteristic of the MSD system prevents it from modeling TC intensity variability at the MPI limit unless stochastic forcing or random parameters are used.

We wish to mention at this point that real TC dynamics is far more complex than a single stable point at the equilibrium captured by the MSD system, as shown in **Figure 5**. As discussed in previous studies (Hakim, 2011; Brown and Hakim, 2013; Kieu and Moon, 2016), long simulations of any full-physics TC model always display a quasi-stationary equilibrium instead of a stable fixed point as in the MSD system or the theoretical MPI framework. Such intensity fluctuation at the MPI limit in real TC models could be attributed to several factors, such as process noises, truncation errors, or the existence of low-dimensional chaotic dynamics, none of which is captured by the MSD system. To better compare

---

[1] Technically, this property is related to the fact that the MSD model can be treated as an extended Markov system (u, v, b, s, T_s, C_d). For this extended system, one first obtains the stationary distribution μ by solving the equation $\mathcal{L}^*\mu = 0$ for the stationary distribution μ, where $\mathcal{L}^*$ is the adjoint of the generator $\mathcal{L}$ of the Markovian system. Then, the error growth at a large time limit can be approximated by the standard deviation of the v-component under the stationary distribution.

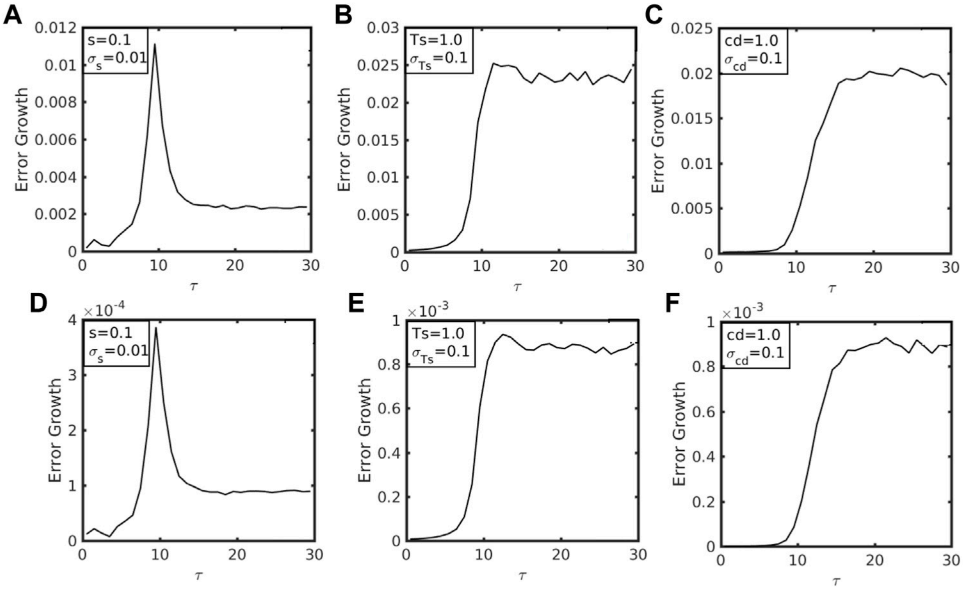

FIGURE 8 | Similar to **Figure 6** but for the random parameter approach with **(A–C)** initial RP method and **(D–F)** time-varying RP method.

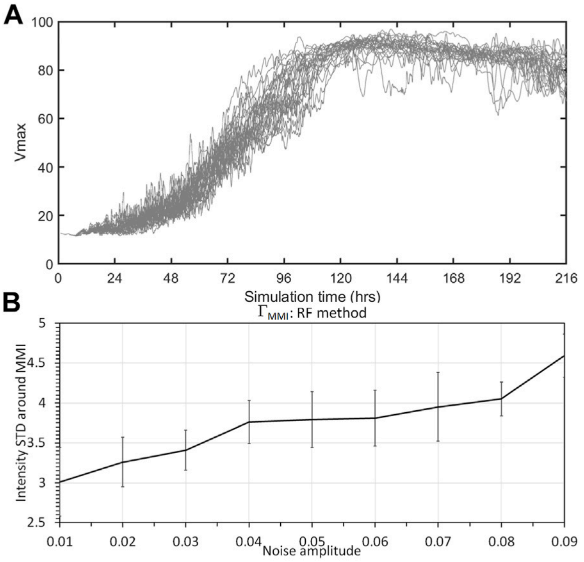

FIGURE 9 | (A) Time series of the maximum tangential wind (V_{MAX}, unit ms^{-1}) as obtained from 100 20-day simulations of the CM1 model that is implemented with the RF method; and **(B)** the standard deviation of V_{MAX} (unit, ms^{-1}) at the maximum intensity equilibrium (day 9–18 into integration) as a function of the random forcing standard deviation. Error bars denote 95% confidence intervals.

the relative effects of the RIC, RF, and RP methods in representing random effects on TC intensity, one must ultimately employ full physics models. For the MSD system, we could at least conclude that the RF method produces the largest impact on TC intensity variability at the long lead times, followed by the initial RP method. To what extent this can be realized in full-physics CM1 models will be presented in **Section 4**.

3.2 Error Growth During RI

Along with the variability of TC intensity at the equilibrium, it is necessary to examine also how intensity fluctuation varies during TC development. In this regard, **Figure 6** shows the TC intensity error growth rate *err* (τ, Δ) as a function of forecast lead time τ for the RF method. Recall that the error growth rate is computed along a reference trajectory with a prescribed lead time Δ. Thus, *err* (τ, Δ) depends on both the integration time (τ) and the lead time Δ, as discussed in **Section 2.3**.

Regardless of the forecast lead time Δ, one can see in **Figure 6** a very specific pattern of *err* (τ, Δ), with the most rapid growth during the pre-conditioning stage, followed by a quick decrease during the intensification period and eventually approaching a constant growth rate at the MPI equilibrium. *err* (τ, Δ) as maximum prior to rapid intensification reflects the fact that the onset moment of TC rapid intensification highly varies among different realizations in the MSD system (cf. **Figure 2**; see also Fan et al. (2021b) for a rigorous treatment), thus resulting in large intensity errors. As the vortex enters its intensification period, TC dynamics becomes more consistent among all realizations, which explains the decrease in error growth. In contrast, the growth rate is minimum when the TC vortex reaches its equilibrium stage because this equilibrium is highly stable and resilient to random fluctuation (Kieu, 2015, NKF). As a result, *err* (τ, Δ) subsides and levels off for $\tau > 16$. These behaviors of the intensity error growth rate accord with a previous study using a full-physics model (Kieu et al., 2018) and highlight the unique properties of TC intensity errors.

Of further significance is that the overall error growth characteristics of *err* (τ, Δ) appear to be less sensitive to the

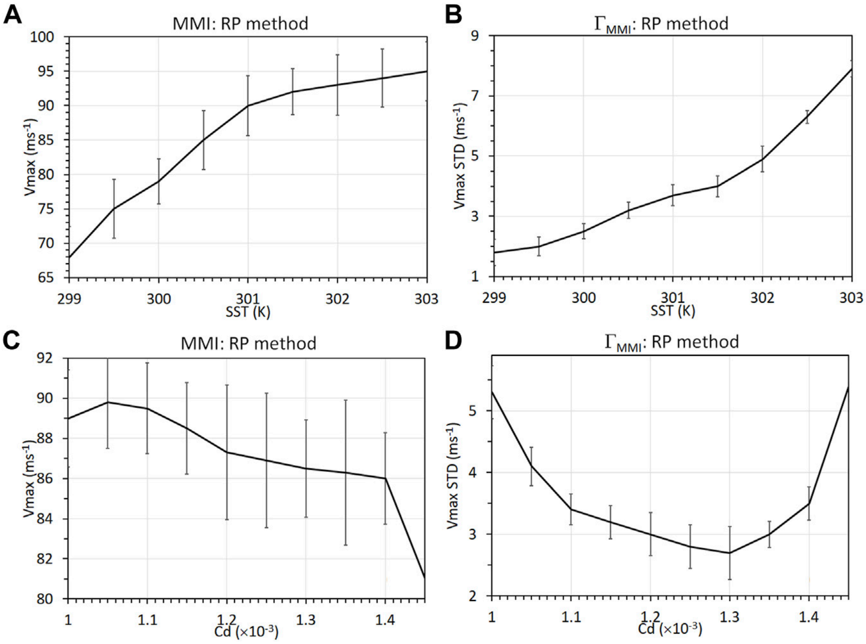

FIGURE 10 | Dependence of V_{MAX} (left panels) and its corresponding standard deviation (right panels) on **(A,B)** SST and **(C,D)** C_d with a fixed noise amplitude in the time-varying RP method.

forecast lead time Δ, so long as Δ is not too large. However, note for the RF method that *err* (*τ*, Δ) is smaller for a longer lead time Δ, as shown in **Figure 6**. This smaller error growth rate for a longer lead time is because TC intensity is bounded by the maximum equilibrium. Therefore, a long forecast lead time Δ must eventually result in a reduced error growth rate, as seen from **Eq. 7** as TC intensity approaches the MPI limit Kieu et al. (2018), consistent with what was shown in **Figure 6**.

For the RIC method, a very similar behavior of *err* (*τ*, Δ) is captured, with the maximum rate during the pre-conditioning period, followed by a decrease during rapid intensification and a stable value at the MPI limit (**Figure 7**). This similar behavior between the RIC and RF representations suggests that different error growth rates at different stages of TC development are inherent to TC dynamics, regardless of the presence of random noise in the initial condition or forcing.

Regarding the RP method, one notices somewhat different behaviors of *err* (*τ*, Δ) compared to the RIC or RF methods, depending on which model parameters are used and whether the RP method employs the initial or time-varying implementation (**Figure 8**). For the initial RP approach, the overall properties of *err* (*τ*, Δ) for the static stability parameter *s* are almost the same as those with the RF or RIC method. In other words, the maximum error growth rate occurs during the pre-conditioning period, followed by a decreasing period and level off at the MPI equilibrium (**Figure 8A**). In contrast, both SST and surface drag parameters show a quick increase in the error growth rate at first but then maintain a large error growth rate during the entire subsequent stage of TC development, instead of subsiding over time as for the RF or RIC method. This unique behavior of *err* (*τ*, Δ) for T_s and C_d is because the uncertainty magnitude of these parameters is much larger than that of *s* at the equilibrium, even though the relative percentage is the same. One can see this directly by looking at the sensitivity analyses for the initial RP method (see **Supplementary Appendix S1**). Apparently, the same 10% variability of each parameter would give a different absolute magnitude in the RP method. That is, a 10% variability of *s* would give an absolute uncertainty magnitude of 0.01, whereas the same 10% variability of T_s or C_d would result in an absolute uncertainty magnitude of 0.1. This explains the difference in the error growth rate at the mature stage, as shown in **Figure 8** for the initial RP implementation.

For the time-varying RP implementation, *err* (*τ*, Δ) is about one order of magnitude smaller than what was obtained from the initial RP method. Recall that such a large difference of *err* (*τ*, Δ) between the initial and time-varying RP approaches is not unique to the rapid intensification period. However, it is, in fact, true for the MPI equilibrium as well (cf. **Figure 4**). This is noteworthy because it suggests that both the RF and the initial RP methods produce more intensity errors than randomizing model parameters during the course of TC development. Again, this conclusion should be cautioned because it is drawn from a simple MSD system that may or may not fully reflect real TC development. Further verification of these results in the full-physics CM1 model will be presented in the following section.

4 CM1 MODEL RESULTS

Although the results obtained from the low-order MSD system are significant, various simplifications in the MSD model naturally raise the question of how much these results can be realized in real TCs. In this section, we examine similar properties of TC intensity error growth and saturation for the CM1 model,

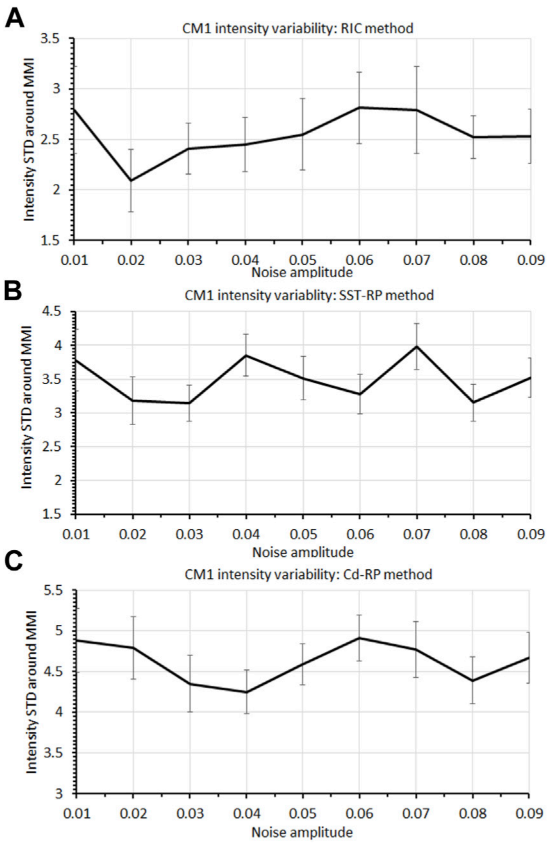

FIGURE 11 | Similar to **Figure 9B** but for **(A)** the RIC method, **(B)** the initial RP method with a random SST parameter, and **(C)** the initial RP method with a random C_d parameter obtained from the CM1 model.

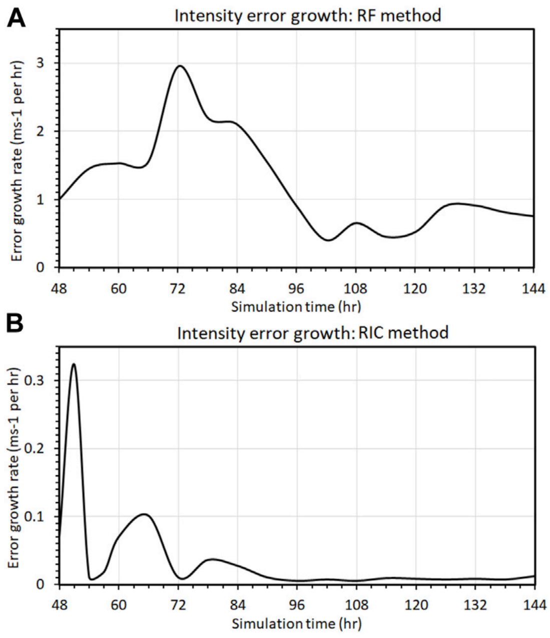

FIGURE 12 | (A) Dependence of the error growth rate (unit $ms^{-1}perhr$) on the stage of TC development for the 12 h lead time obtained from the RF implementation for the CM1 model; and **(B)** similar to **(A)** but for the RIC implementation.

using the same random representation methods as for the MSD system. Unlike the MSD model, it should be emphasized that the CM1 model does not converge to a single MPI equilibrium (**Figure 9A**), even with the axisymmetric setting. Instead, CM1 reaches a statistical quasi-equilibrium state due to the possible existence of low-dimensional chaos at the MPI limit that the MSD model cannot capture, as mentioned in **Section 2.2** (Kieu and Moon, 2016; Kieu et al., 2018). Thus, the MPI equilibrium must be now understood in a statistical sense for all analyses in this section.

4.1 Intensity Variability at the MPI Equilibrium

Figure 9B shows the standard deviation of TC intensity fluctuation (hereinafter denoted as Γ_{MMI} to distinguish from Γ obtained from the MSD system) as a function of noise amplitudes in the RF simulation, which is averaged during the CM1 quasi-stationary maximum intensity (MMI[2]) stage. With more realistic physics, in **Figure 9B**, one notices that the intensity variability tends to increase with the amplitude of stochastic forcing, similar to what was obtained from the MSD model. This result may seem at first somewhat trivial, but it is very noteworthy. Indeed, such an increase in Γ_{MMI} indicates that stochastic forcing can actually introduce further variability to TC intensity, even in the presence of possible low-dimensional chaos at the MMI equilibrium. Sugihara et al. (1994) (NKF) discussed that stochastic and chaotic variability are generally different because deterministic chaos can exist without any stochastic forcing. The fact that Γ_{MMI} increases with random noise amplitude, as shown in **Figure 9B**, suggests that stochastic forcing could contribute to intensity errors at long lead times beyond the chaotic dynamics if the stochastic forcing is sufficiently large.

For the RP method, different intensity variability between T_s and C_d is captured (**Figure 10**). For T_s, both MMI and Γ_{MMI} increase with SST, consistent with previous studies (Keshavamurthy and Kieu, 2021). While the increase in MMI with T_s is well understood, the increase in Γ_{MMI} with T_s is of note here, as it indicates that a warmer SST would also result in higher uncertainty for intensity forecast (Kieu and Moon, 2016; Keshavamurthy and Kieu, 2021).

In contrast, the surface drag coefficient shows a decrease of MMI for a larger C_d as generally expected, yet Γ_{MMI} first decreases and then increases with C_d (**Figure 10D**). This unique behavior of intensity variability in the C_d experiment is due to the dual role of C_d in determining both the MMI and the uncertainty. In other words, when C_d increases from a small value, it will reduce both MMI and the fluctuation around the MMI due to the nature of the frictional forcing against motion. When C_d is sufficiently large, MMI is, however, too weak; it is no longer able to "trap" the intensity

---

[2] It should be noted that the actual CM1 model maximum intensity (MMI) is generally different from the theoretical MPI value.

fluctuation. Therefore, the fluctuation of intensity around the MMI equilibrium becomes larger, as discussed in NKF.

Given such dependence of MMI and the variability around MMI on T_s and C_d in the RP method, **Figures 11B–C** show how Γ_{MMI} depends on the random noise amplitude of T_s and C_d in the CM1 model. Herein, we present results only for the initial RP approach because the time-varying RP method produces a much smaller intensity variability compared to the initial RP method in the CM1 model.

Unlike the MSD model, Γ_{MMI} does not seem to increase with the noise amplitude for the initial RP method. The same is true for the RIC method when increasing the random noise amplitude of initial conditions, capturing no change in Γ_{MMI}, as seen in **Figure 11A**. Such resilience of the intensity variability at the MMI equilibrium for both the RIC and RP methods reflects the fact that this equilibrium is not a point-like equilibrium as in the MSD model. However, it may contain a chaotic attractor of TC dynamics that randomizing model parameters or initial conditions does not help. Consequently, the fluctuation of MMI at the equilibrium is no longer linearly dependent on the random fluctuation of initial conditions or model parameters as in the MSD system. In this regard, the CM1 results shown in **Figure 11** imply that long-term intensity errors in full-physics models may be subject to less of an impact caused by vortex initialization uncertainties or random model parameters/truncation errors, compared to the intrinsic variability of TC dynamics (Du et al., 2013; Kieu et al., 2021).

4.2 Intensity Error Growth

Along with the intensity error saturation, it is important to also validate the characteristics of the intensity error growth obtained from the MSD model. Unlike the MSD model, in which one can add random noise for any representation method in studying error growth, the CM1 model has strong constraints on the model design and numerical stability that prevent one from adding random noise arbitrarily. Therefore, we examine in this section the error growth in the CM1 model only for the RF and RIC methods.

Figure 12A shows the error growth rate for the RF method obtained from the CM1 model between 48 and 180 h into integration (cf. **Figure 9**). For this RF method, the CM1 error growth rate confirms what was obtained from the MSD model, with a larger error growth rate during rapid intensification and much slower growth during the quasi-stationary stage. Detailed comparison of **Figures 9**, **12** shows that the peak in the error growth rate occurs, however, around $t = 72h$ in the CM1 model, which is after the onset of TC rapid intensification, whereas the maximum error growth in the MSD model is prior to the onset of rapid intensification (cf. **Figure 7**). Although this behavior of error growth in the CM1 model is difficult to be explained due to the more complex nature of TC nonlinear dynamics, it could reflect the fact that the onset of TC rapid intensification in the full-physics model is generally less well-defined than that in the MSD model in the presence of stochastic forcing. Thus, any perturbation introduced into the model may be smoothed out until the model vortex enters its rapid intensification period. Of course, this is more or less speculation at this point because there is no effective way to isolate the smoothing effect in the CM1 model. However, it highlights some difficulty when analyzing error growth in full-physics models such as CM1, which is absent in the MSD model.

In contrast to the RF method, the error growth in the RIC method captures somewhat more consistent growth rate characteristics compared to the MSD model, with the largest growth rate prior to the onset of rapid intensification (**Figure 12B**). Moreover, the growth rate also subsides over time and becomes stabilized during the MMI stage. This result also accords with the idealized experiments and real-time intensity verification presented in Kieu et al. (2018) and Keshavamurthy and Kieu (2021), thus supporting 1) larger uncertainty of intensity forecast during TC rapid intensification and 2) the existence of chaotic attractor at the MMI stage.

It should be noted again that the implementation of the RIC method in the CM1 model, by design, does not include stochastic forcing as in the RF method. Thus, the error growth in the RIC experiments with either the CM1 or the MSD model resulted merely from the spread of perturbations under the TC deterministic dynamics, which possesses more well-defined onset of rapid intensification compared to the RF implementation. In this regard, the intensity error growth in the RIC experiment shown in **Figure 11** could truly reflect the behaviors of intensity variability related to the initial condition uncertainty prior to, during, and after TC rapid intensification, similar to the TC dynamics in the MSD model.

5 CONCLUSION

This study examined different methods to represent stochastic processes in TC development, using a fidelity-reduced TC model and a full-physics model. With the focus on TC intensity variability at the equilibrium and the intensity error growth during TC rapid intensification, several significant results have been obtained from both the theoretical and numerical perspectives.

First, our series of Monte Carlo simulations for the fidelity-reduced model based on the TC-scale dynamics (MSD) showed that the random forcing method in which the model forcing is augmented by a stochastic term results in the largest fluctuation of TC intensity at the maximum potential intensity (MPI) limit compared to randomizing either initial conditions or model parameters. In addition, the response of TC intensity to the random forcing method increases with the random noise amplitude, and it is dominated by the tangential wind and warm-core anomaly components, as reported in NKF.

Second, a similar response of TC intensity variability to random noise was also observed for the random parameter method, but the response depends sensitively on how one randomizes model parameters. For the initial random parameter approach in which the model parameters are randomized only at the initial time, TC intensity variability at the MPI limit increases almost linearly with the noise amplitude. For the time-varying random parameter method in which the model parameters are randomized every time step, the intensity fluctuation is one order of magnitude smaller than the initial random parameter method. Such behaviors of TC intensity variability at the MPI limit are consistent with those obtained from stochastic linear models and reveal the importance of how one implements random model parameters in TC models.

Regarding the intensity error growth during TC development, it was found that the error growth rate in the MSD model peaks right before the onset of rapid intensification and then gradually subsides during the intensification period before leveling off at the MPI equilibrium. This characteristic of TC intensity error growth was captured for all random representation methods, except for the initial random parameter methods with two specific parameters T_s (sea surface temperature) and C_d (the surface drag coefficient), due to their unique role in the MPI equilibrium. Specifically the random variation of these two parameters produces an overall larger intensity error growth rate at the MPI limit, which is not applied to other parameters or random methods.

Third, to verify the results obtained from the fidelity-reduced MSD model, cloud-resolving simulations with the CM1 model were conducted. By implementing the same random representation methods for the CM1 axisymmetric configuration, it was confirmed that random forcing plays the most significant role in the overall variability of TC intensity and the intensity error growth during TC development. The CM1 model experiments also confirmed that the random initial condition tends to be more effective during the early stage of TC development but becomes less significant relative to either the random parameter or random forcing method at the later stage of TC development. The findings obtained from both the MSD and CM1 models highlight the importance of choosing a proper random forcing method to represent the variability of TC intensity in operation.

Two major differences between the MSD and the CM1 model that could strongly affect the analyses of TC intensity variability should be noted here. First, unlike the MSD model, which contains a single stable MPI point with no chaos, CM1 possesses some classical chaotic behaviors at the MPI equilibrium similar to other full-physics models (Kieu and Moon, 2016; Keshavamurthy and Kieu, 2021, NKF). While the existence of this chaotic MPI attractor is still elusive, its potential existence is needed to explain the larger intensity variability in the CM1 model, even in the absence of all stochastic forcings. The results shown in **Figure 11** may therefore display the variability of TC intensity due mostly to chaotic dynamics rather than purely random noise as discussed in NKF. The relative contribution between chaotic and stochastic variability is unknown at present, as the CM1 model does not allow for large random noise amplitudes.

The second difference between MSD and CM1 is that the maximum intensity equilibrium in CM1 is sensitive to model configuration and physical parameterizations that may or may not be maintained during arbitrarily long simulation. Unlike the low-order MSD model for which a fixed environment is always assumed, CM1 simulates a TC vortex in a finite domain. Without proper physical schemes such as radiative parameterization or lateral boundary condition adjustment, the model domain will be eventually affected by the subsidence warming in the outer region, thus changing the TC environment and causing the model to spin down. In this regard, the analyses of TC intensity at the maximum intensity equilibrium contain some uncertainty that one has to resolve in future studies before a more definite conclusion of intrinsic TC intensity variability can be obtained.

DATA AVAILABILITY STATEMENT

The original contributions presented in the study are included in the article/**Supplementary Material**. Further inquiries can be directed to the corresponding author.

AUTHOR CONTRIBUTIONS

CK perceived the idea and designed experiments. W-TLF carried out mathematical analyses. MP performed simulations and analyses. All authors contributed to the writing of the manuscript.

FUNDING

This research was partially supported by ONR Awards N000141812588.

ACKNOWLEDGMENTS

CK wishes to thank the NOAA Geophysical Fluid Dynamics Laboratory and Princeton University for their support and hospitality during the sabbatical period that this work was prepared. The authors wish to also thank two anonymous reviewers for their suggestions and comments, which have helped improve this work.

SUPPLEMENTARY MATERIAL

The Supplementary Material for this article can be found online at: https://www.frontiersin.org/articles/10.3389/feart.2022.893781/full#supplementary-material

REFERENCES

Aberson, S. D., Aksoy, A., Sellwood, K. J., Vukicevic, T., and Zhang, X. (2015). Assimilation of High-Resolution Tropical Cyclone Observations with an Ensemble Kalman Filter Using HEDAS: Evaluation of 2008–11 HWRF Forecasts. *Mon. Wea. Rev.* 143, 511–523. doi:10.1175/mwr-d-14-00138.1

Aksoy, A., Aberson, S. D., Vukicevic, T., Sellwood, K. J., Lorsolo, S., and Zhang, X. (2013). Assimilation of High-Resolution Tropical Cyclone Observations with an Ensemble Kalman Filter Using NOAA/AOML/HRD's HEDAS: Evaluation of the 2008–11 Vortex-Scale Analyses. *Mon. Wea. Rev.* 141, 1842–1865. doi:10.1175/mwr-d-12-00194.1

Arakawa, A., and Schubert, W. H. (1974). Interaction of a Cumulus Cloud Ensemble with the Large-Scale Environment, Part I. *J. Atmos. Sci.* 31, 674–701. doi:10.1175/1520-0469(1974)031<0674:ioacce>2.0.co;2

Breil, M., and Schädler, G. (2017). Quantification of the Uncertainties in Soil and Vegetation Parameterizations for Regional Climate Simulations in Europe. *J. Hydrometeorol.* 18, 1535–1548. doi:10.1175/JHM-D-16-0226.1

Brown, B. R., and Hakim, G. J. (2013). Variability and Predictability of a Three-Dimensional Hurricane in Statistical Equilibrium. *J. Atmos. Sci.* 70, 1806–1820. doi:10.1175/JAS-D-12-0112.1

Bryan, G. H., and Fritsch, J. M. (2002). A Benchmark Simulation for Moist Nonhydrostatic Numerical Models. *Mon. Wea. Rev.* 130, 2917–2928. doi:10.1175/1520-0493(2002)130<2917:absfmn>2.0.co;2

Christensen, H. M. (2020). Constraining Stochastic Parametrisation Schemes Using High-resolution Simulations. *Q.J.R. Meteorol. Soc.* 146, 938–962. doi:10.1002/qj.3717

Christensen, H. M., Moroz, I. M., and Palmer, T. N. (2015). Stochastic and Perturbed Parameter Representations of Model Uncertainty in Convection Parameterization*. *J. Atmos. Sci.* 72, 2525–2544. doi:10.1175/jas-d-14-0250.1

Doblas-Reyes, F. J., Weisheimer, A., Déqué, M., Keenlyside, N., McVean, M., Murphy, J. M., et al. (2009). Addressing Model Uncertainty in Seasonal and Annual Dynamical Ensemble Forecasts. *Q. J. R. Meteorol. Soc.* 135, 1538–1559. doi:10.1002/qj.464

Dorrestijn, J., Crommelin, D. T., Siebesma, A. P., and Jonker, H. J. J. (2015). Stochastic Parameterization of Convective Area Fractions with a Multicloud Model Inferred from Observational Data. *J. Atmos. Sci.* 72, 854–869. doi:10.1175/jas-d-14-0110.1

Du, T. D., Ngo-Duc, T., Hoang, M. T., and Kieu, C. Q. (2013). A Study of Connection between Tropical Cyclone Track and Intensity Errors in the Wrf Model. *Meteor. Atmos. Phys.* 122, 55–64. doi:10.1007/s00703-013-0278-0

Fan, W.-T., Jolly, M., and Pakzad, A. (2021a). Three-dimensional Shear Driven Turbulence with Noise at the Boundary. *Nonlinearity* 34, 4764–4786. doi:10.1088/1361-6544/abf84b

Fan, W.-T., Kieu, C., Sakellariou, D., and Patra, M. (2021b). Hitting Time of Rapid Intensification Onset in Hurricane-like Vortices. *Phys. Fluids* 33, 096603. doi:10.1063/5.0062119

Gopalakrishnan, S. G., Marks, F., Zhang, X., Bao, J.-W., Yeh, K.-S., and Atlas, R. (2011). The Experimental HWRF System: A Study on the Influence of Horizontal Resolution on the Structure and Intensity Changes in Tropical Cyclones Using an Idealized Framework. *Mon. Wea. Rev.* 139, 1762–1784. doi:10.1175/2010mwr3535.1

Hakim, G. J. (2011). The Mean State of Axisymmetric Hurricanes in Statistical Equilibrium. *J. Atmos. Sci.* 68, 1364–1376. doi:10.1175/2010jas3644.1

Halperin, D. J., and Torn, R. D. (2018). Diagnosing Conditions Associated with Large Intensity Forecast Errors in the Hurricane Weather Research and Forecasting (HWRF) Model. *Weather Forecast.* 33, 239–266. doi:10.1175/WAF-D-17-0077.1

Hamill, T. M., Whitaker, J. S., Kleist, D. T., Fiorino, M., and Benjamin, S. G. (2011). Predictions of 2010's Tropical Cyclones Using the GFS and Ensemble-Based Data Assimilation Methods. *Mon. Wea. Rev.* 139, 3243–3247. doi:10.1175/mwr-d-11-00079.1

Kain, J. S., and Fritsch, J. M. (1990). A One-Dimensional Entraining/detraining Plume Model and its Application in Convective Parameterization. *J. Atmos. Sci.* 47, 2784–2802. doi:10.1175/1520-0469(1990)047<2784:aodepm>2.0.co;2

Keshavamurthy, K., and Kieu, C. (2021). Dependence of Tropical Cyclone Intrinsic Intensity Variability on the Large-scale Environment. *Q.J.R. Meteorol. Soc.* 147, 1606–1625. doi:10.1002/qj.3984

Kieu, C., Evans, C., Jin, Y., Doyle, J. D., Jin, H., and Moskaitis, J. (2021). Track Dependence of Tropical Cyclone Intensity Forecast Errors in the COAMPS-TC Model. *Weather Forecast.* 36, 469–485. doi:10.1175/waf-d-20-0085.1

Kieu, C. (2015). Hurricane Maximum Potential Intensity Equilibrium. *Q.J.R. Meteorol. Soc.* 141, 2471–2480. doi:10.1002/qj.2556

Kieu, C., Keshavamurthy, K., Tallapragada, V., Gopalakrishnan, S., and Trahan, S. (2018). On the Growth of Intensity Forecast Errors in the Operational Hurricane Weather Research and Forecasting (HWRF) Model. *Q. J. R. Meteorol. Soc.* 144, 1803–1819. doi:10.1002/qj.3344

Kieu, C. Q., and Moon, Z. (2016). Hurricane Intensity Predictability. *Bull. Amer. Meteor. Soc.* 97, 1847–1857. doi:10.1175/BAMS-D-15-00168.1

Kieu, C. Q., and Wang, Q. (2018). On the Scale Dynamics of the Tropical Cyclone Intensity. *Discrete Continuous Dyn. Syst. - B* 23, 3047. doi:10.3934/dcdsb.2017196

Kieu, C., and Wang, Q. (2017). Stability of the Tropical Cyclone Intensity Equilibrium. *J. Atmos. Sci.* 74, 3591–3608. doi:10.1175/jas-d-17-0028.1

Kurihara, Y., Bender, M. A., Tuleya, R. E., and Ross, R. J. (1995). Improvements in the GFDL Hurricane Prediction System. *Mon. Wea. Rev.* 123, 2791–2801. doi:10.1175/1520-0493(1995)123<2791:iitghp>2.0.co;2

Liu, Q., Marchok, T., Pan, H., Bender, M., and Lord, S. (2000). Improvements in Hurricane Initialization and Forecasting at Ncep with Global and Regional (GFDL) Models. *Proced. Bull.* 472. NCEP/EMC. [Available at NOAA/NWS, 1325 East–West Highway, Silver Spring, MD 20910 at: http://205.156.54.206/om/tpb/472.htm.

Nguyen, P., Kieu, C., and Fan, W.-T. L. (2020). Stochastic Variability of Tropical Cyclone Intensity at the Maximum Potential Intensity Equilibrium. *J. Atmos. Sci.* 77(9), 3105–3118. doi:10.1175/jas-d-20-0070.1

Palmer, T. N. (2001). A Nonlinear Dynamical Perspective on Model Error: A Proposal for Non-local Stochastic-Dynamic Parametrization in Weather and Climate Prediction Models. *Q.J R. Met. Soc.* 127, 279–304. doi:10.1002/qj.49712757202

Palmer, T. N. (2012). Towards the Probabilistic Earth-System Simulator: A Vision for the Future of Climate and Weather Prediction. *Q.J.R. Meteorol. Soc.* 138, 841–861. doi:10.1002/qj.1923

Plant, R. S., and Craig, G. C. (2008). A Stochastic Parameterization for Deep Convection Based on Equilibrium Statistics. *J. Atmos. Sci.* 65, 87–105. doi:10.1175/2007jas2263.1

Rappin, E. D., Nolan, D. S., and Majumdar, S. J. (2013). A Highly Configurable Vortex Initialization Method for Tropical Cyclones. *Mon. Weather Rev.* 141, 3556–3575. doi:10.1175/MWR-D-12-00266.1

Richter, D. H., Wainwright, C., Stern, D. P., Bryan, G. H., and Chavas, D. (2021). Potential Low Bias in High-Wind Drag Coefficient Inferred from Dropsonde Data in Hurricanes. *J. Atmos. Sci.* 78, 2339–2352. doi:10.1175/JAS-D-20-0390.1

Song, Y., Wikle, C. K., Anderson, C. J., and Lack, S. A. (2007). Bayesian Estimation of Stochastic Parameterizations in a Numerical Weather Forecasting Model. *Mon. Weather Rev.* 135, 4045–4059. doi:10.1175/2007MWR1928.1

Sugihara, G., Grenfell, B. T., May, R. M., and Tong, H. (1994). Nonlinear Forecasting for the Classification of Natural Time Series. *Phil. Trans. R. Soc. Lond. A* 348, 477–495. doi:10.1098/rsta.1994.0106

Suhas, E., and Zhang, G. J. (2014). Evaluation of Trigger Functions for Convective Parameterization Schemes Using Observations. *J. Clim.* 27, 7647–7666. doi:10.1175/jcli-d-13-00718.1

Tallapragada, V., Bernardet, L., Gopalakrishnan, S., Kwon, Y., Liu, Q., Marchok, T., et al. (2012). Hurricane Weather Research and Forecasting (HWRF) Model: 2012 Scientific Documentation. *Dev. Testbed Cent.* 142(11), 4308–4325. doi:10.1175/MWR-D-13-00010.1

Tong, M., Sippel, J. A., Tallapragada, V., Liu, E., Kieu, C., Kwon, I.-H., et al. (2018). Impact of Assimilating Aircraft Reconnaissance Observations on Tropical Cyclone Initialization and Prediction Using Operational HWRF and GSI Ensemble-Variational Hybrid Data Assimilation. *Mon. Weather Rev.* 146, 4155–4177. doi:10.1175/MWR-D-17-0380.1

Trabing, B. C., and Bell, M. M. (2020). Understanding Error Distributions of Hurricane Intensity Forecasts during Rapid Intensity Changes. *Weather Forecast.* 35, 2219–2234. doi:10.1175/WAF-D-19-0253.1

Van Nguyen, H., and Chen, Y.-L. (2011). High-resolution Initialization and Simulations of Typhoon Morakot (2009). *Mon. Wea. Rev.* 139, 1463–1491. doi:10.1175/2011mwr3505.1

Weisheimer, A., Palmer, T. N., and Doblas-Reyes, F. J. (2011). Assessment of Representations of Model Uncertainty in Monthly and Seasonal Forecast Ensembles. *Geophys. Res. Lett.* 38, a–n. doi:10.1029/2011GL048123

Zhang, F., and Weng, Y. (2015). Predicting Hurricane Intensity and Associated Hazards: A Five-Year Real-Time Forecast Experiment with Assimilation of Airborne Doppler Radar Observations. *Bull. Amer. Meteor. Soc.* 96, 25–33. doi:10.1175/bams-d-13-00231.1

Zhang, J. A. (2010). Estimation of Dissipative Heating Using Low-Level *In Situ* Aircraft Observations in the Hurricane Boundary Layer. *J. Atmos. Sci.* 67, 1853–1862. doi:10.1175/2010jas3397.1

Zhang, J. A., Marks, F. D., Montgomery, M. T., and Lorsolo, S. (2011). An Estimation of Turbulent Characteristics in the Low-Level Region of Intense Hurricanes Allen (1980) and Hugo (1989). *Mon. Wea. Rev.* 139, 1447–1462. doi:10.1175/2010MWR3435.1

Zhang, Z., Tallapragada, V., Kieu, C., Trahan, S., and Wang, W. (2015). HWRF Based Ensemble Prediction System Using Perturbations from GEFS and Stochastic Convective Trigger Function. *Trop. Cyclone Res. Rev.* 3, 145–161. doi:10.6057/2014TCRR03.02

Zou, X., and Tian, X. (2018). Hurricane Warm-Core Retrievals from AMSU-A and Remapped ATMS Measurements with Rain Contamination Eliminated. *J. Geophys. Res. Atmos.* 123, 829. doi:10.1029/2018JD028934

Conflict of Interest: The authors declare that the research was conducted in the absence of any commercial or financial relationships that could be construed as a potential conflict of interest.

frontiers | Frontiers in Earth Science

ORIGINAL RESEARCH
published: 28 June 2022
doi: 10.3389/feart.2022.945058

Wind Gusts Associated with Tornado-Scale Vortices in the Tropical Cyclone Boundary Layer: A Numerical Simulation

Qingyuan Liu[1,2], Liguang Wu[3]*, Nannan Qin[2,3], Jinjie Song[1,2] and Na Wei[1,2]

[1]Key Laboratory of Transportation Meteorology of China Meteorological Administration, Nanjing Joint Institute for Atmospheric Sciences, Nanjing, China, [2]State Key Laboratory of Severe Weather, Chinese Academy of Meteorological Sciences, Beijing, China, [3]Department of Atmospheric and Oceanic Sciences and Institute of Atmospheric Sciences, Fudan University, Shanghai, China

It has been demonstrated that the tornado-scale vortex (TSV) is one of the fine-scale structures associated with extreme updrafts in the tropical cyclone boundary layer (TCBL), but the relationship between surface wind gusts and TSVs is still unclear. In this study, the one-second model output simulated in the Weather Research and Forecast (WRF) model with the large eddy simulation (WRF-LES) is used to investigate the relationships between TSVs and surface wind gusts. Results show that surface wind gust factors in the regions where TSVs are prevalent are significantly larger than those in other regions. 88% of the maximum gust factors associated with TSVs (vertical velocity larger than 20 m s^{-1}) are larger than 1.25 (gust factors larger than 1.25 account for only 1% of the 1-min gust factors in the TC inner core), and the mean maximum 1-min gust factor associated with a TSV is larger than 1.3, while the mean 1-min gust factor in the TC inner core is only 1.1. The surface gust factors associated with TSVs in tropical cyclone eyewall can reach about 1.8, which can cause severe surface wind hazards. This study suggests that potential risk will increase in the regions where TSVs are prevalent because of the large wind gusts and gust factors. Finer real-time observations are needed to monitor the evolution of TSVs for improving the operational TC-related surface gust warnings.

Keywords: tropical cyclone, tropical cyclone boundary layer, large-eddy simulation (LES), tornado-scale vortices, gust factor

Edited by:
Kevin Cheung,
E3-Complexity Consultant, Australia

Reviewed by:
Qingqing Li,
Nanjing University of Information Science and Technology, China
Xu Lu,
University of Oklahoma, United States

***Correspondence:**
Liguang Wu
liguangwu@fudan.edu.cn

Specialty section:
This article was submitted to Atmospheric Science, a section of the journal Frontiers in Earth Science

Received: *16 May 2022*
Accepted: *09 June 2022*
Published: *28 June 2022*

Citation:
Liu Q, Wu L, Qin N, Song J and Wei N (2022) Wind Gusts Associated with Tornado-Scale Vortices in the Tropical Cyclone Boundary Layer: A Numerical Simulation. Front. Earth Sci. 10:945058. doi: 10.3389/feart.2022.945058

INTRODUCTION

The landing of tropical cyclones (TCs) are often accompanied by strong gusts and heavy rainfall, and can even cause mudslides, landslides, and many other disasters, posing a great threat to the lives and property near the coastlines (Pielke and Landsea, 1998; Pielke et al., 2008; Zhang et al., 2009; Liang et al., 2021; Wang et al., 2021; Zhao et al., 2022). Significant variability in damage patterns has been found after the passing of intense TCs, which indicates that the damage caused by TC is not only related to the sustained strong wind but also the localized strong gusts (Wakimoto and Black, 1994; Wurman and Kosiba, 2018). Since the mechanisms on the generation and evolution of strong wind gusts are complicated and have not been fully understood, wind gust forecast is a major challenge for disaster prevention and mitigation in coastlines affected by TCs (Krayer and Marshall, 1992; Black et al., 1999; Harper et al., 2010; Wurman and Kosiba, 2018).

The peak 3-s average wind within a period is typically defined as a "gust". The "gust factor" is a conversion between an estimate of the mean wind speed and the expected highest gust wind speed of a given duration (e.g. 10-min, 5-min, 2-min, 1-min, etc.). The gust factor is an important parameter to describe the characteristics of turbulence (Harper et al., 2010). Wind loads that determine the capability of wind resistances require consideration of gusts and gust factors (American Society of Civil Engineers, 2013). The characteristics of gust and gust factors with the impacts of TCs have been studied in observational studies (Paulsen and Schroeder, 2005; Vickery and Skerlj, 2005; Schroeder et al., 2009). It is found that the gust factor tends to decrease as the mean wind speed increases (Vickery and Skerlj, 2005; Schroeder et al., 2009). The influence of topography on the gust factor during TC landfall has been well studied and the gust tends to be higher due to the effect of topography (Paulsen and Schroeder, 2005; Vickery and Skerlj, 2005; Schroeder et al., 2009). In addition, extreme gusts and gust factors within the TC boundary layer (TCBL) are found in many observational studies (Black et al., 1999; Haper et al., 2010; Wurman and Kosiba 2018). A station at Barrow Island in Western Australia recorded the time series of winds when Hurricane Olivia (1996) passed through the island (Black et al., 1999). The results show that the 3-s average gusts were up to 113 m s^{-1} at 10 m height, with a 5-min gust factor of 2.75 (Black et al., 1999). Extreme gusts were also recorded at the station during the landfall of Hurricane Orson (1989), with extreme gusts reaching more than twice the value of the average wind speed (Harper et al., 2010). They believed that the extreme gusts and gust factors near the eyewall are caused by the small-scale vortices that are associated with extreme downdrafts (Powell et al., 1991; Powell et al., 1996; Black et al., 1999; Harper et al., 2010). Recently, Wurman and Kosiba (2018) found that the surface wind oscillations near the eyewall of Hurricance Harvey (2017) can reach about 30 m s^{-1} compared with the sustained wind speed based on the winds recorded in the weather station. In addition, the 1-min gust factor is larger than 1.5, which is much larger than that (1.11) suggested by the WMO (World Meteorological Organization, Harper et al., 2010). Wurman and Kosiba (2018) analyzed the fine-scale structures on the radar imagery and they believed that the extreme gusts and gust factors can be caused by tornado-scale vortices (TSVs). The TSV is one of the typical fine-scale structures in the TCBL observed by aircraft observations, dropsondes, and doppler radars (Aberson et al., 2006; Marks et al., 2008; Stern et al., 2016; Wurman and Kosiba, 2018). TSVs are usually located inside the TC eyewall and are associated with extreme updrafts and downdrafts, and strong vertical vorticity.

Our understanding of the TCBL process in TC intensity change and structure evolution has been improved with the advances in observational technology, computational power, and numerical models (Willoughby, 1990; Smith, 2003; Bell and Montgomery, 2008; Smith and Montgomery, 2010; Zhang and Montgomery, 2012; Ma and Fei, 2022; Li et al., 2022). The fine-scale (less than 1000 m) features have been explicitly simulated over the past decade (Zhu, 2008; Rotunno et al., 2009; Zhu et al., 2013; Green and Zhang, 2015; Qin and Zhang, 2018; Stern and Bryan, 2018; Wu et al., 2018; Wu et al., 2019; Zheng et al., 2020; Feng et al., 2021; Liu et al., 2021; Qin et al., 2021; Xu et al., 2021; Xu and Wang, 2021). The TSVs occurring inside the TC eyewall can be resolved with the grid spacing of 37 m in the Weather Research and Forecast (WRF) model with the LES (Wu et al., 2018; Wu et al., 2019; Feng et al., 2021; Liu et al., 2021). The three-dimensional structures of TSVs can also be represented in their numerical studies. The simulated TSVs often contain strong updraft/downdraft couplets and may cause strong localized surface winds. However, the characteristics of TSV-induced gusts and gust factors are still unclear since the model output is stored at one-hour intervals in previous numerical experiments (Wu et al., 2018; Wu et al., 2019; Feng et al., 2021; Liu et al., 2021). In this study, a numerical experiment with a horizontal grid spacing of 37 m is conducted using the WRF-LES framework. It should be noted that surface winds during a 22-min period are stored at 1-s intervals to calculate the surface gusts and gust factors. The objective of this study is to analyze the characteristics of surface gusts and gust factors in the TC inner core and examine wind gusts and gust factors associated with TSVs in the TCBL.

Numerical Experiment and Methods

Following, Wu and Chen, (2018), Wu and Chen, (2019), a semi-idealized numerical experiment is conducted with the WRF-LES framework. Here we briefly describe the settings of the numerical experiment. In this experiment, a TC evolved in a realistic low-frequency large-scale background in the western North Pacific and on an open ocean with a spatially uniform sea surface temperature (29°C). Seven domains are used in this experiment, including six interactive nesting domains with the horizontal grid spacing of 9 km, 3 km, 1 km, 333 m, 111 m, and 37 m. Five domains move with the TC center. The innermost domain covers the TC inner core with an area of 90 × 90 km^2. The model consists of 75 vertical levels (12 levels below 1 km) with a top of 50 hPa. The vertical grid spacing is about 70–100 m below 1 km and increases to ~400 m at 4 km. The model output is regularly stored at 1-h intervals. To investigate the characteristics of the surface gusts, surface winds at 10 m height during a 22-min period from the 30th hour of the simulation are stored at 1-s intervals, while the three-dimensional winds are outputted at 3-s intervals to identify the TSVs.

The TC center is determined with the algorithm from previous studies (Wu et al., 2006; Yang et al., 2020), in which the TC center is located until the maximum azimuthally-averaged tangential wind is found. The identification algorithm of TSVs in the numerical experiment is based on the specific threshold of vertical velocity and vorticity similar to that used in the previous studies (Wu et al., 2018; Wu et al., 2019; Feng et al., 2021; Liu et al., 2021). Since the innermost domain moves with the TC, the variables are all projected into a fixed reference

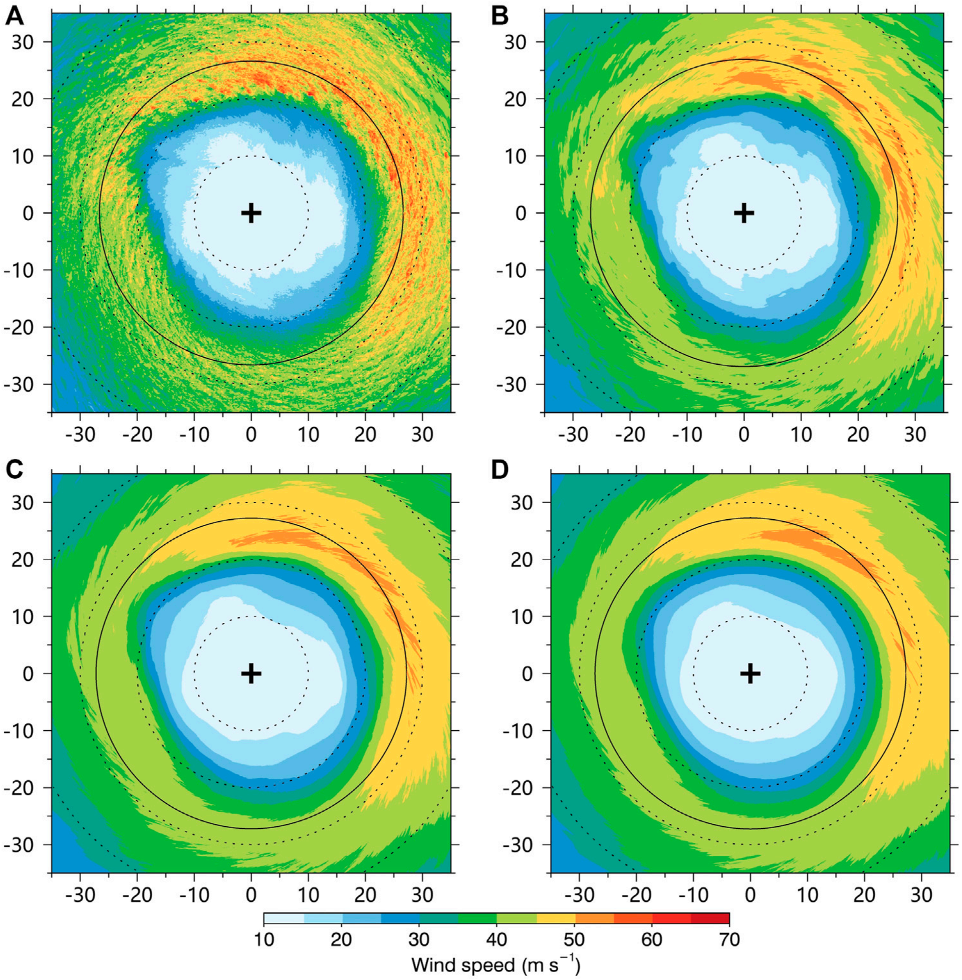

FIGURE 1 | (A) Instantaneous 10-m wind speed (m s^{-1}) at 9 min 30 s during the 22-min period. **(B)** 1-min mean 10-m wind speed (m s^{-1}) at 9min 30 s. **(C)** 5-min mean 10-m wind speed (m s^{-1}) at 9 min 30 s. **(D)** 5-min mean 10-m wind speed (m s^{-1}) at 9 min 30 s. The small cross in the figure is the TC center, the solid circle indicates the RMW. The vertical and horizontal axes indicate the relative distances (kilometers) from the TC center.

framework (overlapped domains within the 22-min) during the 22-min period.

RESULTS

TC Intensity in Terms of Surface Winds

Due to the β effect and the large-scale environmental steering flow (Holland, 1983; Wang and Holland, 1996), the TC moves north-northwestward during the 22-min period. The zonal component of moving speed is ~ −1 m s^{-1} and the meridional component of moving speed is ~4 m s^{-1}.

Figure 1 shows the instantaneous, 1-min, 5-min, and 10-min mean wind fields at 10-m height at 9min 30s during the 22-min period. Significant variability in the wind field at 10-m height can be seen in **Figure 1A**. The variabilities in the surface winds are caused by the fine-scale coherent structures, which have been studied in many observational and numerical studies (Wurman and Winslow, 1998; Morrison et al., 2005; Marks et al., 2008; Rotunno et al., 2009; Lorsolo et al., 2010; Foster, 2013; Gao and Ginis, 2014; Green and Zhang, 2015; Wu et al., 2018; Wurman and Kosiba, 2018; Wu et al., 2019; Liu et al., 2021). 1-min mean wind fields at 10-m height are shown in **Figure 1B**. We can see the variabilities are greatly smoothed in the 1-min mean wind field, although there are still some isolated regions with large values on the northern side of the TC eyewall. The 5-min and 10-min mean wind fields are further shown in **Figure 1C** and **Figure 1D**, respectively. It seems the variabilities have been fully removed in the 5-min and 10-min wind fields and there is no significant difference between them. The maximum wind speed in terms of instantaneous, 1-min, 5-min, and 10-min at this time is 73.7, 54.8, 51.5, and 51.4 m s^{-1}, respectively.

The TC intensities in terms of the instantaneous, 3-s mean, 1-min mean, 5-min mean, 10-min mean, and azimuthal-mean maximum wind speed are examined at the 10-m height (**Figure 2**). TC intensities in terms of the maximum instantaneous and 3-s mean wind speed are significantly larger than those of time-averaged intensities and azimuthal-mean

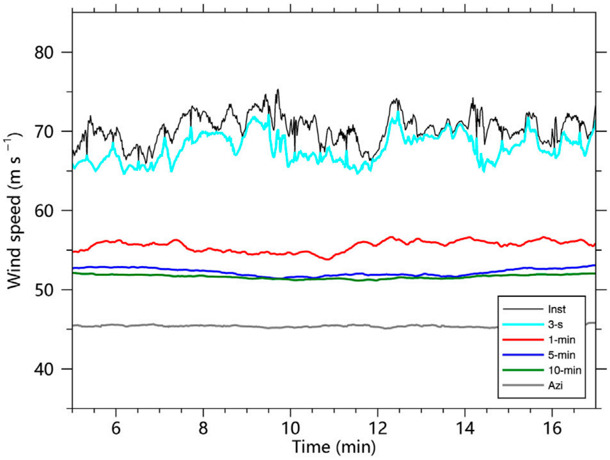

FIGURE 2 | TC intensities (m s^{-1}) in terms of instantaneous (black), 3-s mean (cyan), 1-min mean (red), 5-min mean (blue), 10-min mean (green), and azimuthally-averaged maximum wind speed at 10-m height.

intensity, which may be attributed to the coherent structures in the TCBL (Liu et al., 2021). In addition, the TC intensity in terms of azimuthal mean winds is only about 45 m s^{-1}, which is much smaller than the time-averaged intensities of the TC. This is mainly due to the significant asymmetric structure with the strong convection located on the northern side of the simulated TC (Wu et al., 2018; Wu et al., 2019). TC intensities in terms of 5-min and 10-min are very close to each other, ranging from 51 to 54 m s^{-1}. Although the 1-min mean intensity is slightly larger, the deviations from those of 5-min and 10-min during 22-min are less than 5 m s^{-1}. Harper et al. (2010) gave the ratio of intensity based on 10-min mean wind speed to 1-min mean wind speed as 0.93 from the observations. We calculate the ratio of 10-min intensity to 1-min intensity in the 22 min period, which is also exactly 0.93 and is in good agreement with observational studies. The mean intensity in terms of the maximum instantaneous and 3-s mean wind speed is 71 m s^{-1} and 68 m s^{-1}. The 3-s intensity is about 20% larger than the 1-min intensity and 30% larger than the 5-min intensity, indicating the extreme gust factors exist in the TC inner core at the surface.

Characteristics of the Surface Wind Gust Factors

The mean and maximum 1-min gust factors at 10-m height during the 22-min period are shown in **Figures 3A,B**. It should be noted that all gust factors are firstly calculated in the fixed coordinate, then mean and maximum factors are calculated at every single grid in the TC inner core during the 22-min period. Additionally, the gust factors are calculated when the mean wind speed is no less than 17 m s^{-1}. The surface wind speed larger than 17 m s^{-1} is usually called gale-force wind and the radius of gale-force wind has been widely used to define TC size due to its importance in determining TC potential impacts (Knaff et al., 2007; Wu et al., 2015). The gusts and gust factors corresponding to the mean gale-force wind are closely associated with the TC damages, while the gust factors corresponding to small mean winds are largely random and not very representative. So gust factors corresponding to mean winds less than 17 m s^{-1} are not included in our study. The horizontal distributions of the mean and maximum gust factors are asymmetric as shown in **Figure 3**, with large values in the northern part of the TC eyewall. From **Figure 3A**, we can see that the mean 1-min gust factor is 1.1 at a height of 10 m near the TC eyewall, but it can reach 1.15 on the northern side of the TC eyewall. We further calculate the mean

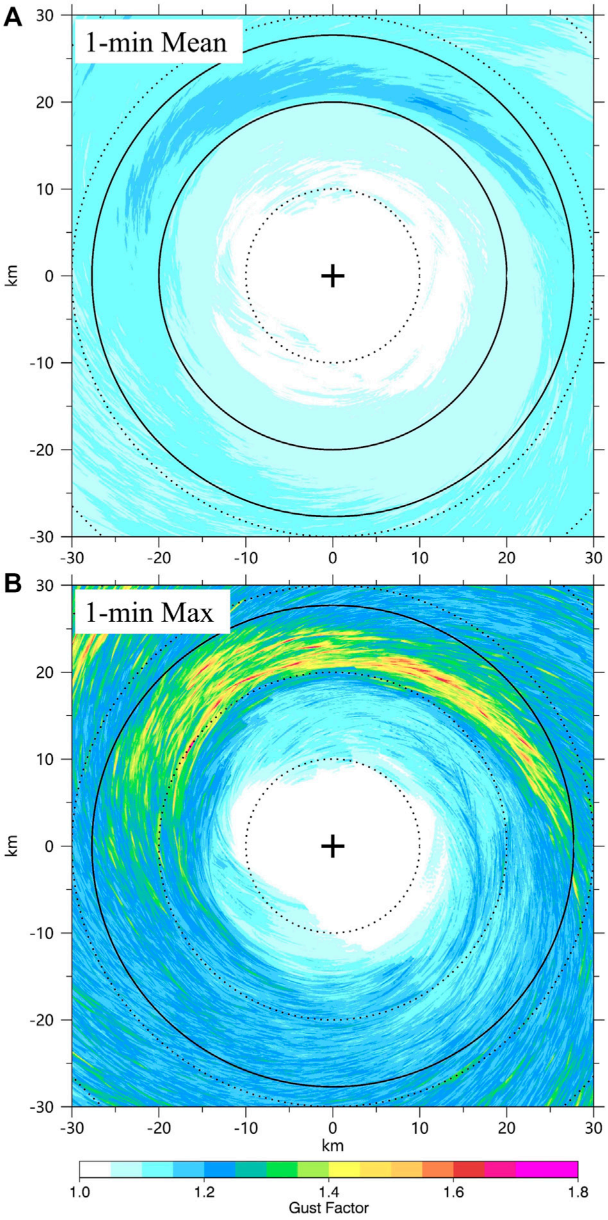

FIGURE 3 | Horizontal distributions of the mean 1-min gust factors **(A)** and maximum 1-min gust factors **(B)** during the 22-min period. The small cross in the figure is the TC center at the 11th minute, the solid circle indicates the RMW. The vertical and horizontal axes indicate the relative distances (kilometers) from the TC center.

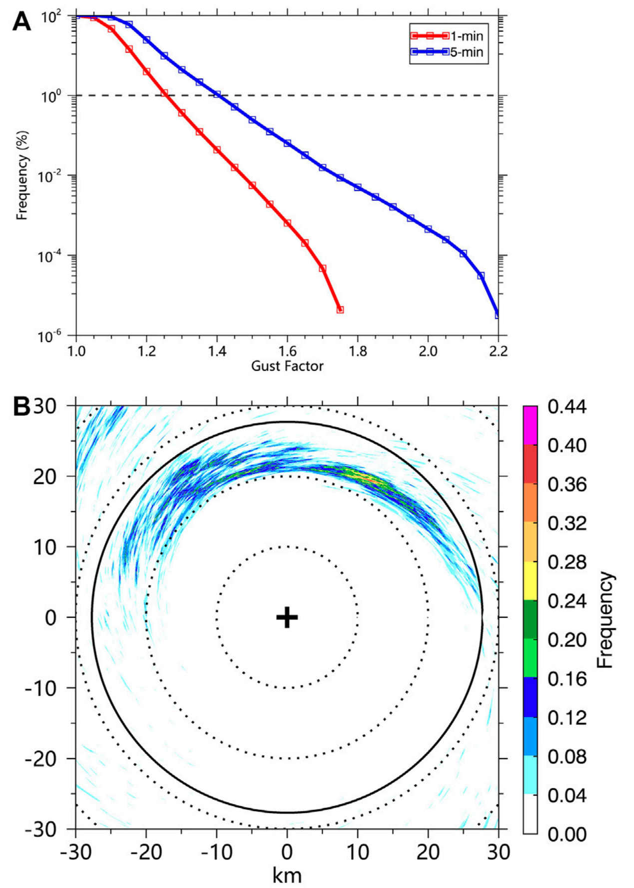

FIGURE 4 | (A) Empirical survival function of 1-min gust factors (red) and 5-min gust factors (blue) averaged in a 60 × 60 km box centered on the TC center over the 22-min period. **(B)** Horizontal distributions of frequencies of 1-min gust factors at every point that are not less than 1.25 during the 22-min period.

and maximum 5-min and 10-min gust factors in the TC inner core and find that the gust factors increase as the time scale increases. The mean 1-min, 5-min, and 10-min gust factors in the TC inner core during the 22-min period are 1.10, 1.17, and 1.21, respectively. Harper et al. (2010) indicated that 1-min mean gust factor recommended by WMO is 1.11 and the 10-min gust factor is 1.23 for the TC at 10-m height over the ocean. Our experiment not only simulated the fine-scale structures in the TCBL (Wu et al., 2018, 2019; Liu et al., 2021), but also the mean values of the gust factors at 10 m height are generally consistent with the observations.

Although extreme gusts and gust factors exist in the TCBL, these extreme values only account for a very small proportion (Black et al., 1999; Harper et al., 2010). The fine-scale structures associated with the extreme gusts and gusts factors have not been detailly discussed (Worsnop et al., 2017; Kapoor et al., 2020). Our simulation indicates that the extreme gust factors prevail inside the TC eyewall. The mean 1-min and 10-min gust factors are only

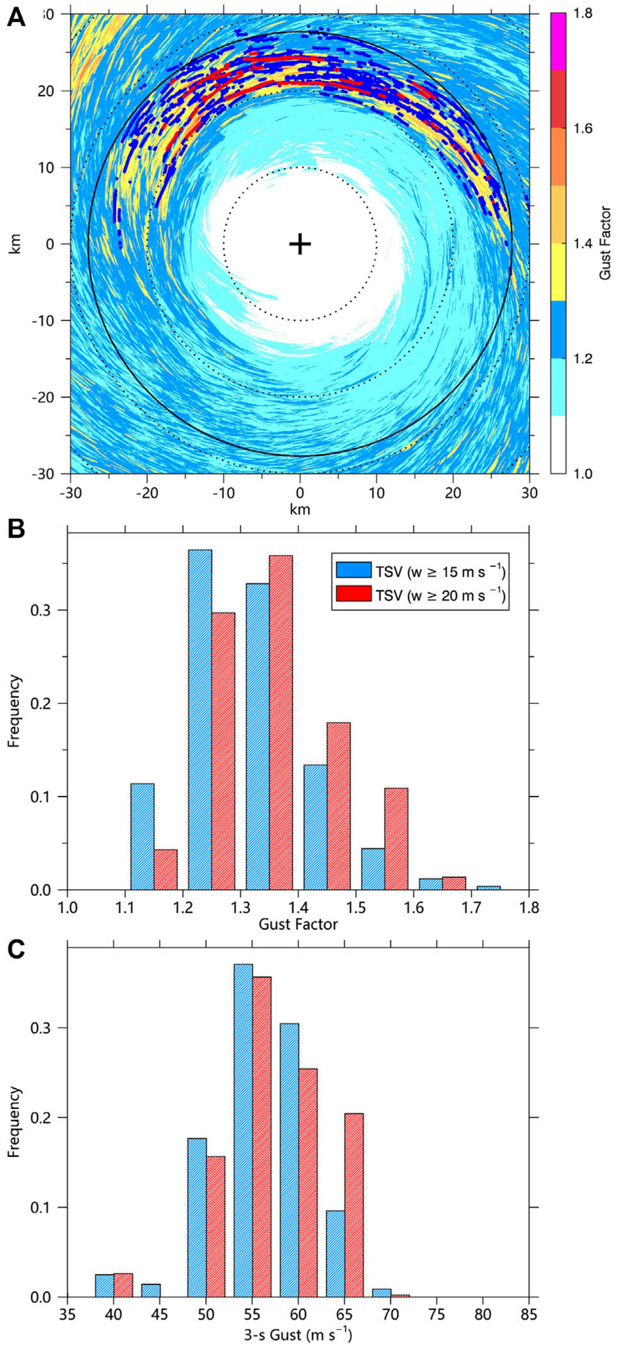

FIGURE 5 | (A) Distributions of the maximum 1-min gust factors and TSV locations during the 22-min period. The small cross in the figure is the TC center, the solid circle indicates the RMW. The vertical and horizontal axes indicate the relative distances (kilometers) from the TC center. **(B)** Frequency of the maximum 1-min gust factors associated with TSVs. **(C)** Frequency of the maximum 3-s gusts associated with TSVs. The red (blue) dots indicate TSVs with a vertical velocity larger than 20 (15) m s^{-1}. The maximum 3-s gust associated with a TSV is the maximum 3-s gust within a 1-km radius around the TSV center. The maximum 1-min gust factor associated with a TSV is the maximum 1-min gust factor at the location where the maximum 3-s gust occurs.

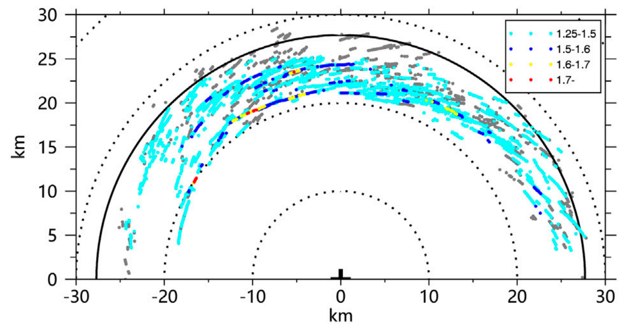

FIGURE 6 | Distributions of TSV locations during the 22-min period. The cyan, blue, yellow, and red points represent the maximum 1-min gust factors with a range of 1.25–1.5, 1.5–1.6, 1.6–1.7, and 1.7–1.8, respectively. The small cross in the figure is the TC center, the solid circle indicates the RMW. The vertical and horizontal axes indicate the relative distances (kilometers) from the TC center.

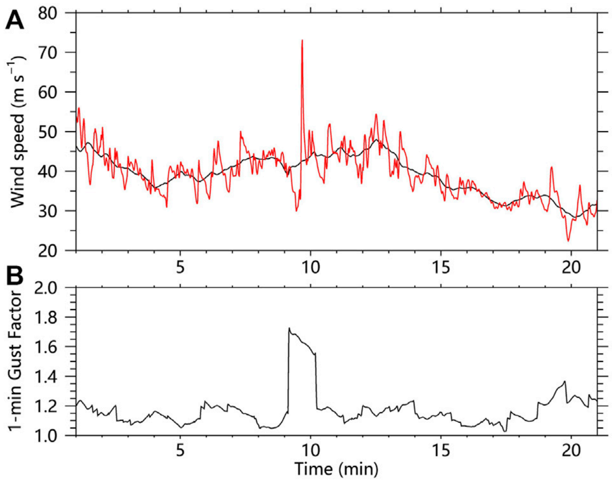

FIGURE 7 | (A) Time sequence of the instantaneous wind speed (red) and 1-min mean wind speed (black). **(B)** Time sequence of the 1-min gust factor.

1.10 and 1.21, but the maximum gust factors can reach 1.79 and 2.23. Furthermore, the mean standard deviation of the 1-min gust factors for the whole field is 0.035, indicating that these extreme gust factors only account for a small percentage of the surface gusts in the TC inner core. The extreme gust factors are checked through the survival functions of the 1-min gust factors and 5-min gust factors averaged in a 60x60 km box centered on the TC center over the 22-min period. The survival function is a function that gives the probability that gust factors will survive past a certain value. The top 1% of the 1-min gust factors and 5-min gust factors are ~1.25 and 1.4, respectively. Based on the simplified statistical approach, the 1-min gust factors larger than 1.25 and 5-min gust factors larger than 1.4 can be treated as extreme gust factors in our study. According to the extreme gust factors recorded in Barrow Island in Western Australia during the passage of Hurricane Olivia (1996), Black et al. (1999) found that it was only 2% of the gusts reached a 5-min gust factor of 1.6, which caused the extreme gusts and damage. Based on our numerical results, the extreme gust and gust factors are smaller than those in their studies. This might be due to the weaker TC intensity in our simulations or the extreme gusts and gust factors are sensitive to the TC-scale structures since the extreme gust factors tend to be prevalent in the inner edge of the enhanced eyewall convection. **Figure 4B** shows the horizontal distribution of the frequency of gust factors that is not less than 1.25 during the 22-min period. It should be noted that most of the points (65%) in the domain (**Figure 4B**) do not have gust factors large than 1.25 during the 22-min period. However, the extreme gust factors tend to occur in the northern side of the TC eyewall with a maximum frequency of 0.4.

Relationships Between TSVs and Surface Wind Gusts

Previous observational and numerical studies show that the TSVs are one of the fine-scale coherent structures in the TCBL which may cause strong localized winds (Wurman and Winslow, 1998; Wu et al., 2018; Wurman and Kosiba 2018; Wu et al., 2019; Liu et al., 2021). Following Wu et al. (2018), the tornado-scale vortex is defined as a small-scale cyclonic circulation with the maximum updraft not less than 15 $m\ s^{-1}$ or 20 $m\ s^{-1}$ and maximum relative vorticity not less than 0.2 s^{-1} below the altitude of 3 km. The grid points that satisfy the thresholds of vertical motion (15 $m\ s^{-1}$ or 20 $m\ s^{-1}$) and relative vorticity (0.2 s^{-1}) belong to the same vortex if they are within a distance of 1 km in the horizontal and vertical direction. There are 3618 (vertical velocity larger than 15 $m\ s^{-1}$) and 493 (vertical velocity larger than 20 $m\ s^{-1}$) TSVs found in our experiment during the 22-min period. The locations of TSVs with the horizontal distribution of the maximum 1-min gust factors are shown in **Figure 5A**. The extreme gust factors (the maximum 1-min gust factors are generally larger than 1.25) usually occur along the tracks of identified TSVs. There seem to be some connections between TSVs and the extreme gust factors.

To further analyze the relations between TSVs and the near-surface extreme gust factors, we calculate the maximum 3-s gusts within a 1-km radius around the TSV centers and the associated maximum 1-min gust factors. The frequency of gust factors and 3-s gusts associated with TSVs are shown in **Figures 5B,C**. According to the statistical results, the mean maximum 1-min gust factor of TSVs with vertical velocity larger than 20 (15) $m\ s^{-1}$ is 1.36 (1.32), and the mean maximum 3-s gust of TSVs with vertical velocity larger than 20 (15) $m\ s^{-1}$ is 59.7 (58.7) $m\ s^{-1}$. According to the previous analysis, the mean frequency of gust factors larger than 1.25 for the whole field is only 1% during the 22 min period, and such a small percentage of the gust factors can be treated as extreme gust factors. Based on our results, the percentage of maximum gust factors associated with the TSVs (vertical velocity larger than 15 $m\ s^{-1}$) larger than 1.25 is 73%, and 88% of maximum gust factors associated with TSVs (vertical velocity larger than 20 $m\ s^{-1}$) are larger than 1.25. From the statistical results, TSVs are significantly associated with extreme gust factors. The extreme 1-min gust factor can reach about 1.8. **Figure 6** shows the scatter plot of the TSV tracks and associated

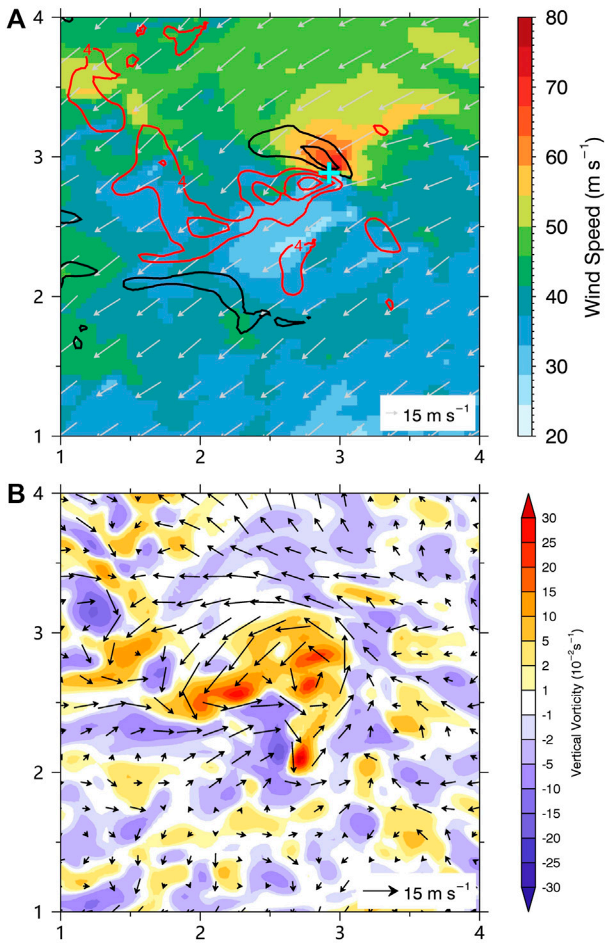

FIGURE 8 | (A) 10-m wind speed (shading), 10-m wind vectors, and vertical motions (contour: 4 m s^{-1}) at 200-m height in the area shown in **Figure 6**. **(B)** the perturbated winds and vertical component of relative vorticity (shading) at 200-m height in the area shown in **Figure 6**. The red (black) contours denote the updrafts (downdrafts) in **Figure 8A**. The cyan cross in **Figure 8A** is the location of maximum wind speed at 10-m height. The vertical and horizontal axes are in kilometers.

1-min gust factors during the 22-min. It can be seen that extreme gust factors caused by TSVs are mostly found in the inner edge of the TC eyewall. We carefully check the gust factors larger than 1.7 (10 cases) and find that they are all associated with typical TSV structures. We choose one of the TSVs in the red box in **Figure 6** to show the detailed TSV structures and the associated time series of gusts and gust factors.

The instantaneous and 1-min mean wind speed at 10-m height during the 22-min are shown in **Figure 7A**. The maximum instantaneous and 3-s gusts are 73 and 69 m s^{-1}, respectively, although the mean 1-min wind speed during the 22-min is only 39 m s^{-1}. We also present the time series of the 1-min gust factor in **Figure 7B**, which shows that it is the instantaneous wind of 73 m s^{-1} associated with the TSV that causes the extreme gust factor at this location. The wind fluctuations can reach 30 m s^{-1}, which is similar to gusts associated with TSV found in observations (Wurman and Kosiba 2018). We further examine the structure of the TSV in **Figure 8**. It can be seen that the extreme gust (maximum instantaneous wind speed is ~73 m/s) is associated with coupled strong updrafts and downdrafts, with maximum updraft (downdraft) up to ~15 (10) m s^{-1} at 200-m height. **Figure 8B** shows the perturbation wind field at 200-m height. The perturbation winds are obtained by subtracting an 8-km moving mean. We can see a small-scale horizontal circulation with a scale of ~1 km in the perturbation wind field, accompanied by strong vertical vorticity up to 0.3 s^{-1}. This structure is consistent with the typical structure of TSVs found in observational and numerical studies (Marks et al., 2008; Wu et al., 2018, 2019; Wurman and Kosiba et al., 2018; Liu et al., 2021). The extreme gust and gust factor at this location is apparently related to a typical TSV.

SUMMARY

Previous studies demonstrated that the strong surface gusts may pose a great threat to the lives and property near the coastlines during TC landfall (Black et al., 1999; Harper 2010; Wurman and Kosiba 2018). Recent observational studies suggest that the TC surface strong gusts may be related to the TSVs in the TCBL (Wurman and Kosiba 2018). In this study, a semi-idealized numerical simulation of TC that evolves in a realistic large-scale environment with the WRF-LES framework is conducted with the finest grid spacing of 37 m and time resolution of 1 s to investigate the characteristics of surface gusts and gust factors in the TC inner core and possible relations between the extreme gust factors and TSVs.

The mean 1-min and 10-min gust factors recommended by WMO are 1.11 and 1.23 for TCs at 10-m height (Harper et al., 2010). Based on the 22-min outputs from the numerical experiment, the mean 1-min and 10-min gust factors are 1.10 and 1.21, which are generally in agreement with those recommended by the WMO. Although the mean 1-min gust factor in the TC inner core is 1.1, the maximum gust factor can reach ~1.8. However, extreme gust factors only account for a small percentage of the surface gusts in the TC inner core and the top 1% of 1-min and 5-min gust factors are 1.25 and 1.4. In addition, there is a strong asymmetry in the horizontal distribution of the mean and maximum gust factors in our experiment, for the extreme gust factors are prevalent in the northern side of the TC eyewall with strong convection. In addition, the TSVs are prevalent on the northern side inside the eyewall, where extreme gust factors tend to occur.

Further analysis shows that the percentage of maximum gust factors associated with the TSVs (vertical velocity larger than 15 m s^{-1}) larger than 1.25 is 73%, and 88% of maximum gust factors associated with TSVs (vertical velocity larger than 20 m s^{-1}) are larger than 1.25. In addition, the stronger the vertical velocity in the TSV, the larger the maximum gust factor. The mean maximum 1-min gust factor associated with a TSV is larger than 1.3, while the mean 1-min gust factor of the TC inner-core is only 1.1. Since the extreme gust factor (top 1% of the 1-min gust factors in the TC inner core) is 1.25, it indicates that most TSVs are associated with localized gusts and extreme gust factors, which can cause severe surface wind hazards, especially near the eyewall region. The surface gust factors associated with TSVs in tropical cyclone eyewall can reach about 1.8, which can cause severe surface wind hazards. Our results suggest that potential risk will increase in the regions where TSVs are prevalent because of the extreme gust factors. Further understanding of the mechanisms on the development and evolution of TSVs is of great significance for gust forecast and resilience against related hazards under the influence of TC.

DATA AVAILABILITY STATEMENT

The raw data supporting the conclusions of this article will be made available by the authors, without undue reservation.

AUTHOR CONTRIBUTIONS

LW designed research. QL conceptualized the analysis and wrote the manuscript. All authors were involved in helpful discussions and contributions to the manuscript.

FUNDING

This work was jointly supported by the National Natural Science Foundation of China (41905001, U2142203, 42075072, 42175007, 42192552, 41730961), the Postdoctoral Science Foundation of China (2019M661342), the National Key R&D Program of China (2021YFC3000901), and the Open Grants of the State Key Laboratory of Severe Weather (2022LASW-B14, 2021LASW-B11). The numerical simulation was carried out on the Shuguang Supercomputer, Nanjing, China.

REFERENCES

Aberson, S. D., Montgomery, M. T., Bell, M., and Black, M. (2006). Hurricane Isabel (2003): New Insights into the Physics of Intense Storms. Part II: Extreme Localized Wind. *Bull. Amer. Meteor. Soc.* 87, 1349–1354. doi:10.1175/BAMS-87-10-1349

American Society of Civil Engineers (2013). *Minimum Design Loads for Buildings and Other Structures. ASCE/SEI 7-10*. American Society of Civil Engineers, 593. doi:10.1061/9780784408094

Bell, M. M., and Montgomery, M. T. (2008). Observed Structure, Evolution, and Potential Intensity of Category 5 Hurricane Isabel (2003) from 12-14 September. *Mon. Wea. Rev.* 136, 2023–2046. doi:10.1175/2007MWR1858.1

Black, P. G., Buchan, S. J., and Cohen, R. L. (1999). "The Tropical Cyclone Eyewall Mesovortex: a Physical Mechanism Explaining Extreme Peak Gust Occurrence in TC Olivia, 4 April 1996 on Barrow Island, Australia," in Paper presented at the Offshore Technology Conference, Houston, Texas, May 1999. doi:10.4043/10792-MS

Feng, Y., Wu, L., Liu, Q., and Zhou, W. (2021). Negative Pressure Perturbations Associated with Tornado-Scale Vortices in the Tropical Cyclone Boundary Layer. *Geophys Res. Lett.* 48, e2020GL091339. doi:10.1029/2020GL091339

Foster, R. (2013). Signature of Large Aspect Ratio Roll Vortices in Synthetic Aperture Radar Images of Tropical Cyclones. *oceanog* 26, 58–67. doi:10.5670/oceanog.2013.31

Gao, K., and Ginis, I. (2014). On the Generation of Roll Vortices Due to the Inflection Point Instability of the Hurricane Boundary Layer Flow. *J. Atmos. Sci.* 71, 4292–4307. doi:10.1175/JAS-D-13-0362.1

Green, B. W., and Zhang, F. (2015). Numerical Simulations of Hurricane Katrina (2005) in the Turbulent Gray Zone. *J. Adv. Model. Earth Syst.* 7, 142–161. doi:10.1002/2014MS000399

Harper, B. A., Kepert, J. D., and Ginger, J. D. (2010). Guidelines for Converting between Various Wind Averaging Periods in Tropical Cyclone Conditions. *World Meteorol. Organ. WMO/TD* 1555, 54.

Holland, G. J. (1983). Tropical Cyclone Motion: Environmental Interaction Plus a Beta Effect. *J. Atmos. Sci.* 40, 328–342. doi:10.1175/1520-0469(1983)040<0328:TCMEIP>2.0.CO

Kapoor, A., Ouakka, S., Arwade, S. R., Lundquist, J. K., Lackner, M. A., Myers, A. T., et al. (2020). Hurricane Eyewall Winds and Structural Response of Wind Turbines. *Wind Energy Sci.* 5, 89–104. doi:10.5194/wes-2019-1410.5194/wes-5-89-2020

Knaff, J. A., Sampson, C. R., DeMaria, M., Marchok, T. P., Gross, J. M., and McAdie, C. J. (2007). Statistical Tropical Cyclone Wind Radii Prediction Using Climatology and Persistence. *Wea. Forecast.* 22, 781–791. doi:10.1175/WAF1026.1

Krayer, W. R., and Marshall, R. D. (1992). Gust Factors Applied to Hurricane Winds. *Bull. Amer. Meteor. Soc.* 73, 613–618. doi:10.1175/1520-0477(1992)073<0613:GFATHW>2.0.CO;2

Li, X., Cheng, X., Fei, J., Huang, X., and Ding, J. (2022). The Modulation Effect of Sea Surface Cooling on the Eyewall Replacement Cycle in Typhoon Trami (2018). *Mon. Wea. Rev.* doi:10.1175/MWR-D-21-0177.1

Liang, Z., Ding, J., Fei, J., Cheng, X., and Huang, X. (2021). Direct/indirect Effects of Aerosols and Their Separate Contributions to Typhoon Lupit (2009): Eyewall versus Peripheral Rainbands. *Sci. China Earth Sci.* 64, 2113–2128. doi:10.1007/s11430-020-9816-7

Liu, Q., Wu, L., Qin, N., and Li, Y. (2021). Storm-Scale and Fine-Scale Boundary Layer Structures of Tropical Cyclones Simulated with the WRF-LES Framework. *JGR Atmos.* 126, e2021JD035511. doi:10.1029/2021JD035511

Lorsolo, S., Zhang, J. A., Marks, F., and Gamache, J. (2010). Estimation and Mapping of Hurricane Turbulent Energy Using Airborne Doppler Measurements. *Mon. Weather Rev.* 138, 3656–3670. doi:10.1175/2010MWR3183.1

Ma, Z., and Fei, J. (2022). A Comparison between Moist and Dry Tropical Cyclones: The Low Effectiveness of Surface Sensible Heat Flux in Storm Intensification. *J. Atmos. Sci.* 79, 31–49. doi:10.1175/JAS-D-21-0014.1

Marks, F. D., Black, P. G., Montgomery, M. T., and Burpee, R. W. (2008). Structure of the Eye and Eyewall of Hurricane Hugo (1989). *Mon. Wea. Rev.* 136, 1237–1259. doi:10.1175/2007MWR2073.1

Morrison, I., Businger, S., Marks, F., Dodge, P., and Businger, J. A. (2005). An Observational Case for the Prevalence of Roll Vortices in the Hurricane Boundary Layer*. *J. Atmos. Sci.* 62, 2662–2673. doi:10.1175/JAS3508.1

Paulsen, B. M., and Schroeder, J. L. (2005). An Examination of Tropical and Extratropical Gust Factors and the Associated Wind Speed Histograms. *J. Appl. Meteor.* 44, 270–280. doi:10.1175/JAM2199.1

Pielke, R. A., Gratz, J., Landsea, C. W., Collins, D., Saunders, M. A., and Musulin, R. (2008). Normalized Hurricane Damage in the United States: 1900-2005. *Nat. Hazards Rev.* 9, 29–42. doi:10.1061/(ASCE)1527-6988

Pielke, R. A., and Landsea, C. W. (1998). Normalized Hurricane Damages in the United States: 1925-95. *Wea. Forecast.* 13, 621–631. doi:10.1175/1520-0434(1998)013<0621:NHDITU>2.0.CO;2

Powell, M. D., Dodge, P. P., and Black, M. L. (1991). The Landfall of Hurricane Hugo in the Carolinas: Surface Wind Distribution. *Wea. Forecast.* 6, 379–399. doi:10.1175/1520-0434(1991)006<0379:TLOHHI>2.0.CO;2

Powell, M. D., Houston, S. H., and Reinhold, T. A. (1996). Hurricane Andrew's Landfall in South Florida. Part I: Standardizing Measurements for Documentation of Surface Wind Fields. *Wea. Forecast.* 11, 304–328. doi:10.1175/1520-0434(1996)011<0304:HALISF>2.0.CO;2

Qin, N., Wu, L., and Liu, Q. (2021). Evolution of the Moat Associated with the Secondary Eyewall Formation in a Simulated Tropical Cyclone. *J. Atmos. Sci.* 78, 4021–4035. doi:10.1175/JAS-D-20-0375.1

Qin, N., and Zhang, D.-L. (2018). On the Extraordinary Intensification of Hurricane Patricia (2015). Part I: Numerical Experiments. *Weather Forecast.* 33, 1205–1224. doi:10.1175/WAF-D-18-0045.1

Rotunno, R., Chen, Y., Wang, W., Davis, C., Dudhia, J., and Holland, G. J. (2009). Large-eddy Simulation of an Idealized Tropical Cyclone. *Bull. Amer. Meteor. Soc.* 90, 1783–1788. doi:10.1175/2009BAMS2884.1

Schroeder, J. L., Edwards, B. P., and Giammanco, I. M. (2009). Observed Tropical Cyclone Wind Flow Characteristics. *Wind Struct. Int. J.* 12, 349–381. doi:10.12989/was.2009.12.4.349

Smith, R. K. (2003). A Simple Model of the Hurricane Boundary Layer. *Q.J.R. Meteorol. Soc.* 129, 1007–1027. doi:10.1256/qj.01.197

Smith, R. K., and Montgomery, M. T. (2010). Hurricane Boundary-Layer Theory. *Q.J.R. Meteorol. Soc.* 136, 1665–1670. doi:10.1002/qj.679

Stern, D. P., Bryan, G. H., and Aberson, S. D. (2016). Extreme Low-Level Updrafts and Wind Speeds Measured by Dropsondes in Tropical Cyclones. *Mon. Wea. Rev.* 144, 2177–2204. doi:10.1175/MWR-D-15-0313.1

Stern, D. P., and Bryan, G. H. (2018). Using Simulated Dropsondes to Understand Extreme Updrafts and Wind Speeds in Tropical Cyclones. *Mon. Weather Rev.* 146, 3901–3925. doi:10.1175/MWR-D-18-0041.1

Vickery, P. J., and Skerlj, P. F. (2005). Hurricane Gust Factors Revisited. *J. Struct. Eng.* 131, 825–832. doi:10.1061/(asce)0733-9445

Wakimoto, R. M., and Black, P. G. (1994). Damage Survey of Hurricane Andrew and its Relationship to the Eyewall. *Bull. Amer. Meteor. Soc.* 75, 189–200. doi:10.1175/1520-0477(1994)075<0189:DSOHAA>2.0.CO;2

Wang, C., Wu, K., Wu, L., Zhao, H., and Cao, J. (2021). What Caused the Unprecedented Absence of Western North Pacific Tropical Cyclones in July 2020? *Geophys. Res. Lett.* 48, 1–9. doi:10.1029/2020GL092282

Wang, Y., and Holland, G. J. (1996). The Beta Drift of Baroclinic Vortices. Part II: Diabatic Vortices. *J. Atmos. Sci.* 53, 3737–3756. doi:10.1175/1520-0469(1996)053<0411:TBDOBV>2.0.CO;2

Willoughby, H. E. (1990). Gradient Balance in Tropical Cyclones. *J. Atmos. Sci.* 47, 265–274. doi:10.1175/1520-0469(1990)047<0265:GBITC>2.0.CO;2

Worsnop, R. P., Lundquist, J. K., Bryan, G. H., Damiani, R., and Musial, W. (2017). Gusts and Shear within Hurricane Eyewalls Can Exceed Offshore Wind Turbine Design Standards. *Geophys. Res. Lett.* 44, 6413–6420. doi:10.1002/2017GL073537

Wu, L., Braun, S. A., Halverson, J., and Heymsfield, G. (2006). A Numerical Study of Hurricane Erin (2001). Part I: Model Verification and Storm Evolution. *J. Atmos. Sci.* 63, 65–86. doi:10.1175/JAS3597.1

Wu, L., and Chen, X. (2016). Revisiting the Steering Principal of Tropical Cyclone Motion in a Numerical Experiment. *Atmos. Chem. Phys.* 16, 14925–14936. doi:10.5194/acp-2016-369

Wu, L., Liu, Q., and Li, Y. (2018). Prevalence of Tornado-Scale Vortices in the Tropical Cyclone Eyewall. *Proc. Natl. Acad. Sci. U.S.A.* 115, 8307–8310. doi:10.1073/pnas.1807217115

Wu, L., Liu, Q., and Li, Y. (2019). Tornado-scale Vortices in the Tropical Cyclone Boundary Layer: Numerical Simulation with the WRF-LES Framework. *Atmos. Chem. Phys.* 19, 2477–2487. doi:10.5194/acp-2018-787

Wurman, J., and Kosiba, K. (2018). The Role of Small-Scale Vortices in Enhancing Surface Winds and Damage in Hurricane Harvey (2017). *Mon. Wea. Rev.* 146, 713–722. doi:10.1175/MWR-D-17-0327.1

Wurman, J., and Winslow, J. (1998). Intense Sub-kilometer-scale Boundary Layer Rolls Observed in Hurricane Fran. *Science* 280, 555–557. doi:10.1126/science.280.5363.555

Xu, H., Wang, H., and Duan, Y. (2021). An Investigation of the Impact of Different Turbulence Schemes on the Tropical Cyclone Boundary Layer at Turbulent Gray-Zone Resolution. *JGR Atmos.* 126, e2021JD035327. doi:10.1029/2021JD035327

Xu, H., and Wang, Y. (2021). Sensitivity of Fine-Scale Structure in Tropical Cyclone Boundary Layer to Model Horizontal Resolution at Sub-kilometer Grid Spacing. *Front. Earth Sci.* 9, 707274. doi:10.3389/feart.2021.707274

Yang, H., Wu, L., and Xie, T. (2020). Comparisons of Four Methods for Tropical Cyclone Center Detection in a High-Resolution Simulation. *J. Meteorological Soc. Jpn.* 98, 379–393. doi:10.2151/jmsj.2020-020

Zhang, J. A., and Montgomery, M. T. (2012). Observational Estimates of the Horizontal Eddy Diffusivity and Mixing Length in the Low-Level Region of Intense Hurricanes. *J. Atmos. Sci.* 69, 1306–1316. doi:10.1175/JAS-D-11-0180.1

Zhang, Q., Wu, L., and Liu, Q. (2009). Tropical Cyclone Damages in China 1983-2006. *Bull. Amer. Meteor. Soc.* 90, 489–496. doi:10.1175/2008BAMS2631.1

Zhao, H., Zhao, K., Klotzbach, P. J., Wu, L., and Wang, C. (2022). Interannual and Interdecadal Drivers of Meridional Migration of Western North Pacific Tropical Cyclone Lifetime Maximum Intensity Location. *J. Clim.* 35, 2709–2722. doi:10.1175/JCLI-D-21-0797.1

Zheng, Y., Wu, L., Zhao, H., Zhou, X., and Liu, Q. (2020). Simulation of Extreme Updrafts in the Tropical Cyclone Eyewall. *Adv. Atmos. Sci.* 37, 781–792. doi:10.1007/s00376-020-9197-4

Zhu, P., Menelaou, K., and Zhu, Z. (2013). Impact of Subgrid-Scale Vertical Turbulent Mixing on Eyewall Asymmetric Structures and Mesovortices of Hurricanes. *Q.J.R. Meteorol. Soc.* 140, 416–438. doi:10.1002/qj.2147

Zhu, P. (2008). Simulation and Parameterization of the Turbulent Transport in the Hurricane Boundary Layer by Large Eddies. *J. Geophys. Res.* 113, D17104. doi:10.1029/2007JD009643

Conflict of Interest: The authors declare that the research was conducted in the absence of any commercial or financial relationships that could be construed as a potential conflict of interest.

ORIGINAL RESEARCH
published: 11 July 2022
doi: 10.3389/feart.2022.929115

Tropical Cyclones Intensity Prediction in the Western North Pacific Using Gradient Boosted Regression Tree Model

Gangya Zhu[1], *Qinglan Li*[1]*, *Wei Zhao*[1], *Xinyan Lv*[2], *Chuanhai Qian*[2] *and Qifeng Qian*[2]

[1]*Shenzhen Institute of Advanced Technology, Chinese Academy of Sciences, Shenzhen, China,* [2]*National Meteorological Center, Beijing, China*

As an artificial intelligence method, machine learning (ML) has been widely used in prediction models of high-dimensional datasets. This study proposes an ML method, the Gradient Boosted Regression Tree (GBRT), to predict the intensity changes of tropical cyclones (TCs) in the Western North Pacific at 12-, 24-, 36-, 48-, 60-, and 72-h (hr) forecasting lead time and the model is optimized by the Bayesian Optimization algorithm. The model predictands are the TCs intensity changes at different forecasting lead times, obtained from the best track data of the Shanghai Typhoon Institute (STI) and the Joint Typhoon Warning Center (JTWC) from 2000 to 2019. The model predictors are the synoptic variables, climatological and persistent variables derived from the reanalysis data obtained from the National Centers for Environmental Prediction (NCEP), and the sea surface temperature (SST) data obtained from the National Oceanic and Atmospheric Administration (NOAA). The results show that the GBRT model can capture the TCs intensity changes well for the succeeding 12-h, 24-h, 36-h, and 72-h. Compared with the traditional multiple linear regression (MLR) model, the GBRT model has better performance in predicting TCs intensity changes. Compared with the MLR model, R^2 of the GBRT model for TCs intensity forecast increases by an average of 8.47% and 4.45% for STI data and JTWC data. MAE (RMSE) drops by 26.24% (25.14%) and 10.51% (4.68%) for the two datasets, respectively. The potential future intensity change (POT), the intensity changes during the previous 12 h (Dvmax), Initial storm maximum wind speed (Vmax), SST, and the Sea-Land ratio are the most significant predictors for the GBRT model in predicting TCs intensity change over the Western North Pacific.

Keywords: tropical cyclones, intensity change, prediction, Western North Pacific, gradient boosted regression tree, Bayesian optimization

Edited by:
Liguang Wu,
Fudan University, China

Reviewed by:
Chao Wang,
Nanjing University of Information Science and Technology, China
Jinjie Song,
Chinese Academy of Meteorological Sciences, China

Correspondence:
Qinglan Li
ql.li@siat.ac.cn

Specialty section:
This article was submitted to Atmospheric Science, a section of the journal Frontiers in Earth Science

Received: *27 April 2022*
Accepted: *20 June 2022*
Published: *11 July 2022*

Citation:
Zhu G, Li Q, Zhao W, Lv X, Qian C and Qian Q (2022) Tropical Cyclones Intensity Prediction in the Western North Pacific Using Gradient Boosted Regression Tree Model. Front. Earth Sci. 10:929115. doi: 10.3389/feart.2022.929115

1 INTRODUCTION

Tropical cyclones (TCs) usually bring substantial economic losses and casualties through strong winds, heavy rainfall, and storm surge during and after TCs landfall, especially in the coastal area which is vulnerable to TCs (Zhang et al., 2009). Therefore, an accurate and timely forecast of TCs track and intensity is crucial for local disaster mitigation. During the past century, scientists and meteorological administrations tried to improve their ability in TCs observation technology, forecasting techniques, and understanding TCs intensification

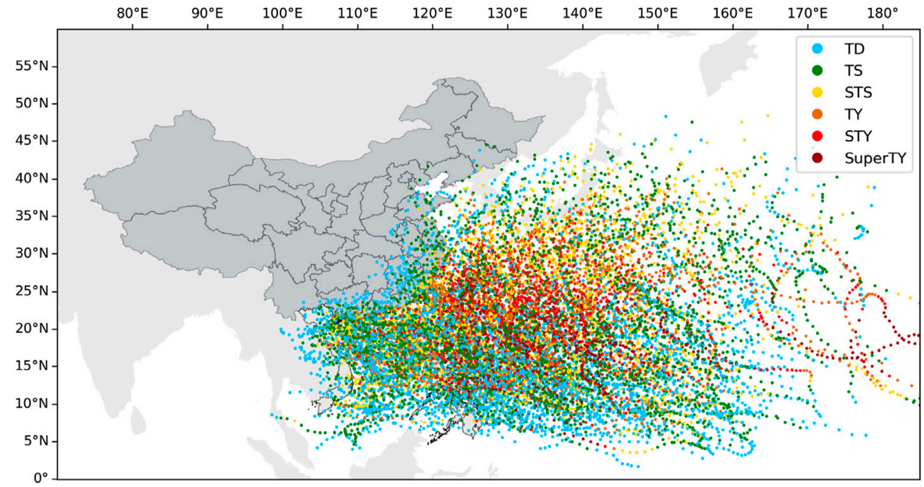

FIGURE 1 | Tracks of the TCs in the Western North Pacific from 2000 to 2019 based on the best track data from STI at 6-h interval.

TABLE 1 | The 26 potential predictors available for the GBRT model.

Predictor	Description
Lat	Initial storm latitude
Lon	Initial storm longitude
Vmax	Initial storm maximum wind speed
Dvmax	Intensity change during the previous 12 h
JDATE	Absolute value of Julian day
SHRS	Area-average (200–800 km) wind shear at 850–500 hpa
SHRD	Area-average (200–800 km) wind shear at 850–200 hpa
LSHRS	SHRS times the sine of the latitude
LSHRD	SHRD times the sine of the latitude
USHRS	Area-average (200–800 km) zonal wind shear at 850–500 hpa
USHRD	Area-average (200–800 km) zonal wind shear at 850–200 hpa
MPI_Vmax	MPI[a] times the initial intensity
POT	Maximum possible intensity - initial intensity
RHHI	Area-average (200–800 km) relative humidity at 500–300 hpa
RHLO	Area-average (200–800 km) relative humidity at 850–700 hpa
SPD	Storm translational speed
T200	Area-average (200–800 km) temperature at 200 hpa
D200	Area-average (200–800 km) divergence at 200 hpa
WVF500	Area-average (200–800 km) water vapor flux at 500 hpa
WVF850	Area-average (200–800 km) water vapor flux at 850 hpa
Z500	Area-average (200–800 km) vorticity at 500 hpa
Z850	Area-average (200–800 km) vorticity at 850 hpa
U200	Area-average (200–800 km) zonal wind at 200 hpa
V200	Area-average (200–800 km) meridional wind at 200 hpa
SST	Area-average (0–800 km) sea surface temperature
SL ratio	Ratio of sea area with a certain radius

[a] *MPI, refers to the maximum potential intensity, following the methodology employed by DeMaria and Kaplan (1994b) and Knaff et al. (2005).*

TABLE 2 | Sample numbers for different TCs' lead time prediction models.

Lead time	Source	Over land	Near the coast	Over open ocean	All samples
12	STI	814	6782	6525	14121
	JTWC	384	6388	6437	13209
24	STI	547	6272	6220	13003
	JTWC	175	5746	6143	12064
36	STI	—	5592	5931	11891
	JTWC	—	5016	5853	10946
48	STI	—	4920	5639	10814
	JTWC	—	4273	5547	9860
60	STI	—	4257	5340	9785
	JTWC	—	3557	5228	8809
72	STI	—	3622	5041	8803
	JTWC	—	2925	4875	7819

mechanism (Emanuel, 2018). In the past 30 years, with the application of meteorological satellites and the popularity of ensemble forecasts for TCs track, the track prediction has been greatly improved (Zhang and Krishnamurti, 1997; Fraedrich et al., 2003; Langmack et al., 2012; Jun et al., 2017). However, the intensity forecast is still poor compared with the track forecast and is a huge challenge around the world (DeMaria et al., 2014).

TCs intensity is influenced by two main physical processes (Wang and Wu, 2004; Elsberry et al., 2013), which are synoptic variables such as vertical wind shear, humidity, sea surface temperature, water vapor, divergency (DeMaria, 1996; Ge et al., 2013; Gao et al., 2016; Mercer and Grimes, 2017), and climatological and persistent variables such as latitude, longitude, Julian day, and sea-land ratio (SL ratio) (DeMaria and Kaplan, 1994a; Gao et al., 2016; Li et al., 2018). Statistical-dynamical models were used to predict TCs intensity and rapid intensification probability and outperformed the forecasts of individual physics-based dynamical models (Knaff et al., 2005; Kaplan et al., 2010; Gao and Chiu, 2012). For decades, scientists have dedicated themselves to improving the skill of TCs intensity forecast. Jarvinen and Neumann (1979) proposed a statistical regression equation (Statistical Hurricane Intensity FORecast, SHIFOR) using predictors derived from climatic and persistent variables to predict TCs intensity changes over the North Atlantic Basin for the future 72 h. DeMaria and Kaplan (1994a) proposed a Statistical Hurricane Intensity Prediction Scheme (SHIPS), which considered more synoptic predictors to predict the changes in TCs intensity over the Atlantic Ocean Basin. The

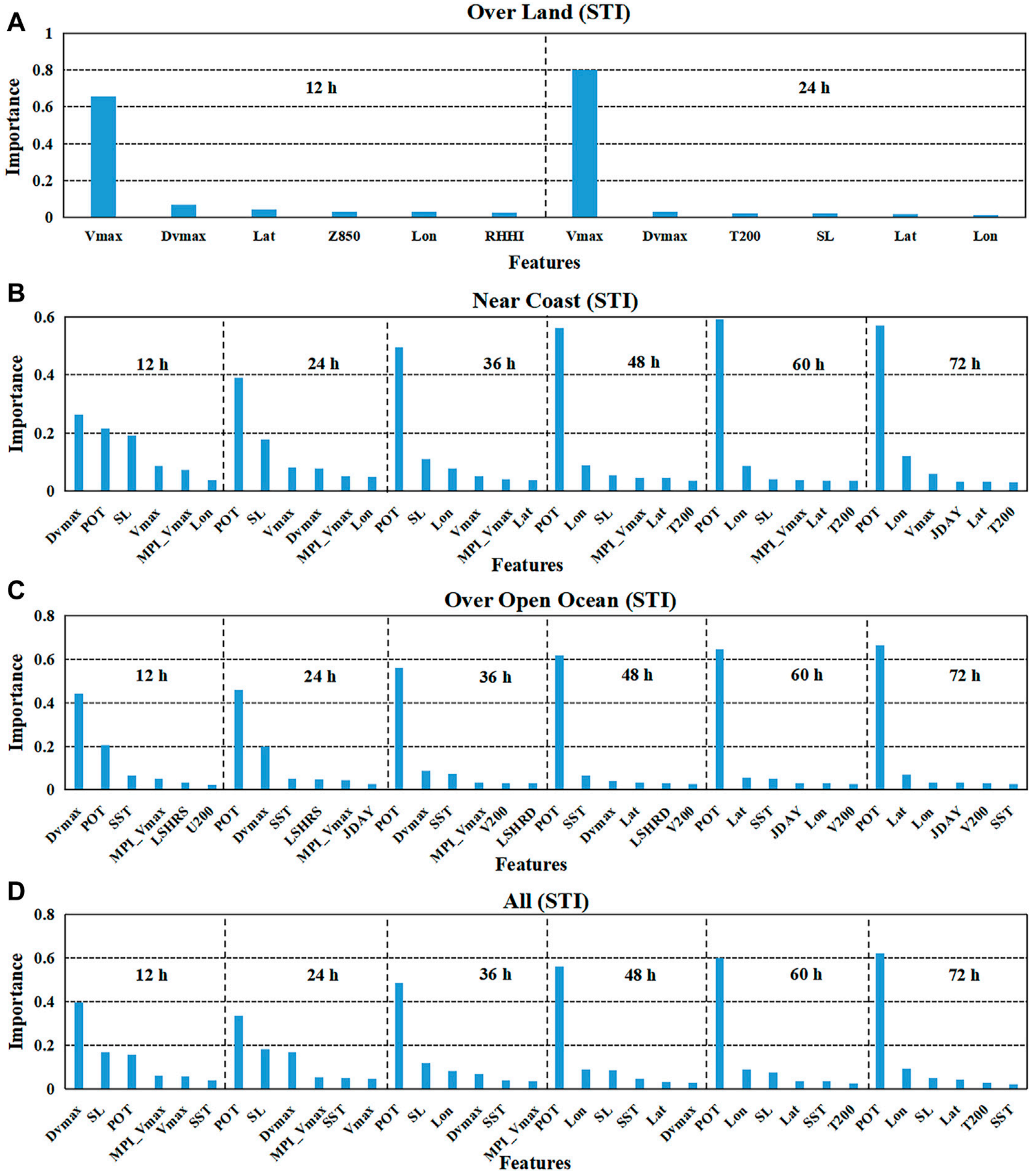

FIGURE 2 | Selection results of the significant variables for TCs intensity prediction models for the STI datasets by the GBRT method. The vertical axis represents the percentage of the feature importance of the variable in the corresponding prediction model, and the horizontal axis refers to the predictor variable. Only the six most important variables are displayed for each lead time forecasting model. **(A)** for TC samples over land; **(B)** for TC samples near the coast; **(C)** for TC samples over the open ocean; **(D)** for all TC samples.

results showed that the average errors by SHIPS were 10%–15% smaller than the errors by the SHIFOR model that used only climatic and persistent variables. The storm decay over land was further considered by SHIPS (DeMaria et al., 2005). Besides the conventional synoptic and climatological variables, Li et al. (2018) paid close attention to the land effect on TCs intensity change by proposing a new factor involving the ratio of seawater area to land area (SL ratio) in the statistical regression model. TCs intensity changes over the entire TCs life span, including over the ocean basin, near the coast, and after landfall, were considered in the model (Li et al., 2018). Intensity forecasting accuracy for TCs near the coast and over land was improved with the addition of the SL ratio, compared with that of the models that did not consider the index of SL ratio (Li et al., 2018).

Based on previous observations and studies, in most cases, intensity changes are usually slow and steady over a certain period. However, in some situations, the TCs intensity may vary rapidly. Predicting these rapid intensifications is very challenging (Emanuel and Zhang, 2016). Many factors, such as the complex and chaotic energy exchange process between the sea

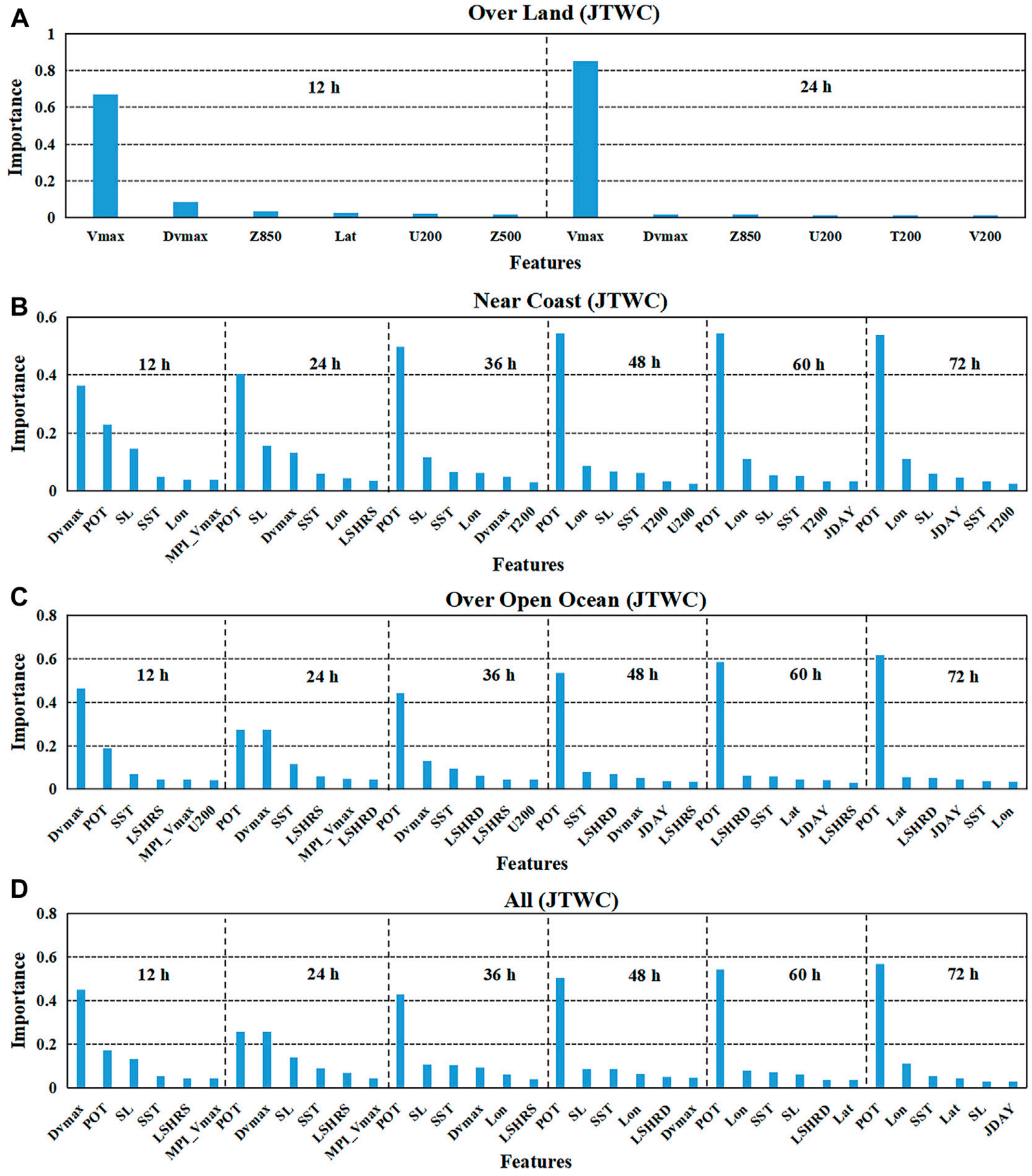

FIGURE 3 | Selection results of the significant variables for TCs intensity prediction models for the JTWC datasets by the GBRT method. The vertical axis represents the percentage of the feature importance of the variable in the corresponding prediction model, and the horizontal axis refers to the predictor variable. Only the six most important variables are displayed for each lead time forecasting model. **(A)** for TC samples over land; **(B)** for TC samples near the coast; **(C)** for TC samples over the open ocean; **(D)** for all TC samples.

and the atmosphere, and the imperfection of real-time data collection, may influence the prediction of TCs intensity change. These rapid intensification processes are challenging to explain, and therefore, neither numerical nor statistical-dynamic models can predict TCs intensity changes accurately (Chen et al., 2020). A vital weakness for numerical methods is insufficient representation of the complicated dynamical process; however, increasing the number of variables or equations would exponentially demand the computation (Gao et al., 2016). On the other hand, statistical methods, usually based on regression and lower computational costs, may not be effective in capturing nonlinear relationships. Therefore, their forecast results need to be further improved (Lin et al., 2009; Sandery et al., 2010).

To solve these problems, scientists began to use machine learning (ML) to predict the TCs intensity in recent years (Gao et al., 2016; Cloud et al., 2019; Chen et al., 2020; Xu et al., 2021). Some ML algorithms, such as support vector machine, artificial neural network, decision tree, and random forest, have been gradually introduced into meteorology (Breiman, 1996; Mas and Flores, 2008; Behrangi et al., 2009;

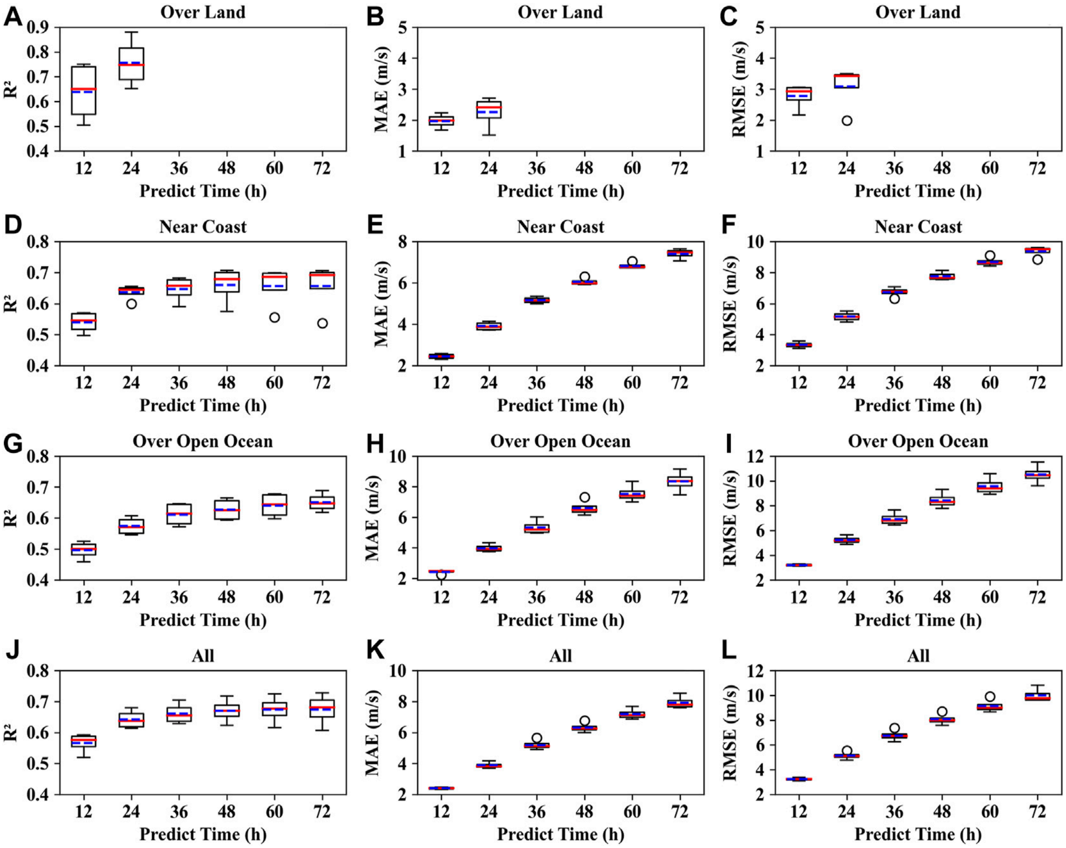

FIGURE 4 | Evaluation of the performance of the GBRT model in predicting the TCs future 12-h, 24-h, 36-h, 48-h, 60-h, and 72-h intensity changes with four cross validations in terms of R^2 (the first column), MAE (the second column), and RMSE (the third column) based on the STI TCs best track data. **(A–C)** for TC samples over land; **(D–F)** for TC samples near the coast; **(G–I)** for TC samples over the open ocean; **(J–L)** for all TC samples.

Mountrakis et al., 2011; Pan et al., 2019). ML is applicable to high-dimensional datasets and can deal with nonlinear relationships between predictors and predictand. It is used to explore satellite, radar, and *in-situ* data to improve the TCs intensity forecast skills (Gao et al., 2016; Zhang et al., 2016; Griffin et al., 2017; Jin et al., 2020). Generally, ML models combine historical storm characteristics, physically motivated information, and storm-specific features to make predictions (Xu et al., 2021).

The gradient boosted regression tree (GBRT) is an ensemble ML algorithm consisting of multiple decision trees, which is robust in model training (Zhang et al., 2020). First, the decision tree algorithm is a classical ML method, and it can deal with inherent nonlinear relationships in variables and missing values (Quinlan, 1987; Fayyad and Stolorz, 1997). In addition, the algorithm can quantify the relative importance of variables and establish decision rules for prediction (Quinlan, 1987). It has been successfully applied in the analyses of the re-curvature, landfall, and intensity change of TCs in the Western North Pacific Ocean (Zhang et al., 2013; Gao et al., 2016). Second, like most ensemble methods, a combination of decision trees can provide more robust and accurate regressions than a single one. The greater-than and less-than structures of the tree module make the GBRT less affected by outliers (Bishop and Nasrabadi, 2006; Ma et al., 2018). Furthermore, GBRT is able to capture the complicated and nonlinear relationships between TCs intensity change and other related features. Compared with a single decision tree, GBRT pays more attention to the regression errors with less calculation time for high-dimension data (Xie and Coggeshall, 2010; Ding et al., 2016; Yang et al., 2016; Ma et al., 2017; Ma et al., 2018). Therefore, GBRT is used in this study to predict the future change of TCs intensity in the Western North Pacific Ocean.

Most of the studies mainly focused on TCs intensity change over the open ocean. However, TCs that make landfall or approach the coast usually cause most of the loss of life and damage. Forecasting the intensity of TCs near the coast and over land should be, therefore, more critical than forecasting TCs intensity over the open ocean (Li et al., 2018). Li et al. (2018) explored the TCs intensity change over the entire TCs life span by considering a new factor, the "ratio of seawater area to the land area," in the multiple linear regression model (MLR). However, MLR usually performs poorly in handling the nonlinear relationship between predictors and predictand. In this study, the GBRT is proposed to forecast future TCs intensity at 12-, 24-, 36-, 48-, 60-, and 72-h forecasting lead time in the Western North Pacific region for different TCs life spans. GBRT's performance in predicting TCs intensity change over the Western North Pacific is compared with the performance of the MLR model used by Li et al. (2018). The remaining of the paper is as

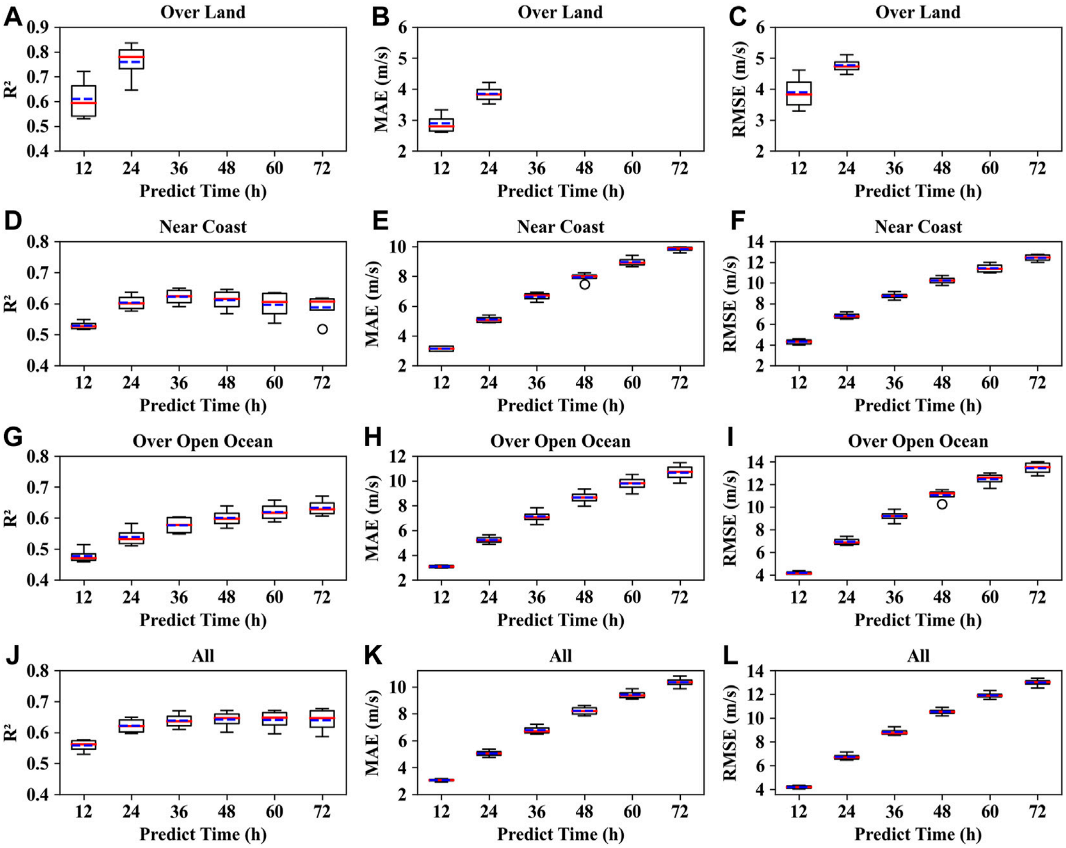

FIGURE 5 | Evaluation of the performance of the GBRT model in predicting the TCs future 12, 24, 36, 48, 60, and 72-h intensity changes with four cross validations in terms of R^2 (the first column), MAE (the second column), and RMSE (the third column) based on the JTWC TCs best track data. (A–C) for TC samples over land; (D–F) for TC samples near the coast; (G–I) for TC samples over the open ocean; (J–L) for all TC samples.

follows. The data and methodology are described in **Section 2**. **Section 3** contains the results and discussion. In the final section, summaries are presented.

2 DATA AND METHODS

2.1 Data

At present, there is no standardized TCs intensity estimation method, and the most widely used methods are artificial algorithms based on satellite cloud images; therefore, there is uncertainty about TCs intensity values (Jiang et al., 2019; Lee et al., 2019). To account for the uncertainty, this study used two different TCs datasets: the best track data from the Shanghai Typhoon Institute (STI, 2020) and the best track data from the Joint Typhoon Warning Center (JTWC, 2020) for the period of 2000–2019 in the Western North Pacific region, covering the area with latitude north of 0°N and longitude west of 180°. It is worth noting that for TCs that affect China, STI data might have more advantages than JTWC, as there are more direct observations for those TCs in China (Ren et al., 2011).

The best track datasets include the TCs time (year, month, day, hour), location (latitude and longitude of the TCs center), TCs central pressure, and the maximum sustained wind speed near the TCs center. **Figure 1** shows the tracks of the TCs in the Western North Pacific from 2000 to 2019 based on the data from STI. In addition to the TCs data, synoptic variables, climatological and persistent variables are derived from the reanalysis data obtained from the National Centers for Environmental Prediction (NCEP, 2020) at 6-h temporal and $1^\circ \times 1^\circ$ spatial resolution. The NCEP FNL (Final) Operational Global analysis data has incorporated the most complete set of observational data and is possibly the best choice for a long-term operational model archive from NCEP (NCEP, 2020). The analyses are available at the surface and 26 mandatory levels from 1,000 to 10 hpa. Furthermore, this study applies global daily means of SST provided by the National Oceanic and Atmospheric Administration (NOAA, 2020), as warm seawater is the energy source for TCs. The data from 2000 to 2019 are divided into four groups according to five consecutive years (i.e., 2000–2004 is a group; 2005–2009 is another group). We use one group as the test set and the other three groups as the training set to build the prediction model and perform cross-validation.

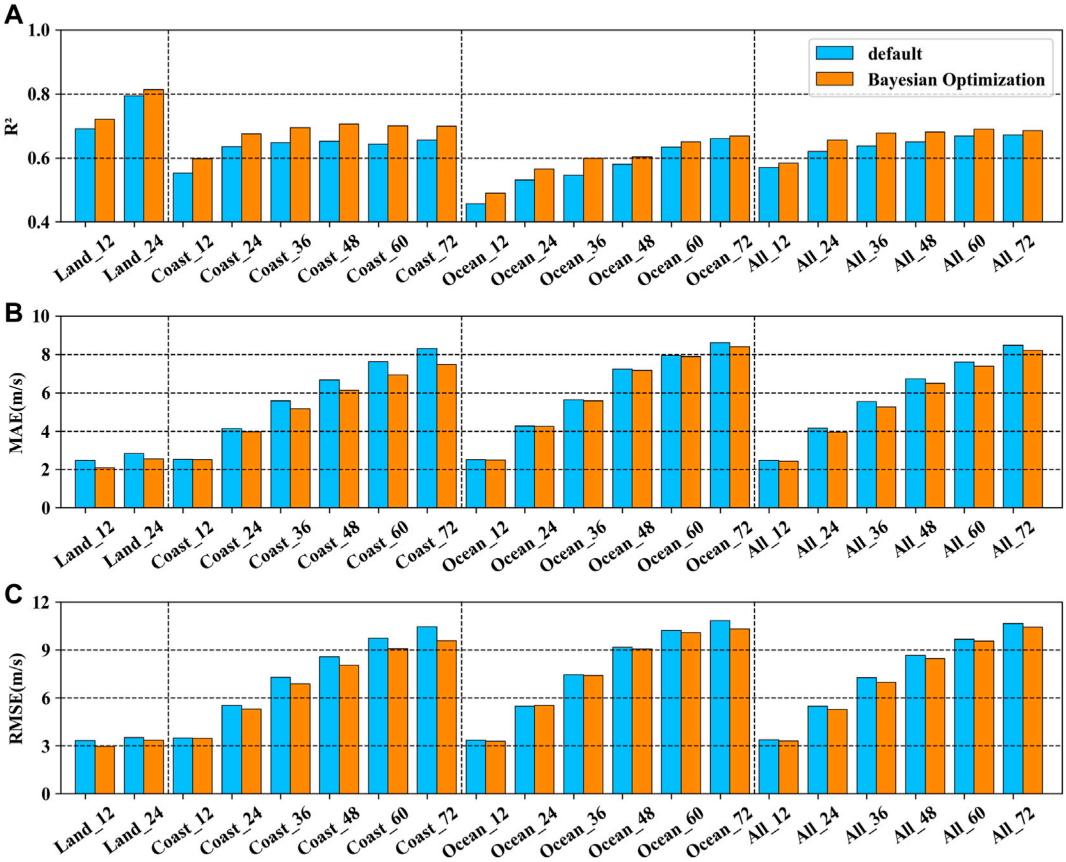

FIGURE 6 | Performance comparison between the GBRT model with the default hyperparameters and Bayesian optimized GBRT model in terms of **(A)** R^2, **(B)** MAE, and **(C)** RMSE for TCs intensity change prediction based on the STI data. The labels of Land, Coast, Ocean, and All in the figures refer to TC samples over land, near the coast, over the open ocean, and all TC samples, respectively.

2.2 Method

2.2.1 Gradient Boosted Regression Tree Model

In this study, the Gradient Boosted Regression Tree (GBRT) model is applied to predict the TCs intensity change over the entire TCs life span. The GBRT model is popular for its ability to describe the complicated relationships between input and output data and the explanation of input features (Yang et al., 2020). It enhances the traditional decision tree approach by boosting technology (Friedman, 2001; Friedman, 2002). In boosting, base learners are built sequentially, and each base learner tries to reduce the bias of the previous combined learner (Yang et al., 2020). This approach can combine multiple weak models to make the ensemble model more powerful (Zhou et al., 2021). One of the core ideas of GBRT is to use the value of the negative gradient of the loss function in the current model as an approximation of the residual, which is essentially a first-order Taylor expansion of the loss function to fit a regression tree. Besides, the samples in the training set with the largest residuals are weighted the most heavily in GBRT (Schapire, 2003), encouraging the model to improve its worst predictions (McGovern et al., 2019). In addition, the importance of each input variable can be ranked in GBRT model.

The GBRT is additive models, which can be expressed as the following form:

$$\hat{y}_i = F_M(x_i) = \sum_{m=1}^{M} h_m(x_i). \tag{1}$$

where the h_m are estimators, which are called weak learners in boosting. The GBRT uses fixed-size decision tree models as weak learners. The constant M corresponds to the parameters of the estimator.

Then the GBRT learners are updated continuously, similar to other boosting algorithms.

$$F_m(x) = F_{m-1}(x) + h_m(x), \tag{2}$$

where the newly added tree h_m is fitted to minimize the sum of losses L_m, based on the previous ensemble F_{m-1}:

$$h_m(x) = \underset{h}{arg\,min}\, L_m = \underset{h}{arg\,min} \sum_{i=1}^{n} l(y_i, \mathrm{F}(x_i) + h(x_i)). \tag{3}$$

2.2.2 Bayesian Optimization Algorithm

Bayesian optimization is a very effective global optimization algorithm whose goal is to find the global optimal solution, which is a kind of black-box function without assuming any function form (Brochu et al., 2010; Snoek et al., 2012). As ML

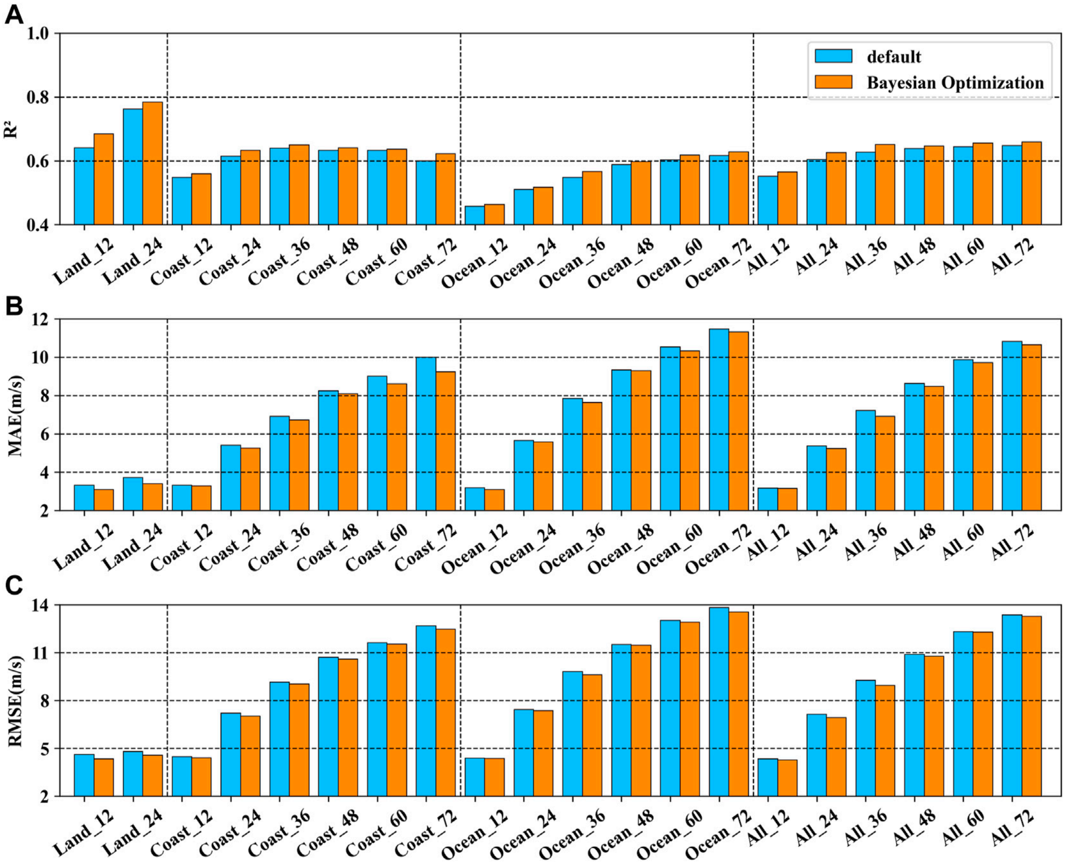

FIGURE 7 | Performance comparison between the GBRT model with the default hyperparameters and Bayesian optimized GBRT model in terms of **(A)** R^2, **(B)** MAE, and **(C)** RMSE for TCs intensity change prediction based on the JTWC data. The labels of Land, Coast, Ocean, and All in the figures refer to TC samples over land, near the coast, over the open ocean, and all TC samples, respectively.

models are widely used to process large amounts of data, the space and process required for hyperparametric tuning become more and more complex. Nowadays, people prefer Bayesian optimization parameter tuning which has been shown to lead to high model performance after the convenient and efficient tuning (Swersky et al., 2013). The corresponding algorithm for the Bayesian optimization is as follow:

Suppose we have a function $f: X \rightarrow R$ and we need to find the maximum within $x \in X$:

$$x_{opt} = \underset{x \in X}{arg\,max} f(x), \tag{4}$$

where X is a set of hyperparameters, and $X \subset R^d$. The computational cost of evaluating model changes is high with a usually small d, and hyperparametric gradients are often not available; therefore, hyperparametric optimization of ML models is important (SIGOPT, 2020). It is worth mentioning that the Bayesian optimization algorithm remains robust for random, non-convex, and even discontinuous fundamental functions f. In this study, we use the Bayesian optimization algorithm to iteratively tune the hyperparameters of the GBRT model, and apply the optimal hyperparameter combination to the prediction model, thereby improving the accuracy of the model.

2.2.3 Potential Predictors

The 26 potential predictors used in the MLR model by Li et al. (2018) are also applied for the GBRT model in this study, which are listed in **Table 1**. All synoptic variables are generally averaged from the corresponding data within a specific radius of the TCs center, usually within a ring with an outer diameter of 800 km and an inner diameter of 200 km. Note that SST is calculated as the average value of the data with a radius of 800 km. The maximum potential intensity (MPI) and TCs potential future intensity change (POT) are calculated by SST. Following Li et al. (2018), the life spans of TCs are divided into the samples over the open ocean, near the coast, and over land according to the values of SL ratio with the range of SL ratio > 0.99, 0.5 < SL ratio < 0.99, SL ratio < 0.5, respectively, which are computed within the radius of 500 km around the TCs center. The numbers of TC samples over the open ocean, near the coast, and over land, as well as the total TC samples (all TC samples without categorization), for the TCs intensity change prediction models with 12-, 24-, 36-, 48-, 60-, and 72-h forecasting lead time are shown in **Table 2**.

The performance of the forecasting models for the testing periods are evaluated in terms of the statistical properties of

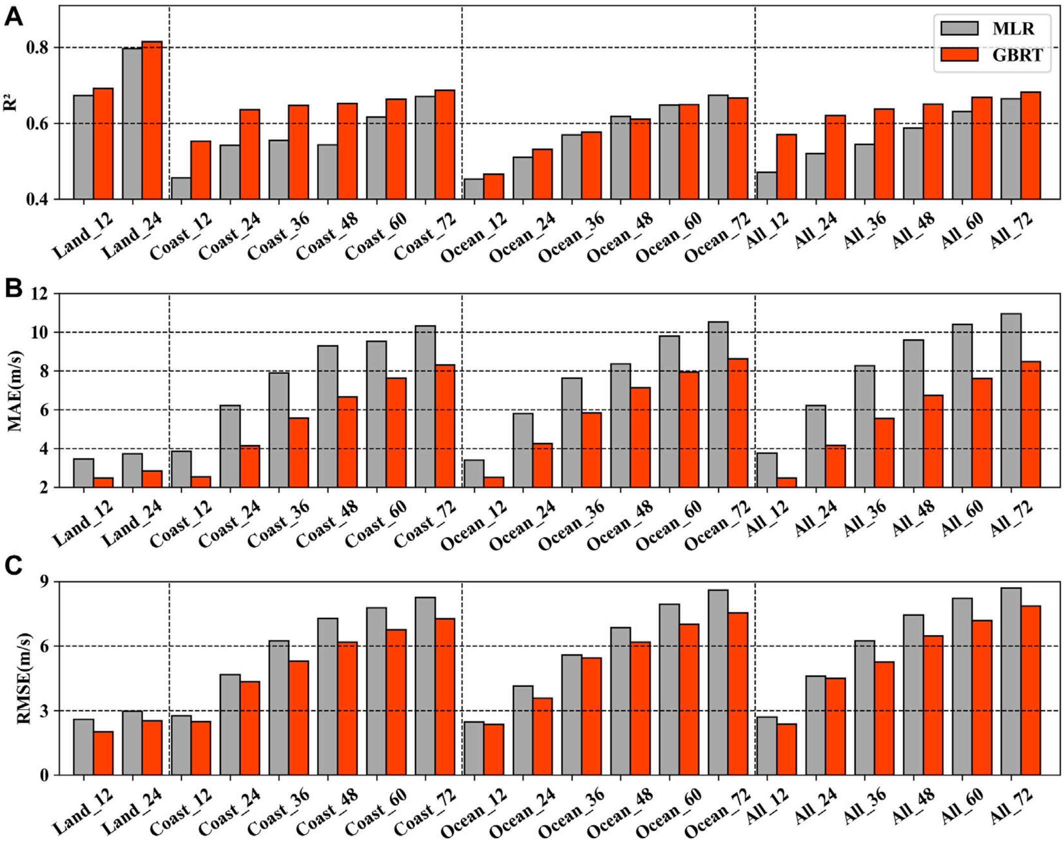

FIGURE 8 | Performance comparisons between the MLR model and GBRT model in terms of **(A)** R^2, **(B)** MAE, and **(C)** RMSE for the TCs intensity change prediction based on the STI data from 2000 to 2015. The Land, Coast, Ocean, and All from the *x*-axis labels refer to TCs over land, near the coast, over the open ocean, and all TC samples, respectively.

coefficient of determination (commonly known as R^2), mean absolute error (MAE) and root mean square error (RMSE).

3 RESULTS AND DISCUSSION

3.1 Computation and Selection of the Model Predictors

For the TCs intensity prediction models, the dependent variables are the TCs intensity changes for the future 12-h, 24-h, to 60-h, and 72-h, and the potential predictors are listed in **Table 1**. Because TCs usually decay quickly after their landfall, this study only considers TCs intensity changes within 24 h (including 12-h and 24-h) after landfall. **Figures 2**, **3** show the importance of the variables in the prediction models with different lead times over the open ocean, near the coast, over land, as well as the all TC samples, based on the STI and the JTWC datasets, respectively. As can be seen from **Figures 2**, **3**, the feature importance of variables varies for the STI and JTWC datasets with different prediction periods, and the six most important variables for each prediction period have accounted for more than 80% of the total feature importance for the prediction models.

Figures 2, **3** show that POT plays the most crucial role in TCs intensity change for TCs over the open ocean (**Figures 2C**, **3C**) and near the coast (**Figures 2B**, **3B**), as well as all TC samples (**Figures 2D**, **3D**). The importance of POT is generally increasing with the forecasting lead time. Besides POT, SST is also essential for TCs intensity change for TCs over the open ocean and near the coast, especially based on the JTWC datasets. Dvmax is an important factor affecting TCs intensity change for TCs over the open ocean and near the coast, as well as all TC samples, for short forecasting lead time, i.e., 12 h and 24 h. Dvmax is no longer an important factor for TCs intensity changes when the forecasting lead time is longer than 24 h for TCs near the coast and the forecasting lead time is longer than 48 h for TCs over the ocean. It is reported that vertical wind shear is one of the most critical dynamic parameters influencing TCs intensity change (DeMaria and Kaplan, 1999; DeMaria et al., 2005; Zeng et al., 2010; Wang et al., 2015). In the GBRT model, vertical wind shear variables of LSHRS and LSHRD play important roles in affecting the TCs intensity when TCs are over the open ocean; however, vertical wind shear is not important for TCs intensity change when TCs are near the coast.

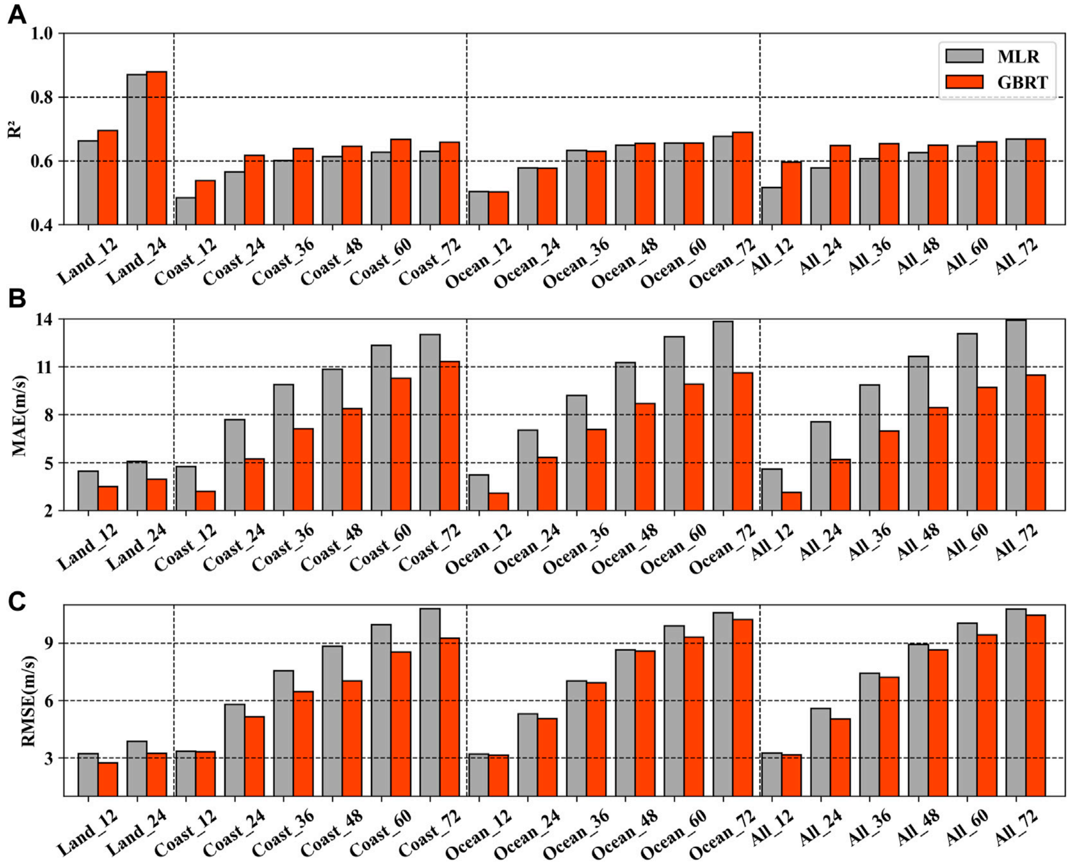

FIGURE 9 | Performance comparisons between the MLR model and GBRT model in terms of **(A)** R^2, **(B)** MAE, and **(C)** RMSE for the TCs intensity change prediction based on the JTWC data from 2000 to 2015. The Land, Coast, Ocean, and All from the x-axis labels refer to TCs over land, near the coast, over the open ocean, and all TC samples, respectively.

It can be seen from **Figures 2B**, **3B**, SL ratio is a crucial variable affecting TCs intensity change when TCs are near the coast. Different from the MLR model used by Li et al. (2018), SL ratio is not an important predictor for the future 12-h TCs' intensity change after TCs landfall. For TCs after landfall, the significant predictors are Vmax and Dvmax, and the importance of Vmax reaches 0.65–0.85 (**Figures 2A**, **3A**).

3.2 Evaluation of the Prediction Model for TCs Intensity Change

As described in **Section 2**, we divide the 2000–2019 data into four groups, i.e., 2000–2004, 2005–2009, 2010–2014, 2015–2019. We use any three groups as the training datasets, and the remaining one as the test datasets to build the prediction model and perform cross validation. We evaluate the GBRT model's performance in predicting the TCs future intensity changes for TCs over land, near the coast, and over the open ocean, as well as all TC samples in terms of R^2, MAE, and RMSE. **Figures 4**, **5** show the evaluation results of the prediction models' performance with the four cross validations by boxplots based on STI data and JTWC data, respectively.

It can be seen from **Figures 4**, **5** that the R^2 value will generally increase with the forecasting lead time. For the GBRT model based on all TC samples, the median and mean of R^2 values are 0.58 (0.56) and 0.57 (0.56) by the 12-h lead time forecast and are 0.68 (0.65) and 0.67 (0.64) by the 72-h lead time forecast based on STI (JTWC) datasets. MAE and RMSE also increase with the forecasting lead time. For all sample models of STI (JTWC) data, the MAE median and mean values are approximately 2.39 (3.08) and 2.40 (3.06) ms^{-1} by the 12-h lead time forecast and are 7.79 (10.35) and 7.93 (10.29) ms^{-1} by the 72-h lead time forecast. The RMSE median and mean values are 3.23 (4.19) and 3.24 (4.20) ms^{-1} by the 12-h lead time forecast and are approximately 9.75 (12.99) and 9.98 (12.94) ms^{-1} by the 72-h lead time forecast. From the comparison of the statistical properties, the quality of the best track data from STI might be slightly better than the one from JTWC.

Specifically, for the GBRT model for TCs over land, the median and mean of R^2 are 0.65 (0.61) and 0.64 (0.62) by the 12-h lead time forecast, and are 0.75 (0.74) and 0.76 (0.76) by the 24-h lead time forecast based on STI (JTWC) datasets. The median and mean of MAE are 1.98 (2.81) and 1.96 (2.88) ms^{-1}

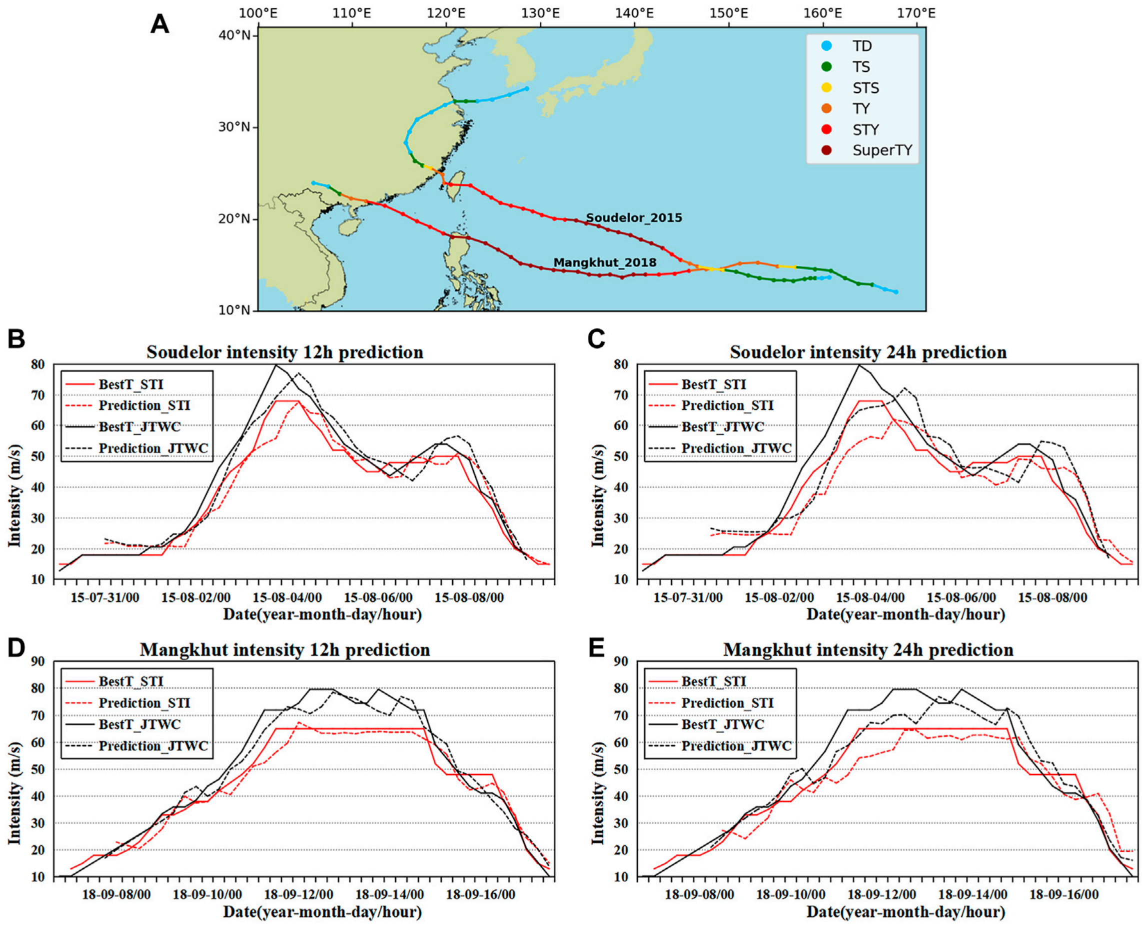

FIGURE 10 | (A) The tracks of Soudelor (201513) and Mangkhut (201822) based on the STI best track data; the comparison of the time series of Soudelor's intensity values from the STI and JTWC best track data and the intensity prediction by the GBRT model by **(B)** 12-h and **(C)** 24-h lead time forecasts, respectively; the comparison of the time series of Mangkhut's intensity values from the STI and JTWC best track data and the intensity prediction by the GBRT model by **(D)** 12-h and **(E)** 24-h lead time forecasts, respectively.

by the 12-h lead time forecast, and are 2.4 (3.82) and 2.26 (3.84) ms^{-1} by the 24-h lead time forecast based on STI (JTWC) datasets. The median and mean of RMSE are 2.93 (3.83) and 2.77 (3.89) ms^{-1} by the 12-h lead time forecast, and are 3.42 (4.74) and 3.08 (4.76) ms^{-1} by the 24-h lead time forecast based on STI (JTWC) datasets. Again, from the comparison of the statistical properties, the quality of the STI best track data is slightly better than the JTWC best track data. The MAE and RMSE for TC samples over land are less than those values for TCs near the coast and TCs over the open ocean. The reason may be that TCs intensity will usually decay quickly after landfall, and the number of essential variables that affect the TCs intensity change after landfall is less than the number of essential variables when TCs are near the coast and over the open ocean. Therefore, the TCs intensity changing process after landfall is not as complicated as the processes for TCs near the coast and over the open ocean. And consequently, the performance of TCs intensity forecast after landfall is generally better.

3.3 Performance Comparison Between the GBRT Model With Default Hyperparameters and Bayesian Optimized GBRT Model

As described in **Section 2**, We use the Bayesian optimization algorithm to tune the hyperparameters of the GBRT model to improve the accuracy of the prediction model. The prediction results of the GBRT model with default hyperparameters are compared with the performance of the GBRT model with Bayesian optimization. The historical data from 2000 to 2014 are used for model training, and the data from 2015 to 2019 are used for model testing. The performance of the two prediction models is evaluated by the statistical properties of R^2, MAE, and RMSE. **Figures 6, 7** show the performance comparison based on STI and JTWC datase-ts, respectively.

In the figures, it can be seen that the performance of the Bayesian optimized GBRT model for the TCs over land, near the coast, over the open ocean, and for all TC samples is generally better than the performance of the model with default hyperparameters. For STI data and JTWC data, after Bayesian optimization for the prediction model, R^2 will increase by an average of 3.37% and 3.26%. MAE (RMSE) will decrease by an average of 3.22% (2.62%) and 3.82% (3.71%).

3.4 Performance Comparison Between the GBRT Model and MLR Model

The performance of the GBRT model is compared with that of the MLR model (Li et al., 2018) during the testing period to forecast TCs intensity over the entire TCs life span in the Western North Pacific. Li et al. (2018) used historical data from 2000 to 2011 for model calibration and data from 2012 to 2015 for model validation. To ensure a fair comparison, the same training datasets and testing datasets are selected in the GBRT model. Similarly, the performance of the different prediction models is evaluated in terms of R^2, MAE, and RMSE.

Figures 8, **9** show the performance comparison results based on STI and JTWC datasets, respectively. It can be seen from the two figures that the GBRT model outperforms the MLR model in TCs intensity forecast for both datasets. Compared with the performance of the MLR model, R^2 of the GBRT model increases by an average of 8.47% and 4.45% for STI data and JTWC data, respectively. MAE (RMSE) drops by an average of 26.24% (25.14%) and 10.51% (4.68%) for the two datasets, respectively.

3.5 Performance of the GBRT Model for Intensity Prediction of Real TCs Cases

In order to further evaluate the performance of the GBRT prediction model, we apply the model to predict the intensity variation for two TC cases in the Western North Pacific, Soudelor (201513) and Mangkhut (201822), which have long life spans and have impacted China significantly. We use historical data from 2000 to 2014 to train the GBRT model. The trained GBRT model is then used to predict the intensity changes for Soudelor and Mangkhut, respectively. The TCs intensity prediction results are compared with the corresponding values from the best track data. The time series of the TCs intensity of Soudelor and Mangkhut from the two best tack data and the GBRT prediction by the 12-h and 24-h lead time forecast are compared in **Figure 10**. **Figure 10A** shows the tracks of these two TCs, which have experienced all three processes: over the open ocean, near the coast, and over land. The different colors in **Figure 10A** represent the different TCs intensity levels.

Figures 10B,C show the comparison between the time series of Soudelor's intensity prediction by the GBRT model with 12-h and 24-h forecasting lead time, and the corresponding TCs intensity values from the STI and JTWC best track data. The solid lines refer to the TCs intensity values from the best track data, and the dashed lines refer to the intensity forecast by the GBRT model. The red color indicates the comparison based on the STI data, and the black color indicates the comparison based on the JTWC data. **Figures 10D,E** show similar comparisons as **Figures 10B,C**, but for TCs Mangkhut. From the figures, it can be seen that the prediction model can generally capture the TCs intensity variation by 12-h and 24-h lead time forecast. However, when the TCs experience rapid intensification, the models' performance is not satisfactory.

4 CONCLUSION

Based on the TCs best track datasets from STI and JTWC from 2000 to 2019, this study proposes TCs intensity prediction models by the GBRT method. Using the index of SL ratio, TCs data are grouped into four parts: TC samples over the open ocean, near the coast, over land, and all TC samples. The future TCs intensity changes of 12 h, 24 h, 36 h, 48 h, 60 h, and 72 h are the model predictands, which are obtained from the best track datasets. Synoptic variables, climatological and persistent variables, which are derived from the NCEP reanalysis data and the SST data from NOAA, are used for the model predictors. Unlike the MLR model, the GBRT model can describe well the nonlinear relationship between predictors and predictands. Compared with the MLR model, R^2 of the GBRT model for TCs intensity forecast increases by an average of 8.47% and 4.45% for STI data and JTWC data, respectively. MAE (RMSE) drops by an average of 26.24% (25.14%) and 10.51% (4.68%) for the two datasets. By comparing the statistical properties for the prediction models based on different datasets, the quality of the TCs best track data over the Western North Pacific from STI might be slightly better than that from JTWC.

According to the feature importance of the GBRT model, for TCs after landfall, the significant predictors are Vmax and Dvmax. Dvmax plays the most crucial role in TCs intensity change for TCs over the open ocean and near the coast, as well as for all TC samples when the forecasting lead time is 12 h. And POT is essential for TCs intensity change when the forecasting lead time is more than 24 h. Besides, SL ratio is an important variable affecting TCs intensity change when TCs are near the coast and for all TC samples when the forecasting lead time is 24–36 h.

In addition, we use the Bayesian optimization algorithm to tune the hyperparameters of the GBRT model to improve the accuracy of the prediction model. For the prediction performance based on the STI data and JTWC data, the R^2 value increases by approximately 3.37% and 3.26% on average. The MAE (RMSE) decreases by an average of 3.22% (2.62%) and 3.82% (3.71%).

Overall, the GBRT model can describe well the complex nonlinear relationship between predictors and TCs intensity change and improves the performance of the intensity prediction of the TCs throughout their life span, compared with the MLR model. Therefore, the GBRT prediction model is practically valuable, and can be referred to for operational TCs intensity forecast.

DATA AVAILABILITY STATEMENT

The original contributions presented in the study are included in the article/supplementary material, further inquiries can be directed to the corresponding author.

AUTHOR CONTRIBUTIONS

Conceptualization: QL and GZ; Data collection and analysis: GZ and QL; Methodology: QL, GZ, and WZ; Writing original draft: GZ and QL. All the co-authors participated the manuscript review and editing.

FUNDING

This research is funded by the Science and Technology Department of Guangdong Province (grant 2019B111101002) and the Innovation of Science and Technology Commission of Shenzhen Municipality Ministry with Grant JCYJ20210324101006016.

REFERENCES

Behrangi, A., Hsu, K.-l., Imam, B., Sorooshian, S., Huffman, G. J., and Kuligowski, R. J. (2009). PERSIANN-MSA: A Precipitation Estimation Method from Satellite-Based Multispectral Analysis. *J. Hydrometeorol.* 10 (6), 1414–1429. doi:10.1175/2009JHM1139.1

Bishop, C. M., and Nasrabadi, N. M. (2006). *Pattern Recognition and Machine Learning*. New York: Springer, 695.

Breiman, L. (1996). Bagging Predictors. *Mach. Learn* 24 (2), 123–140. doi:10.1007/BF00058655

Brochu, E., Brochu, T., and De Freitas, N. (2010). “A Bayesian Interactive Optimization Approach to Procedural Animation Design,” in Proceedings of the 2010 ACM SIGGRAPH/Eurographics Symposium on Computer Animation, Madrid, Spain, July 2–4, 2010, 103–112. doi:10.2312/SCA/SCA10/103-112

Chen, R., Zhang, W., and Wang, X. (2020). Machine Learning in Tropical Cyclone Forecast Modeling: A Review. *Atmosphere* 11 (7), 676. doi:10.3390/atmos11070676

Cloud, K. A., Reich, B. J., Rozoff, C. M., Alessandrini, S., Lewis, W. E., and Delle Monache, L. (2019). A Feed Forward Neural Network Based on Model Output Statistics for Short-Term Hurricane Intensity Prediction. *Wea. Forecast.* 34 (4), 985–997. doi:10.1175/WAF-D-18-0173.1

DeMaria, M., and Kaplan, J. (1994a). A Statistical Hurricane Intensity Prediction Scheme (SHIPS) for the Atlantic Basin. *Wea. Forecast.* 9 (2), 209–220. doi:10.1175/1520-0434(1994)009<0209:aships>2.0.co;2

DeMaria, M., and Kaplan, J. (1999). An Updated Statistical Hurricane Intensity Prediction Scheme (SHIPS) for the Atlantic and Eastern North Pacific Basins. *Wea. Forecast.* 14 (3), 326–337. doi:10.1175/1520-0434(1999)014<0326:auship>2.0.co;2

DeMaria, M., and Kaplan, J. (1994b). Sea Surface Temperature and the Maximum Intensity of Atlantic Tropical Cyclones. *J. Clim.* 7 (9), 1324–1334. doi:10.1175/1520-0442(1994)007<1324:sstatm>2.0.co;2

DeMaria, M., Mainelli, M., Shay, L. K., Knaff, J. A., and Kaplan, J. (2005). Further Improvements to the Statistical Hurricane Intensity Prediction Scheme (SHIPS). *Wea. Forecast.* 20 (4), 531–543. doi:10.1175/WAF862.1

DeMaria, M., Sampson, C. R., Knaff, J. A., and Musgrave, K. D. (2014). Is Tropical Cyclone Intensity Guidance Improving? *Bull. Am. Meteorol. Soc.* 95 (3), 387–398. doi:10.1175/BAMS-D-12-00240.1

DeMaria, M. (1996). The Effect of Vertical Shear on Tropical Cyclone Intensity Change. *J. Atmos. Sci.* 53 (14), 2076–2088. doi:10.1175/1520-0469(1996)053<2076:teovso>2.0.co;2

Ding, C., Wang, D., Ma, X., and Li, H. (2016). Predicting Short-Term Subway Ridership and Prioritizing its Influential Factors Using Gradient Boosting Decision Trees. *Sustainability* 8 (11), 1100. doi:10.3390/su8111100

Elsberry, R. L., Chen, L., Davidson, J., Rogers, R., Wang, Y., and Wu, L. (2013). Advances in Understanding and Forecasting Rapidly Changing Phenomena in Tropical Cyclones. *Trop. Cyclone Res. Rev.* 2 (1), 13–24. doi:10.6057/2013TCRR01.02

Emanuel, K. (2018). 100 Years of Progress in Tropical Cyclone Research. *Meteorol. Monogr.* 59, 1–15. doi:10.1175/AMSMONOGRAPHS-D-18-0016.1

Emanuel, K., and Zhang, F. (2016). On the Predictability and Error Sources of Tropical Cyclone Intensity Forecasts. *J. Atmos. Sci.* 73 (9), 3739–3747. doi:10.1175/JAS-D-16-0100.1

Fayyad, U., and Stolorz, P. (1997). Data Mining and KDD: Promise and Challenges. *Future Gener. Comput. Syst.* 13 (2-3), 99–115. doi:10.1016/S0167-739X(97)00015-0

Fraedrich, K., Raible, C. C., and Sielmann, F. (2003). Analog Ensemble Forecasts of Tropical Cyclone Tracks in the Australian Region. *Wea. Forecast.* 18 (1), 3–11. doi:10.1175/1520-0434(2003)018<0003:aefotc>2.0.co;2

Friedman, J. H. (2001). Greedy Function Approximation: A Gradient Boosting Machine. *Ann. Statistics* 29 (5), 1189–1232. Available at: https://www.jstor.org/stable/2699986. doi:10.1214/aos/1013203451

Friedman, J. H. (2002). Stochastic Gradient Boosting. *Comput. Stat. Data Anal.* 38 (4), 367–378. doi:10.1016/s0167-9473(01)00065-2

Gao, S., and Chiu, L. S. (2012). Development of Statistical Typhoon Intensity Prediction: Application to Satellite-Observed Surface Evaporation and Rain Rate (STIPER). *Wea. Forecast.* 27 (1), 240–250. doi:10.1175/WAF-D-11-00034.1

Gao, S., Zhang, W., Liu, J., Lin, I.-I., Chiu, L. S., and Cao, K. (2016). Improvements in Typhoon Intensity Change Classification by Incorporating an Ocean Coupling Potential Intensity Index into Decision Trees. *Wea. Forecast.* 31 (1), 95–106. doi:10.1175/WAF-D-15-0062.1

Ge, X., Li, T., and Peng, M. (2013). Effects of Vertical Shears and Midlevel Dry Air on Tropical Cyclone Developments. *J. Atmos. Sci.* 70 (12), 3859–3875. doi:10.1175/JAS-D-13-066.1

Griffin, S. M., Otkin, J. A., Rozoff, C. M., Sieglaff, J. M., Cronce, L. M., and Alexander, C. R. (2017). Methods for Comparing Simulated and Observed Satellite Infrared Brightness Temperatures and What Do They Tell Us? *Wea. Forecast.* 32 (1), 5–25. doi:10.1175/WAF-D-16-0098.1

Jarvinen, B. R., and Neumann, C. J. (1979). Statistical Forecasts of Tropical Cyclone Intensity for the North Atlantic Basin. *NOAA Tech. Memo. NWS NHC-10*, 22.

Jiang, H., Tao, C., and Pei, Y. (2019). Estimation of Tropical Cyclone Intensity in the North Atlantic and Northeastern Pacific Basins Using TRMM Satellite Passive Microwave Observations. *J. Appl. Meteorol. Climatol.* 58 (2), 185–197. doi:10.1175/JAMC-D-18-0094.1

Jin, Q., Fan, X., Liu, J., Xue, Z., and Jian, H. (2020). Estimating Tropical Cyclone Intensity in the South China Sea Using the XGBoost Model and FengYun Satellite Images. *Atmosphere* 11 (4), 423. doi:10.3390/atmos11040423

JTWC (2020). Western North Pacific Ocean Best Track Data. Available at: http://www.metoc.navy.mil/jtwc/jtwc.html?western-pacifific (Accessed August 20, 2020).

Jun, S., Kang, N.-Y., Lee, W., and Chun, Y. (2017). An Alternative Multi-Model Ensemble Forecast for Tropical Cyclone Tracks in the Western North Pacific. *Atmosphere* 8 (9), 174. doi:10.3390/atmos8090174

Kaplan, J., DeMaria, M., and Knaff, J. A. (2010). A Revised Tropical Cyclone Rapid Intensification Index for the Atlantic and Eastern North Pacific Basins. *Wea. Forecast.* 25 (1), 220–241. doi:10.1175/2009WAF2222280.1

Knaff, J. A., Sampson, C. R., and DeMaria, M. (2005). An Operational Statistical Typhoon Intensity Prediction Scheme for the Western North Pacific. *Wea. Forecast.* 20 (4), 688–699. doi:10.1175/WAF863.1

Langmack, H., Fraedrich, K., and Sielmann, F. (2012). Tropical Cyclone Track Analog Ensemble Forecasting in the Extended Australian Basin: NWP Combinations. *Q. J. R. Meteorol. Soc.* 138 (668), 1828–1838. doi:10.1002/qj.1915

Lee, J., Im, J., Cha, D.-H., Park, H., and Sim, S. (2019). Tropical Cyclone Intensity Estimation Using Multi-Dimensional Convolutional Neural Networks from Geostationary Satellite Data. *Remote Sens.* 12 (1), 108. doi:10.3390/rs12010108

Li, Q., Li, Z., Peng, Y., Wang, X., Li, L., Lan, H., et al. (2018). Statistical Regression Scheme for Intensity Prediction of Tropical Cyclones in the Northwestern Pacific. *Wea. Forecast.* 33 (5), 1299–1315. doi:10.1175/WAF-D-18-0001.1

Lin, I.-I., Chen, C.-H., Pun, I.-F., Liu, W. T., and Wu, C.-C. (2009). Warm Ocean Anomaly, Air Sea Fluxes, and the Rapid Intensification of Tropical Cyclone Nargis (2008). *Geophys. Res. Lett.* 36 (L03817), 1–5. doi:10.1029/2008GL035815

Ma, L., Zhang, G., and Lu, E. (2018). Using the Gradient Boosting Decision Tree to Improve the Delineation of Hourly Rain Areas during the Summer from Advanced Himawari Imager Data. *J. Hydrometeorol.* 19 (5), 761–776. doi:10.1175/JHM-D-17-0109.1

Ma, X., Ding, C., Luan, S., Wang, Y., and Wang, Y. (2017). Prioritizing Influential Factors for Freeway Incident Clearance Time Prediction Using the Gradient Boosting Decision Trees Method. *IEEE Trans. Intell. Transp. Syst.* 18 (9), 2303–2310. doi:10.1109/TITS.2016.2635719

Mas, J. F., and Flores, J. J. (2008). The Application of Artificial Neural Networks to the Analysis of Remotely Sensed Data. *Int. J. Remote Sens.* 29 (3), 617–663. doi:10.1080/01431160701352154

McGovern, A., Karstens, C. D., Smith, T., and Lagerquist, R. (2019). Quasi-Operational Testing of Real-Time Storm-Longevity Prediction via Machine Learning. *Wea. Forecast.* 34 (5), 1437–1451. doi:10.1175/WAF-D-18-0141.1

Mercer, A., and Grimes, A. (2017). Atlantic Tropical Cyclone Rapid Intensification Probabilistic Forecasts from an Ensemble of Machine Learning Methods. *Procedia Comput. Sci.* 114, 333–340. doi:10.1016/j.procs.2017.09.036

Mountrakis, G., Im, J., and Ogole, C. (2011). Support Vector Machines in Remote Sensing: A Review. *ISPRS J. Photogramm. Remote Sens.* 66 (3), 247–259. doi:10.1016/j.isprsjprs.2010.11.001

NCEP (2020). National Center for Atmospheric Research, Computational and Information Systems Laboratory. Available at: https://rda.ucar.edu/datasets/ds083.2/#! (Accessed August 21, 2020).

NOAA (2020). NOAA Optimum Interpolation (OI) Sea Surface Temperature (SST) V2. Available at: https://psl.noaa.gov/data/gridded/data.noaa.oisst.v2.highres.html (Accessed August 25, 2020).

Pan, B., Xu, X., and Shi, Z. (2019). Tropical Cyclone Intensity Prediction Based on Recurrent Neural Networks. *Electron. Lett.* 55 (7), 413–415. doi:10.1049/el.2018.8178

Quinlan, J. R. (1987). "Decision Trees as Probabilistic Classifiers," in Proceedings of the Fourth International Workshop on Machine Learning, Irvine, CA, June 22–25, 1987, 31–37. doi:10.1016/B978-0-934613-41-5.50007-6

Ren, F., Liang, J., Wu, G., Dong, W., and Yang, X. (2011). Reliability Analysis of Climate Change of Tropical Cyclone Activity over the Western North Pacific. *J. Clim.* 24 (22), 5887–5898. doi:10.1175/2011JCLI3996.1

Sandery, P. A., Brassington, G. B., Craig, A., and Pugh, T. (2010). Impacts of Ocean-Atmosphere Coupling on Tropical Cyclone Intensity Change and Ocean Prediction in the Australian Region. *Mon. Wea. Rev.* 138 (6), 2074–2091. doi:10.1175/2010MWR3101.1

Schapire, R. E. (2003). "The Boosting Approach to Machine Learning: An Overview," in *Nonlinear Estimation and Classification*. Editors D. D. Denison, M. H. Hansen, C. C. Holmes, B. Mallick, and B. Yu (New York, NY: Springer), 149–171. doi:10.1007/978-0-387-21579-2_9

SIGOPT (2020). Bayesian Optimization Primer. Available at: https://sigopt.com/static/pdf/SigOpt_Bayesian_Optimization_Primer.pdf (Accessed Sept 6, 2020).

Snoek, J., Larochelle, H., and Adams, R. P. (2012). "Practical Bayesian Optimization of Machine Learning Algorithms," in *Advances in Neural Information Processing Systems* (Nevada, U.S.A, Curran Associates, Inc.), 25, 2960–2968.

STI (2020). Shanghai Typhoon Institute. TC Best Track Data. Available at: http://tcdata.typhoon.org.cn/zjljsjj_zlhq.html (Accessed August 28, 2020).

Swersky, K., Snoek, J., and Adams, R. P. (2013). "Multi-task Bayesian Optimization," in *Advances in Neural Information Processing Systems*. Editors C. J. C. Burges, L. Bottou, M. Welling, Z. Ghahramani, and K. Q. Weinberger (Red Hook, NY: Curran Associates, Inc.), 26. Available at: http://nrs.harvard.edu/urn-3:HUL.InstRepos:12561002.

Wang, Y., Rao, Y., Tan, Z.-M., and Schönemann, D. (2015). A Statistical Analysis of the Effects of Vertical Wind Shear on Tropical Cyclone Intensity Change over the Western North Pacific. *Mon. Wea. Rev.* 143 (9), 3434–3453. doi:10.1175/MWR-D-15-0049.1

Wang, Y., and Wu, C.-C. (2004). Current Understanding of Tropical Cyclone Structure and Intensity Changes–A Review. *Meteorol. Atmos. Phys.* 87 (4), 257–278. doi:10.1007/s00703-003-0055-6

Xie, J., and Coggeshall, S. (2010). Prediction of Transfers to Tertiary Care and Hospital Mortality: A Gradient Boosting Decision Tree Approach. *Stat. Analy. Data Min.* 3 (4), 253–258. doi:10.1002/sam.10079

Xu, W., Balaguru, K., August, A., Lalo, N., Hodas, N., DeMaria, M., et al. (2021). Deep Learning Experiments for Tropical Cyclone Intensity Forecasts. *Wea. Forecast.* 36 (4), 1453–1470. doi:10.1175/WAF-D-20-0104.1

Yang, F., Wang, D., Xu, F., Huang, Z., and Tsui, K.-L. (2020). Lifespan Prediction of Lithium-Ion Batteries Based on Various Extracted Features and Gradient Boosting Regression Tree Model. *J. Power Sources* 476, 228654. doi:10.1016/j.jpowsour.2020.228654

Yang, T., Chen, W., and Cao, G. (2016). Automated Classification of Neonatal Amplitude-Integrated EEG Based on Gradient Boosting Method. *Biomed. Signal Process. Control* 28, 50–57. doi:10.1016/j.bspc.2016.04.004

Zeng, Z., Wang, Y., and Chen, L. (2010). A Statistical Analysis of Vertical Shear Effect on Tropical Cyclone Intensity Change in the North Atlantic. *Geophys. Res. Lett.* 37 (L02802), 1–6. doi:10.1029/2009GL041788

Zhang, C.-J., Qian, J.-F., Ma, L.-M., and Lu, X.-Q. (2016). Tropical Cyclone Intensity Estimation Using RVM and DADI Based on Infrared Brightness Temperature. *Wea. Forecast.* 31 (5), 1643–1654. doi:10.1175/WAF-D-15-0100.1

Zhang, Q., Wu, L., and Liu, Q. (2009). Tropical Cyclone Damages in China 1983-2006. *Bull. Amer. Meteor. Soc.* 90 (4), 489–496. doi:10.1175/2008BAMS2631.1

Zhang, W., Gao, S., Chen, B., and Cao, K. (2013). The Application of Decision Tree to Intensity Change Classification of Tropical Cyclones in Western North Pacific. *Geophys. Res. Lett.* 40 (9), 1883–1887. doi:10.1002/grl.50280

Zhang, Z., and Krishnamurti, T. N. (1997). Ensemble Forecasting of Hurricane Tracks. *Bull. Amer. Meteor. Soc.* 78 (12), 2785–2795. doi:10.1175/1520-0477(1997)078<2785:efoht>2.0.co;2

Zhang, Z., Yang, W., and Wushour, S. (2020). Traffic Accident Prediction Based on LSTM-GBRT Model. *J. Control Sci. Eng.* 2020, 1–10. doi:10.1155/2020/4206919

Zhou, M., Chen, J., Huang, H., Zhang, D., Zhao, S., and Shadabfar, M. (2021). Multi-Source Data Driven Method for Assessing the Rock Mass Quality of a NATM Tunnel Face via Hybrid Ensemble Learning Models. *Int. J. Rock Mech. Min. Sci.* 147, 104914. doi:10.1016/j.ijrmms.2021.104914

Conflict of Interest: The authors declare that the research was conducted in the absence of any commercial or financial relationships that could be construed as a potential conflict of interest.

frontiers | Frontiers in Earth Science

TYPE Original Research
PUBLISHED 07 September 2022
DOI 10.3389/feart.2022.994647

OPEN ACCESS

EDITED BY
Wei Zhang,
Utah State University, United States

REVIEWED BY
Kevin Cheung,
E3-Complexity Consultant, Australia
Yuqing Wang,
University of Hawaii at Manoa,
United States

*CORRESPONDENCE
Liguang Wu,
liguangwu@fudan.edu.cn
Jinhua Yu,
jhyu@nuist.edu.cn

SPECIALTY SECTION
This article was submitted to
Atmospheric Science,
a section of the journal
Frontiers in Earth Science

RECEIVED 15 July 2022
ACCEPTED 03 August 2022
PUBLISHED 07 September 2022

CITATION
Xie T, Wu L and Yu J (2022), Application of potential vorticity tendency diagnosis method to high-resolution simulation of tropical cyclones.
Front. Earth Sci. 10:994647.
doi: 10.3389/feart.2022.994647

Application of potential vorticity tendency diagnosis method to high-resolution simulation of tropical cyclones

Tong Xie[1,2], Liguang Wu[3,4]* and Jinhua Yu[1]*

[1]Key Laboratory of Meteorological Disaster of Ministry of Education (KLME)/ Collaborative Innovation Center on Forecast and Evaluation of Meteorological Disasters (CIC-FEMD), Nanjing, China, [2]State Key Laboratory of Severe Weather, Chinese Academy of Meteorological Sciences, Beijing, China, [3]Department of Atmospheric and Oceanic Sciences and Institute of Atmospheric Sciences, Fudan University, Shanghai, China, [4]Innovation Center of Ocean and Atmosphere System, Zhuhai Fudan Innovation Research Institute, Zhuhai, China

As the grid spacing in the numerical simulation decreases to ~1 km, the potential vorticity (PV) structure of the simulated tropical cyclone (TC) is an annular tower of high PV with low PV in the eye and the resulting reversal of the radial PV gradient in the inner core is subject to dynamic instability, leading to complicated small-scale features in the PV field. While the PV tendency (PVT) method has been successfully used to diagnose TC motion in numerical simulations with relatively coarse resolution (~10 km), it has been found that the PVT diagnosis method fails in the TC simulation with grid spacing of ~1 km. This study reveals that the failure of the PVT diagnosis method in the high-resolution simulation with grid spacing of ~1 km arises from the induced small-scale features in the PV field. The high localized PV features do not affect TC motion, but make it difficult to calculate the gradient of azimuthal mean PV when the time interval of the model output is ~1 h. It is suggested that the PVT method can be applied to high-resolution simulations by increasing the time interval of the model output and/or smoothing the model output to reduce the influence of small-scale PV features.

KEYWORDS

tropical cyclone motion, nurmerical simulation, potential vorticity (PV), small-scale features, model resolution

Introduction

The potential vorticity (PV) tendency (PVT) method proposed by Wu and Wang (2000) treats a tropical cyclone (TC) as a positive PV anomaly relative to its environment and TC motion is essentially the propagation of the PV anomaly. The PVT method has been successfully used to diagnose the influences of various physical processes on TC motion in numerical simulations, such as the effects of diabatic heating, land surface friction, river deltas, coastal lines, mountains, islands, cloud-radiative processes, and sea surface pressure gradients (e.g., Wu and Wang 2001a, Wu and Wang 2001b; Wong and Chan, 2006; Yu et al., 2007; Fovell et al., 2010; Hsu et al., 2013; Wang et al., 2013; Choi et al., 2013). Over the past two decades, numerical models for TC simulation have been greatly improved and the horizontal grid spacing has been decreased from ~10 to ~1 km, even to 100 m or less (Zhu 2008; Rotunno et al., 2009; Zhu et al., 2013; Green and Zhang 2015; Wu et al., 2018, Wu et al., 2019). However, it has been found that the PVT method cannot be applied to the high-resolution (1 km or less) simulations of TCs (Zhao et al., 2019).

Over the past two decades, the PVT method was used to diagnose the influences of various physical processes on TC motion (e.g., Wu and Wang 2001a, Wu and Wang 2001b; Wong and Chan, 2006; Yu et al., 2007; Fovell et al., 2010; Hsu et al., 2013; Wang et al., 2013; Choi et al., 2013). Using the hourly model output with the 9-km horizontal resolution, Wu and Chen (2016) demonstrated that the conventional steering calculated over a certain radius from the TC center in the horizontal and a deep pressure layer in the vertical plays a dominant role in TC motion since the coherent structure of TC circulation makes the contributions of other processes largely cancelled out, but the instantaneous motion and the trochoidal motion around a mean track can considerably deviate from the conventional steering (Chan et al., 2002) also found that the horizontal PV advection played a dominant role when there were no significant changes in the speed and direction of the TC motion. Using the hourly model output with the 9-km horizontal resolution, (Liang and Wu 2015) investigated the sudden northward track turning of the western North Pacific TCs embedded in a monsoon gyre, which is a low-frequency, cyclonic vortex in the lower troposphere with a diameter of about 2500 km (Lander 1994; Carr and Elsberry 1995; Wu et al., 2013). They showed that the sudden northward track turning can be generally accounted for by changes in the synoptic-scale steering flow resulted from the interaction between the TC and the monsoon gyre. Note that the PVT method used in these studies were based on simulation data with relatively coarse resolution (~10 km), although some numerical simulations include nested domains with the horizontal resolution (~1 km).

As the grid spacing decreases to ~1 km or less, the PV structure of the simulated TC is an annular tower of high PV with low PV in the inner-core region, rather than a tower of high PV (e.g., Möller and Smith 1994; Yang et al., 2020). The reversal of the radial PV gradient in the eyewall is subject to dynamic instability (Montgomery and Shapiro 1995; Menelaou et al., 2018), leading to a complicated PV structure due to breaking and mixing of the PV distribution (Schubert et al., 1999). With the increase of the model resolution, the simulated PV structure in the TC inner core is increasingly complicated due to the presence of small-scale structures (Ito et al., 2017; Wu et al., 2018, Wu et al., 2019). Given that the tendency and horizontal gradient in the PVT method are calculated using the difference method, it is necessary to reevaluate the PVT method in the high-resolution (~1 km) simulation, which is an important approach to understand TC intensity and structure change.

High-resolution simulation of TCs

The simulation data used in this study are from two numerical experiments, which were conducted in previous studies (Chen et al., 2011; Wu and Chen 2016). While the first simulation mainly provides the 1-h outputs with different horizontal resolutions, the second simulation provides the 5-min output in the 1-km resolution domain.

The first numerical experiment is a semi-idealized numerical simulation conducted with the version 3.2.1 of the WRF model. The details of the experimental design can be found in Wu and Chen (2016). It was designed with four two-way interactive domains embedded in the 27-km resolution domain. The grid spacing decreases by a factor of 3 for the nested domains. The corresponding horizontal grid sizes of the nested domains are 9 km, 3 km, 1 km, 1/3 km (333 m) and the number of their grid meshes is 230 × 210, 432 × 399, 333 × 333, 501 × 501, and 720 × 720, respectively. The three innermost domains move with the simulated TC. The model includes 75 vertical levels with a model top of 50 hPa. The Kain-Fritsch cumulus parameterization scheme and the WRF single-moment 3-class scheme are used in the outermost domain (Kain and Fritch 1993), and in the four nested domains the WRF 6-class microphysics scheme is selected (Hong et al., 2006). The Yonsei University scheme was adopted for PBL parameterization in the outer domains (Noh et al., 2003) and the LES simulation was used in the sub-kilometer domains (Mirocha et al., 2010). In this study we focus only on the evaluation of the PVT method and the evolution of the TC structure simulated with the different grid sizes is not discussed. The multi-domain datasets can be used to examine the influence of the small-scale PV features in the inner core of the simulated TC.

Following (Wu and Chen 2016), the low-frequency background was from that of Typhoon Matsa (2005) from 0000 UTC on 5 August to 0000 UTC on 9 August 2005 (Duchon 1979). A symmetric vortex was first spun up for 18-h on an f-plane and then put in the low-frequency background at the center of Matsa (25.4°N, 123.0°E). The experiment was run for 72 h over an open ocean with a constant sea surface temperature of 29°C. Considering the possible adjustment of the vortex structure, we used the output from 24 to 72 h. Figure 1 shows the 48-h track and intensity of the simulated TC in the semi-idealized experiment at 1-h intervals. The simulated storm takes a generally recurving track. The minimum sea-level pressure fluctuates around 950 hPa, while the 10-m maximum wind generally decreases during the 48-h period. The simulated TC maintains the strength of categories 2 and 3.

The other experiment is the prediction of Hurricane Wilma (2005) from (Chen et al., 2011). The initial and lateral boundary conditions were from then-operational GFDL model data. The details about the setup of the WRF model and the corresponding verification can be found in (Chen et al., 2011). The experiment included four interactive domains with the horizontal grid

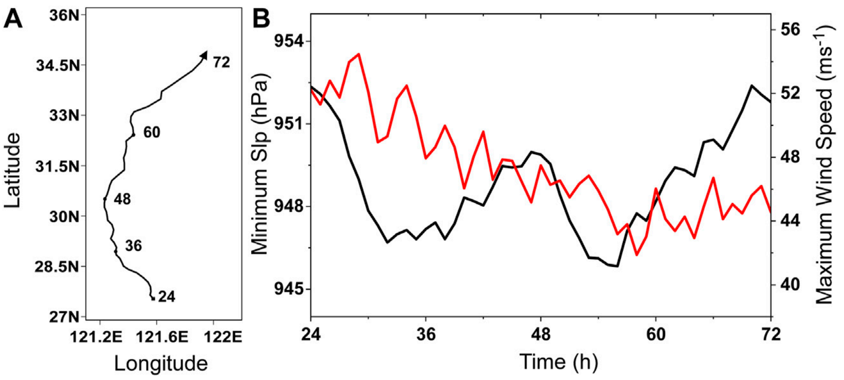

FIGURE 1
The 48-h track **(A)** and intensity **(B)** of the simulated TC in the semi-idealized experiment. The TC intensity is indicated by the minimum sea level pressure (SLP) (black, hPa) and 10-m maximum wind speed (red, ms^{-1}).

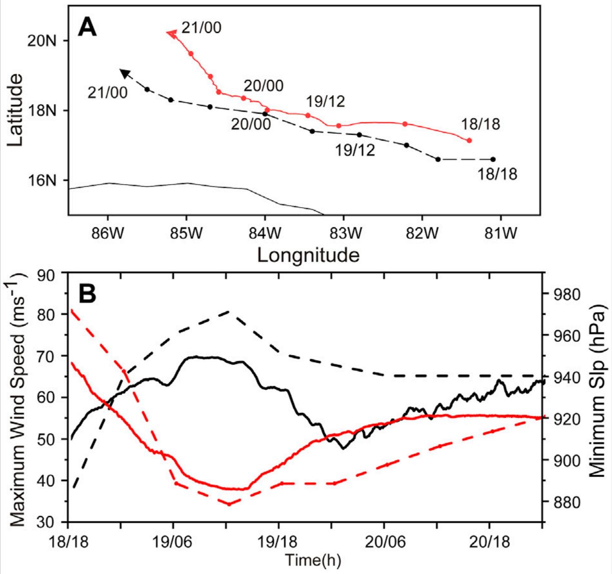

FIGURE 2
The observed (dashed) and predicted (solid) tracks **(A)** and intensity **(B)** of Hurricane Wilma (2005) during the period 1800 UTC 18 October 2005 (18 h) to 0000 UTC 21 October 2005 (72 h). The intensity is indicated by the minimum sea level pressure (SLP) (red, hPa) and 10-m maximum wind speed (black, ms^{-1}).

spacing of 27 km, 9 km, 3 km and 1 km, respectively, with 55 vertical levels. The output of the innermost domain at 5-min intervals is used in this study. The 72-h experiment was initialized at 0000 UTC 18 October 2005 and terminated at 0000 UTC 21 October 2005. Figure 2 shows the predicted track and intensity of Wilma after the first 18-h spin-up. The predicted storm generally takes a northwestward track. Consistent with the observation, the predicted storm experiences an initial spin-up, the rapid intensification from 18 to 36 h and the intensity change associated with the eyewall replacement during the last 36 h.

PVT method and TC center detection

The PV tendency in the coordinates moving with a TC is written as (Wu and Wang 2000)

$$\left(\frac{\partial P}{\partial t}\right)_{1m} = \left(\frac{\partial P}{\partial t}\right)_{1f} + \vec{C}\cdot\nabla P_s, \tag{1}$$

where subscript 1 represents the wavenumber-1 component of the PV tendency and subscripts m and f denote the moving and fixed reference frames relative to the TC center, respectively. $\vec{C}$ is the translation velocity of the TC, and P_s is the symmetric component of PV with respect to the TC center. In (1), the Ertel PV (P) is written as

$$P = \frac{1}{\rho}\vec{\eta}\cdot\nabla\theta_v, \tag{2}$$

where the absolute vorticity $\vec{\eta} = 2\vec{\Omega} + \nabla\times\vec{V}$, and $\vec{\Omega}$ and $\vec{V}$ are the angular velocity of rotation of Earth and three-dimensional velocity, respectively. The total air density (ρ) includes the densities of dry air, water vapor, condensed water, and hydrometeors. θ_v is the virtual potential temperature.

In (Wu and Wang 2000), the PV tendency in the moving reference frame was neglected since it is much smaller than the one in the fixed reference frame in their study. In this study, we retain the term and calculate it with the time difference method. The PV tendency in the fixed reference frame can be calculated with the time difference or from the PV tendency equation. The gradient of the symmetric component of PV are calculated with the space difference method. The least square method is used to solve the zonal and meridional components of the translation velocity within a radius of 90 km (Wu and Wang 2000). In fact, when the calculation area covers the inner-core region, the results are insensitive to the selection of the radius since the TC translation velocity is weighed by the gradient of the symmetric component of PV.

When quantifying the contributions of individual physical processes, we use the PV tendency equation in the fixed reference as follows

$$\left(\frac{\partial P}{\partial t}\right)_{1f} = \wedge_1\left(-\overrightarrow{V_h}\cdot\nabla_h P - w\frac{\partial P}{\partial z} + \frac{\vec{\eta}}{\rho}\cdot\nabla\frac{d\theta_v}{dt} + R\right), \qquad (3)$$

where $\overrightarrow{V_h}$ and w are the horizontal and vertical components of the wind velocity. The right-hand side of (3) includes the horizontal advection (HA), vertical advection (VA), diabatic heating (DH) terms. R includes the friction term and the effects related to momentum flux. In this study, R is calculated as a residual of (3) and thus also includes the calculation error. The operator $\wedge_1$ is used to obtain the wavenumber one component. In addition to the PV tendency in the moving coordinates (PVTm), as indicated in (1) and (3), the TC translation velocity calculated with the PVT method can result from five physical processes: the development of the wavenumber-one component (PVTm), HA, VA, DH and R.

As indicated in (1), the symmetric and wavenumber one components with respect to the TC center are calculated in the PVT method. The accuracy of the decomposed symmetric and asymmetric components of the TC circulation depends critically on the TC center position due to strong wind speed and the associated strong radial gradient in the inner-core region (Willoughby 1992; Yang et al., 2020). Focusing on the resulting symmetric and asymmetric inner-core structures, Yang et al. (2020) evaluated four center-detecting methods that are often used in TC simulations by comparing the evolution of the small-scale track oscillation and vortex tilt. The centers detected with the four methods are the pressure centroid center (PCC), the PV centroid center (PVC), the maximum tangential wind center (MTC), and the minimum pressure variance center (MVC). They found that the maximun symmetric inner-core structures can be obtained with the MVC and MTC, while the resulting track oscillations and vortex tilt are smoother with the MVC than with the MTC. It is suggested that the MVC and MTC can be used in high-resolution simulations.

The method for detecting the MVC was described in Braun et al. (2006) and Yang et al. (2020). That is, the azimuthally-averaged variance of the pressure field in the inner core is calculated with an assumed TC center in the inner-core region until the minimum azimuthally-averaged variance is reached. The radius for calculating pressure variance is 90 km in this study. The method for detecting the MTC was described in Marks et al. (1992), Wu et al. (2006) and Reasor et al. (2013). The MTC is associated with the maximum azimuthal mean tangential wind. To reduce abrupt changes in the track oscillations, we detect the maximum azimuthal mean tangential wind in an annulus, rather than a single circle. The annulus is defined between 0.7 and 1.3 times the radius of maximum wind (RMW).

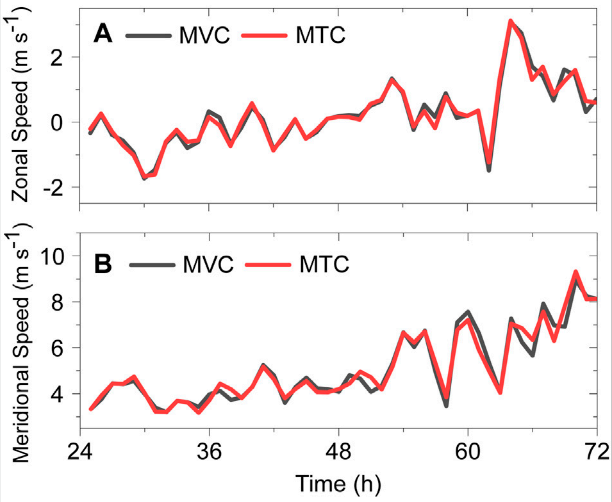

FIGURE 3
Comparisons of the zonal **(A)** and meridional **(B)** TC translation speed based on the MVC (black) and MTC (red) at the 5-km altitude. The 1-h model output in the 9-km domain is used from the semi-idealized experiment.

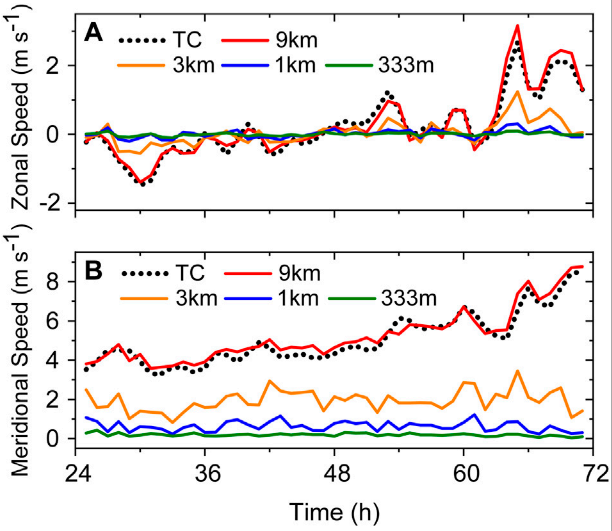

FIGURE 4
Time series of the zonal **(A)** and meridional **(B)** components of TC velocity based on the MVC (black dashed) and the PVT velocity from the 9-km domain (red), the 3-km domain (orange), the 1-km domain (blue) and the 1/3-km domain (green) at 5-km altitude in the semi-idealized experiment.

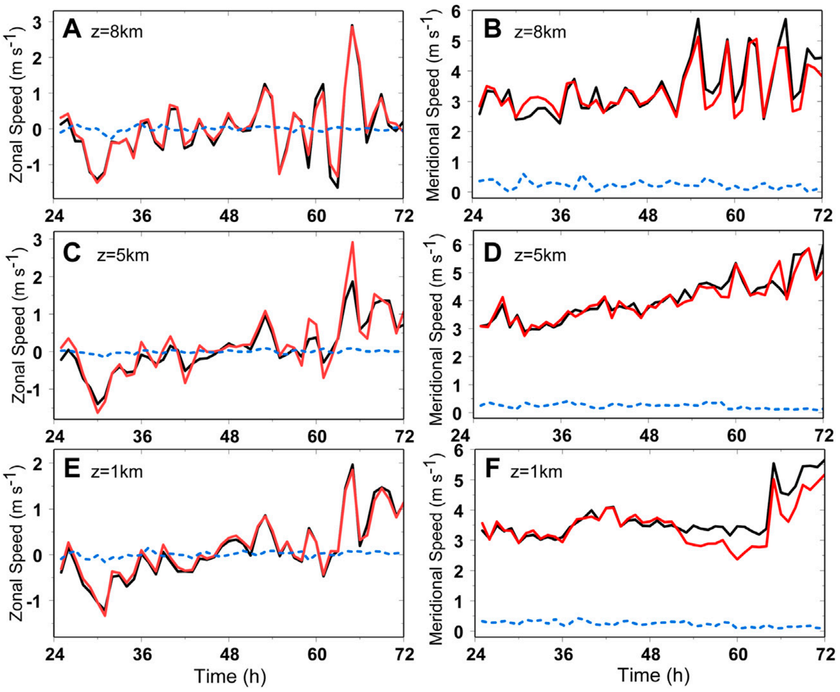

FIGURE 5
The zonal (left) and meridional (right) components of the PVT translation velocity based on the symmetric PV gradient from the 9-km domain and the wave-number-one component of PV tendency from the 1/3-km domain (red), the symmetric PV gradient from the 1/3-km domain and the wave-number-one component of PV tendency from the 9-km domain (blue), and the symmetric PV gradient from the 9-km domain and the wave-number-one component of PV tendency from the 9-km domain (black) at **(A,B)** 8 km, **(C,D)** 5 km and **(E,F)** 1 km in the semi-idealized experiment. The TC speed is based on the MVC.

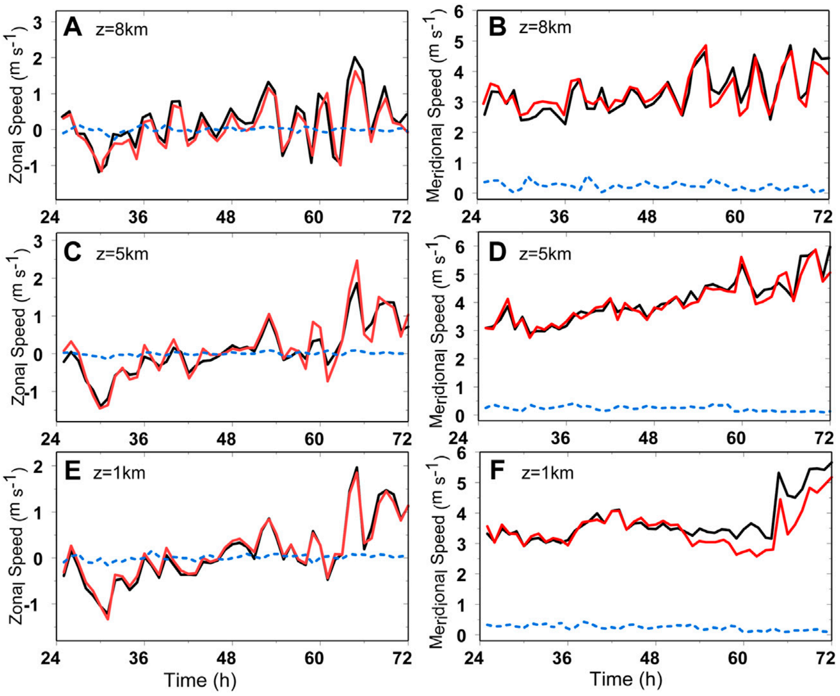

FIGURE 6
The zonal (left) and meridional (right) components of the PVT translation velocity based on the symmetric PV gradient from the 9-km domain and the wave-number-one component of PV tendency from the 1/3-km domain (red), the symmetric PV gradient from the 1/3-km domain and the wave-number-one component of PV tendency from the 9-km domain (blue), and the symmetric PV gradient from the 9-km domain and the wave-number-one component of PV tendency from the 9-km domain (black) at **(A,B)** 8 km, **(C,D)** 5 km and **(E,F)** 1 km in the semi-idealized experiment. The TC speed is based on the MTC.

In the semi-idealized experiment, the RMW is about 30 km, and the width of the annulus is about 18 km. Figure 3 shows the comparisons of the zonal and meridional components of the translation velocity of the center at the 5-km altitude based on the data from the 9-km domain at 1-h intervals in the semi-idealized experiment. Despite the small differences, Figure 3 indicates that the TC velocity can be calculated based on both the MVC and MTC.

Failure of the PVT diagnostic method in the high-resolution simulation

We first demonstrate the failure of the PVT diagnostic method in the high-resolution simulation when the hourly model output is used. The TC translation velocity (hereafter PVT velocity) is retrieved by using the 1-h instantaneous outputs from the various model domains in the semi-idealized experiment. Note that the TC translation velocity calculated with the center position (hereafter TC velocity) at 1-h intervals are nearly identical in these domains despite the varying grid sizes (figure not shown). In this section, the MVC is used as the TC center to demonstrate that the PVT velocity can be very different when the grid sizes become smaller than 9 km.

Figure 4 shows the time series of the zonal and meridional components of the TC translation velocity retrieved with the PVT method at the 5-km altitude. The PVT tendency terms were calculated with the time difference method. As shown in Figure 4, while the PVT velocity in the 9-km domain is in good agreement with the TC velocity, the PVT method fails to retrieve the TC velocity in the 3-km, 1-km and 1/3-km domains. Moreover, as the grid size becomes finer, the PVT velocity is closer to zero.

With the increase of the numerical model resolution, the simulated PV structure contains complicated small-scale structures (Ito et al., 2017; Wu et al., 2018, 2019). To understand the influence of the complicated small-scale features on the PVT method, we first conducted two experiments, in which we replaced the wave-number-one component of PVT and horizontal gradient of the symmetric PV component with those in the 1/3-km domain, respectively. By doing this we can pinpoint the influence of the complicated small-scale features. Figures 5, 6 show the comparisons of the resulting zonal and meridional components of the PVT velocity for the three selected levels, which represent the TC motion at the lower, middle and upper levels. When the wavenumber-one component of PV tendency is replaced with that in the 1/3-km domain, the TC motion can be well retrieved with the MVC and MTC. However, when the horizontal gradient of the symmetric PV component in (1) is replaced with that in the 1/3-km domain (blue), the TC motion is poorly retrieved. Both the zonal and meridional components are close to zero. It is suggested that the failure of the PVT method in the 1/3-km domain arises from the calculation of the horizontal gradient of the symmetric PV component.

Why cannot we use the 1-h instantaneous output to represent the horizontal gradient of PV over the 1-h period? Figure 7 shows the radius-altitude cross section of the azimuthal mean PV in the 9-km and 1/3-km domains at 48 h. In the 9-km domain, as shown in Figure 7A, the simulated TC exhibits a bowl-shaped PV anomaly within the radius of ~30 km, extending to 12 km. The maximum of PV is more than 35 PVU (1 PVU = 10^{-6} kg^{-1} K m^{2} s^{-1}) in the eye, with large radial PV gradient in the inner side of the eyewall. The simulated PV structure agrees well with previous studies (e.g., Chen and Yau 2001; Martinez et al., 2019). As the horizontal grid spacing decreases to 1/3 km (Figure 7B), there are many small-scale features although the bowl-shaped structure can be generally identified. A significant difference is localized PV maxima in the inner side of the eyewall. Figure 8 further shows the comparison of the horizontal cross section of PV in the two domains and their difference at the 5-km altitude. Comparing with the PV in the 9-km domain (Figure 8A), there are small-scale features outside of the high-PV core (Figure 8B). The small-scale structures are clearly seen in their difference (Figure 8C). It is suggested that the presence of the small-scale features can make difference in the calculated horizontal gradient of the symmetric PV component.

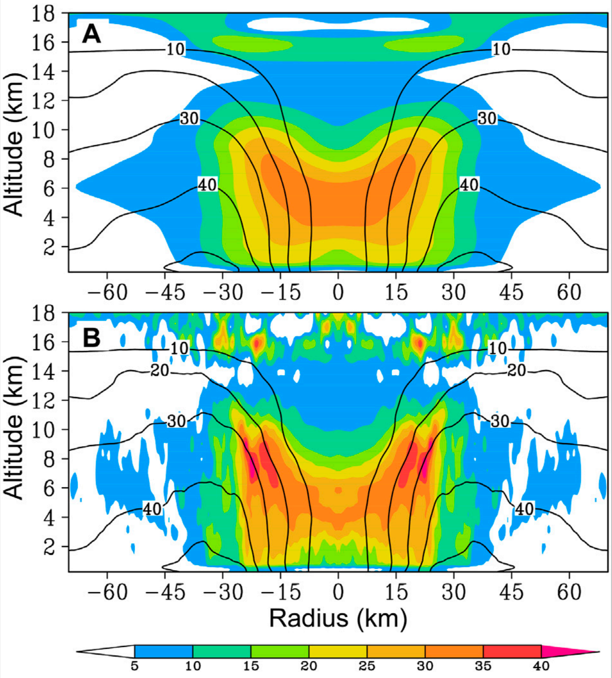

FIGURE 7
The radius-altitude cross section of the azimuthal mean PV (shaded, unit: 10^{-6} m^{2}s^{-1} Kkg^{-1}) and the azimuthal mean wind (contour, unit: ms^{-1}) at 48 h in the semi-idealized experiment. The PV is calculated with the outputs from **(A)** the 9-km domain and **(B)** 1/3-km domain, respectively.

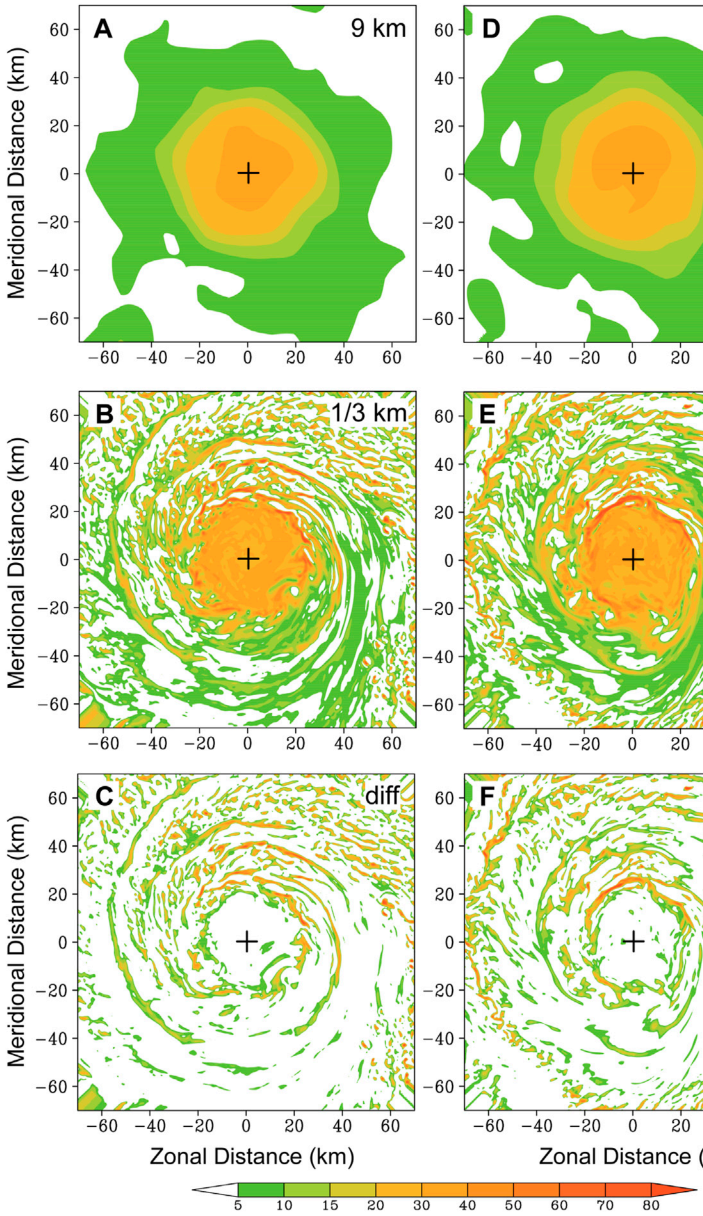

FIGURE 8
The 5-km PV (10^{-6} m^{2}s^{-1} Kkg^{-1}) field calculated from **(A,D)** the 9-km domain and **(B,E)** the 1/3-km domain and **(C,F)** their difference at 48 h (left) and 57 h (right) in the semi-idealized experiment. The plus symbol denotes the position of the TC center.

Figure 9 shows the comparisons of the zonal and meridional gradients of the azimuthal mean PV calculated from the 9-km domain and the 1/3-km domain at 48 h at the altitude of 5-km in the semi-idealized experiment. Compared with the 9-km domain, the PV gradient in the 1/3-km domain exhibits complicated radial structures, which result from the azimuthal mean of the small-scale features characterized by localized high PV maxima. In other words, the symmetric PV component is distorted by the localized PV maxima when making the azimuthal average.

Improvement of the PVT method for high-resolution simulations

In the last section, we show that the presence of the small-scale PV features can distort the resulting symmetric PV component. If the simulation with the high spatial resolution can resolve the small-scale features with very high PV, the evolution of the small-scale features must be represented in the calculation of the PV tendency. On the other hand, the

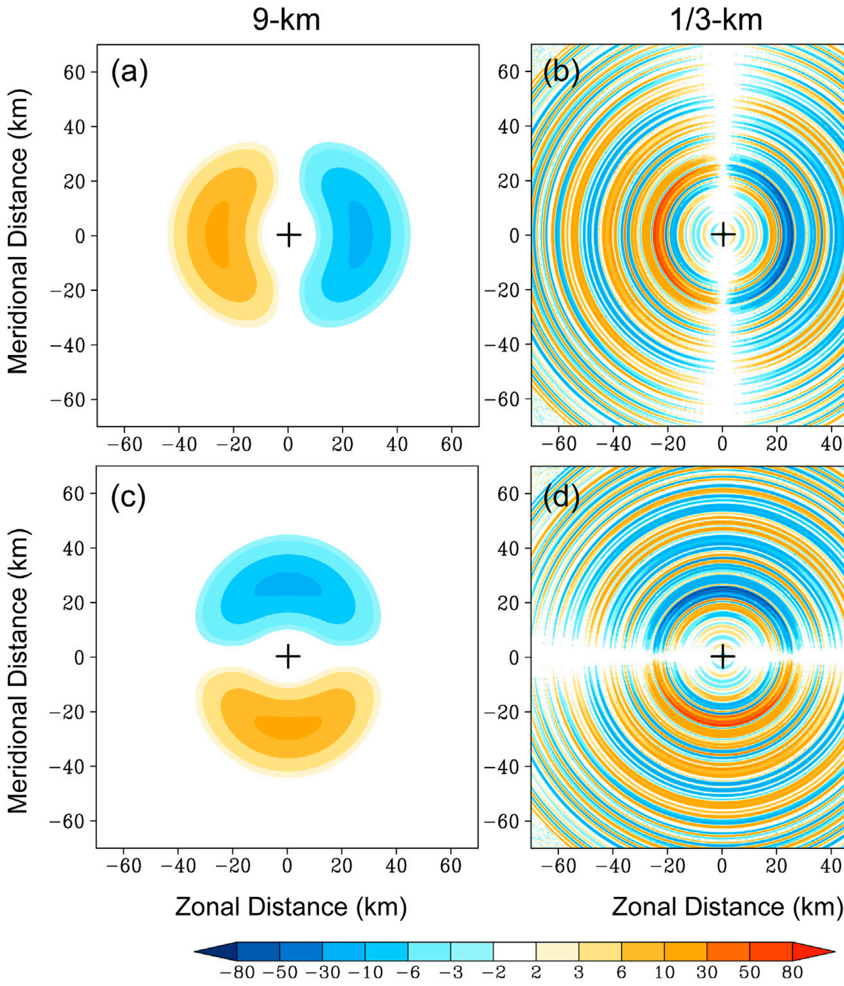

FIGURE 9
The zonal **(A,B)** and meridional **(C,D)** gradients of the azimuthal mean PV (unit: 10^{-10} m^2s^{-2} Kkg^{-1}) calculated from the 9-km domain (left) and the 1/3-km domain (right) at 48 h at the altitude of 5-km in the semi-idealized experiment.

small-scale features must be smoothed out as the PVT method is applied to the data at longer time intervals. Thus we can have two approached to improve the PVT method for high-resolution simulations.

Increasing time intervals

Since the PV structure cannot be well resolved with the 1-h model output, we first calculated the PV tendency and TC velocities with the 2-h model output of the semi-idealized experiment at 1-min intervals. Figure 10 shows the comparison between the PVT velocity and TC velocity based on the MTC and MVC, respectively. We can see that the TC motion at 1-min intervals can be retrieved with the PVT method, the correlation coefficients of zonal and meridional velocities are 0.95 (0.80) and 0.91 (0,72) for the MTC (MVC), respectively. The fluctuations of PVT velocity with the MVC are smaller than that with the MTC. Note that the TC translation velocity from the 1-min output can also have larger errors than that from 1-h output.

We also examined the retrieved PVT velocity using the prediction data of Hurricane Wilma (2005). Using the 5-min data, the TC velocity can be well retrieved with both the MTC and MVC although there are differences of the PVT velocity between the MVC and the MTC (Figure 11). For clarity, the 1-h running average is applied to the time series. Taking the MTC as an example, the zonal and meridional correlation coefficients between the TC and PVT velocities are 0.94 and 0.98, respectively. It is suggested that the TC velocity in the high-resolution simulation can be retrieved with the PVT method using the minute-interval output.

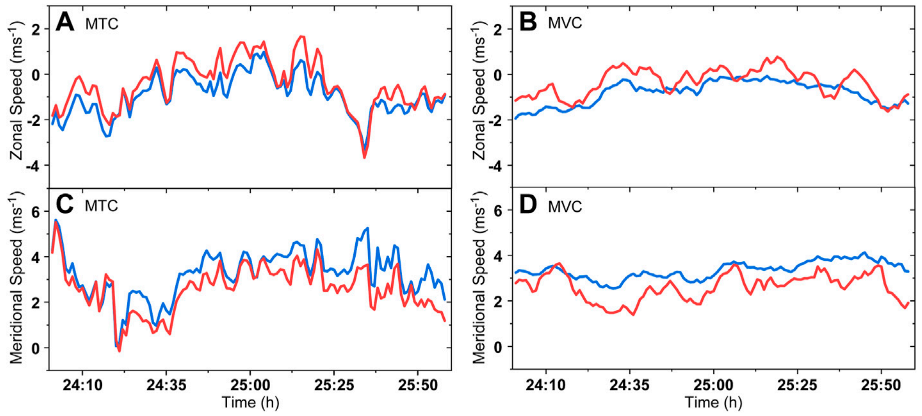

FIGURE 10
Comparisons of the zonal **(A,B)** and meridional **(C,D)** TC translation velocity derived from the TC center position (blue) and PV tendency (red) based on the MTC **(A,C)** and MVC **(B,D)** in the 1-min output and the 1/3-km domain at 5-km altitude in the semi-idealized experiment.

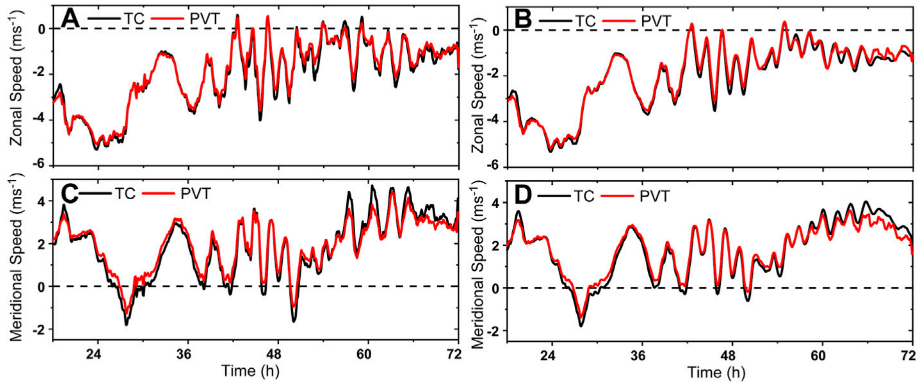

FIGURE 11
Comparisons of the zonal **(A,B)** and meridional **(C,D)** TC translation velocity derived from the TC center position (black) and PV tendency (red) based on the MTC **(A,C)** and MVC **(B,D)** of the 5-min output in the 1-km domain at 5-km altitude in the prediction of Hurricane Wilma. The 1-h running average is applied to the time series.

Reducing influence of small-scale PV features

(Zhao et al., 2019) suggested that the PVT method can be improved by smoothing the meteorological fields such as wind speed and temperature. However, the smoothing method and time were subjectively selected in (Zhao et al., 2019). In this study, a horizontal-thinning method is introduced to smooth the model output. The model output is horizontally thinned to the resolution of ~10 km for the calculation of the PVT velocity at the interval of ~1 h.

The thinning method can be illustrated by calculating the PVT velocity in the simulation of Hurricane Wilma. Here we use the instantaneous output in the 1-km domain at a time interval of 1 h. First, a 9-point smoothing is applied to the fields required in the PVT method, and then we have the resulting fields with the horizontal resolution of 3 km. Note that we cannot directly smooth the PV field since it is dominated by the positive PV. Second, using the smoothed fields, we repeat the first step and then we have the thinned output with the horizontal resolution of 9 km. Finally, we use the thinned, smoothed model output to calculate the PVT velocity.

Figure 12 shows the comparisons between the PVT velocity and TC velocity based on the instantaneous 1-h output in the 1-km domain. The PVT velocity is retrieved with the original output (black dashed) and thinned output (red dashed), respectively. For clarity, a 3-h running average is applied to the time series. While the PVT velocity from the original output

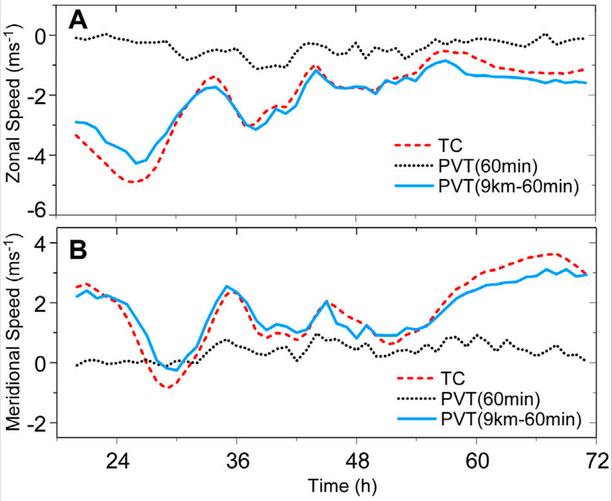

FIGURE 12
Comparisons of the zonal **(A)** and meridional **(B)** components of the TC velocity (red dashed) and the PVT velocity (blue solid) derived from the prediction of Hurricane Wilma (2005). The PVT velocity is calculated with the original 1-h output with the 1-km grid spacing (black dotted) and the corresponding thinned one (blue solid).

deviates significantly from the TC velocity, the TC velocity is well retrieved from the thinned output. The correlation between the TC and PVT velocities is 0.94 and 0.95 in the zonal and meridional components, respectively. Note that we can improve the performance of the PVT method by increasing time intervals and spatially smoothing model output.

Diagnosing contributions of physical processes

As shown in the last section, the TC translation velocity in the high-resolution can be well retrieved by increasing the output time interval or/and thinning the model output. In this section, we show that using the PV tendency equation, we can examine the individual contributions of the five physical processes: HA, VA, DH, the development of the wavenumber-one component (PVTm), and R. Since the PVT method can retrieve the TC translation velocity with 1-km resolution predicted data of Hurricane Wilma (2005), here we use the experiment as an example to illustrate the diagnosis of the contributions from various physical processes. Figure 13 shows the contributions of the five processes to the PVT velocity at the altitudes of 1 km, 5 and 8 km at 28 h. Note that the PVT velocity at each level is the vector sum of the contributions of the five processes. Consistent with the TC velocity, the retrieved PVT velocities at the three levels are nearly the same, and direct to the southwest. The PVT velocity is dominated by the contributions of HA, VA, and DH at

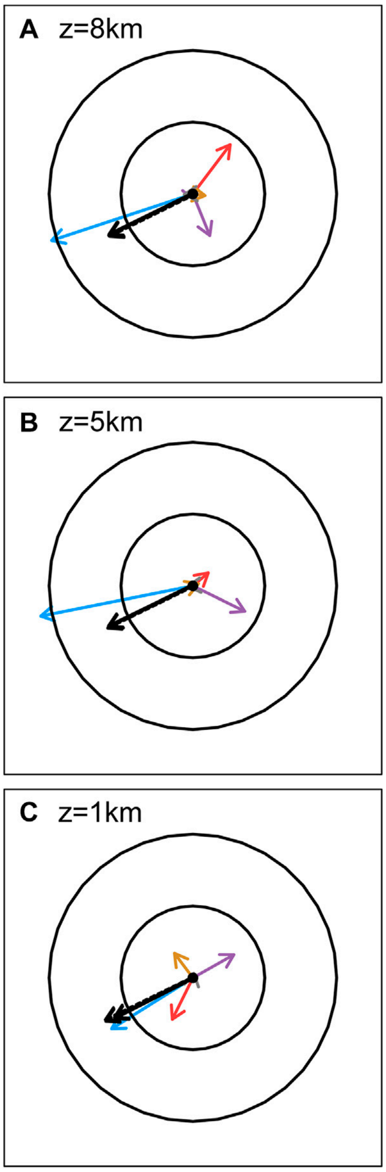

FIGURE 13
PVT velocity (black) and variations of contributions of HA (blue), VA (purple), DH (red), R (brown) and PVTm (grey) at 1 km **(A)**, 5 km **(B)** and 8 km **(C)** at 28 h of the prediction of Hurricane Wilma. The black circles represent speeds of 3 and 6 ms^{-1}, respectively. The black dash line vector indicates the TC velocity at the same altitude.

5 and 8 km, while R also plays a role in the boundary layer at 1 km. Although the individual contributions vary in the vertical, the TC vortex can maintain its coherent structure in the vertical.

Figure 14 further shows the time series of the contributions of the individual contributions at 5 km. Since the predicted Wilma maintains a relatively symmetric structure, the contribution of PVTm is generally small during the period, while the contribution of R increases since 60 h. As indicated in Wu and Chen (2016), the

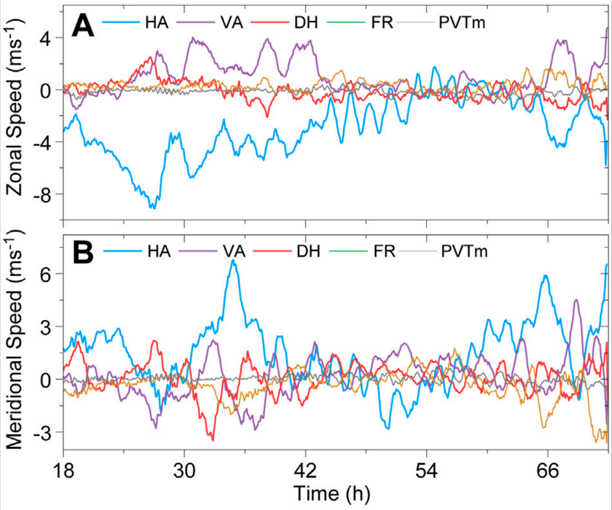

FIGURE 14
Comparisons of the zonal **(A)** and meridional **(B)** contributions of HA (blue), VA (purple), DH (red), R (brown) and PVTm (grey) terms at the 5-km altitude in the prediction of Hurricane Wilma.

contributions of these processes are not physically independent due to the coherent structure of the TC. For example, the correlation between the contributions of VA and HA is −0.53 in the zonal component and the correlation between the contributions of VA and DH is −0.4 in the meridional component. It is suggested that the contributions of these processes to the TC motion can partially cancelled each other.

Summary

As the model grid spacing decreases to ~1 km, the PV structure of the simulated TC is an annular tower of high PV with relatively low PV in the eye and the resulting reversal of the radial PV gradient in the eyewall is subject to dynamic instability. While the PVT method has been successfully used to understand TC motion in numerical simulations with relatively coarse resolution (~10 km), this study reevaluates the performance of the PVT diagnosis method by using the model output from two high-resolution TC simulations with grid spacing of ~1 km.

It is indicated that the failure of the PVT method in the high-resolution simulation arises from the influence of small-scale PV features on the calculation of the horizontal gradient of the symmetric PV component. This study demonstrates that the TC translation velocity in the high-resolution can be well retrieved by increasing the output time interval and thinning the model output. As the grid spacing decreases to ~1 km, the minute-interval model output can be used to calculate the PVT velocity. Alternatively, when the 1-h model output is available, a 9-point smoothing is successively used to thin the fields required in the PVT method, until the grid spacing of the smoothed fields is ~10 km. The thinned model output can be used to calculate the PVT velocity.

In this study, we also demonstrate that the PV tendency can be divided into two parts: one for TC motion and the other for the development of the asymmetric structure of TCs. It is suggested that the PVT method can be useful to understand the changes of TC structure and the associated intensity.

Data availability statement

Publicly available datasets were analyzed in this study. This data can be found here: https://mygeohub.org/resources/1601.

Author contributions

LW and TX conducted analysis and writing. TX contributed to figures included in this manuscript. JY offered advices to the writing.

Acknowledgments

The detail of the predicted data of Hurricane Wilma (2005) was described in (Chen et al., 2011). The authors thank Da-Lin Zhang of University of Maryland for providing the prediction data. This study was jointly supported by the National Natural Science Foundation of China (41730961, 42192551 and 421507100531).

Conflict of interest

The reviewer YW is currently organizing a Research Topic with the author LW.

The remaining authors declare that the research was conducted in the absence of any commercial or financial relationships that could be construed as a potential conflict of interest.

Publisher's note

References

Braun, S. A., Montgomery, M. T., and Pu, Z. (2006). High resolution simulation of Hurricane Bonnie (1998). Part I: The organization of eyewall vertical motion. *J. Atmos. Sci.* 63, 19–42. doi:10.1175/jas3598.1

Carr, L. E., and Elsberry, R. L. (1995). Monsoonal interactions leading to sudden tropical cyclone track changes. *Mon. Weather Rev.* 123, 265–290. doi:10.1175/1520-0493(1995)123<0265:miltst>2.0.co;2

Chan, J. C. L., Ko, F. M. F., and Lei, Y. M. (2002). Relationship between potential vorticity tendency and tropical cyclone motion. *J. Atmos. Sci.* 59, 1317–1336. doi:10.1175/1520-0469(2002)059<1317:rbpvta>2.0.co;2

Chen, H., Zhang, D.-L., Carton, J., and Atlas, R. (2011). On the rapid intensification of Hurricane Wilma (2005). Part I: Model prediction and structural changes. *Weather Forecast.* 26, 885–901. doi:10.1175/waf-d-11-00001.1

Chen, Y., and Yau, M. K. (2001). Spiral bands in a simulated hurricane. Part I: Vortex rossby wave verification. *J. Atmos. Sci* 58 (15), 2128–2145. doi:10.1175/1520-0469(2001)058<2128:sbiash>2.0.co;2

Choi, Y., Yun, K.-S., Ha, K.-J., Kim, K.-Y., Yoon, S.-J., and Chan, J.-C.-L. (2013). Effects of asymmetric SST distribution on straight-moving typhoon ewiniar (2006) and recurving typhoon maemi (2003). *Mon. Weather Rev.* 141, 3950–3967. doi:10.1175/mwr-d-12-00207.1

Duchon, C. E. (1979). Lanczos filtering in one and two dimensions. *J. Appl. Meteor.* 18, 1016–1022. doi:10.1175/1520-0450(1979)018<1016:lfioat>2.0.co;2

Fovell, R. G., Corbosiero, K. L., Seifert, A., and Liou, K.-N. (2010). Impact of cloud-radiative processes on hurricane track. *Geophys. Res. Lett.* 37, L07808. doi:10.1029/2010GL042691

Green, B. W., and Zhang, F. (2015). Numerical simulations of Hurricane Katrina (2005) in the turbulent gray zone. *J. Adv. Model. Earth Syst.* 7, 142. doi:10.1175/JAS-D-14-0244.1

Hong, S.–Y., Lim, J., and Kim, J-H. (2006). The WRF single–moment 6–class microphysics scheme (WSM6). *J. Korean Meteor. Soc.* 42, 129.

Hsu, L.-H., Kuo, H.-C., and Fovell, R. G. (2013). On the geographic asymmetry of typhoon translation speed across the mountainous island of taiwan. *J. Atmos. Sci.* 70, 1006–1022. doi:10.1175/jas-d-12-0173.1

Ito, J., Oizumi, T., and Niino, H. (2017). Near-surface coherent structures explored by large eddy simulation of entire tropical cyclones. *Sci. Rep.* 7, 3798. doi:10.1038/s41598-017-03848-w

Kain, J. S., and Fritch, J. M. (1993). Convective parameterization for mesoscale models: The kain–fritch scheme. The representation of cumulus convection in numerical models. *Meteorol. Monogr.* 46, 165–170. doi:10.1007/978-1-935704-13-3_16

Lander, M. A. (1994). Description of a monsoon gyre and its effects on the tropical cyclones in the Western North Pacific during August 1991. *Wea. Forecast.* 9, 640–654. doi:10.1175/1520-0434(1994)009<0640:doamga>2.0.co;2

Liang, J., and Wu, L. (2015). Sudden track changes of tropical cyclones in monsoon gyres: Full-physics, idealized numerical experiments. *J. Atmos. Sci.* 72, 1307–1322. doi:10.1175/jas-d-13-0393.1

Marks, F. D., Jr., Houze, R. A., Jr., and Gamache, J. F. (1992). Dual-aircraft investigation of the inner core of Hurricane Norbert. Part I: Kinematic structure. *J. Atmos. Sci.* 49, 919–942. doi:10.1175/1520-0469(1992)049<0919:daioti>2.0.co;2

Martinez, J., Bell, M. M., Rogers, R. F., and Doyle, J. D. (2019). Axisymmetric potential vorticity evolution of hurricane patricia (2015). *J. Atmos. Sci.* 76 (7), 2043–2063. doi:10.1175/jas-d-18-0373.1

Menelaou, K., Yau, M. K., and Lai, T.-K. (2018). A possible three-dimensional mechanism for oscillating wobbles in tropical cyclone–like vortices with concentric eyewalls. *J. Atmos. Sci.* 75 (7), 2157–2174. doi:10.1175/jas-d-18-0005.1

Mirocha, J. D., Lundquist, J. K., and Kosović, B. (2010). Implementation of a nonlinear subfilter turbulence stress model for large-eddy simulation in the advanced research WRF model. *Mon. Weather Rev.* 138, 4212–4228. doi:10.1175/2010mwr3286.1

Möller, J. D., and Smith, R. K. (1994). The development of potential vorticity in a hurricane-like vortex. *Q. J. R. Meteorol. Soc.* 120, 1255–1265. doi:10.1002/qj.49712051907

Montgomery, M. T., and Shapiro, L. J. (1995). Generalized charney–stern and fjortoft theorems for rapidly rotating vortices. *J. Atmos. Sci.* 52 (10), 1829–1833. doi:10.1175/1520-0469(1995)052<1829:gcaftf>2.0.co;2

Noh, Y., Cheon, W. G., Hong, S.-Y., and Raasch, S. (2003). Improvement of the K-profile model for the planetary boundary layer based on large-eddy simulation data. *Bound. Layer. Meteorol.* 107, 401–427. doi:10.1023/a:1022146015946

Reasor, P. D., Rogers, R., and Lorsolo, S. (2013). Environmental flow impacts on tropical cyclone structure diagnosed from airborne Doppler radar composites. *Mon. Weather Rev.* 141, 2949–2969. doi:10.1175/mwr-d-12-00334.1

Rotunno, R., Chen, Y., Wang, W., Davis, C., Dudhia, J., and Holland, G. J. (2009). Large-Eddy simulation of an idealized tropical cyclone. *Bull. Am. Meteorol. Soc.* 90, 1783–1788. doi:10.1175/2009bams2884.1

Schubert, W. H., Montgomery, M. T., Taft, R. K., Guinn, T. A., Fulton, S. R., Kossin, J. P., et al. (1999). Polygonal eyewalls, asymmetric eye contraction, and potential vorticity mixing in hurricanes. *J. Atmos. Sci.* 56, 1197–1223. doi:10.1175/1520-0469(1999)056<1197:peaeca>2.0.co;2

Wang, C.-C., Chen, Y.-H., Kuo, H.-C., and Huang, S.-Y. (2013). Sensitivity of typhoon track to asymmetric latent heating/rainfall induced by taiwan topography: A numerical study of typhoon fanapi(2010). *J. Geophys. Res. Atmos.* 118, 3292–3308. doi:10.1002/jgrd.50351

Willoughby, H. E. (1992). Linear motion of a shallow-water barotropic vortex as an initial-value problem. *J. Atmos. Sci.* 49, 2015–2031. doi:10.1175/1520-0469(1988)045<1906:LMOASW>2.0.CO;2

Wong, M. L. M., and Chan, J. C. L. (2006). Tropical cyclone motion in response to land surface friction. *J. Atmos. Sci.* 63, 1324–1337. doi:10.1175/jas3683.1

Wu, L., Braun, S. A., Halverson, J., and Heymsfield, G. (2006). A numerical study of Hurricane Erin (2001). Part I: Model verification and storm evolution. *J. Atmos. Sci.* 63, 65–86. doi:10.1175/jas3597.1

Wu, L., and Chen, X. (2016). Revisiting the steering principal of tropical cyclone motion in a numerical experiment. *Atmos. Chem. Phys.* 16, 14925–14936. doi:10.5194/acp-16-14925-2016

Wu, L., Liu, Q., and Li, Y. (2018). Prevalence of tornado-scale vortices in the tropical cyclone eyewall. *Proc. Natl. Acad. Sci. U. S. A.* 115, 8307–8310. doi:10.1073/pnas.1807217115

Wu, L., Liu, Q., and Li, Y. (2019). Tornado-scale vortices in the tropical cyclone boundary layer: Numerical simulation with the WRF–LES framework. *Atmos. Chem. Phys.* 19, 2477–2487. doi:10.5194/acp-19-2477-2019

Wu, L., and Wang, B. (2000). A potential vorticity tendency diagnostic approach for tropical cyclone motion. *Mon. Wea. Rev.* 128, 1899–1911. doi:10.1175/1520-0493(2000)128<1899:apvtda>2.0.co;2

Wu, L., and Wang, B. (2001b). Effects of convective heating on movement and vertical coupling of tropical cyclones: A numerical study. *J. Atmos. Sci.* 58, 3639–3649. doi:10.1175/1520-0469(2001)058<3639:eochom>2.0.co;2

Wu, L., and Wang, B. (2001a). Movement and vertical coupling of adiabatic baroclinic tropical cyclones. *J. Atmos. Sci.* 58, 1801–1814. doi:10.1175/1520-0469(2001)058<1801:mavcoa>2.0.co;2

Wu, L., Zong, H., and Liang, J. (2013). Observational analysis of tropical cyclone formation associated with monsoon gyres. *J. Atmos. Sci.* 70, 1023–1034. doi:10.1175/jas-d-12-0117.1

Yang, H., Wu, L., and Xie, T. (2020). Comparisons of four methods for tropical cyclone center detection in a high-resolution simulation. *J. Meteorological Soc. Jpn.* 98, 379–393. doi:10.2151/jmsj.2020-020

Yu, H., Huang, W., Duan, Y. H., Chan, J. C. L., Chen, P. Y., and Yu, R. L. (2007). A simulation study on pre-landfall erratic track of typhoon Haitang (2005). *Meteorol. Atmos. Phys.* 97, 189–206. doi:10.1007/s00703-006-0252-1

Zhao, J., Xie, T., Yang, H., Wu, L., and Liu, Q. (2019). Application of PVT method for diagnosing typhoon motion with high-resolution data. *Acta Meteorol. Sin.* 77, 1062. doi:10.11676/qxxb2019.065

Zhu, P., Menelaou, K., and Zhu, Z. (2013). Impact of subgrid-scale vertical turbulent mixing on eyewall asymmetric structures and mesovortices of hurricanes: Impact of SGS vertical turbulent mixing on eyewall asymmetries. *Q. J. R. Meteorol. Soc.* 140, 416–438. doi:10.1002/qj.2147

Zhu, P. (2008). Simulation and parameterization of the turbulent transport in the hurricane boundary layer by large eddies. *J. Geophys. Res.* 113, D17104. doi:10.1029/2007jd009643

frontiers | Frontiers in Earth Science

TYPE Original Research
PUBLISHED 15 September 2022
DOI 10.3389/feart.2022.997925

OPEN ACCESS

EDITED BY
Liguang Wu,
Fudan University, China

REVIEWED BY
Dajun Zhao,
Chinese Academy of Meteorological Sciences, China
Yuanlong Li,
Nanjing University, China

*CORRESPONDENCE
Zifeng Yu,
yuzf@typhoon.org.cn

SPECIALTY SECTION
This article was submitted to Atmospheric Science, a section of the journal Frontiers in Earth Science

RECEIVED 19 July 2022
ACCEPTED 22 August 2022
PUBLISHED 15 September 2022

CITATION
Duan J, Yu Z, Hu B, Zhen Y, Cheung KKW, Li Y and Cai Z (2022), Sensitivity of boundary layer schemes in simulating the asymmetric rainfall of landfalling typhoon Lekima (2019). *Front. Earth Sci.* 10:997925. doi: 10.3389/feart.2022.997925

Sensitivity of boundary layer schemes in simulating the asymmetric rainfall of landfalling typhoon Lekima (2019)

Jingjing Duan[1,2], Zifeng Yu[1]*, Bo Hu[2], Yan Zhen[3], Kevin K. W. Cheung[4], Yubin Li[5,6] and Zhiying Cai[2]

[1]Key Laboratory of Numerical Modeling for Tropical Cyclone of China Meteorological Administration, Shanghai Typhoon Institute, Shanghai, China, [2]Ningbo Meteorological Bureau of Zhejiang Province, Ningbo, China, [3]Ningbo Zhenhai Meteorological Bureau of Zhejiang Province, Ningbo, China, [4]E3-Complexity Consulting, Eastwood, NSW, Australia, [5]Key Laboratory for Aerosol-Cloud-Precipitation of China Meteorological Administration, Collaborative Innovation Center on Forecast and Evaluation of Meteorological Disasters, School of Atmospheric Physics, Nanjing University of Information Science and Technology, Nanjing, China, [6]Southern Marine Science and Engineering Guangdong Laboratory (Zhuhai), Zhuhai, China

A group of control (CTL) plus ten sensitivity numerical experiments have been conducted to investigate the sensitivity of planetary boundary layer (PBL) schemes in simulating the asymmetric precipitation distribution of typhoon Lekima (2019) during landfall. The simulated track and intensity are quite sensitive to the choice of the PBL scheme. In CTL that applies the Mellor–Yamada Nakanishi and Niino (MYNN) PBL and the surface layer scheme, the observed eyewall replacement 6 h prior to landfall and the asymmetric precipitation during landfall have been simulated well. However, in the PBL1 experiment that applies the Yonsei University (YSU) PBL scheme and the Revised Mesoscale Model version 5 (MM5) Monin–Obukhov surface layer scheme, no double eyewall is simulated. PBL1 and the other sensitivity experiments also simulate more axisymmetric precipitation distribution. PBL1 simulates intensification just before landfall, sustains intensity longer after landfall, but then dissipates quite rapidly. Such differences from CTL are due to larger enthalpy flux, higher PBL height (which is almost unchanged in CTL), and eddy diffusivity extending more into the free atmosphere in PBL1. These factors lead to outward expansion of the radius of maximum wind, larger radial inflow, larger axisymmetric tangential wind in the boundary layer, and larger updrafts in the eyewall. After landfall, larger momentum flux and larger friction velocity in PBL1 enable the more rapid dissipation. The intensification before landfall in PBL1 makes the axisymmetric component stronger. Asymmetry developed in the outer eyewall, and PBL1 was less successful in simulating the eyewall replacement that affects the degree of rainfall asymmetry. These results indicate that the model PBL schemes largely influence the simulated tropical cyclone (TC) intensity and structure including asymmetric rainfall distribution during landfall.

KEYWORDS

planetary boundary layer, PBL parameterization, landfall typhoon, asymmetric precipitation, tropical cyclone (TC)

1 Introduction

China experiences the most landfalling tropical cyclones (TCs) in the world, with an average of seven to eight such events per year (Zhang et al., 2011). Most TC damage occurs during the landfall. Strong wind, torrential rain, and storm surges caused by TCs may lead to heavy casualties and property damages. Despite the considerably improved accuracy of TC track forecasts over the last decades (Emanuel, 2000; DeMaria et al., 2007), the accuracy of precipitation forecasts during TC landfalls remains low (Yu et al., 2013, 2020). When the 24 h accumulated precipitation reaches 100 mm, the equitable threat score for the current operational numerical model forecasts is approximately 0.2, while the precipitation is 250 mm or higher, the score drops below 0.1 or even lower (Yu et al., 2020).

With the rapid advancement of modern weather observing systems such as satellites and radars (Yu et al., 2009), the analysis of precipitation distribution characteristics in TCs has greatly improved. Environmental vertical wind shear (VWS) is regarded as a crucial factor affecting the precipitation distribution in TCs over the ocean (Lonfat et al., 2004; Chen et al., 2006; Reasor et al., 2013). When VWS is greater than 5 m s^{-1}, the asymmetry of precipitation distribution in TCs is noticeable (Chen et al., 2006). Such asymmetry is more noticeable in an environment with strong westerly wind shear than one with strong easterly wind shear (Wingo and Cecil, 2010). These observational results indicate that the radial precipitation differences in a TC are predominantly dependent on the intensity of TC itself, whereas the azimuthal precipitation differences are mainly affected by VWS (Hence and Houze, 2012). The asymmetric precipitation distribution is attributable to the asymmetric vertical air motion, specifically the relative updraft and downdraft in downshear and upshear locations, respectively. The convective precipitation mainly occurs in the downshear-right quadrant in the eyewall region (Hence and Houze, 2011), and thus heavy precipitation generally concentrates in the downshear-left quadrant when

TABLE 1 Numerical experiment design.

Experiment name	PBL scheme description	Surface layer scheme
CTL	MYNN2.5	MYNN
PBL1	YSU	Revised MM5 Monin–Obukhov
PBL2	MYJ	Monin–Obukhov
PBL3	QNSE	QNSE
PBL4	MYNN3	MYNN
PBL5	ACM2	Revised MM5 Monin–Obukhov
PBL6	BouLac	Revised MM5 Monin–Obukhov
PBL7	UW	Revised MM5 Monin–Obukhov
PBL8	TEMF	TEMF
PBL9	SH	Revised MM5 Monin–Obukhov
PBL10	GBM	Revised MM5 Monin–Obukhov

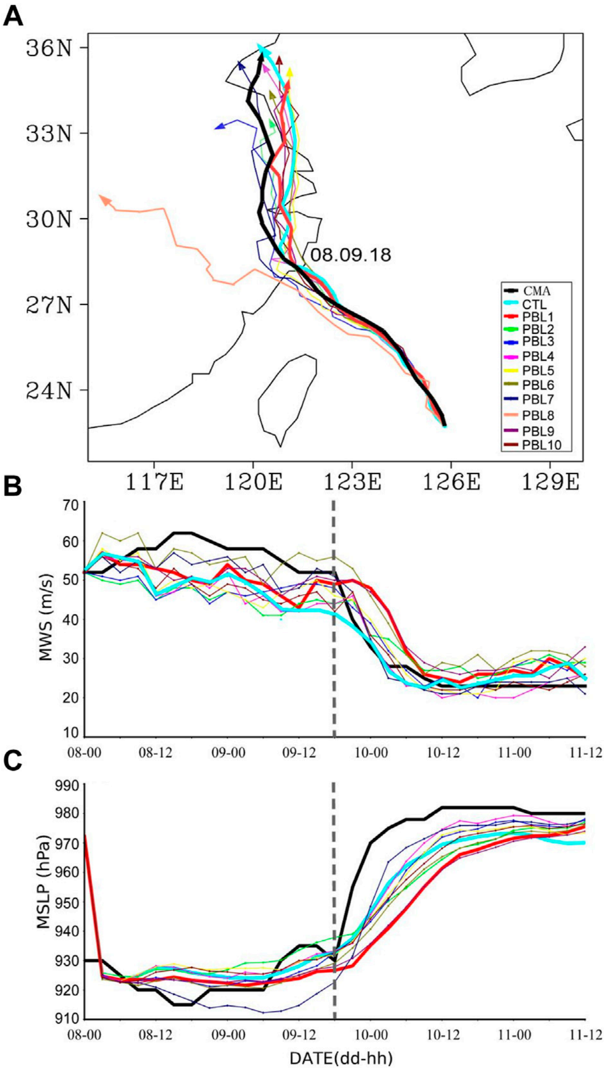

FIGURE 1
Observed and simulated **(A)** tracks, **(B)** MWS (unit: m/s), and **(C)** MSLP (unit: hPa) of typhoon Lekima. Dotted line denotes the observed landing time.

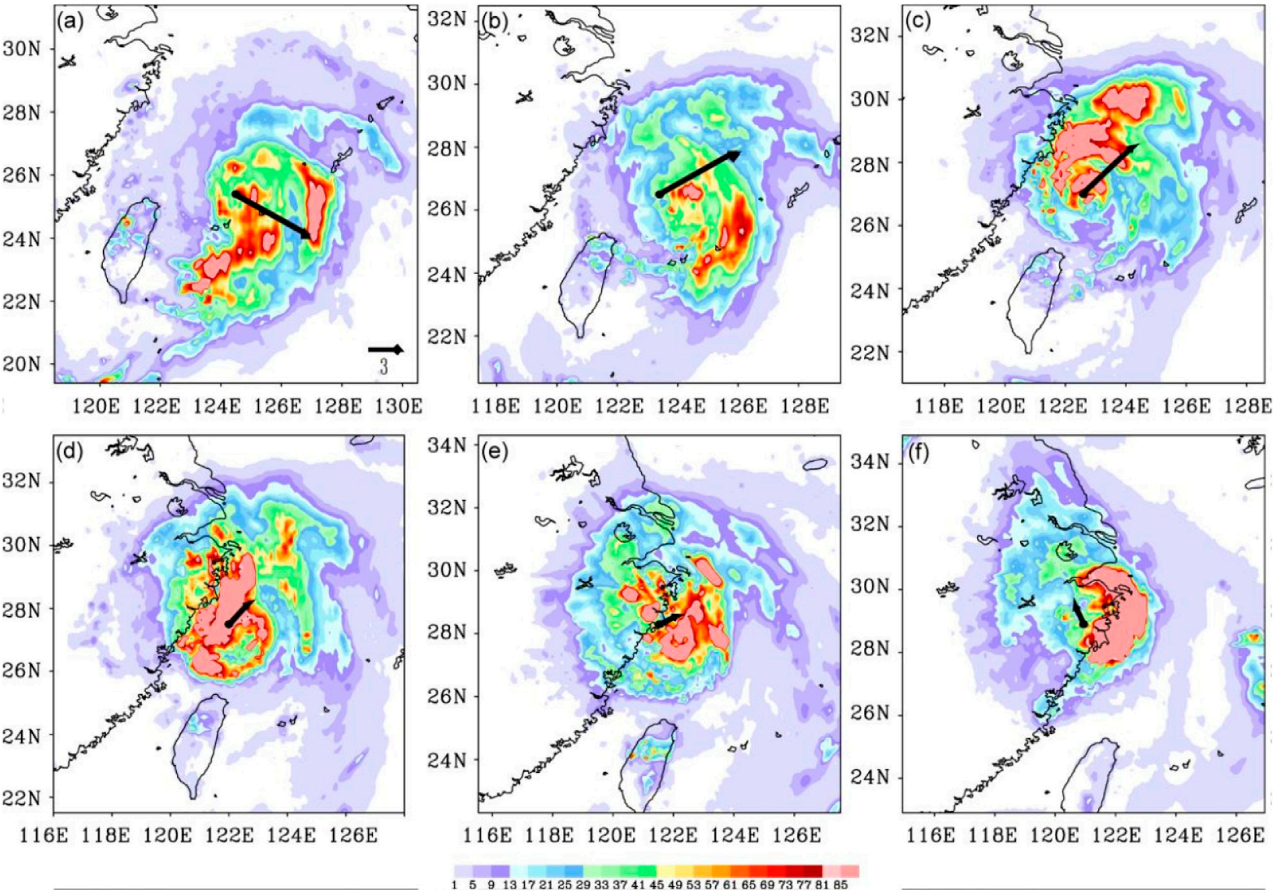

FIGURE 2
Six-hour accumulated precipitation of GPM (unit: mm) at **(A)** 18:00 UTC on 8 August 2019, **(B)** 00:00 UTC on 9 August 2019, **(C)** 06:00 UTC on 9 August 2019, **(D)** 12:00 UTC on 9 August 2019, **(E)** 18:00 UTC on 9 August 2019, and **(F)** 00:00 UTC on 10 August 2019. The black arrow denotes VWS between 200 and 850 hPa (reference magnitude in a), with black dots indicating the center of typhoon.

advected by the TC cyclonic circulation (Hence and Houze, 2011; Yu et al., 2017).

Compared with TCs over the ocean, landfalling TCs exhibit a complex precipitation process (Ren and Xiang 2017). The large-scale environmental field, TC intensity, land–sea contrast, forcing of complex underlying surfaces such as water body and topography, and mesoscale convective activities all can cause TC structural change substantially, resulting in the asymmetric distribution of precipitation (Chan and Liang 2003; Chen and Yau 2003; Yu et al., 2010; Li et al., 2014, Li et al., 2015; Yu et al., 2022). Based on satellite precipitation estimates, the asymmetric distribution of TC precipitation (wavenumber-1) is mostly associated with VWS, whereas the axisymmetric distribution of precipitation (wavenumber-0) is closely related to the intensity of TC. When the environmental VWS is less than 5 m s^{-1}, heavy rain often concentrates on the onshore side (Yu et al., 2017). Nevertheless, under internal vortex dynamics (i.e., no environmental factor for asymmetry such as vertical wind shear) rainfall maximum over the offshore side is also possible (Li et al., 2014, Li et al., 2015).

In addition, high-resolution numerical models have been used to investigate precipitation processes in TCs. Tao et al. (2011) compared the effects of microphysical and planetary boundary layer (PBL) parameterization schemes through a high-resolution numerical simulation of extreme precipitation of TC Morakot (2009) and found that forecasts were more sensitive to microphysical schemes than to PBL schemes. However, some studies applying numerical simulations have concluded equal importance of PBL and cloud microphysical schemes in TC precipitation simulations (Li and Pu, 2008). Some other studies have revealed the importance of PBL parameterization in the numerical simulations of TCs (Davis and Bosart, 2002; Li and Pu, 2008; Hill and Lackmann, 2009). For example, the simulation performance for the track and intensity of TCs depends on whether PBL parameterization is used, and performances in terms of the structure, intensity change, and track of TCs differ

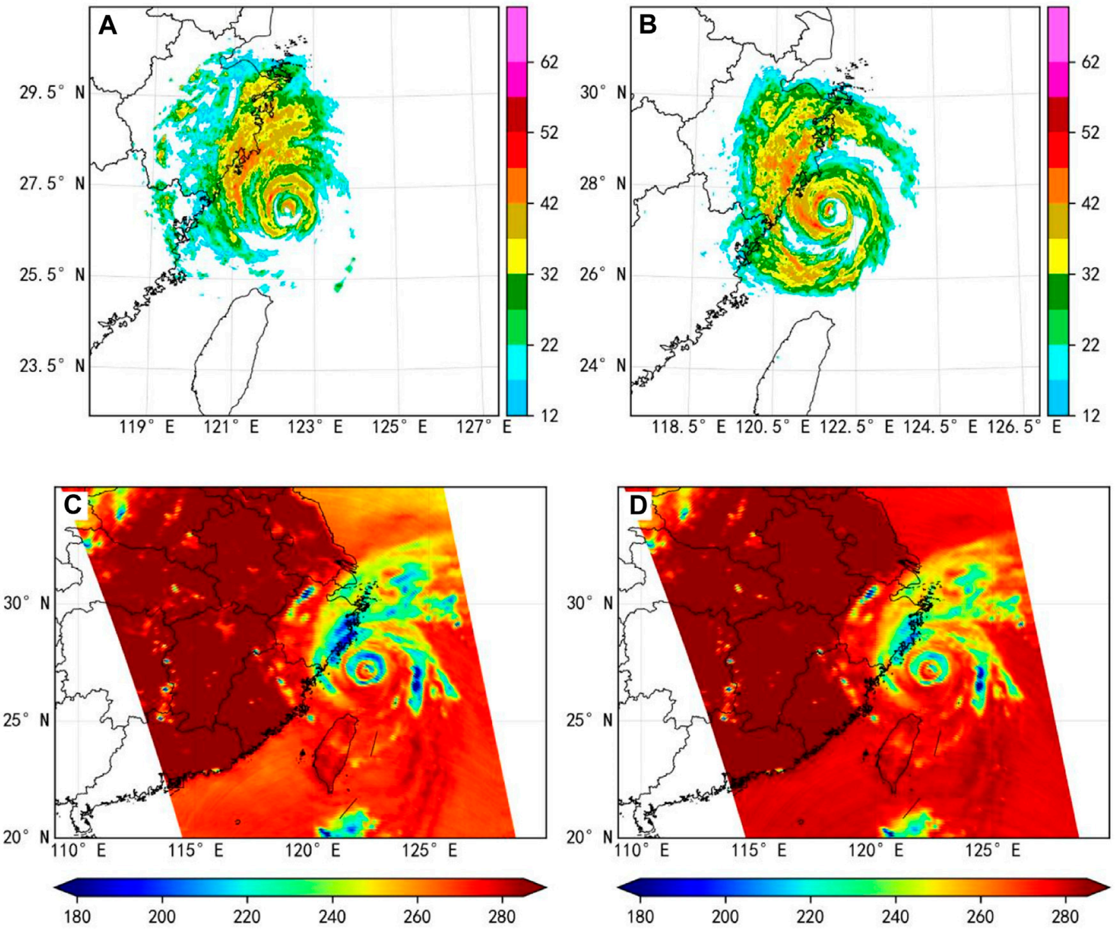

FIGURE 3
Horizontal distribution of reflectivity (unit: dBz) at 0.5° elevation at **(A)** 06:00, **(B)** 12:00 UTC on 9 August 2019. FY-3B polar orbit satellite MWRI 89 GHz channel **(C)** vertical and **(D)** horizontal polarization detection brightness temperature (unit: K) at 15:00 on 9 August.

with various PBL parameterization schemes. Xu et al. (2017) selected a variety of microphysical and boundary layer schemes to simulate nine typhoons affecting Zhejiang province. They found that typhoon track and intensity closer to the observations were simulated with the MYNN2 and Boulac boundary layer schemes, and the Boulac scheme was also better for precipitation simulation. Wang and Zhao (2020) used seven boundary layer parameterization schemes in the WRF model to simulate typhoon Meranti (2016). It was found that the PBL schemes had a significant influence on the TC track and intensity in the weakening phase of landfall, accompanied by significantly different latent heat flux and sensible heat flux in the surface layer.

TC Lekima (2019) was a super typhoon when it made the landfall and became the third most intense landfall typhoon in the Zhejiang province of China according to China meteorological records. Many recent studies have investigated typhoon Lekima. Shi et al. (2020) and Shi and Chen (2021) studied the rapid intensification (RI) of typhoon Lekima, focusing on its kinetic energy and double warm-core structure during the RI period. Xu and Liang (2021) identified an eyewall replacement in typhoon Lekima on 8 August and 9 August over the ocean. Xiang et al. (2021) found that before typhoon Lekima made the landfall, there was an obvious concentric eyewall structure. The extreme rainfall distribution prior to, during, and post-landfall associated with typhoon Lekima presented significant features of asymmetry. Dai et al. (2021) used radar observations to show the substantial contribution of vortex Rossby waves to the asymmetric structure of the typhoon's outer eyewall. He et al. (2021) examined the operational rainfall forecast errors in the different stages of typhoon Lekima after landfall. They concluded that the asymmetric rainfall distribution of Lekima can hardly be predicted, resulting in weak or even totally missed rainfall forecasts in northern Zhejiang. This study aims to discuss the influence of different PBL schemes on the asymmetric precipitation distribution of typhoon Lekima (2019) prior to and during

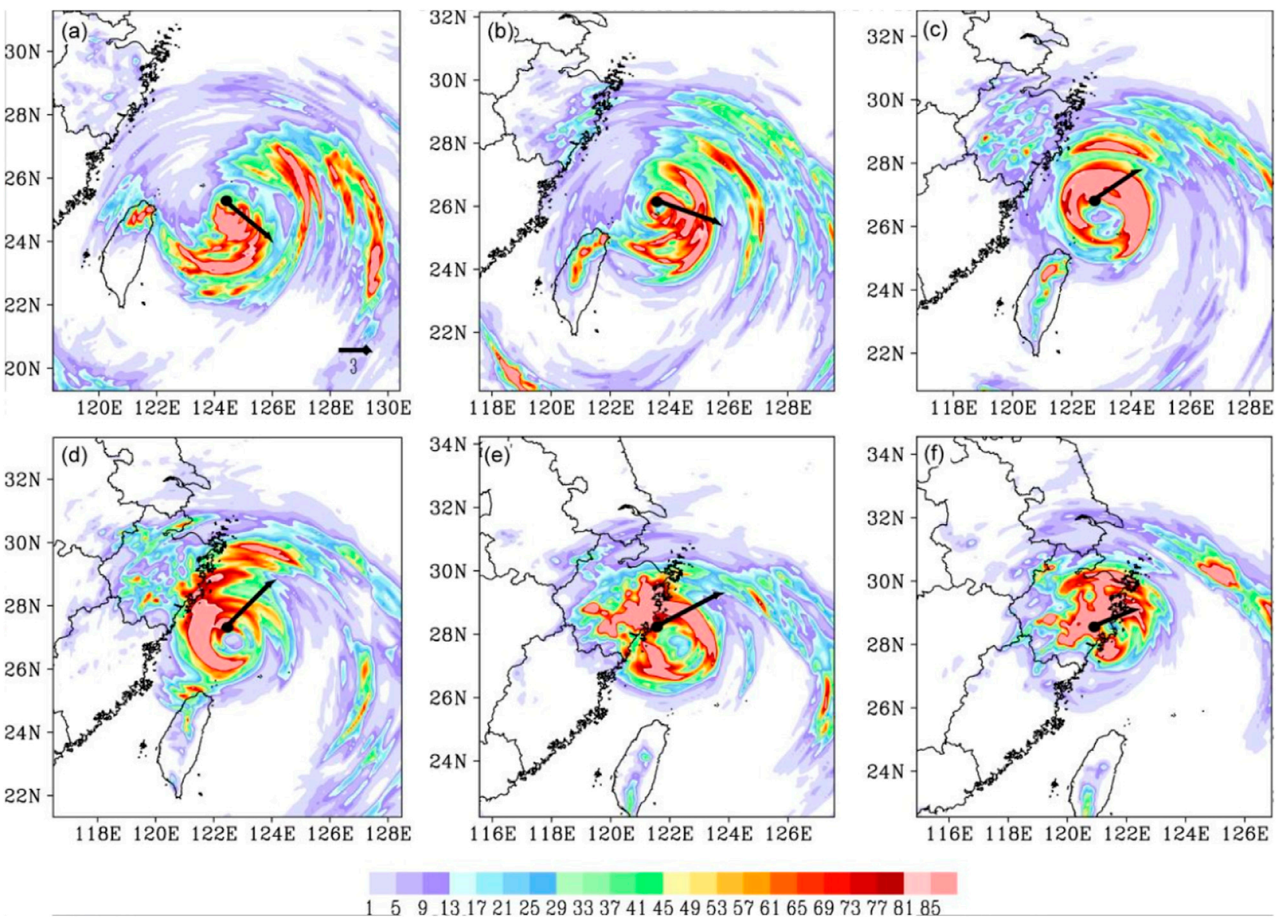

FIGURE 4
Simulated 6-h accumulated precipitation (unit: mm) at **(A)** 18:00 UTC on 8 August, **(B)** 00:00 UTC on 9 August, **(C)** 06:00 UTC on 9 August, **(D)** 12:00 UTC on 9 August, **(E)** 18:00 UTC on 9 August, and **(F)** 00:00 UTC on 10 August 2019 in the CTL experiment. The black arrow denotes VWS between 200 and 850 hPa, with black dots indicating the center of typhoon.

landfall by using multiple sources of observation and high-resolution numerical simulation.

2 Data and methods

Intensities and locations of typhoon Lekima were extracted from the 3-hourly best track data officially released by the Shanghai Typhoon Institute of China Meteorological Administration (Ying et al., 2014). The hourly Global Precipitation Measurement (GPM) precipitation data with a spatial resolution of 0.1° was obtained from the National Aeronautics and Space Administration (NASA) (https://pmm.nasa.gov/data-access) were used in this study. The structure associated with typhoon Lekima was examined by using the brightness temperature from Feng-Yuan FY-3B polar orbit satellite's Micro Wave Radiation Imager (MWRI) 89-GHz channel vertical and horizontal polarization detection (http://satellite.nsmc.org.cn), and the 6-minute radar reflectivity from the S-band Doppler radar at Wenzhou, Zhejiang Province, China.

Numerical experiments (one control and ten sensitivity tests) were conducted with the Advanced Research Weather Research and Forecasting (WRF) model Version 4.1. These simulations all had three two-way interactive, nested domains with horizontal resolutions of 27, 9, and 3 km, and grid numbers of 211 × 241, 355 × 355, and 319 × 319, respectively. The innermost domain was designed to move with the typhoon center. Thirty-four vertical levels were set with a top at 50 hPa. The initial and lateral boundary conditions were from the (0.5° × 0.5°) Global Forecast System of National Center for Environmental Prediction (https://nomads.ncep.noaa.gov/). The Kain–Fritch convective scheme (Kain and Fritch 1993) was used in the outermost (27 km) domain, but

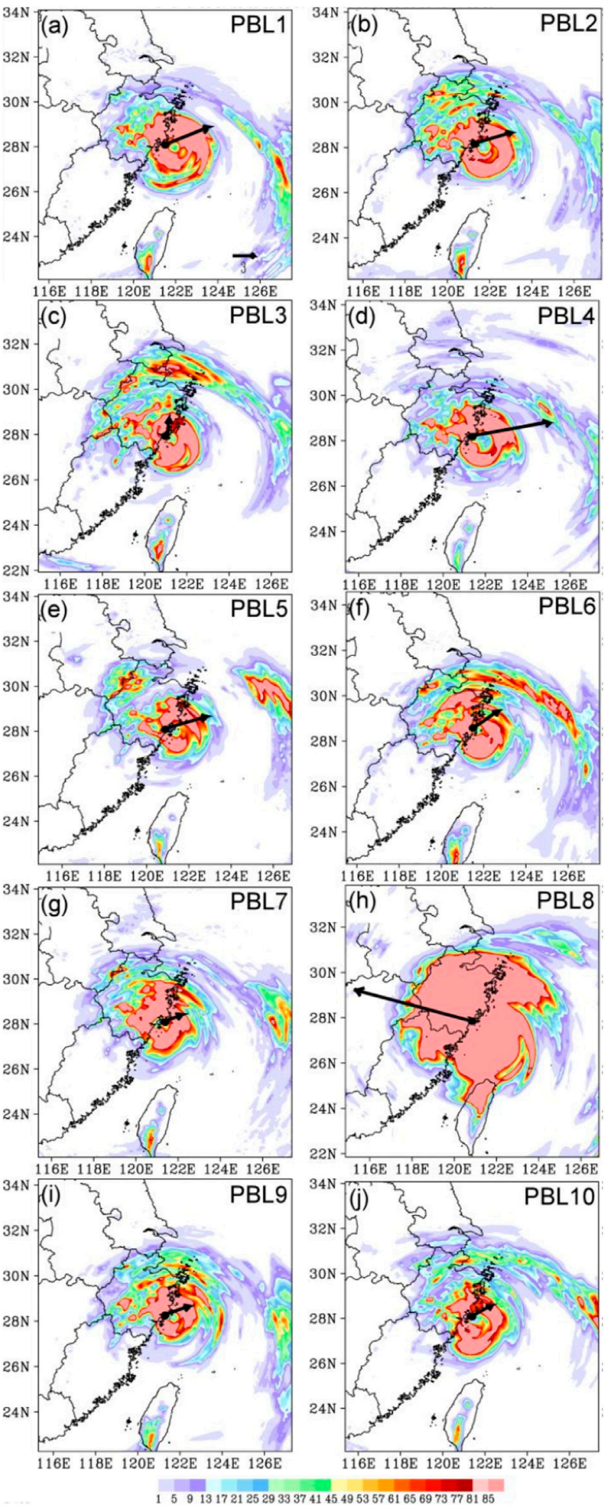

FIGURE 5
Simulated 6-h accumulated precipitation (unit: mm) at the TC landfall time in experiment **(A)** PBL1, **(B)** PBL2, **(C)** PBL3, **(D)** PBL4, **(E)** PBL5, **(F)** PBL6, **(G)** PBL7, **(H)** PBL8, **(I)** PBL9, and **(J)** PBL10. The black arrow denotes the VWS between 200 and 850 hPa, with black dots indicating the center of typhoon.

without convective parameterization for the other two domains. The Lin microphysical scheme (Lin et al., 1983), Dudhia shortwave scheme (Dudhia 1989), and Rapid Radiative Transfer Model (RRTM) longwave parameterization (Mlawer et al., 1997) were used in the three domains.

To investigate the possible effects of different boundary layer schemes on the typhoon asymmetric precipitation simulation during landfall, the MYNN 2.5 level turbulent kinetic energy (TKE) PBL scheme was used in the control (CTL) run. In addition, ten sensitivity experiments (PBL1 to PBL10) are successively carried out by using the other ten PBL schemes (Table 1). Here, YSU (Hong et al., 2006), Asymmetrical Convective Model version 2 (ACM2) (Pleim, 2007), Bougeault and Lacarrere (BouLac) (Bougeault and Lacarrere, 1989), University Washington (UW) Moist Turbulence (Bretherton and Park, 2009), Shin-Hong “scale-aware” (SH) (Shin and Hong, 2011), and Grenier-Bretherton-McCaa (GBM) schemes (Grenier and Bretherton, 2001) were coupled with the Revised MM5 Monin–Obukhov surface layer scheme (Jimenez et al., 2012). Mellor-Yamada-Janjic (MYJ) (Janjić, 1994) scheme was coupled with the Monin–Obukhov surface layer scheme (Janjic, 1994). The quasi-normal scale (QNSE) (Sukoriansky et al., 2005) scheme was coupled with the QNSE surface layer scheme (Sukoriansky et al., 2005), while MYNN2.5 and MYNN third (MYNN3)-level TKE PBL schemes (Nakanishi and Niino, 2006; Nakanishi and Niino, 2009) were coupled with the MYNN surface layer scheme (Nakanishi and Niino, 2006) and the total energy mass flux (TEMF) (Angevine et al., 2010) scheme used the TEMF surface layer scheme (Angevine et al., 2010). The numerical simulations cover an 84 h period from 00:00 UTC on 8 August to 12:00 UTC on 11 August 2019.

3 Overview of typhoon lekima

Typhoon Lekima (2019) formed over the north-western Pacific at 09:00 UTC on 4 August 2019. It reached its maximum wind speed (MWS) of 62 m s^{-1} and minimum central sea level pressure (MSLP) of 915 hPa at 15:00 UTC on August 8. At 17:45 UTC on August 9, Lekima made landfall in Wenling city of Zhejiang province of China, with MWS of 52 m s^{-1} and MSLP of 930 hPa. After landing, MWS further rapidly decreased to 23 m s^{-1}. At about 13:00 UTC on August 10, Lekima made a northward deflection (Huang et al., 2022) and moved further into Jiangsu province, with its intensity further weakening (Figure 1).

Figure 2 shows GPM 6 h accumulated precipitation and the 200–850-hPa VWS just before and after the landfall. As early as 6-7 August, typhoon Lekima underwent a rapid intensification under an environment with easterly VWS and rainfall asymmetry emerged (Huang et al., 2021). From 8 August, rainfall was clearly distributed asymmetrically, with heavy

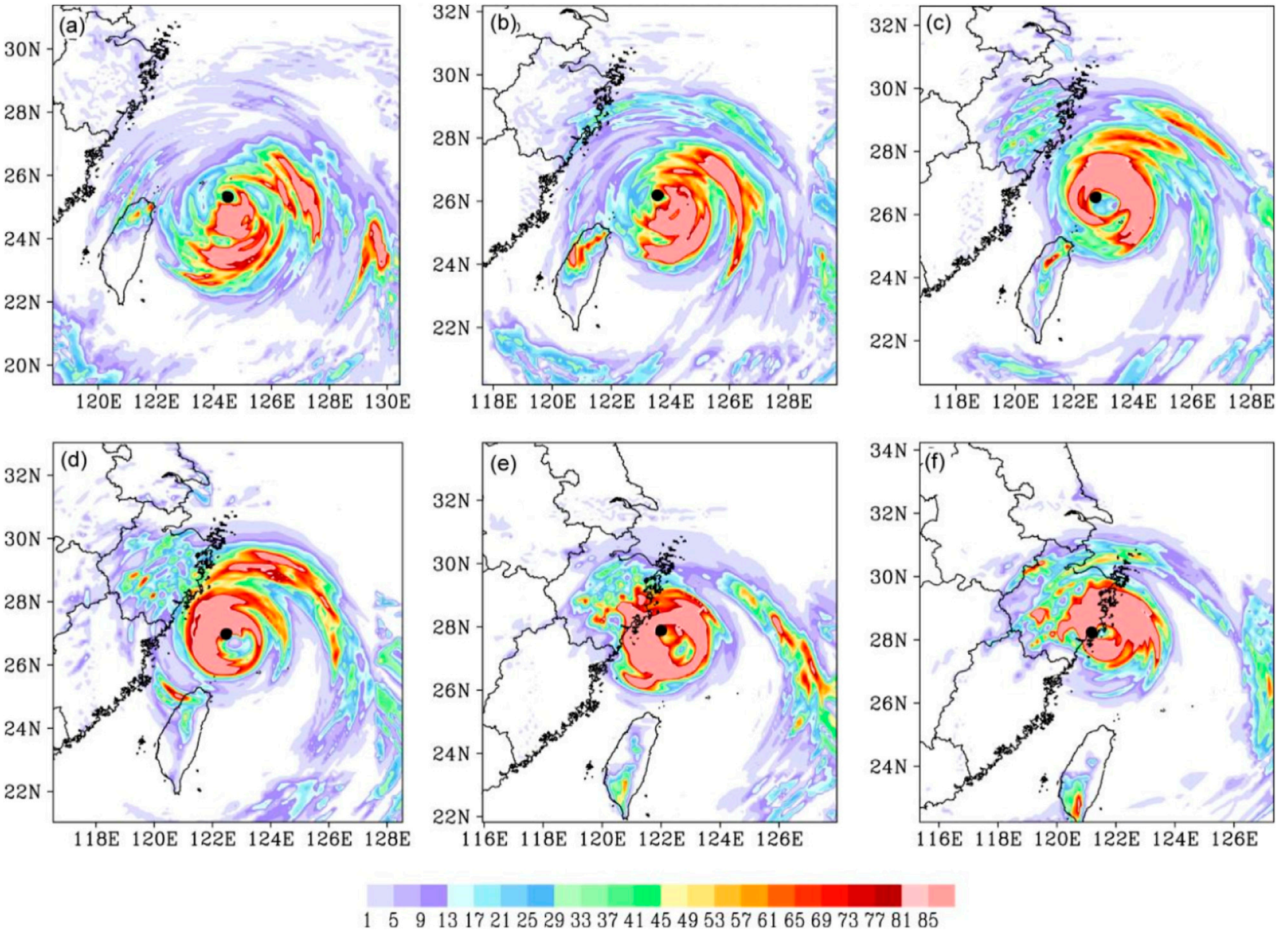

FIGURE 6
Simulated 6 h accumulated precipitation (unit: mm) at **(A)** 18:00 UTC on 8 August, **(B)** 00:00 UTC on 9 August, **(C)** 06:00 UTC on 9 August, **(D)** 12:00 UTC on 9 August, **(E)** 18:00 UTC on 9 August, and **(F)** 00:00 UTC on 10 August 2019 in the PBL1 experiment. The black dots indicating the center of typhoon.

rainfall located on the downshear side at 18:00 UTC on 8 August (Figure 2A). VWS showed a counterclockwise rotation and its magnitude decreased during the landfall (Figures 2A–C). At 06:00 UTC on 9 August, the heavy precipitation region was located on the right of shear (Figure 2B). Six hours later, the heavy precipitation was distributed mainly on the left of shear (Figure 2C). At 12:00 UTC on 9 August, the shear was orientated toward the northeast while the maximum rainfall occurred on the left of shear in the coastal area (Figure 2D). VWS continued decreasing to 2.6 m s^{-1}. During and after the landfall (Figures 2E,F), VWS remained low and further rotated counterclockwise. However, the asymmetric rainfall maximum did not rotate and is still on the downshear and offshore side.

According to the radar observation (Figures 3A,B), concentric eyewalls developed before the landfall, accompanied by an eyewall replacement, which is also identified by the satellite TBB analysis (Figures 3C,D). It can be seen that along the shear at these times, the major convection in the second concentric eyewall as well as the outer spiral rainbands concentrated on the north/northwest side of the typhoon center, which has seriously impacted the coastal areas of Zhejiang (He et al., 2021; Ao et al., 2022).

4 Analysis of simulation results

4.1 Tracks and intensities

Figure 1 shows that the tracks of typhoon Lekima simulated by CTL and the sensitivity experiments are relatively consistent with each other before 06:00 UTC on 9 August (Figure 1A). After that, the different influences of subgrid-scale turbulence under the PBL parameterization schemes, together with their interaction with the free atmosphere, on the typhoon motion

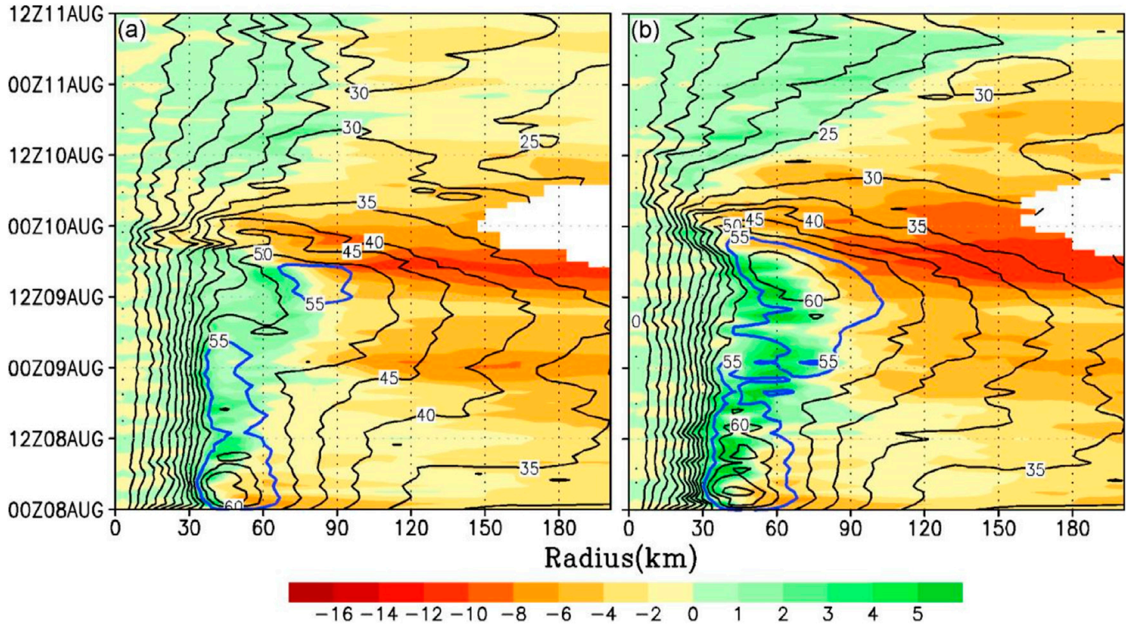

FIGURE 7
Radius–time evolution of the azimuthal-mean radial wind (shaded, unit: m s^{-1}) and tangential wind (contour, unit: m s^{-1}) at 1 km altitude in the **(A)** CTL and **(B)** PBL1 experiment. The white areas denote missing data.

gradually accumulated. Since 06:00 UTC on 9 August, the divergence of typhoon tracks gradually increase which is apparent by the time of the landfall. As the track simulated by PBL8 differs greatly from the observation, only the results from CTL and other nine sensitivity experiments are analyzed here. The simulated landfall locations by CTL, PBL1, PBL2, PBL4, PBL9, and PBL10 are relatively close to the observation. The landing locations in PBL3, PBL5, and PBL7 are more southward, while those in PBL6 are more northward. At the moment of the typhoon landfall, the maximum distance error is 110.5 km in PBL3, while the minimum is 17.8 km in CTL.

After the landfall, the track errors in simulations are more evident, which shows that the track over land is also sensitive to the PBL parameterization scheme. The typhoon makes landfall at 18:00 UTC on 9 August in CTL that is close to the observation. It is to be noted that in PBL1, PBL4, PBL5, PBL6, PBL7, and PBL10, the typhoon makes landfall at 21:00 UTC on 9 August which is 3 h later the observation, while the landfall time in the other four experiments is about 6 h later than that observed.

All the numerical simulations capture quite well the variation trends of MWS and MSLP (Figures 1B,C). The maximum 10-m wind speed is used to define MWS in the simulations. The exception is MWS and MSLP simulated by PBL8 that reaches 132 m s^{-1} and 676 hPa, which is thus not shown in the figure. The tangential wind speed of the local scheme UW is much larger than the other schemes, and the larger tangential wind continues to strengthen the energy of the typhoon, so the intensity of the typhoon simulated by PBL8 is too strong. Moreover, the low-level convergence and high-level divergence of typhoon simulated by PBL8 are the most significant, and vertical ascent velocities is the largest, so typhoon intensity is stronger than those of other experiments. We noticed that although MWS in the PBL1 experiment is quite close to the observation during the landfall, the simulated typhoon intensifies by about 8 m s^{-1} from 12:00 UTC to 21:00 UTC on 9 August just before the landfall time in the experiment, while the observed MWS was almost unchanged. In addition, the intensity of typhoon in PBL1 slowly intensify after the landfall and maintains an MWS of about 50 m s^{-1} 6 h after the landfall. In general, the simulated track and intensity in CTL are the closest to the observation although this experiment underestimates the intensity before the landfall.

4.2 Typhoon precipitation

The 6-h accumulated precipitation processes just before and after landfall in the CTL experiment are shown in Figure 4. The simulated precipitation distribution is close to that observed (Figures 4A–C). At 12:00 UTC on 9 August just before the landfall over Zhejiang, VWS in both simulation and observation are orientated toward the northeast. However, VWS has weakened to 2.6 m s^{-1} in the observation,

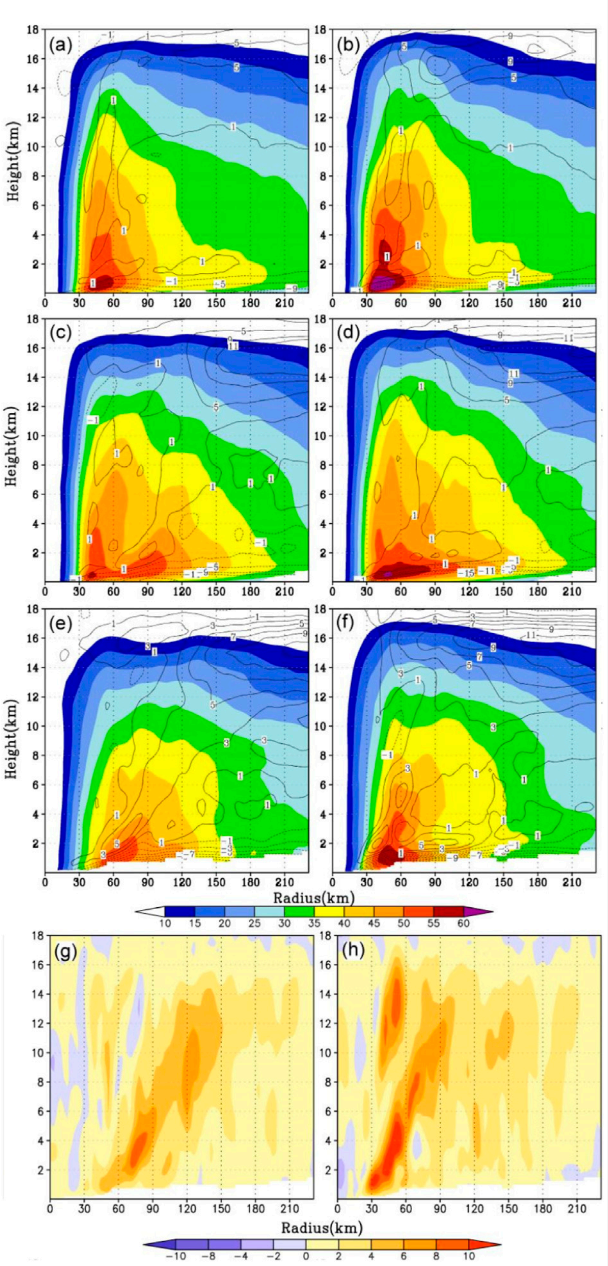

FIGURE 8
Radius–height distribution of the azimuthal-mean tangential wind (shaded, unit: m s^{-1}) and radial wind (contour, unit: m s^{-1}) at **(A,B)** 12:00 UTC on 8 August 2019, **(C,D)** 06:00 UTC on 9 August 2019, and **(E,F)** at the landing time in the **(A,C,E)** CTL and **(B,D,F)** PBL1 experiment. **(G,H)** as in **(E,F)** but for vertical velocity (shaded, unit: 10^{-1} m s^{-1}).

while it is maintained at about 6.2 m s^{-1} in the simulation (Figure 4D). During the landfall, VWS remains at 6.3 m s^{-1} in CTL (Figure 4E) but further decreases to 1.4 m s^{-1} in the observation. In addition, unlike observation, VWS in CTL remains orientated toward the northeast after landfall with a magnitude of about 4.3 m s^{-1} Figure 4F). In other words, while the simulated VWS is too strong in CTL, the asymmetric distribution of rainfall maximum agrees well with the observation.

Figure 5 shows the distribution of 6 h accumulated precipitation simulated by the ten sensitivity experiments during the typhoon landfall. The precipitation area simulated by PBL8 (Figure 5H) is much larger than that observed and the other nine sensitivity experiments (Figure 2E, Figures 5A–G, I–J), presenting a more axisymmetrical distribution. The latent heat flux simulated by PBL8 is much larger than that simulated by other experiments, and the simulated typhoon intensity and precipitation are the largest. In addition, the landfall time in PBL8 is 9 h earlier than the observation. It can also be seen that generally the precipitation distributions simulated in the sensitivity experiments all display remarkable axisymmetry, which differs largely from the observation.

The sensitivity experiment PBL1 adopts the YSU boundary layer scheme, which is a common scheme in typhoon simulation (Kepert, 2012). The 6 h accumulated precipitation processes just before and after landfall in PBL1 experiments are further compared (Figure 6). Before 06:00 UTC on 9 August, rainfall distribution in PBL is similar to the CTL experiment, showing an asymmetric distribution (Figures 6A–C). After that, the distribution of precipitation in CTL maintains asymmetry until the typhoon makes landfall (Figures 5D–F). Compared to CTL, the precipitation in PBL1 turned more symmetric even after the landfall (Figures 6D–F).

4.3 Further analysis of the CTL and PBL1 experiments

4.3.1 Typhoon structure

Figure 7 shows the distributions of azimuthally averaged tangential wind and radial wind near the top of the boundary layer simulated by CTL and PBL1. In CTL, the average tangential wind reaches 60 m s^{-1} before 09:00 UTC on 8 August, which then weakens to about 55 m s^{-1} and remains 30–60 km from the typhoon center. A double-eyewall structure appears from 06:00 UTC on 9 August (Figures 7A, 8A,C), which has been observed (Figure 3; Xu and Liang 2021; Dai et al., 2021). The outer eyewall is 70–100 km from the typhoon center, with a wind speed of about 55 m s^{-1} (Figures 7A, 8C). At about 12:00 UTC on 9 August, the inner eyewall is replaced by the outer one. After landfall, the eyewall convection begins to weaken (Figure 7A). On the other hand, the maximum average tangential wind in PBL1 maintains at 60 m s^{-1} until about 15:00 UTC on 8 August and then weakens to 55 m s^{-1}, and resides stably about 30–60 km from the typhoon center (Figure 7B). At 06:00 UTC on 9 August, the eyewall had already expanded outward to 60–90 km from the typhoon center (Figure 8D), and after 6 h, the average tangential wind strengthens to 60 m s^{-1} and begins to shrink inward. The simulated typhoon makes landfall at around

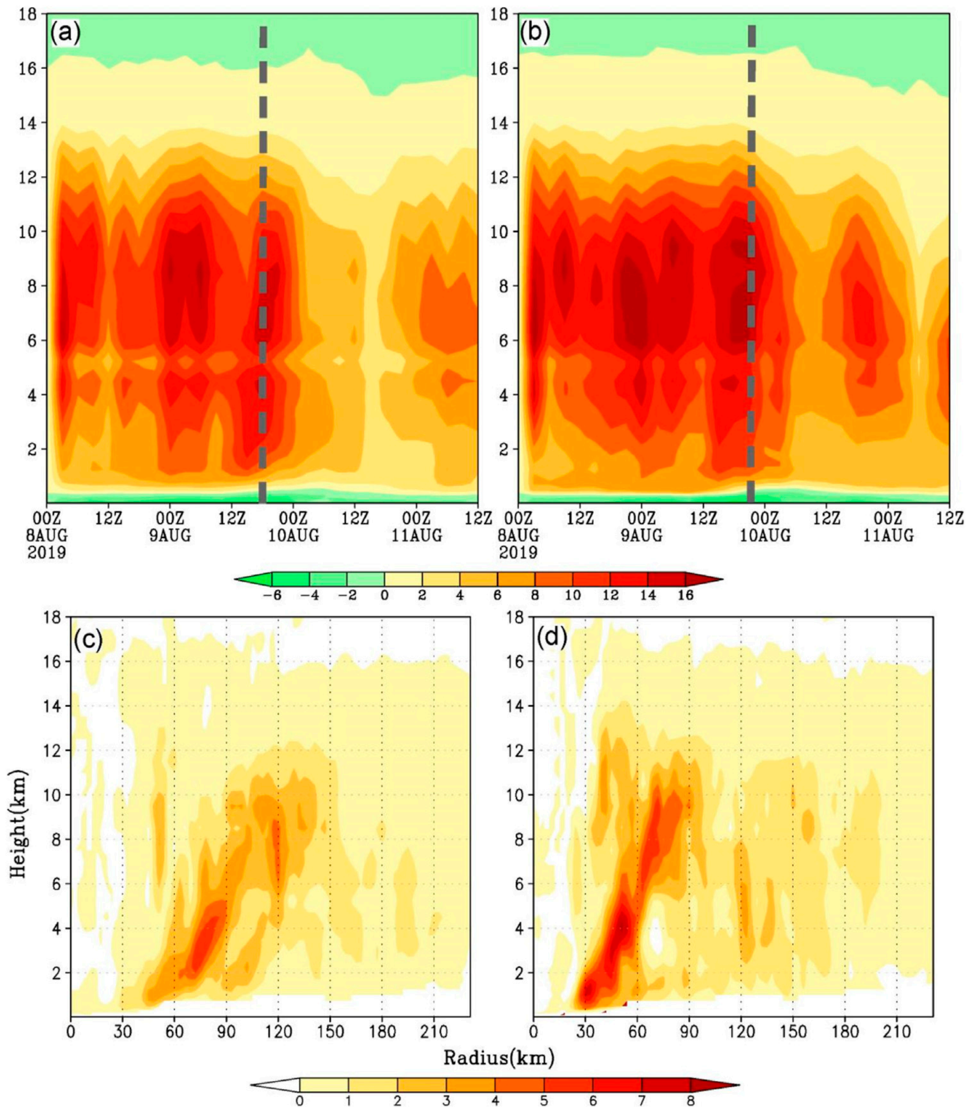

FIGURE 9
Time evolution of the vertical distribution of the azimuthal-mean diabatic heating (shaded, unit: K s^{-1}) averaged within 200 km from the typhoon center in **(A)** CTL and **(B)** PBL1. Radius−height distribution of the azimuthal-mean diabatic heating (shaded, unit: K s^{-1}) at the landing time in **(C)** CTL and **(D)** PBL1. The grey dotted line indicates the landing time.

21:00 UTC on 9 August, during which the eyewall contracts to about 40–60 km from the typhoon center (Figure 7B). In summary, the major difference between the two experiments is that there is no double eyewall and eyewall replacement simulated in PBL1, however, the single eyewall goes through the process of expansion, strengthening, contraction, and weakening after the landfall (Figures 7B, 8B,D,F).

Focusing on the secondary circulation, the maximum inflow in CTL is about 60 km away from the typhoon center and begins to weaken from 03:00 UTC on 8 August. With the inflow (beyond 100 km from the typhoon center) beginning to strengthen, the outer eyewall appears. During the typhoon making the landfall, the maximum inflow reaches 10 m s^{-1} (Figure 7A). In PBL1, the maximum inflow is also located on the outer side of the eyewall and begins to decrease. When the inflow beyond 100 km strengthens, the eyewall expands outward to 60–90 km from the typhoon center. After that, the inflow further strengthens, reaching 12 m s^{-1} during the landfall. During landfall, the inflow simulated in PBL1 is larger than that in CTL (Figure 7B).

At the moment of landfall, the azimuthally average tangential wind in the lower layer increases with height and reaches the

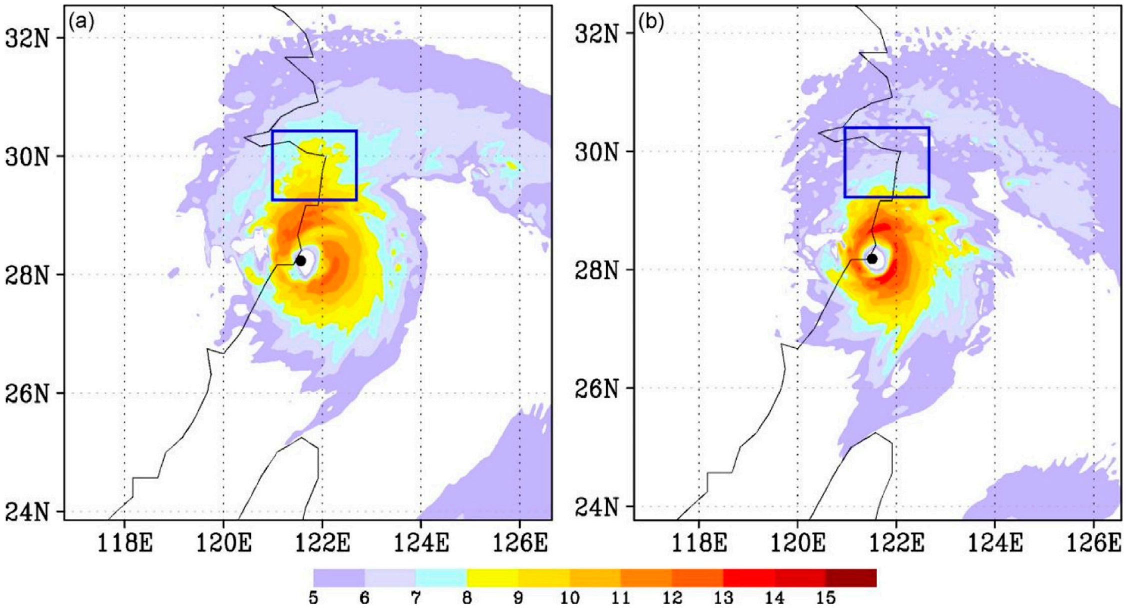

FIGURE 10
850 hPa water vapor flux (shaded, unit: 10 g hPa^{-1} cm^{-1} s^{-1}) at the landing time in **(A)** CTL and **(B)** PBL1. Black dots indicate the center of typhoon. The blue box represents the coastal area north of Zhejiang.

maximum near the top of the boundary layer (Figures 8E,F). After that, the wind speed further decreased with the increase in height. The maximum tangential wind in PBL1 is slightly larger than that in CTL (60 m s^{-1} vs. 55 m s^{-1}), and the location is also closer to the typhoon center (40–60 km vs. 50–80 km). In addition, the maximum tangential wind in the PBL1 over 50 m s^{-1} extends to a height as high as 4 km, while that in CTL is below 2 km. In both experiments, the maximum outflow near the eyewall is about 5 m s^{-1}. It can be seen that the outflow in PBL1 is much stronger and tilted outward, and thus strong outflow speed extends outside 90 km from the center.

During the landfall, the eyewall in both CTL and PBL1 tilts outward (Figures 8G,H). The maximum vertical velocity in CTL (about 9×10^{-1} m s^{-1}) appears at the height of 2–4 km around 60–90 km from the typhoon center. However, in PBL1, the eye size is smaller about 30–60 km from the typhoon center, a nd the maximum vertical speed exceeding 10×10^{-1} m s^{-1} extends up to a height of 6 km.

4.3.2 Thermodynamic and water vapor factors

Figures 9A,B show the time evolution of diabatic heating within a radius of 200 km from the typhoon center for the two experiments CTL and PBL1. When typhoon Lekima reaches its maximum intensity, the diabatic heating is also the highest that is located at the height of 8 km. In CTL, the diabatic heating decreases when the double-eyewall structure appears, however, it increases again during the period from the replacement of the eyewall to the landfall time. It is obvious that the diabatic heating in PBL1 changes intermittently, similar to that in CTL. However, the diabatic heating in PBL1 is higher than that in CTL during the landfall (Figures 9C,D), which indicates enhanced convection and is consistent with the intensification right before landfall in this experiment (Figure 1).

During the landfall, the water vapor flux in CTL is mainly in the northwest and southeast quadrant of the typhoon, with maximum up to 12×10^{-4} kg m^{-2} s^{-1} (Figure 10A). The water vapor flux in the coastal area north of Zhejiang is also relatively larger, which is generally above 8×10^{-4} kg m^{-2} s^{-1}. It is indicated that the outer spiral rainbands concentrated on the north side of the typhoon center simulated in CTL agree well with the observation (Figure 3; Ao et al., 2022; He et al., 2021). While in PBL1, the water vapor flux is axisymmetrically distributed. Although the landing location is close to that in CTL, the water vapor flux in the coastal area north of Zhejiang is relatively smaller (Figure 10B).

4.3.3 Surface layer fluxes

Surface latent and sensible heat fluxes are the sources of energy for TC intensification and are the primary physical processes in the boundary layer (Li and Chen, 2005). Surface momentum flux, on the other hand, is the sink of energy for TC to weaken. Since the magnitude of sensible heat flux is much smaller than latent heat flux, surface sensible heat flux distribution is not analyzed here. Figures 11, 12 show the surface latent heat and momentum fluxes from 12:00 UTC on 9 August to 00:00 UTC on 10 August 2019. It can be seen that the

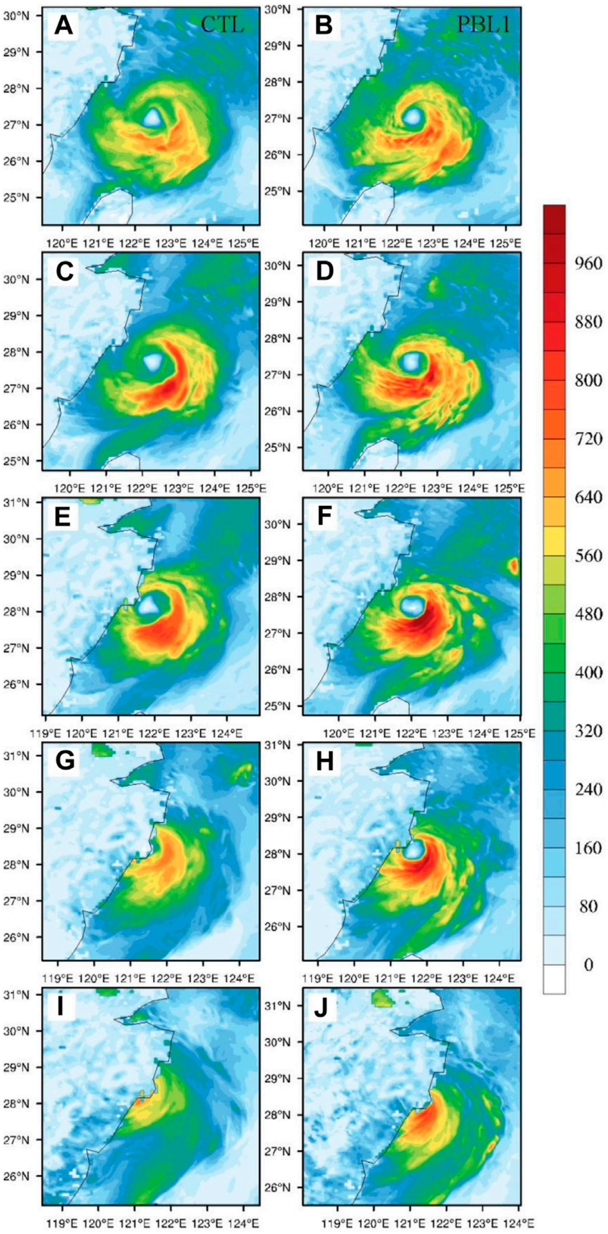

FIGURE 11
Surface latent heat flux (unit: W m^{-2}) during 12:00 UTC on 9 August 2019 to 00:00 UTC on 10 August 2019 from **(A,C,E,G,I)** CTL, and **(B,D,F,H,J)** PBL1, at **(A,B)** 12:00 UTC on 9 August, **(C,D)** 15:00 UTC on 9 August, **(E,F)** 18:00 UTC on 9 August, **(G,H)** 21:00 UTC on 9 August, and **(I,J)** 00:00 UTC on 10 August 2019.

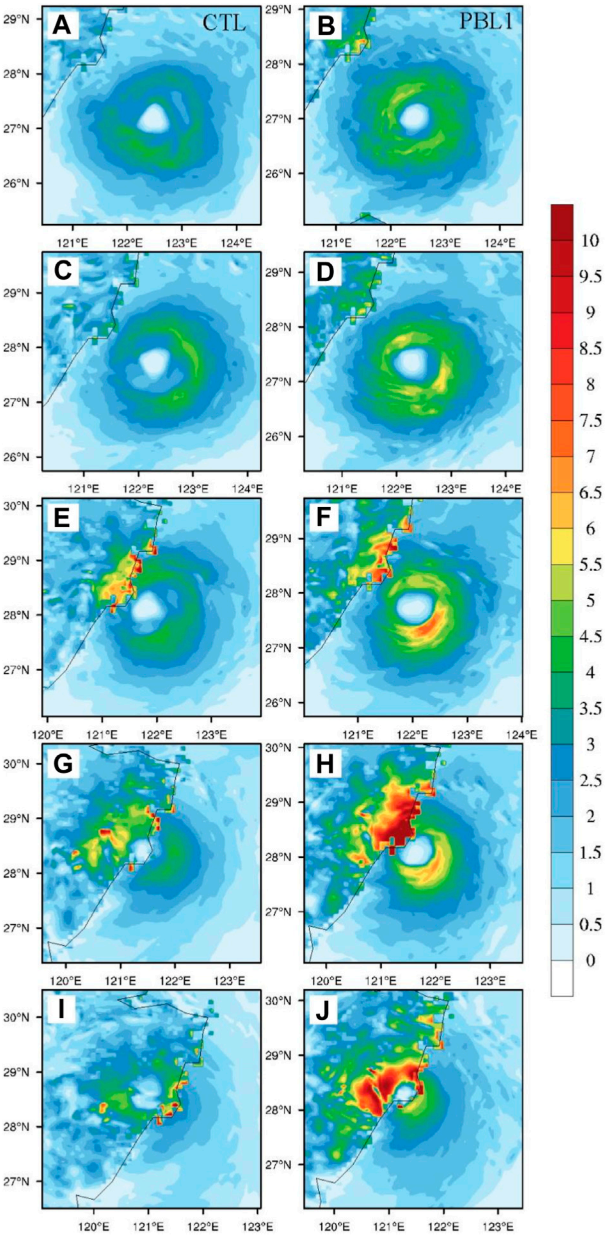

FIGURE 12
Surface momentum flux [unit:kg/(m s^2)].during 12:00 UTC on 9 August 2019 to 00:00 UTC on 10 August 2019 from **(A,C,E,G,I)** CTL, and **(B,D,F,H,J)** PBL1, at **(A,B)** 12:00 UTC on 9 August, **(C,D)** 15:00 UTC on 9 August, **(E,F)** 18:00 UTC on 9 August, **(G,H)** 21:00 UTC on 9 August, and **(I,J)** 00:00 UTC on 10 August 2019.

Revised MM5 Monin–Obukhov surface layer scheme used in the PBL1 experiment tends to generate larger latent heat and momentum fluxes than CTL using the MYNN surface layer scheme, especially southeast of the typhoon center. The higher latent heat flux in PBL1 is conducive to intensification near landfall and sustaining the intensity longer after landfall, which has not been simulated in CTL. On the contrary, it can be seen that the momentum flux in PBL1 over land is also larger than that in CTL. Such larger momentum flux enables rapid dissipation on 10 August.

Figure 13A shows the time evolution of surface latent flux within a radius of 200 km centered on the typhoon in the CTL and PBL1 experiments, where a positive value indicates that the surface flux is upward. In the first 3 h of the simulation,

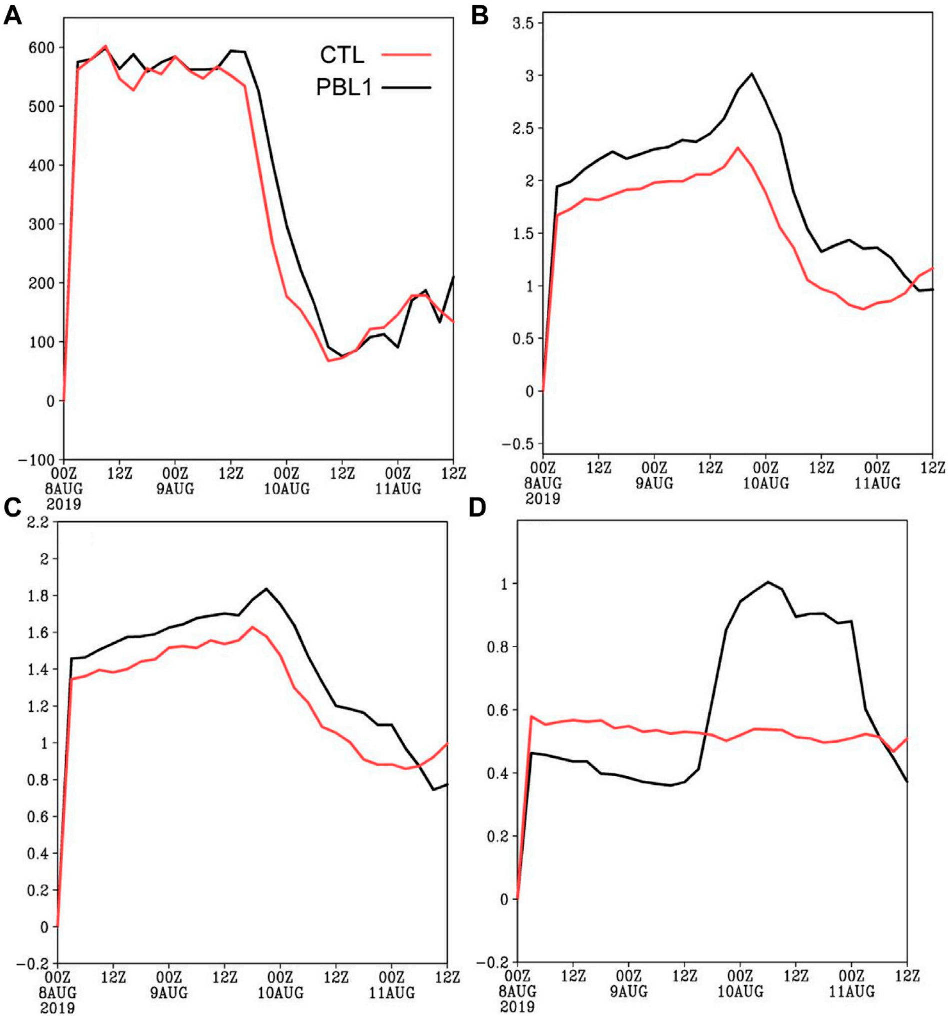

FIGURE 13
Time series of **(A)** surface latent heat flux (unit: W m^{-2}), **(B)** momentum flux (unit: kg m^{-1} s^{-2}), **(C)** friction velocity (unit: m s^{-1}), and **(D)** boundary layer height (unit: km) within 200 km from the typhoon center.

the latent heat flux increases significantly. From then until the typhoon makes landfall, although the simulated latent flux varies with different PBL schemes, they all maintain relatively large values. After the typhoon landfall, the latent flux decreases significantly. The latent heat flux is positive over both sea and land. The values of latent heat in PBL1 are larger than those in CTL, which is consistent with the simulated intensity (Figure 1). Also, the Revised MM5 Monin–Obukhov in PBL1 promotes a faster intensification rate before landfall, and produced the largest momentum flux (3.06 kg m^{-1} s^{-2}) at 21:00 UTC on 9 August, followed by the MYNN2.5 (2.32 kg m^{-1} s^{-2}) at 18:00 UTC on 9 August in CTL (Figure 13B). After the typhoon makes landfall, the momentum flux decreases substantially.

4.3.4 PBL eddy diffusivity

Eddy diffusivity is a key parameter in PBL parameterization schemes (Zhu, 2014; Zhu, 2019), which is related to turbulent mixing. Some different behaviors of the PBL schemes can be explained by the distribution of the eddy diffusivity (Smith et al., 2014). PBL eddy diffusivity includes eddy diffusivity for momentum (Km) and heat (Kh), and Kh was computed from Km using the relationship of the Prandtl number (Gopalakrishnan et al., 2013). This subsection investigates the PBL eddy diffusivity during the typhoon landfall period.

The distributions of Kh and Km are similar, thus, only that of Km is examined here. Figure 14 shows the height–radius distribution of azimuthally averaged Km from the CTL and

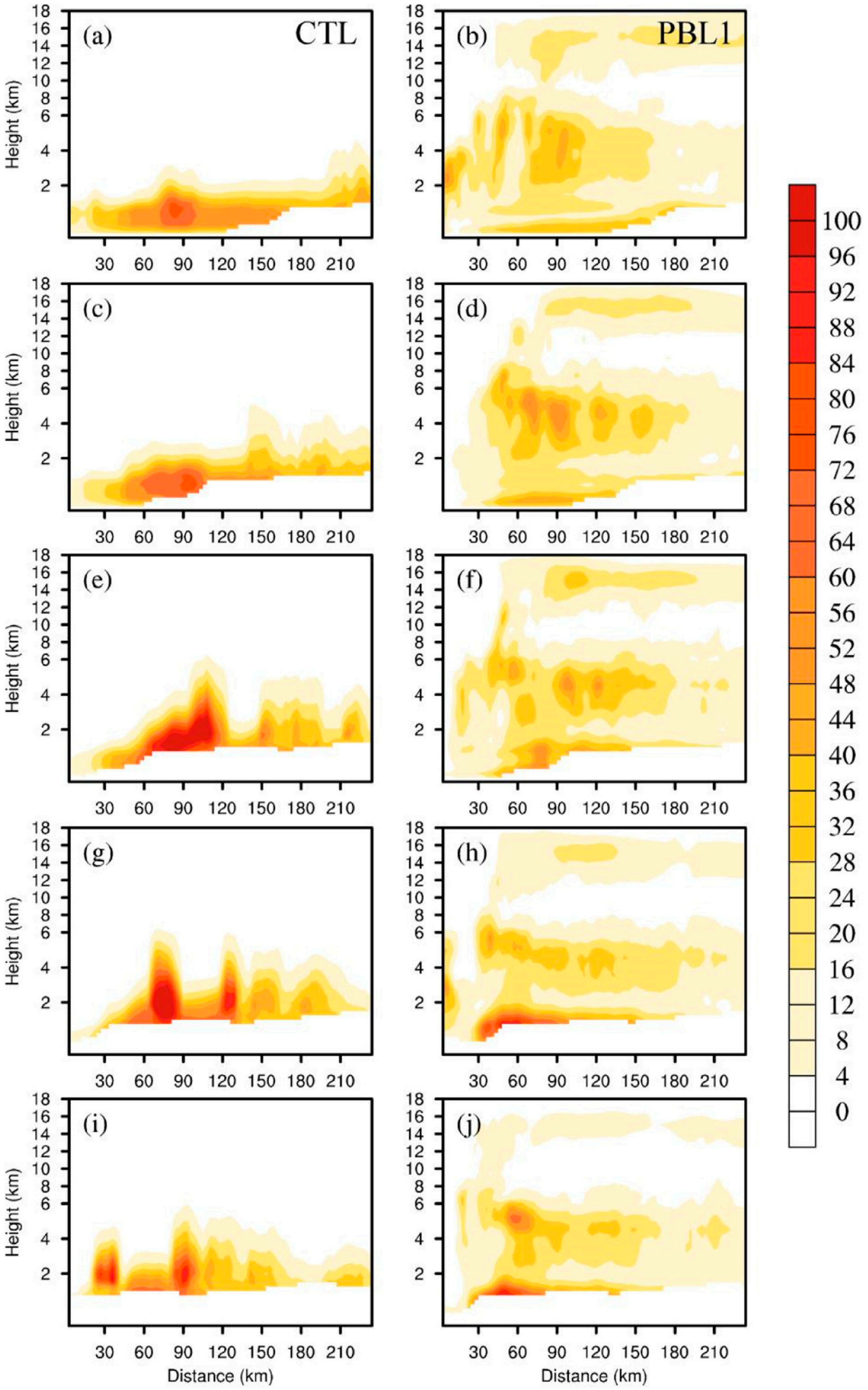

FIGURE 14
Height–radius distribution of azimuthal-mean eddy diffusivity for momentum (unit: m^2/s) from **(A,C,E,G,I)** CTL and **(B,D,F,H,J)** PBL1 at **(A,B)** 12:00 UTC on 9 August, **(C,D)** 15:00 UTC on 9 August, **(E,F)** 18:00 UTC on 9 August, **(G,H)** 21:00 UTC on 9 August, and **(I,J)** 00:00 UTC on 10 August 2019. The *y*-axis is for height above ground (0 m). The white areas below the height of 2 km denote missing data.

PBL1 experiments from 12:00 UTC on 9 August 2019 to 00:00 UTC on 10 August 2019. Km mainly concentrates below 6 km in CTL, however, Km from the YSU scheme extends into the free atmosphere in PBL1. In CTL, Km increases until the typhoon makes landfall and weakens afterward. In PBL1, Km is generally smaller in magnitude than that in CTL but has been increasing even after the typhoon made landfall. The spatial distribution of Km in PBL1 is likely related to the more extensive outflow circulation shown in Figure 8.

4.3.5 PBL structure

The friction velocity increases before landfall and decreases afterward, indicating that the turbulence intensity changes from strong to weak (Figure 13C). The friction velocity in PBL1 is larger than that in CTL, especially, during the typhoon making landfall. Larger friction velocity leads to stronger vertical momentum flux, which is consistent with the variation of typhoon intensity. Different PBL schemes correspond to different vertical diffusion processes, which have different effects on the dynamic, thermal structure, and intensity evolutions of the typhoon. PBL heights simulated in the two experiments of CTL and PBL1 are quite different (Figure 13D). In this study, the PBL height is defined as the radial velocity being 10% of the peak inflow (Zhang et al., 2011). The PBL height reaches over 500 m in the CTL after 6 h of simulation and remains at this height until typhoon landfall. However, the PBL height reaches about 400 m in PBL1 after 6 h of simulation and remains until 12:00 UTC on 9 August. From 12:00 UTC on 9 August, the PBL height in PBL1 increases rapidly, approaching 700 m at the time of landfall, which exceeds in CTL. After the landfall, the PBL height in PBL1 is much higher than that in CTL, reaching about 1 km, and gradually decreases 24 h after landfall. A higher boundary layer corresponds to stronger vertical mixing that can transport the surface flux to a larger height, which provides energy for the development of typhoons. This is likely related to the longer sustained intensity during landfall in PBL1.

5 Conclusion and discussion

Typhoon Lekima's precipitation distribution possessed asymmetry both over the sea and after the landfall. Moreover, typhoon Lekima had a concentric eyewall structure before landfall and showed evident asymmetric precipitation distribution. Numerical experiments are conducted to investigate the sensitivity of boundary layer schemes in simulating the asymmetric precipitation distribution of typhoon Lekima. To a moderate degree, the simulated track and intensity are sensitive to the choice of the PBL scheme. The CTL simulation (with model configurations in Table 1) well captures the development and asymmetric distribution of precipitation, while the group of ten sensitivity experiments has shown much more axisymmetric precipitation distribution near landfall. Thus, in terms of asymmetry, the simulated precipitation distribution seems to be less sensitive to the different PBL schemes (albeit with quite different spatial extent), however, the physics in CTL has captured the appropriate processes for asymmetric precipitation development.

The CTL and PBL1 experiments, which apply two of the most popular PBL and surface layer schemes, simulate the general trend in intensity change before landfall and similarly show the different intensity and structural changes during landfall. Therefore, these two experiments are further compared in detail. It is found that the simulated typhoon has experienced different evolutions before and during landfall. In CTL, the double-eyewall structure is simulated well as observed 12 h prior to landfall. The eyewall replacement is completed 6 h prior to landfall, accompanied by the weakening of the typhoon. After that and until the typhoon makes landfall, MWS, and PBL height remain unchanged. The asymmetric precipitation associated with outer spiral rainbands concentrated on the north side of the typhoon center during landfall is simulated reasonably.

Comparatively, no double eyewall occurs in the PBL1 experiment, while the radius of maximum wind expands outward from 00:00 UTC on 9 August (21 h prior to landfall), accompanied by the weakening of the typhoon. After 12 h, the average tangential wind strengthens to 60 m s^{-1} and begins to shrink inward. Until the typhoon makes landfall, MWS and PBL height increase rapidly, which is very different from CTL. The precipitation distribution turned more symmetric even as approaching landfall, which may be due to the re-intensification before landfall in PBL1. The stronger axisymmetric component associated with higher intensity before landfall would be more resistant to vertical wind shear. In addition, Dai et al. (2021) have analyzed the mechanism for the asymmetry that developed in the outer eyewall. Since there was no eyewall replacement simulated in PBL1, the process of vortex Rossby wave propagation analyzed by Dai et al. (2021) likely was not simulated well in the experiment, which would affect the degree of precipitation asymmetry too. Nevertheless, these processes must be further studied to clarify. During landfall, the simulated spatial scale of the typhoon core in PBL1 (eyewall at 40–60 km) is smaller than in CTL (70–100 km). It might affect the TC rainfall distribution, as newly concluded in an observational study by Yu et al. (2022) that small inner-core TCs have higher intensity with higher rainfall axisymmetry. After landfall, the precipitation distribution becomes asymmetric while dissipating, which is similar for CTL.

Diagnosis of boundary layer processes has been performed to reveal the differences between CTL and PBL1. Surface layer parameterization adopted by the PBL scheme determines the surface exchange coefficient and surface flux, and a larger enthalpy flux leads to larger typhoon intensity. The Revised MM5 Monin–Obukhov surface layer scheme used in the PBL1 experiment tends to generate larger enthalpy fluxes than CTL that uses the MYNN surface layer scheme. The YSU PBL scheme in PBL1, having smaller eddy diffusivity, larger friction velocity, and higher PBL height, simulates larger radial inflow and tangential wind in the boundary and larger updraft in the eyewall and thus higher typhoon intensity, especially, noticeable before landfall. On the other hand, the momentum fluxes in PBL1 are also higher, especially, over land during landfall, enabling rapid dissipation in the model. These results indicate that the model boundary layer schemes may largely influence the typhoon intensity and structure including the asymmetric rainfall distribution during landfall. However, majority of the sensitivity experiments here do not simulate the asymmetric precipitation properly and would affect the quality of impact forecast such as in the case of typhoon Lekima. Therefore, the complexity of the impacts of PBL processes makes it necessary to study the influences of PBL parameterization schemes on typhoon structural changes based on more cases in the future.

In addition, since both microphysical and boundary layer schemes could largely affect the precipitation processes in simulation, six additional sensitivity experiments by six microphysical schemes and a YSU scheme are also carried out to investigate the possible effects of different microphysical schemes on the typhoon asymmetric precipitation simulation during landfall. The results of the preliminary analysis indicate that microphysical schemes also affect the simulated typhoon asymmetric rainfall distribution during landfall. While the current study focuses on the PBL schemes, the in-depth analyses of the microphysics schemes will be continued in the second part of the study.

Data availability statement

The datasets presented in this study can be found in online repositories. The names of the repository/repositories and accession number(s) can be found in the article/ Supplementary Material.

Author contributions

JD and ZY conceived the study and wrote the manuscript. BH, YZ, and ZC helped with the data analysis. KC and YL provided critical feedback and helped shape the research and manuscript. All authors contributed to the manuscript and approved the submitted version.

Funding

The work was supported in part by the National Key Research and Development Program of China (2021YFC3000804), the National Natural Science Foundation of China (U2142206, 41875080), the Natural Science Foundation of Shanghai (22ZR1482000), the Program of Shanghai Academic/Technology Research Leader (21XD1404500), and the Typhoon Scientific and Technological Innovation group of Shanghai Meteorological Service.

Acknowledgments

The authors thank two reviewers for their careful review of the manuscript and constructive suggestions.

Conflict of interest

Author KC was employed by E3-Complexity Consulting, Eastwood, NSW, Australia.

The remaining authors declare that the research was conducted in the absence of any commercial or financial relationships that could be construed as a potential conflict of interest.

Publisher's note

References

Angevine, W. M., Jiang, H., and Mauritsen, T. (2010). Performance of an eddy diffusivity-mass flux scheme for shallow cumulus boundary layers. *Mon. Weather Rev.* 138 (7), 2895–2912. doi:10.1175/2010mwr3142.1

Ao, X., Yue, C., Yang, X., Deng, L., and Huang, W. (2022). Urbanization effects on rainfall processes induced by landfalling typhoon Lekima (2019) over the Shanghai metropolitan area. *J. Hydrometeorol.* 23, 1075–1093. doi:10.1175/JHM-D-21-0170.1

Bougeault, P., and Lacarrere, P. (1989). Parameterization of orography-induced turbulence in a mesobeta-scale model. *Mon. Weather Rev.* 117 (8), 1872–1890. doi:10.1175/1520-0493(1989)117<1872:POOITI>2.0.CO;2

Bretherton, C. S., and Park, S. (2009). A new moist turbulence parameterization in the community atmosphere model. *J. Clim.* 22 (12), 3422–3448. doi:10.1175/2008JCLI2556.1

Chan, J. C. L., and Liang, X. (2003). Convective asymmetries associated with tropical cyclone landfall. Part I: F-Plane simulations. *J. Atmos. Sci.* 60, 1560–1576. doi:10.1175/1520-0469(2003)60<1560:caawtc>2.0.co;2

Chen, S., Knaff, J. A., and Marks, F. D. (2006). Effects of vertical wind shear and storm motion on tropical cyclone rainfall asymmetries deduced from TRMM. *Mon. Weather Rev.* 134 (11), 3190–3208. doi:10.1175/mwr3245.1

Chen, Y., and Yau, M. K. (2003). Asymmetric structures in a simulated landfalling hurricane. *J. Atmos. Sci.* 60, 2294–2312. doi:10.1175/1520-0469(2003)060<2294:asiasl>2.0.co;2

Dai, H., Zhao, K., Li, Q., Lee, W. C., Ming, J., Zhou, A., et al. (2021). Quasiperiodic intensification of convective asymmetries in the outer eyewall of Typhoon Lekima (2019). *Geophys. Res. Lett.* 48, e2020GL091633. doi:10.1029/2020GL091633

Davis, C., and Bosart, L. F. (2002). Numerical simulations of the Genesis of Hurricane Diana (1984). Part II: Sensitivity of track and intensity prediction. *Mon. Weather Rev.* 130 (5), 1100–1124. doi:10.1175/1520-0493(2002)130<1100:nsotgo>2.0.co;2

DeMaria, M., Knaff, J. A., and Sampson, C. R. (2007). Evaluation of long-term trends in tropical cyclone intensity forecasts. *Meteorol. Atmos. Phys.* 59, 19–28. doi:10.1007/s00703-006-0241-4

Dudhia, J. (1989). Numerical study of convection observed during the winter monsoon experiment using a mesoscale two-dimensional model. *J. Atmos. Sci.* 46, 3077–3107. doi:10.1175/1520-0469(1989)046<3077:nsocod>2.0.co;2

Emanuel, K. A. (2000). A statistical analysis of tropical cyclone intensity. *Mon. Weather Rev.* 128, 1139–1152. doi:10.1175/1520-0493(2000)128<1139:asaotc>2.0.co;2

Gopalakrishnan, S. G., Marks, F., Jr, Zing, J. A., Zhang, X., Bao, J. W., and Tallapragada, V. (2013). A study of the impacts of vertical diffusion on the structure and intensity of the tropical cyclones using the high-resolution HWRF system. *J. Atmos. Sci.* 70, 524–541. doi:10.1175/jas-d-11-0340.1

Grenier, H., and Bretherton, C. S. (2001). A moist PBL parameterization for large-scale models and its application to subtropical cloud-topped marine boundary layers. *Mon. Weather Rev.* 129 (3), 357–377. doi:10.1175/1520-0493(2001)129<0357:AMPPFL>2.0.CO;2

He, B., Yu, Z., Tan, Y., Shen, Y., and Chen, Y. (2021). Rainfall forecast errors in different landfall stages of Super Typhoon Lekima (2019). *Front. Earth Sci.* 16, 34–51. doi:10.1007/s11707-021-0894–9

Hence, D. A., and Houze, R. A. (2011). Vertical structure of hurricane eyewalls as seen by the TRMM Precipitation Radar. *J. Atmos. Sci.* 68 (8), 1637–1652. doi:10.1175/2011jas3578.1

Hence, D. A., and Houze, R. A. (2012). Vertical structure of tropical cyclone rainbands as seen by the TRMM Precipitation Radar. *J. Atmos. Sci.* 69 (9), 2644–2661. doi:10.1175/jas-d-11-0323.1

Hill, K. A., and Lackmann, G. M. (2009). Analysis of idealized tropical cyclone simulations using the weather research and forecasting model: Sensitivity to turbulence parameterization and grid spacing. *Mon. Weather Rev.* 137 (2), 745–765. doi:10.1175/2008mwr2220.1

Hong, S. Y., Noh, Y., and Duchies, J. (2006). A new vertical diffusion package with an explicit treatment of entrainment processes. *Mon. Weather Rev.* 134 (9), 2318–2341. doi:10.1175/mwr3199.1

Huang, C., Sha, S., and Kuo, H. (2022). A modeling study of typhoon Lekima (2019) with the topographic influence of taiwan. *Mon. Weather Rev.* 150, 1993–2011. doi:10.1175/MWR-D-21-0183.1

Huang, Q., Ge, X., and Peng, M. (2021). Simulation of rapid intensification of Super Typhoon Lekima (2019). Part I: Evolution characteristics of asymmetric convection under upper-level vertical wind shear. *Front. Earth Sci. (Lausanne).* 9, 739507. doi:10.3389/feart.2021.739507

Janjić, Z. I. (1994). The step-mountain eta coordinate model: Further developments of the convection, viscous sublayer, and turbulence closure schemes. *Mon. Weather Rev.* 122 (5), 927–945. doi:10.1175/1520-0493(1994)122<0927:TSMECM>2.0.CO;2

Jiménez, P. A., Dudhia, J., Gonzalez–Rouco, J. F., Navarro, J., Montavez, J. P., and Garci–Bustamante, E. (2012). A revised scheme for the WRF surface layer formulation. *Mon. Weather Rev.* 140, 898–918. doi:10.1175/MWR-D-11-00056.1

Kain, J. S., and Fritch, J. M. (1993). Convective parameterization for mesoscale models: The kain-fritch scheme. The representation of cumulus convection in numerical models. *Meteor Monogr.* 46, 165–170. doi:10.1007/978-1-935704-13-3_16

Kepert, J. D. (2012). Choosing a boundary layer parameterization for tropical cyclone modeling. *Mon. Weather Rev.* 140 (5), 1 427–1445. doi:10.1175/mwr-d-11-00217.1

Li, X. L., and Pu, Z. X. (2008). Sensitivity of numerical simulation of early rapid intensification of Hurricane Emily (2005) to cloud microphysical and planetary boundary layer parameterizations. *Mon. Weather Rev.* 136 (12), 4819–4838. doi:10.1175/2008mwr2366.1

Li, Y., and Chen, L. S. (2005). Numerical study of impacts of boundary layer fluxes over wetland on sustention and rainfall of landfalling tropical cyclone. *J. Meteor Res.* 63 (5), 683–693.

Li, Y., Cheung, K. K. W., and Chan, J. C. L. (2015). Modelling the effects of land-sea contrast on tropical cyclone precipitation under environmental vertical wind shear. *Q. J. R. Meteorol. Soc.* 141, 396–412. doi:10.1002/qj.2359

Li, Y., Cheung, K. K. W., and Chan, J. C. L. (2014). Numerical study on the development of asymmetric convection and vertical wind shear during tropical cyclone landfall. *Q. J. R. Meteorol. Soc.* 140, 1866–1877. doi:10.1002/qj.2259

Lin, Y. L., Farley, R. D., and Orville, H. D. (1983). Bulk parameterization of the snow field in a cloud model. *J. Clim. Appl. Meteor.* 22, 1065–1092. doi:10.1175/1520-0450(1983)022<1065:bpotsf>2.0.co;2

Mlawer, E. J., Taubman, S. J., BrownP, D., Iacono, M. J., and Clough, S. A. (1997). Radiative transfer for inhomogeneous atmospheres: RRTM, a validated correlated-k model for the longwave. *J. Geophys. Res.* 102 (D14), 16663–16682. doi:10.1029/97jd00237

Nakanishi, M., and Niino, H. (2006). An improved mellor–Yamada level-3 model: Its numerical stability and application to a regional prediction of advection fog. *Bound. Layer. Meteorol.* 119, 397–407. doi:10.1007/s10546-005-9030-8

Nakanishi, M., and Niino, H. (2009). Development of an improved turbulence closure model for the atmospheric boundary layer. *J. Meteorological Soc. Jpn.* 87, 895–912. doi:10.2151/jmsj.87.895

Pleim, J. E. (2007). A combined local and nonlocal closure model for the atmospheric boundary layer. Part II: Application and evaluation in a mesoscale meteorological model. *J. Appl. Meteorol. Climatol.* 46 (9), 1396–1409. doi:10.1175/jam2534.1

Reasor, P. D., Rogers, R., and Lorsolo, S. (2013). Environmental flow impacts on tropical cyclone structure diagnosed from airborne Doppler radar composites. *Mon. Weather Rev.* 141 (9), 2949–2969. doi:10.1175/mwr-d-12-00334.1

Ren, F., and Xiang, C. (2017). Review and prospect of researches on the prediction of precipitation associated with landfalling tropical cyclones. *J. Mar. Meteorology (in Chinese)* 37 (4), 8–18. doi:10.19513/j.cnki.issn2096-3599.2017.04.002

Shi, D., Chen, G., Wang, K., Bi, X., and Chen, K. (2020). Evaluation of two initialization schemes for simulating the rapid intensification of Typhoon Lekima (2019). *Adv. Atmos. Sci.* 37 (9), 987–1006. doi:10.1007/s00376-020-2038-7

Shi, D. L., and Chen, H. (2021). Double warm-core structure and potential vorticity diagnosis during the rapid intensification of supertyphoon Lekima (2019). *J Atmos Sci* 78, 2471–2492. doi:10.1175/JAS-D-20-0383.1

Shin, H. H., and Hong, S. Y. (2011). Intercomparison of planetary boundary-layer parametrizations in the WRF model for a single day from CASES-99. *Boundary. Layer. Meteorol.* 139 (2), 261–281. doi:10.1007/s10546-010-9583-z

Smith, R. K., Montgomery, M. T., and Thomsen, G. L. (2014). Sensitivity of tropical-cyclone models to the surface drag coefficient in different boundary-layer schemes. *Q. J. R. Meteorol. Soc.* 140 (680), 792–804. doi:10.1002/qj.2057

Sukoriansky, S., Galperin, B., and Perov, V. (2005). Application of a new spectral theory of stably stratified turbulence to the atmospheric boundary layer over sea ice. *Boundary. Layer. Meteorol.* 117 (2), 231–257. doi:10.1007/s10546-004-6848-4

Tao, W. K., Shi, J. J., Lin, P. L., Chen, J., Lang, S., Chang, M. Y., et al. (2011). Highresolution numerical simulation of the extreme rainfall associated with Typhoon Morakot. Part I: Comparing the impact of microphysics and PBL parameterizations with observations. *Terr. Atmos. Ocean. Sci.* 22, 673–696. doi:10.3319/tao.2011.08.26.01(tm)

Wang, Y., and Zhao, Y. (2020). Numerical investigation of the effects of boundary layer parameterization schemes on typhoon Meranti (1614) landing process. *Chinese Journal of Atmospheric Sciences (in Chinese)* 44 (5), 935–995. doi:10.3878/j.issn.1006-9895.2004.19135

Xiang, C., Wu, L., and Qin, N. (2021). Characteristics of extreme rainfall and rainbands evolution of Super Typhoon Lekima (2019) during its landfall. *Front. Earth Sci.* 1, 64–74. doi:10.1007/s11707-021-0871–3

Xu, F., and Liang, X. (2021). Drastic change in dynamics as Typhoon Lekima experiences an eyewall replacement cycle. *Front. Earth Sci.* 16, 121–131. doi:10.1007/s11707–020–0865–6

Xu, Y., Zhai, G., Li, G., Yu, Z., and Yan, H. (2017). Optimization experiment for microphysical and boundary layer parameterization of high-impact Zhejiang typhoons by WRF model. *Journal of Tropical Meteorology (in Chinese)* 33 (2), 201–211.

Ying, M., Zhang, W., Yu, H., Lu, X., Feng, J., Fan, Y., et al. (2014). An overview of the China Meteorological Administration tropical cyclone database. *J. Atmos. Ocean. Technol.* 31, 287–301. doi:10.1175/JTECH-D-12-00119.1

Yu, H., Chen, P., Li, Q., and Tang, B. (2013). Current capability of operational numerical models in predicting tropical cyclone intensity in the western north pacific. *Weather Forecast.* 28 (2), 353–367. doi:10.1175/waf-d-11-00100.1

Yu, Z., Chen, J. Y., Ebert, B., Davidson, N., Xiao, Y., Yu, H., et al. (2020). Benchmark rainfall verification of landfall tropical cyclone forecasts by operational ACCESS-TC over China. *Meteorol. Appl.* 27 (1), 1–18. doi:10.1002/met.1842

Yu, Z., Liang, X., Yu, H., and Chan, J. C. L. (2010). Mesoscale vortex generation and merging process: A case study associated with a post-landfall tropical depression. *Adv. Atmos. Sci.* 27 (2), 356–370. doi:10.1007/s00376-009-8091-x

Yu, Z., Wang, Y., Xu, H., Davidson, N., Chen, Y., Chen, Y., et al. (2017). On the relationship between intensity and rainfall distribution in tropical cyclones making landfall over China. *J. Appl. Meteorol. Climatol.* 56 (10), 2883–2901. doi:10.1175/jamc-d-16-0334.1

Yu, Z., Wang, Y., Yu, H., and Duan, Y. (2022). The relationship between the inner-core size and the rainfall distribution in landfalling tropical cyclones over China. *Geophys. Res. Lett.* 49, e2021GL097576. doi:10.1029/2021gl097576

Yu, Z., Yu, H., Chen, P., Qian, C., and Yue, C. (2009). Verification of tropical cyclone–related satellite precipitation estimates in mainland China. *J. Appl. Meteorol. Climatol.* 48 (11), 2227–2241. doi:10.1175/2009jamc2143.1

Zhang, J. A., Rogers, R. F., Nolan, D. S., and Marks, F. D. (2011). On the characteristic height scales of the hurricane boundary layer. *Mon. Weather Rev.* 139, 2523–2535. doi:10.1175/mwr-d-10-05017.1

Zhu, P., Menelaou, K., and Zhu, Z. (2014). Impact of subgrid-scale vertical turbulent mixing on eyewall asymmetric structures and mesovortices of hurricanes. *Q. J. R. Meteorol. Soc.* 140 (679), 416–438. doi:10.1002/qj.2147

Zhu, P., Tyner, B., Zhang, J. A., Aligo, E., Tallapragada, V., Marks, F. D., et al. (2019). Role of eyewall and rainband eddy forcing in tropical cyclone intensification. *Atmos. Chem. Phys.* 19 (22), 14289–14310. doi:10.5194/acp-19-14289-2019

frontiers | Frontiers in Earth Science

TYPE Original Research
PUBLISHED 26 September 2022
DOI 10.3389/feart.2022.987001

OPEN ACCESS

EDITED BY
Liguang Wu,
Fudan University, China

REVIEWED BY
Dong-Hyun Cha,
Ulsan National Institute of Science and Technology, South Korea
Eric Hendricks,
National Center for Atmospheric Research (UCAR), United States

*CORRESPONDENCE
Fumin Ren,
fmren@163.com

SPECIALTY SECTION
This article was submitted to Atmospheric Science, a section of the journal Frontiers in Earth Science

RECEIVED 05 July 2022
ACCEPTED 07 September 2022
PUBLISHED 26 September 2022

CITATION
Li L, Chen Y, Ren F, Liu C, Ma Y and Wan Q (2022), Experiment with the dynamical–statistical–analog ensemble forecast model for landfalling typhoon gale over South China.
Front. Earth Sci. 10:987001.
doi: 10.3389/feart.2022.987001

Experiment with the dynamical–statistical–analog ensemble forecast model for landfalling typhoon gale over South China

Lifang Li[1,2], Yuxu Chen[3], Fumin Ren[1]*, Chunxia Liu[2], Yunqi Ma[1] and Qilin Wan[2]

[1]State Key Laboratory of Severe Weather, Chinese Academy of Meteorological Sciences, Beijing, China, [2]Guangzhou Institute of Tropical and Marine Meteorology, Guangzhou, China, [3]Shantou Meteorological Bureau, Shantou, China

In this study, an experiment based on the Dynamical-Statistical-Analog Ensemble Forecast model for Landfalling Typhoon Gale (DSAEF_LTG model) was conducted to predict tropical cyclone (TC)-induced potential maximum gales in South China for the first time. A total of 21 TCs with maximum gales greater than or equal to 17.2 m/s (at least one station) during 2011–2018 were selected for this experiment. Among them, 16 TCs in 2011–2015 were selected as the training samples aimed at identifying the best forecast scheme, while 5 TCs in 2016–2018 were selected as the independent samples to verify the best forecast scheme. Finally, the forecast results were compared with four numerical weather prediction (NWP) models (i.e., CMA, ECMWF, JMA and NCEP) based on four forecasting skill scores (Threat Score, False Alarm Ratio, Missing Ratio and Bias Score) at thresholds above Beaufort Scale 7 and 10, and two more indicators (Mean Absolute Error and pearson correlation coefficient). The results revealed encouraging forecasting ability in South China for the DSAEF_LTG model. In general, the DSAEF_LTG model showed higher forecasting skill than the NWP models above the critical thresholds. While the DSAEF_LTG model was prone to false alarms, the NWP models were prone to missing alarms, especially for an intense scale (≥Beaufort Scale 10). In addition, the DSAEF_LTG model also performed best with the smallest forecasting error. Furthermore, the DSAEF_LTG model had distinct advantages in predicting target TCs with typical tracks and widespread gales, both in terms of the wind field pattern and the magnitude of central wind speeds. However, for sideswiping TCs with small-scale gales, the DSAEF_LTG model tended to over-predict and held no advantage over the NWP models, which could perhaps be improved by introducing more reasonable ensemble forecast schemes in further research.

KEYWORDS

landfalling tropical cyclone, potential maximum gale, DSAEF_LTG model, South China, forecasting

1 Introduction

A tropical cyclone (TC, also known as a typhoon in the western North Pacific) refers to a low-pressure system with a warm core that forms over tropical and subtropical warm oceans (Roy and Rita, 2012). China is one of the countries frequently affected by TC-related disasters in the world, with about 15 TCs affecting it each year and about 7 making landfall in coastal areas (Chen and Meng, 2001). Landfalling TCs are associated with heavy rainfall, strong winds and damaging storm surges (Peduzzi et al., 2012), of which strong winds is a non-negligible disaster-causing factor that triggers storm surges and further aggravates heavy-rain disasters (Powell and Reinhold, 2011). For example, the strong winds generated by super typhoon Rammasun in 2014 caused a huge number of casualties and the direct economic losses reached approximately CNY 26.55 billion (equivalent to approximately USD 4.2 billion) in South China (Wan et al., 2016). Therefore, accurate and timely forecasting of TC gales is of great significance in the prevention and mitigation of TC-related disasters.

At present, the main approaches to the prediction of TC-induced gales include empirical forecasts, statistical forecasts, numerical weather prediction (NWP) and their interpretations (Dong, 2014). Empirical forecasting is based on synoptic principles and the experience of forecasters, and an example would be the empirical model developed by Kaplan and DeMaria (1995) for predicting the decay of TC gales after landfall. More recently, the application of satellite cloud imagery (Chen and Zhang, 2008) and radar images (Zhi and Huang, 2020) have enhanced the reliability of empirical forecasts in short-impending predictions. Statistical forecasting utilizes large amounts of historical TC data as well as effective statistical methods to obtain objective and quantitative predictions. For instance, Li et al. (2016) proposed a quantitative forecast model for predicting the potential TC maximum gust in South China by exploring the relationship between observations and the main characteristics of TCs. In addition, Knaff et al. (2007) established a statistical-parametric model that adopted climatology and persistence to predict TC wind radii. Relying on the integration of atmospheric dynamic equations under certain initial conditions, NWP plays a key role in the forecasting of TC gales, and many forecasting institutions around the world have developed relevant products (e.g., high-resolution gridded forecasts of wind speed and TC wind speed probability) (Demaria et al., 2013; Lin et al., 2015). The interpretations of NWP indicate further analysis and modification on NWP outputs by statistical, dynamic or artificial intelligence methods are needed; for example, He et al. (2018) provided a model for predicting TC gust by introducing improved fruit fly optimization algorithm into fuzzy support vector machine to raise the applicability of WRF outputs.

Although the approaches mentioned above have shown encouraging results in research and operations, they still face complex challenges and need to overcome certain shortcomings for further improvements. For example, empirical forecasting is not objective enough, while statistical forecasting lacks consideration of TC physical mechanisms, and NWP as well as its interpretation are limited by the descriptions of physical processes (Li et al., 2021). Considerable attention has been paid in recent decades to improving the performance of TC forecasts, significantly, based on statistical methods and dynamical models (Zhang et al., 2016). The statistical–dynamical approach combines forecast information from dynamical model within a statistical framework to make the forecast (Charney et al., 1969; Carter et al., 1989). Knaff et al. (2017) developed a statistical–dynamical model to predict TC wind structure in terms of wind radii, which not only compared well with NWP, but its inclusion boosted the skill of consensus forecast. At the same time, there is a notable absence in existing models of applying the statistical–dynamical approach to provide forecast guidance on TC-induced potential maximum gales, which contributes to estimating the intensity and affected area of TC-related disasters about strong winds (Wang et al., 2017). With this deficiency in mind, Chen (2021) developed the Dynamical–Statistical–Analog Ensemble Forecast model for Landfalling Typhoon Gales (i.e., TC-induced potential maximum gale) (hereafter abbreviated to the DSAEF_LTG model), based on the DSAEF theory proposed by Ren et al. (2020). Preliminary application in a simulation experiment on Mangkhut in 2018 demonstrated that the DSAEF_LTG model was able to accurately simulate the pattern and central wind speeds of the potential maximum gale, performing better than NWP models.

Completed simulation experiments with single sample and large number of samples have both confirmed that the DSAEF_LTG model did well in simulating the intensity and spatial distributions of the potential maximum gale. Nevertheless, more attention needs to be paid to whether the model can show high forecast skill in operational application. Hence, it is necessary to carry out multi-sample forecast experiments to examine the forecasting ability of the DSAEF_LTG model, which is the motivation behind our study. Accordingly, 21 TCs that severely affected South China during the period 2011–2018 were selected to conduct forecast experiment in this paper.

Following this introduction, Section 2 presents the data and methods, including the forecasting procedures of the DSAEF_LTG model. Section 3 introduces the experimental design and how the best forecasting scheme was obtained and its performance verified. Section 4 compares the forecasting results of the DSAEF_LTG model to those from four select dynamic models. The summaries and discussions are given in Section 5.

2 Data and methods

2.1 Data

Based on revised NWP model outputs, the observed and predicted information of the target TCs in our experiment, including their tracks and intensity, were obtained from the

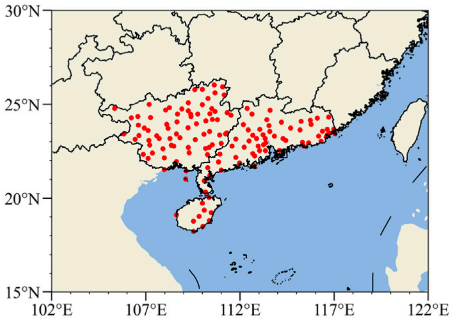

FIGURE 1
Spatial distribution of 140 stations in South China (Guangdong, Guangxi and Hainan provinces).

National Meteorological Information Center (NMIC) of China Meteorological Administration (CMA). Historical TC best-track data, comprising the TC position and intensity at 6-h intervals since the 1960s (Ying et al., 2014), and Beaufort scale of wind speeds were both obtained from Shanghai Typhoon Institute of CMA (available from https://tcdata.typhoon.org.cn/).

Historical observed maximum 2-min average wind speeds of 10-m above the surface at 1-h intervals were provided by the NMIC of CMA from 1980 to 2018. For consistency, the stations with a cumulative absence time of more than 24 months were discarded, as were the stations above the mean station height of 894.7-m, in order to reduce the interference of alpine stations in separating TC-induced gales. Ultimately, the original data with 140 stations in South China (Guangdong, Guangxi and Hainan provinces) were retained in this study, and their geographical distribution is shown in Figure 1. Furthermore, the TC-induced potential maximum gale refers to the peak value of hourly maximum 2-min-averaged wind speed within a certain TC's life for each station.

The gridded forecast datasets of 10-m zonal (*u*) and meridional (*v*) winds from The Observing System Research and Predictability Experiment (THORPEX) Interactive Grand Global Ensemble (TIGGE) control forecasts (available from https://apps.ecmwf.int/datasets/data/tigge/) were used to evaluate the forecasting performance of the DSAEF_LTG model. Specifically, the datasets were derived from following forecast centers: CMA, European Centre for Medium-Range Weather Forecasts (ECMWF), Japan Meteorological Agency (JMA) and National Centers for Environmental Prediction (NCEP), available on 1 × 1 grids with lead times of about 1–10 days at 6-h intervals and an initial time of 1200 UTC. For comparison, the resultant u and v wind speeds at each grid point were firstly calculated and then interpolated to the 140 stations mentioned above. Correspondingly, the TC-induced potential maximum gales of the NWP models refer to the maximum value of resultant wind speed at 6-h intervals within a certain TC's life for each station.

2.2 DSAEF_LTG model

Figure 2 is a flowchart of how to apply the DSAEF_LTG model, which is composed of following four forecasting steps: 1) obtain the forecast track of the target TC; 2) construct generalized initial values (GIVs), including TC track, landfall date and current TC intensity; 3) identify the similarity of the GIVs constructed in the previous step between target and historical TCs; and 4) make an ensemble prediction about the potential maximum gale of target TCs. Table 1 lists the eight parameters and their physical significances involved in the DSAEF_LTG model (referring to the DSAEF_LTP model improved by Jia et al. (2020). For better understanding, values 16–20 of the similarity region (P2) in the parameters are shown in Figure 3. According to Table 1, each parameter has multiple values and they can combine randomly between different parameters. One combination is referred to as a forecast scheme and, as a result, 2,880,000 forecast schemes can be generated from eight parameters under idealized conditions.

The forecasting procedures of the DSAEF_LTG model can be summarized in more detail as follows: 1) first, the observed track before the initial time (P1) and the forecast track after the initial time, both obtained from NMIC of CMA, were merged into a complete track as the target TC track. 2) Next, the objective TC Track Similarity Area Index (TSAI) was calculated between the target TC track and all the historical TC tracks (before the target TC since 1980) in an established similarity region (P2), and then sorted in ascending order. A smaller TSAI implies a higher track similarity. In other words, P2, P3 and P4 codetermined the TC track similarity in this part. 3) based on the TC track similarity, the TC landfall season (P5) and TC intensity (P6) similarities were identified to eliminate the historical TCs that differed greatly from the target TC in landfall time and intensity. 4) Finally, an optimized ensemble forecast scheme (P8) was adopted to assemble the TC wind fields of the remaining top N historical TCs (where N was determined by P7), and the predicted potential maximum gale of the target TC was obtained.

2.3 Other methods

2.3.1 Track similarity area index

The TSAI is an objective technique to select analogous tracks from historical TC data (Ren et al., 2018). The principle of TSAI is to calculate the area enclosed by any 2 TC tracks—namely, the target TC and the historical TC in this study. The smaller the area value, the higher the similarity.

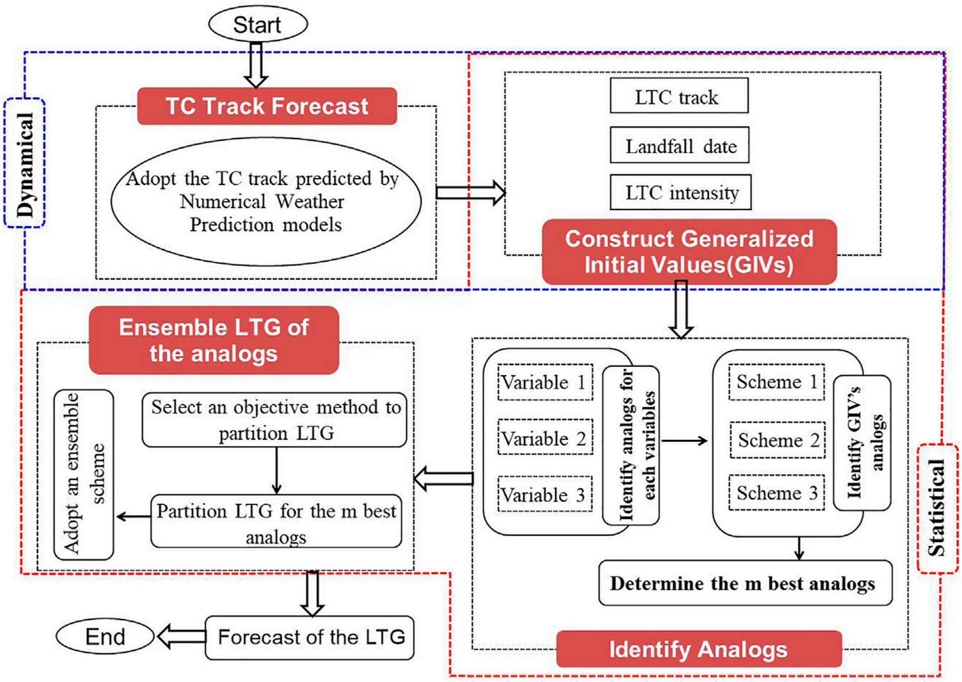

FIGURE 2
Flowchart of the DSAEF_LTG model.

2.3.2 The improved objective synoptic analysis technique for landfalling TC-induced gale (OSAT_LTG)

The OSAT_LTG is used to separate and obtain TC-induced gales (i.e., wind speeds reaching 10.8 m/s and above) (Lu et al., 2016) and includes four steps as follows: 1) divide the gales into independent natural wind fields; 2) identify the potential TC wind field; 3) separate the gales for each station; and 4) combine the complete TC wind field. In this study, OSAT_LTG was also employed to obtain the list of historical TCs (i.e., experimental samples) with TC-induced gales in South China.

2.3.3 Forecast evaluations and skill scores

In this paper, four skill scores including Threat Score (TS), False Alarm Ratio (FAR), Missing Ratio (MR) and Bias Score (BS) are applied to compare the forecasting skill of the models above two critical thresholds. Meanwhile, two more indicators including Mean Absolute Error (MAE) and pearson correlation coefficient (R) are used to get a more complete evaluation of the forecast performances. Their calculation formulae are as follows:

$$TS = \frac{hits}{hits + misses + false\,alarms}$$

$$FAR = \frac{false\,alarms}{hits + false\,alarms}$$

$$MR = \frac{misses}{hits + misses}$$

$$BS = \frac{hits + false\,alarms}{hits + misses}$$

$$MAE = \frac{\sum_{i=1}^{N} \left| x_i - y_i \right|}{N}$$

$$R = \frac{\sum_{i=1}^{N} \left(x_i - \overline{x_i} \right) \left(y_i - \overline{y_i} \right)}{\sqrt{\sum_{i=1}^{N} \left(x_i - \overline{x_i} \right)^2 \left(y_i - \overline{y_i} \right)^2}}$$

The value of "hits" indicates the number of stations at which the prediction and observation both reach a certain magnitude; and"false alarms" is the number of stations where the prediction reaches a certain magnitude but the observation does not; while "misses" is the number of stations where the observation reaches a certain magnitude but the prediction does not. The TS, FAR and MR vary from 0 to 1. The closer the TS is to 1, the higher the forecast skill. However, for FAR and MR, higher values denote more serious false alarms and missing alarms, respectively. For better comparisons, all the BS values in this study were reduced by 1, and they further indicate whether the forecast results have tendencies to over-predictions (BS>0) or under-predictions (BS<0) (Wang et al., 2020).

The MAE and R are defined as where x_i and y_i denote the predicted and observed wind speeds, at the i th station,

TABLE 1 Parameters of the DSAEF_LTG model.

Parameters (1–8)	Description	Number of values
Initial time (P1)	1: 1200 UTC on Day1, 2: 0000 UTC on Day1, 3: 1200 UTC on Day2, 4: 0000 UTC on Day2. (Day1: the day of TC gales occurring on land; Day2: the day before Day1)	4
Similarity region (P2)	A parameter of TSAI with rectangular shape. Its southeastern vertex (C) can be the TC position at 0, 12, 24, 36 or 48 h prior to the initial time, and the northwestern vertex (A) can be the TC position at 0, 6 or 12 h prior to the maximum lead time, the values of 1st–15th are combined by C and A. The 16th–20th values are based on the first value; namely, C represents the TC position at the initial time and A represents the TC position at the maximum lead time. More details about the 16th–20th values are given in Figure	20
Threshold of the segmentation ratio of a latitude extreme point (P3)	A parameter of TSAI. 1: 0.1, 2: 0.2, 3: 0.3	3
The overlapping percentage threshold of 2 TC tracks (P4)	A parameter of TSAI. 1: 0.9, 2: 0.8, 3: 0.7 4: 0.6, 5: 0.5, 6: 0.4	6
Seasonal similarity (P5)	A parameter indicating the TC landfall date 1: whole year; 2: May–Nov; 3: Jul–Sep 4: same landfall month as the target TC 5: within 15 days of the target TC landfall time	5
Intensity similarity (P6)	Four categories 1: average intensity on the first windy day 2: maximum intensity on the first windy day 3: average intensity on all windy days 4: maximum intensity on all windy days Five levels 1: all grades; 2: the target TC intensity is the same grade or above the historical TC 3: the same grade or below; 4: only the same grade 5: the same grade or one grade difference	4×5
Number (*N*) of analogue TCs screened for the ensemble forecast (P7)	1–10 for 1, 2, . . . , 10, respectively	10
Ensemble forecast scheme (P8)	1: mean 2: maximum	2
Total number of schemes	4 × 20 × 3 × 6 × 5 × 20 × 10 × 2 = 2,880,000	

respectively. N is the station size, $\overline{x_i}$ and $\overline{y_i}$ represent the corresponding mean values. The lower the MAE is, the smaller the gaps between prediction and observation are, namely the forecasting performance is better. While for R, higher values represent closer relationships between prediction and observation and better performance (Wilks, 2006).

3 Experimental design

3.1 The target TCs

Considering that the “landfalling typhoon” in the DSAEF_LTG model refers to the TC that had serious impacts caused by TC-induced gales on China, we set a primary inclusion criterion for a target TC—namely, a TC having maximum gale ≥17.2 m/s for at least one station in South China.

To keep a moderate sample size for the first forecasting application of the DSAEF_LTG model, together considering that 2018 is the last year for available historical observed wind speeds, 2011–2018 was selected as the analysis period of the target TCs. Specifically, the target TCs consist of training samples and independent samples, for the simulation and forecast experiments, respectively. For the forecast experiment, archived TIGGE data of NWP models is required for comparison. Then, considering that none of the target TCs in 2015 has archived TIGGE data, 16 TCs in 2011–2015 and 5 TCs in 2016–2018 were selected as training samples (Figure 4A) and independent samples (Figure 4B), respectively.

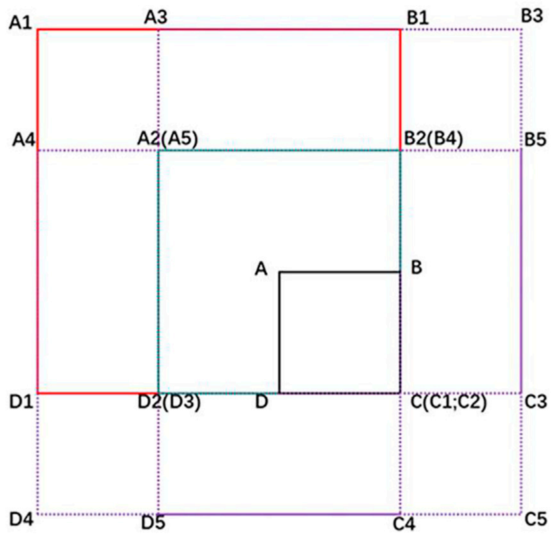

FIGURE 3
Schematic diagram of the 16th–20th similarity region (P2). C is the TC position at the initial time and A is the TC position at the maximum lead time, with ABCD denoting the first value of P2. The 16th value is a square (A1B1C1D1) with C as the southeastern vertex and a side length of 2000 km. B2 is the midpoint of B and B1, while D2 is the midpoint of D and D1, and A2B2C2D2 is a medium-sized rectangle as the 17th value of P2. Shifting A1B1C1D1 to the right by the distance of D1D2, down by the distance of B1B2, right by the distance of D1D2, and down by the distance of B1B2, simultaneously, produces A3B3C3D3, A4B4C4D4, and A5B5C5D5 as the 18th–20th values of P2, respectively.

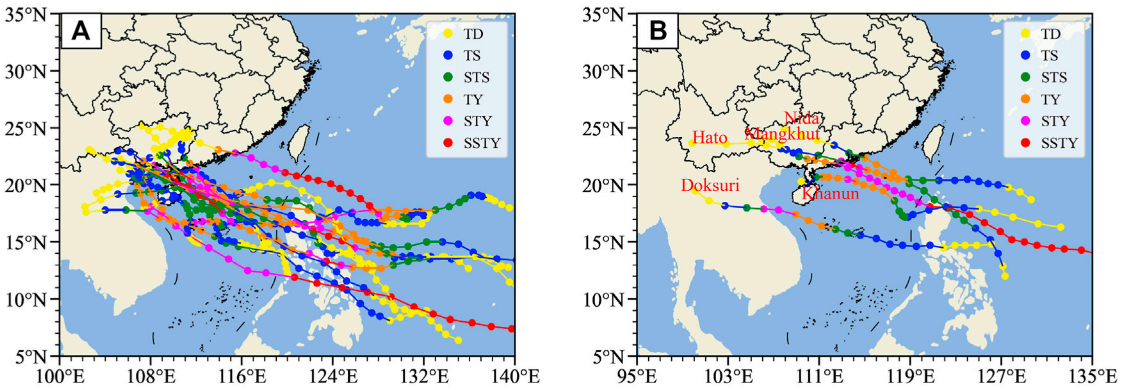

FIGURE 4
Tracks of the target TCs, including **(A)** 16 training samples in 2011–2015 and **(B)** five independent samples in 2016–2018. The names of the independent samples are also shown in **(B)**.

3.2 Experimental design of the DSAEF_LTG model

We conducted both simulation and forecast experiment to explore the forecasting ability of the DSAEF_LTG model in predicting the TC-induced potential maximum gale in South China. The simulation experiment based on the training samples was aimed at identifying the best forecast scheme suitable for South China—in other words, the optimal value of each parameter in Table 2 with the best forecast performance. The purpose of the forecast experiment based on the independent samples was to verify the best forecast scheme. Meanwhile, we also compared the forecast results with those of the NWP models (CMA, ECMWF, JMA and NCEP) to gain a comprehensive and objective understanding of the DSAEF_LTG model.

Specifically, there are two steps to determine the best forecast scheme: firstly, screen the forecast schemes, applicable to all the training samples, from the forecast schemes generated by the simulation experiment; then, set an appropriate criterion to pick out the best forecast scheme. Significantly, some training samples aren't able to be fully valued on certain parameters, such as the initial time (P1) and the similarity region (P2), so the number of forecast schemes will be equal to or less than 2,880,000.

The Beaufort Wind Scale is commonly used in research and operations. In this study, we concentrated on TC-induced gales greater than Beaufort Scale 6 (the wind speeds of Beaufort Scale from 6 to 13 are listed in Table 3). As shown in Figure 5, the TC-induced gales in the training samples mainly ranged within Beaufort Scale 6–8, the proportion being more than 80%. Thus, in order to pick out the best forecast scheme with high efficiency, we calculated the TS values above the thresholds of Beaufort Scale 6 and 8 (hereafter TS6 and TS8, respectively), and the forecast scheme with maximal TSsum (i.e., TSsum = TS6 + TS8) was selected as the best forecast scheme. However, the TC warnings issued by operational centers pay more attention to Beaufort Scale 7 and 10, due to the fact that Beaufort Scale 7 is related to TC scale and Beaufort Scale 10 is a critical reference for TC defense (Sampson and Knaff, 2015; Xiang et al., 2016). Hence

TABLE 2 List of training samples and independent samples for TCs.

Sample classification	Names of TCs from 2011 to 2018
Training samples (16 TCs from 2011 to 2015)	2011: Haima, Nock-ten, Nesat, Nalgae 2012: Kai-tak, Son-tinh 2013: Rumbia, Jebi, Utor, Usagi, Wutip, Haiyan 2014: Rammasun, Kalmaegi 2015: Kujira, Mujigae
Independent samples (5 TCs from 2016 to 2018)	2016: Nida 2017: Hato, Doksuri, Khanun 2018: Mangkhut

TABLE 3 Beaufort scale of wind speeds.

Beaufort number	Wind speed (m/s)
6	10.8–13.8
7	13.9–17.1
8	17.2–20.7
9	20.8–24.4
10	24.5–28.4
11	28.5–32.6
12	32.7–36.9
13	37.0–41.4

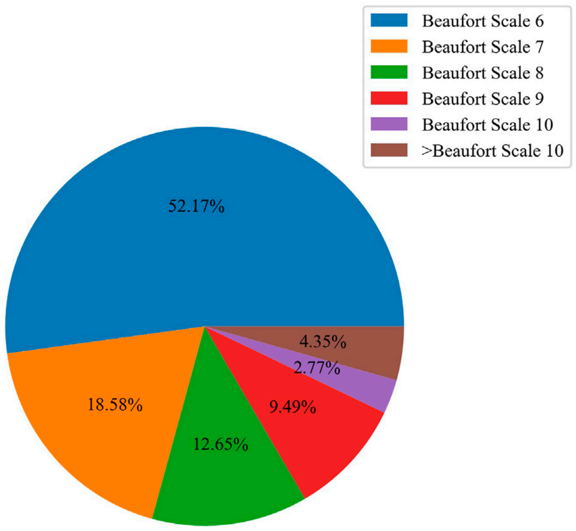

FIGURE 5
Proportions of different wind speed magnitudes of the TC-induced gales in 16 training samples.

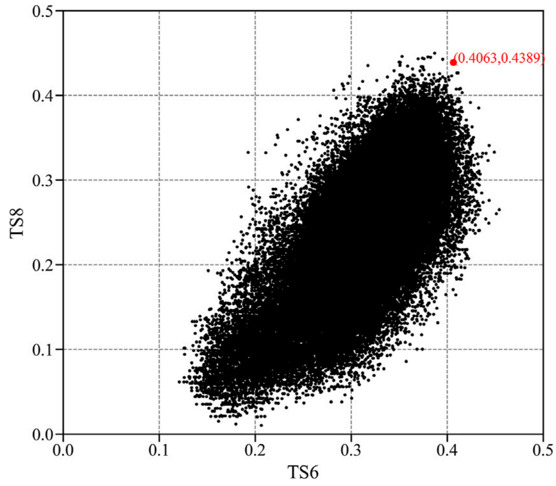

FIGURE 6
Scatter plots of the threat scores (TS6–TS8) from 241,186 forecast schemes generated by the simulation experiment. TS6 and TS8 represent the threat scores for predicting the potential maximum gale of ≥ Beaufort Scale 6 and ≥ Beaufort Scale 8, respectively. The red scatter point indicates the best forecast scheme with maximal TSsum (TS6 + TS8).

the TS, FAR, MR and BS were calculated above the thresholds of Beaufort Scale 7 and 10 to evaluate the forecasting performances in the forecast experiment.

4 Results

4.1 Simulation experiment of training samples

The results of the simulation experiment indicated that there were 241,186 forecast schemes for the 16 training samples, which are shown in Figure 6 by the black scatter points. Taking TS6 as the *x*-axis and TS8 as the *y*-axis, each

TABLE 4 Optimized values for the best forecast scheme in the simulation experiment.

Parameters (1–8)	Optimized value and its description
Initial time (P1)	3: 1200 UTC on the day before the day of TC gales occurring on land
Similarity region (P2)	20
Threshold of the segmentation ratio of a latitude extreme point (P3)	2: 0.2
Overlapping percentage threshold of 2 TC tracks (P4)	5: 0.5
Seasonal similarity (P5)	1: Whole year
Intensity similarity (P6)	(2, 5): maximum intensity on the first windy day with the same grade or one grade difference
Number (*N*) of analogue TCs screened for the ensemble forecast (P7)	2
Ensemble forecast scheme (P8)	2: maximum

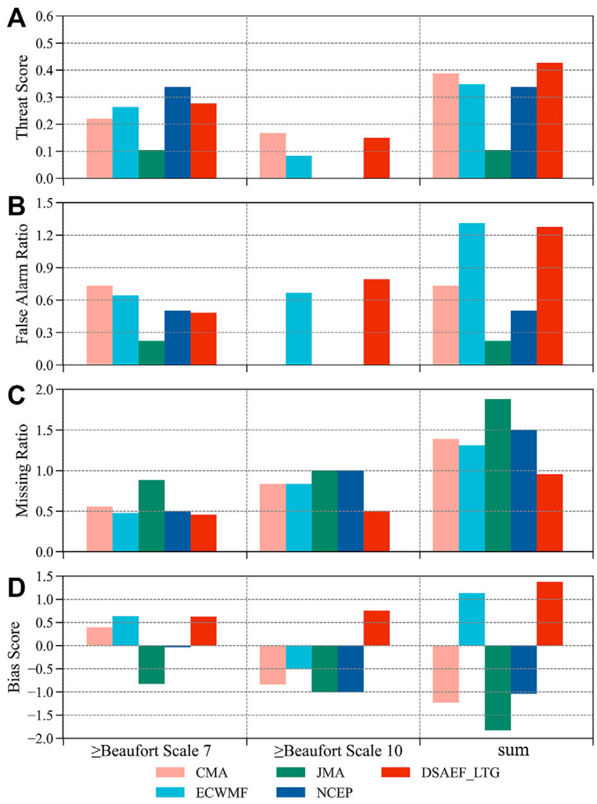

FIGURE 7
Comparison of the average forecast skill scores (i.e., **(A)** TS, **(B)** FAR, **(C)** MR and **(D)** BS) of different models (CMA, ECWMF, JMA, NCEP, and the best forecast scheme of the DSAEF_LTG model) at thresholds above Beaufort Scale 7 and 10. Note that all the BS values were reduced by 1 for better comparisons, and the sum of average BS was defined as ± (|BS7|+|BS10|), where the symbol depended on BS7+BS10.

scatter point in Figure 6 represents a forecast scheme, and the red scatter point denotes the best forecast scheme determined by TSsum (i.e., TS6 = 0.4063 and TS8 = 0.4389). Furthermore, the values of eight parameters in the best forecast scheme are listed in Table 4.

4.2 Forecast experiment of independent samples

Based on the average forecast skill scores (i.e., TS, FAR, MR and BS) of five independent samples under two critical thresholds—Beaufort Scale 7 and 10, Figure 7 further compares the best forecast scheme of the DSAEF_LTG model to the four NWP models (i.e., CMA, ECMWF, JMA and NCEP). For brevity, TS7 (FAR7, MR7 and BS7) and TS10 (FAR10, MR10 and BS10) denote the TS (FAR, MR and BS) at two thresholds above Beaufort Scale 7 and 10, respectively. Note that the average TS, FAR and MR were calculated only when the scores were greater than or equal to 0. In addition, the sum of average BS was defined as ± (|BS7|+|BS10|), where the symbol depended on the BS7+BS10.

According to Figure 7A, NCEP ranked first in the average TS7, followed by the DSAEF_LTG model; while in the average TS10, the DSAEF_LTG model was still in the second place, and CMA ranked first. Consequently, the DSAEF_LTG model outperformed the four NWP models in terms of the sum (i.e., TS7 + TS10), with a total score of 0.4273. As shown in Figures 7B,C, the DSAEF_LTG model ranked fourth in FAR7, first in FAR10, and its sum of average FAR was only slightly lower than CMA, which indicated the FAR of the DSAEF_LTG model was on the high side; but for the average MR, the minimums were calculated by the DSAEF_LTG model both in the average MR7 and MR10, confirming it has a distinct advantages over the NWP models in terms of missing alarms. Figure 7D compares the average BS of different models. The DSAEF_LTG model tends to over-predictions in BS7 and BS10, with scores of 0.6232 and 0.75, respectively; while the NWP models tend to under-predictions, especially for an intense scale (≥Beaufort Scale 10).

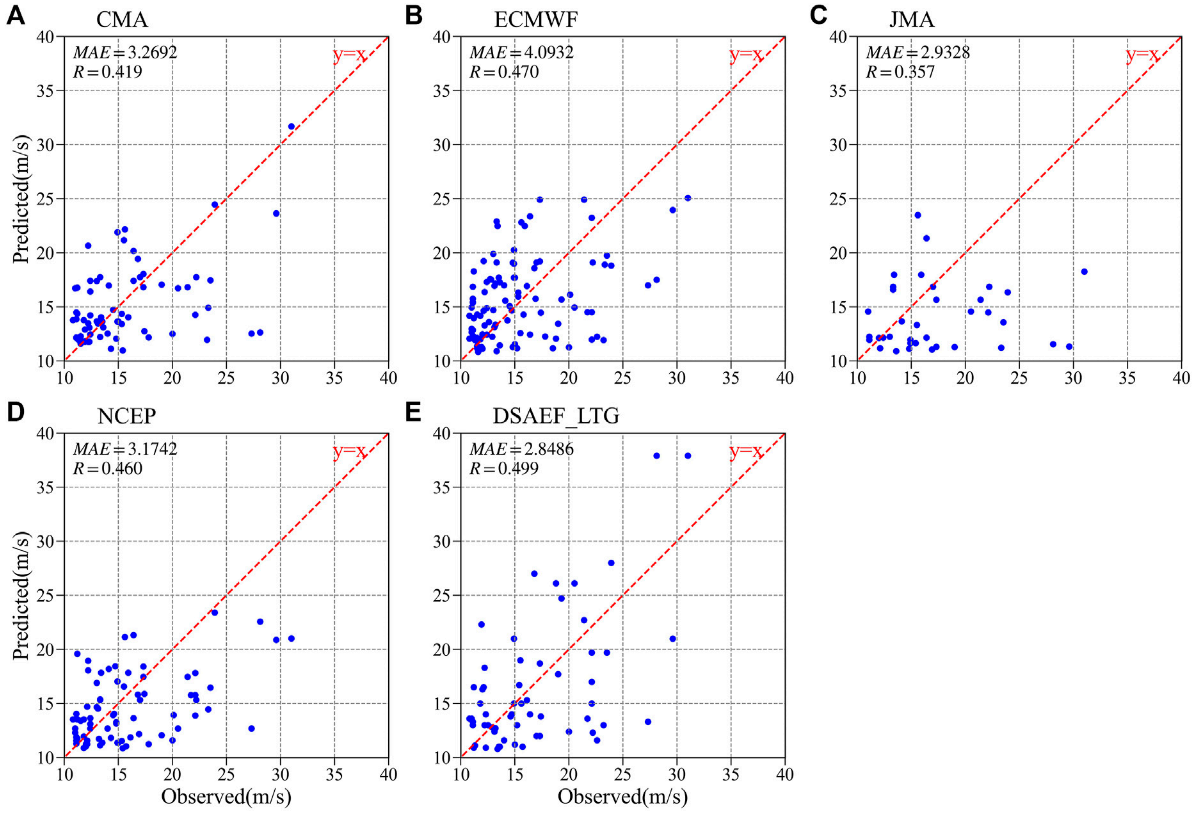

FIGURE 8
Scatter distributions of the predicted and observed wind speeds from five independent samples according to **(A)** CMA, **(B)** ECMWF, **(C)** JMA, **(D)** NCEP and **(E)** the DSAEF_LTG model. The MAE and R (passing the 0.01 significance test) of each model are also provided in the upper left. The red dotted line is a reference line where the prediction is equal to observation.

In conclusion, on the whole, the DSAEF_LTG model showed higher forecasting skill than the NWP models at two critical thresholds (i.e., Beaufort Scale 7 and 10). Moreover, according to the results of the average FAR, MR and BS, the DSAEF_LTG model was prone to false alarms, while the NWP models were prone to missing alarms, especially for an intense scale.

According to the scatter distribution between predicted and observed wind speeds of five independent samples and relevant statistical indicators (i.e., MAE and R), the forecasting deviation of each model can be compared directly. As all above presented in Figure 8, the forecasting deviations of all models were increased (i.e., the scatters were further away from the reference line) in the case of stronger wind speeds. Among the 5 models, the minimum of MAE and the maximum of R (passing the 0.01 significance test) were both derived from the best forecast scheme of the DSAEF_LTG model with the values of 2.8486 and 0.499, respectively. Thus in general, the DSAEF_LTG model performed best with smallest forecasting error.

Figure 9 further show the TS7 and TS10 associated with individual independent samples forecasted by the different models mentioned above. As indicated by the black dotted line, the stronger the maximum gale (the largest value selected from the potential maximum gale of all stations for each TC), the better the forecasting performance at Beaufort Scale 7 for each model. However, this feature was not obvious at Beaufort Scale 10.

In terms of TS7 (Figure 9A), among all the independent samples, Mangkhut had the best forecast performance with scores above 0.25 for all models, while Nida performed the worst with scores below 0.15 for all models. From the perspective of comparing between different models, the DSAEF_LTG model had a prominent advantage over the four NWP models in its performance for Hato, with a score of 0.375, and was tied for first place with ECMWF for Nida. For the remaining 3 TCs (Doksuri, Khanun and Mangkhut), the DSAEF_LTG model ranked third or fourth, the biggest difference with the first-place model was for Doksuri, at 0.3334, and the smallest difference was for Mangkhut, at 0.0302.

From the black dotted line in Figure 9B, we can see that only the potential maximum gales of Hato, Doksuri and Mangkhut exceeded Beaufort Scale 10. The remaining 2 TCs (Nida and Khanun), without TS10 values, indicate that neither observations

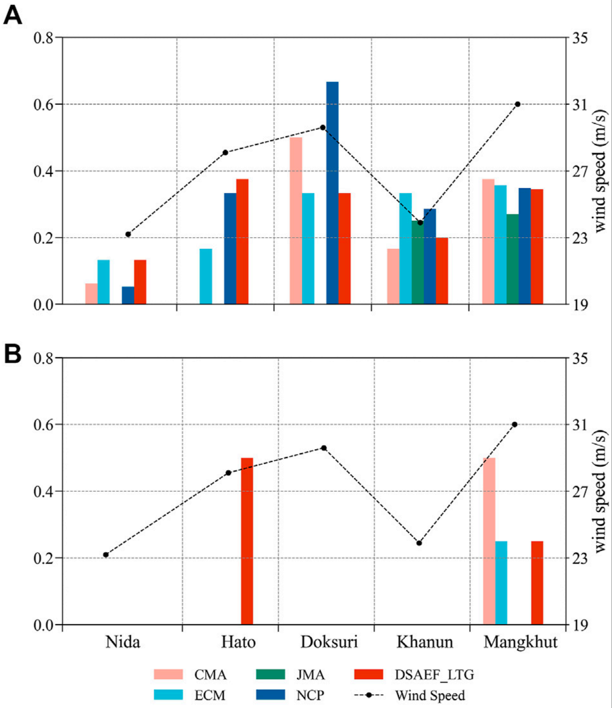

FIGURE 9
Comparison of the TS from different models associated with individual independent samples at the threshold above **(A)** Beaufort Scale 7 and **(B)** Beaufort Scale 10. The wind speed (black dotted line) is the largest value selected from the potential maximum gales of all stations for each TC (unit: m/s).

nor predictions have reached the threshold of Beaufort Scale 10. In addition, the TS10 values of Doksuri were unable to present positive forecast skills, with scores of 0 for all models. For the TS10 of Hato, none of the NWP models could provide satisfactory forecast results, whereas the DSAEF_LTG model still kept a high forecast level, with score as high as 0.5. With regard to the TS10 of Mangkhut, CMA had the highest score of 0.5; the DSAEF_LTG model tied with ECMWF for second place with a score of 0.25; while NCEP and JMA showed no forecasting capability.

4.3 Analysis of representative cases

To obtain a better insight into the forecasting capacity of the DSAEF_LTG model, two typical cases, Hato and Doksuri, were selected for further analysis (Figures 10, 11). They shared the common attribute that the largest value selected from the potential maximum gales of all stations was greater than Beaufort Scale 10, which was apt to trigger gale-related disasters and raise operational concerns. Their difference came in the forecasting performances of the DSAEF_LTG model compared with the NWP models: for Hato, the DSAEF_LTG model was in a superior position; but for Doksuri, it was at a disadvantage. Hence, it is worth trying to unpack the reasons behind this distinction.

For Hato, its gales were observed to be mainly concentrated on the right side of the TC track, including the Pearl River Delta region and south Guangxi, with the center located on the west bank of the Pearl River Estuary (Figure 10A). From the spatial distributions of the gales predicted by different models, the pattern of the DSAEF_LTG model (Figure 10B) was closest to observation among all models, but it missed the gales in Guangxi. Meanwhile, ECWMF (Figure 10D) and NCEP (Figure 10F) produced significant over-prediction with an overly large region, while the windy areas predicted by CMA (Figure 10C) and JMA (Figure 10E) were underestimated. In terms of the magnitude of the central wind speeds, the four NWP models were weaker than observed, but the deviation of the DSAEF_LTG model was negligible. Previous research (Zhang et al., 2018; Qin et al., 2019) suggested that Hato underwent rapid intensification twice in the offshore area after the initial time mentioned in Section 4.1 (i.e., 1200 UTC 22 August 2017), and its convection was asymmetric, both of which made it a harder task for the NWP models to make accurate prediction. Meanwhile, the track of Hato belonged to typical TC category in South China (i.e., westbound after making landfall) with observed gales nearby, contributing to the prediction of the DSAEF_LTG model whose merit is taking full advantage of TC track.

For Doksuri, the number of windy stations was less than for Hato: one station with wind speed exceeding Beaufort Scale 10 and four stations below Beaufort Scale 8, scattered over south Hainan, south Guangdong and south Guangxi (Figure 11A). All the models performed well in their predicted spatial distributions of gales, with their prominent differences manifesting in the predicted magnitude of wind speeds. Specifically, NCEP performed the best (Figure 11F); the DSAEF_LTG model (Figure 11B) and CMA (Figure 11C) were over-prediction; and ECWMF (Figure 11D) as well as JMA (Figure 11E) were underestimated. On the one hand, Doksuri did not make direct landfall in China [i.e., sideswiping TC (Feng et al., 2020)] and was accompanied by weak gales and small numbers of windy stations, thus partly accounting for the limited forecasting ability of the DSAEF_LTG model. On the other hand, according to the best forecast scheme mentioned in Section 4.1, the maximum was adopted to assemble the TC-induced wind fields of two analogous historical TCs, which may have resulted in the over-prediction of the DSAEF_LTG model. These two reasons may have led to the big gap in TS between the DSAEF_LTG model and NCEP, whose TS was ranked first.

From the above analysis of two representative TC cases, we can conclude that the DSAEF_LTG model had advantages over (for Hato) or was equivalent to (for Doksuri) dynamic models in the prediction of gale spatial distributions, and it could successfully capture the center with wind speeds above

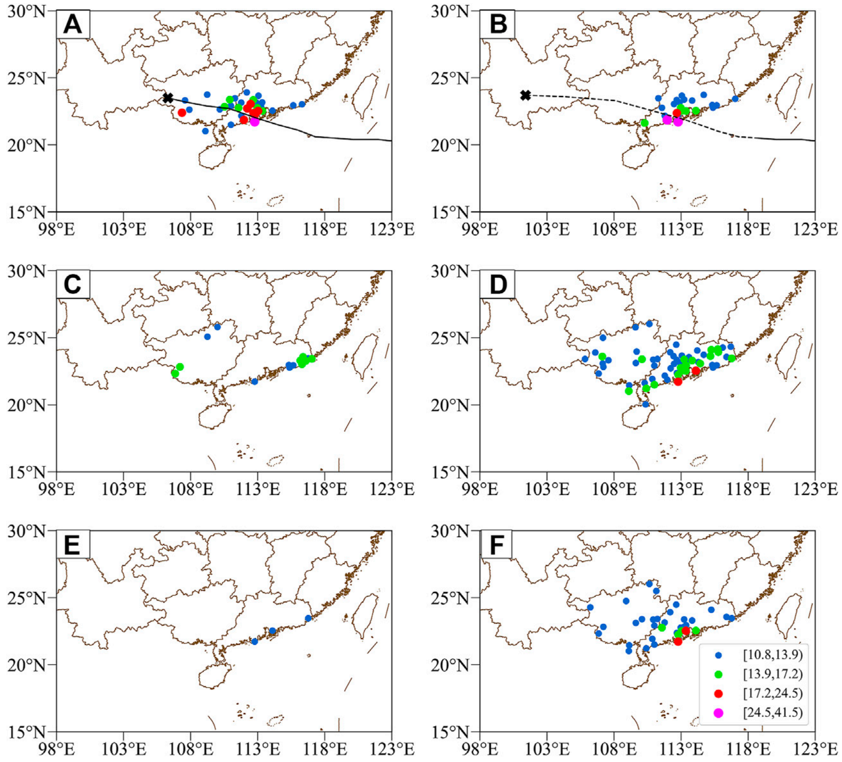

FIGURE 10
Spatial distributions of the potential maximum gale (m/s) associated with Hato according to **(A)** observations, **(B)** the DSAEF_LTG model, **(C)** CMA, **(D)** ECMWF, **(E)** JMA, and **(F)** NCEP. The observed and forecasted tracks are also plotted (black line and black dotted line, respectively). The marker "x" represents the end of the TC track.

Beaufort Scale 10. Nevertheless, the overall wind speed scale of Doksuri forecasted by the DSAEF_LTG model was greater than observed. The status quo is likely to be improved by adding more reasonable ensemble forecast schemes and including more analogous historical TCs.

5 Summary and discussion

In this study, the DSAEF_LTG model was used to conduct an experiment for forecasting the TC-induced potential maximum gale in South China. Our major results can be summarized as follows:

1) As the first forecasting application of the DSAEF_LTG model, encouraging forecasting ability in South China was demonstrated. In this experiment, the best forecast scheme was crucial and can be described as follows: For TC track similarity, the initial time of the target TC was set at 1200 UTC on the day before TC-induced gales occurred on land and the historical TCs were screened in the 20th similarity region. For landfall time similarity, the analogous historical TCs could make landfall at any time of year (i.e., the landfall time was not restricted). For intensity similarity, the historical TCs with the same grade or one grade difference as target TC would be reserved, using the maximum intensity on the first windy day as a reference. After the screening via the above three similarity conditions, the maximum was adopted to assemble the analogous historical TCs in the top two.
2) In general, the DSAEF_LTG model had higher forecasting skills than the NWP models at the critical thresholds of Beaufort Scale 7 and 10, with a total average TS of 0.4273. The TS values also showed that, the stronger the maximum gale (the largest value selected from the potential maximum gales of all stations for each TC), the better the forecasting performance of TS7 for each model. However, this feature was not obvious in TS10. On the basis of the average FAR, MR and BS, the DSAEF_LTG model was prone to false alarms, while the NWP models were prone to missing alarms, especially for an intense scale (≥Beaufort Scale 10). Additionally, the DSAEF_LTG model also had the smallest forecasting error among five models, with the MAE of 2.8486 and the R of 0.499.

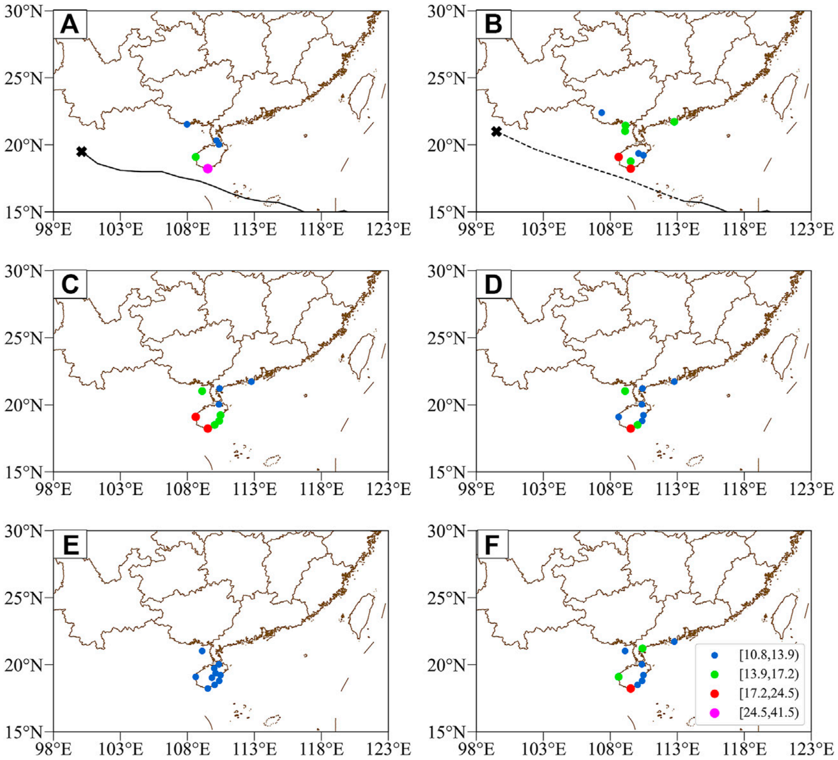

FIGURE 11
Spatial distributions of the potential maximum gale (m/s) associated with Doksuri according to **(A)** observations, **(B)** the DSAEF_LTG model, **(C)** CMA, **(D)** ECMWF, **(E)** JMA, and **(F)** NCEP. The observed and forecasted tracks are also plotted (black line and black dotted line, respectively). The marker "x" represents the end of the TC track.

3) The analysis of two typical cases (Hato and Doksuri) further demonstrated that target TC with typical track and widespread gale (e.g., Hato) makes it easier for the DSAEF_LTG model to make accurate prediction which was superior to those of NWP models, both in the wind field pattern and magnitude of central wind speeds. However, for sideswiping TC with small-scale gales (e.g., Doksuri), the DSAEF_LTG model tends to over-predict and fails to achieve satisfactory forecasting results.

The results mentioned above illustrate that the DSAEF_LTG model is able to provide effective predictions of TC-induced potential maximum gales in South China, one of the regions most frequently affected by typhoons, and it is likely to offer a promising tool for local forecasters and hazard mitigation administrators to make decisions. Meanwhile, the weaknesses of the DSAEF_LTG model were also highlighted in our results, namely it was inclined to over-prediction and short in forecasting the target TC with weak and small-scale gales.

Consequently, further work should concentrate on how to further improve the forecasting performances of the DSAEF_LTG model. Some possible solutions are: 1) more reasonable ensemble forecast schemes to reduce the FAR; 2) constructing the GIV is an important step in the DSAEF_LTG model, so it is necessary to incorporate more physical variables related to TC-induced gales, including TC characteristics (e.g., size, translation speed) and environmental conditions (e.g., subtropical high, vertical wind shear); and 3) historical TC datasets with a longer period of time need to be adopted to identify more analogous historical TCs for the target TC.

Data availability statement

The original contributions presented in the study are included in the article/Supplementary Material, further inquiries can be directed to the corresponding author.

Author contributions

FR designed research. LL conceptualized the analysis and wrote the manuscript. All authors were involved in helpful discussions and contributions to the manuscript.

Funding

This work was supported by Guangdong Province Key Research and Development Project (Grant No. 2019B111101002) and Shenzhen Science and Technology Project (Grant No. KCXFZ2020122173610028).

Conflict of interest

The authors declare that the research was conducted in the absence of any commercial or financial relationships that could be construed as a potential conflict of interest.

Publisher's note

Supplementary material

The Supplementary Material for this article can be found online at: https://www.frontiersin.org/articles/10.3389/feart.2022.987001/full#supplementary-material

References

Carter, G. M., Paul, D. J., and Glahn, H. R. (1989). Statistical forecasts based on the national meteorological center's numerical weather prediction system. *Weather Forecast.* 4 (3), 401–412. doi:10.1175/1520-0434(1989)004<0401:sfbotn>2.0.co;2

Charney, J. G., Halem, M., and Jastrow, R. (1969). Use of incomplete historical data to infer the present state of the atmosphere. *J. Atmos. Sci.* 26 (5), 1160–1163. doi:10.1175/1520-0469(1969)026<1160:uoihdt>2.0.co;2

Chen, H. Y., and Zhang, M. (2008). Practical skill of using satellite cloud pictures in tropical cyclone forecasting. *Meteorological Sci. Technol.* 5 (7), 547–550. (in Chinese). doi:10.19517/j.1671-6345.2008.05.007

Chen, L. S., and Meng, Z. Y. (2001). Researches on tropical cyclones in China in the past decade. *Chin. J. Atmos. Sci.* 3, 420–432. (in Chinese). doi:10.3878/j.issn.1006-9895.2001.03.11

Chen, Y. X. (2021). *Research on the dynamical-statistical-analog ensemble forecast model for landfalling typhoon gale (DSAEF_LTG)*. Chengdu: Chengdu University of Information Technology. in Chinese.

Demaria, M., Knaff, J. A., Brennan, M. J., Brown, D., Knabb, R. D., DeMaria, R. T., et al. (2013). Improvements to the operational tropical cyclone wind speed probability model. *Weather Forecast.* 28 (3), 586–602. doi:10.1175/waf-d-12-00116.1

Dong, Y. (2014). *Research on distribution characteristics and forecast for tropical cyclone gale in Guangxi*. Nanning: Guangxi Teachers Education University. in Chinese.

Feng, T., Ren, F. M., Zhang, D. L., Li, G., Qiu, W., and Yang, H. (2020). Sideswiping tropical cyclones and their associated precipitation over China. *Adv. Atmos. Sci.* 37 (7), 707–717. doi:10.1007/s00376-020-9224-5

He, C. F., Qian, K. B., and Jin, W. (2018). Precision forecasting of typhoon wind speed in WRF model based on IFOA-FSVM. *J. Ningbo Univ. (Nsee)* 31 (6), 20–26. in Chinese. doi:10.3969/j.issn.1001-5132.2018.06.004

Jia, L., Jia, Z., Ren, F., Ding, C., Wang, M., and Feng, T. (2020). Introducing TC intensity into the DSAEF_LTP model and simulating precipitation of super-typhoon *Lekima* (2019). *Q. J. R. Meteorol. Soc.* 146, 3965–3979. doi:10.1002/qj.3882

Kaplan, J., and DeMaria, M. (1995). A simple empirical model for predicting the decay of tropical cyclone winds after landfall. *J. Appl. Meteor.* 34 (11), 2499–2512. doi:10.1175/1520-0450(1995)034<2499:asemfp>2.0.co;2

Knaff, J. A., Sampson, C. R., and Chirokova, G. (2017). A global statistical–dynamical tropical cyclone wind radii forecast scheme. *Weather Forecast.* 32 (2), 629–644. doi:10.1175/waf-d-16-0168.1

Knaff, J. A., Sampson, C. R., DeMaria, M., Marchok, T. P., Gross, J. M., and McAdie, C. J. (2007). Statistical tropical cyclone wind radii prediction using climatology and persistence. *Weather Forecast.* 22 (4), 781–791. doi:10.1175/waf1026.1

Li, Q. L., Xu, P. C., Wang, X. B., Lan, H., Cao, C., Li, G., et al. (2016). An operational statistical scheme for tropical cyclone induced wind gust forecasts. *Weather Forecast.* 31 (6), 1817–1832. doi:10.1175/waf-d-16-0015.1

Li, Y., Liu, Y. B., and Xu, X. F. (2021). Advances and challenges for improving numerical weather prediction models and forecasting using deep learning. *Adv. Meteorological Sci. Technol.* 11 (3), 103–112. in Chinese. doi:10.3969/j.issn.2095-1973.2021.03.012

Lin, Z. P., Zhou, S. W., and Wen, J. C. (2015). Application of ECMWF thin-grid 10m wind fields in "tiantu" heavy wind forecast. *Meteorological, Hydrological Mar. Instrum.* 32 (3), 7–12. in Chinese. doi:10.19441/j.cnki.issn1006-009x.2015.03.002

Lu, Y., Zhu, W. J., and Ren, F. M. (2016). Changes of tropical cyclone high winds and extreme winds during 1980-2014 over China. *Clim. Change Res.* 12 (05), 413–421. in Chinese. doi:10.12006/j.issn.1673-1719.2016.030

Peduzzi, P., Chatenoux, B., Dao, H., De Bono, A., Herold, C., Kossin, J., et al. (2012). Global trends in tropical cyclone risk. *Nat. Clim. Chang.* 2 (4), 289–294. doi:10.1038/nclimate1410

Powell, M. D., and Reinhold, T. A. (2011). *Predicting tropical cyclone destructive potential by integrated kinetic energy according to the Powell/Reinhold scale.* US. US7970543 B2[P].

Qin, L., Wu, Q. S., and Zeng, X. T. (2019). Analysis on cause of rapid intensification of asymmetrical Typhoon Hato (1713) over the offshore of China. *Torrential Rain Disasters* 38 (3), 212–220. in Chinese. doi:10.3969/j.issn.1004-9045.2019.03.003

Ren, F. M., Ding, C., Zhang, D. L., Chen, D., Ren, H. l., and Qiu, W. (2020). A dynamical-statistical-analog ensemble forecast model: Theory and an application to heavy rainfall forecasts of landfalling tropical cyclones. *Mon. Weather Rev.* 148 (4), 1503–1517. doi:10.1175/mwr-d-19-0174.1

Ren, F. M., Qiu, W. Y., and Jiang, X. L. (2018). An objective track similarity index and its preliminary application to predicting precipitation of landfalling tropical cyclones. *Weather Forecast.* 33, 1725–1742. doi:10.1175/waf-d-18-0007.1

Roy, C., and Rita, K. (2012). Tropical cyclone track forecasting techniques — A review. *Atmos. Res.* 9 (12), 40–69. doi:10.1016/j.atmosres.2011.09.012

Sampson, C. R., and Knaff, J. A. (2015). A consensus forecast for tropical cyclone gale wind radii. *Weather Forecast.* 30 (5), 1397–1403. doi:10.1175/waf-d-15-0009.1

Wan, J. H., Chen, W., and Zhang, B. W. (2016). Analysis on flood disaster characteristics and disaster mechanism caused by the super typhoon Rammasun in 2014. *J. Catastrophology* 31 (3), 78–83. in Chinese. doi:10.3969/j.issn.1000-811X.2016.03.013

Wang, S. S., Zhou, H. M., and Zhu, S. P. (2020). Station forecast calibration of daily precipitation using categorized rainfall regression. *Meteorological Sci. Technol.* 48 (3), 422–427. in Chinese. doi:10.19517/j.1671-6345.20190159

Wang, X. F., Xu, X. L., and Yang, X. C. (2017). The NWP models evaluation of landfall processes of the strong typhoon Fitow. *Trans. Atmos. Sci.* 40 (5), 609–618. in Chinese. doi:10.13878/j.cnki.dqkxxb.20170124001

Wilks, D. (2006). Statistical methods in the atmospheric sciences. *Technometrics* 102 (477), 380. doi:10.1198/jasa.2007.s163

Xiang, C. Y., Wu, L. G., and Tian, W. (2016). Applications of MTCSWA data to the characteristic analysis of tropical cyclone structure. *Meteorol. Mon.* 42 (11), 1316–1324. in Chinese. doi:10.7519/j.issn.1000-0526.2016.11.003

Ying, M., Zhang, W., Yu, H., Lu, X., Feng, J., Fan, Y., et al. (2014). An overview of the China Meteorological Administration tropical cyclone database. *J. Atmos. Ocean. Technol.* 31, 287–301. doi:10.1175/jtech-d-12-00119.1

Zhang, J., Shi, D. W., and Li, C. (2018). Analysis on the sudden change and its cause of Typhoon Hato. *Mar. Forecasts* 35 (2), 37–43. in Chinese. doi:10.11737/j.issn.1003-0239.2018.02.005

Zhang, W., Villarini, G., Vecchi, G. A., Murakami, H., and Gudgel, R. (2016). Statistical-dynamical seasonal forecast of Western North Pacific and East Asia landfalling tropical cyclones using the high-resolution GFDL FLOR coupled model. *J. Adv. Model. Earth Syst.* 8 (2), 538–565. doi:10.1002/2015ms000607

Zhi, J. L., and Huang, X. X. (2020). Comparion and cause analysis of high wind processes in NO.1713 typhoon Hato and NO.1822 typhoon Mangkhut. *Mid-low Latit. Mt. Meteorol.* 44 (5), 54–60. in Chinese. doi:10.3969/j.issn.1003-6598.2020.05.008

frontiers | Frontiers in Earth Science

TYPE Original Research
PUBLISHED 08 November 2022
DOI 10.3389/feart.2022.1038351

OPEN ACCESS

EDITED BY
Eric Hendricks,
National Center for Atmospheric Research (UCAR), United States

REVIEWED BY
Zifeng Yu,
China Meteorological Administration, China
Binod Sreenivasan,
Indian Institute of Science (IISc), India

*CORRESPONDENCE
Richard K. Taft,
rick.taft@colostate.edu

SPECIALTY SECTION
This article was submitted to Atmospheric Science, a section of the journal Frontiers in Earth Science

RECEIVED 06 September 2022
ACCEPTED 11 October 2022
PUBLISHED 08 November 2022

CITATION
Schubert WH and Taft RK (2022), Tropical cyclone rapid intensification and the excitation of inertia-gravity waves on the edges of an evolving potential vorticity structure.
Front. Earth Sci. 10:1038351.
doi: 10.3389/feart.2022.1038351

Tropical cyclone rapid intensification and the excitation of inertia-gravity waves on the edges of an evolving potential vorticity structure

Wayne H. Schubert and Richard K. Taft*

Department of Atmospheric Science, Colorado State University, Fort Collins, CO, United States

The problem of tropical cyclone rapid intensification is reduced to a potential vorticity (PV) equation and a second order, inhomogeneous, partial differential equation for the azimuthal wind. The latter equation has the form of a Klein-Gordon equation, the right-hand side of which involves the radial derivative of the evolving PV field. When the PV field evolves rapidly, inertia-gravity waves are excited at the edges of the evolving PV structure. In contrast, when the PV field evolves slowly, the second order time derivative term in the Klein-Gordon equation is negligible, inertia-gravity waves are not excited, and the equation reduces to an invertibility principle for the PV. The above concepts are presented in the context of an axisymmetric shallow water model, in both its linear and nonlinear forms. The nonlinear results show a remarkable sensitivity of vortex intensification to the percentage of mass that is diabatically removed from the region inside a given absolute angular momentum surface.

KEYWORDS

tropical cyclone, rapid intensification, inertia-gravity waves, potential vorticity, axisymmetric shallow water model, Klein-Gordon equation

1 Introduction

While modern numerical weather prediction has produced significant skill in forecasting tropical cyclone tracks, the forecasting of rapid intensification remains an important challenge (DeMaria et al., 2014). The status of present observational, theoretical, and numerical modeling efforts to improve intensity forecasting can be found in the special collection of thirty articles that have appeared recently in five of the journals published by the American Meteorological Society (see the Doyle and Ferek, 2017, reference for the website that describes this special collection associated with the Tropical Cyclone Intensity Experiment). A concise and excellent review of much of this previous work can be found in Martinez et al. (2019). The present paper explores some of the theoretical aspects of the rapid intensification problem. In particular, this paper discusses how the problem of tropical cyclone intensification can be reduced to the solution of a coupled pair of partial differential equations—a first order equation for the time evolution of the potential vorticity (PV) field, and a second order, Klein-Gordon equation for the evolution of the rotational wind field. In many interesting cases the potential vorticity equation can be solved analytically and the result used as a forcing term in the Klein-Gordon equation. Examples of this approach, in the case when the Klein-Gordon equation reduces to an elliptic invertibility principle, are given in Schubert and Alworth (1987) and Möller and Smith (1994).

The forcing term in the Klein-Gordon equation can be especially large at the edges of an evolving PV structure. When this forcing effect varies slowly in time, the second order time derivative term in the Klein-Gordon equation can be neglected, which converts this hyperbolic equation into an elliptic, PV invertibility principle. When the forcing does not vary slowly in time, the second order time derivative term must be retained and the Klein-Gordon equation maintains its hyperbolic character, thereby describing both the balanced flow and the generation and propagation of inertia-gravity waves. These basic concepts are presented in the simple context of the axisymmetric shallow water model (Section 2), where curvature effects and gradient balance come into play. In the linear case (Section 3), the primary results are the PV solution, given in Eq. 8, and the linear Klein-Gordon equation for v (r, t), given in the middle entry of Eq. 11, or the linear invertibility principle for v_b (r, t), given by the middle entry of Eq. 12. These linear results are generalized to the nonlinear case through the use of a Lagrangian description of the flow (Section 4). In the nonlinear case, the primary results are the PV solution, given in Eq. 21, and the nonlinear Klein-Gordon equation for V (R, τ), given by Eq. 24, or the nonlinear invertibility principle for $V_b(R, \tau)$, given by Eq. 26. Solutions of the nonlinear problem illustrate how rapid intensification can occur when a large percentage of the original lower tropospheric mass inside a given absolute angular momentum surface is diabatically removed *via* eyewall convection.

2 Shallow water model

Consider the inviscid, axisymmetric, nonlinear shallow water equations

$$\frac{Du}{Dt} - \left(f + \frac{v}{r}\right)v + g\frac{\partial h}{\partial r} = 0,$$

$$\frac{Dv}{Dt} + \left(f + \frac{v}{r}\right)u = 0, \qquad \frac{Dh}{Dt} + h\frac{\partial (ru)}{r\,\partial r} = -hS, \tag{1}$$

where u (r, t) is the radial velocity component, v (r, t) the azimuthal velocity component, h (r, t) the fluid depth, g the acceleration of gravity, f the constant Coriolis parameter, $(D/Dt) = (\partial/\partial t) + u\,(\partial/\partial r)$ the material derivative, and S (r, t) the specified mass sink. The potential vorticity principle associated with Eq. 1 is

$$\frac{DP}{Dt} = PS \qquad \text{where} \qquad P = \frac{(f + \zeta)\bar{h}}{h} \qquad \text{and} \qquad \zeta = \frac{\partial (rv)}{r\,\partial r}, \tag{2}$$

with the constant $\bar{h}$ denoting the far-field fluid depth. Our goal in Section 4 is to solve Eq. 1 as a forced, nonlinear, transient, gradient adjustment problem. The approach is to solve analytically for P and then use this solution as a forcing in the second order partial differential equation for v. However, the derivation of a single nonlinear partial differential equation for v is not a straightforward task. For example, one approach might be as follows. First, take $(\partial/\partial r)$ of $hP = \bar{h}(f + \zeta)$, and use the result to eliminate $(\partial h/\partial r)$ from the radial momentum equation. Then, write the azimuthal momentum equation in an angular momentum form. The momentum equations then take the form

$$\frac{Du}{Dt} - \left(f + \frac{v}{r}\right)v + \frac{g\bar{h}}{P}\frac{\partial}{\partial r}\left(\frac{\partial (rv)}{r\,\partial r}\right)$$
$$= \frac{gh}{P}\frac{\partial P}{\partial r} \qquad \text{and} \qquad \frac{1}{r}\frac{D(rv)}{Dt} + fu = 0, \tag{3}$$

which we can regard as a coupled pair of equations for u (r, t) and v (r, t) if P (r, t) is regarded as known from the solution of the PV principle (Eq. 2). Taking D/Dt of the second entry in Eq. 3 and using the result to eliminate Du/Dt from the first entry, we obtain

$$\begin{aligned} &\frac{\partial}{\partial r}\left(\frac{\partial (rv)}{r\,\partial r}\right) - \frac{\hat{f}^2}{gh}v - \frac{P}{fg\bar{h}}\frac{D}{Dt}\left(\frac{1}{r}\frac{D(rv)}{Dt}\right) = \frac{h}{\bar{h}}\frac{\partial P}{\partial r}, \\ &\text{where} \qquad \frac{\hat{f}^2}{gh} = \frac{1}{gh}\left(f + \frac{v}{r}\right)\left(f + \frac{\partial (rv)}{r\partial r}\right) = \frac{1}{g\bar{h}}\left(f + \frac{v}{r}\right)P. \end{aligned} \tag{4}$$

It is tempting to regard Eq. 4 as a nonlinear Klein-Gordon equation for the single variable v (r, t), with a time dependent forcing term that is proportional to the radial derivative of the potential vorticity. However, it is important to note that the variables u (r, t) and h (r, t) have not been completely eliminated from Eq. 4, with u (r, t) appearing in the D/Dt operator. In Section 4 we discuss the transformation of Eqs 2–4 to a Lagrangian coordinate, which simplifies the material derivative D/Dt to a local derivative. This not only simplifies the (D/Dt)-terms in Eqs 2–4, but also allows for time integration of the potential vorticity equation (Eq. 2), thereby making the forcing term in Eq. 4 a known function. If the forcing term varies slowly enough in time, the term in Eq. 4 involving D/Dt becomes negligible, so that the diagnostic equation for the gradient balanced wind v_b (r, t) is

$$\begin{aligned} &\frac{\partial}{\partial r}\left(\frac{\partial (rv_b)}{r\,\partial r}\right) - \frac{\hat{f}_b^2}{gh}v_b = \frac{h}{\bar{h}}\frac{\partial P}{\partial r}, \\ &\text{where} \qquad \frac{\hat{f}_b^2}{gh} = \frac{1}{gh}\left(f + \frac{v_b}{r}\right)\left(f + \frac{\partial (rv_b)}{r\partial r}\right) \end{aligned} \tag{5}$$

which is the shallow water version of the nonlinear invertibility relation discussed by Hoskins et al. (1985). However, before discussing the nonlinear problem, we consider in Section 3 the linearized version of the shallow water dynamics (Eq. 1).

Although it is limited to weak vortices, the linear analysis of Section 3 provides a useful guide to the nonlinear analysis of Section 4.

Although the analysis presented here is in the context of the shallow water equations, a more general interpretation is that these equations approximately describe the dynamics of an atmospheric layer confined between two isentropic surfaces. The analogy is as follows. When there is a mass sink in the shallow water continuity equation, the two isentropic surfaces bounding the layer should be regarded as lower tropospheric surfaces (e.g., with the layer defined by $320 \leq \theta \leq 325$K). In contrast, when there is a mass source, the two isentropic surfaces should be regarded as upper tropospheric surfaces (e.g., with the layer defined by $355 \leq \theta \leq 360$K). This interpretation is justified by noting that the shallow water continuity equation in the independent variables (r, t) and the continuity equation for a stratified hydrostatic model in the independent variables (r, θ, t) can respectively be written as

$$\frac{\partial h}{\partial t} + \frac{\partial (ruh)}{r\partial r} = -hS \qquad \text{and} \qquad \frac{\partial \sigma}{\partial t} + \frac{\partial (ru\sigma)}{r\partial r} = -\sigma\left(\frac{\partial\left(\sigma\dot{\theta}\right)}{\sigma\partial\theta}\right), \tag{6}$$

where $\sigma = -(1/g)\,(\partial p/\partial\theta)$ is the pseudodensity, p is the pressure, θ is the potential temperature, and $\sigma\dot{\theta}$ is the diabatic mass flux. Because of the close correspondence of the two equations in Eq. 6, we can make the following analogies: $h \Leftrightarrow \sigma$ and $S \Leftrightarrow [\partial(\sigma\dot{\theta})/\sigma\partial\theta]$. Note that in regions where the fractional variation of σ with respect to θ is much less than the fractional variation of $\dot{\theta}$ with respect to θ, this analogy simplifies to $S \Leftrightarrow (\partial\dot{\theta}/\partial\theta)$. In the lower tropospheric core region of a tropical cyclone, $[\partial(\sigma\dot{\theta})/\sigma\partial\theta] > 0$, so there should be an analogous mass sink in the shallow water equations to simulate a lower tropospheric layer. In the upper tropospheric core region of a tropical cyclone, $[\partial(\sigma\dot{\theta})/\sigma\partial\theta] < 0$, so there should be an analogous mass source in the shallow water equations to simulate an upper tropospheric layer. In Section 4 and Supplementary Appendix C we develop an alternative analogy based on potential vorticity dynamics rather than simply the mass conservation principles in Eq. 6. Although these analogies help interpret the shallow water model results in terms of the dynamics of a continuously stratified fluid, the analysis of the detailed vertical structure of tropical cyclones requires a complete θ-coordinate model, in which case the Klein-Gordon equations and the invertibility principles discussed in Section 3 and Section 4 would include terms that involve second order partial derivatives in θ.

3 Linear dynamics

As a guide to the nonlinear analysis of Section 4, let us first linearize the system Eq. 1 about a state of rest with constant mean depth $\bar{h}$. The linear equations are

$$\frac{\partial u}{\partial t} - fv + g\frac{\partial h'}{\partial r} = 0, \qquad \frac{\partial v}{\partial t} + fu = 0, \qquad \frac{\partial h'}{\partial t} + \bar{h}\frac{\partial (ru)}{r\,\partial r} = -\bar{h}S, \tag{7}$$

where $h'(r,t) = h(r,t) - \bar{h}$ is the deviation depth. As initial conditions for Eq. 7 we assume there is no flow and no anomaly in the fluid depth, i.e., $u\,(r, 0) = 0$, $v\,(r, 0) = 0$, and $h'(r, 0) = 0$. With these assumptions, any flow that develops is due to the mass sink $S\,(r, t)$. The equation for the potential vorticity anomaly $P'(r, t)$, derived from the second and third entries in Eq. 7, and its solution are given by

$$\frac{\partial P'}{\partial t} = fS \qquad \text{where} \qquad P' = P - f = \frac{\partial (rv)}{r\,\partial r} - \frac{f}{\bar{h}}h' \quad \Rightarrow \quad P'(r,t) = f\int_0^t S(r,t')\,dt'. \tag{8}$$

In order to better understand the stationary and oscillatory solutions of the unforced version of Eq. 7, assume the solutions are separable in r and t, with the time dependent part given by $e^{i\omega t}$, where ω is the frequency of oscillation. It can then be shown that the radially dependent part of h' satisfies an order zero Bessel equation and the radially dependent parts of u and v satisfy order one Bessel equations (for further discussion, see Schubert et al., 1980). In other words, we can simply begin with the assumed separable forms $u(r,t) = c\hat{u}J_1(kr)e^{i\omega t}$, $v(r,t) = c\hat{v}J_1(kr)e^{i\omega t}$, and $h'(r,t) = (c^2/g)\hat{h}J_0(kr)e^{i\omega t}$, where $\hat{u}, \hat{v}, \hat{h}$ are dimensionless complex constants, k is the radial wavenumber, J_0 and J_1 are Bessel functions of order zero and order one respectively, and $c = (g\bar{h})^{1/2}$ is the pure gravity wave speed. Substituting these assumed solutions into the unforced version of Eq. 7 and using the Bessel function derivative relations $dJ_0\,(kr)/dr = -kJ_1\,(kr)$ and $d\,[rJ_1\,(kr)]/rdr = kJ_0\,(kr)$, we obtain

$$\begin{pmatrix} i\omega & -f & -ck \\ f & i\omega & 0 \\ ck & 0 & i\omega \end{pmatrix}\begin{pmatrix} \hat{u} \\ \hat{v} \\ \hat{h} \end{pmatrix} = 0 \Rightarrow \quad \omega\left(\omega^2 - f^2 - c^2k^2\right) = 0 \quad \Rightarrow \quad \omega = \begin{cases} \omega_0 = 0 \\ \omega_1 = \left(f^2 + c^2k^2\right)^{1/2} \\ \omega_2 = -\left(f^2 + c^2k^2\right)^{1/2}. \end{cases} \tag{9}$$

The three eigenvectors corresponding to the three eigenvalues ω_0, ω_1, ω_2 are

$$\begin{pmatrix} \hat{u} \\ \hat{v} \\ \hat{h} \end{pmatrix}_0 = A\begin{pmatrix} 0 \\ ck \\ -f \end{pmatrix}, \quad \begin{pmatrix} \hat{u} \\ \hat{v} \\ \hat{h} \end{pmatrix}_1 = \frac{A}{\sqrt{2}}\begin{pmatrix} -i\omega_1 \\ f \\ ck \end{pmatrix}, \quad \begin{pmatrix} \hat{u} \\ \hat{v} \\ \hat{h} \end{pmatrix}_2 = \frac{A}{\sqrt{2}}\begin{pmatrix} -i\omega_2 \\ f \\ ck \end{pmatrix}, \tag{10}$$

where $A = (f^2 + c^2k^2)^{-1/2}$ is the normalization constant. Using the assumed form of solution and the derivative relation for $rJ_1\,(kr)$, the potential vorticity anomaly can be written as $P' = (ck\hat{v} - f\hat{h})J_0(kr)e^{i\omega t}$. For the eigenvector corresponding to the eigenvalue ω_0, the potential vorticity anomaly is $P' = (f^2 + c^2k^2)^{1/2}J_0(kr)$. In contrast, since the factor $ck\hat{v} -$

$f\hat{h}$ vanishes for both the eigenvector corresponding to the eigenvalue ω_1 and the eigenvector corresponding to the eigenvalue ω_2, both of these inertia-gravity modes have $P' = 0$. In other words, although the inertia-gravity waves contribute to the $u(r,t)$, $v(r,t)$, and $h'(r,t)$ fields, these waves are invisible in the $P'(r,\ t)$ field. The remainder of this section is devoted to understanding how inertia-gravity waves can be excited on the edge of a rapidly intensifying PV disk or the edges of a rapidly intensifying PV annulus.

Single, independent, second order partial differential equations for $u\ (r,\ t)$, $v\ (r,\ t)$, and $h'(r,\ t)$ can be found. The easiest to derive is the equation for the divergent component $u\ (r,\ t)$, which can be found by taking $\partial/\partial t$ of the radial momentum equation and then using the other two equations to eliminate $\partial v/\partial t$ and $\partial h'/\partial t$. Then, including boundary and initial conditions, the complete linear problem for the radial flow is given in the first entry of Eq. 11. Since the rotational wind component $v\ (r,\ t)$ plays such a central role in tropical cyclone dynamics, the single partial differential equation for $v\ (r,\ t)$ is of particular interest. This equation can be obtained by taking $(\partial/\partial t)$ of the v-equation in Eq. 7, then using the u-equation to eliminate $(\partial u/\partial t)$, and finally using the second entry in Eq. 8 to eliminate h'. Then, including boundary and initial conditions, the complete linear problem for the azimuthal flow is given in the second entry of Eq. 11. Similarly, and again making use of the second entry in Eq. 8, we can derive the single partial differential equation for $h'(r,\ t)$, which is given in the third entry of Eq. 11. To summarize, the linear primitive equation problems for $u\ (r,\ t)$, $v\ (r,\ t)$, and $h'(r,\ t)$ as independent equations are as follows:

$$\underline{\textbf{Linear Klein – Gordon Equations for } u(r,t),\ v(r,t),\ h'(r,t)}$$

$$\begin{gathered}
\frac{\partial}{\partial r}\left(\frac{\partial (ru)}{r\,\partial r}\right) - \frac{1}{c^2}\left(f^2 + \frac{\partial^2}{\partial t^2}\right)u = -\frac{\partial S}{\partial r} \\
\text{with } \left\{\begin{array}{ll} \text{BCs}: & u = 0 \text{ at } r = 0,\ \ ru \to 0 \text{ as } r \to \infty \\ \text{ICs}: & u = 0 \text{ and } u_t = 0 \text{ at } t = 0 \end{array}\right\}, \\
\frac{\partial}{\partial r}\left(\frac{\partial (rv)}{r\,\partial r}\right) - \frac{1}{c^2}\left(f^2 + \frac{\partial^2}{\partial t^2}\right)v = \frac{\partial P'}{\partial r} \\
\text{with } \left\{\begin{array}{ll} \text{BCs}: & v = 0 \text{ at } r = 0,\ \ rv \to 0 \text{ as } r \to \infty \\ \text{ICs}: & v = 0 \text{ and } v_t = 0 \text{ at } t = 0 \end{array}\right\}, \\
\frac{\partial}{r\partial r}\left(r\frac{\partial h'}{\partial r}\right) - \frac{1}{c^2}\left(f^2 + \frac{\partial^2}{\partial t^2}\right)h' = \frac{f}{g}P' + \frac{1}{g}\frac{\partial S}{\partial t} \\
\text{with } \left\{\begin{array}{ll} \text{BCs}: & \dfrac{\partial h'}{\partial r} = 0 \text{ at } r = 0,\ \ rh' \to 0 \text{ as } r \to \infty \\ \text{ICs}: & h' = 0 \text{ and } h'_t = -\bar{h}S \text{ at } t = 0 \end{array}\right\}.
\end{gathered} \tag{11}$$

Equations of the type Eq. 11 are often referred to as linear, inhomogeneous, Klein-Gordon equations (Whitham, 1974), or, in the context of electromagnetic theory, as equations of telegraphy (see Cahn Jr, 1945, and sections 4.10 and 5.6 of Copson, 1975). See Supplementary Appendix A for historical notes on the Klein-Gordon equation. The initial conditions listed in Eq. 11 guarantee that the evolving flow results entirely from the forcing $S\ (r,\ t)$. Note that the three equations in Eq. 11 contain time-dependent inhomogeneities that depend on the forcing. For the idealized forcing given below in the first entry of Eq. 13, $P'(r,t)$ grows as shown in the second entry of Eq. 13, so that $|\partial P'/\partial r|$ at the PV edge increases with time and inertia-gravity waves can be excited there. Thus, more generally, the inner and outer edges of a PV annulus can be regions for the generation of inertia-gravity waves. Since the three Klein-Gordon equations in Eq. 11 are linear, they can be solved by transform methods, e.g., Laplace transforms in time or Hankel transforms in radius. The Hankel transform solution of the Klein-Gordon equation for $v\ (r,\ t)$ is discussed in Supplementary Appendix B.

When the forcing is slow enough, the pressure field and the azimuthal wind field remain close to a state of balance, so that the radial wind equation could be discarded and replaced by $v_b = (g/f)(\partial h'_b/\partial r)$. This is equivalent to saying that the $(\partial^2/\partial t^2)$ terms in Eq. 11 all become negligible. Also, when the forcing is slow enough, the time derivative of the forcing becomes small and can be neglected. Thus, in this slow forcing case, each of the equations in Eq. 11 simplifies to a diagnostic equation, with the first equation in Eq. 11 reducing to a diagnostic equation for the slowly evolving divergent flow $u_b\ (r,\ t)$, the second equation in Eq. 11 reducing to an invertibility principle for the balanced rotational flow $v_b\ (r,\ t)$, and the third equation in Eq. 11 reducing to an invertibility principle for the balanced mass field $h'_b(r,t)$. The only initial condition required is on $P'(r,\ t)$, so that the hyperbolic problems in Eq. 11 reduce to

$$\underline{\textbf{Linear Balanced Problems for } u_b(r,t),\ v_b(r,t),\ h'_b(r,t)}$$

$$\begin{array}{ll}
\dfrac{\partial}{\partial r}\left(\dfrac{\partial (ru_b)}{r\,\partial r}\right) - \mu^2 u_b = -\dfrac{\partial S}{\partial r} & \text{with BCs}: \ u_b = 0 \text{ at } r = 0,\ \ ru_b \to 0 \text{ as } r \to \infty, \\
\dfrac{\partial}{\partial r}\left(\dfrac{\partial (rv_b)}{r\,\partial r}\right) - \mu^2 v_b = \dfrac{\partial P'}{\partial r} & \text{with BCs}: \ v_b = 0 \text{ at } r = 0,\ \ rv_b \to 0 \text{ as } r \to \infty, \\
\dfrac{\partial}{r\partial r}\left(r\dfrac{\partial h'_b}{\partial r}\right) - \mu^2 h'_b = \dfrac{f}{g}P' & \text{with BCs}: \ \dfrac{\partial h'_b}{\partial r} = 0 \text{ at } r = 0,\ \ rh'_b \to 0 \text{ as } r \to \infty,
\end{array} \tag{12}$$

where $\mu = f/c$ is the inverse of the Rossby length.

In order to provide examples of the solutions of the linear balanced flow problems (Eq. 12), we now assume that the mass sink $S\ (r,\ t)$ vanishes for $r > r_0$ and is horizontally uniform for $r \le r_0$, where r_0 is a specified constant. The time dependence of the mass sink is assumed to be $(t/t_s^2)\,e^{-t/t_s}$, where the specified constant t_s is the time at which the mass sink is a maximum. Small values of t_s correspond to rapid forcing and large values of t_s to slow forcing, but the total forcing is independent of t_s since $\int_0^\infty (t/t_s^2)e^{-t/t_s}dt = 1$. This forcing $S\ (r,\ t)$ and the result of using it in Eq. 8 are given by

$$\begin{aligned}
S(r,t) &= \frac{\mathcal{V}}{\pi r_0^2 \bar{h}} \begin{cases} (t/t_s^2)\,e^{-t/t_s} & 0 \le r \le r_0 \\ 0 & r_0 < r < \infty \end{cases} \\
\Rightarrow \quad P'(r,t) &= \frac{f\mathcal{V}}{\pi r_0^2 \bar{h}} \begin{cases} 1 - (1 + t/t_s)\,e^{-t/t_s} & 0 \le r \le r_0 \\ 0 & r_0 < r < \infty, \end{cases}
\end{aligned} \tag{13}$$

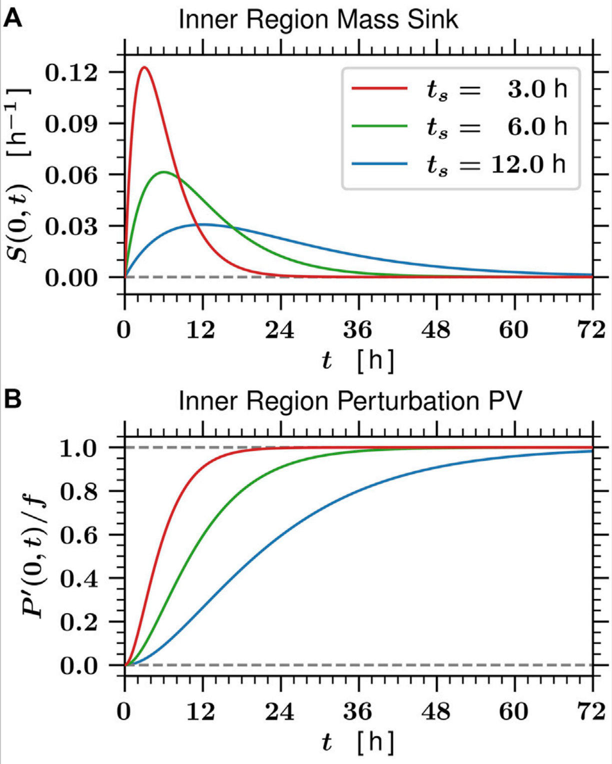

FIGURE 1
Panel **(A)** shows the time dependence of the mass sink S (r, t) for $r \leq r_0$, as given by the first entry in Eq. 13, with $\mathcal{V} = \pi r_0^2 \bar{h}$, for the three choices t_s =3,6,12 h, where the specified constant t_s is the time at which the mass sink is a maximum. Since the areas under the three curves are identical, the total mass removed by the mass sink is independent of t_s. Panel **(B)** shows the corresponding time dependence of $P'(r, t)/f$ for $r \leq r_0$, as given by the second entry in Eq.13, again for the three choices t_s =3,6,12 h. Although the rate of increase of $P'(r, t)$ depends on t_s, the ultimate value of the $P'(r, t)$ is independent of t_s, with $P'(r, t) \to f$ as $t \to \infty$ for $r \leq r_0$.

where $\mathcal{V}$ is a specified constant. Thus, the P' field is a disk of fixed radius r_0, with the value of P' in its interior increasing in time. The ultimate value of P' in the disk is independent of the specified constant t_s since $P'(r,t) \to f\,(\mathcal{V}/\pi r_0^2 \bar{h})$ as $t \to \infty$ for $r \leq r_0$. With this particular forcing S (r, t), integration of the linearized continuity equation over all r and all t yields $2\pi \int_0^\infty [\bar{h} - h(r,\infty)] r\, dr = \mathcal{V}$, so the constant $\mathcal{V}$ can be interpreted as the total volume of fluid removed by the mass sink over its life cycle. We now assume that $\mathcal{V} = \pi r_0^2 \bar{h}$, i.e., the mass sink removes all the fluid initially inside $r = r_0$. Because the linear dynamics have the limitation that $|P'| < f$, this value of $\mathcal{V}$ is essentially the maximum allowable value, since, according to the second entry in Eq. 13, it allows the magnitude of the growing PV jump at $r = r_0$ to maximize at the value f. The time dependence of the mass sink S (r, t) for $r \leq r_0$ is shown in Figure 1A for the three choices $t_s = 3, 6, 12$ h. The time dependence of $P'(r, t)/f$ for $r \leq r_0$, as given by the second entry in Eq. 13, is shown in Figure 1B. Thus, without restating the boundary conditions, the linear balanced problems (Eq. 12) with this forcing (Eq. 13) take the forms

Linear Balanced Problems for the Specified Forcing(13)

$$r^2\frac{\partial^2 u_b}{\partial r^2} + r\frac{\partial u_b}{\partial r} - (\mu^2 r^2 + 1)u_b = 0 \quad \text{for } r \neq r_0$$

$$\text{with} \quad [u_b]_{r_0-}^{r_0+} = 0 \quad \text{and} \quad \left[\frac{\partial(r u_b)}{r\partial r}\right]_{r_0-}^{r_0+} = (t/t_s^2)\, e^{-t/t_s},$$

$$r^2\frac{\partial^2 v_b}{\partial r^2} + r\frac{\partial v_b}{\partial r} - (\mu^2 r^2 + 1)v_b = 0 \quad \text{for } r \neq r_0$$

$$\text{with} \quad [v_b]_{r_0-}^{r_0+} = 0 \quad \text{and} \quad \left[\frac{\partial(r v_b)}{r\partial r}\right]_{r_0-}^{r_0+} = -f\left[1 - (1 + t/t_s)\, e^{-t/t_s}\right],$$

$$r^2\frac{\partial^2 h_b'}{\partial r^2} + r\frac{\partial h_b'}{\partial r} - \mu^2 r^2 h_b' = \frac{f^2 r^2}{g}\begin{cases} 1 - (1 + t/t_s)\, e^{-t/t_s} & \text{if } 0 \leq r < r_0 \\ 0 & \text{if } r_0 < r < \infty, \end{cases}$$

$$\text{with} \quad [h_b']_{r_0-}^{r_0+} = 0 \quad \text{and} \quad \left[\frac{\partial h_b'}{\partial r}\right]_{r_0-}^{r_0+} = 0. \tag{14}$$

Note that the relations Eq. 13 for S (r, t) and $P'(r, t)$ result in Dirac delta functions on the right-hand sides of the u_b and v_b equations in Eq. 12. In Eq. 14, these become jump conditions on the radial derivatives of ru_b and rv_b. The equations governing u_b (r, t) and v_b (r, t) for $r \neq r_0$ are homogeneous modified Bessel equations of order one, while the equation governing $h_b'(r,t)$ is an inhomogeneous modified Bessel equation of order zero. This difference in orders arises from the difference in the radial derivative operators in Eq. 12. The jump conditions on the radial derivatives of ru_b and rv_b can be derived *via* integration of the first two equations in Eq. 12 over a narrow radial interval surrounding $r = r_0$.

As can be checked by direct substitution, the solutions of Eq. 14, along with the associated formula for the relative vorticity, are

Solutions of the Linear Balanced Problems(14)

$$u_b(r,t) = -r_0\,(t/t_s^2)\, e^{-t/t_s} \begin{cases} I_1(\mu r)\, K_1(\mu r_0) & \text{if } 0 \leq r \leq r_0 \\ I_1(\mu r_0)\, K_1(\mu r) & \text{if } r_0 \leq r < \infty, \end{cases}$$

$$v_b(r,t) = r_0 f\left[1 - (1 + t/t_s)e^{-t/t_s}\right] \begin{cases} I_1(\mu r)\, K_1(\mu r_0) & \text{if } 0 \leq r \leq r_0 \\ I_1(\mu r_0)\, K_1(\mu r) & \text{if } r_0 \leq r < \infty, \end{cases}$$

$$h_b'(r,t) = -\bar{h}\left[1 - (1 + t/t_s)e^{-t/t_s}\right] \begin{cases} 1 - \mu r_0\, I_0(\mu r)\, K_1(\mu r_0) & \text{if } 0 \leq r \leq r_0 \\ \mu r_0\, I_1(\mu r_0)\, K_0(\mu r) & \text{if } r_0 \leq r < \infty, \end{cases}$$

$$\zeta_b(r,t) = f\left[1 - (1 + t/t_s)e^{-t/t_s}\right] \begin{cases} \mu r_0\, I_0(\mu r)\, K_1(\mu r_0) & \text{if } 0 \leq r \leq r_0 \\ -\mu r_0\, I_1(\mu r_0)\, K_0(\mu r) & \text{if } r_0 < r < \infty, \end{cases} \tag{15}$$

where I_0 and K_0 are the zero order modified Bessel functions, and I_1 and K_1 are the first order modified Bessel functions. All four of the solution fields in Eq. 15 are continuous across $r = r_0$ except ζ_b (r, t). The fact that the solutions u_b (r, t) and v_b (r, t) given in Eq. 15 satisfy the jump conditions can be checked by using the derivative relations $d\,[rI_1\,(\mu r)]/rdr = \mu I_0\,(\mu r)$ and $d\,[rK_1\,(\mu r)]/rdr = -\mu K_0\,(\mu r)$, and the Wronskian $I_0\,(\mu r_0)K_1\,(\mu r_0) + K_0\,(\mu r_0)I_1\,(\mu r_0) = 1/(\mu r_0)$. Using this Wronskian, it is easily seen that the jump in ζ_b across $r = r_0$ is the same as the jump in P'. The maximum inflow occurs at $r = r_0$ when $t = t_s$, while the maximum azimuthal flow occurs at $r = r_0$ as $t \to \infty$

TABLE 1 Parameters used for the linear balanced and linear primitive equation solutions.

Specified Constants	Computed Quantities
$r_0 = 200$ km	$r_0 f = 10$ m s^{-1}
$f = 5 \times 10^{-5}$ s^{-1}	$c = (g\bar{h})^{1/2} = 50$ m s^{-1}
$g = 9.8$ m s^{-1}	$\mu^{-1} = (g\bar{h})^{1/2}/f = 1000$ km
$\bar{h} = 255.1$ m	$\mu r_0 = 0.2$
	$I_1\,(\mu r_0)K_1\,(\mu r_0) = 0.47999$

and the minimum fluid depth anomaly occurs at $r = 0$ as $t \to \infty$.

We now examine actual solutions of the linear balanced model and the linear primitive equation model, using the parameters specified in Table 1 and the three forcing cases shown in Figure 1. The solutions of the linear primitive equation model (Eq. 7) are obtained numerically using a second-order, centered finite differencing scheme radially, a fourth-order Runge-Kutta scheme temporally, an outer radial boundary set at $r = 5000$ km, a 100 m radial resolution, and a 1 s temporal resolution. Select properties of the linear balanced solutions, specifically the values of $u_b\,(r_0, t_s)$, $v_b\,(r_0, \infty)$, and $h_b'(0, \infty)$, are given in Table 2. For the rapid forcing case $t_s = 3$ h, the linear balanced solutions $u_b(r,t)$, $v_b(r,t)$, $h_b'(r,t)$ and the linear primitive equation solutions $u\,(r, t)$, $v\,(r, t)$, $h'(r, t)$ are respectively plotted in the left and right columns of Figure 2. Similarly, Figure 3 shows linear balanced (left column) and linear primitive equation (right column) results for parameter settings identical to those in Figure 2, except that the time scale t_s has been increased from 3 h to 6 h. Note from Figures 2, 3 that the differences between the balanced and primitive equation results become smaller as the forcing time scale t_s increases from 3 h to 6 h. In fact, we have chosen not to show the $t_s = 12$ h case because the balanced solutions and the primitive equation solutions are so similar for this case. To better understand the nature of the inertia-gravity wave motion excited in the primitive equation model, Figure 4 shows the time behavior of the u, v, h' fields at $r = 200$, 400, 600, 800, 1000 km for the $t_s = 3$ h case (left column) and for the $t_s = 6$ h case (right column). The $h'(r, t)$ field most clearly shows the outward-propagating inertia-gravity wave packet. For the $t_s = 3$ h case, that wave packet causes the negative depth anomaly to overshoot before returning to an equilibrium value that is the same as that given by the balanced solution $h_b'(r, \infty)$. Although individual inertia-gravity wave components can have shorter time scales, the superposition of these individual components into an inertia-gravity wave packet results in an outward-propagating wave pattern that has a time scale (period) of approximately 11 h.

The fundamental difference between the radial and azimuthal wind fields plotted in Figures 2, 3 can be understood as follows. The Dirac delta function on the right-hand side of the Klein-Gordon equation for $u\,(r, t)$ and on the right-hand side of the diagnostic equation for $u_b\,(r, t)$ is characterized by a single pulse in time, so that both $u\,(r, t)$ and $u_b\,(r, t)$ go to zero as $t \to \infty$, similar to $S\,(r, t)$. In contrast, the Dirac delta function on the right-hand side of the Klein-Gordon equation for $v\,(r, t)$ and on the right-hand side of the invertibility principle for $v_b\,(r, t)$ is characterized by the same time behavior as the PV, so that both $v(r, 17$ and $v_b\,(r, t)$ approach nonzero values as $t \to \infty$.

The solution of the invertibility problem for $v_b\,(r, t)$ or the solution of the invertibility problem for $h_b'(r, t)$ can be viewed as essentially converting the radial distribution of P' into the radial distributions of ζ_b and h_b'. This is a nonlocal process since it involves the solution of a second order differential equation. Since $P' = \zeta - (f/\bar{h})h'$ and since $P' = 0$ for $r > r_0$, we obtain $\zeta_b = (f/\bar{h})h_b' < 0$ for $r > r_0$. The situation is quite different in the region $r \leq r_0$, where $P' > 0$. In this region, $\zeta_b > 0$ and $h_b' < 0$, so both the wind field and the mass field contribute to the positive PV anomaly. To better understand how the partitioning between ζ_b and h_b' in the core ($r \leq r_0$) depends on vortex size, note that the average vorticity in the core is given by $2v_b\,(r_0, t)/r_0$, which allows us to write

$$\begin{aligned} \frac{\text{Average Core Vorticity}}{\text{Core PV Anomaly}} &= \frac{2v_b\,(r_0, t)/r_0}{P'\,(0, t)} = 2I_1\,(\mu r_0)K_1\,(\mu r_0) \\ &= (0.960,\ 0.891,\ 0.817,\ 0.746,\ 0.680) \\ &\quad \text{for } \ \mu r_0 = (0.2,\ 0.4,\ 0.6,\ 0.8,\ 1.0), \end{aligned} \tag{16}$$

where the second equality follows from the cancellation of the time dependence of $v_b\,(r_0, t)$ with the time dependence of $P'(0, t)$. Thus, as long as the radius of the vortex core is less than a Rossby length (i.e., $\mu r_0 < 1$), most of the PV anomaly in the core is partitioned to the vorticity field rather than to the mass field.

Since $P'(r, t)$ grows as shown in Eq. 8, then $|\partial P'/\partial r|$ at the PV edge increases with time and inertia-gravity waves can be excited there. Thus, the outer edge of a PV tower can be a region for the spontaneous generation of inertia-gravity waves. The inertia-gravity wave packets initiated at $r = 200$ km propagate inward and outward at $c = (g\bar{h})^{1/2} = 50$ m s^{-1} = 180 km h^{-1}, so that at $r = 920$ km the radial flow u, the azimuthal flow v, and the free surface height anomaly h' remain zero for the first 4 hours, immediately after which the height anomaly quickly becomes negative, the radial flow quickly becomes inward, and the azimuthal flow becomes cyclonic. Although the inertia-gravity wave packets are visible in the $u\,(r, t)$, $v\,(r, t)$, and $h'(r, t)$ fields, they are invisible in the $P'(r, t)$ field. Even though the balanced solutions $u_b(r,t)$, $v_b(r,t)$, $h_b'(r,t)$ filter inertia-gravity waves, they are useful approximations of the primitive equation solutions $u\,(r, t)$, $v\,(r, t)$, $h'(r, t)$ even when the time scale of the mass sink is as short as $t_s = 3$ h. Since the balanced dynamics have an elliptic rather than a hyperbolic character, the response at large radius to a mass sink at small radius is immediate, i.e., it can be described as "action at a distance." In this regard, the following analogy is useful: The balanced model is to the primitive equation model as Newton's gravitational theory is to general relativity, i.e., in the shallow water primitive equations information cannot radially

TABLE 2 The maximum radial inflow, maximum azimuthal wind, and final central depth anomaly for the three forcing cases t_s =3,6,12 h, as computed from the linear balanced solutions (Eq. 15) using the specified and computed constants listed in Table 1. The maximum radial inflow is proportional to $1/t_s$, but the weaker inflows last progressively longer. Since the same volume of fluid is removed in each case, the final values $v_b\,(r_0,\infty)$ and $h_b'(0,\infty)$ are the same. Even though all the original mass inside $r = r_0$ has been removed by the mass sink, almost all of this mass has been replaced by the time-integrated inflow at $r = r_0$, so that the final central depth anomaly is only –11.43 m. Detailed plots of the t_s =3 h and t_s =6 h cases are presented in Figures 2, 3. The t_s =12 h case is not shown since the balanced solutions and the primitive equation solutions are so similar.

Property	**Forcing Case**		
	$t_s = 3$ **h**	$t_s = 6$ **h**	$t_s = 12$ **h**
Maximum Radial Inflow $u_b\,(r_0, t_s) = -(r_0/t_s)e^{-1}I_1\,(\mu r_0)K_1\,(\mu r_0)$	-3.27 m s^{-1}	-1.63 m s^{-1}	-0.82 m s^{-1}
Maximum Azimuthal Wind $v_b\,(r_0, \infty) = r_0 f I_1\,(\mu r_0)K_1\,(\mu r_0)$	4.80 m s^{-1}	4.80 m s^{-1}	4.80 m s^{-1}
Final Central Depth Anomaly $h_b'(0,\infty) = -\bar{h}[1 - \mu r_0 K_1\,(\mu r_0)]$	-11.43 m	-11.43 m	-11.43 m

propagate faster than $c = (g\bar{h})^{1/2}$, while in general relativity information cannot propagate faster than the speed of light.

We may use the results of this section as the basis for the following physical picture. Each pulse of eyewall convective mass transport from the lower to the upper troposphere is accompanied by a corresponding pulse in the divergent circulation, which ratchets up the rotational circulation and ratchets down the fluid depth. According to the balanced model, the time dependence of the divergent circulation is in lock-step with the forcing $S\,(r,\,t)$; this behavior is due to the mathematically elliptic character of the balanced divergent flow (i.e., action at a distance). Convection in the hurricane eyewall can fluctuate on a variety of time scales, so the secondary circulation is expected to fluctuate in a roughly similar fashion. If the convective fluctuations have a vertical structure similar to the first internal mode of the troposphere, the associated gravity wave speed is approximately 50 m s^{-1} (180 km h^{-1}), so the information from eyewall convective fluctuations will propagate outward to 1000 km in approximately 4.5 h. For eyewall convective fluctuations having time scales larger than 6 h, the amplitude of the associated inertia-gravity wave packet is small, but for eyewall convective fluctuations with time scales less than 3 h, the amplitude of the associated wave packets may be considerably larger. In a continuously stratified fluid the inertia-gravity wave packets also propagate vertically, an important aspect that is further discussed in Section 5.

Although the linear analysis presented in this section provides a helpful guide to the nonlinear analysis of Section 4, the linearization used in Eq. 7 means that we are not analyzing true gradient adjustment and are restricting applications of the analytical results to situations where $\zeta < f$, whereas real tropical cyclones involve situations in which $\zeta \sim 100f$. In Section 4 we examine the full nonlinear case.

4 Nonlinear dynamics in the Lagrangian coordinate

We now return to the nonlinear shallow water equations of Section 2, and perform numerical integrations using two types of forcing. The first type uses the mass sink defined by Eq. 13, i.e., the mass sink is confined within a disk of fixed radius ($0 \le r \le r_0$). The second type, defined below in Eq. 27, uses a mass sink that is confined within the disk $0 \le R \le R_0$, where R is a Lagrangian coordinate that collapses as the vortex intensifies. As we shall see, there are some remarkable differences in the vortices that can be produced by these two types of forcing.

Figure 5 compares the nonlinear (left panels) and linear (right panels) numerical integrations using the identical parameter settings and forcing used to obtain the results shown in the right column of Figure 2. A major difference between the linear and nonlinear cases is the inward shift of the radius of maximum wind in the nonlinear case. In the linear case the azimuthal equation is $(\partial v/\partial t) = -fu$, so the radial distributions of $(\partial v/\partial t)$ and $-u$ are identical. In the nonlinear case the azimuthal equation is $(\partial v/\partial t) = -(f+\zeta)u$, so the radial distribution of $(\partial v/\partial t)$ is shifted inward when compared to the radial distribution of $-u$. During the first 24 h, the radius of maximum azimuthal wind shifts inward from 200 km to about 150 km and the maximum azimuthal wind approaches 5.3 m s^{-1}. Thus, for $24 \le t \le 48$ h, the average relative vorticity inside $r = 150$ km is approximately $1.4f$, somewhat outside the range of validity for linear theory.

Before discussing results of the second type of forcing, we note that insight into nonlinear model results can be obtained by transforming from the original independent variables $(r,\,t)$ to the new independent variables $(R,\,\tau)$, where $\tau = t$ and R is defined by $\frac{1}{2}fR^2 = \frac{1}{2}fr^2 + rv = \frac{1}{2}fr^2 + RV$, with $V = (r/R)v$ denoting the new dependent variable. Note that in general $(\partial/\partial\tau) \ne (\partial/\partial t)$ since $(\partial/\partial\tau)$ implies fixed R while $(\partial/\partial t)$ implies fixed r. We can think of

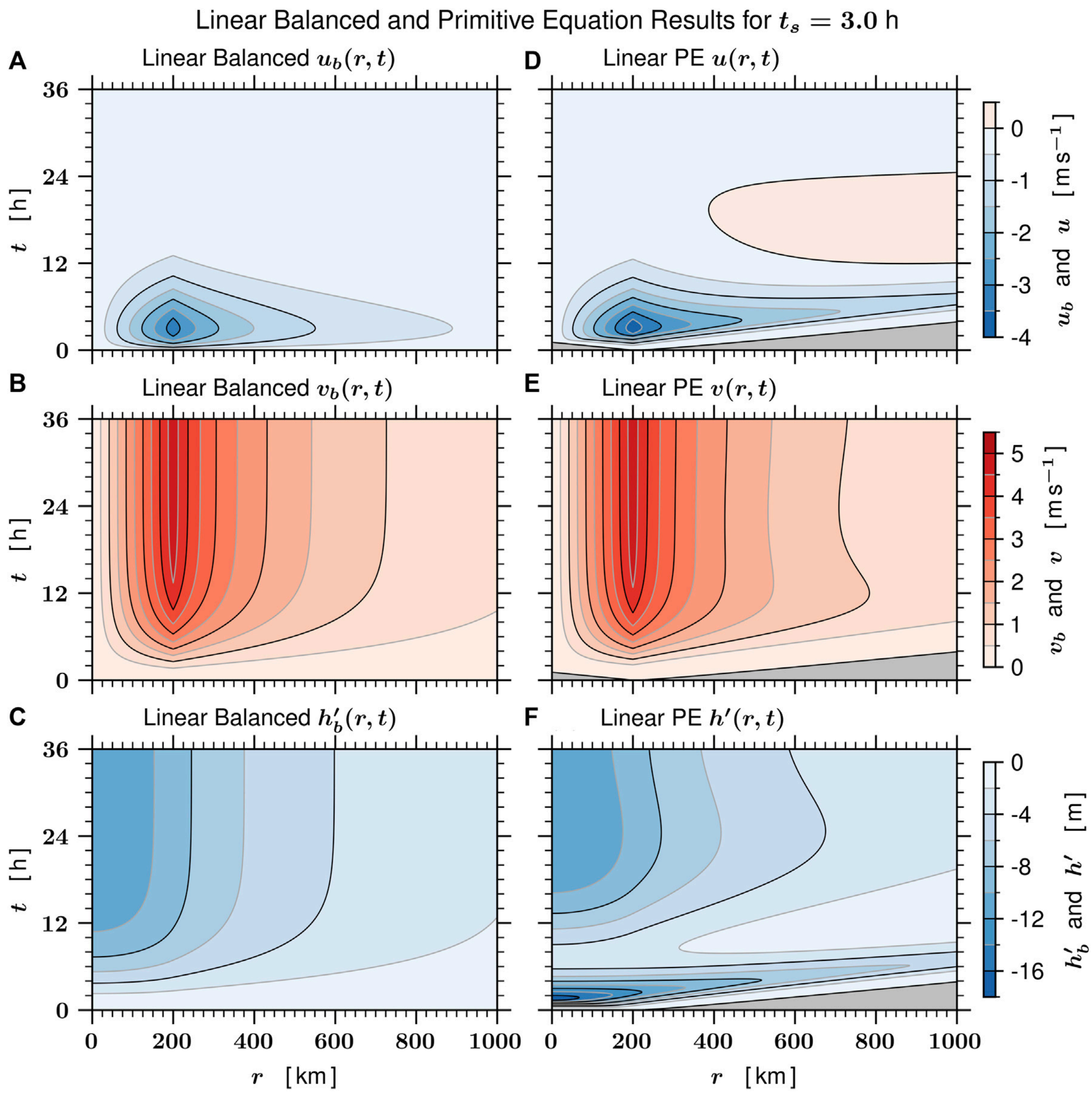

FIGURE 2
Panels **(A-C)** show the linear balanced solutions $u_b(r,t)$, $v_b(r,t)$, $h_b'(r,t)$ obtained from Eq. 15, while panels **(D-F)** show the corresponding linear primitive equation (PE) solutions $u(r,t)$, $v(r,t)$, $h'(r,t)$ obtained from Eq. 7 or equivalently from Eq. 11, all for the rapid forcing case $t_s = 3$ h. The isoline intervals are 0.5 m s^{-1} for the radial and azimuthal flow and 2.0 m for the perturbation depth, and the gray regions indicate initial regions where the plotted field is zero. The peak radial inflow is –3.3 m s^{-1} for the balanced case and –3.8 m s^{-1} for the primitive equation case, which has a slight overshoot. As $t \to \infty$, both $v_b(r_0, t)$ and $v(r_0, t)$ approach 4.8 m s^{-1}, while both $h_b'(0,t)$ and $h'(0,t)$ approach –11.4 m. Note that in the outer region $800 < r < 1000$ km, the balanced model response to the inner core forcing is instantaneous (action at a distance), while in the primitive equation model there is a 4–5 h delay as the inertia-gravity wave packet propagates outward at 50 m s^{-1}. The pink area in the $u(r,t)$ panel is weak outward radial velocity and is associated with inertia-gravity waves having very small radial wavenumber k, so that the relevant frequency $(f^2 + c^2k^2)^{1/2}$ is close to the inertia frequency $\omega \approx f$ (i.e., a period of approximately 34.9 h).

R as an absolute angular momentum coordinate with the unit of length, or equivalently, as the potential radius, i. e., the radius to which a fluid particle must be moved, conserving its absolute angular momentum, in order for its azimuthal wind to vanish. Finally, in the present context of inviscid flow, R can also be viewed as a Lagrangian coordinate, i. e., as a fluid particle label. Noting that

$$\left(1 + \frac{2v}{fr}\right)\left(1 - \frac{2V}{fR}\right) = 1, \tag{17}$$

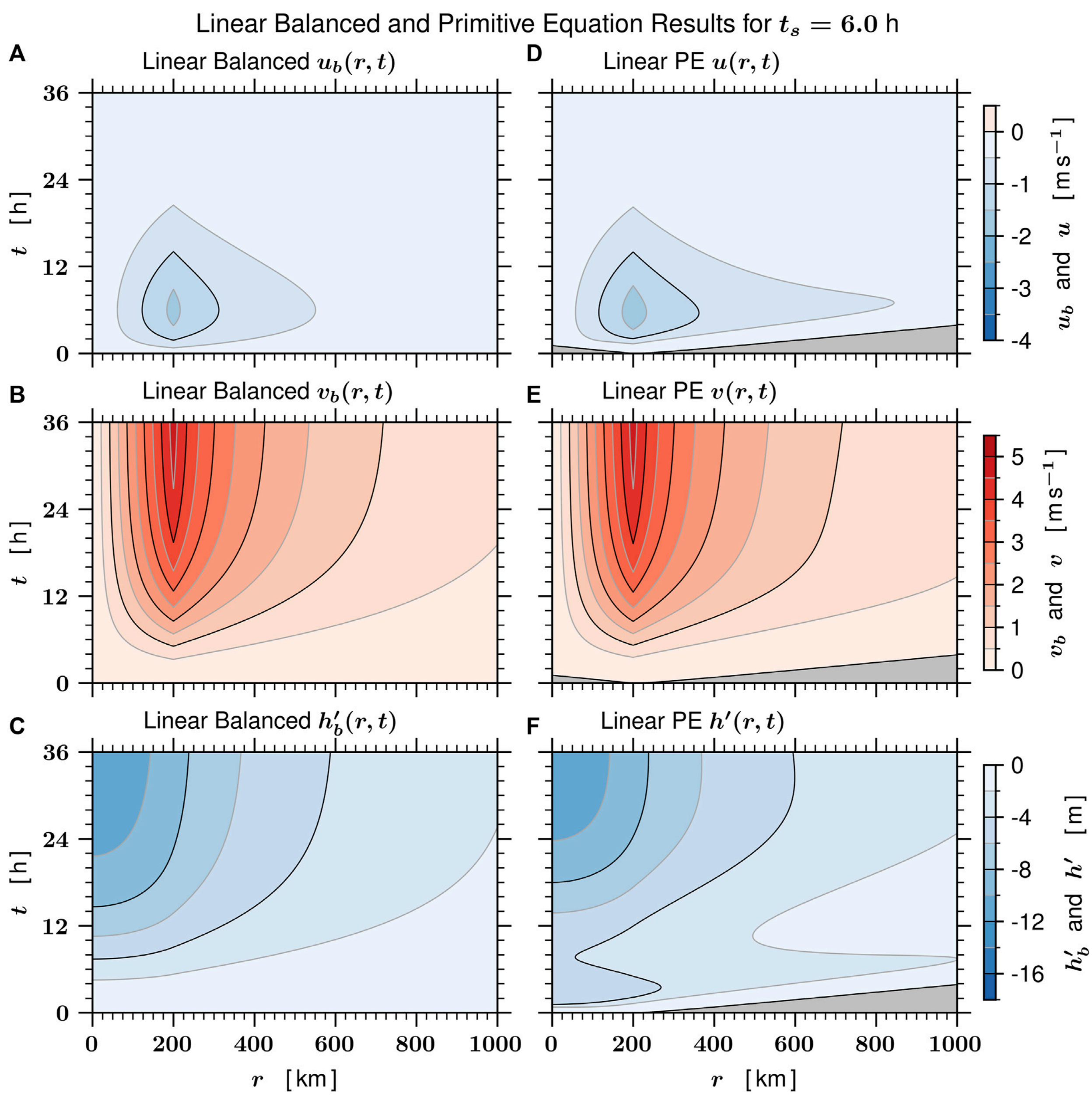

FIGURE 3
As in Figure 2, panels **(A-C)** show the linear balanced solutions $u_b(r,t)$, $v_b(r,t)$, $h_b'(r,t)$ while panels **(D-F)** show the corresponding linear primitive equation solutions $u(r,t)$, $v(r,t)$, $h'(r,t)$. All parameter settings used in this figure are identical to those used in Figure 2, except that t_s has been changed, i.e., Figure 2 corresponds to the rapid forcing case $t_s = 3$ h, while the present figure corresponds to the less rapid forcing $t_s = 6$ h. Note that, with less rapid forcing, the differences between the balanced and primitive equation solutions are smaller.

we can easily confirm that transformations between r, v and R, V can be written in the form

$$\left\{\begin{array}{l} R = \left(1+\dfrac{2v}{fr}\right)^{1/2} r \\ V = \left(1+\dfrac{2v}{fr}\right)^{-1/2} v \end{array}\right\} \Leftrightarrow \left\{\begin{array}{l} r = \left(1-\dfrac{2V}{fR}\right)^{1/2} R \\ v = \left(1-\dfrac{2V}{fR}\right)^{-1/2} V \end{array}\right\}. \qquad (18)$$

Since the relative circulation $2\pi rv$ divided by the area πr^2 is $2v/r$, the factor $(1 + 2v/fr)$ can be interpreted as the absolute circulation per unit area, measured in units of f, or equivalently, as the dimensionless average absolute vorticity inside the radius r. In the core of a hurricane we typically find $(1 + 2v/fr) \sim 100$ and $(1 - 2V/fR) \sim (1/100)$, so that $r \sim (1/10)\ R$ and $v \sim 10\ V$. Because of the conservation of absolute angular momentum, the material derivative is $(D/Dt) = (\partial/\partial t) + u\,(\partial/\partial r) = (\partial/\partial\tau)$. As discussed below, this simplification

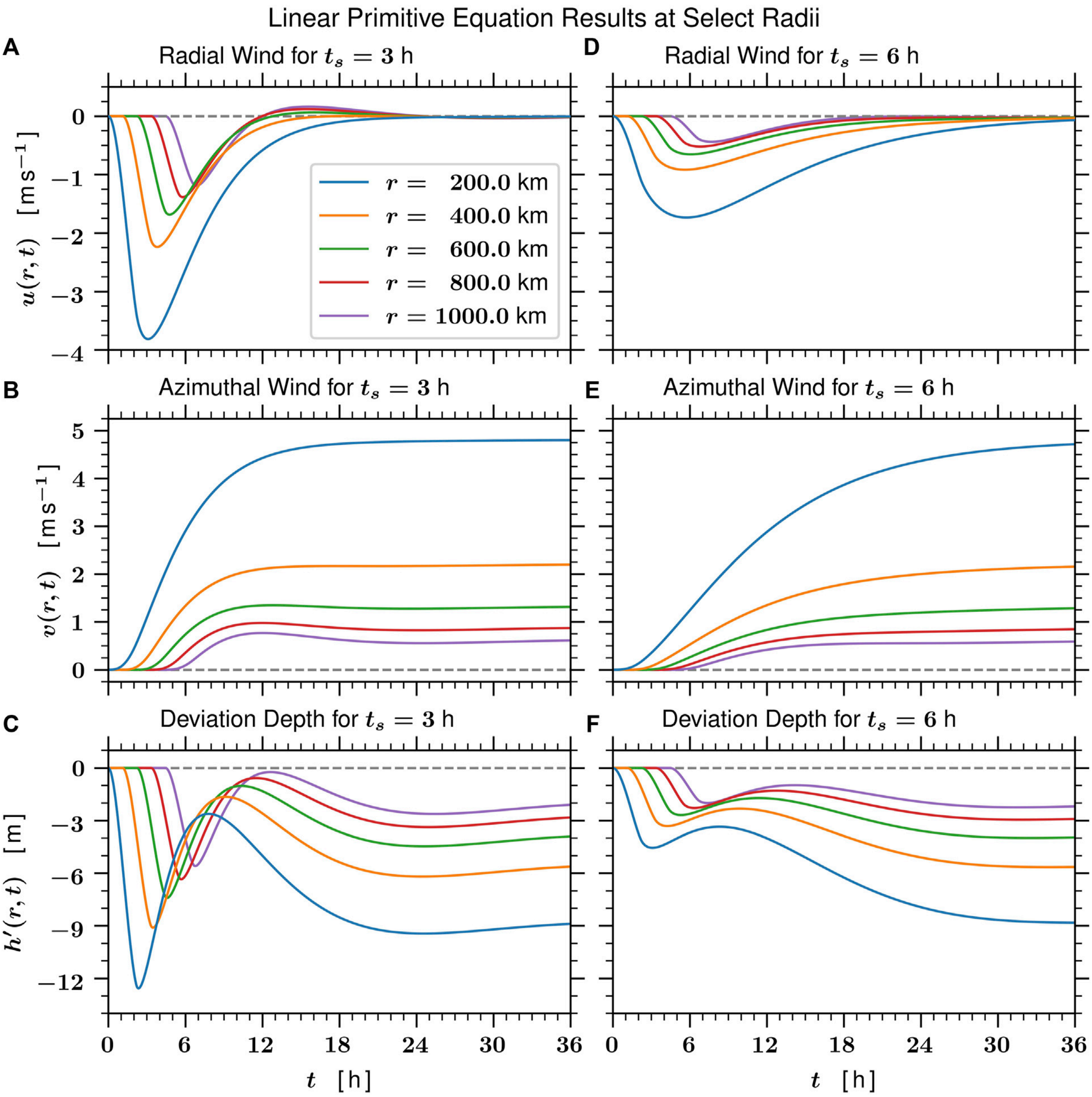

FIGURE 4
This figure shows the time dependence of the linear primitive equation solutions for the radial flow u (r, t), the azimuthal flow v (r, t), and the deviation depth $h'(r, t)$ at the selected radii r =200,400,600,800,1000 km for the rapid forcing case t_s =3 h **(A-C)** and for the less rapid forcing case t_s =6 h **(D-F)**. Note that these curves are simply vertical cross sections from Figures 2, 3. The outward propagating inertia-gravity wave packet is most readily apparent in the $h'(r, t)$-field, where it is immediately seen at r =200 km, and is seen, for example, with an approximately 4.5 h delay at r =1000 km. At each radius for the rapid forcing case (t_s =3 h) these linear primitive equation solutions for $h'(r, t)$ overshoot before coming into adjustment at a value that equals $h_b'(r, \infty)$. The less rapid forcing case (t_s =6 h) generates a weaker inertia-gravity wave packet that does not result in such an overshoot in the $h'(r, t)$ solutions.

of the material derivative will allow the PV equation to be directly integrated in time, so that the PV part of the dynamics can be treated analytically. The fact that $(D/Dt) = (\partial/\partial\tau)$ means that the radial advective effects $u\ (\partial u/\partial r)$, $u\ (\partial v/\partial r)$, $u\ (\partial h/\partial r)$, and $u\ (\partial P/\partial r)$ become implicit in the coordinate transformation $r \rightarrow R$. If the solutions of the nonlinear shallow water equations are obtained in R-space, the effects of the radial advection terms do not appear until the final step of transforming the results back to r-space. Many of the characteristics of rapid intensification appear in this transformation $R \rightarrow r$.

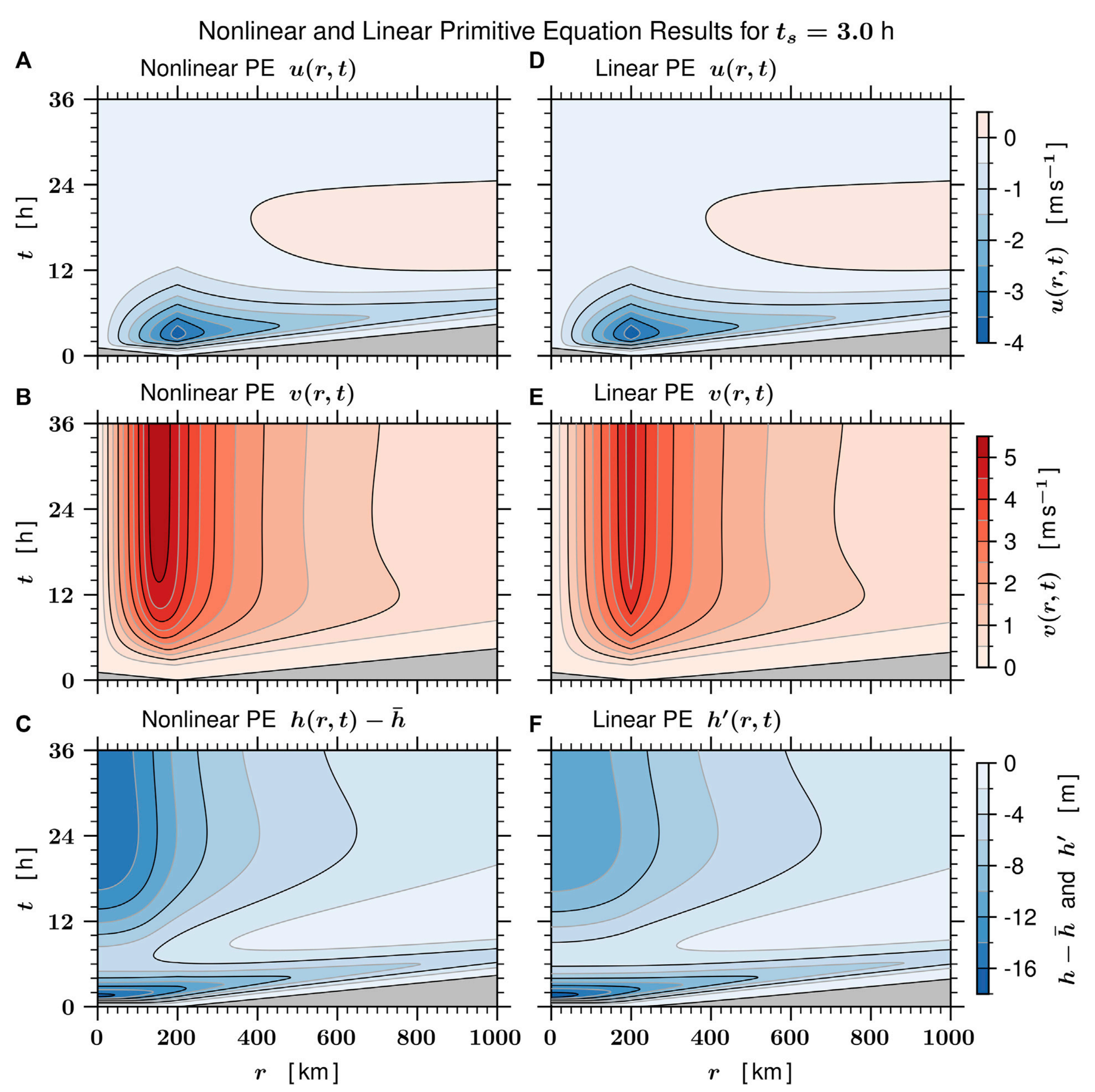

FIGURE 5

Panels **(D-F)** show the linear primitive equation solutions $u\,(r,\,t)$, $v\,(r,\,t)$, $h'(r,\,t)$ for the rapid forcing case $t_s = 3$ h as shown previously in the right panels of Figure 2. Panels **(A-C)** show the nonlinear primitive equation solutions $u\,(r, t)$, $v\,(r, t)$, $h\,(r, t) - \bar{h}$ obtained from Eq. 1 for the rapid forcing case $t_s = 3$ h obtained using the same parameters and forcing as those used for the linear results. The isoline intervals are identical to those used in the linear case (Figure 2), i.e., 0.5 m s^{-1} for the radial and azimuthal flow and 2.0 m for the perturbation depth, and the gray regions again indicate initial regions where the plotted field is zero. For the nonlinear results, the peak radial inflow is −3.8 m s^{-1} and occurs at $r = 200$ km, the central depth anomaly $h\,(0, t) - \bar{h}$ approaches −15.4 m as $t \to \infty$, and the maximum azimuthal flow approaches 5.3 m s^{-1} at about $r = 150$ km. It follows that, for $24 \leq t \leq 48$ h, the average relative vorticity inside $r = 150$ km is approximately 1.47 f. A major difference between the linear and nonlinear cases is the inward shift of the radius of maximum wind in the nonlinear case. Further discussion of this effect is given in Hack and Schubert (1986).

To further understand the transformation between $v(r)$ and $V(R)$, it is useful to consider the special case of a Rankine vortex. This example is simple because if V has a Rankine structure in R, then v has a Rankine structure in r, i. e.,

$$V\,(R) = V_0 \begin{cases} R/R_0 & \text{if } \ 0 \leq R \leq R_0 \\ R_0/R & \text{if } \ R_0 \leq R < \infty \end{cases} \quad \Leftrightarrow$$

$$v\,(r) = v_0 \begin{cases} r/r_0 & \text{if } \ 0 \leq r \leq r_0 \\ r_0/r & \text{if } \ r_0 \leq r < \infty, \end{cases} \qquad (19)$$

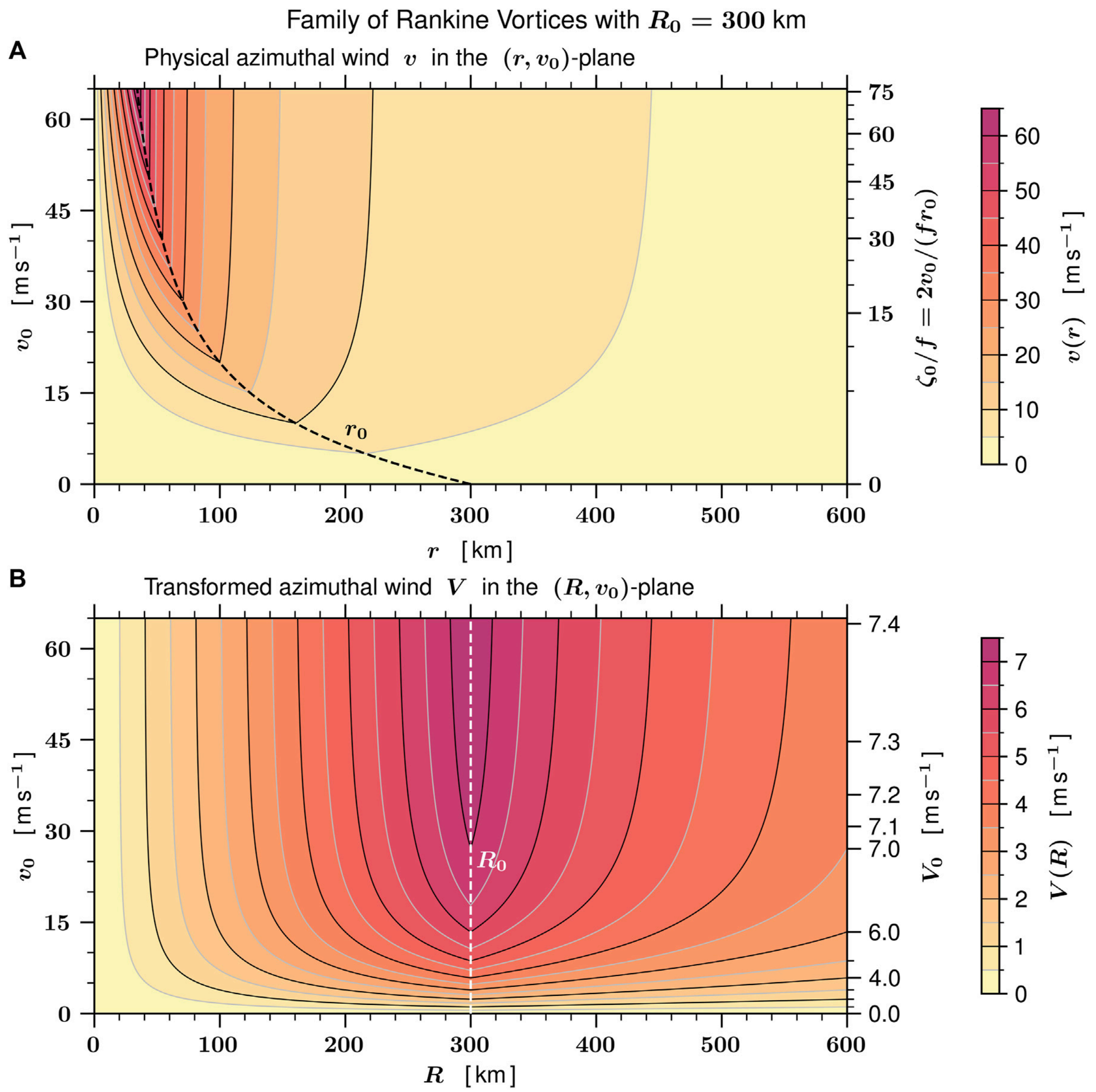

FIGURE 6
An illustration of the transformation relations Eq. 18 for the special case of a family of Rankine vortices, as defined in Eqs. 19, 20, with R_0=300 km and f =5×10^{-5} s^{-1}, so that $\frac{1}{2}fR_0$ = 7.5 m s^{-1}. Panel **(A)** shows isolines of the physical azimuthal wind v in the (r, v_0)-plane with an isoline interval of 5 m s^{-1}, and panel **(B)** shows isolines of the transformed azimuthal wind V in the (R, v_0)-plane with an isoline interval of 0.5 m s^{-1}. In both **(A,B)** the range on the left ordinate is $0 \le v_0 \le 65$ m s^{-1}. This corresponds to the range $0 \le V_0 \le 7.403$ m s^{-1}, as shown on the right ordinate of panel **(B)**, and to the range $0 \le \zeta_0/f \le 76.10$, as shown on the right ordinate of panel **(A)**, where $\zeta_0/f = 2v_0/(fr_0)$ is the dimensionless core vorticity. Note the striking difference in the behavior of $V(R)$ and $v(r)$. As $V(R_0)$ increases from rest to 7.403 m s^{-1}, $v(r_0)$ increases from rest to 65 m s^{-1} and the radius of maximum wind decreases from r_0=300 km to r_0=34.17 km.

where r_0, v_0 are related to R_0, V_0 by

$$r_0 = \left(1 - \frac{2V_0}{fR_0}\right)^{1/2} R_0 \qquad \text{and} \qquad v_0 = \left(1 - \frac{2V_0}{fR_0}\right)^{-1/2} V_0. \quad (20)$$

Thus, if we specify R_0 and V_0, then compute r_0 and v_0 from Eq. 20, we can plot $V(R)$ and $v(r)$ using Eq. 19. Figure 6 shows a family of Rankine vortices with R_0 = 300 km and $0 \le v_0 \le 65$ m s^{-1} where isolines of the physical azimuthal wind v in the (r, v_0)-plane are shown in the top panel and isolines of the transformed azimuthal wind V in the (R, v_0)-plane are shown in the bottom panel. For a particular value of v_0, the associated horizontal cross section from the top panel gives $v(r)$ for that particular Rankine vortex and the same

TABLE 3 Rankine vortex properties for a variety of storm categories, ranging from tropical depression (TD), to tropical storm (TS), to the five hurricane categories (C1–C5), and computed using Eq. 20 with R_0=300 km and f =5×10^{-5} s^{-1}. A range of values of the maximum physical azimuthal wind v_0 is specified in the second column followed by computed values in the next three columns of the radius of maximum wind r_0, the maximum transformed azimuthal wind V_0, and the quantity $2v_0/(fr_0)$, which can be interpreted as the core's relative vorticity, measured in units of f. Since the validity of the linearized dynamics discussed in Section 3 requires that $2v_0/(fr_0)<1$, seven of the eight storm categories shown here fall outside the scope of linear theory.

Storm Category	v_0 (m s^{-1})	r_0 (km)	V_0 (m s^{-1})	$2v_0/(fr_0)$ Vorticity/f
TD	5	216.2	3.604	0.93
TD	15	124.3	6.213	4.8
TS	25	83.1	6.925	12.0
C1	35	61.6	7.184	22.7
C2	45	48.7	7.303	37.0
C3	55	40.2	7.366	54.8
C4	65	34.2	7.403	76.1
C5	75	29.7	7.427	101.0

horizontal cross section from the bottom panel gives the corresponding $V(R)$ for that same Rankine vortex. Since all the effects of radial advection are implicit in the R-coordinate, these often striking radial advective effects appear in the transformation back from R to r, i.e., in going from the bottom panel to the top panel in Figure 6. Some of the information in Figure 6 can also be presented in tabular form, as shown in Table 3. In constructing Table 3 we have chosen R_0 = 300 km and a convenient set of values for v_0, and then used Eq. 20 to determine r_0 and V_0. The determination of r_0 is easily accomplished by noting that the two equations in Eq. 20 can be combined into $r_0 = [(\alpha^2+1)^{1/2} - \alpha]R_0$, where $\alpha = v_0/(fR_0)$. Once r_0 is thereby found, V_0 can be computed from $V_0 = (r_0/R_0)v_0$. Table 3 shows properties for a sequence of Rankine vortices with R_0 = 300 km, running from tropical depression (TD), to tropical storm (TS), and on upward to category five hurricane strength.

Because of the conservation of absolute angular momentum, the material derivative is $(D/Dt) = (\partial/\partial t) + u\,(\partial/\partial r) = (\partial/\partial\tau)$. This allows the potential vorticity equation (Eq. 2) and its solution to be written as

$$\frac{\partial P}{\partial\tau} = PS \quad\Rightarrow\quad \left\{\begin{array}{l} P(R,\tau) = f\exp\left(\displaystyle\int_0^\tau S(R,\tau')\,d\tau'\right) \\ \quad\text{and} \\ h^*(R,\tau) = \bar{h}\exp\left(-\displaystyle\int_0^\tau S(R,\tau')\,d\tau'\right), \end{array}\right. \tag{21}$$

where the potential depth h^* is related to the potential vorticity by $Ph^* = f\bar{h}$. Comparing the second entry in Eq. 21 with the linear version (Eq. 8), note that the appearance of the exponential function in Eq. 21 will lead to much faster growth of the P field in the nonlinear case. In fact, it is the appearance of this exponential function that is the crux of the rapid intensification process. In order to make practical use of this and related theoretical results, Hendricks et al. (2021) have introduced and tested a minimal, axisymmetric, shallow water modeling system (SWAMI) as an aid to forecasting short-term tropical cyclone intensity and wind structure changes.

Now consider the transformation of the nonlinear equations (Eq. 3). Using Eqs. 17, 18, and the definitions for R and V, the following useful relationships can be derived

$$\begin{array}{ll} \dfrac{\partial}{r\partial r} = \left(\dfrac{f+\zeta}{f}\right)\dfrac{\partial}{R\partial R}, & \left(f + \dfrac{\partial(rv)}{r\,\partial r}\right)\left(f - \dfrac{\partial(RV)}{R\,\partial R}\right) = f^2 = \left(f + \dfrac{2v}{r}\right)\left(f - \dfrac{2V}{R}\right), \\ r^2\left(f + \dfrac{v}{r}\right) = R^2\left(f - \dfrac{V}{R}\right), \quad \text{and} & \dfrac{\partial}{r\partial r}\left(\dfrac{\partial(rv)}{r\partial r}\right) = \left(\dfrac{f+\zeta}{f}\right)^3\dfrac{\partial}{R\partial R}\left(\dfrac{\partial(RV)}{R\partial R}\right). \end{array} \tag{22}$$

Using Eq. 22 and the definitions for P and h^*, the nonlinear equations (Eq. 3) become

$$\begin{array}{c} \dfrac{\partial u}{\partial\tau} - \left(\dfrac{R}{r}\right)^3\left(f - \dfrac{V}{R}\right)V + \dfrac{gh}{f}\left(\dfrac{h^2 r}{h^{*2}R}\right)\dfrac{\partial}{\partial R}\left(\dfrac{\partial(RV)}{R\partial R}\right) = -g\left(\dfrac{h^2 r}{h^{*2}R}\right)\dfrac{\partial h^*}{\partial R} \\ \text{and} \qquad \dfrac{R}{r}\dfrac{\partial V}{\partial\tau} + fu = 0. \end{array} \tag{23}$$

The single, nonlinear partial differential equation for $V(R,\tau)$ can now be obtained by eliminating u from the system in Eq. 23. Taking $(r/R)\,(\partial/\partial\tau)$ of the V-equation in Eq. 23, and then making use of the u-equation, we obtain

$$\underline{\textbf{Nonlinear Klein} - \text{Gordon Equation for } V(R,\tau)}$$

$$\begin{array}{c} \dfrac{\partial}{\partial R}\left(\dfrac{\partial(RV)}{R\,\partial R}\right) - \dfrac{1}{gh}\left(\dfrac{h^* R}{hr}\right)^2\left\{f\left(\dfrac{R}{r}\right)^2\left(f - \dfrac{V}{R}\right)V + r\dfrac{\partial}{\partial\tau}\left(\dfrac{1}{r}\dfrac{\partial V}{\partial\tau}\right)\right\} = -\dfrac{f}{h}\dfrac{\partial h^*}{\partial R} \\ \text{with}\left\{\begin{array}{ll} \text{BCs}: & V(0,\tau) = 0,\, RV(R,\tau) \to 0 \text{ as } R \to \infty \\ \text{ICs}: & V(R,0) = 0,\, V_\tau(R,0) = 0 \end{array}\right\}, \end{array} \tag{24}$$

which is the nonlinear generalization of the middle entry in Eq. 11. The initial conditions and boundary conditions in Eq. 24 result from the assumption that the evolving flow is due entirely to a localized forcing $S\,(R,\tau)$. The factors r and h appearing in Eq. 24 can be expressed in terms of V by

$$r = R\left(1 - \frac{2V}{fR}\right)^{1/2} \quad \text{and} \quad h = h^* f\left(f - \frac{\partial(RV)}{R\,\partial R}\right)^{-1}. \tag{25}$$

When the forcing term on the right-hand side of Eq. 24 is slow enough, the azimuthal flow remains close to gradient balance. Then, the $r\,(\partial/\partial\tau)[(1/r)\,(\partial V/\partial\tau)]$ term becomes negligible and Eq. 24 simplifies to the following invertibility principle for the balanced transformed azimuthal wind $V_b(R,\tau)$:

$$\underline{\textbf{Nonlinear Invertibility Problem for } V_b(R,\tau)}$$

$$\begin{array}{l} R^2\dfrac{\partial^2 V_b}{\partial R^2} + R\dfrac{\partial V_b}{\partial R} - (\mu_b^2 R^2 + 1)V_b = -\dfrac{fR^2}{h}\dfrac{\partial h^*}{\partial R} \\ \qquad \text{with BCs}: \quad V_b(0,\tau) = 0, \quad RV_b(R,\tau) \to 0 \text{ as } R \to \infty \\ \qquad \text{where} \quad \mu_b(R,\tau) = \left[\dfrac{f}{gh}\left(f - \dfrac{V_b}{R}\right)\right]^{1/2}\left(f - \dfrac{2V_b}{R}\right)^{-1}\left(f - \dfrac{\partial(RV_b)}{R\partial R}\right). \end{array} \tag{26}$$

Once again the h appearing in Eq. 26 can be expressed in terms of V by using Eq. 25.

In analogy with the argument given in Section 3 for the linear case, we now assume that the mass sink $S(R, \tau)$ vanishes for $R > R_0$ and is horizontally uniform for $R \le R_0$, where R_0 is a specified constant. The time dependence of $S(R, \tau)$ is again assumed to be $(\tau/\tau_s^2)\, e^{-\tau/\tau_s}$, where τ_s is a specified constant. Again, small values of τ_s correspond to fast forcing and large values of τ_s to slow forcing. This forcing $S(R, \tau)$ and the result of using it in Eq. 21 are given by

$$S(R,\tau) = -\ln(1-\epsilon)\begin{cases} (\tau/\tau_s^2)\, e^{-\tau/\tau_s} & \text{if } 0 \le R \le R_0 \\ 0 & \text{if } R_0 < R < \infty, \end{cases} \tag{27}$$

and

$$h^*(R,\tau) = \bar{h}\begin{cases} (1-\epsilon)^{1-(1+\tau/\tau_s)e^{-\tau/\tau_s}} & \text{if } 0 \le R \le R_0 \\ 1 & \text{if } R_0 < R < \infty, \end{cases} \tag{28}$$

where $\epsilon = \mathcal{V}/(\pi R_0^2 \bar{h})$ and, as confirmed below, the specified constant $\mathcal{V}$ is the total volume of fluid removed by the mass sink. Note that ϵ is the percentage of the initial fluid volume inside the potential radius R_0 that is removed by the mass sink and that $-\ln(1-\epsilon) \approx \epsilon$ for $\epsilon \ll 1$, in which case the forcing for the nonlinear case (Eq. 27) is essentially the same as the forcing for the linear case (Eq. 13). The h^* field is a disk of potential radius R_0, with values of h^* in its interior decreasing with time. To confirm that the constant $\mathcal{V}$ is the total volume of fluid removed, integrate the mass continuity equation over the entire spatial domain to obtain

$$\begin{aligned} \frac{\partial}{\partial t}\left\{2\pi\int_0^\infty \left[\bar{h} - h(r,t)\right] r\, dr\right\} &= 2\pi\int_0^\infty S h\, r\, dr \\ &= 2\pi\int_0^{R_0} S h^*\, R\, dR = -\pi R_0^2 \frac{\partial h^*(0,\tau)}{\partial \tau}, \end{aligned} \tag{29}$$

where we have made use of $hr\, dr = h^*R\, dR$, the assumption that $S = 0$ for $R > R_0$, and the assumption that $S(R, \tau)$ and $h^*(R, \tau)$ are independent of R for $R \le R_0$. The last equality in Eq. 29 results from writing the first entry of Eq. 21 in the form $(\partial h^*/\partial \tau) = -Sh^*$. The total volume of fluid removed is now obtained by integrating Eq. 29 over time, giving

$$2\pi\int_0^\infty \left[\bar{h} - h(r,\infty)\right] r\, dr = \pi R_0^2\left[\bar{h} - h^*(0,\infty)\right] = \pi R_0^2 \bar{h}\epsilon = \mathcal{V}, \tag{30}$$

where the second to last equality in Eq. 30 results from the use of Eq. 28 to show that $h^*(0,\infty) = (1-\epsilon)\bar{h}$. This confirms that $\mathcal{V}$ is the total volume of fluid removed by the mass sink over its life cycle. In other words, for a fixed value of $\mathcal{V}$ in Eq. 27, the total volume of fluid removed by the mass sink is independent of the choice of the constants τ_s and R_0, although the choice of R_0 should satisfy $\pi R_0^2 \bar{h} > \mathcal{V}$ so that $1 - \epsilon > 0$. Note that since R is a Lagrangian coordinate, fluid does not flow across R surfaces, so ϵ is constrained to be less than unity. As we shall now discuss, a crucial aspect of the forcing (Eq. 27) is its confinement to $R \le R_0$, i.e., in physical space the forcing collapses as the angular momentum surface R_0 collapses. This confines the forcing to the high PV region (Musgrave et al., 2012) and leads to rapid increases in the core PV.

Since $P/f = \bar{h}/h^*$, the solution in Eq. 28 can also be expressed in the potential vorticity form

$$\begin{aligned} P(R,\tau) &= f\begin{cases} (1-\epsilon)^{(1+\tau/\tau_s)e^{-\tau/\tau_s}-1} & \text{if } 0 \le R \le R_0 \\ 1 & \text{if } R_0 < R < \infty, \end{cases} \\ \Rightarrow \quad P(0,\infty) &= \frac{f}{1-\epsilon} = f\left(1 - \frac{\mathcal{V}}{\pi R_0^2 \bar{h}}\right)^{-1}, \end{aligned} \tag{31}$$

A plot of $P(0, \infty)/f$ as a function of $\mathcal{V}/(\pi R_0^2 \bar{h})$ is given in Figure 7. As discussed in Supplementary Appendix D, the solution Eq. 31 can be used to obtain a simple upper bound on the rotational flow $v(r, t)$. If we regard R_0 as fixed, the abscissa of Figure 7 can be interpreted as a measure of the total volume of fluid removed by the mass sink. If the total volume of fluid removed is $\mathcal{V} = 0.5\,(\pi R_0^2 \bar{h})$, then $P(0, \infty) = 2f$. If the total volume of fluid removed is $\mathcal{V} = 0.90\,(\pi R_0^2 \bar{h})$, then $P(0, \infty) = 10f$. In the extreme case when the total volume of fluid removed is $\mathcal{V} = 0.99\,(\pi R_0^2 \bar{h})$, then $P(0, \infty) = 100f$. In other words, it is the removal of the last vestiges of the original mass inside R_0 that spins up the PV to such large values. This effect can also be seen in Figure 8, which shows plots of $P(0, \tau)/f$, as given by Eq. 31, for the time range $0 \le \tau \le 72$ h and for the fixed volume parameter $\mathcal{V} = 3.174 \times 10^{13}$ m³. The nine curves correspond to combinations of the three choices τ_s = 3, 6, 12 h and the three choices R_0 = 200, 300, 400 km, the latter of which give ϵ = 0.990, 0.440, 0.248. The nine curves illustrate the sensitivity of the core PV to the value of R_0 for fixed $\mathcal{V}$. They also illustrate the concepts of long incubation times and vortex preconditioning (see section 15 of Ooyama, 1969). For example, although all nine cases in Figure 8 have the same value of $\mathcal{V}$, the R_0 = 400 km case has the mass sink spread over the largest area, so the vortex experiences a long period of incubation, with the PV increasing to only ~ $1.3f$ by the end of the mass sink. The R_0 = 300 km case also experiences long incubation, with the PV increasing to ~ $1.7f$ by the end of the mass sink. In contrast, the PV in the R_0 = 200 km case increases to ~ $100f$ in 72 h when developing from a resting initial state. However, if the R_0 = 200 km case were initialized with $P(0, 0) = 5f$, it could reach a core PV of ~ $100f$ in less than 24 h. Such a vortex might be said to be preconditioned for rapid development. The most detailed observations and analyses of a rapidly intensifying hurricane are those of Hurricane Patricia, which occurred in the northeast Pacific in October 2015. The potential vorticity analysis of Martinez et al. (2019) indicates that Hurricane Patricia could be roughly interpreted as the preconditioned R_0 = 200 km case, although any detailed comparison would involve the important roles of frictional boundary layer pumping and moist physical processes.

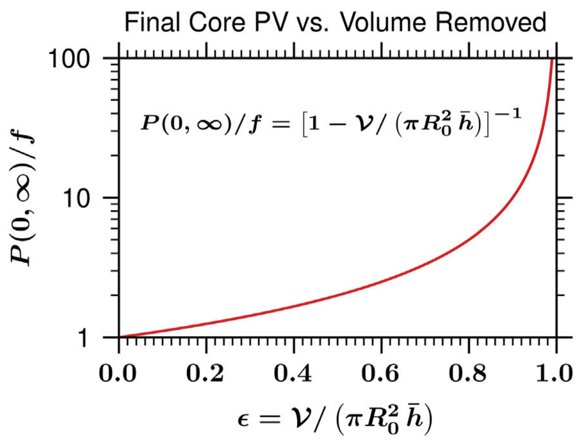

FIGURE 7
The final, dimensionless core potential vorticity $P(0,\infty)/f$ as a function of $\epsilon = \mathcal{V}/(\pi R_0^2\bar{h})$, as given by Eq. 31 and shown by the displayed formula. Note that the scale on the ordinate is logarithmic. If we regard R_0 as given, the abscissa is a measure of the total volume of fluid removed by the mass sink. This graph implies that it is the removal of the last 10% of the initial volume of fluid inside R_0 that can rapidly spin up the PV from $10f$ to more than $100f$. Since $P = (f+\zeta)(\bar{h}/h)$, large values of P are associated with large values of the absolute vorticity $(f+\zeta)$ and small values of the fluid depth h.

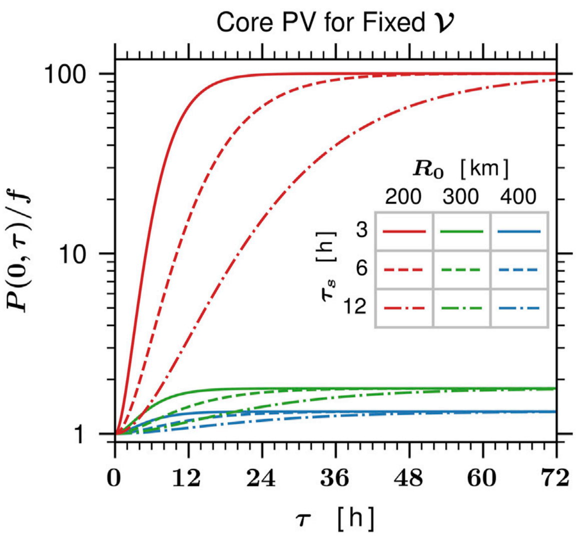

FIGURE 8
Plots of $P(0,\tau)/f$, as given by Eq. 31 for the three choices τ_s =3,6,12 h, and for the three choices R_0=200,300,400 km. The time evolution of $P(0,\tau)/f$ is plotted for $0\leq\tau\leq 72$ h, and the volume parameter is chosen to be $\mathcal{V} = 3.174 \times 10^{13}$ m^3. This specified value of $\mathcal{V}$ is 99.0% of the initial volume inside the potential radius R_0=200 km, 44.0% of the initial volume inside the potential radius R_0=300 km, and 24.8% of the initial volume inside the potential radius R_0=400 km.

As a final illustration of the remarkable intensification that can result with the second type of forcing, Figure 9 shows the results of two nonlinear primitive equation model integrations using the forcing in Eq. 27 with $t_s = 3$ h. The right three panels show the time evolution of $u(r,t)$, $v(r,t)$, and $h(r,t) - \bar{h}$ for the parameter settings $R_0 = 300$ km and $\epsilon = 0.44$, while the left three panels show the corresponding results for $R_0 = 200$ km and $\epsilon = 0.99$. Since $\mathcal{V} = \pi R_0^2\bar{h}\epsilon$, the same total volume of fluid is removed in each case. However, the vortex intensification is quite different in the two cases, with the $\epsilon = 0.99$ case intensifying to hurricane strength and the $\epsilon = 0.44$ case intensifying to only about 4 m s^{-1}. This is consistent with the sensitivity of PV evolution illustrated in Figures 7, 8.

5 Concluding remarks

It is important to note that the simple axisymmetric shallow water model framework of this work does not include environmental effects and the frictional boundary layer, both of which certainly play a role in the rapid intensification process. Nevertheless, the nonlinear results presented here provide what we believe is an important part of the puzzle and are consistent with the notion that intensity forecasting is a difficult problem. For example, suppose (quite hypothetically) that we have a tropical cyclone with its core diabatic forcing (convection) confined by the absolute angular momentum surface $R = R_0$. As can be see from Figures 7–9, if that diabatic forcing is able to remove 99% of the original mass inside that R_0 surface over the next 24 h, then that tropical cyclone will undergo rapid intensification, but if the forcing only removes 50% of the original mass, then it will only slightly intensify. This does not mean that larger storms, i.e., storms with larger R_0 values, cannot undergo rapid intensification, just that such a larger storm may require a longer incubation period before rapid intensification can occur.

Concerning the frictional boundary layer, consider a region bounded by two R-surfaces and two lower tropospheric θ-surfaces just above the boundary layer, i.e., an $(R,\ \theta)$-pseudovolume. The removal of mass from such a pseudovolume involves both diabatic processes and boundary layer pumping. Boundary layer pumping may play a dual role, helping to keep the diabatic heating radially confined so that it collapses with the R-surfaces, but also limiting the percentage of mass that can be removed from that $(R,\ \theta)$-pseudovolume. We might conclude that accurate determination of the location and magnitude of both frictional and diabatic mass fluxes is necessary for forecasting rapid intensification. The inclusion of environmental effects, such as vertical shear, would require fully three-dimensional arguments and thus a more

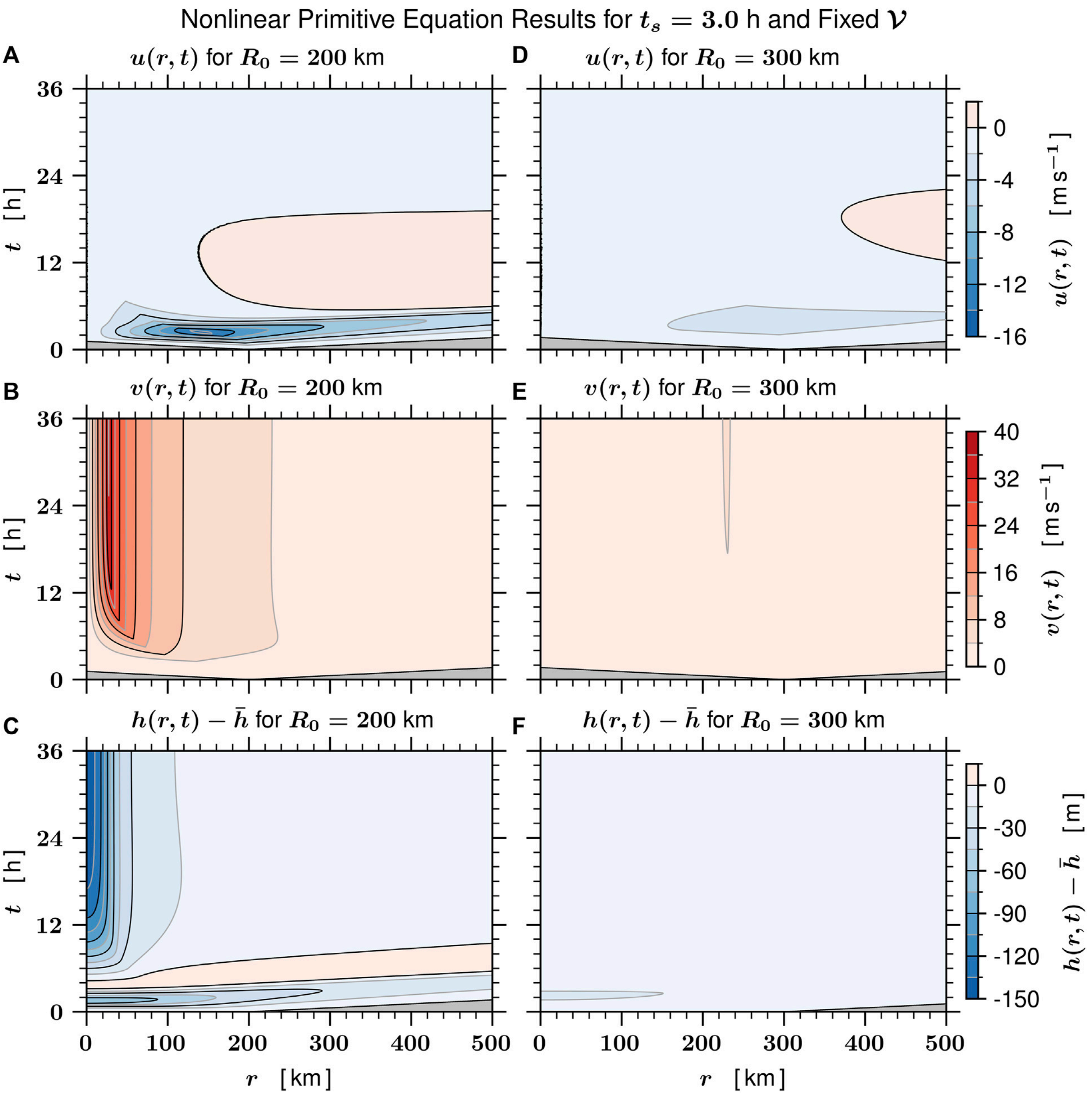

FIGURE 9
Panels **(A–F)** show the nonlinear primitive equation solutions obtained from Eq. 1 for the radial flow u (r, t), the azimuthal flow v (r, t), and the deviation depth $h(r,t) - \bar{h}$ for the forcing in Eq. 27 with t_s =3 h. Panels **(A-C)** use the parameters R_0=200 km and ϵ =0.99, while panels **(D-F)** use R_0=300 km and ϵ =0.44. Since $\mathcal{V} = \pi R_0^2 \bar{h} \epsilon$, the same volume of fluid is removed in each case. For the ϵ =0.44 case shown in **(D-F)**, the maximum azimuthal winds are only about 4 m s^{-1}, while for the ϵ =0.99 case shown in **(A-C)**, the maximum azimuthal winds increase to hurricane strength. The gray regions indicate initial regions where the plotted field is zero.

detailed PV analysis or a generalized omega equation analysis (DeMaria, 1996; Wang and Zhang, 2003), which is an important topic for future research. While the present paper certainly does not solve the rapid intensification problem, perhaps it better defines the nature of the problem.

In closing we note that it can be argued that inertia-gravity waves generated by tropical cyclones are simply "the zero-PV icing on the cake" of what is fundamentally a balanced, potential vorticity phenomenon. Although there is merit to this argument, the observational monitoring of inertia-gravity waves as they propagate upward into the stratosphere and mesosphere can

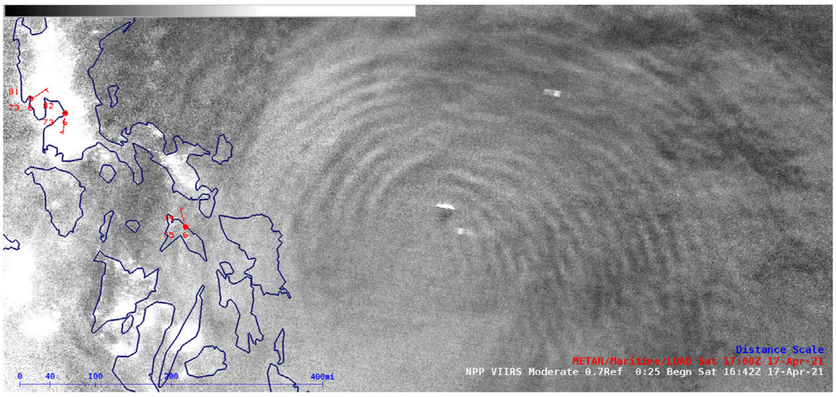

FIGURE 10
A nocturnal (several hours before sunrise) Suomi-NPP VIIRS Day/Night Band image (0.7 μm) showing concentric mesospheric airglow waves that have propagated upward from the convective core of Super Typhoon Surigae near the time of its peak intensity on 17 April 2021, when it was just east of the Philippines. From Bachmeier (2021).

reveal information about eyewall convection. Some of this information might be of practical use in the prediction of rapid intensification. Inertia-gravity waves excited by inner core tropical cyclone convection can sometimes be observed at mesosphere levels by airglow observations from the Earth's surface or from low Earth orbit (Miller et al., 2012, 2015). For example, Suzuki et al. (2013) described inertia-gravity wave patterns in the mesopause region caused by tropospheric convection in Typhoon Pongsona on 10 December 2002. Concentric rings of inertia-gravity waves in the OH airglow were observed simultaneously by all-sky imagers in a Japanese network of surface stations located between 31.0N and 43.5N. Such ground-based optical measurements require clear-sky conditions, so must be obtained at some distance from the tropical cyclone core in order to avoid persistent cirrus overcast. Such concentric mesospheric airglow waves can also be observed from space (Yue et al., 2014). As a recent example, Figure 10 shows a nocturnal Suomi-NPP VIIRS Day/Night Band image that captured concentric mesospheric airglow waves propagating upward from Super Typhoon Surigae near the time of its peak intensity on 17 April 2021. Concerning evidence from data at stratospheric levels, signatures of stratospheric inertia-gravity waves that have large vertical wavelengths can be found in Atmospheric Infrared Sounder (AIRS) radiance measurements in the 4.3 μm CO_2 waveband. Such measurements detect the wave-induced perturbations in stratospheric temperature at levels between 30 and 40 km. Using such data, Hoffmann et al. (2018) searched for an association of stratospheric inertia-gravity waves with the intensification of tropical cyclones. They found a statistical correlation between stratospheric inertia-gravity wave activity and tropical cyclone intensification, lending support to the idea that variability in inertia-gravity wave signatures as a result of changing storm behavior may constitute a useful diagnostic tool for rapid intensification. This interesting possibility led Tratt et al. (2018) to propose a satellite mission concept for monitoring stratospheric inertia-gravity waves from geostationary orbit, which would open up the possibility of continuous monitoring. Although the theoretical results presented here are limited to shallow water dynamics, they do highlight some of the subtleties that are involved in linking inertia-gravity wave activity to rapid intensification. Thus, as research on this topic evolves with the use of full physics numerical models, it would not be surprising to encounter subtleties in the relationship of stratospheric inertia-gravity wave activity to rapid intensification.

An important result presented here is the nonlinear, inhomogeneous, Klein-Gordon equation (Eq. 24), which describes essential aspects of the rapid intensification of the potential vorticity and azimuthal wind fields in a tropical cyclone. Although this equation has an unfamiliar form, it may be of interest to note a relevant point made by Weinberg (1977, page 131) concerning results derived from sound physical and mathematical principles: "This is often the way it is in physics—our mistake is not that we take our theories too seriously, but that we do not take them seriously enough. It is always hard to realize that these numbers and equations we play with at our desks have something to do with the real world."

Data availability statement

The original contributions presented in the study are included in the article/Supplementary Material. Further inquiries can be directed to the corresponding author.

Author contributions

WS researched and derived the scientific aspects of this work and wrote the majority of this paper. RT developed and ran the numerical models, created all of the figures, and provided editing and LaTeX support.

Funding

Our research has been supported by the National Science Foundation under grant AGS-1841326.

Acknowledgments

We thank Chris Slocum and Mark DeMaria for their helpful comments and Eric Hendricks, Jonathan Vigh, and Chris Rozoff for sharing with us their ideas on how PV concepts associated with a forced, balanced, axisymmetric shallow water model can be used for understanding short-term tropical cyclone intensification and wind structure changes. We would also like to thank the two reviewers for their useful comments and suggestions.

Conflict of interest

The authors declare that the research was conducted in the absence of any commercial or financial relationships that could be construed as a potential conflict of interest.

Publisher's note

Supplementary material

The Supplementary Material for this article can be found online at: https://www.frontiersin.org/articles/10.3389/feart.2022.1038351/full#supplementary-material

References

Bachmeier, S. (2021). *Rapid intensification of super Typhoon Surigae*. Wisconsin: University of Wisconsin. CIMSS Satellite Blog. Available at: https://cimss.ssec.wisc.edu/satellite-blog/archives/date/2021/04/16 (Accessed 04 25, 2022).

Cahn, A., Jr. (1945). An investigation of the free oscillations of a simple current system. *J. Meteor.* 2, 113–119. doi:10.1175/1520-0469(1945)002<0113:AIOTFO>2.0.CO;2

Copson, E. T. (1975). *Partial differential equations*. Cambridge: Cambridge University Press, 280.

DeMaria, M., Sampson, C. R., Knaff, J. A., and Musgrave, K. D. (2014). Is tropical cyclone intensity guidance improving? *Bull. Am. Meteorol. Soc.* 95, 387–398. doi:10.1175/BAMS-D-12-00240.1

DeMaria, M. (1996). The effect of vertical shear on tropical cyclone intensity change. *J. Atmos. Sci.* 53, 2076–2088. doi:10.1175/1520-0469(1996)053<2076:TEOVSO>2.0.CO;2

Doyle, J. D., and Ferek, R. (2017). *Tropical cyclone intensity experiment (TCI)*. AMS Special Collection. Boston: American Meteorological Society. Available at: https://journals.ametsoc.org/collection/TCI (Accessed 10 07, 2022).

Hack, J. J., and Schubert, W. H. (1986). Nonlinear response of atmospheric vortices to heating by organized cumulus convection. *J. Atmos. Sci.* 43, 1559–1573. doi:10.1175/1520-0469(1986)043<1559:NROAVT>2.0.CO;2

Hendricks, E. A., Vigh, J. L., and Rozoff, C. M. (2021). Forced, balanced, axisymmetric shallow water model for understanding short-term tropical cyclone intensity and wind structure changes. *Atmosphere* 12, 1308. doi:10.3390/atmos12101308

Hoffmann, L., Wu, X., and Alexander, M. J. (2018). Satellite observations of stratospheric gravity waves associated with the intensification of tropical cyclones. *Geophys. Res. Lett.* 45, 1692–1700. doi:10.1002/2017GL076123

Hoskins, B. J., McIntyre, M. E., and Robertson, A. W. (1985). On the use and significance of isentropic potential vorticity maps. *Q. J. R. Meteorol. Soc.* 111, 877–946. doi:10.1002/qj.49711147002

Martinez, J., Bell, M. M., Rogers, R. F., and Doyle, J. D. (2019). Axisymmetric potential vorticity evolution of Hurricane Patricia (2015). *J. Atmos. Sci.* 76, 2043–2063. doi:10.1175/JAS-D-18-0373.1

Miller, S. D., Mills, S. P., Elvidge, C. D., Lindsey, D. T., Lee, T. F., and Hawkins, J. D. (2012). Suomi satellite brings to light a unique frontier of nighttime environmental sensing capabilities. *Proc. Natl. Acad. Sci. U. S. A.* 109, 15706–15711. doi:10.1073/pnas.1207034109

Miller, S. D., Straka, W. C., III, Yue, J., Smith, S. M., Alexander, M. J., Hoffmann, L., et al. (2015). Upper atmospheric gravity wave details revealed in nightglow satellite imagery. *Proc. Natl. Acad. Sci. U. S. A.* 112, E6728–E6735. doi:10.1073/pnas.1508084112

Möller, J. D., and Smith, R. K. (1994). The development of potential vorticity in a hurricane-like vortex. *Q. J. R. Meteorol. Soc.* 120, 1255–1265. doi:10.1002/qj.49712051907

Musgrave, K. D., Taft, R. K., Vigh, J. L., McNoldy, B. D., and Schubert, W. H. (2012). Time evolution of the intensity and size of tropical cyclones. *J. Adv. Model. Earth Syst.* 4, 15. doi:10.1029/2011MS000104

Ooyama, K. (1969). Numerical simulation of the life cycle of tropical cyclones. *J. Atmos. Sci.* 26, 32–40. doi:10.1175/1520-0469(1969)026<0003:NSOTLC>2.0

Schubert, W. H., and Alworth, B. T. (1987). Evolution of potential vorticity in tropical cyclones. *Q. J. R. Meteorol. Soc.* 113, 147–162. doi:10.1002/qj.49711347509

Schubert, W. H., Hack, J. J., Silva Dias, P. L., and Fulton, S. R. (1980). Geostrophic adjustment in an axisymmetric vortex. *J. Atmos. Sci.* 37, 1464–1484. doi:10.1175/1520-0469(1980)037<1464:GAIAAV>2.0.CO;2

Suzuki, S., Vadas, S. L., Shiokawa, K., Otsuka, Y., Kawamura, S., and Murayama, Y. (2013). Typhoon-induced concentric airglow structures in the mesopause region. *Geophys. Res. Lett.* 40, 5983–5987. doi:10.1002/2013GL058087

Tratt, D. M., Hackwell, J. A., Valant-Spaight, B. L., Walterscheid, R. L., Gelinas, L. J., Hecht, J. H., et al. (2018). Ghost: A satellite mission concept for persistent monitoring of stratospheric gravity waves induced by severe storms. *Bull. Am. Meteorol. Soc.* 99, 1813–1828. doi:10.1175/BAMS-D-17-0064.1

Wang, X., and Zhang, D.-L. (2003). Potential vorticity diagnosis of a simulated hurricane. Part I: Formulation and quasi-balanced flow. *J. Atmos. Sci.* 60, 1593–1607. doi:10.1175/2999.1

Weinberg, S. (1977). *The first three minutes: A modern view of the origin of the universe*. New York: Basic Books, 188.

Whitham, G. B. (1974). *Linear and nonlinear waves*. New York: John Wiley & Sons, 636.

Yue, J., Miller, S. D., Hoffmann, L., and Straka, W. C., III (2014). Stratospheric and mesospheric concentric gravity waves over tropical cyclone Mahasen: Joint AIRS and VIIRS satellite observations. *J. Atmos. Sol. Terr. Phys.* 119, 83–90. doi:10.1016/j.jastp.2014.07.003

frontiers | Frontiers in Earth Science

TYPE Original Research
PUBLISHED 05 December 2022
DOI 10.3389/feart.2022.1058262

OPEN ACCESS

EDITED BY
Eric Hendricks,
National Center for Atmospheric Research (UCAR), United States

REVIEWED BY
Tao Gao,
Institute of Atmospheric Physics, CAS, China
Kelvin T. F. Chan,
Sun Yat-sen University, China

*CORRESPONDENCE
Kosuke Ito,
itokosk@sci.u-ryukyu.ac.jp

SPECIALTY SECTION
This article was submitted to Atmospheric Science, a section of the journal Frontiers in Earth Science

RECEIVED 30 September 2022
ACCEPTED 23 November 2022
PUBLISHED 05 December 2022

CITATION
Ito K and Yamamoto R (2022), Thermodynamic and kinematic structure of tropical cyclones in the western North Pacific based on ACARS/AMDAR.
Front. Earth Sci. 10:1058262.
doi: 10.3389/feart.2022.1058262

Thermodynamic and kinematic structure of tropical cyclones in the western North Pacific based on ACARS/AMDAR

Kosuke Ito[1,2]* and Ren Yamamoto[1]

[1]Department of Physics and Earth Sciences, University of the Ryukyus, Nishihara, Japan, [2]Typhoon Science and Technology Research Center, Yokohama National University, Yokohama, Japan

Meteorological variables are often reported by commercial aircraft flying around tropical cyclones (TCs). They are archived in Aircraft Communications, Addressing, and Reporting System/Aircraft Meteorological Data Relay (ACARS/AMDAR). Therefore, they are potentially useful for constructing a composite mean structure of TCs based on *in-situ* measurements. The number of temperature and wind observations are 4.0×10^6 and 1.0×10^4 within the radius of 1,200 km and 100 km from the TC center during 2010–2020, respectively. The warm-core potential temperature anomaly with respect to the climatology is 6.4 K, 9.1 K, and 14.4 K maximized around 300 hPa for weak, moderate, and strong TCs, respectively. The composite of the potential temperature anomaly potentially extends more than 1,000 km from the TC center in the upper troposphere, cautioning the typical definition of the environment. The region of significant upper-level positive potential temperature anomalies extends broadly with increasing TC intensity. Moreover, large TCs tend to have a broad and deep upper-level warm core for a given intensity. In addition, we ensured that a single observation of potential temperature around 300 hPa could be used as a proxy for minimum sea level pressure. Low-level inflow and upper-level outflow were detected in the ACARS/AMDAR data.

KEYWORDS

warm core, tropical cyclone, aircraft, wind, temperature

1 Introduction

The structure of the temperature and wind profiles of tropical cyclones (TCs) is important for understanding them and disaster prevention. Although *in-situ* observations are preferable to describe the true structure, aircraft observation missions of TCs by the Joint Typhoon Warning Center in the western North Pacific, where strong TCs appear most frequently in the world, were terminated in 1987. Since then, several aircraft observation campaigns have been conducted for research and operation (Chan et al., 2018; D'Asaro et al., 2014; Elsberry 1990; Elsberry and Harr 2008; Hirano et al., 2022; Ito

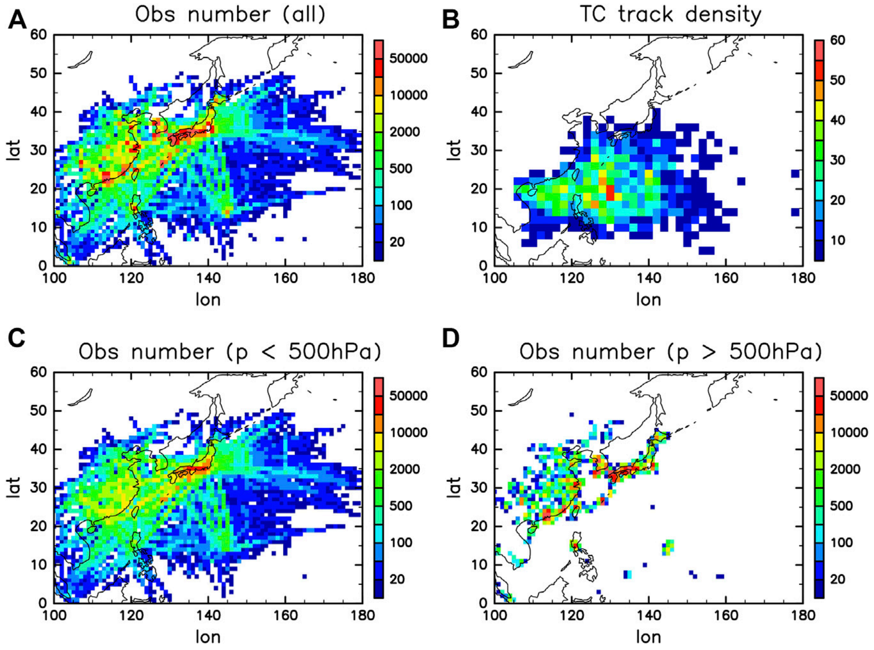

FIGURE. 1
(A) The number of the ACARS/AMDAR temperature observations within $r < 1,200$ km during 2010–2020 used in this study. **(B)** TC track density obtained from 6-hourly best track data during 2010–2020. The number of ACARS/AMDAR observations is divided into those **(C)** above 500 hPa and **(D)** below 500 hPa.

et al., 2018; Newell et al., 1996; Wu et al., 2005; Yamada et al., 2021). However, *in-situ* measurements from these campaigns are still insufficient to construct a composite mean structure of TCs in the western North Pacific. In particular, the upper-tropospheric portion of the inner core is rarely observed, except during the Tropical Cyclones-Pacific Asian Research Campaign for the Improvement of Intensity Estimations/Forecasts (T-PARCII) projects (Ito et al., 2018; Yamada et al., 2021; Hirano et al., 2022), in which dropsondes were released from 43,000 ft.

The upper-level warm core is connected with the minimum sea level pressure (MSLP) through hydrostatic balance. Therefore, the MSLP has been estimated based on upper-level temperature observations using satellite microwave sounding (Knaff et al., 2000; Oyama et al., 2016). Komaromi and Doyle (2017) inferred that the maximum wind speed ($V_{\max}$) is related to the magnitude of warm cores based on the Global Hawk AV-6 flying above 100 hPa in the Atlantic Ocean. However, in the western North Pacific, it is difficult to validate the relationship between TC intensity and warm core magnitude based on *in-situ* observations, because of the insufficient number of samples.

Commercial aircraft data are potentially useful for addressing the thermodynamic and kinematic fields based on *in-situ* measurements. Commercial aircraft sometimes fly over TCs. In addition, meteorological variables are reported and compiled as Aircraft Communications, Addressing, and Reporting System/Aircraft Meteorological Data Relay [ACARS/AMDAR; NOAA/ESRL (2011)]. It has been used to construct climatological meteorological fields (Frehlich and Sharman 2010) and in data assimilation studies (Cardinali et al., 2003). However, to the best of our knowledge, a detailed analysis of the temperature and wind fields of TCs in the western North Pacific has not been carried out with ACARS/AMDAR. In fact, as envisioned, several *in-situ* observations are available around TCs, particularly the upper air sounding. They are useful to describe the composite mean structure of TCs in the western North Pacific.

The remainder of this paper is organized as follows. Section 2 explains the data used and the methodology. Section 3 describes the climatological mean of the warm core and the wind field. Section 4 contains the concluding remarks.

2 Method

We used the ACARS/AMDAR data from 2010 to 2020. The sampling rate varied from 10 s to 30 min. The accuracy of each horizontal wind component and temperature are $\sigma_v \sim 1.25$–$1.5\ \mathrm{ms}^{-1}$ and $\sigma_T \sim 0.5$ K, respectively (Benjamin et al., 1999; Drüe et al., 2008). When the icing condition is suggested by a quality control flag, the data were not utilized. In addition, the data were not used when the horizontal position, pressure height, time consistency, and physical variables did not pass quality control. The pressure altitude was converted to pressure, using a standard atmosphere.

The TC center position, intensity, and size refer to the 6-hourly best track data from the Regional Specialized Meteorological Center (RSMC) Tokyo–Typhoon Center of the Japan Meteorological Agency (JMA). The RSMC Tokyo best track data were not considered before the TC reached the threshold of tropical storm status or an extratropical cyclone subjected to transition from the TC. The best track data were linearly interpolated in time to match the observation time of ACARS/AMDAR. To plot a figure in radius-pressure coordinates, we grouped the data into bins with radial and pressure intervals of 50 km and 50 hPa, respectively. When the number of observations is less than 10 in each grid, the composite mean was not shown.

Figure 1A displays the number of temperature observations that were used within 1,200 km from the TC center (hereafter represented as $r < 1{,}200$ km) in the western North Pacific. The total number was approximately 4.0×10^6. As expected, several data were obtained around the major airports in Japan, China, Korea, the Philippines, the Guam, and the flight routes connecting them. Thus, the data density during 2010–2020 was higher in the north, as compared to the TC track density in the western North Pacific based on 6-hourly RSMC Tokyo best track records of TC center locations (Figure 1B). Upper-tropospheric conditions (above 500 hPa) were sufficiently observed over land, the East China Sea, the South China Sea, the northwestern portion of the western North Pacific, and the region between Japan and Guam (Figure 1C). Below 500 hPa, observations were limited to land or coastal regions (Figure 1D). This reflects that the cruise altitude is higher for a long flight over the ocean and the marginal seas.

Figure 2 displays the observation density at each pressure level and radius from the TC center. The observation density peaked at 200–300 hPa, 500–700 hPa, and near the surface. These presumably correspond to the cruising altitudes of aircraft and departure/landings. The number of observations within $r < 100$ km was approximately 1.0×10^4. The large number of observations in the upper troposphere enabled analysis of the warm core magnitude and structure. To check the difference in the temperature and wind speed among different intensities, we divided the data according to $V_{\max}$ into three groups that roughly contained a similar number of samples: $V_{\max} < 25\ \mathrm{ms}^{-1}$, $25\ \mathrm{ms}^{-1} \leq V_{\max} < 33\ \mathrm{ms}^{-1}$, and $V_{\max} \geq 33\ \mathrm{ms}^{-1}$ (Figures 2B–D). These values correspond to the categories of tropical storms, strong tropical storms, and typhoons (including very strong typhoons and violent typhoons), respectively, used by JMA. For representation, we refer to these categories as weak, moderate, and strong TCs, respectively. The number of observations of the inner core in the low- and middle-troposphere is quite rare for strong TCs, probably because of aviation safety reasons. Nevertheless, more than 200 observations are available at 200–300 hPa within $r < 100$ km, even for strong TCs; thus, they can be used as important *in-situ* observations. Notably, many observations were available in the upper to lower troposphere for $r = 100$–$1{,}000$ km from the center of strong TCs.

The warm core is defined as the temperature or potential temperature deviation with respect to the reference temperature. Typically, the reference temperature using the average within $r < 1{,}000$ km or a few hundred kilometers is implemented. However, the magnitude of the warm core depends on the choice of reference temperature (Durden 2013; Stern and Zhang 2016; Yamada et al., 2021). In this study, we employed the temperature and potential temperature anomaly with respect to the climatology for a given longitude, latitude, pressure, and pentad day of the year as a reference state. This clarifies the composite mean difference from that of the ordinary state. This approach is not compatible for the case study of a single TC, but it clarifies the impact of TCs and the favorable conditions for TC development. The climatology was constructed based on the 11-years (2010–2020) averaged ACARS/AMDAR data. The temperature and potential temperature anomalies obtained using these climatological values were represented as follows:

$$\delta T_{clim} \equiv T - \overline{T_{clim}} \tag{1}$$

$$\delta \theta_{clim} \equiv \theta - \overline{\theta_{clim}} \tag{2}$$

where T and θ are the observed temperature and potential temperature in ACARS/AMDAR, respectively, $\overline{T_{clim}}$ and $\overline{\theta_{clim}}$ are the climatological mean temperature and potential temperature for the same longitude, latitude, pressure, and pentad-day of the year based on the climatology, and δT_{clim} and $\delta\theta_{clim}$ are temperature and potential temperature anomalies, respectively, with respect to the climatology. We show the composite mean of anomalies, $\langle \delta T_{clim} \rangle$ and $\langle \delta\theta_{clim} \rangle$, where an angle bracket indicates the composite mean.

For comparison, we further calculated the temperature and potential temperature anomalies with a reference state averaged over the region between the rings of 800–1,200 km (hereafter, a 1,000 km ring for simplicity).

$$\langle \delta T_{1000} \rangle \equiv \langle T \rangle - \langle T_{1000} \rangle \tag{3}$$

$$\langle \delta \theta_{1000} \rangle \equiv \langle \theta \rangle - \langle \theta_{1000} \rangle \tag{4}$$

where $\langle T_{1000} \rangle$ and $\langle \theta_{1000} \rangle$ are the composite means of the temperature and potential temperatures for a 1000-km ring based on the ACARS/AMDAR. $\langle \delta T_{1000} \rangle$ and $\langle \delta\theta_{1000} \rangle$ represent the composite mean with respect to the environment.

3 Result

3.1 Potential temperature field

Figure 3 shows the composite mean of the temperature, potential temperature and their anomalies throughout the

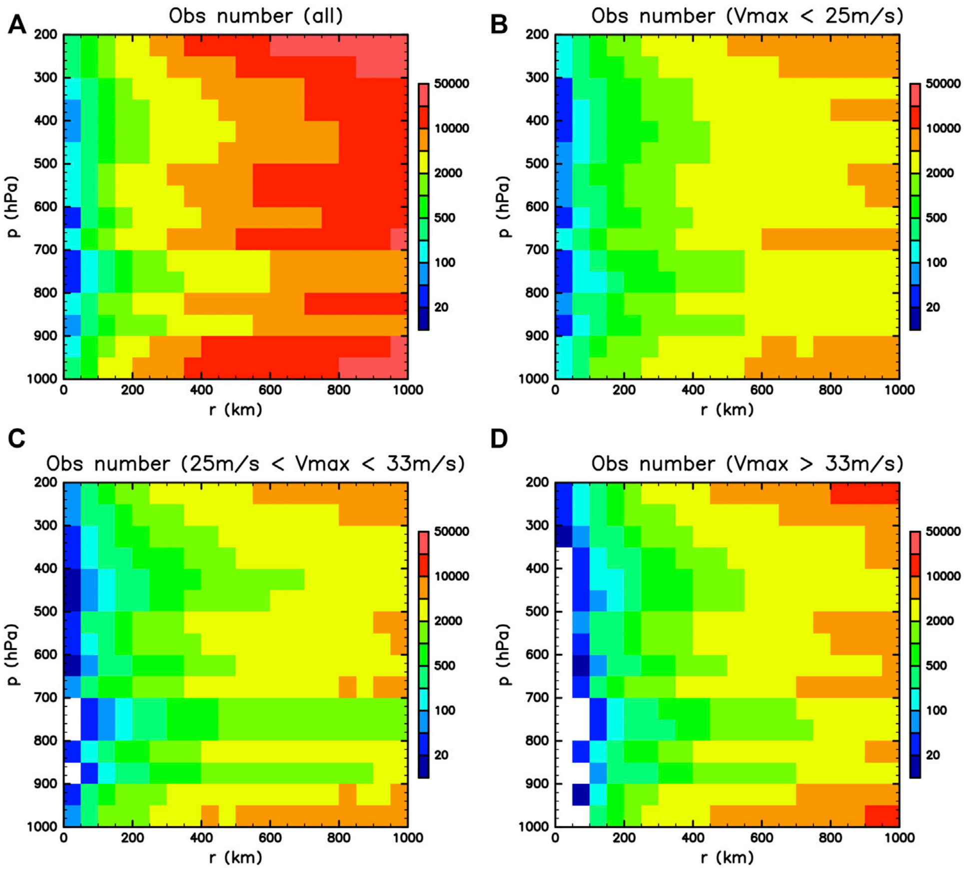

FIGURE. 2
(A) The number of the ACARS/AMDAR temperature observations during 2010–2020 used in this study in a radius-pressure coordinate. The observations are classified according to the maximum wind speed: **(B)** $V_{max} < 25$ ms^{-1}, **(C)** 25 ms^{-1} < V_{max} < 33 ms^{-1}, and **(D)** $V_{max} > 33$ ms^{-1}.

observations. The contours of the temperature and potential temperature in the inner core region indicate the warm core of TCs in the upper-troposphere (200–400 hPa) (Figures 3A,B). The maximum composite mean temperature and potential temperature anomaly with respect to the climatology (1,000 km ring) is 6.0 K and 8.4 K (4.6 K and 7.1 K) within $r < 50$ km in the upper troposphere, respectively (Figures 3C–F). Strictly speaking, it is not the composite mean of the warm core magnitude of TCs, because the pressure level of the maximum temperature anomaly may differ depending on each TC. Nevertheless, the current result suggests that the composite mean warming is maximized around 300 hPa, and it can be used as a reference value for the warm core magnitude. The lower warm cores described by Stern and Nolan (2012) were not clearly observed in the current composite analysis. However, the temperature and potential temperature anomalies in the inner core region were weakly positive in the lower troposphere. The negative potential temperature anomaly around the surface represents cold air. Considering that low-level observations were mostly obtained over land, the results should be carefully interpreted. Presumably this is due to cold pool or evaporation over the land.

The potential temperature anomaly more than 2.0 K with respect to climatology extends to more than 1,000 km in the upper troposphere (Figure 3D). This differs from the lower tropospheric warm anomaly, which is limited to a narrow region. The broad temperature and potential temperature anomaly in the upper troposphere is beyond 1,000 km, which is typically used as the definition of “environmental region”. Thus, if one defines a reference temperature with respect to the 1,000 km ring or less, one underestimates the warming influence of a TC in the upper troposphere. Temperature and potential temperature anomalies are negative above 200 hPa in the outer region. One possible explanation might be that the cold tropopause (relative to climatology) is favorable for TC development through the mechanism of wind-induced surface heat exchange (Emanuel 1986; Emanuel 2012).

To check the influence of reference states, Figures 3E,F shows the temperature and potential temperature anomalies with respect to values at the 1,000 km radius. The structures of the

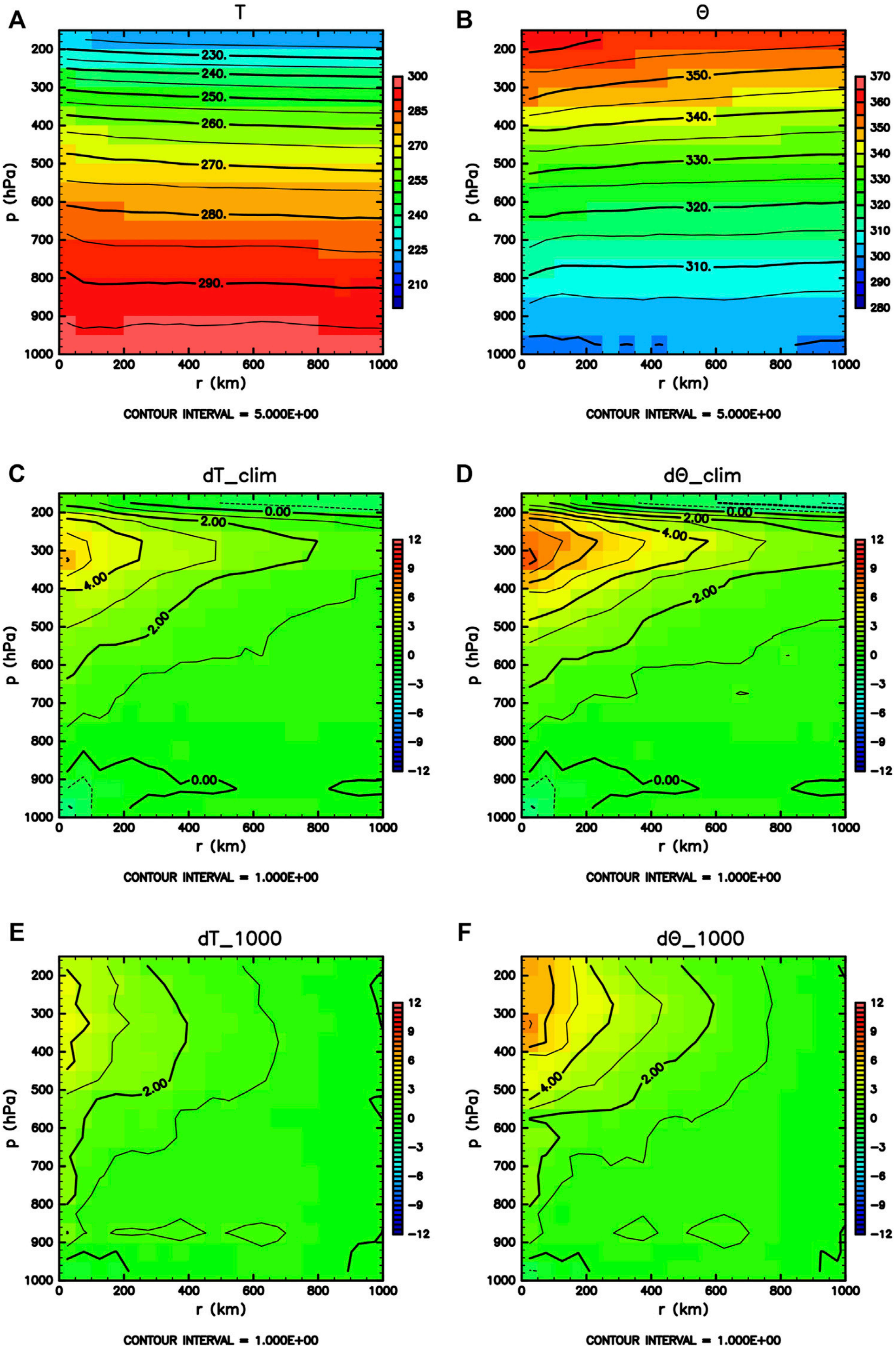

FIGURE. 3
Composite of **(A)** T, **(B)** θ, **(C)** δT_{clim}, **(D)** $\delta\theta_{clim}$, **(E)** δT_{1000}, and **(F)** $\delta\theta_{1000}$ in a radial-pressure coordinate.

temperature and potential temperature anomalies are basically similar to those with respect to climatology. However, the warm anomaly is weaker in the upper troposphere and is confined within several hundred kilometers. As for the anomaly with respect to the 1,000 km ring, notable, most observations were obtained in the mid-latitudes where the meridional temperature

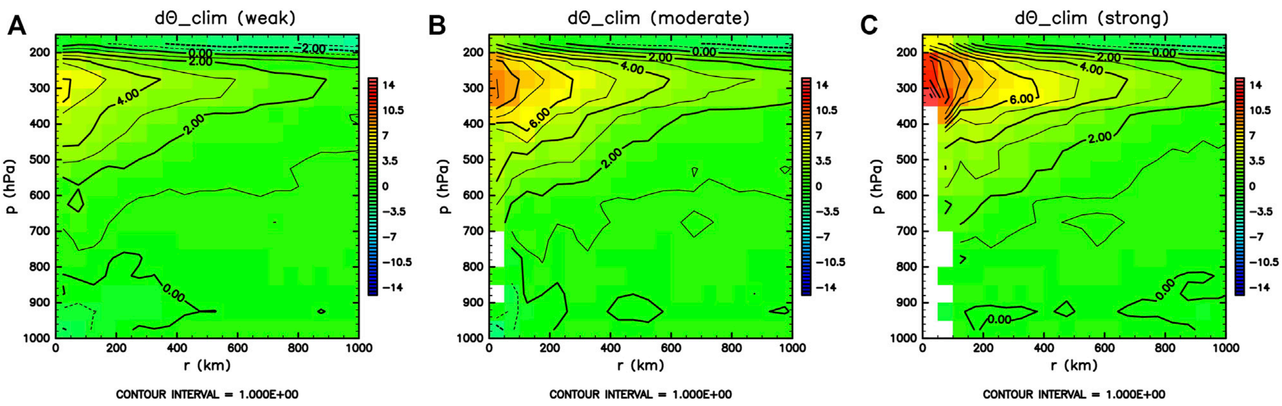

FIGURE. 4
$\delta\theta_{clim}$ in radial-pressure coordinates for **(A)** $V_{\max} < 25$ ms^{-1}, **(B)** 25 ms^{-1} < $V_{\max} < 33$ ms^{-1}, and **(C)** $V_{\max} > 33$ ms^{-1}.

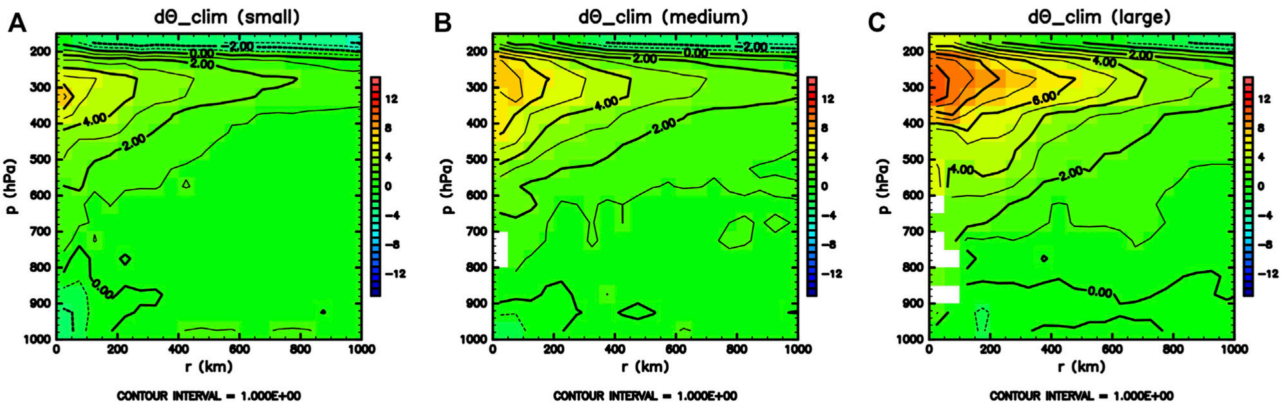

FIGURE. 5
$\delta\theta_{clim}$ in a radial-pressure coordinate for **(A)** $R_{15} < 270$ km, **(B)** 270 km < $R_{15} < 390$ km, and **(C)** $R_{15} > 390$ km. Note that we use the cases particularly with 25 ms^{-1} < $V_{\max} < 33$ ms^{-1}.

gradient was large. Currently, the climatological-mean temperature at the center is colder than that at the 1,000 km ring by approximately 2 K in the lower troposphere and 0.5 K in the upper troposphere (figures not shown). This affects the difference in anomalies with different references.

The magnitude of the maximum warm potential temperature anomaly with respect to the climatology in the TC centers depends on the TC intensity (Figure 4). The anomaly is 6.4 K, 9.1 K, and 14.4 K for weak, moderate, and strong TCs, respectively. The region of warm air extends away from the TC center above 500 hPa with increasing intensity. The pressure level of the core magnitude of the warm anomaly does not depend on TC intensity. However, the warm anomaly region at the TC center became deeper for the stronger TCs.

By grouping the potential temperature anomalies from the moderate TCs (25 ms^{-1} < $V_{\max} < 33$ ms^{-1}) by size defined as a radius of 15 ms^{-1} wind (R_{15}) in the best track, the depth and radius of the upper warm anomaly varied. Figure 5 shows that small TCs yield radially small and shallow upper-tropospheric warming. By contrast, large TCs yield a radially large and deep upper-tropospheric warming. We also found that the maximum of composite mean of potential temperature anomaly is stronger for large TCs (7.3 K, 7.8 K, and 10.8 K for small, medium, and large TCs, respectively). Therefore, the magnitude of the warm core was stronger for larger TCs. We consider the radial integration of the pressure gradient term in gradient wind balance to explain this.

$$p_c = -\int_{r_c}^{r_{env}} \rho\left(\frac{v^2}{r} + fv\right)dr + p_{env} \tag{5}$$

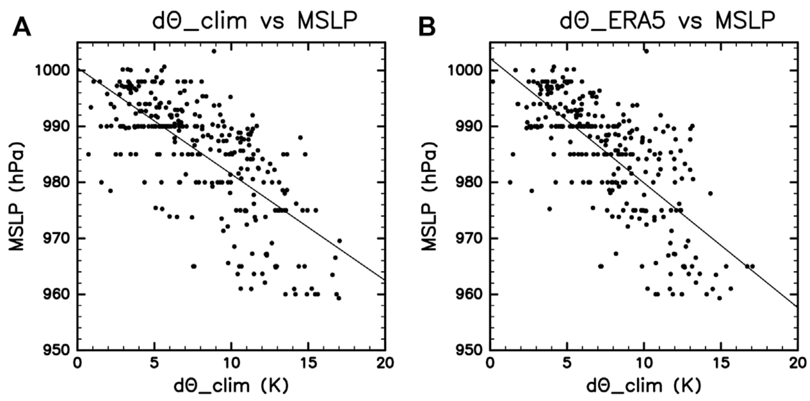

FIGURE. 6
The relationship between MSLP in the best track and potential temperature anomaly in 250–350 hPa within $r < 50$ km with respect to **(A)** climatology and **(B)** ERA5. The regression line is overplotted.

where p_c is the sea-level pressure at the radius of interest (including MSLP), v is the tangential wind, ρ is the air density, f is the Coriolis parameter, subscripts c and env are the radius of interest and environment. Eq. 5 states that the radially integrated tangential wind is related to a deficit of pressure, and thus a large R_{15} indicates a low pressure at the radius of interest for the given $V_{\max}$. It leads vertically deep and intense warm core in a large TC because a low pressure is connected to vertically integrated density through hydrostatic balance.

Therefore, the vertical profile of the potential temperature is highly relevant to the MSLP. However, it is not clear whether a single-level observation observed by aircraft can be used as a proxy for the MSLP. Figure 6A shows the relationship between the potential temperature anomaly with respect to the climatology at 250–350 hPa within $r < 50$ km, where the composite mean exhibited the maximum value (Figure 3), and MSLP in the best track. The increasing potential temperature anomaly was clearly associated with a decrease in the MSLP. The simple linear regression yields the MSLP (hPa) as shown below:

$$\text{MSLP} = -1.900\delta\theta_{clim} + 1000.475 \tag{6}$$

The root mean square difference (RMSD) between this simple statistical model and the best track was 7.33 hPa, which is comparable to, or smaller than the uncertainties in the best track and other techniques (Hoshino and Nakazawa 2007; Nakazawa and Hoshino 2009; Shimada et al., 2016; Ito et al., 2018; Higa et al., 2021). Although $\delta\theta_{1000}$ is difficult to calculate for individual case because aircrafts does not densely observe the whole region between rings of 800 km and 1,200 km in most cases, we can calculate the potential temperature anomaly with respect to the corresponding region based on the ERA5 reanalysis by European Centre for Medium-Range Weather Forecasts (Hersbach et al., 2020). The comparison between MSLP and the potential temperature anomaly with respect to ERA5 reanalysis is shown in Figure 6B, and the simple linear regression yields the MSLP (hPa) as follows:

$$\text{MSLP} = -2.227\delta\theta_{clim} + 1002.155 \tag{7}$$

with the RMSD of 7.20 hPa. In other words, a single commercial aircraft observation flying over a TC is beneficial for estimating the MSLP of TCs through Eqs. 6, 7, while we should be prudent to apply these equations to very strong TCs whose MSLP is lower than 960 hPa because the samples were rarely taken. It supports the validity of methodologies that use satellite-derived potential temperature anomalies for TC intensity estimation.

3.2 Wind field

Figure 7 shows the composite mean of the radial and tangential wind in radial-pressure coordinates. The depth of the strong cyclonic wind ranges from the lower troposphere to the upper troposphere for strong TCs. However, cyclonic wind is observed only in the middle and lower troposphere for weak TCs. In the main cruising altitudes for a longer flight (200–300 hPa), the composite-mean wind speed is much weaker than in the lower troposphere, while there is a chance that strong turbulence exists. Anticyclonic circulation was observed in the outer upper troposphere. This anticyclonic circulation became stronger with increasing TC intensity. The composite mean of the tangential wind was maximized at approximately 800 hPa. The corresponding height was higher than that observed (500–1,000 m) in dropsondes in the Atlantic Ocean (Powell et al., 2003). This might be because ACARS/AMDAR observations in the lower troposphere are mostly obtained over land, where the surface friction is very strong.

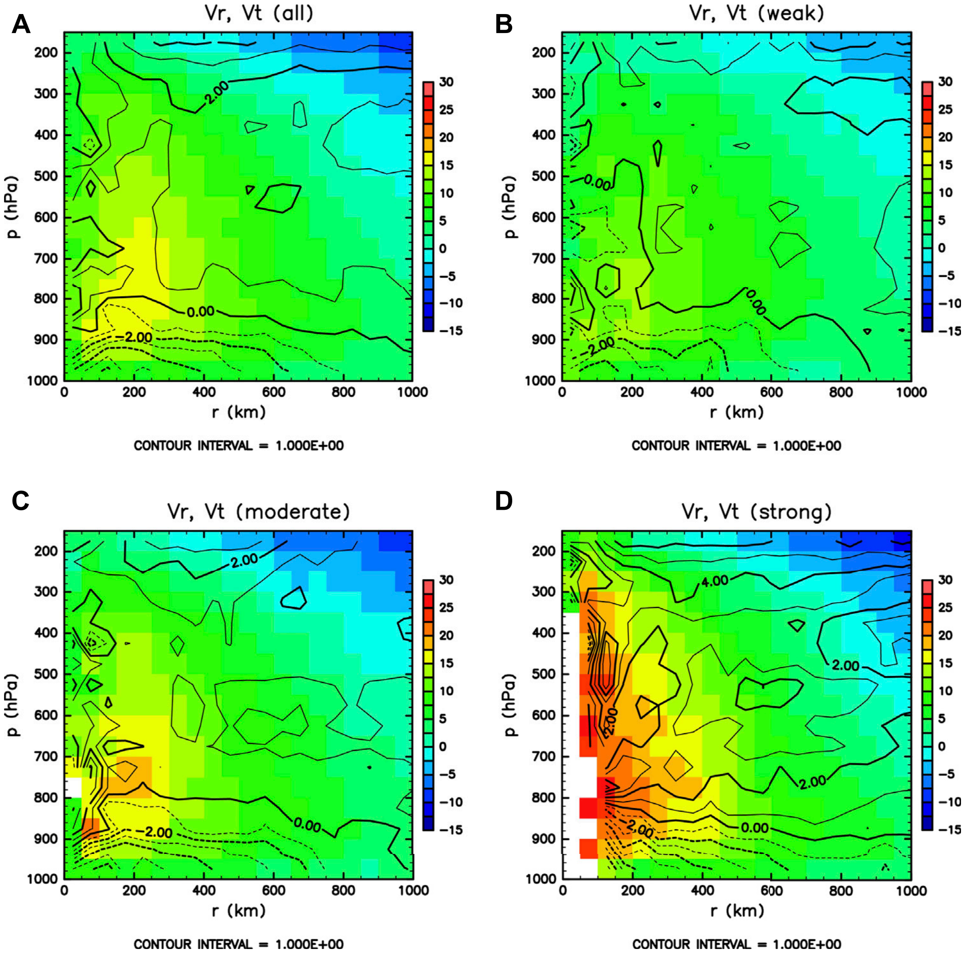

FIGURE. 7
The radial velocity (contour) and tangential velocity (shade) in a radial-pressure coordinate for **(A)** all TCs, **(B)** $V_{max} < 25$ ms^{-1}, **(C)** 25 ms$^{-1} < V_{max} <$ 33 ms^{-1}, and **(D)** $V_{max} > 33$ ms^{-1}.

The radial wind profile indicates that low-level inflow and upper-level outflow can be clearly detected based on ACARS/AMDAR observations below 850 hPa and above 300 hPa, respectively. With increasing intensity, the inflow and outflow regions were larger. A low-level inflow of more than 1 ms^{-1} was observed within 600 km for weak TCs, whereas it was 1,000 km for strong TCs. The outflow became stronger with decreasing pressure, whereas the core of the outflow might be located above 200 hPa. Upper-level outflow was clearly observed above 300 hPa for strong TCs. The outflow was discernible beyond $r = 1{,}000$ km, supporting the idea that positive $\langle \delta T_{clim} \rangle$ and $\langle \delta \theta_{clim} \rangle$ stem from the TCs.

The composite mean of absolute angular momentum (AAM) for each intensity category is shown in Figure 8. A relatively larger AAM is advected close to the TC center for strong TCs. As the AAM is nearly conserved except for the frictional loss at the surface and mixing around the tropopause (Hioki and Tsuboki 2021), the slantwise tilt of the constant AAM and radial gradient of radial wind indicate upward motion at 200 hPa even for weak TCs. In addition, the core height of the outflow is thought to be above 200 hPa. This core height is as high as observed in the Atlantic (Komaromi and Doyle 2017) or higher. The slope becomes flatter for strong TCs, implying that the upward air parcel experiences more outward motion. The calculus for an axisymmetric balanced vortex yields the slope along the constant AAM surface as follows:

$$\left(\frac{\partial z}{\partial r}\right)_{AAM} = \frac{(f+\zeta)(f+2v/r)}{-(g/\theta)(\partial\theta/\partial r)} \tag{8}$$

where f is the Coriolis parameter, ζ is the vorticity, v is the tangential velocity, and g is the gravitational constant. Thus, it is the inertial stability divided by baroclinicity. In this case, inertical stability is strong for strong TCs. In other words, the

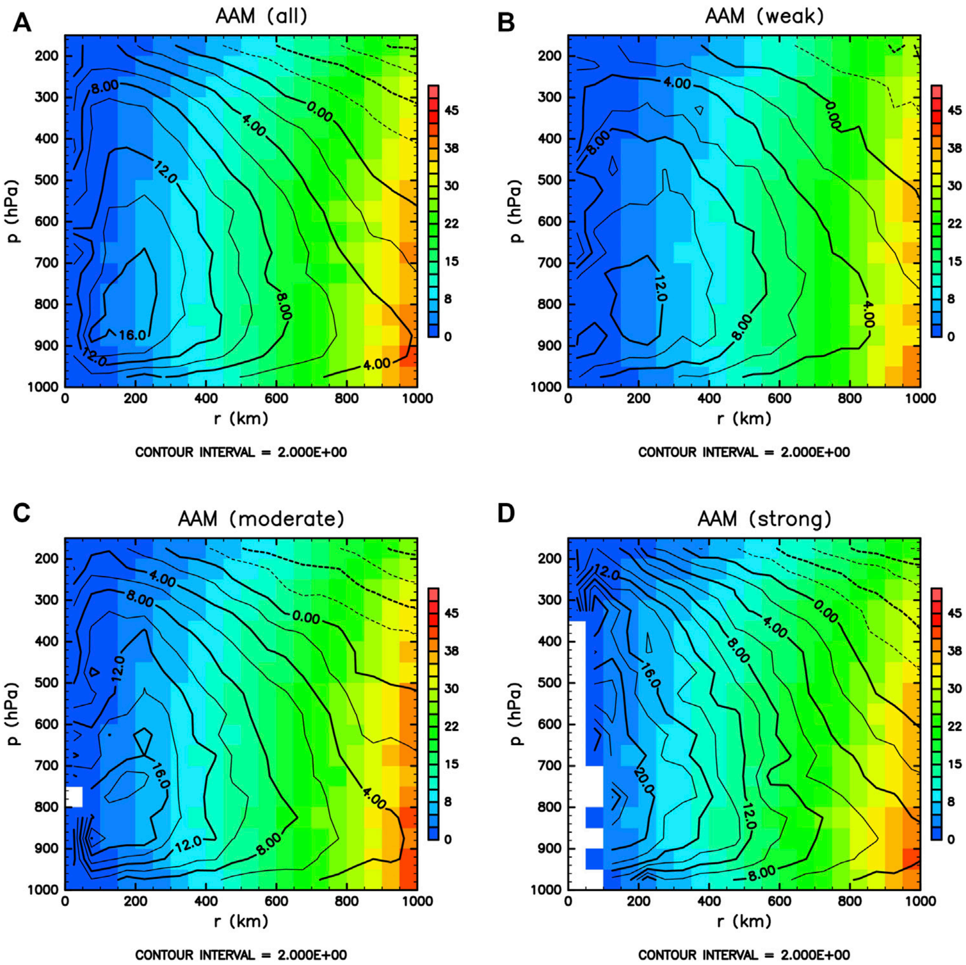

FIGURE. 8
AAM (x 10^6 m^2s^{-1}; color shadings) in a radial-pressure coordinate overplotted by the tangential wind (contours) for **(A)** all TCs, **(B)** weak TCs, **(C)** moderate TCs, and **(D)** strong TCs.

flat structure (smaller $(\partial z/\partial r)_{AAM}$) can be attributed to the strong potential temperature gradient of strong TCs (Figure 4C).

4 Concluding remarks

In-situ observations of TCs are very important for describing the true TC structure. Moreover, it has long been believed that such observations have become rare in the western North Pacific since 1987. The current study reveals that meteorological variables reported and archived in the ACARS/AMDAR are beneficial for several purposes. Due to the large number of observations, they are sufficient to construct the mean vertical-pressure cross section of potential temperature and wind fields, particularly for upper tropospheric conditions and weak-to-moderate TCs.

The well-known basic structures are reproduced in our composite analysis: Upper-level warm core, inflow in the lower troposphere, outflow in the upper troposphere, and slantwise upward motion. Several important findings have been produced in this study are summarized as follows. First, the upper-level warm potential temperature anomaly can be extended more than 1,000 km away from the center of the TCs, with respect to the climatology. It cautions a typical definition of a warm temperature anomaly from the environment, represented as a 1,000 km ring or less. Second, a large TC tends to have a deep and strong upper-level warm core for a given maximum wind speed. It is reasonable that a large TC for the given maximum wind speed has a low MSLP through gradient wind balance and that the low MSLP is connected to the vertically integrated thermodynamic property. Third, the peak pressure level of the potential temperature anomaly did not depend on the intensity. In addition, the core of the outflow was expected to be above 200 hPa, considering the AAM surface and weak radial wind at 200 hPa. Another contribution of this work is to provide the usefulness of potential temperature anomaly as a proxy for MSLP based on the *in-situ* observations.

Although the current study demonstrates the advantages of ACARS/AMDAR data for constructing the composite mean of the TC structure, few sections must be interpreted with caution. Low- and middle-tropospheric observations were mostly obtained over land. Therefore, it does not entirely represent the characteristics of TCs in the western North Pacific. In addition, the middle-to-low troposphere of the inner core is rarely observed for strong TCs. For this purpose, coordinated aircraft campaigns that penetrate the eyewalls of strong TCs such as T-PARCII are considered powerful in the western North Pacific.

Data availability statement

The original contributions presented in the study are included in the article/supplementary material, further inquiries can be directed to the corresponding author.

Author contributions

KI designed the study, discussed the results, and wrote the manuscript. RY performed the data analysis.

Funding

This research was supported by JST Moonshot R&D Grant Number JPMJMS2282 and MEXT KAKENHI Grant JP21H04992, JP21K03657, and JP18H01283.

Acknowledgments

We would like to thank NCAR/EOL for providing the data under the sponsorship of the National Science Foundation https://data.eol.ucar.edu/.

Conflict of interest

The authors declare that the research was conducted in the absence of any commercial or financial relationships that could be construed as a potential conflict of interest.

Publisher's note

References

Benjamin, S. G., Schwartz, B. E., and Cole, R. E. (1999). Accuracy of ACARS wind and temperature observations determined by collocation. *Wea. Forecast.* 14, 1032–1038. doi:10.1175/1520-0434(1999)014<1032:aoawat>2.0.co;2

Cardinali, C., Isaksen, L., and Andersson, E. (2003). Use and impact of automated aircraft data in a global 4DVAR data assimilation system. *Mon. Weather Rev.* 131, 1865–1877. doi:10.1175//2569.1

Chan, P., Wu, N., Zhang, C., Deng, W., and Hon, K. (2018). The first complete dropsonde observation of a tropical cyclone over the South China Sea by the Hong Kong Observatory. *Weather* 73, 227–234. doi:10.1002/wea.3095

D'Asaro, E., Black, P., Centurioni, L. R., Chang, Y-T., Chen, S., Foster, R. C., et al. (2014). Impact of typhoons on the ocean in the Pacific. *Bull. Amer. Meteor. Soc.* 95, 1405–1418.

Drüe, C., Frey, W., Hoff, A., and Hauf, T. (2008). Aircraft type-specific errors in AMDAR weather reports from commercial aircraft. *Q. J. R. Meteorol. Soc.* 134, 229–239. doi:10.1002/qj.205

Durden, S. L. (2013). Observed tropical cyclone eye thermal anomaly profiles extending above 300 hPa. *Mon. Weather Rev.* 141, 4256–4268. doi:10.1175/mwr-d-13-00021.1

Elsberry, R. L., and Harr, P. A. (2008). Tropical cyclone structure (TCS08) field experiment science basis, observational platforms, and strategy. *Asia-Pacific J. Atmos. Sci.* 44, 209–231.

Elsberry, R. L. (1990). International experiments to study tropical cyclones in the Western North Pacific. *Bull. Amer. Meteor. Soc.* 71, 1305–1316. doi:10.1175/1520-0477(1990)071<1305:ietstc>2.0.co;2

Emanuel, K. A. (1986). An air-sea interaction theory for tropical cyclones. Part I: Steady-state maintenance. *J. Atmos. Sci.* 43, 585–605. doi:10.1175/1520-0469(1986)043<0585:aasitf>2.0.co;2

Emanuel, K. (2012). Self-stratification of tropical cyclone outflow. Part II: Implications for storm intensification. *J. Atmos. Sci.* 69, 988–996. doi:10.1175/jas-d-11-0177.1

Frehlich, R., and Sharman, R. (2010). Climatology of velocity and temperature turbulence statistics determined from rawinsonde and ACARS/AMDAR data. *J. Appl. Meteorology Climatol.* 49, 1149–1169. doi:10.1175/2010jamc2196.1

Hersbach, H., Bell, B., Berrisford, P., Hirahara, S., Horányi, A., Muñoz-Sabater, J., et al. (2020). The ERA5 global reanalysis. *Quart. J. Roy. Meteor. Soc.* 146, 1999–2049.

Higa, M., Tanahara, S., Adachi, Y., Ishiki, N., Nakama, S., Yamada, H., et al. (2021). Domain knowledge integration into deep learning for typhoon intensity classification. *Sci. Rep.* 11, 1–10. doi:10.1038/s41598-021-92286-w

Hioki, T., and Tsuboki, K. (2021). Trajectory analyses on the warm core development and pressure falls of a developing typhoon as simulated by a cloud-resolving model. *J. Meteorological Soc. Jpn.* 99, 064–1350. doi:10.2151/jmsj.2021-064

Hirano, S., Ito, K., Yamada, H., Tsujino, S., Tsuboki, K., and Wu, C.-C. (2022). Deep eye clouds in tropical cyclone trami (2018) during T-PARCII dropsonde observations. *J. Atmos. Sci.* 79, 683–703. doi:10.1175/jas-d-21-0192.1

Hoshino, S., and Nakazawa, T. (2007). Estimation of tropical cyclone's intensity using TRMM/TMI brightness temperature data. *J. Meteorological Soc. Jpn.* 85, 437–454. doi:10.2151/jmsj.85.437

Ito, K., Yamada, H., Yamaguchi, M., Nakazawa, T., Nagahama, N., Shimizu, K., et al. (2018). Analysis and forecast using dropsonde data from the inner-core region of Tropical Cyclone Lan (2017) obtained during the first aircraft missions of T-PARCII. *SOLA* 14, 105–110. doi:10.2151/sola.2018-018

Knaff, J. A., Zehr, R. M., Goldberg, M. D., and Kidder, S. Q. (2000). An example of temperature structure differences in two cyclone systems derived from the

Advanced Microwave Sounder Unit. *Wea. Forecast.* 15, 476–483. doi:10.1175/1520-0434(2000)015<0476:aeotsd>2.0.co;2

Komaromi, W. A., and Doyle, J. D. (2017). Tropical cyclone outflow and warm core structure as revealed by HS3 dropsonde data. *Mon. Weather Rev.* 145, 1339–1359. doi:10.1175/mwr-d-16-0172.1

Nakazawa, T., and Hoshino, S. (2009). Intercomparison of Dvorak parameters in the tropical cyclone datasets over the Western North Pacific. *SOLA* 5, 33–36. doi:10.2151/sola.2009-009

Newell, R., Hu, W., Wu, Z. X., Zhu, Y., Akimoto, H., Anderson, B. E., et al. (1996). Atmospheric sampling of supertyphoon mireille with NASA DC-8 aircraft on september 27, 1991, during PEM-west A. *J. Geophys. Res.* 101, 1853–1871. doi:10.1029/95jd01374

NOAA/ESRL, 2011: Aircraft meteorological data reports (AMDAR) and aircraft Communications addressing and reporting system (ACARS) data. Version 1.0. UCAR/NCAR - Earth Observing Laboratory.

Oyama, R., Nagata, K., Kawada, H., and Koide, N. (2016). *Development of a product based on consensus between Dvorak and AMSU tropical cyclone central pressure estimates at JMA*, 18. JMA: RSMC Tokyo-Typhoon Center Technical Review

Powell, M. D., Vickery, P. J., and Reinhold, T. A. (2003). Reduced drag coefficient for high wind speeds in tropical cyclones. *Nature* 422, 279–283. doi:10.1038/nature01481

Shimada, U., Sawada, M., and Yamada, H. (2016). Evaluation of the accuracy and utility of tropical cyclone intensity estimation using single ground-based Doppler radar observations. *Mon. Wea. Rev.* 144, 1823–1840. doi:10.1175/mwr-d-15-0254.1

Stern, D. P., and Nolan, D. S. (2012). On the height of the warm core in tropical cyclones. *J. Atmos. Sci.* 69, 1657–1680. doi:10.1175/jas-d-11-010.1

Stern, D. P., and Zhang, F. (2016). The warm-core structure of Hurricane Earl (2010). *J. Atmos. Sci.* 73, 3305–3328. doi:10.1175/jas-d-15-0328.1

Wu, C.-C., Lin, P-H., Aberson, S., Yeh, T-C., Huang, W-P., Chou, K-H., et al. (2005). Dropwindsonde observations for typhoon surveillance near the taiwan region (DOTSTAR) an overview. *Bull. Amer. Meteor. Soc.* 86, 787–790.

Yamada, H., Ito, K., Tsuboki, K., Shinoda, T., Ohigashi, T., Yamaguchi, M., et al. (2021). The double warm-core structure of Typhoon Lan (2017) as observed through the first Japanese eyewall-penetrating aircraft reconnaissance. *J. Meteorological Soc. Jpn.* 99, 063–1327. Ser. II. doi:10.2151/jmsj.2021-063

frontiers | Frontiers in Earth Science

TYPE Original Research
PUBLISHED 12 December 2022
DOI 10.3389/feart.2022.1082181

OPEN ACCESS

EDITED BY
Haishan Chen,
Nanjing University of Information
Science and Technology, China

REVIEWED BY
Si Gao,
Sun Yat-sen University, China
Jia Liang,
Nanjing University of Information
Science and Technology, China

*CORRESPONDENCE
Yuqing Wang,
✉ yuqing@hawaii.edu

SPECIALTY SECTION
This article was submitted to
Atmospheric Science,
a section of the journal
Frontiers in Earth Science

RECEIVED 27 October 2022
ACCEPTED 01 December 2022
PUBLISHED 12 December 2022

CITATION
Han W, Wang Y and Liu L (2022), The
relationship between pre-landfall
intensity change and post-landfall
weakening of tropical cyclones
over China.
Front. Earth Sci. 10:1082181.
doi: 10.3389/feart.2022.1082181

The relationship between pre-landfall intensity change and post-landfall weakening of tropical cyclones over China

Wenjun Han[1,2], Yuqing Wang[3]* and Lu Liu[1]

[1]State Key Laboratory of Severe Weather, Chinese Academy of Meteorological Sciences, China Meteorological Administration, Beijing, China, [2]College of Earth and Planetary Sciences, University of Chinese Academy of Sciences, Beijing, China, [3]International Pacific Research Center and Department of Atmospheric Sciences, School of Ocean and Earth Science and Technology, University of Hawaii at Manoa, Honolulu, HI, United States

The accurate prediction of the weakening of landfalling tropical cyclones (TC) is of great importance to the disaster prevention but is still challenging. In this study, based on the 6-hourly TC best-track data and global reanalysis data, the relationship between the intensity change prior to landfall of TCs and the energy dissipation rate after landfall over mainland China is statistically analyzed, and the difference between East and South China is compared. Results show that TCs making landfall over East China often experienced pre-landfall weakening and usually corresponded to a rapid decay after landfall, while most TCs making landfall over South China intensified prior to landfall and weakened slowly after landfall. The key factors affecting both pre-landfall intensity change and post-landfall energy dissipation rate are quantitatively analyzed. It is found that the decreasing sea surface temperature (SST), increasing SST gradient, and increasing environmental vertical wind shear are the major factors favoring high pre-landfall weakening occurrence, leading to rapid TC weakening after landfall over East China. In South China, changes in the large-scale environmental factors are relatively small and contribute little to the post-landfall weakening rate.

KEYWORDS

landfalling tropical cyclones, intensity change, post-landfall weakening rate, large-scale environmental factors, statistical analysis

Introduction

Landfalling tropical cyclones (LTCs), especially those weakening slowly after landfall, seriously threaten to our life and property (Klotzbach et al., 2018). LTCs caused annual deaths of 472 and annual economic loss of 28.7 billion RMB in China during 1983–2006 (Zhang et al., 2009). Typhoon Nina (7503) triggered a disastrous dam collapse in the inland province of Henan in 1975, which led to flood spread to more than 1 million hectares of farmland in 29 counties and cities and eventually caused a total economic loss of about 10 billion RMB (Liu et al., 2009). Therefore, it is important but challenging for accurate prediction of LTC intensity and thus for disaster prevention because of dramatically changes in tropical cyclone (TC) structure and intensity (Elsberry and Tsai, 2014). From a social and economic point of view, it is also very important to accurately predict the regional changes in the intensity of LTCs (Walsh et al., 2016).

The weakening of TCs after landfall is driven by many factors, including LTC intensity (Tuleya et al., 1984), land-atmosphere interaction (Andersen et al., 2013; Andersen and Shepherd, 2014), and topographic effect (Done et al., 2020). The sudden reduction of surface enthalpy source and the increase of surface roughness would lead to weakening of the eyewall convection and the decrease of surface wind speed, and thus the filling of a TC over land (Miller, 1964; Ooyama, 1969; Powell et al., 1991; Tuleya, 1994). Li and Chakraborty. (2020) statistically analyzed the TCs making landfall over the North Atlantic in recent fifty years and found that the increasing sea surface temperature (SST) increases the moisture stored in TCs during its passage over the coastal ocean, which can supply extra enthalpy source and help maintain warm-core structure and thus the intensity of TCs after landfall. However, some other studies have found that the SST may not be a major factor determining the weakening rate of LTCs over the western North Pacific (Chen et al., 2021). In addition, the influence of large-scale environmental conditions on LTC weakening cannot be ignored. Wood and E Ritchie (2015) studied the rapid weakening events of TCs in the North Atlantic and eastern North Pacific during 1982–2013. Their results showed that the strong SST gradient and the contribution by dry air intrusion induced more rapid weakening events in the eastern North Pacific than in the North Atlantic. The increase in coastal SST, land surface temperature and soil moisture, the decrease in low-level vertical wind shear (VWS), and the increase in upper-level divergence are all favorable for intensification of TCs and their survival after landfall (Jiang, 1989; Wang et al., 2015; Liang et al., 2016; Liu et al., 2020). Previous studies have qualitatively examined how environmental factors affect the weakening of TCs while a quantitative study on the environmental factors affecting the weakening of TCs after landfall has not been comprehended.

In recent years, more attention has been given to how nearshore intensity change of TCs may affect the post-landfall weakening. TCs that experienced rapid intensification prior to landfall are more destructive, such as Hurricanes Andrew (1992), Opal (1995), and Charley (2004), all resulted in devastating to the coastal regions in the United States (Franklin et al., 2006). Rappaport et al. (2010) discussed the intensity change of TCs within 48 h before landfall along the Gulf coast and concluded that weak (intense) TCs strengthened (weakened) prior to landfall. Park et al. (2011) analyzed TCs making landfall in Korea and Japan and found a trend of increasing duration after landfall relative to the intensity prior to landfall, and further affect the temporal variation of the TC-induced rainfall in the region. Zhu et al. (2021) found that hurricanes undergoing rapid intensification prior to landfall weakened at a slower rate after landfall in the Continental United States and the weakening rate was also weakly and positively correlated with the landfall intensity. They also indicated that the pre-landfall intensification was more common along the Gulf Coast but there was no significant correlation between regions and weakening rate. Song et al. (2021) further showed that a slower weakening rate prior to landfall of TCs over the South China Sea and an increased intensification rate prior to landfall of TCs east of the Philippines had a significant linkage to warmer ocean and greater upper-level divergence.

The aforementioned studies have mainly focused on either the TC pre-landfall intensity change or regional distribution of weakening rate after landfall. In particular, few studies have involved whether the post-landfall weakening rate of LTCs over China exhibits any obvious regional characteristics related to the pre-landfall intensity change (Kruk et al., 2010;

TABLE 1 **The factors analyzed in this study with their units and descriptions given.**

Factors	Unit	Description
SST	°C	Sea surface temperature within a radius of 3 degrees of the TC center
SST Gradient	°C km^{-1}	SST gradient within a radius of 3 degrees of the TC center
VOR850	s^{-1}	Environmental relative vorticity averaged within a radius of 9 degrees of the TC center at 850 hPa
DIV200	s^{-1}	Environmental divergence averaged within a radius of 9 degrees of the TC center at 200 hPa
VWS300-1000	m s^{-1}	Environmental vertical wind shear averaged within a radius of 4.5 degrees of the TC center between 1000 hPa and 300 hPa
UVWS300-1000	m s^{-1}	Zonal environmental vertical wind shear averaged within a radius of 4.5 degrees of the TC center between 1000 hPa and 300 hPa
VWS700-1000	m s^{-1}	As in VWS300-1000 but between 1000 hPa and 700 hPa
UVWS700-1000	m s^{-1}	As in UVWS300-1000 but between 1000 hPa and 700 hPa
q500	g kg^{-1}	Environmental specific humidity averaged within a radius of 5 degrees of the TC center at 500 hPa
QVDIV	s^{-1}	Environmental water vapor flux divergence within a radius of 9 degrees of the TC center between 1000 hPa and 850 hPa

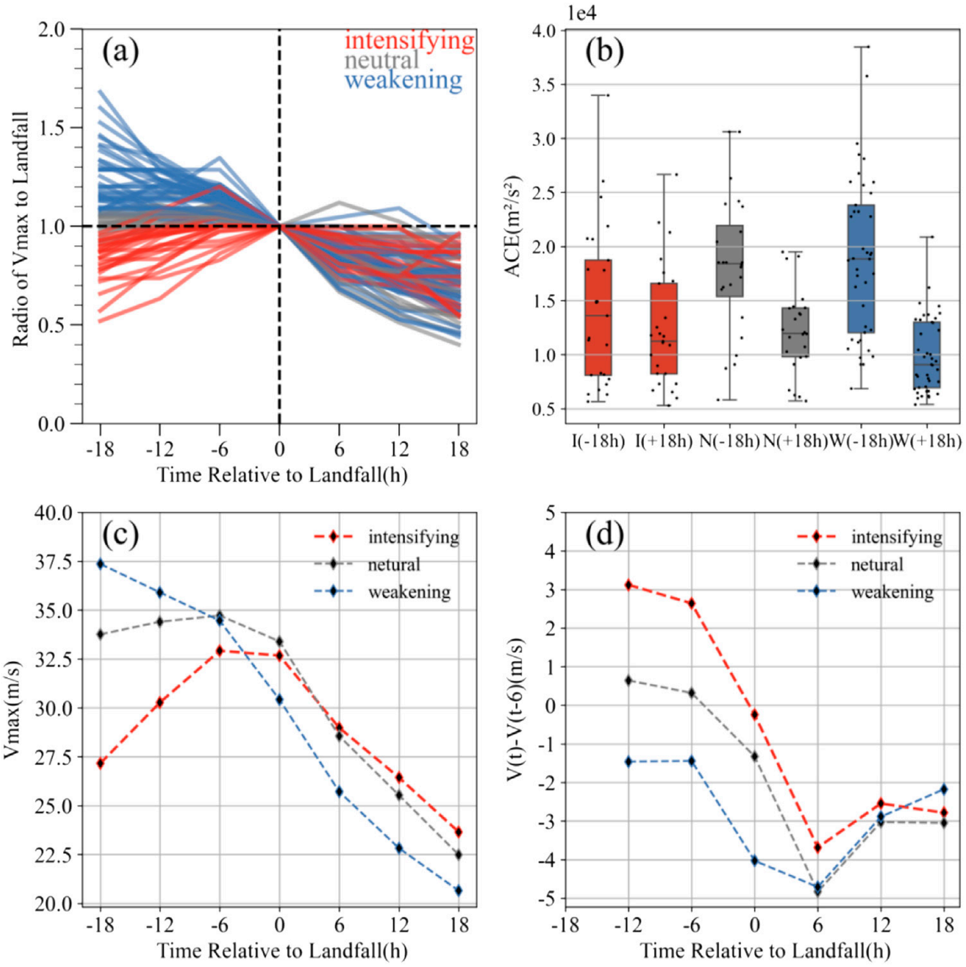

FIGURE 1
(A) Time evolutions of the ratio of maximum sustained near-surface wind to that at the time of landfall ($V_{max}/V_{0\,max}$); **(B)** the accumulated cyclone energy (ACE) within 18 h prior to landfall (Figures 2A–C 18 h) and 18 h after landfall (+18 h), with black dots representing the TC cases and the horizontal line representing the median; **(C)** the average V_{max} from −18 h to +18 h during landfall; and **(D)** the average 6-h intensity change. The red, gray and blue colors represent intensifying, neutral and weakening TCs, respectively.

Zhu et al., 2021). Furthermore, it is still unclear how oceanic and atmospheric environmental factors regulate the relationship between the pre-landfall intensity change and the post-landfall weakening of TCs. The main objectives of this study are 1) to explore the intensity change characteristics of LTCs prior to landfall over China, 2) to analyze the difference in the weakening rate of TCs over South China and East China, 3) to identify key factors affecting LTC dissipation and quantify their relative contributions based on the box difference index (BDI) method. The rest of the paper is organized as follows. Section 2 describes the data and analysis methods used in this study. The intensity change of TCs prior to landfall over China and the weakening of TCs after landfall are presented in *Post-landfall Weakening of TCs in the Three Categories Section*. *Characteristics of Spatial Distribution Section* shows the spatial distribution characteristics of LTCs. The relative importance of various factors affecting the decay and regional differences is analyzed and discussed in *Factors Affecting LFDR Over South China and East China Section*. The main findings are summarized in the last section.

Data and methods

Data

The 6-hourly TC best-track data used in this study were obtained from the China Meteorological Administration-

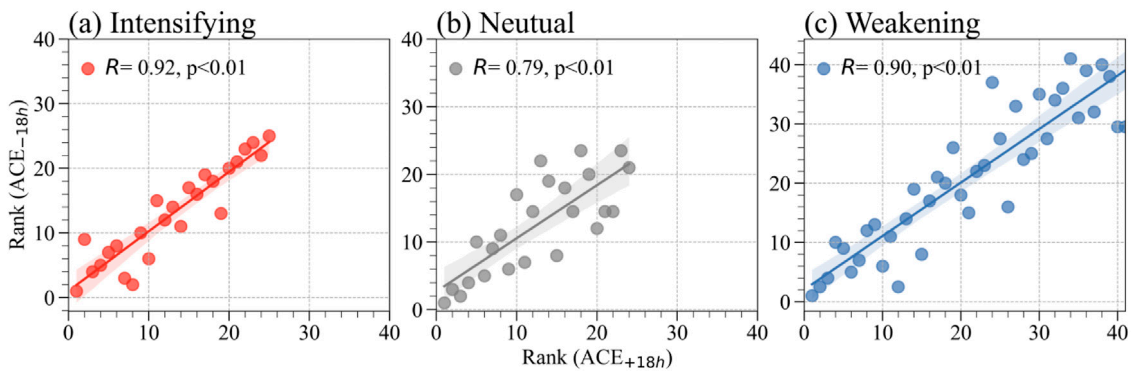

FIGURE 2
Mann-Kendall's tau-b correlation (non-parametric) of the rank between accumulated cyclone energy (ACE) within 18 h prior to landfall (−18 h) and 18 h after landfall (+18 h) for **(A)** intensifying, **(B)** neutral, and **(C)** weakening TCs.

Shanghai Typhoon Institute (CMA/STI), which include 6-hourly TC center location (longitude and latitude), maximum sustained (2-min mean) near-surface wind speed (V_{max}) and minimum central sea level pressure (Ying et al., 2014). The 6-hourly best track data were linearly interpolated to hourly data (Liu et al., 2021) for the subsequent calculations of the accumulated cyclone energy (ACE), the change rate of V_{max}, and landfalling dissipation rate (LFDR).

We have focused on TCs whose centers crossed the coastline of mainland China (except Taiwan Island) at least once during their lifetimes. We first checked the hourly data to determine whether a TC was on land and then calculated the intersection of the line between 6-h pre-landfall and 6-h post-landfall using the coastline to determine the TC landfalling location and intensity (Hu et al., 2017). We only considered the landfall location south of 40°N in the peak TC season from June to October (Wang et al., 2015) during 1979–2018. In total, 90 TCs cases including at least three continuous 6-h records prior to and after landfall were selected in our study.

The environmental data were acquired from the European Centre for Medium-Range Weather Forecasts (ECMWF) interim reanalysis (ERA-Interim) data at the horizontal resolution of 0.75°×0.75°, including the horizontal winds, vertical *p*-velocity, and specific humidity (Dee and Coauthors, 2011). The filtering algorithm of Kurihara et al. (1993) was used to remove the disturbance field, including the TC vortex, with the wavelengths less than 1,000 km from the unfiltered large-scale environmental fields at a given time. The filtered data were used to calculate the environmental vorticity, divergence, vertical wind shear (between 1000 and 300-hPa and 700–300-hPa, respectively), and water vapor flux divergence (QVDIV) (Table 1), in our analyses on environmental effect on TC intensity change during landfall.

Methods

The average change rate in sustained near-surface wind speed V_{max} (r_{vmax}) is introduced as an index to characterize a TC that is intensifying or weakening within 18 h prior to landfall following Zhu et al. (2021):

$$r_{vmax} = \frac{V_{max,t} - V_{max,t-18}}{18h}$$

where $V_{max,t}$ and $V_{max,t-18}$ represent the sustained near-surface wind speed at the time of landfall and the time of 18 h prior to landfall. The intensifying TCs and weakening TCs are bounded by the 90th percentiles of positive values and negative values of r_{vmax}, respectively, and the remaining are considered as neutral TCs. Finally, 25 intensifying cases, 41 weakening cases, and 24 neutral cases were identified in our following analyses. Note that we used the period of 18 h instead of 24 h used in Zhu et al. (2021) because most TCs that made landfall over China weakened to tropical depression about 18 h after landfall. We also examined the 24 h period with the results quite similar to those obtained using 18 h discussed herein.

Accumulated cyclone energy (ACE) is a metric to express the energy released by a TC during its lifetime (Bell et al., 2000; Trenberth et al., 2005; Emanual, 2005). We used hourly interpolated data to compute the pre-landfall ACE (ACE_{-18h}) and post-landfall ACE (ACE_{+18h}) of a TC during its landfalling period (Vitart, 2009; Truchelut and Staehling, 2017):

$$\mathrm{ACE} = 10^{-4} \sum V_{max}^{2}$$

where V_{max} is sustained near-surface wind speed with four continuous 6 hourly records prior to (−18 h, −12 h, −6 h, 0 h) or after (0 h, 6 h, 12 h, 18 h) landfall. The index is scaled by 10^{-4} to make them more manageable.

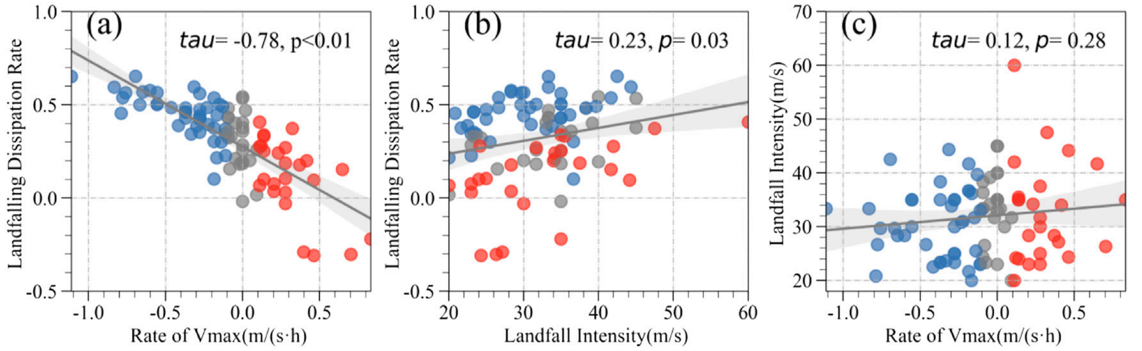

FIGURE 3
(A) The relationship between the rate of V_{max} (r_{vmax}) and landfalling dissipation rate (LFDR) in intensifying (red), neutral (gray) and weakening (blue) TCs. Solid line represents the linear regression trend. Dashed lines show the 99% confidence interval. **(B)** As in **(A)** but for landfall intensity (V_{0max}) and LFDR. **(C)** As in **(A)** but for r_{vmax} and landfall intensity.

In addition to quantifying the post-landfall weakening of TCs, Zhu et al. (2021) also defined the landfalling dissipation rate (LFDR) given below:

$$\mathrm{LFDR} = 1 - \frac{\mathrm{ACE}_{+18\mathrm{h}}}{\mathrm{ACE}_{-18\mathrm{h}}}$$

A TC with higher $\mathrm{ACE}_{-18\mathrm{h}}$ and lower $\mathrm{ACE}_{+18\mathrm{h}}$ has greater LFDR, which means that the TC weakens more rapidly because of the larger energy dissipation.

A box difference index (BDI) was used to quantitatively measure the difference of key factors in intensifying (weakening) TCs compared to neutral TCs (Fu et al., 2012; Li and Chakraborty, 2020):

$$\mathrm{BDI}_{\mathrm{ITC}} = \frac{\mathrm{M}_{\mathrm{ITC}} - \mathrm{M}_{\mathrm{NTC}}}{\sigma_{\mathrm{ITC}} - \sigma_{\mathrm{NTC}}};\ \mathrm{BDI}_{\mathrm{WTC}} = \frac{\mathrm{M}_{\mathrm{WTC}} - \mathrm{M}_{\mathrm{NTC}}}{\sigma_{\mathrm{WTC}} - \sigma_{\mathrm{NTC}}}$$

where $\mathrm{M}_{\mathrm{ITC}}$ and σ_{ITC} ($\mathrm{M}_{\mathrm{WTC}}$ and σ_{WTC}, $\mathrm{M}_{\mathrm{NTC}}$ and σ_{NTC}) represent the mean and standard deviation of the variables for the intensifying (weakening, neutral) TC cases within 18 h prior to landfall. The BDI is a number between -1.0 and 1.0. If the absolute value of index is greater, the corresponding factor is easier to trigger the intensifying (or weakening) process.

Post-landfall weakening of TCs in the three categories

Figure 1 shows the intensity change characteristics of TCs in, respectively, the intensifying, weakening, and neutral categories during landfall. To compare the intensity evolution during landfall, we defined the ratio of the maximum near-surface wind speed (V_{max}) to that at the time of landfall (V_{0max}), which can also be termed relative intensity (V_{max}/V_{0max}). The ratios in all weakening cases are greater than 1.0 because the TC intensity decreases with time prior to landfall while those in intensifying TCs are less than 1.0 except for in a few intensifying cases whose ratios are still greater than 1 because their maximum intensities appeared at 6 h prior to landfall (Figure 1A), indicating that the weakening started 6 h prior to landfall rather than at the time of landfall. The mixed distribution pattern of TC cases after landfall illustrates that some individual TCs weakened rapidly while some others weakened slowly or a few even maintained. The pre- and post-landfall ACE distributions are compared in Figure 1B. The weakening TCs with an average ACE of 1.75×10^4 m^2 s^{-2} possess more energy prior to landfall but less energy after landfall relative to that at the time of landfall. This means that the weakening cases prior to landfall would experience greater energy dissipation after landfall. For intensifying TCs, the post-landfall ACE decreased slowly or even maintained their intensities. The time evolutions of the average V_{max} and the average 6-h intensity change from Figures 2A–C 18 h to +18 h in the three categories are compared in Figures 1C, D, respectively. The average V_{max} of intensifying TCs increased from −18 h to −6 h and then decreased toward landfall while that of weakening TCs decreased during the whole landfalling process. The average V_{max} after landfall in weakening TCs is less than that in intensifying TCs. From the 6-h intensity decay rate, we can see that the intensification rate of the pre-landfall intensifying TCs decreases and the weakening rate of the pre-landfall weakening TCs increases prior to landfall. Both types of the TCs weaken rapidly within 6 h after landfall and then the weakening rate shows a decreasing trend.

To explore whether the pre-landfall intensity change has a direct relationship with the post-landfall intensity decay, we first examined the correlation between $\mathrm{ACE}_{-18\mathrm{h}}$ and $\mathrm{ACE}_{+18\mathrm{h}}$ and found that they are highly correlated, which is statistically significant over the 99% confidence level (Figures 2A–C). Namely, a strong TC that undergoes slow weakening prior to landfall possesses relatively higher intensity at landfall and tends to decay more rapidly after landfall, while a weak TC with lower

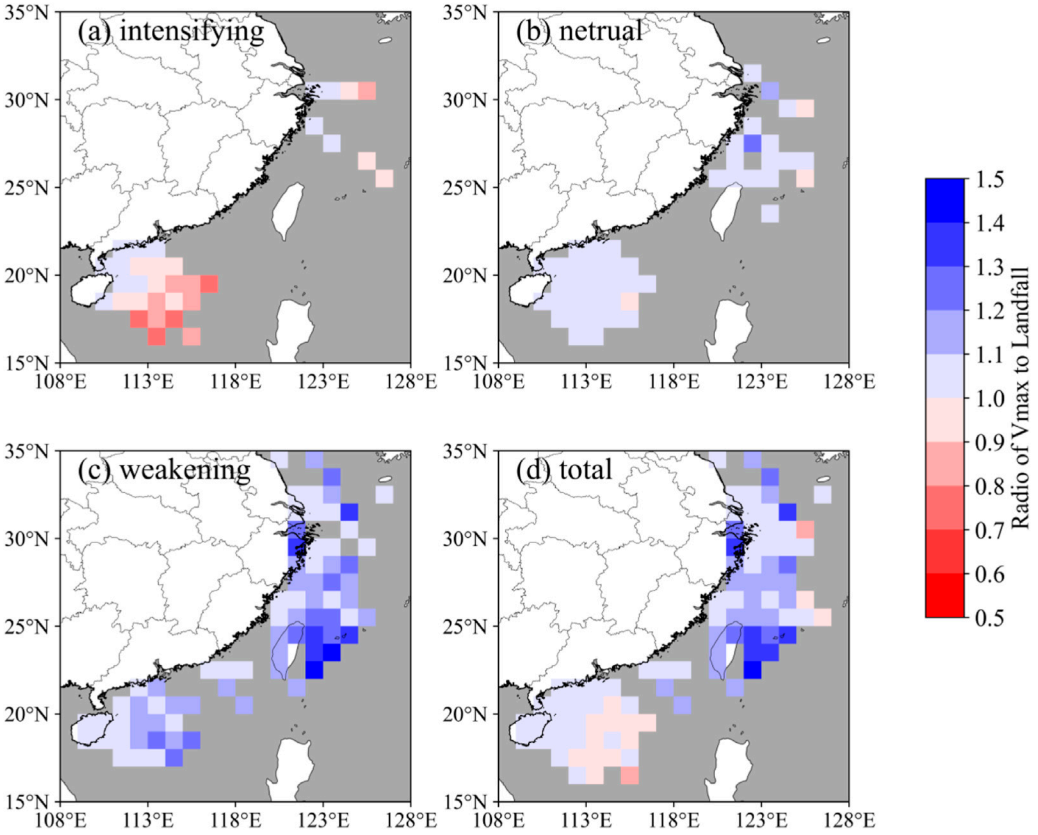

FIGURE 4
Spatial distribution of relative intensity ($V_{max}/V_{0\,max}$) for **(A)** intensifying, **(B)** neutral, **(C)** weakening, and **(D)** total TCs prior to landfall.

ACE prior to landfall decays more slowly after landfall. This is different from those documented in Zhu et al. (2021), who found that the correlation for the weakening TCs is very weak and insignificant. The difference may be due to the different environmental conditions in the United States and mainland China.

We further choose LFDR as a metric to describe the energy dissipation process during landfall, which can help quantify the influence of pre-landfall intensity on the subsequent post-landfall dissipation. As we can see from Figure 3A, r_{vmax} has a significant negative correlation with LFDR with a correlation coefficient as high as −0.6, which is statistically significant over the 99% confidence level. This indicates that a TC undergoing pre-landfall intensification would be filled slowly after landfall while a TC that weakens prior to landfall would dissipate rapidly, which is consistent with the results for hurricanes making landfall over the United States reported by Zhu et al. (2020). Previous studies have also demonstrated that the landfall intensity is one of the factors related to the weakening characteristics of TCs after landfall. Li et al. (2017) found that increasing landfall intensity would result in greater destruction over China. However, recent studies have revealed that TCs with higher landfall intensity usually have longer duration after landfall (Liu et al., 2020; Chen et al., 2021; Liu et al., 2021; Song et al., 2021). This does not necessarily mean that the weakening of a strong TC is slower. We found that the LFDR is significantly correlated with the landfall intensity over the 95% confidence level (Figure 3B). Since r_{vmax} depends on landfall intensity (Figure 3C), we can conclude that the landfall intensity also has a weak effect on the post-landfall weakening.

Characteristics of spatial distribution

Figure 4 depicts the spatial distribution of the relative intensity ($V_{max}/V_{0\,max}$) for TCs in the three individual categories and for all TCs as a whole. The relative intensity of TCs making landfall in northern Taiwan Island and East China Sea shows a maximum and decreases toward the north (Figure 4D), which is dominated by the weakening TCs (Figure 4C). However, the pre-landfall relative intensity in the South China Sea shows little change. This is mainly because of the high landfall frequency over the South China Sea (Liu et al., 2020), dominated by both northwestward moving intensifying

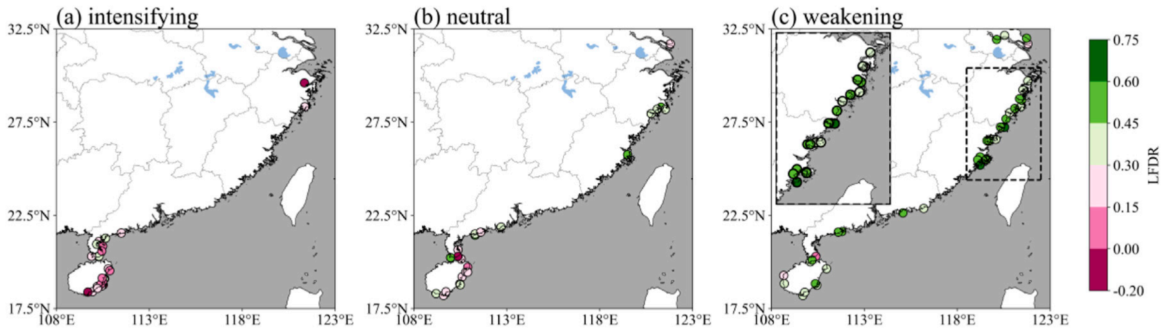

FIGURE 5
Spatial distribution of landfalling dissipation rate (LFDR) for **(A)** intensifying, **(B)** neutral, **(C)** weakening TCs. The weakening TCs over East China is magnified in the inset box for clarity in **(C)**.

TCs (Figure 4A) and westward moving weakening TCs (Figure 4C).

We next examine the spatial distribution of the relationship between pre-landfall TC intensity change (r_{vmax}) and the inland LFDR, with the results shown in Figure 5. Most frequent landfalls of TCs occurred in the southeastern Hainan Island, which are classified into South China in our study, and the northern Fujian Province and Zhejiang Province (namely East China). Due to the blocking effect of the Central Range over the Taiwan Island, TCs making landfall in Guangdong and southern Fujian often decayed too quickly to maintain over 18 h, which were not included in our analysis. As we can see from Figure 5A, the intensifying TCs with larger r_{vmax} were distributed in South China. Only two cases are located in the northern Zhejiang, namely Bill (8807) in 1988 and YAGI (1814) in 2018 because of the sufficient water vapor supply to support active convection in the inner core of the TCs (Jiang, 1989; Huang et al., 2018; Ji et al., 2019). The weakening TCs were densely distributed over East China (Figure 5C), and neutral TCs were distributed in both South and East China (Figure 5B). This indicates that TCs making landfall in East China would carry larger pre-landfall ACE and tend to have greater landfall intensity.

We now discuss the spatial distribution of inland LFDR in East and South China. Intensifying TCs in South China show weak LFDR, with values ranging from −0.2 to 0.45. Note that a few weakening TCs with small LFDR also made landfall in this area, making the dissipation pattern a little bit complicated there. The larger LFDR ranging from 0.45 to 0.60 appeared in East China, all of which came from the weakening TCs. This indicates that the pre-landfall weakening TCs in East China experienced rapid dissipation after landfall. Some previous studies have shown that the apparent regional difference over mainland China might be controlled by various large-scale environmental conditions (Wong et al., 2008; Song et al., 2021). Whether the large-scale environmental factors affect r_{vmax} and LFDR will be discussed in detail in the next section.

TABLE 2 The average factors and Mann-Kendall correlation coefficients with LFDR. Change (T_{0h} -T_{-18h}), average values indicate the pre-landfall change and average value, respectively.

Factors	Change values		Average values	
	Change.	Corr coef.	Avg.	Corr coef.
SST	−0.44	**−0.31**	28.47	**−0.28**
SST Gradient	1.25×10^{-3}	**0.20**	3.67×10^{-3}	**0.26**
VOR850	0.06×10^{-7}	−0.04	-0.96×10^{-6}	0.11
DIV200	-0.60×10^{-6}	−0.04	-0.12×10^{-5}	**−0.22**
VWS300-1000	0.31	**0.14**	4.88	**0.19**
UVWS300-1000	0.92	**0.22**	−2.19 m s^{-1}	**0.23**
VWS700-1000	0.38	−0.01	1.78 m s^{-1}	0.05
UVWS700-1000	0.10	0.09	−0.34 m s^{-1}	0.01
q500	0.067	**−0.19**	4.08	−0.03
QVDIV	0.045×10^{-6}	0.01	-0.06×10^{-6}	**0.25**

Correlation coefficients that are statistically significant above 95% confidence level are boldfaced.

Factors affecting LFDR over south China and east China

Most studies have shown that the rapid weakening of TCs may be caused by low SST and large SST gradient (Zhang et al., 2007; DeMaria et al., 2012; Qian and Zhang, 2013; Wood and E Ritchie, 2015) and large-scale environmental factors, such as strong vertical wind shear and dry air intrusion (Frank and Ritchie, 2001; Wang et al., 2015; Wood and E Ritchie, 2015; Fei et al., 2020). In our study, we selected SST, SST gradient, environmental low-level vorticity, upper-level divergence, vertical wind shear, mid-level specific humidity, and low-level

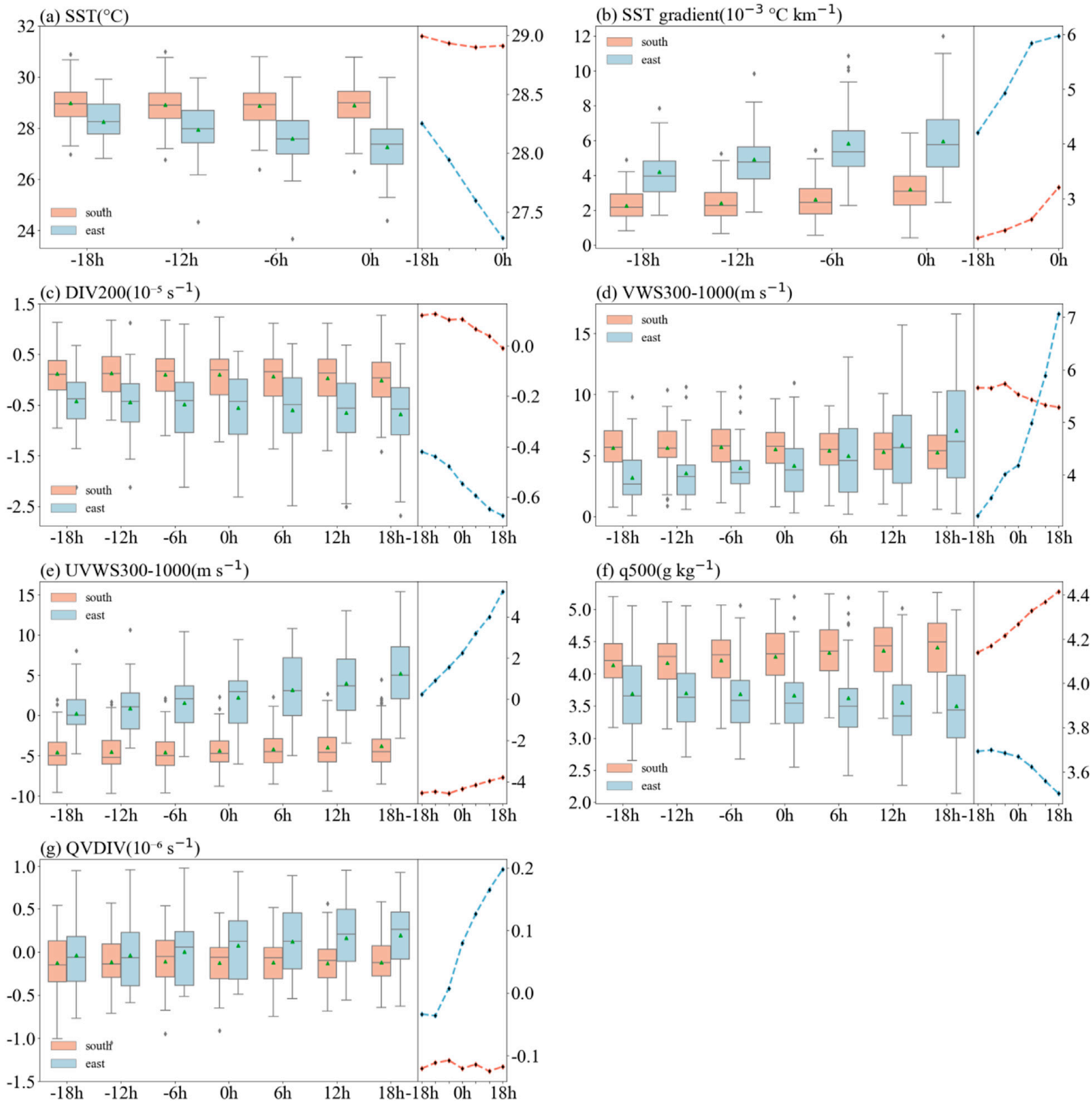

FIGURE 6
Evolutions of **(A)** SST (°C), **(B)** SST gradient (10^{-3}°C km^{-1}), **(C)** divergence at 200 hPa (10^{-5} s^{-1}), **(D)** vertical wind shear (m s^{-1}) between 1000 hPa and 300 hPa, **(E)** zonal vertical wind shear (m s^{-1}) between 1000 hPa and 300 hPa, **(F)** specific humidity (g kg^{-1}) at 500 hPa, **(G)** low-level water vapor flux divergence (10^{-6} s^{-1}) between 1000 hPa and 850 hPa during TC landfall over East China (red) and South China (blue). Green dots and horizontal lines represent mean value and median lines, respectively. Right part in each panel represents the evolution of the corresponding mean value of the factor over East China (red) and South China (blue).

water vapor flux divergence as possible environmental factors affecting LFDR after landfall over mainland China and compare the different characteristics of persistence of these factors in South China and East China (Table 1).

Table 2 compares the linear correlation coefficients between the change and average value of each of the pre-landfall factors and LFDR. Among them, SST, SST gradient, zonal deep vertical wind shear (UVWS), and low-level water vapor flux divergence (QVDIV) are highly correlated with LFDR, while upper-level divergence (DIV200) and mid-level specific humidity (q500) show weak correlations with LFDR, while low-level vorticity has no obvious correlation with LFDR. We can see that the

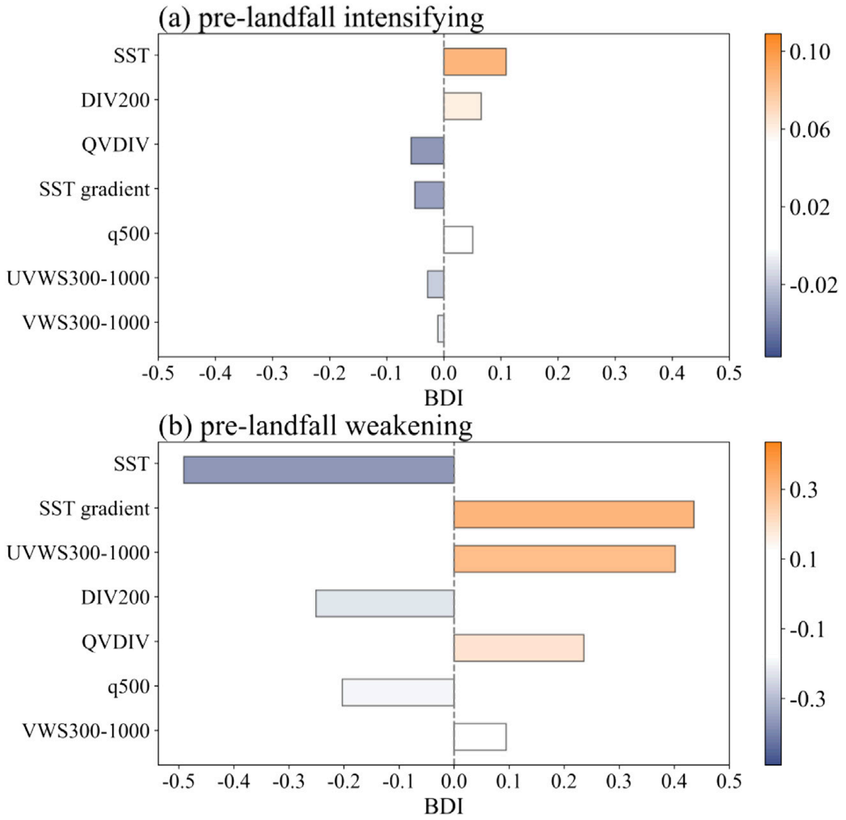

FIGURE 7
Key factors in **(A)** intensifying TCs and **(B)** weakening TCs and their corresponding box difference index (BDI) values prior to landfall. The factors are ordered based on the average values within 18 h prior to landfall.

average SST was 28.47°C with the negative correlation coefficient of –0.28 with LFDR. Compared with 18 h prior to landfall, the SST decreased by 0.44°C at the time of landfall with a negative correlation of –0.31 with LFDR. This implies that a TC crossing a region with lower SST and greater decreasing SST trend has a larger LFDR. This is consistent with previous result in Li et al. (2021), who drawn a conclusion that the water content carried by a hurricane would be reduced to retard the supply of ocean heat when the nearshore SST was cooler and decreased faster. However, Bender et al. (1993) showed that the upwelling and vertical mixing under a TC had a negative effect on TC intensity and could lead to rapid TC weakening after landfall. In addition to SST, the SST gradient is another key ocean parameter. Prior to landfall, the average SST gradient was 3.67×10^{-3}°C km^{-1} and increased by 1.25×10^{-3}°C $km^{-1}$with the significant positive correlation with LFDR, which implies that the large SST gradient favors rapid decay of TC after landfall.

The large-scale environmental atmospheric conditions are also important to TC intensity change and thus the weakening of LTCs. From Table 2, we can see that the low-level vorticity shows little correlation with LFDR, while the upper-level divergence is negatively correlated with LFDR. This suggests that the upper tropospheric convergence forcing (-0.12×10^{-5} s^{-1}) may contribute to the weakening of TCs after landfall over China. The VWS is considered a detrimental dynamical environmental factor that is unfavorable for TC intensification (Zeng et al., 2010; Wang et al., 2015; Liang et al., 2016). We examined both the deep-layer VWS between 300 and 1000 hPa and the low-level VWS between 700 and 1000 hPa, representative of the VWS effect on TC intensity change over the western North Pacific (Wang et al., 2015). As we can see from Table 2, the deep-layer VWS and the deep-layer vertical shear of zonal wind have higher linear correlations with LFDR (r=0.19 and 0.23, respectively) than the low-level VWS, which implies that TCs with larger VWS may weaken more rapidly after landfall over China. This is different from the results of Wang et al. (2015), who found the low-level VWS during the active TC season is more significantly correlated with TC intensity change than the VWS at other layers. This is mainly because they considered the area of 123°E–180°E while we focused on the area west of 127°E. Importantly, the vertical shear of zonal wind can have a more detrimental effect on TC intensity after landfall, or equivalently more beneficial to LFDR. This suggests that the effect of VWS on TC intensity depends not only on the magnitude of the shear but also on the direction of the shear. For example, Wang and Yu. (2013) found that nearly 70% of the rapid intensification of TCs occurred in easterly shear while westerly shear inhibits TC development, suggesting that westerly shear has a greater negative effect on TC intensity than easterly shear.

The dry air intrusion and water vapor supply are two other factors that may affect the weakening rate of landfalling TCs (Wood and E Ritchie, 2015; Fei et al., 2020). We thus examined the mid-level environmental specific humidity and low-level water vapor flux divergence. The change in 500-hPa specific humidity prior to landfall shows a weakly negative correlation with the LFDR, with the correlation coefficient of -0.19, indicating that the TCs experiencing large decreasing specific humidity nearshore usually tend to weaken rapidly after landfall. Note that the specific humidity decreased little prior to landfall with one possible reason is that changes in the environmental humidity in South China and East China offset each other, which will be discussed later (Figure 6G). The water vapor flux divergence prior to landfall is positively correlated with LFDR, with the correlation coefficient of 0.25, which is statistically significant above 95% confidence level, indicating that the reduced moisture supply with weak horizontal water vapor flux convergence provides favorable environmental conditions for TC post-landfall weakening.

Based on the above correlation analysis, we examine the trends of key factors, including SST, SST gradient, DIV200, VWS300-1000, UVWS300-1000, q500, and QVDIV during landfall over South China and East China, with the results shown in Figure 6. The average SST over East China is lower and the SST gradient is greater than those over South China, with a decreasing trend of the former and an increasing trend of the latter (Figures 6A, B). The high-level divergence in both East and South China is decreasing during the landfall from -18 h to +18 h (Figure 6C). However, the high-level flow is dominated by decreasing divergence in South China while that in East China shows convergence (around -1.5×10^{-5} s^{-1}). This means that the upper-level flow is more unfavorable for the maintenance of TCs making landfall over East China. This seems to be consistent with the predominant pre-landfall weakening TCs over East China and intensifying TCs in South China. Moreover, the VWS initially is weaker but increases rapidly over East China while that is moderate over South China (Figure 6D). The westerly vertical shear (UVWS>0) increases during landfall over East China, which implies that a TC would dissipate rapidly after landfall over East China (Figure 6E), consistent with the significant correlation coefficient of 0.22 between LFDR and UVWS300-1000 (Table 2). In contrast, both the deep-layer total VWS and the deep-layer easterly vertical shear (UVWS<0) did not change much during landfall over South China. This implies that the large-scale environmental VWS may not be the key factor affecting TC intensity and post-landfall weakening of TCs over South China.

The mid-tropospheric specific humidity during landfall shows different evolutions over East and South China (Figure 6F). South China is characterized by high mid-tropospheric specific humidity due to the effect of South China Sea summer monsoon compared with East China. Note that the specific humidity increased and decreased the equivalent range over South China and East China, respectively. This explains why the average change in specific humidity for all TC cases is feeble in Table 2. Because of the negative correlation between the mid-tropospheric humidity trend and LFDR (r=−0.19, Table 2), the decreasing humidity over East China contributes to post-landfall weakening while increasing humidity over South China has an opposite effect. The low-level water vapor flux in East China changed from convergence to divergence at 6 h prior to landfall (Figure 6G), indicating that the reduction of water vapor transport into the TC core. Over South China, the low-level water vapor flux maintained a weak convergence of $-0.1\times10^{-6}s^{-1}$. The above results suggest that the faster post-landfall weakening of TCs over East China than over East China was primarily due to lower SST, larger SST gradient, and stronger zonal vertical wind shear, together with the convergence of upper-level flow and the divergence of lower-level water vapor flux.

Factors analyzed above are linked to the ACE prior to and after landfall and can represent their effects of TC intensity change prior to landfall on TC weakening after landfall. This means that the environmental conditions that affect the post-landfall dissipation are mediated by pre-landfall intensity change of TCs. Figure 7 quantifies the relative contributions of key factors to pre-landfall intensifying and weakening TCs using the BDI index, respectively. The results show that the most important factors for distinguishing intensifying TCs from neutral TCs are SST with the BDI value of 0.109. The contributions by other factors are generally secondary with the BDI less than 0.1. As intensifying TCs mostly occurs in South China, the least contribution of UVWS300–1000 (−0.029) and VWS (−0.011) also confirms the above-mentioned conclusion that the large-scale environmental VWS may not be the main factor affecting the pre-landfall weakening of TCs over South China (Figures 6D, E). The q500 also contributes little to LFDR of intensifying TCs over South China, which explains why the specific humidity increases but the TC intensity weakens after landfall in South China. The key factors contributing to the weakening of TCs are SST, SST gradient, and UVWS300–1000 with the BDI values of -0.491, 0.436, and 0.402, respectively. The rests are DIV200 (-0.251), QVDIV (0.236), q500 (-0.203) and VWS300-1000 (0.095). It is worth noting that the contribution by ocean thermodynamic conditions (SST and SST gradient) is very significant, especially for pre-landfall weakening TCs, which is followed by environmental

UVWS, consistent with the higher correlation of these factors with LFDR shown in Table 2. In addition, it is clear to see that the BDI values in the intensifying TCs are much smaller than those in the weakening TCs. In other words, environmental factors play a more crucial role in the post-landfall weakening of TCs over East China while the post-landfall dissipation over South China may be controlled by other factors, such as the TC size and structure. As a result, the post-landfall weakening is largely regulated by the intensity change of TCs prior to landfall, which is affected significantly by the coastal ocean thermodynamic and large-scale environmental atmospheric dynamic and thermodynamic conditions.

Conclusion

In this study, we first analyzed the intensity change of TCs within 18 h prior to landfall over mainland China during 1979–2018 in the active typhoon season (June–October). The results show that the pre-landfall intensifying TCs usually tend to have small accumulation cyclone energy (ACE_{-18}) and easily maintain larger post-landfall energy (ACE_{+18}) while the weakening TCs with great intensity tend to experience larger energy dissipation after landfall. This indicates that there is a relationship between the pre-landfall intensity change and post-landfall weakening. We also found that the average intensity of intensifying TCs prior to landfall is small and the increasing rate decreases during landfall, while the decreasing rate after landfall is smaller than that of the weakening TCs. The results thus demonstrate that the post-landfall weakening difference of LTCs may result from intensity change prior to landfall.

The distribution of the average change rate in V_{max} (r_{vmax}) and LFDR show different regional characteristics over East China and South China. The intensifying TCs are mostly concentrated southeast of Hainan Island, mainly with a southeast-northwest track. The weakening TCs are distributed in both Hainan Province and northern Guangdong to Zhejiang Provinces, moving westward and north-northwestward, respectively. Compared with South China, due to pre-landfall weakening of TCs, TCs making landfall over East China present relatively higher pre-landfall intensity than the intensity at the time of landfall (relative intensity), but possess faster weakening prior to landfall and high LFDR after landfall.

To determine what caused the regional dependence, relevant oceanic and atmospheric environmental factors are statistically analyzed and quantified. Five factors are found to be significantly correlated with LFDR, including SST, SST gradient, environmental VWS between 1000 hPa and 300 hPa (VWS300–1000), zonal environmental VWS between 1000 hPa and 300 hPa (UVWS300–1000), and low-level water vapor flux divergence (QVDIV). This indicates that TCs with greater post-landfall weakening rate usually cross the region with lower SST and greater SST gradient, and are embedded in environment with larger environmental westerly VWS, larger high-level flow convergence and smaller low-level moisture convergence prior to landfall. In addition, decreasing environmental moisture at 500 hPa (q500) are weakly correlated with LFDR, often under 95% significance level.

Results from this study illustrate that the cooling SST and the sharper SST gradient nearshore would promote the high occurrence of rapid weakening prior to landfall because of high BDI values in both intensifying and weakening TCs. For the environmental atmospheric factors, the large deep westerly VWS is also favorable for pre-landfall weakening of TCs, favoring LFDR over mainland China. Nevertheless, above-considered environmental conditions are not key factors leading to pre-landfall intensifying of TCs with very small BDI values over South China and thus play weak role in post-landfall dissipation of intensifying TCs.

The oceanic thermodynamic conditions and the environmental atmospheric conditions over East China show more drastic changes, characterized by smaller and decreasing SST, larger and increasing SST gradient and increasing VWS (particularly, the increasing zonal VWS) in weakening LTCs, resulting in faster energy dissipation after landfall. In addition, upper-tropospheric convergence, decreasing environmental moisture and decreasing convergence of low-level water vapor flux are additional factors conducive to rapid weakening of TCs after landfall over East China. In general, most of these factors changed little over South China but with average values featured with larger SST, small SST gradient, lower VWS, eastern VWS ranging from -2.5 m s^{-1} to -5 m s^{-1} and wetter environment, all being favorable for pre-landfall weakening TCs over South China to maintain great landfall intensify and weak post-landfall dissipation, and weakly affecting the intensity change of pre-landfall intensifying TCs.

Although we evaluated the relationship between the post-landfall weakening and the pre-landfall TC intensity change of LTCs over mainland China, the conclusions are subject to the limited sample size and the involvements of complex ocean-atmospheric, ocean-land, and land-atmospheric interactions. Note that land surface properties, such as land surface temperature, soil temperature and moisture, vegetation coverage, etc. also affect the post-landfall weakening of TCs (Tuleya and Kurihara, 1978; Tuleya, 1994; Song et al., 2021; Liu and Wang, 2022; Thomas and Shepherd, 2022). In future studies, the possible effects of land surface properties, including mesoscale terrains (Liu and Wang, 2022), on TC post-landfall weakening can be further examined in combination with large-scale environmental conditions. In addition, it can be also a good topic to introduce the pre-landfall intensity change into the empirical decay model of TCs after landfall (Kaplan and Demaria, 1995; Vickery, 2005; Wong et al., 2008; Liu et al., 2021; Liu and Wang, 2022). With improved understanding of key factors affecting TC post-landfall weakening, the forecast accuracy of landfalling TC intensity could be improved.

Data availability statement

The datasets presented in this study can be found in online repositories. The names of the repository/repositories and accession number(s) can be found in the article/Supplementary material.

Author contributions

YW developed the main idea. WH analyzed the datasets and generated figures. WH and YW wrote the manuscript. LL helped with data pre-processing and provided feedback on the manuscript.

Funding

This study has been supported by the National Natural Science Foundation of China under grants 41730960 and 42175011. YW has been supported by the NSF grant AGS-1834300.

Conflict of interest

The authors declare that the research was conducted in the absence of any commercial or financial relationships that could be construed as a potential conflict of interest.

Publisher's note

References

Andersen, T. K., Radcliffe, D. E., and Shepherd, J. M. (2013). Quantifying surface energy fluxes in the vicinity of inland-tracking tropical cyclones. *J. Appl. Meteorol. Climatol.* 52, 2797–2808. doi:10.1175/jamc-d-13-035.1

Andersen, T. K., and Shepherd, J. M. (2014). A global spatiotemporal analysis of inland tropical cyclone maintenance or intensification. *Int. J. Climatol.* 24, 391–402. doi:10.1002/joc.3693

Bell, G. D., Halpert, M. S., Ropelewski, C. F., Kousky, V. E., Douglas, A. V., Schnell, R. C., et al. (2000). Climate assessment for 1998. *Bull. Am. Meteorol. Soc.* 80, S1. doi:10.1175/1520-0477(2000)81[s1:CAF]2.0.CO;2

Bender, M. A., Ginis, I., and Kurihara, Y. (1993). Numerical simulations of tropical cyclone-ocean interaction with a high-resolution coupled model. *J. Geophys. Res.* 98, 23245–23263. doi:10.1029/93jd02370

Chen, J. L., Tam, C. Y., Cheung, K., Wang, Z., Murakami, H., Lau, N. C., et al. (2021). Changing impacts of tropical cyclones on East and Southeast Asian inland regions in the past and a globally warmed future climate. *Front. Earth Sci.* 9, 769005. doi:10.3389/feart.2021.769005

Dee, D. P., Uppala, S. M., Simmons, A. J., Berrisford, P., Poli, P., Kobayashi, S., et al. (2011). The ERA-interim reanalysis: Configuration and performance of the data assimilation system. *Q. J. R. Meteorol. Soc.* 137, 553–597. doi:10.1002/qj.828

DeMaria, M., DeMaria, R. T., Knaff, J. A., and Molenar, D. (2012). Tropical cyclone lightning and rapid intensity change. *Mon. Weather Rev.* 140, 1828–1842. doi:10.1175/mwr-d-11-00236.1

Done, J. M., Ge, M., Holland, G., Dima-West, I., Phibbs, S., Saville, G. R., et al. (2020). Modelling global tropical cyclone wind footprints. *Nat. Hazards Earth Syst. Sci.* 20, 567–580. doi:10.5194/nhess-20-567-2020

Elsberry, R. L., and Tsai, H. C. (2014). Situation-dependent intensity skill metric and intensity spread guidance for Western North Pacific tropical cyclones. *Asia. Pac. J. Atmos. Sci.* 50, 297–306. doi:10.1007/s13143-014-0018-5

Emanuel, K. (2005). Increasing destructiveness of tropical cyclones over the past 30 years. *Nature* 436, 686–688. doi:10.1038/nature03906

Fei, R., Xu, J., Wang, Y., and Yang, C. (2020). Factors affecting the weakening rate of tropical cyclones over the Western North Pacific. *Mon. Weather Rev.* 148, 3693–3712. doi:10.1175/mwr-d-19-0356.1

Frank, W. M., and Ritchie, E. A. (2001). Effects of vertical wind shear on the intensity and structure of numerically simulated hurricanes. *Mon. Weather Rev.* 129, 2249–2269. doi:10.1175/1520-0493(2001)129<2249:eovwso>2.0.co;2

Franklin, C. N., Holland, G. J., and May, P. T. (2006). Mechanisms for the generation of mesoscale vorticity features in tropical cyclone rainbands. *Mon. Weather Rev.* 134, 2649–2669. doi:10.1175/mwr3222.1

Fu, B., Peng, M. S., Li, T., and Stevens, D. E. (2012). Developing versus nondeveloping disturbances for tropical cyclone formation. Part II: Western north Pacific. *Mon. Weather Rev.* 140, 1067–1080. doi:10.1175/2011mwr3618.1

Hu, H., Duan, Y., Wang, Y., and Zhang, X. (2017). Diurnal cycle of rainfall associated with landfalling tropical cyclones in China from rain gauge observations. *J. Appl. Meteorol. Climatol.* 56, 2595–2605. doi:10.1175/jamc-d-16-0335.1

Huang, M., Li, Q., Xu, H., Lou, W., and Lin, N. (2018). Non-stationary statistical modeling of extreme wind speed series with exposure correction. *Wind Struct.* 26, 129–146. doi:10.12989/was.2018.26.3.129

Ji, Q., Xu, F., Xu, J., Liang, M., Tu, S., and Chen, S. (2019). Large-scale characteristics of landfalling tropical cyclones with abrupt intensity change. *Front. Earth Sci.* 13, 808–816. doi:10.1007/s11707-019-0792-6

Jiang, J. (1989). Analysis of some important characteristics of typhoon No.7 in 1988. *Mar. Forecasts* 6, 41–49. doi:10.11737/j.issn.1003-0239.1989.04.008

Kaplan, J., and DeMaria, M. (1995). A simple empirical model for predicting the decay of tropical cyclone winds after landfall. *J. Appl. Meteor.* 34, 2499–2512. doi:10.1175/1520-0450(1995)034<2499:asemfp>2.0.co;2

Kaplan, J., and DeMaria, M. (2001). On the decay of tropical cyclone winds after landfall in the New England area. *J. Appl. Meteor.* 40, 280–286. doi:10.1175/1520-0450(2001)040<0280:otdotc>2.0.co;2

Klotzbach, P. J., Steven, S. G., and Bell, M. (2018). Continental U.S. hurricane landfall frequency and associated damage: Observations and future risks. *Bull. Am. Meteorol. Soc.* 99, 1359–1376. doi:10.1175/BAMS-D-17-0184.1

Kruk, M. C., Gibney, E. J., Levinson, D. H., and Squires, M. (2010). A climatology of inland winds from tropical cyclones for the eastern United States. *J. Appl. Meteorol. Climatol.* 49, 1538–1547. doi:10.1175/2010jamc2389.1

Kurihara, Y. M., Bender, M. A., and Ross, R. J. (1993). An initialization scheme of hurricane models by vortex specification. *Mon. Weather Rev.* 121, 2030–2045. doi:10.1175/1520-0493(1993)121<2030:AISOHM>2.0.CO;2

Li, L., and Chakraborty, P. (2020). Slower decay of landfalling hurricanes in a warming world. *Nature* 587, 230–234. doi:10.1038/s41586-020-2867-7

Li, R. C. Y., Zhou, W., Shun, C. M., and Lee, T. C. (2017). Change in destructiveness of landfalling tropical cyclones over China in recent decades. *J. Clim.* 30, 3367–3379. doi:10.1175/jcli-d-16-0258.1

Li, X., Zhan, R., Wang, Y., and Xu, J. (2021). Factors controlling tropical cyclone intensification over the marginal seas of China. *Front. Earth Sci.* 9, 795186. doi:10.3389/feart.2021.795186

Liang, J., Wu, L., Gu, G., and Liu, Q. (2016). Rapid weakening of Typhoon Chan-Hom (2015) in a monsoon gyre. *J. Geophys. Res. Atmos.* 121, 9508–9520. doi:10.1002/2016jd025214

Liu, D., Pang, L., and Xie, B. (2009). Typhoon disaster in China: Prediction, prevention, and mitigation. *Nat. Hazards* 49, 421–436. doi:10.1007/s11069-008-9262-2

Liu, L., and Wang, Y. (2022). A physically based statistical model with the parameterized topographic effect for predicting the weakening of tropical cyclones after landfall over China. *Geophys. Res. Lett.* 49, 1–8. doi:10.1029/2022gl099630

Liu, L., Wang, Y., and Wang, H. (2021). The performance of three exponential decay models in estimating tropical cyclone intensity change after landfall over China. *Front. Earth Sci.* 9, 792005. doi:10.3389/feart.2021.792005

Liu, L., Wang, Y., Zhan, R., Xu, J., and Duan, Y. (2020). Increasing destructive potential of landfalling tropical cyclones over China. *J. Clim.* 33, 3731–3743. doi:10.1175/jcli-d-19-0451.1

Liu, Q., Song, J., and Klotzbach, P. J. (2021). Trends in Western North Pacific tropical cyclone intensity change before landfall. *Front. Earth Sci.* 9, 780353. doi:10.3389/feart.2021.780353

Miller, B. I. (1964). A study of the filling of Hurricane Donna (1960) over land. *Mon. Weather Rev.* 92, 389–406. doi:10.1175/1520-0493(1964)092<0389:asotfo>2.3.co;2

Ooyama, K. (1969). Numerical simulation of the life cycle of tropical cyclones. *J. Atmos. Sci.* 26, 3–40. doi:10.1175/1520-0469(1969)026<0003:NSOTLC>2.0.CO;2

Park, D. S. R., Ho, C. H., Kim, J. H., and Kim, H. S. (2011). Strong landfall typhoons in Korea and Japan in a recent decade. *J. Geophys. Res.* 116, D07105–D07111. doi:10.1029/2010jd014801

Powell, M. D., Dodge, P. P., and Black, M. L. (1991). The landfall of hurricane hugo in the carolinas: Surface wind distribution. *Wea. Forecast.* 6, 379–399. doi:10.1175/1520-0434(1991)006<0379:tlohhi>2.0.co;2

Qian, Y., and Zhang, S. (2013). Cause of the rapid weakening of typhoon bebinca (0021) in the SouthSouth China sea. *Trop. Cycl. Res. Rev.* 2, 159–168. doi:10.6057/2013TCRR03.03

Rappaport, E. N., Franklin, J. L., Schumacher, A. B., DeMaria, M., Shay, L. K., and Gibney, E. J. (2010). Tropical cyclone intensity change before U.S. Gulf coast landfall. *Weather Forecast.* 25, 1380–1396. doi:10.1175/2010waf2222369.1

Song, J. J., Klotzbach, P. J., Zhao, H., and Duan, Y. H. (2021). Slowdown in the decay of Western North Pacific tropical cyclones making landfall on the Asian continent. *Front. Earth Sci.* 9, 749287. doi:10.3389/feart.2021.749287

Thomas, A. M., and Shepherd, J. M. (2022). A machine-learning based tool for diagnosing inland tropical cyclone maintenance or intensification events. *Front. Earth Sci.* 10, 818671. doi:10.3389/feart.2022.818671

Trenberth, K. (2005). Uncertainty in hurricanes and global warming. *Science* 308, 1753–1754. doi:10.1126/science.1112551

Truchelut, R. E., and Staehling, E. M. (2017). An energetic perspective on United States tropical cyclone landfall droughts. *Geophys. Res. Lett.* 44, 12013–12019. doi:10.1002/2017gl076071

Tuleya, R. E., Bender, M. A., and Kurihara, Y. (1984). A simulation study of the landfall of tropical cyclones. *Mon. Weather Rev.* 112, 124–136. doi:10.1175/1520-0493(1984)112<0124:assotl>2.0.co;2

Tuleya, R. E., and Kurihara, Y. (1978). A numerical simulation of the landfall of tropical cyclones. *J. Atmos. Sci.* 35, 242–257. doi:10.1175/1520-0469(1978)035<0242:ANSOTL>2.0.CO;2

Tuleya, R. E. (1994). Tropical storm development and decay: Sensitivity to surface boundary conditions. *Mon. Weather Rev.* 122, 291–304. doi:10.1175/1520-0493(1994)122<0291:tsdads>2.0.co;2

Vickery, P. J. (2005). Simple empirical models for estimating the increase in the central pressure of tropical cyclones after landfall along the coastline of the United States. *J. Appl. Meteor.* 44, 1807–1826. doi:10.1175/jam2310.1

Vitart, F. (2009). Impact of the Madden Julian Oscillation on tropical storms and risk of landfall in the ECMWF forecast system. *Geophys. Res. Lett.* 36, 6. doi:10.1029/2009gl039089

Walsh, K. J. E., McBride, J. L., Klotzbach, P. J., Balachandran, S., Camargo, S. J., Holland, G., et al. (2016). Tropical cyclones and climate change. *WIREs Clim. Change* 7, 65–89. doi:10.1002/wcc.371

Wang, W., and Yu, J. (2013). Characteristic comparison between the rapid intensification of tropical cyclones in easterly and westerly wind shear over the Northwest Pacific. (in Chinese). *Trans. Atmos. Sci.* 36, 337–345. doi:10.13878/j.cnki.dqkxxb.2013.03.011

Wang, Y., Rao, Y., Tan, Z., and Schonemann, D. (2015). A statistical analysis of the effects of vertical wind shear on tropical cyclone intensity change over the Western North Pacific. *Mon. Weather Rev.* 143, 3434–3453. doi:10.1175/mwr-d-15-0049.1

Wong, M. L. M., Chan, J. C. L., and Zhou, W. (2008). A simple empirical model for estimating the intensity change of tropical cyclones after landfall along the South China coast. *J. Appl. Meteorol. Climatol.* 47, 326–338. doi:10.1175/2007jamc1633.1

Wood, K. M., and E Ritchie, A. (2015). A definition for rapid weakening of North Atlantic and eastern North Pacific tropical cyclones. *Geophys. Res. Lett.* 42, 10091–10097. doi:10.1002/2015gl066697

Ying, M., Zhang, W., Yu, H., Lu, X., Feng, J., Fan, Y., et al. (2014). An overview of the China Meteorological Administration tropical cyclone database. *J. Atmos. Ocean. Technol.* 31, 287–301. doi:10.1175/jtech-d-12-00119.1

Zeng, Z., Wang, Y., and Chen, L. (2010). A statistical analysis of vertical shear effect on tropical cyclone intensity change in the North Atlantic. *Geophys. Res. Lett.* 37, L02802. doi:10.1029/2009gl041788

Zhang, Q., Wu, L., and Liu, Q. (2009). Tropical cyclone damages in China 1983-2006. *Bull. Am. Meteorol. Soc.* 90, 489–496. doi:10.1175/2008bams2631.1

Zhang, X., Xiao, Q., and Fitzpatrick, P. J. (2007). The impact of multisatellite data on the initialization and simulation of Hurricane Lili's (2002) rapid weakening phase. *Mon. Weather Rev.* 135, 526–548. doi:10.1175/mwr3287.1

Zhu, Y. J., Collins, J. M., and Klotzbach, P. J. (2021). Nearshore hurricane intensity change and post-landfall dissipation along the United States Gulf and east coasts. *Geophys. Res. Lett.* 48, 1–10. doi:10.1029/2021gl094680

frontiers | Frontiers in Earth Science

TYPE Original Research
PUBLISHED 19 December 2022
DOI 10.3389/feart.2022.1062465

OPEN ACCESS

EDITED BY
Eric Hendricks,
National Center for Atmospheric Research (UCAR), United States

REVIEWED BY
Richard Rotunno,
University Corporation for Atmospheric Research (UCAR), United States
Nannan Qin,
Fudan University, China

*CORRESPONDENCE
Richard K. Taft,
rick.taft@colostate.edu

SPECIALTY SECTION
This article was submitted to Atmospheric Science, a section of the journal Frontiers in Earth Science

RECEIVED 05 October 2022
ACCEPTED 22 November 2022
PUBLISHED 19 December 2022

CITATION
Schubert WH, Taft RK and Slocum CJ (2022), Baroclinic effects on the distribution of tropical cyclone eye subsidence.
Front. Earth Sci. 10:1062465.
doi: 10.3389/feart.2022.1062465

Baroclinic effects on the distribution of tropical cyclone eye subsidence

Wayne H. Schubert[1], Richard K. Taft[1]* and Christopher J. Slocum[2]

[1]Department of Atmospheric Science, Colorado State University, Fort Collins, CO, United States, [2]NOAA Center for Satellite Applications and Research, Colorado State University, Fort Collins, CO, United States

Solutions of the secondary (transverse) circulation equation for an axisymmetric, gradient balanced vortex are used to better understand the distribution of subsidence in the eye of a tropical cyclone. This secondary circulation equation is derived using both the physical radius coordinate r and the potential radius coordinate R. In the R-coordinate version, baroclinic effects are implicit in the coordinate transformation and are recovered in the final step of transforming the solution for the streamfunction Ψ back from R-space to r-space. Two types of elliptic problems for Ψ are formulated: 1) the full secondary circulation problem, which is formulated on $0 \le R < \infty$, with the diabatic forcing due to eyewall convection appearing on the right-hand side of the elliptic equation; 2) the restricted secondary circulation problem, which is formulated on $0 \le R \le R_{\mathrm{ew}}$, where the constant R_{ew} is the potential radius of the inside edge of the eyewall, with no diabatic forcing but with the streamfunction specified along $R = R_{\mathrm{ew}}$. The restricted secondary circulation problem can be solved semi-analytically for the case of vertically sheared, Rankine vortex cores. The solutions identify the conditions under which large values of radial and vertical advection of θ are located in the lower troposphere at the outer edge of the eye, thereby producing a warm-ring thermal structure.

KEYWORDS

tropical cyclone, eye subsidence, baroclinic effects, secondary circulation, gradient balanced vortex

1 Introduction

The concept of hub clouds and eye moats comes from aircraft observations made by Simpson and Starrett (1955). Figure 1 is adapted from their schematic diagram of Hurricane Edna (9–10 September 1954). Of particular interest is the hub cloud near the circulation center and the clear moat at the edge of the eye. In later years, intense storms like Edna have been found that also possess a warm-ring thermal structure in the lower troposphere—where the temperature surrounding the center of a tropical cyclone is greater than the center, which is in contrast to a warm-core thermal structure where temperature decreases radially outward from the center. A good example is Hurricane Isabel on 13 September 2003, when it had tangential winds in excess of 70 m s^{-1}. Figure 2

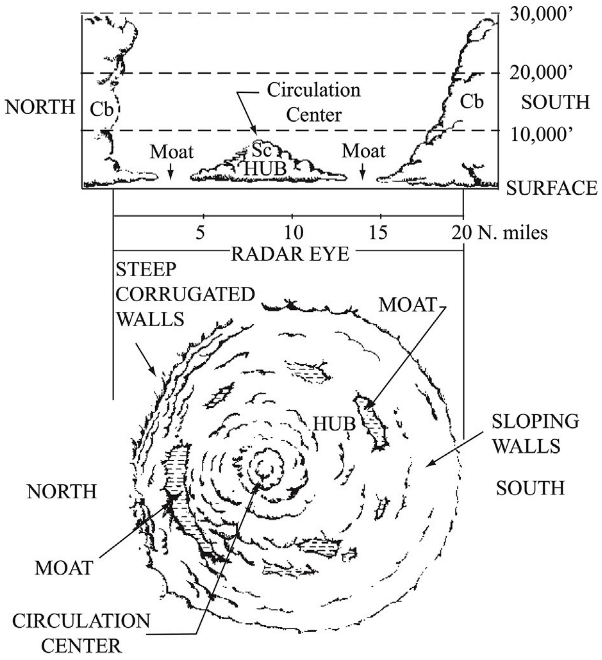

FIGURE 1
Schematic diagram of the eye of Hurricane Edna, 9–10 September 1954, as adapted from Simpson and Starrett (1955). At this time, Hurricane Edna had a steep corrugated eyewall on its north side and a sloping (≈ 45°) eyewall on its south side. Such variations in eyewall slope are often interpreted as an effect of environmental vertical shear (see Hazelton and Hart, 2013; Hazelton et al., 2015; and the recent review by Rogers, 2021). The stratocumulus "hub cloud" near the circulation center and the moat near the edge of the eye indicate that in strong hurricanes the subsidence is not uniform across the eye, but rather is concentrated near the edge of the eye. Enhanced subsidence in the lower troposphere near the edge of the eye leads to a lower-tropospheric warm-ring thermal structure, as shown in Figure 2 for Hurricane Isabel (2003). A photograph of Isabel's hub cloud is shown in Figure 3, which indicates that the hub clouds in Isabel and Edna were of approximately the same height, although Isabel's eye diameter was somewhat larger than that of Edna.

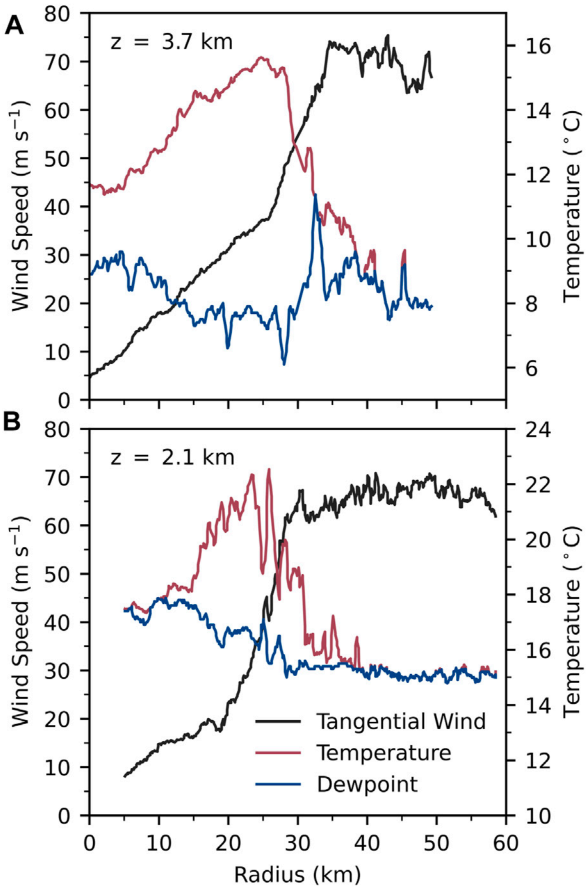

FIGURE 2
Radial profiles of NOAA WP-3D aircraft data for Hurricane Isabel on 13 September 2003. The panel **(B)** is for the z = 2.1 km flight leg (1922 to 1931 UTC) and the panel **(A)** for the z = 3.7 km flight leg (1948 to 1956 UTC). Black curves are for tangential wind, red curves for temperature, and blue curves for dewpoint temperature. Adapted from Schubert et al. (2007).

shows NOAA WP-3D aircraft data for this storm. The two panels show tangential wind (black curves), temperature (red curves), and dewpoint temperature (blue curves) for a 2.1 km altitude radial leg (lower panel) and a 3.7 km altitude radial leg (upper panel). A warm-ring thermal structure occurs at both levels, with the warmest and driest air at 25 km radius, which is at the outer edge of the eye. In temperature, the warm ring is approximately 4.2°C warmer than the vortex center at 3.7 km and 5.0°C warmer than the vortex center at 2.1 km. As can be seen from the dewpoint depressions, the warm-ring region near 25 km radius is associated with dry, subsiding air at the outer edge of the eye. Enhanced subsidence at the outer edge of the eye tends to produce an eye-moat. Note that the center of the eye is saturated at z = 2.1 km but is not saturated at z = 3.7 km, which is consistent with the top of the hub cloud being located at $z \approx 3$ km. The tangential wind profiles reveal a vorticity structure more complicated than the simple structure that will be assumed in Section 3. This is evident from the kinks that occur near $r \approx 20$ km for z = 2.1 km and near $r \approx 27$ km for z = 3.7 km. In other words, Isabel had a somewhat "hollow" vorticity structure compared to the radially uniform structure that is assumed in Section 3.

The photograph shown here as Figure 3 was taken from the WP-3D aircraft near the edge of the eye, looking towards the hub cloud at the center of the eye. The top of the hub cloud is near 3 km altitude, so the radial leg in the upper panel of Figure 2 is just above the top of the hub cloud, while the radial leg in the lower panel is just below the top of the hub cloud, as is evident in the dewpoint depressions. Since the first internal mode Rossby length in the eye of Isabel at this time is on the order of 10–15 km, the eye diameter (~ 60 km) is approximately 5 Rossby lengths, allowing for the rare opportunity to view balanced dynamical

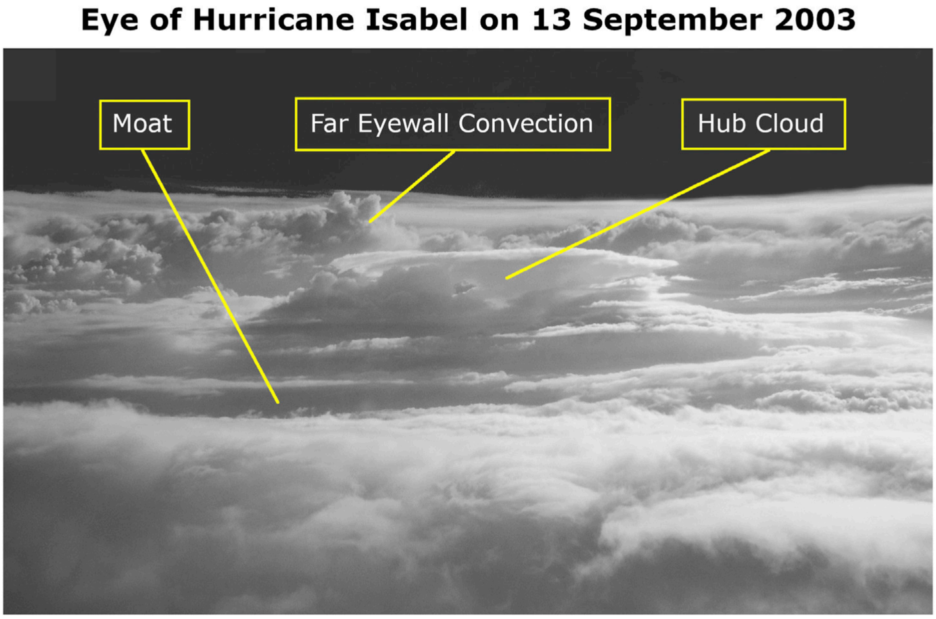

FIGURE 3
Photograph of the eye of Hurricane Isabel on 13 September 2003. The 3 km tall hub cloud at the center of the eye is surrounded by a moat of clear air or shallow stratocumulus. Beyond the hub cloud and on the opposite side of the eye (at a distance of ~ 60 km) lies eyewall convection extending up to 12–14 km. Photo courtesy of Sim Aberson.

structure over several Rossby lengths in a single photograph. For comprehensive discussions of Hurricane Isabel, see Montgomery et al. (2006), Aberson et al. (2006), Bell and Montgomery (2008), Nolan et al. (2009b,a), and Stern et al. (2016). The eye-moat and mesovortex structure of Hurricane Isabel on 12 September 2003 is discussed by Kossin and Schubert (2004) and Rozoff et al. (2006).

Another common feature of intense tropical cyclones is the "stadium effect," caused by the outward slope of the eyewall. An example of this effect, taken from the CloudSat data archive, is shown in Figure 4. This vertical cross-section was obtained when CloudSat's 94 GHz Cloud Profiling Radar made a fortuitous pass directly over the eye of Typhoon Choi-Wan on 15 September 2009. In the top panel of Figure 4, the vertical scale is stretched to highlight the vertical structure of the radar reflectivity. In the bottom panel, only the region inside a radius of 50 km is shown, so the aspect ratio is one-to-one, which clearly reveals the approximate 45° baroclinic tilt of the eyewall updraft. The incorporation of such baroclinic tilt is an important aspect of the theoretical analysis presented here in Sections 2 and 3.

An interesting feature of nonhydrostatic, full-physics, tropical cyclone models is that they can produce intense storms with a temperature field that has a warm-core structure at upper levels, but a warm-ring structure at lower levels. The first example of this was presented by Yamasaki (1983), whose Figure 10A is reproduced here as Figure 5. The upper tropospheric warm-core anomaly is 17°C and is centered at a height of 14 km. A warm-ring thermal structure is found between heights of 2 and 8 km, and at a radius of approximately 7–8 km. Much of the present paper is devoted to a balanced dynamical interpretation of the production of such an overall thermal structure.

For the study of eye subsidence, one can envision using (at least) four different sets of independent variables in space: radius and log-pressure, (r, z); potential radius and log-pressure, (R, Z); radius and potential temperature, (r, θ); or potential radius and potential temperature, (R, Θ). Note that $Z = z$ and $\Theta = \theta$, but the upper case symbols Z and Θ are used because $(\partial/\partial Z) \neq (\partial/\partial z)$ and $(\partial/\partial\Theta) \neq (\partial/\partial\theta)$. Concerning the use of (R, Θ)-coordinates, since the flow in the eye is inviscid and adiabatic, both R and Θ are Lagrangian coordinates, which means that a given parcel in the eye stays on its original R-surface and its original Θ-surface. In other words, when the mathematical analysis is performed in (R, Θ)-space, there is no need for a transverse circulation equation, and the dynamics is more easily understood in the framework of PV and its invertibility principle, as discussed in a theoretical context by Schubert and Alworth (1987), Möller and Smith (1994), and Schubert (2018), and in an observational context by Martinez et al. (2019). This is in sharp contrast to the use of (r, z)-coordinates, where neither r nor z is a Lagrangian coordinate. In this paper, we have analyzed the transverse circulation problem in (R, Z)-coordinates, a setting in which one coordinate is Lagrangian and the other is not. There is a duality between the use of (R, Z)-coordinates and the use of (r, θ)-coordinates, since in the (r, θ)-formulation, one coordinate is Lagrangian (recall that $\dot{\theta} = 0$ in the eye) and the other is not.

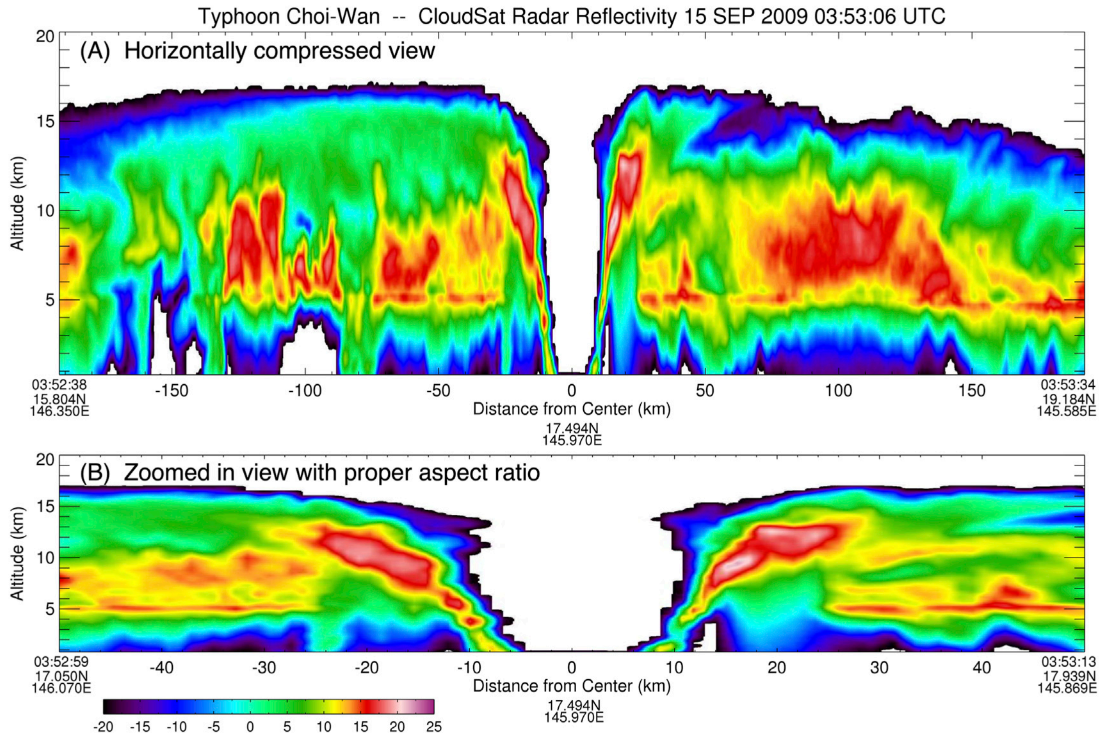

FIGURE 4
At 0353 UTC on 15 September 2009, CloudSat's 94 GHz Cloud Profiling Radar passed directly over Typhoon Choi-Wan. This figure shows a north-south vertical cross-section of radar reflectivity for the 65 m s^{-1} storm (north is to the right) when it was located approximately 450 km north of Guam. In the panel **(A)**, the horizontal scale is compressed to exaggerate the vertical structure. In the panel **(B)**, only the region inside a radius of 50 km is shown (which excludes the secondary eyewall), but the aspect ratio is one-to-one, thus showing the sloping eyewall (or "stadium effect") as would be seen by an observer on a research aircraft. Reflectivity values less than – 20 dBZ have been removed for clarity. This figure has been adapted from Schubert and McNoldy (2010) and is based on radar data made available through the NASA CloudSat Project.

Thus, the essential results obtained in Section 3 using the (R, Z)-formulation could also be obtained using the (r, θ)-formulation. However, some details involved in the two formulations are different. For example, in the (r, θ)-formulation, a convenient vertically sheared Rankine core has solid-body rotation on each isentropic surface rather than on each isobaric surface. Also, in the elliptic problem (Eq. 16), the outer boundary is the coordinate surface $R = R_{ew}$, while in the (r, θ)-formulation a sloping eyewall outer boundary would not be an r-surface, thereby producing an additional difficulty in the solution of the elliptic problem. Thus, while the difficulties of including baroclinic effects in the (r, z)-formulation can be overcome by using either the (R, Z)-formulation or the (r, θ)-formulation, the analysis presented in this paper is indicative of our slight preference for the (R, Z)-formulation.

The paper is organized as follows. Section 2 first presents the balanced vortex equations in the (r, z)-formulation, and then transforms to the (R, Z)-formulation. For certain baroclinic vortices, the (R, Z) formulation of the transverse circulation equation can be solved semi-analytically using a vertical transform approach (Section 3). These semi-analytical solutions are used to generalize the barotropic vortex results of Schubert et al. (2007) and to better understand the role of baroclinicity in the distribution of subsidence in the eye of an intense tropical cyclone.

2 Gradient balance theory

For simplicity, the analysis presented here considers an axisymmetric, balanced flow in the inviscid fluid that lies above the frictional boundary layer. To simplify the primitive equation model to a balanced vortex model, we assume that the azimuthal flow remains in a gradient balanced state, i.e., we discard the exact radial equation of motion and replace it with the gradient balance condition given below as the first entry in Eq. 1. A sufficient condition for the validity of this assumption is that the diabatic forcing effects have slow enough time scales that significant, azimuthal mean inertia-gravity waves are not excited. We shall describe this inviscid flow using the log-pressure vertical coordinate $z = H \ln(p_0/p)$, where $H = R_d T_0/g$ is the constant scale height, p_0 and T_0 are constant reference values of pressure and temperature, R_d is the gas constant for dry air, and g is the

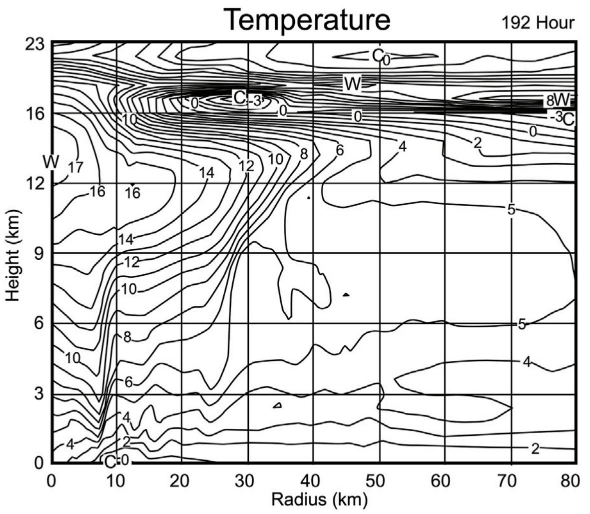

FIGURE 5
Vertical cross-section of the temperature anomaly (°C) from the nonhydrostatic, full-physics model simulation of an intense tropical cyclone by Yamasaki (1983). A warm-core thermal structure (17°C anomaly) is found at heights near 14 km, while a warm-ring thermal structure is found near $r \approx 7$–8 km between heights of 2 and 8 km. As shown in Eq. 35 the warm-ring thermal structure is associated with absolute angular momentum surfaces that are tilted in opposite directions on the two sides of the warm ring. The upper troposphere/lower stratosphere cold anomaly produced by this model is similar to that observed by Johnson and Kriete (1982) for tropical mesoscale systems using radiosonde data (their Figure 3) and by Rivoire et al. (2016) using COSMIC GPS radio occultation data. Adapted from Figure 10A of Yamasaki (1983).

acceleration of gravity. Under the balance condition, the governing equations are

$$\begin{aligned} \left(f+\frac{v}{r}\right)v &= \frac{\partial \phi}{\partial r}, \\ \frac{\partial v}{\partial t}+w\frac{\partial v}{\partial z}+\left(f+\frac{\partial (rv)}{r\,\partial r}\right)u &= 0, \\ \frac{\partial \phi}{\partial z} &= \frac{g}{T_0}T, \\ \frac{\partial (ru)}{r\,\partial r}+\frac{\partial (\rho w)}{\rho\,\partial z} &= 0, \\ \frac{\partial T}{\partial t}+u\frac{\partial T}{\partial r}+w\left(\frac{\partial T}{\partial z}+\frac{\kappa T}{H}\right) &= \frac{Q}{c_{\mathrm{p}}}, \end{aligned} \tag{1}$$

where $\kappa = R_{\mathrm{d}}/c_{\mathrm{p}}$, c_{p} is the specific heat at constant pressure, f the constant Coriolis parameter, $\rho(z) = \rho_0 e^{-z/H}$ the pseudo-density in the log-pressure coordinate, $\rho_0 = p_0/(R_{\mathrm{d}}T_0)$ the constant reference density, ϕ the geopotential, u the radial velocity component, v the azimuthal velocity component, w the log-pressure vertical velocity, and Q the diabatic heating. The potential vorticity (PV) equation, derived from Eq. 1, is

$$\frac{DP}{Dt} = \frac{1}{\rho}\left[-\frac{\partial v}{\partial z}\frac{\partial \dot{\theta}}{\partial r}+\left(f+\frac{\partial (rv)}{r\,\partial r}\right)\frac{\partial \dot{\theta}}{\partial z}\right], \tag{2}$$

where $D/Dt = (\partial/\partial t) + u(\partial/\partial r) + w(\partial/\partial z)$ is the material derivative,

$$P = \frac{1}{\rho}\left[-\frac{\partial v}{\partial z}\frac{\partial \theta}{\partial r}+\left(f+\frac{\partial (rv)}{r\,\partial r}\right)\frac{\partial \theta}{\partial z}\right] = \frac{fR}{\rho r}\frac{\partial (R,\theta)}{\partial (r,z)} \tag{3}$$

is the potential vorticity, $\theta = T\,(p_0/p)^{\kappa} = Te^{\kappa z/H}$ is the potential temperature, $c_{\mathrm{p}}\dot{\theta}/\theta = Q/T$, and the potential radius R is defined in terms of the absolute angular momentum by $\frac{1}{2}fR^2 = rv + \frac{1}{2}fr^2$.

Using the mass conservation principle, we define a streamfunction ψ such that

$$\rho u = -\frac{\partial \psi}{\partial z} \quad \text{and} \quad \rho w = \frac{\partial (r\psi)}{r\,\partial r}. \tag{4}$$

For convenience, we shall refer to ψ as the “streamfunction,” although it is worth noting that it is actually $r\psi$, rather than ψ, that is the “streamfunction” for the transverse mass flux. This flexibility with the factor r proves convenient for the analytical solutions presented in Section 3. Using the gradient balance relation in the tangential wind equation, and using the hydrostatic relation in the thermodynamic equation, we can write

$$\begin{aligned} \frac{\partial \phi_t}{\partial r} - \rho B w + \rho C u &= 0, \\ \frac{\partial \phi_t}{\partial z} + \rho A w - \rho B u &= \frac{gQ}{c_{\mathrm{p}}T_0}, \end{aligned} \tag{5}$$

where $\phi_t = (\partial\phi/\partial t)$ is the geopotential tendency, and where the static stability A, the baroclinicity B, and the inertial stability C are given by

$$\begin{aligned} \rho A &= \frac{g}{T_0}\left(\frac{\partial T}{\partial z}+\frac{\kappa T}{H}\right), \\ \rho B &= -\left(f+\frac{2v}{r}\right)\frac{\partial v}{\partial z} = -\frac{g}{T_0}\frac{\partial T}{\partial r}, \\ \rho C &= \left(f+\frac{2v}{r}\right)\left(f+\frac{\partial (rv)}{r\,\partial r}\right). \end{aligned} \tag{6}$$

Eliminating ϕ_t between the two equations in Eq. 5, then expressing u and w in terms of ψ *via* Eq. 4, and requiring that $w = 0$ at the top and bottom boundaries, we obtain the following transverse circulation problem (Eliassen, 1951).

$$\begin{gathered} \textbf{Secondary Circulation Problem on the Full}\,(\boldsymbol{r},\boldsymbol{z})-\textbf{Domain :} \\ \frac{\partial}{\partial r}\left(A\frac{\partial (r\psi)}{r\,\partial r}+B\frac{\partial \psi}{\partial z}\right)+\frac{\partial}{\partial z}\left(B\frac{\partial (r\psi)}{r\,\partial r}+C\frac{\partial \psi}{\partial z}\right) = \frac{g}{c_{\mathrm{p}}T_0}\frac{\partial Q}{\partial r} \\ \text{for} \quad 0 \le r < \infty \quad \text{and} \quad 0 \le z \le z_{\mathrm{T}} \quad \text{with} \\ \begin{cases} \psi(0,z) = \psi(r,0) = \psi(r,z_{\mathrm{T}}) = 0, \\ r\psi(r,z) \to 0 \quad \text{as} \quad r \to \infty\,. \end{cases} \end{gathered} \tag{7}$$

Note that $AC - B^2 = gT_0^{-1}\rho_0^{-1}e^{(1-\kappa)z/H}(f + 2v/r)P$, so that this problem is elliptic if $(f + 2v/r)P > 0$, which is typically the case for the tropical cyclone core region studied in this paper.

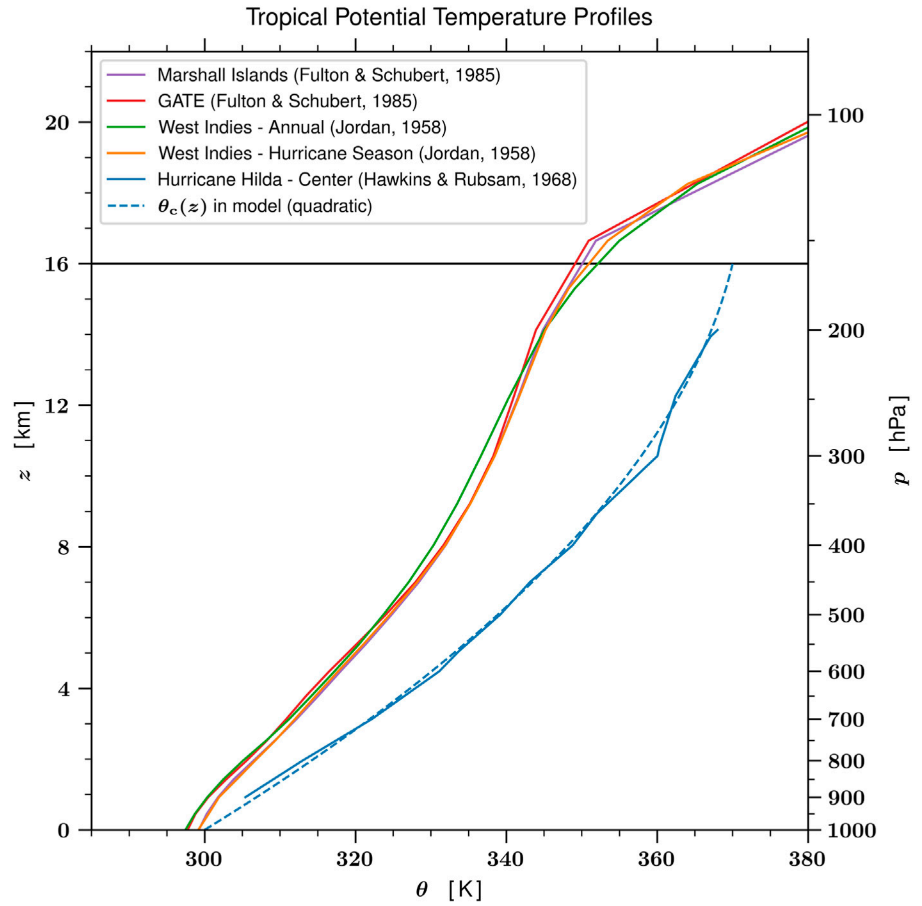

FIGURE 6
The solid blue curve is the θ profile in the core of Hurricane Hilda, as described by Hawkins and Rubsam (1968). The dashed blue curve is the quadratic approximation $\theta_c(z)$ given by Eq. 18. For reference, the annual mean and hurricane season mean profiles for the West Indies (Jordan, 1958) and the mean profiles for the Marshall Islands and GATE (Fulton and Schubert, 1985) are shown by the other colored curves. The maximum warm-core anomaly in θ occurs at 300 hPa and is approximately 21 K. The horizontal line at z = 16 km denotes the upper boundary used in the calculations presented in Section 3.

According to Eq. 7, subsidence in the hurricane eye at a particular time is forced by the $(\partial Q/\partial r)$ term and is shaped by the three spatially varying coefficients A, B, C at that time. Analytical progress in understanding eye subsidence can more easily be made if we obtain a transformed version of Eq. 7 that contains only two spatially varying coefficients and does not contain any second order mixed derivative terms. The balanced vortex model and the associated transverse circulation equation take simple forms when the original independent variables (r, z, t) are replaced by the new independent variables (R, Z, τ), where $Z = z$ and $\tau = t$ but $\partial/\partial Z$ and $\partial/\partial \tau$ imply fixed potential radius R. This transformation (Schubert and Hack, 1983) makes use of

$$\left(\frac{\partial}{\partial r}, \frac{\partial}{\partial z}, \frac{\partial}{\partial t}\right) = \left(\frac{\partial R}{\partial r}\frac{\partial}{\partial R}, \frac{\partial R}{\partial z}\frac{\partial}{\partial R} + \frac{\partial}{\partial Z}, \frac{\partial R}{\partial t}\frac{\partial}{\partial R} + \frac{\partial}{\partial \tau}\right), \tag{8}$$

from which it follows that

$$\frac{D}{Dt} = \frac{\partial}{\partial t} + u\frac{\partial}{\partial r} + w\frac{\partial}{\partial z} = \frac{\partial}{\partial \tau} + w\frac{\partial}{\partial Z}. \tag{9}$$

Defining U, V, W, and Φ by

$$\begin{aligned} U &= \frac{r}{R}u + \frac{w}{f}\frac{\partial V}{\partial Z}, & W &= \left(\frac{f}{f+\zeta}\right)w, \\ V &= \frac{r}{R}v, & \Phi &= \phi + \frac{1}{2}v^2, \end{aligned} \tag{10}$$

where $\zeta = r^{-1}\partial(rv)/\partial r$ is the relative vorticity, the governing equations (Eq. 1) transform to (see Appendix A for further details)

$$\begin{aligned} \hat{f}V &= \frac{\partial \Phi}{\partial R}, & \frac{\partial (RU)}{R\,\partial R} + \frac{\partial (\rho W)}{\rho\,\partial Z} &= 0, \\ \frac{\partial V}{\partial \tau} + fU &= 0, & & \\ \frac{\partial \Phi}{\partial Z} &= \frac{g}{T_0}T, & \frac{\partial T}{\partial \tau} + \frac{T_0}{g}N^2 W &= \frac{Q}{c_p}, \end{aligned} \tag{11}$$

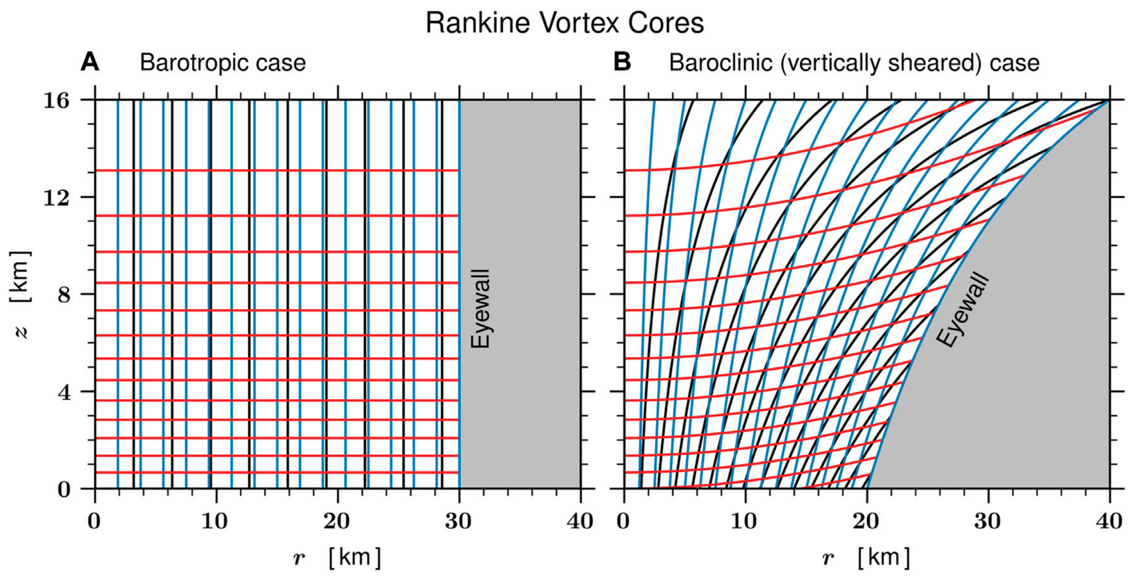

FIGURE 7
Structure of the Rankine vortex core, as described by Eq. 17, for both the barotropic case **(A)** where $\hat{f}_0 = \hat{f}_T = 64\,f$ and the baroclinic (vertically sheared) case **(B)** where $\hat{f}_0 = 144\,f$ and $\hat{f}_T = 36\,f$. The three sets of contours (black, blue, and red) are for $v(r, z)$, $R(r, z)$ and $\theta(r, z)$ in the eye region, which is bounded by an eyewall at $R = R_{ew} = 240$ km. The physical radius for the eyewall, given by $r_{ew}(z) = [f/\hat{f}(z)]^{1/2} R_{ew}$, has a constant value of 30 km in the barotropic case but slopes outward between $r = 20$ km and $r = 40$ km in the baroclinic case. In panel **(A)**, the black contours for $v(r, z)$ run from 5 to 45 $\mathrm{m\,s^{-1}}$ in increments of 5 $\mathrm{m\,s^{-1}}$, the blue contours for $R(r, z)$ run from 15 to 240 km in increments of 15 km, while the red contours for $\theta(r, z)$ run from 305 K to 365 K in increments of 5 K. In panel **(B)**, the black contours for $v(r, z)$ run from 5 to 70 $\mathrm{m\,s^{-1}}$ in increments of 5 $\mathrm{m\,s^{-1}}$, the blue contours for $R(r, z)$ run from 15 to 240 km in increments of 15 km, while the red contours for $\theta(r, z)$ run from 295 K to 365 K in increments of 5 K.

where the effective inertial frequency $\hat{f}$ and the effective buoyancy frequency N are defined by

$$\begin{aligned} \hat{f}^2 &= \left(f + \frac{2v}{r}\right)^2 = f^2 \frac{R^4}{r^4} = f^4 \left(f - \frac{2V}{R}\right)^{-2}, \\ N^2 &= \left(\frac{f+\zeta}{f}\right) \frac{g}{T_0} \left(\frac{\partial T}{\partial Z} + \frac{\kappa T}{H}\right) \\ &= e^{-\kappa Z/H} \left(\frac{f+\zeta}{f}\right) \frac{g}{T_0} \frac{\partial \theta}{\partial Z} = e^{-\kappa Z/H} \frac{g \rho P}{T_0 f}. \end{aligned} \tag{12}$$

It follows that r and R are related by $r = (f/\hat{f})^{1/2} R$ and that $rv = RV$. Note that the system in Eq. 11 is formally simpler than the system in Eq. 1, even though no additional approximations have been introduced. Also note that the effective buoyancy frequency N can differ greatly from the usual buoyancy frequency in the cyclone core, but they are essentially the same in far-field regions where $|\zeta| \ll f$ and the angular momentum surfaces are nearly vertical, so that $(\partial T/\partial Z) \approx (\partial T/\partial z)$ and $(\partial \theta/\partial Z) \approx (\partial \theta/\partial z)$.

Using the fourth entry in Eq. 11, we define the streamfunction Ψ such that

$$\rho U = -\frac{\partial \Psi}{\partial Z} \quad \text{and} \quad \rho W = \frac{\partial (R\Psi)}{R\,\partial R}. \tag{13}$$

From Eqs. 4 and 13, and the transformation relations in Eq. 8, it can be shown that $R\Psi$ and $r\psi$ differ only by a constant, which, without loss of generality, we can take to be zero, so that $R\Psi = r\psi$. Using the gradient balance relation in the tangential wind equation, and using the hydrostatic relation in the thermodynamic equation, we can write

$$\frac{\partial \Phi_\tau}{\partial R} + \hat{f}^2 U = 0 \quad \text{and} \quad \frac{\partial \Phi_\tau}{\partial Z} + N^2 W = \frac{gQ}{c_p T_0}, \tag{14}$$

where $\Phi_\tau = (\partial \Phi/\partial \tau) = (\partial \phi/\partial t)$ is the "geopotential tendency." Eliminating Φ_τ between these two equations, and then expressing U and W in terms of Ψ *via* Eq. 13, we obtain the following transverse circulation problem.

Secondary Circulation Problem on the Full (R, Z) – Domain :

$$\frac{\partial}{\partial R}\left(N^2 e^{Z/H} \frac{\partial (R\Psi)}{R\,\partial R}\right) + \frac{\partial}{\partial Z}\left(\hat{f}^2 e^{Z/H} \frac{\partial \Psi}{\partial Z}\right) = \frac{g\rho_0}{c_p T_0} \frac{\partial Q}{\partial R}$$

$$\text{for} \quad 0 \le R < \infty \quad \text{and} \quad 0 \le Z \le Z_T \quad \text{with}$$

$$\begin{cases} \Psi(0, Z) = \Psi(R, 0) = \Psi(R, Z_T) = 0, \\ R\Psi(R, Z) \to 0 \quad \text{as} \quad R \to \infty\,. \end{cases} \tag{15}$$

The boundary conditions on Ψ come from the requirement that the log-pressure vertical velocity vanishes at the bottom and top boundaries, that the radial component of the secondary circulation vanishes at $R = 0$, and that the secondary circulation goes to zero as $R \to \infty$. To summarize, the secondary circulation in

TABLE 1 Numerical results for the barotropic case (top table) and the baroclinic case (bottom table). The first column lists the vertical mode index ℓ, while the second column lists the corresponding values of the Rossby length μ_ℓ^{-1}, which are determined from the eigenvalues of the Sturm–Liouville problem in Eq. 23. Note that the crude approximation $\mu_\ell^{-1} \approx \mu_1^{-1}/\ell$, which can be derived for the special case where N^2 and $\hat{f}$ are constants, works better for the barotropic case, for which $\hat{f}(z)$ is a constant. The five corresponding eigenfunctions are shown in the left and right panels of Figure 8. For the choice $R_{ew} = 240$ km, the third column lists values of $\mu_\ell R_{ew}$, which can be interpreted as the number of Rossby lengths (in R-space) between the vortex center $R = 0$ and the inner edge of the eyewall $R = R_{ew}$. The fourth column lists values of $I_0(\mu_\ell R_{ew})$, which can be interpreted as the factor by which (for given ℓ) the subsidence at the center is reduced from that at the edge of the eye. The large value of $I_0(\mu_\ell R_{ew})$ for $\ell \geq 2$ indicate the importance of the higher vertical modes in producing a lower-tropospheric warm-ring structure. Columns 5 and 6 tabulate the projection of $\Psi_{ew}(Z)$ onto the first five vertical modes, as computed from Eq. 29.

(A) Barotropic Case: $\hat{f}_0 = \hat{f}_T = 64\, f$ **and** $R_{ew} = 240$ **km**

ℓ	μ_ℓ^{-1} (km)	$\mu_\ell R_{ew}$	$I_0(\mu_\ell R_{ew})$	A_ℓ for $Z_m/Z_T = 0.25$	A_ℓ for $Z_m/Z_T = 0.5$
1	133.15	1.80	1.99	−1,005.32	−1,129.26
2	66.78	3.59	7.98	−250.87	304.33
3	44.46	5.40	38.96	−20.77	−81.47
4	33.30	7.21	204.10	−28.60	39.88
5	26.62	9.01	1,108.54	−4.07	−17.82

(B) Baroclinic Case: $\hat{f}_0 = 144\, f$, $\hat{f}_T = 36\, f$, **and** $R_{ew} = 240$ **km**

ℓ	μ_ℓ^{-1} (km)	$\mu_\ell R_{ew}$	$I_0(\mu_\ell R_{ew})$	A_ℓ for $Z_m/Z_T = 0.25$	A_ℓ for $Z_m/Z_T = 0.5$
1	122.53	1.96	2.22	−765.54	−899.72
2	58.44	4.11	12.40	−419.44	−28.88
3	38.54	6.23	82.79	−109.89	14.81
4	28.78	8.34	587.22	−53.50	−7.15
5	22.98	10.45	4,298.18	−23.14	3.72

the entire region is obtained by solving the elliptic problem in Eq. 15 for specified $N(R, Z)$, $\hat{f}(R, Z)$, and $Q(R, Z)$. Note that Eq. 15 is formally simpler than Eq. 7 since it does not contain baroclinic, second order cross derivative terms. Baroclinic effects are implicit in Eq. 15 and are recovered when the solution $\Psi(R, Z)$ is transformed back to the physical space form $\psi(r, z)$ using $\psi = (R/r)\Psi$.

We can understand several aspects of eye subsidence by solution of a restricted version of the full elliptic problem in Eq. 15. In this simplified problem, we restrict our attention to the eye region $0 \leq R \leq R_{ew}$, where the eyewall potential radius R_{ew} (i.e., the inner edge of the eyewall) is assumed to be a constant. In the eye region, we assume that $Q = 0$, so that the elliptic problem in Eq. 15 simplifies as follows.

Secondary Circulation Problem on the Restricted (R, Z) – Domain :

$$\frac{\partial}{\partial R}\left(N^2 e^{Z/H}\frac{\partial(R\Psi)}{R\,\partial R}\right) + \frac{\partial}{\partial Z}\left(\hat{f}^2 e^{Z/H}\frac{\partial\Psi}{\partial Z}\right) = 0$$

$$\text{for} \quad 0 \leq R \leq R_{ew} \quad \text{and} \quad 0 \leq Z \leq Z_T \quad \text{with}$$

$$\begin{cases} \Psi(0, Z) = \Psi(R, 0) = \Psi(R, Z_T) = 0, \\ \Psi(R_{ew}, Z) = \Psi_{ew}(Z). \end{cases} \tag{16}$$

To summarize, the secondary circulation in the eye is obtained by solving the homogeneous, elliptic problem in Eq. 16 with specified $N(R, Z)$, $\hat{f}(R, Z)$, and $\Psi_{ew}(Z)$. Note that all the dynamics in the region $R_{ew} < R < \infty$, described explicitly in Eq. 15, has been replaced in Eq. 16 by the specification of $\Psi(R, Z)$ at $R = R_{ew}$. Because the elliptic problem in Eq. 16 is homogeneous, the solution $\Psi(R, Z)$ has no local maxima or minima in the interior of the restricted domain (i.e., in the eye). For the problems considered here, we have chosen $\Psi_{ew}(Z) \leq 0$, so that $\Psi(R, Z)$ attains its minimum value on the outer boundary $R = R_{ew}$ and its maximum value of zero on the other three boundaries, $R = 0$ and $Z = 0$, Z_T, where $Z_T = z_T$ represents the tropopause. By concentrating attention on the restricted problem (Eq. 16), the goal is to understand how the spatial structure of eye subsidence is shaped by $N(R, Z)$, $\hat{f}(R, Z)$, and $\Psi_{ew}(Z)$. A semi-analytical solution of a simplified version of Eq. 16 is given in Section 3, using vertical transform methods. An alternative approach, not explored here, is to study solutions of the geopotential tendency equation (see Appendix B).

3 Subsidence in a vertically sheared, Rankine vortex core

3.1 The specified vortex

We now solve Eq. 16 semi-analytically for particular choices of the coefficients $\hat{f}(R, Z)$ and $N(R, Z)$. For the example given here, the vortex core is assumed to have constant angular velocity (i.e., solid body rotation) on each isobaric surface, but with the angular velocity varying in the vertical. In terms of $v(r, z)$ and $\theta(r, z)$, the specified vortex for $0 \le r \le r_{\mathrm{ew}}(z)$ and $0 \le z \le z_{\mathrm{T}}$ is given by

$$\begin{cases} v(r,z) = \dfrac{1}{2}\left(\hat{f}(z) - f\right)r, \\ \hat{f}(z) \;\; = \hat{f}_{\mathrm{T}} + \left(\hat{f}_0 - \hat{f}_{\mathrm{T}}\right)\left(\dfrac{e^{-\kappa z/H} - e^{-\kappa z_{\mathrm{T}}/H}}{1 - e^{-\kappa z_{\mathrm{T}}/H}}\right), \\ \theta(r,z) = \theta_{\mathrm{c}}(z) - \dfrac{\left(\hat{f}_0 - \hat{f}_{\mathrm{T}}\right)\hat{f}(z)r^2}{4c_{\mathrm{p}}\left(1 - e^{-\kappa z_{\mathrm{T}}/H}\right)}, \end{cases} \tag{17}$$

where, for this vertically sheared Rankine core, the effective inertial frequency $\hat{f}(z)$ is also the absolute vorticity in the eye, the constants $\hat{f}_0$ and $\hat{f}_{\mathrm{T}}$ are the specified values of $\hat{f}(z)$ at $z = 0$ and $z = z_{\mathrm{T}}$ respectively, and $r_{\mathrm{ew}}(z) = [f/\hat{f}(z)]^{1/2}R_{\mathrm{ew}}$, with the constant R_{ew} denoting the potential radius of the inner edge of the eyewall. The specified function $\theta_{\mathrm{c}}(z)$ is the potential temperature at the vortex center, which is simply taken as a quadratic function of z varying from 300 K at $z = 0$ to 370 K at $z = z_{\mathrm{T}} = 16$ km, i.e.,

$$\theta_{\mathrm{c}}(z) = 300\,\mathrm{K} + \frac{z}{z_{\mathrm{T}}}\left[70\,\mathrm{K} + 52\,\mathrm{K}\left(1 - \frac{z}{z_{\mathrm{T}}}\right)\right]. \tag{18}$$

This profile, shown by the dashed blue line in Figure 6, has been constructed to approximate the θ-profile for the center of Hurricane Hilda, as described by Hawkins and Rubsam (1968) and shown by the solid blue curve in Figure 6. For reference, the mean profiles for the West Indies, as given by Jordan (1958), and the mean profiles for the Marshall Islands and GATE, as given by Fulton and Schubert (1985), are shown by the other colored curves, thereby illustrating the warming of the core of Hilda relative to a far-field environment. In addition to this profile, we have chosen the following parameters for our analyses of both the barotropic and baroclinic cases: $R_{\mathrm{d}} = 287\,\mathrm{J\,kg^{-1}\,K^{-1}}$, $T_0 = 300$ K, $p_0 = 1000$ hPa, $g = 9.81\,\mathrm{m\,s^{-2}}$, $H = R_{\mathrm{d}}T_0/g = 8{,}777$ m, $f = 5 \times 10^{-5}\,\mathrm{s^{-1}}$, and $z_{\mathrm{T}} = 16$ km.

As is easily confirmed, the $v(r, z)$ and $\theta(r, z)$ fields given in Eq. 17 satisfy the thermal wind relation $\hat{f}(\partial v/\partial z) = (g/T_0)(\partial\theta/\partial r)e^{-\kappa z/H}$. The choice $\hat{f}_0 = \hat{f}_{\mathrm{T}}$ corresponds to a barotropic vortex, which is the case studied by Schubert et al. (2007). The vortex specified in Eq. 17 is plotted in the left panel of Figure 7 for the barotropic case $\hat{f}_0 = \hat{f}_{\mathrm{T}} = 64\,f$ and $R_{\mathrm{ew}} = 240$ km, so that $r_{\mathrm{ew}}(z) = 30$ km and $v(r_{\mathrm{ew}}(z), z) = 47.3\,\mathrm{m\,s^{-1}}$. For barotropic cases such as the one shown in Figure 7A, the isolines of v and R are vertical, while the isentropes are parallel to the isobars. The right panel of Figure 7 is for the baroclinic case $\hat{f}_0 = 144\,f$, $\hat{f}_{\mathrm{T}} = 36\,f$, and $R_{\mathrm{ew}} = 240$ km, so that $\frac{1}{2}fR_{\mathrm{ew}} = 6\,\mathrm{m\,s^{-1}}$, $r_{\mathrm{ew}}(0) = 20$ km, $r_{\mathrm{ew}}(z_{\mathrm{T}}) = 40$ km, $v(r_{\mathrm{ew}}(0), 0) = 71.5\,\mathrm{m\,s^{-1}}$, and $v(r_{\mathrm{ew}}(z_{\mathrm{T}}), z_{\mathrm{T}}) = 35\,\mathrm{m\,s^{-1}}$. Note that this baroclinic vortex is warm-core at all levels, with the highest values of θ on any isobaric surface occurring at $r = 0$ and with outward-tilting R-surfaces. The maximum values of $v(r, z)$ occur on the $R_{\mathrm{ew}} = 240$ km surface, which is consistent with the observation (Stern and Nolan, 2009) that, for the majority of storms, the radius of maximum wind is closely approximated by an R-surface.

Written in terms of $V(R, Z)$ and $\theta(R, Z)$, the specified vortex in Eq. 17 for $0 \le R \le R_{\mathrm{ew}}$ and $0 \le Z \le Z_{\mathrm{T}}$ is given by

$$\begin{cases} V(R,Z) = \dfrac{1}{2}f\left(\dfrac{\hat{f}(Z) - f}{\hat{f}(Z)}\right)R, \\ \hat{f}(Z) \;\;\; = \hat{f}_{\mathrm{T}} + \left(\hat{f}_0 - \hat{f}_{\mathrm{T}}\right)\left(\dfrac{e^{-\kappa Z/H} - e^{-\kappa Z_{\mathrm{T}}/H}}{1 - e^{-\kappa Z_{\mathrm{T}}/H}}\right), \\ \theta(R,Z) = \theta_{\mathrm{c}}(Z) - \dfrac{\left(\hat{f}_0 - \hat{f}_{\mathrm{T}}\right)fR^2}{4c_{\mathrm{p}}\left(1 - e^{-\kappa Z_{\mathrm{T}}/H}\right)}. \end{cases} \tag{19}$$

As is also easily confirmed, the $V(R, Z)$ and $\theta(R, Z)$ fields given in Eq. 19 satisfy the thermal wind relation $(\hat{f}^2/f)(\partial V/\partial Z) = (g/T_0)(\partial\theta/\partial R)e^{-\kappa Z/H}$. A crucial property of this vertically sheared Rankine-like vortex core is that the $\theta(R, Z)$ field, given by the last line in Eq. 19, is the sum of a function of Z and a function of R. Using the last line of Eq. 19, we find that N^2 and P take the simplified forms

$$\begin{aligned} N^2(z) &= e^{-\kappa z/H}\,\frac{\hat{f}(z)}{f}\,\frac{g}{T_0}\,\frac{d\theta_{\mathrm{c}}(z)}{dz}, \\ P(z) &= \frac{1}{\rho(z)}\,\hat{f}(z)\,\frac{d\theta_{\mathrm{c}}(z)}{dz}, \end{aligned} \tag{20}$$

so that both N^2 and P are functions of z only for the vertically sheared Rankine core. This allows the solution of Eq. 16 to be written in separable form, i.e., it allows for the analytical solution of Eq. 16 using the vertical normal mode transform method discussed below. The shape of the secondary circulation in the eye depends on the outward tilt of the $R = R_{\mathrm{ew}}$ absolute angular momentum surface and on the ratio of the two variable coefficients in Eq. 16. It is convenient to multiply this ratio by the constant scale height H to obtain the local Rossby length $[N(Z)/\hat{f}(Z)]H \sim [\hat{f}(Z)]^{-1/2}$, so that in the typical situation for which $\hat{f}$ decreases with height, the local Rossby length is smallest in the lower troposphere. This leads to the expectation that the compensating subsidence in the eye occurs closer to the eyewall in the lower troposphere than in the upper troposphere. An alternative interpretation of the dynamics involves the definition of Rossby length *via* vertical mode rather than locally. This alternative interpretation is given in the discussion of the results shown in Table 1.

3.2 Solution *via* the vertical transform method

For the vertically sheared Rankine vortex core, the restricted problem given in Eq. 16 simplifies considerably because N and $\hat{f}$ are functions of Z only. Then, the elliptic partial differential equation reduces to

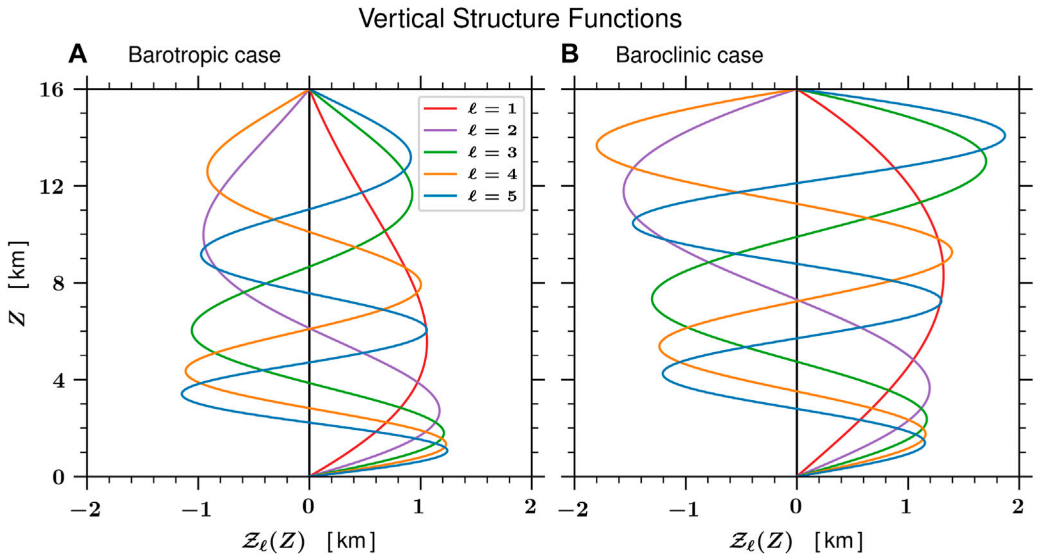

FIGURE 8
Barotropic **(A)** and baroclinic **(B)** vertical structure functions $\mathcal{Z}_\ell(Z)$ for ℓ = 1, 2, 3, 4, 5. These are the eigenfunctions of the Sturm–Liouville problem in Eq. 23, satisfying the orthonormality relation in Eq. 40. The associated eigenvalues are given in the top (barotropic) and bottom (baroclinic) halves of Table 1.

$$\frac{\partial^2\Psi}{\partial R^2} + \frac{\partial\Psi}{R\,\partial R} - \frac{\Psi}{R^2} + \frac{e^{-Z/H}}{N^2}\frac{\partial}{\partial Z}\left(\hat{f}^2 e^{Z/H}\frac{\partial\Psi}{\partial Z}\right) = 0. \tag{21}$$

We now solve Eq. 21 using the vertical transform method. The vertical transform pair is

$$\begin{aligned} \Psi(R,Z) &= \sum_{\ell=1}^{\infty}\Psi_\ell(R)\,\mathcal{Z}_\ell(Z), \\ \Psi_\ell(R) &= \frac{1}{N_0^2 H}\int_0^{Z_T}\Psi(R,Z)\,\mathcal{Z}_\ell(Z)\,N^2(Z)\,e^{Z/H}\,dZ, \end{aligned} \tag{22}$$

where the kernel $\mathcal{Z}_\ell(Z)$ of the transform is defined to be the solution of

$$\begin{gathered} \frac{e^{-Z/H}}{N^2}\frac{d}{dZ}\left(\hat{f}^2 e^{Z/H}\frac{d\mathcal{Z}_\ell}{dZ}\right) + \mu_\ell^2\mathcal{Z}_\ell = 0 \\ \text{with} \quad \mathcal{Z}_\ell(0) = \mathcal{Z}_\ell(Z_T) = 0, \end{gathered} \tag{23}$$

which is a second order differential problem of the Sturm–Liouville type (e.g., Arfken and Weber, 2005, Chapter 10). In this method of solution, the streamfunction $\Psi(R,\ Z)$ is represented as an infinite series of eigenfunctions $\mathcal{Z}_\ell(Z)$ with corresponding eigenvalues μ_ℓ. The constant surface value of the effective buoyancy frequency, denoted by N_0, has been introduced into the weight function $[N^2(Z)/N_0^2][e^{Z/H}/H]$ so that, if $\mathcal{Z}_\ell(Z)$ is normalized in such a way that it is dimensionless, then $\Psi(R,\ Z)$ and $\Psi_\ell(R)$ will have the same units. The orthonormality of the vertical structure functions $\mathcal{Z}_\ell(Z)$ is discussed in Appendix C, as is the derivation of the second entry in Eq. 22 using this orthonormality relation.

To take the vertical transform of Eq. 21, first multiply it by $\mathcal{Z}_\ell(Z)\,[N^2(Z)/N_0^2]\,[e^{Z/H}/H]$ and integrate over Z to obtain

$$\begin{aligned} &\frac{\partial^2\Psi_\ell}{\partial R^2} + \frac{\partial\Psi_\ell}{R\,\partial R} - \frac{\Psi_\ell}{R^2} \\ &\quad + \frac{1}{N_0^2 H}\int_0^{Z_T}\mathcal{Z}_\ell\frac{\partial}{\partial Z}\left(\hat{f}^2 e^{Z/H}\frac{\partial\Psi}{\partial Z}\right)dZ = 0. \end{aligned} \tag{24}$$

Integrating by parts twice, making use of the top and bottom boundary conditions on $\Psi(R,\ Z)$ and $\mathcal{Z}_\ell(Z)$, we obtain

$$\begin{aligned} &\frac{\partial^2\Psi_\ell}{\partial R^2} + \frac{\partial\Psi_\ell}{R\,\partial R} - \frac{\Psi_\ell}{R^2} \\ &\quad + \frac{1}{N_0^2 H}\int_0^{Z_T}\Psi\frac{d}{dZ}\left(\hat{f}^2 e^{Z/H}\frac{d\mathcal{Z}_\ell}{dZ}\right)dZ = 0. \end{aligned} \tag{25}$$

Making use of Eq. 23, the horizontal structure equation (Eq. 25) becomes

$$\begin{gathered} R^2\frac{d^2\Psi_\ell}{dR^2} + R\frac{d\Psi_\ell}{dR} - (\mu_\ell^2 R^2 + 1)\Psi_\ell = 0 \\ \text{for} \quad 0 \le R \le R_{\text{ew}} \quad \text{with} \quad \Psi_\ell(0) = 0. \end{gathered} \tag{26}$$

The solution of Eq. 26 is a linear combination of the order one modified Bessel functions $I_1(\mu_\ell R)$ and $K_1(\mu_\ell R)$. Because $K_1(\mu_\ell R)$ is singular at $R = 0$, only the $I_1(\mu_\ell R)$ solution is

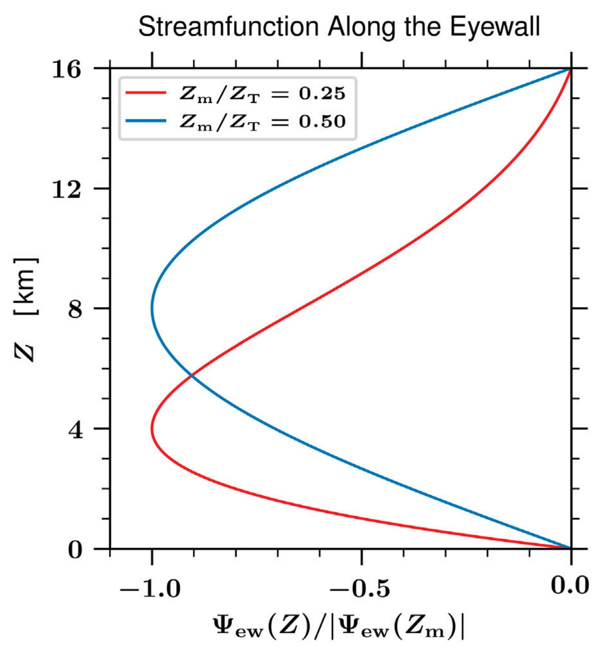

FIGURE 9
The specified function $\Psi_{ew}(Z)/\Psi_{ew}(Z_m)$, as given by Eq. 33, for $Z_m = 0.5\, Z_T = 8$ km and $Z_m = 0.25\, Z_T = 4$ km. In all the results presented here we have chosen the normalization factor $\Psi_{ew}(Z_m)$ such that $2\pi R_{ew}\Psi_{ew}(Z_m) = -1.8 \times 10^9$ kg s^{-1}. According to Eq. 32, the vertical distribution of the horizontally integrated downward mass flux in the eye is given by $2\pi R_{ew}\Psi_{ew}(Z)$. Specification of the constant R_{ew} also specifies $r_{ew}(z)$ since $r_{ew}(z) = [f/\hat{f}(z)]^{1/2} R_{ew}$. Determination of the detailed spatial distribution of the downward mass flux $\rho w(r, z) = \partial[r\psi(r, z)]/r\partial r$ requires solution of the homogeneous, restricted elliptic problem given in Eq. 16 for $\Psi(R, Z)$, from which $\psi(r, z)$ is obtained *via* $\psi(r, z) = (R/r)\Psi(R, Z)$.

accepted in the region $0 \le R < R_{ew}$. Thus, the solution of the horizontal structure problem (Eq. 26) is

$$\Psi_\ell(R) = A_\ell \frac{I_1(\mu_\ell R)}{I_1(\mu_\ell R_{ew})}, \tag{27}$$

where the A_ℓ are constants. Using Eq. 27 in the top entry of Eq. 22, the final solution for the streamfunction becomes

$$\Psi(R, Z) = \sum_{\ell=1}^{\infty} A_\ell \frac{I_1(\mu_\ell R)}{I_1(\mu_\ell R_{ew})} \mathcal{Z}_\ell(Z) \qquad \text{for} \quad 0 \le R \le R_{ew} \quad \text{and} \quad 0 \le Z \le Z_T, \tag{28}$$

where the coefficients A_ℓ are computed from the specified function $\Psi_{ew}(Z)$ *via*

$$A_\ell = \frac{1}{N_0^2 H} \int_0^{Z_T} \Psi_{ew}(Z)\, \mathcal{Z}_\ell(Z)\, N^2(Z)\, e^{Z/H}\, dZ. \tag{29}$$

The solution given in Eq. 28 is valid for vortices with the vertical profiles of $\hat{f}(Z)$ and $N(Z)$ given by Eqs. 17 and 19. With these vertical profiles, the first five eigenvalues of the vertical structure problem (Eq. 23) are given in the top part of Table 1 for the barotropic case, and the bottom part of Table 1 for the baroclinic case. The corresponding five eigenfunctions $\mathcal{Z}_\ell(Z)$ are shown in the left (barotropic) and right (baroclinic) panels of Figure 8. Note that we have solved the vertical structure problem (Eq. 23) using the Mathematica package NDEigensystem, which returns the eigenvalues and eigenfunctions of a user-defined linear operator, along with user-defined boundary conditions. This Mathematica package returns eigenfunctions with a default normalization, so we have renormalized the Mathematica output to satisfy the normalization given in Eq. 40 in Appendix C. There is general similarity in the appearance of the vertical structure functions for the barotropic and baroclinic cases. However, the inclusion of vertical dependence of $\hat{f}$ in the Sturm–Liouville problem in Eq. 23 does lead to vertical shifts (~ 1 km) in the nodes and to changes in the upper tropospheric amplitudes of the $\mathcal{Z}_\ell(Z)$ functions.

Using Eq. 28, along with the derivative relation $d\,[RI_1(\mu_\ell R)]/dR = \mu_\ell R I_0(\mu_\ell R)$, it can be shown that the formula for $\rho W(R, Z)$ is

$$\rho W(R, Z) = \sum_{\ell=1}^{\infty} A_\ell \frac{\mu_\ell I_0(\mu_\ell R)}{I_1(\mu_\ell R_{ew})} \mathcal{Z}_\ell(Z) \qquad \text{for} \quad 0 \le R \le R_{ew} \quad \text{and} \quad 0 \le Z \le Z_T, \tag{30}$$

and the formula for $\rho w(r, z)$ is

$$\rho w(r, z) = \left(\frac{\hat{f}(z)}{f}\right) \sum_{\ell=1}^{\infty} A_\ell \frac{\mu_\ell I_0\left(\mu_\ell \left[\hat{f}(z)/f\right]^{1/2} r\right)}{I_1\left(\mu_\ell \left[\hat{f}(z)/f\right]^{1/2} r_{ew}(z)\right)} \mathcal{Z}_\ell(z) \qquad \text{for} \quad 0 \le r \le r_{ew}(z) \quad \text{and} \quad 0 \le z \le z_T. \tag{31}$$

Note that the vertical mass flux ρw is related to the vertical p-velocity by $\rho w = -(1/g)\omega$ and that $w(r, z)$ can have a quite different vertical dependence than $W(R, Z)$, for example due to the leading $\hat{f}(z)/f$ factor, which can have large values in the lower troposphere.

We now specify $\Psi_{ew}(Z)$ in such a way that it vanishes at $Z = 0$, Z_T and has only one local minimum for $0 < Z < Z_T$. The specification of $\Psi_{ew}(Z)$ constrains the problem in an important way. To see this, note that

$$\begin{aligned} 2\pi \int_0^{r_{ew}(z)} \rho w\, r\, dr &= 2\pi \int_0^{R_{ew}} \rho W\, R\, dR \\ &= 2\pi \int_0^{R_{ew}} \frac{\partial(R\Psi)}{\partial R}\, dR = 2\pi R_{ew} \Psi_{ew}(Z), \end{aligned} \tag{32}$$

which shows that the specification of $2\pi R_{ew}\Psi_{ew}(Z)$ is equivalent to specification of the vertical distribution of the horizontally integrated vertical mass flux in the eye. However, the details of the spatial distribution of vertical motion in the eye comes from the elliptic equation, whose solution yields Eqs. 30 and 31. In order to make the height of the minimum value of $\Psi_{ew}(Z)$ adjustable, we have chosen the form

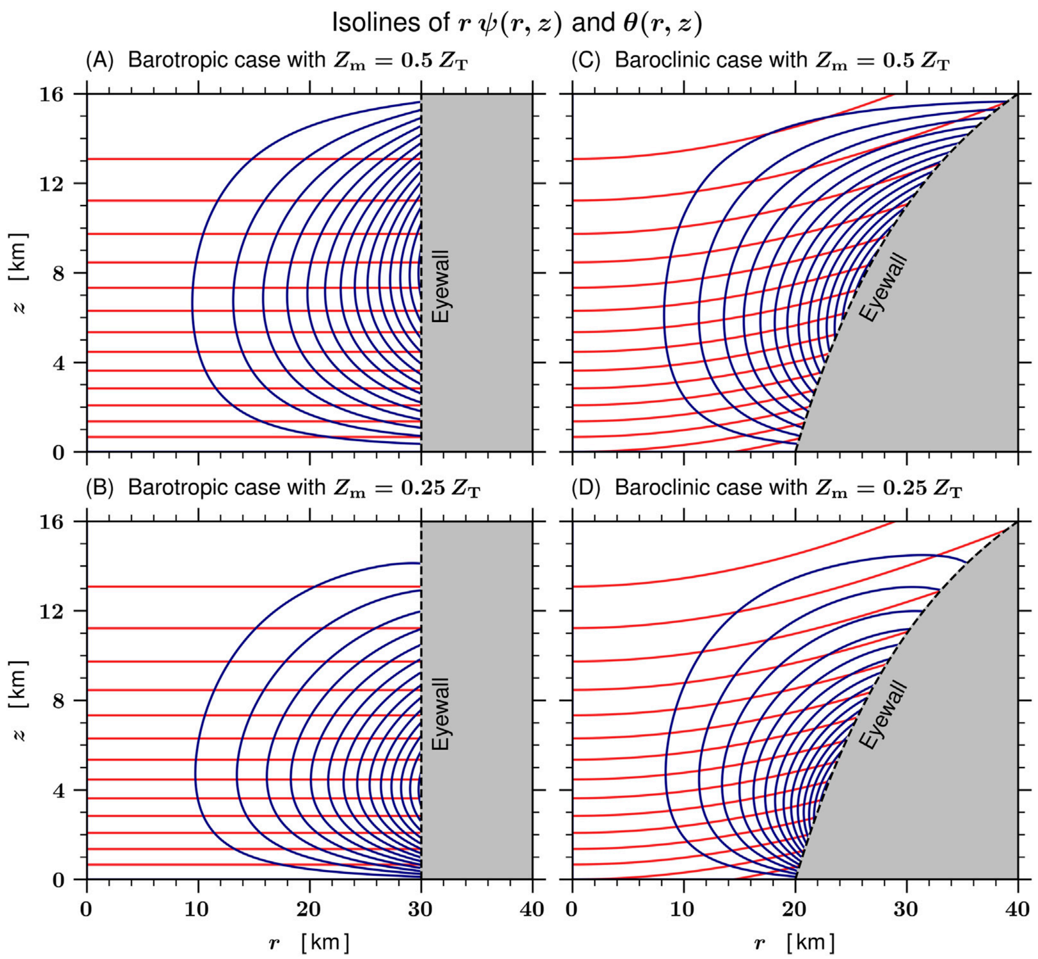

FIGURE 10

Isolines of the solution $r\psi(r, z)$ (navy blue contours) and of $\theta(r, z)$ (red contours) for the barotropic case **(A,B)** and for the baroclinic case **(C,D)**, both shown for the two eyewall forcing cases $Z_{\mathrm{m}} = 0.5\,Z_{\mathrm{T}} = 8$ km **(A,C)** and $Z_{\mathrm{m}} = 0.25\,Z_{\mathrm{T}} = 4$ km **(B,D)**. The specified functions $\Psi_{\mathrm{ew}}(Z)$ for these two eyewall forcing cases are shown in Figure 9. The isolines of $r\psi$ have been computed from the solution given in Eq. 28 using the relation $r\psi = R\Psi$, with the sum over ℓ truncated at $\ell = 20$. The blue contours for $r\psi$ indicate the direction of fluid flow for the secondary circulation within the eye and have a contour interval of 2.0×10^7 kg s^{-1}. The red contours for $\theta(r, z)$ are identical to those shown in Figure 7 and run from 305 K to 365 K for the barotropic case (left column) and from 295 K to 365 K for the baroclinic case (right column), both in increments of 5 K. In regions where a small area is enclosed by two neighboring blue lines and two neighboring red lines, the Jacobian $\partial(r\psi, \theta)/r\partial(r, z)$ tends to be large, so that $\partial\theta/\partial t$ tends to be large, as shown in Figure 11.

$$\Psi_{\mathrm{ew}}(Z) = \Psi_{\mathrm{ew}}(Z_{\mathrm{m}})\,\exp\left(\frac{\pi(Z_{\mathrm{m}} - Z)/Z_{\mathrm{T}}}{\tan(\pi Z_{\mathrm{m}}/Z_{\mathrm{T}})}\right)\frac{\sin(\pi Z/Z_{\mathrm{T}})}{\sin(\pi Z_{\mathrm{m}}/Z_{\mathrm{T}})}, \quad (33)$$

where the specified parameter Z_{m} is the height of the minimum value of $\Psi_{\mathrm{ew}}(Z)$. In all the results presented here, the normalization factor $\Psi_{\mathrm{ew}}(Z_{\mathrm{m}})$ has been chosen such that $2\pi R_{\mathrm{ew}}\Psi_{\mathrm{ew}}(Z_{\mathrm{m}}) = -1.8 \times 10^9\,\mathrm{kg\,s^{-1}}$. Plots of $\Psi_{\mathrm{ew}}(Z)/\Psi_{\mathrm{ew}}(Z_{\mathrm{m}})$ for the two choices $Z_{\mathrm{m}} = 0.5\,Z_{\mathrm{T}} = 8\,\mathrm{km}$ (a middle-tropospheric forcing case) and $Z_{\mathrm{m}} = 0.25\,Z_{\mathrm{T}} = 4\,\mathrm{km}$ (a lower-tropospheric forcing case) are shown in Figure 9. The normalization factor chosen here results in horizontally averaged eye subsidence rates, defined by $\bar{w}(z) = [2/r_{\mathrm{ew}}^2(z)]\int_0^{r_{\mathrm{ew}}(z)} w(r,z)\,r\,dr$, of approximately 1–2 m s^{-1}, which is consistent with the aircraft observations reported by Jorgensen (1984). The projection of these two $\Psi_{\mathrm{ew}}(Z)$ profiles onto the first five vertical modes, as computed from Eq. 29, is shown in Table 1.

Figure 10 shows isolines of $r\psi(r, z)$ for the middle-tropospheric eyewall forcing case $Z_{\mathrm{m}} = 8\,\mathrm{km}$ (upper two panels) and for the lower-tropospheric eyewall forcing case $Z_{\mathrm{m}} = 4\,\mathrm{km}$ (lower two panels). These isolines of $r\psi$ have been computed from Eqs. 28 and 29 using the relation $r\psi = R\Psi$. The sum over ℓ in Eq. 28 has been truncated at $\ell = 20$. Also shown in Figure 10 are isolines of $\theta(r, z)$; these isolines are identical to those shown in Figure 7. Alternative views of the adiabatic temperature changes in the eye are provided by $(\partial\theta/\partial t)$, the tendency at fixed

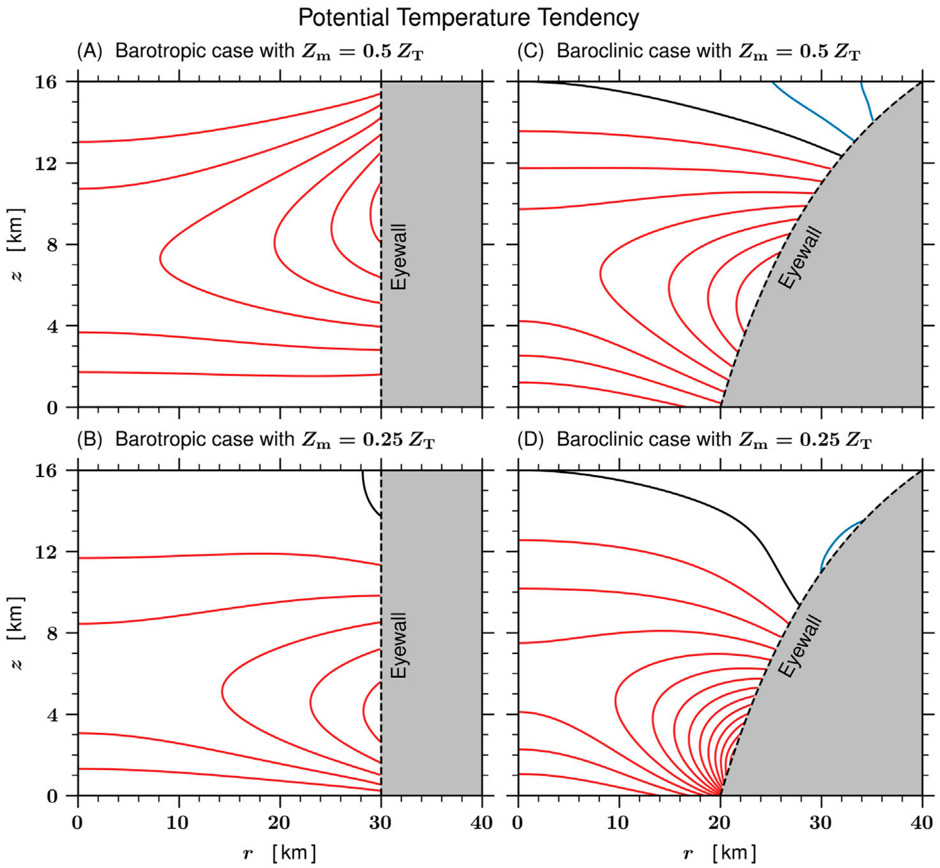

FIGURE 11
The potential temperature tendency $\partial\theta/\partial t$ for the barotropic case **(A,B)** and for the baroclinic case **(C,D)**, both shown for the two eyewall forcing cases $Z_m = 0.5\,Z_T = 8$ km **(A,C)** and $Z_m = 0.25\,Z_T = 4$ km **(B,D)**. The contour interval for $\partial\theta/\partial t$ is 5.0 K h^{-1} with positive contours shown in red, the zero contour level shown in black, and negative contours shown in blue. The $-w(\partial\theta/\partial z)$ term contributes to positive $(\partial\theta/\partial t)$ at all radii and all levels, except in a small region of the upper troposphere in the baroclinic cases. In the two baroclinic cases the $-u(\partial\theta/\partial r)$ term generally opposes the $-w(\partial\theta/\partial z)$ at upper-tropospheric levels (i.e., radial advection of colder air), but enhances the $-w(\partial\theta/\partial z)$ term at lower-tropospheric levels (i.e., radial advection of warmer air). This results in a $(\partial\theta/\partial t)$ field that is more radially uniform in the upper troposphere, but enhanced near the edge of the eye at lower-tropospheric levels.

radius r, and by $(\partial\theta/\partial\tau)$, the tendency at fixed potential radius R. Here, we discuss only the tendency $(\partial\theta/\partial t)$, which is governed by

$$\begin{aligned}\frac{\partial\theta}{\partial t} = -u\frac{\partial\theta}{\partial r} - w\frac{\partial\theta}{\partial z} &= -\frac{1}{\rho}\frac{\partial(r\psi,\theta)}{r\,\partial(r,z)}\\ &= -\frac{1}{\rho}\frac{\partial(R\Psi,\theta)}{R\,\partial(R,Z)}\left(\frac{f+\zeta}{f}\right).\end{aligned} \tag{34}$$

From the above Jacobian form in (r, z), we conclude that the formation of lower-tropospheric warm-ring structures, where $(\partial\theta/\partial t)$ is large, tends to occur where small areas are produced by the intersection of θ-isolines and $(r\psi)$-isolines. Figure 11 shows the corresponding potential temperature tendencies produced by the secondary circulations shown in Figure 10. The lower-tropospheric baroclinic case $Z_m = 4$ km, shown in Figure 11D, clearly illustrates the tendency to produce an upper-tropospheric warm-core and a lower-tropospheric warm-ring structure. For example, at $z \approx 10$ km, the values of $\partial\theta/\partial t$ are uniform for $0 < r < 15$ km and somewhat smaller for $15 < r < 28$ km. In contrast, at $z \approx 3$ km, the values of $\partial\theta/\partial t$ near $r \approx 21$ km are approximately five times as large as those at $r = 0$. These results indicate that a full-tropospheric warm-core structure such as that shown in Figure 10D could transform into a lower-tropospheric warm-ring structure very quickly, perhaps in less than an hour.

4 Concluding remarks

Two problems for the secondary circulation in R-space have been formulated. The first is the full domain elliptic problem (Eq. 15), which requires knowledge of the coefficients $\hat{f}(R, Z)$ and $N(R, Z)$, and the forcing $Q(R, Z)$ over $0 \le R < \infty$. The second is the restricted domain elliptic problem (Eq. 16), which requires knowledge of the coefficients $\hat{f}(R, Z)$] and $N(R, Z)$ over $0 \leq R \leq R_{ew}$ and specification of the lateral boundary values $\Psi_{ew}(Z)$ at $R = R_{ew}$. For the barotropic vortex core and the vertically sheared Rankine core, the restricted domain elliptic problem has been solved semi-analytically in Section 3. The results for the middle-tropospheric forcing barotropic case shown in the upper left panels of Figure 10 and Figure 11 are closest to the results shown in the previous study (Schubert et al., 2007), which were based on full domain, physical space solutions of the transverse circulation equation with forcing of the first internal mode only. In the results for the lower-tropospheric forcing barotropic case shown in the lower left panels of Figure 10 and Figure 11, the minimum value of $\Psi_{ew}(Z)$ has been shifted to a lower level, which has the effect of producing an enhancement of $\partial\theta/\partial t$ in the lower troposphere at the edge of the eye. The results for the vertically sheared (baroclinic) Rankine core, shown in the right panels of Figure 10 and Figure 11, more realistically capture the outward tilt of the eyewall and illustrate to a greater degree the preference for the potential temperature tendency to be largest in the lower troposphere at the edge of the eye in baroclinic vortices for which the minimum value of the eyewall streamfunction $\Psi_{ew}(Z)$ occurs below middle-tropospheric levels. The right two panels of Figure 11 are consistent with the concept of a potential temperature tendency field that is nearly uniform in radius at upper tropospheric levels but highly biased toward the edge of the eye at lower tropospheric levels, i.e., consistent with the development of a warm core at upper levels and a warm ring at lower levels, as seen in the full-physics simulations of Figure 5.

It is important to note that the model of eye subsidence used here is highly idealized, i.e., it is axisymmetric, gradient balanced, inviscid, adiabatic, and for a restricted domain. The adiabatic idealization results because, in the formulation of the restricted problem (Eq. 16), it has been assumed that $Q = 0$ for $R \leq R_{ew}$. Careful inspection of the lower panel of Figure 4 indicates that this assumption might be violated in the upper troposphere near the edge of the eye, where frozen condensate can be advected inward and subsequently sublimated, producing a region where $Q < 0$. Malkus (1958), Willoughby (1998), and Zhang et al. (2002) have considered the role that such cooling might play in producing deep, narrow downdrafts at the edge of the eye. The relative roles of such diabatic dynamics and the adiabatic dynamics studied here deserve further study. The idealization of gradient balance filters inertia-gravity waves, which results in a "slow manifold" view of eye dynamics. With their mesoscale scanning techniques, the GOES-R series of geostationary satellites can image a 1000 km × 1000 km hurricane area with 30 s time resolution. When viewing such rapid-scan loops of a major hurricane, one is struck by the highly dynamic nature of the inner core. Some of the high frequency variability of the inner core is probably due to inertia-gravity wave oscillations that are not captured by the simplified dynamics of the balanced vortex model. However, the balanced vortex model does capture the slow-manifold dynamics upon which we can crudely imagine the higher frequency inertia-gravity waves are superposed. To improve this crude view, much work remains to understand how the inner core PV dynamics can become frequency matched with the inertia-gravity wave oscillations, so the two types of dynamics can evolve in a strongly coupled fashion.

In closing, we comment on the possible effects of lower-tropospheric warm-ring structure on the stadium effect. General experience with solutions of the Eliassen transverse circulation equation supports the notion that baroclinic effects play an important role in determining the outward tilt of the eyewall, as seen for example in the CloudSat observations of Figure 4. We have studied the secondary circulation in the eye when the vortex has a warm-core structure at all levels, as shown in the right panel of Figure 7. The results indicate that a lower-tropospheric warm-core structure can be modified to a lower-tropospheric warm-ring structure when the subsidence is enhanced in the lower troposphere at the edge of the eye, as shown in panels D of Figure 10 and Figure 11. When a lower-tropospheric warm ring develops in a tropical cyclone, the baroclinic terms acquire a more complicated spatial structure, which means the absolute angular momentum surfaces also acquire a correspondingly more complicated spatial structure. To see this, consider the thermal wind equation written in the form $f^2(R/r)^3(\partial R/\partial z) = (g/T_0)(\partial T/\partial r)$. From this form of the thermal wind equation, we can easily deduce the following general rules.

$$\begin{aligned}
&\text{Radially inward of a warm ring :}\\
&\qquad \frac{\partial T}{\partial r} > 0 \;\Rightarrow\; \frac{\partial R}{\partial z} > 0\\
&\qquad\qquad\quad \Rightarrow\; R - \text{surfaces tilt inward with height;}\\
&\text{Radially outward of a warm ring :}\\
&\qquad \frac{\partial T}{\partial r} < 0 \;\Rightarrow\; \frac{\partial R}{\partial z} < 0\\
&\qquad\qquad\quad \Rightarrow\; R - \text{surfaces tilt outward with height.}
\end{aligned} \tag{35}$$

Thus, if a tropical cyclone has a warm core at all pressure levels, the R-surfaces tilt outward with height everywhere. Since the R-surfaces help shape the secondary circulation, the eyewall updraft would generally be expected to tilt outward at all levels. However, if a tropical cyclone has a warm-core structure in the upper troposphere but a warm-ring structure in the lower troposphere, the R-surfaces tilt inward with height in the lower troposphere just inside the radius with maximum temperature anomaly. The effect is to make the secondary circulation outward-tilted at upper levels but more vertical at lower levels—an interesting refinement of the stadium effect. To better understand such refinements, additional solutions of Eq. 16 for baroclinic vortices with warm-ring structure would be helpful and are a topic for future work since such solutions would require a numerical approach to Eq. 16. The semi-analytical approach used here is restricted to the vertically sheared, Rankine vortex and simply provides a snapshot in time (rather than a complete time evolution) that illustrates the tendency for a vortex with a warm-core structure to transition to a vortex with a lower-tropospheric warm-ring structure.

Data availability statement

The original contributions presented in the study are included in this article. Further inquiries can be directed to the corresponding author.

Author contributions

WS researched and derived the scientific aspects of this work and wrote the majority of this paper. RT developed and ran the numerical models, created the figures related to those model runs, and provided editing and LaTeX support. CS assisted with the research and derivations and with the preparation of some of the figures.

Funding

Our research has been supported by the National Science Foundation under grant AGS-1841326.

Acknowledgments

We would like to thank Eric Hendricks for his helpful comments and Brian McNoldy, Natalie Tourville, and Graeme Stephens for their advice on the Typhoon Choi-Wan data. We would also like to thank Jon Martinez, Marie McGraw, and the two official reviewers for their insightful reviews and valuable suggestions. The scientific results and conclusions, as well as any views or opinions expressed herein, are those of the author(s) and do not necessarily reflect those of NOAA or the Department of Commerce.

Conflict of interest

The authors declare that the research was conducted in the absence of any commercial or financial relationships that could be construed as a potential conflict of interest.

Publisher’s note

References

Aberson, S. D., Montgomery, M. T., Bell, M., and Black, M. (2006). Hurricane Isabel (2003): New insights into the physics of intense storms. Part II: Extreme localized wind. *Bull. Am. Meteorol. Soc.* 87, 1349–1354. doi:10.1175/BAMS-87-10-1349

Arfken, G. B., and Weber, H. J. (2005). *Mathematical methods for physicists*. Sixth Edition. Amsterdam and Boston: Elsevier Academic Press.

Bell, M. M., and Montgomery, M. T. (2008). Observed structure, evolution, and potential intensity of category 5 Hurricane Isabel (2003) from 12 to 14 September. *Mon. Wea. Rev.* 136, 2023–2046. doi:10.1175/2007MWR1858.1

Eliassen, A. (1951). Slow thermally or frictionally controlled meridional circulation in a circular vortex. *Astrophys. Norv.* 5, 19–60.

Fulton, S. R., and Schubert, W. H. (1985). Vertical normal mode transforms: Theory and application. *Mon. Wea. Rev.* 113, 647–658. doi:10.1175/1520-0493(1985)113⟨0647:VNMTTA⟩2.0.CO;2

Hawkins, H. F., and Rubsam, D. T. (1968). Hurricane Hilda, 1964. II. Structure and budgets of the hurricane on October 1, 1964. *Mon. Wea. Rev.* 96, 617–636. doi:10.1175/1520-0493(1968)096<0617:hh>2.0.co;2

Hazelton, A. T., and Hart, R. E. (2013). Hurricane eyewall slope as determined from airborne radar reflectivity data: Composites and case studies. *Wea. Forecast.* 28, 368–386. doi:10.1175/WAF-D-12-00037.1

Hazelton, A. T., Rogers, R., and Hart, R. E. (2015). Shear-relative asymmetries in tropical cyclone eyewall slope. *Mon. Wea. Rev.* 143, 883–903. doi:10.1175/MWR-D-14-00122.1

Johnson, R. H., and Kriete, D. C. (1982). Thermodynamic and circulation characteristics of winter monsoon tropical mesoscale convection. *Mon. Wea. Rev.* 110, 1898–1911. doi:10.1175/1520-0493(1982)110<1898:taccow>2.0.co;2

Jordan, C. L. (1958). Mean soundings for the West Indies area. *J. Meteor.* 15, 91–97. doi:10.1175/1520-0469(1958)015<0091:MSFTWI>2.0.CO;2

Jorgensen, D. P. (1984). Mesoscale and convective-scale characteristics of mature hurricanes. Part II: Inner core structure of Hurricane Allen (1980). *J. Atmos. Sci.* 41, 1287–1311. doi:10.1175/1520-0469(1984)041<1287:macsco>2.0.co;2

Kossin, J. P., and Schubert, W. H. (2004). Mesovortices in Hurricane Isabel. *Bull. Am. Meteorol. Soc.* 85, 151–153.

Malkus, J. S. (1958). On the structure and maintenance of the mature hurricane eye. *J. Meteor.* 15, 337–349. doi:10.1175/1520-0469(1958)015<0337:otsamo>2.0.co;2

Martinez, J., Bell, M. M., Rogers, R. F., and Doyle, J. D. (2019). Axisymmetric potential vorticity evolution of Hurricane Patricia (2015). *J. Atmos. Sci.* 76, 2043–2063. doi:10.1175/JAS-D-18-0373.1

Möller, J. D., and Smith, R. K. (1994). The development of potential vorticity in a hurricane-like vortex. *Q. J. R. Meteorol. Soc.* 120, 1255–1265. doi:10.1002/qj.49712051907

Montgomery, M. T., Bell, M. M., Aberson, S. D., and Black, M. L. (2006). Hurricane Isabel (2003): New insights into the physics of intense storms. Part I: Mean vortex structure and maximum intensity estimates. *Bull. Am. Meteorol. Soc.* 87, 1335–1348. doi:10.1175/BAMS-87-10-1335

Nolan, D. S., Stern, D. P., and Zhang, J. A. (2009a). Evaluation of planetary boundary layer parameterizations in tropical cyclones by comparison of *in situ* observations and high-resolution simulations of Hurricane Isabel (2003). Part II: Inner-core boundary layer and eyewall structure. *Mon. Wea. Rev.* 137, 3675–3698. doi:10.1175/2009MWR2786.1

Nolan, D. S., Zhang, J. A., and Stern, D. P. (2009b). Evaluation of planetary boundary layer parameterizations in tropical cyclones by comparison of *in situ* observations and high-resolution simulations of Hurricane Isabel (2003). Part I:

Initialization, maximum winds, and the outer-core boundary layer. *Mon. Wea. Rev.* 137, 3651–3674. doi:10.1175/2009MWR2785.1

Rivoire, L., Birner, T., and Knaff, J. A. (2016). Evolution of the upper-level thermal structure in tropical cyclones. *Geophys. Res. Lett.* 43 (10), 537. doi:10.1002/2016GL070622

Rogers, R. F. (2021). Recent advances in our understanding of tropical cyclone intensity change processes from airborne observations. *Atmosphere* 12 (650), 650. doi:10.3390/atmos12050650

Rozoff, C. M., Schubert, W. H., McNoldy, B. D., and Kossin, J. P. (2006). Rapid filamentation zones in intense tropical cyclones. *J. Atmos. Sci.* 63, 325–340. doi:10.1175/JAS3595.1

Schubert, W. H., and Alworth, B. T. (1987). Evolution of potential vorticity in tropical cyclones. *Q. J. R. Meteorol. Soc.* 113, 147–162. doi:10.1002/qj.49711347509

Schubert, W. H. (2018). Bernhard Haurwitz memorial lecture (2017): Potential vorticity aspects of tropical dynamics. http://arXiv.org/abs/1801.08238.

Schubert, W. H., and Hack, J. J. (1983). Transformed Eliassen balanced vortex model. *J. Atmos. Sci.* 40, 1571–1583. doi:10.1175/1520-0469(1983)040<1571:tebvm>2.0.co;2

Schubert, W. H., and McNoldy, B. D. (2010). Application of the concepts of Rossby length and Rossby depth to tropical cyclone dynamics. *J. Adv. Model.. Earth Syst.* 2, 7. doi:10.3894/JAMES.2010.2.7

Schubert, W. H., Rozoff, C. M., Vigh, J. L., McNoldy, B. D., and Kossin, J. P. (2007). On the distribution of subsidence in the hurricane eye. *Q. J. R. Meteorol. Soc.* 133, 595–605. doi:10.1002/qj.49

Simpson, R. H., and Starrett, L. G. (1955). Further studies of hurricane structure by aircraft reconnaissance. *Bull. Am. Meteorol. Soc.* 36, 459–468. doi:10.1175/1520-0477-36.9.459

Stern, D. P., Bryan, G. H., and Aberson, S. D. (2016). Extreme low-level updrafts and wind speeds measured by dropsondes in tropical cyclones. *Mon. Wea. Rev.* 144, 2177–2204. doi:10.1175/MWR-D-15-0313.1

Stern, D. P., and Nolan, D. S. (2009). Reexamining the vertical structure of tangential winds in tropical cyclones: Observations and theory. *J. Atmos. Sci.* 66, 3579–3600. doi:10.1175/2009JAS2916.1

Willoughby, H. E. (1998). Tropical cyclone eye thermodynamics. *Mon. Wea. Rev.* 126, 3053–3067. doi:10.1175/1520-0493(1998)126<3053:TCET>2.0.CO;2

Yamasaki, M. (1983). A further study of the tropical cyclone without parameterizing the effects of cumulus convection. *Pap. Meteorol. Geophys.* 34, 221–260. doi:10.2467/mripapers.34.221

Zhang, D.-L., Liu, Y., and Yau, M. K. (2002). A multiscale numerical study of Hurricane Andrew (1992). Part V: Inner-core thermodynamics. *Mon. Wea. Rev.* 130, 2745–2763. doi:10.1175/1520-0493(2002)130<2745:amnsoh>2.0.co;2

Appendix A: Coordinate transformation

This appendix provides an outline of the transformation from the (r, z, t)-version of the gradient balanced model, given in Eq. 1, to the (R, Z, τ)-version, which is given in Eq. 11.

- To transform the gradient wind formula in Eq. 1, note that

$$\left(f + \frac{v}{r}\right)v = \frac{\partial \phi}{\partial r} \quad \Rightarrow \quad (f + \zeta)v = \frac{\partial \Phi}{\partial r}$$
$$\Rightarrow \quad f\frac{R}{r}v = \frac{\partial \Phi}{\partial R}.$$

Using $v = (R/r)V$, we then obtain the first entry in Eq. 11.

- To transform the second entry in Eq. 1, we start with the absolute angular momentum form and write

$$\frac{D\left(RV + \frac{1}{2}fr^2\right)}{Dt} = 0 \quad \Rightarrow \quad \frac{DV}{Dt} + f\frac{r}{R}u = 0$$
$$\Rightarrow \quad \frac{\partial V}{\partial \tau} + f\left(\frac{r}{R}u + \frac{w}{f}\frac{\partial V}{\partial Z}\right) = 0$$
$$\Rightarrow \quad \frac{\partial V}{\partial \tau} + fU = 0,$$

where we have made use of $(Dr/Dt) = u$ and the absolute angular momentum conservation relation $DR/Dt = 0$. The final form results from the definition of U, which is given in the first entry of Eq. 10.

- To transform the hydrostatic formula in Eq. 1, note that

$$\frac{\partial \Phi}{\partial Z} = \frac{\partial \Phi}{\partial z} - \frac{\partial R}{\partial z}\frac{\partial \Phi}{\partial R}$$
$$= \frac{\partial \phi}{\partial z} + v\left(\frac{\partial v}{\partial z} - f\frac{R}{r}\frac{\partial R}{\partial z}\right) = \frac{\partial \phi}{\partial z},$$

where the second equality results from $\Phi = \phi + \frac{1}{2}v^2$ and the transformed gradient wind equation, while the last equality follows from cancellation of the terms within the parentheses. The third entry in Eq. 11 immediately follows. A closely related formula is

$$\frac{\partial \Phi}{\partial \tau} = \frac{\partial \Phi}{\partial t} - \frac{\partial R}{\partial t}\frac{\partial \Phi}{\partial R}$$
$$= \frac{\partial \phi}{\partial t} + v\left(\frac{\partial v}{\partial t} - f\frac{R}{r}\frac{\partial R}{\partial t}\right) = \frac{\partial \phi}{\partial t},$$

which justifies the use of the term "geopotential tendency equation" for Eq. 36.

- Interestingly, a short derivation of the fourth entry in Eq. 11 begins with the vorticity equation and proceeds as follows:

$$\frac{D\zeta}{Dt} + \frac{\partial w}{\partial r}\frac{\partial v}{\partial z} - (f + \zeta)\frac{\partial(\rho w)}{\rho\,\partial z} = 0$$
$$\Rightarrow \quad \frac{D\zeta}{Dt} - (f + \zeta)\frac{\partial(\rho w)}{\rho\,\partial Z} = 0$$
$$\Rightarrow \quad \frac{\partial}{\partial \tau}\left(\frac{f}{f + \zeta}\right) + \frac{\partial(\rho W)}{\rho\,\partial Z} = 0,$$

where the second entry follows by combining the twisting and divergence terms and the third entry follows from the use of $(D/Dt) = (\partial/\partial\tau) + w(\partial/\partial Z)$ and the relationship between W and w. Now start with the tangential wind equation and proceed as follows:

$$\frac{\partial V}{\partial \tau} + fU = 0 \quad \Rightarrow \quad \frac{\partial}{\partial \tau}\left(\frac{\partial(RV)}{R\,\partial R}\right) + f\frac{\partial(RU)}{R\,\partial R} = 0$$
$$\Rightarrow \quad \frac{\partial}{\partial \tau}\left(\frac{f}{f + \zeta}\right) = \frac{\partial(RU)}{R\,\partial R},$$

where the second entry follows by differentiation of R times the first entry, and the third entry from $f^2/(f + \zeta) = f - [\partial(RV)/R\partial R]$. Combining the last entries of the above two results yields the fourth entry in Eq. 11.

- Finally, the transformation of the thermodynamic equation in Eq. 1 proceeds as follows:

$$\frac{DT}{Dt} + \frac{\kappa T}{H}w = \frac{Q}{c_p} \quad \Rightarrow \quad \frac{\partial T}{\partial \tau} + \left(\frac{\partial T}{\partial Z} + \frac{\kappa T}{H}\right)w = \frac{Q}{c_p}$$
$$\Rightarrow \quad \frac{\partial T}{\partial \tau} + \frac{T}{\theta}\frac{\partial \theta}{\partial Z}w = \frac{Q}{c_p}$$
$$\Rightarrow \quad \frac{\partial T}{\partial \tau} + \frac{T_0}{g}N^2 W = \frac{Q}{c_p},$$

where the final form results from the definitions of N^2 and W.

Appendix B: Geopotential tendency equation

The secondary circulation problems defined in Eqs. 15 and 16 were derived by eliminating Φ_τ between the two equations in Eq. 14. An alternative approach is to make use of the fourth entry in Eq. 11 to eliminate U and W between the two equations in Eq. 14, thereby obtaining the geopotential tendency equation. Then, translating the Dirichlet boundary conditions on U and W into Neumann boundary conditions on the normal derivatives of Φ_τ, the geopotential tendency problem for the restricted domain can be written as follows.

Geopotential Tendency Problem on the Restricted Domain :

$$\frac{\partial}{R\,\partial R}\left(\frac{Re^{-Z/H}}{\hat{f}^2}\frac{\partial\Phi_\tau}{\partial R}\right)+\frac{\partial}{\partial Z}\left(\frac{e^{-Z/H}}{N^2}\frac{\partial\Phi_\tau}{\partial Z}\right)=0$$
$$\text{for}\ \ 0\le R<R_{\mathrm{ew}}\ \ \text{and}\ \ 0\le Z\le Z_{\mathrm{T}}\ \ \text{with}$$
$$\begin{cases}\dfrac{\partial\Phi_\tau}{\partial Z}=0 & \text{at}\ \ Z=0,Z_{\mathrm{T}},\\ \dfrac{\partial\Phi_\tau}{\partial R}=0 & \text{at}\ \ R=0,\\ \dfrac{\partial\Phi_\tau}{\partial R}\ \text{given} & \text{at}\ \ R=R_{\mathrm{ew}}.\end{cases}\tag{36}$$

All the conclusions reached in Section 3 could also be reached through an analysis of Eq. 36.

Appendix C: Orthonormality of the vertical structure functions

The orthonormality of the vertical structure functions is proved as follows. Let $\mathcal{Z}_\ell(Z)$ and $\mathcal{Z}_{\ell'}(Z)$ be eigenfunctions with corresponding eigenvalues μ_ℓ and $\mu_{\ell'}$. Then, multiplying the equation for $\mathcal{Z}_{\ell'}$ by $\mathcal{Z}_\ell$, and the equation for $\mathcal{Z}_\ell$ by $\mathcal{Z}_{\ell'}$, we obtain

$$\begin{aligned}\mathcal{Z}_\ell\frac{d}{dZ}\left(\hat{f}^2e^{Z/H}\frac{d\mathcal{Z}_{\ell'}}{dZ}\right)+\mu_{\ell'}^2N^2e^{Z/H}\mathcal{Z}_\ell\mathcal{Z}_{\ell'}&=0,\\ \mathcal{Z}_{\ell'}\frac{d}{dZ}\left(\hat{f}^2e^{Z/H}\frac{d\mathcal{Z}_\ell}{dZ}\right)+\mu_\ell^2N^2e^{Z/H}\mathcal{Z}_\ell\mathcal{Z}_{\ell'}&=0.\end{aligned}\tag{37}$$

The difference of these two equations can be written in the form

$$\frac{d}{dZ}\left\{\hat{f}^2e^{Z/H}\left(\mathcal{Z}_\ell\frac{d\mathcal{Z}_{\ell'}}{dZ}-\mathcal{Z}_{\ell'}\frac{3}{d\mathcal{Z}_\ell}dZ\right)\right\}$$
$$+(\mu_{\ell'}^2-\mu_\ell^2)N^2e^{Z/H}\mathcal{Z}_\ell\mathcal{Z}_{\ell'}=0.\tag{38}$$

Integrating over Z and noting that both $\mathcal{Z}_\ell(Z)$ and $\mathcal{Z}_{\ell'}(Z)$ vanish at $Z=0$ and $Z=Z_{\mathrm{T}}$, we obtain

$$(\mu_{\ell'}^2-\mu_\ell^2)\int_0^{Z_{\mathrm{T}}}\mathcal{Z}_\ell(Z)\mathcal{Z}_{\ell'}(Z)\,N^2(Z)\,e^{Z/H}\,dZ=0.\tag{39}$$

Thus, in the absence of degenerate eigenvalues and with proper normalization of $\mathcal{Z}_\ell(Z)$, the orthonormality relation for the vertical structure functions is

$$\int_0^{Z_{\mathrm{T}}}\mathcal{Z}_\ell(Z)\mathcal{Z}_{\ell'}(Z)\,N^2(Z)\,e^{Z/H}\,dZ=\begin{cases}N_0^2H & \text{if}\ \ell'=\ell,\\ 0 & \text{if}\ \ell'\neq\ell.\end{cases}\tag{40}$$

The proof of the second entry in Eq. 22 is as follows. Change the dummy index ℓ to ℓ' in the first entry of Eq. 22, multiply the resulting formula by $\mathcal{Z}_\ell(Z)\,N^2(Z)\,e^{Z/H}$, and then integrate over Z to obtain

$$\begin{aligned}&\int_0^{Z_{\mathrm{T}}}\Psi(R,Z)\mathcal{Z}_\ell(Z)\,N^2(Z)\,e^{Z/H}\,dZ\\ &\quad=\sum_{\ell'=1}^{\infty}\Psi_{\ell'}(R)\int_0^{Z_{\mathrm{T}}}\mathcal{Z}_\ell(Z)\mathcal{Z}_{\ell'}(Z)N^2(Z)\,e^{Z/H}\,dZ\\ &\quad=N_0^2H\,\Psi_\ell(R),\end{aligned}\tag{41}$$

where the final equality follows from the orthonormality relation (Eq. 40).

frontiers | Frontiers in Earth Science

TYPE Original Research
PUBLISHED 05 January 2023
DOI 10.3389/feart.2022.1018851

OPEN ACCESS

EDITED BY
Yuqing Wang,
University of Hawaii at Manoa,
United States

REVIEWED BY
Jianqi Sun,
Institute of Atmospheric Physics (CAS),
China
Kelvin T. F. Chan,
Sun Yat-sen University, China

*CORRESPONDENCE
Fumin Ren,
fmren@163.com

SPECIALTY SECTION
This article was submitted to
Atmospheric Science,
a section of the journal
Frontiers in Earth Science

RECEIVED 14 August 2022
ACCEPTED 21 September 2022
PUBLISHED 05 January 2023

CITATION
Su Z, Ma Y, Jia L, Ren F and Ding C (2023), Application of the improved dynamical–Statistical–Analog ensemble forecast model for landfalling typhoon precipitation in Fujian province. *Front. Earth Sci.* 10:1018851.
doi: 10.3389/feart.2022.1018851

Application of the improved dynamical–Statistical–Analog ensemble forecast model for landfalling typhoon precipitation in Fujian province

Zhizhong Su[1,2], Yunqi Ma[3,4], Li Jia[5], Fumin Ren[5]* and Chenchen Ding[6]

[1]Xiamen Key Laboratory of Straits Meteorology, Xiamen Meteorological Bureau, Xiamen, China, [2]Fujian Key Laboratory of Severe Weather, Fuzhou, China, [3]CMA·Henan Key Laboratory of Agrometeorological Support and Applied Technique, Zhengzhou, China, [4]Henan Meteorological Observatory, Zhengzhou, China, [5]State Key Laboratory of Severe Weather, Chinese Academy of Meteorological Sciences, Beijing, China, [6]Public Meteorological Service Center of CMA, Beijing, China

The forecasting performance of the Dynamical–Statistical–Analog Ensemble Forecast (DSAEF) model for Landfalling Typhoon [or tropical cyclone (TC)] Precipitation (DSAEF_LTP), with new values of two parameters (i.e., similarity region and ensemble method) for landfalling TC precipitation over Fujian Province, is tested in four experiments. Forty-two TCs with precipitation over 100 mm in Fujian Province during 2004–2020 are chosen as experimental samples. Thirty of them are training samples and twelve are independent samples. First, simulation experiments for the training samples are used to determine the best scheme of the DSAEF_LTP model. Then, the forecasting performance of this best scheme is evaluated through forecast experiments. In the forecast experiments, the TSsum (the sum of threat scores for predicting TC accumulated rainfall of ≥250 mm and ≥100 mm) of experiments DSAEF_A, B, C, D is 0.0974, 0.2615, 0.2496, and 0.4153, respectively. The results show that the DSAEF_LTP model performs best when both adding new values of the similarity region and ensemble method (DSAEF_D). At the same time, the TSsum of the best performer of numerical weather prediction (NWP) models is only 0.2403. The improved DSAEF_LTP model shows advantages compared to the NWP models. It is an important method to improve the predictability of the DSAEF_LTP model by adopting different schemes in different regions.

KEYWORDS

landfalling typhoon, accumulated precipitation forecast, DSAEF_LTP model, forecasting performance, Fujian province

1 Introduction

Tropical cyclones (TCs, or typhoons) are among the top 10 global natural disasters (Lei et al., 2019). The Northwest Pacific (including the South China Sea) is the most active region for TCs worldwide, with about 27 TCs per year and accounting for about one-third of the total number of TCs globally (Matsuura et al., 2013). Studies have shown that most TCs move westward and northwestward immediately after their generation, making China one of the most severely affected countries (Chen and Meng, 2001; Zhang et al., 2019), especially with the regard to landfalling TCs (LTCs).

Forecasting LTC precipitation is one of the major challenges of TC science. China has made remarkable progress in improving the prediction error of tropical cyclone track, but the progress in forecasting TC precipitation is still relatively slow. Besides, current understanding of TC rainfall distribution change is more qualitative than quantitative (AMS, 2000). Therefore, it is of great scientific significance and practical value to continue researching LTC precipitation and improving the quality and skill of its forecasting.

With regard to research approaches for forecasting LTC precipitation, three methods are widely applied: dynamical models, statistical methods, and dynamical–statistical methods. Among them, the dynamical–statistical method is an important approach to improving the forecasting skill for LTC precipitation, and can be generally divided into three categories (Ren and Xiang, 2017). The first category involves using the TC tracks forecasted by dynamical models along with historical rainfall observations, and the TC precipitation forecast is obtained from the perspective of the climatic average (Marks et al., 2002; Lee et al., 2006; Lonfat et al., 2007). The second type adopts TC track forecasts and the integration of rainfall from the initial rainfall rates to forecast the LTC precipitation (Kidder et al., 2005; Liu, 2009; Ebert et al., 2011). And the third type works by constructing a dynamical–statistical scheme that consists of various internal TC variables and its environmental fields (Li and Zhao, 2009; Zhong et al., 2009). There have been some important recent studies on hybrid analog-ensemble-based forecasts. For instance, Elsberry and Tsai (2014) developed a situation-dependent intensity prediction technique for western North Pacific TCs, based on the mean intensity changes from the 10 best historical track analogs, and successfully applied the technique to other TC cases (Tsai and Elsberry, 2015, Tsai and Elsberry, 2016, Tsai and Elsberry, 2017).

Recently, Ren et al. (2020) proposed the theory of the Dynamical–Statistical–Analog Ensemble Forecast (DSAEF) and applied it to LTC accumulated precipitation forecasting, developing the DSAEF model for landfalling TC precipitation (the DSAEF_LTP model). The initial model contained two physical factors: TC track and TC landfalling season. Subsequently, Ding et al. (2020) introduced TC intensity into the model and conducted rainfall forecast experiments for 21 LTCs over South China. Furthermore, Jia et al. (2020) added five new parameter values of similarity regions (2020) into the model and conducted simulation experiments on a single TC in 2019 (Lekima). In a follow-up study (Jia et al., 2022), the authors added five new values of ensemble forecast schemes and carried out further experiments on 10 TCs in 2018, which further improved the DSAEF_LTP model.

The above review reveals that so far only a small number of samples have thus far been adopted to conduct forecast experiments with the new similarity regions and ensemble forecast schemes added into the DSAEF_LTP model. In other words, evidence based on large-sample experiments are still missing. And how about? The forecast skill of the model for a small area, such as a province? This is the motivation behind the present study in which large-sample experiments are carried out with the improved model (with new parameter values added) in Fujian Province, which is located on the southeast coast of China and experiences frequent typhoon impacts as well as severe disaster-related losses, to evaluate the model's forecast performance in this region.

The paper is structured as follows: The next section describes data and methods. Section 3 explains the experiments (samples and design). Results are presented in Section 4. A summary and discussion are given in Section 5.

2 Data and methods

2.1 Data

(1) The observed historical precipitation data during 1960–2020 with 24-h intervals at 1200 UTC used in this paper are from the National Meteorological Information Center (NMIC) of the China Meteorological Administration (CMA), covering 2027 meteorological stations, including 66 in Fujian.

(2) The historical best-track data at 6-h intervals during 1960–2020, including the position and strength of TCs, are from the Shanghai Typhoon Institute (Ying et al., 2014; Lu et al., 2021). The tracks of target TCs [both the best tracks and operational numerical weather prediction (NWP) model forecast tracks] are from the NMIC of the CMA.

(3) Forecasted precipitation data from NWP models are used to compare their forecast performance with that of the DSAEF_LTP model. The following four models are used: the European Centre for Medium-Range Weather Forecasts (ECMWF) model ($0.125^\circ \times 0.125^\circ$); the Global Forecast System (GFS) of the National Centers for Environmental Prediction ($0.25^\circ \times 0.25^\circ$); the Global/Regional Assimilation and Prediction System (GRAPES) model run by the CMA ($0.25^\circ \times 0.25^\circ$); and the Shanghai Meteorological Service WRF ADAS Real-Time Modeling System (SMS-WARMS)

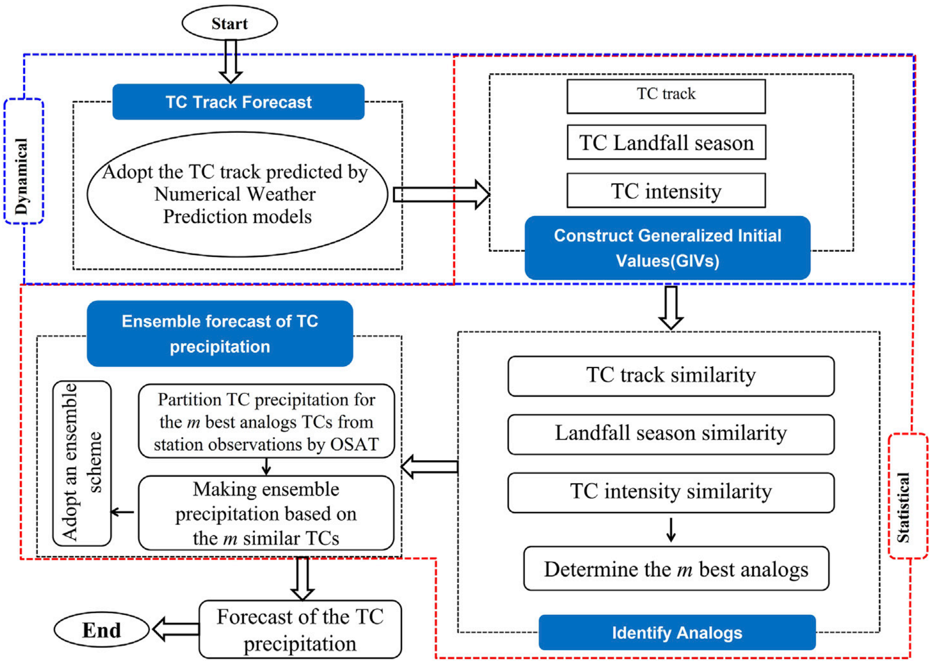

FIGURE 1
Flowchart of the DSAEF_LTP model.

(0.09°×0.09°). For simplicity, the four NWP models, i.e., ECMWF, GFS, GRAPES and SMS-WARMS, are referred to as ECM, NCP, GRP, and mSH, respectively in the following.

2.2 Methods

2.2.1 The DSAEF_LTP model

The DSAEF_LTP model is used to predict the accumulated precipitation of the target TCs in this study. Figure 1 shows the flowchart of the forecasting procedure of the DSAEF_LTP model, and the procedure consists of four main steps: 1) obtaining the complete track of the target TC; 2) constructing the generalized initial values (GIVs); 3) discriminating the similarity of the GIV; and 4) ensemble-forecasting the LTC precipitation.

In the first step, the complete track of the target TC is obtained by combining the observed track before the initial time and the forecast track after the initial time. The forecast track is based on the TC track forecast of the NWP model, and the initial time depends on the first parameter presented in Table 1.

In the second step, GIVs are constructed *via* physical factors that affect TC precipitation. Certain variables of TC characteristics (e.g., TC track, TC landfall season, TC intensity, TC translation speed, TC structure) and environmental fields (e.g., monsoons, subtropical high, low-level jet) that are important factors influencing TC precipitation should be considered. In this study, only three TC characteristic factors—TC track, TC landfall season and TC intensity—have been introduced into the model. The environmental factors will be considered to be introduced into the model in the future.

The third step is to distinguish the similarity of the GIVs. Specifically, it is used to discriminate the similarity of the GIVs constructed in the second step between the target TC and the historical TCs, and then *m* historical TCs that are most similar to the target TC can be selected. This step is determined by parameters (P) 2–6 in Table 1. The TC track similarity is determined by the TC track Similarity Area Index (TSAI) (Ren et al., 2018), which is calculated by using P2–P4. Meanwhile, P5 and P6 are used to determine the similarity of TC landfall season and intensity, respectively. Based on the above steps, *m* historical TCs are finally screened, and *m* is determined by P7.

The fourth step is the LTC precipitation ensemble forecast and the ensemble members are the similar historical TCs. In this context, the accumulated precipitation of *m* similar historical TCs screened during the third step are assembled to obtain the precipitation forecast of the target TC. The ensemble method is determined by P8. Here, the Objective Synoptic Analysis Technique is used to partition the precipitation generated by TCs from the historical accumulated precipitation (Ren et al., 2001, Ren et al., 2007).

TABLE 1 Parameters of the DSAEF_LTP model.

Parameter	Description	Experimented values
P1 Initial time	The complete track of the target TC consists of the observed track before the initial time and the forecast track after the initial time	1: 1200 UTC on Day 1 2: 0000 UTC on Day 1 3: 1200 UTC on Day0 4: 0000 UTC on Day 0 5: 1200 UTC on Day −1 6: 0000 UTC on Day −1 (Day 0: the day of TC precipitation occurring on land; Day 1: the day after Day 0; Day −1: the day before Day 0)
P2 Similarity region	A designated region within which the TSAI is calculated. It is a rectangle with diagonal points A and B	Decided by the predicted TC track, initial time and diameter of the TC. There are 20 experimental values (1–20)
P3 Threshold of the segmentation ratio of a latitudinal extreme point	A parameter of TSAI that represents the bending degree of TC tracks	1: 0.1 2: 0.2 3: 0.3
P4 Overlapping percentage threshold of two TC tracks	A parameter of TSAI that represents the degree of longitudinal (latitudinal) overlap of TC tracks	1: 0.9 2: 0.8 3: 0.7 4: 0.6 5: 0.5 6: 0.4
P5 Seasonal similarity	A parameter that indicates the TC landfall time	1: the whole year 2: May–Nov 3: Jul–Sept 4: the same landfall month as the target TC 5: within 15 days of the target TC landfall time
P6 Intensity similarity	A parameter that indicates the differences between the TC intensity of the target TC and historical TCs. There are four categories of TC intensity that can be chosen. The similarity of TC intensity is divided into five levels	Four categories 1: average intensity on the first rainy day 2: maximum intensity on the first rainy day 3: average intensity on all rainy days 4: maximum intensity on all rainy days Five levels 1: all grades 2: the target TC intensity is the same grade or above the historical TC 3: the same grade or below 4: only the same grade 5: the same grade or one grade difference
P7 Number of analog TCs screened for the ensemble forecast	*m* historical TCs with the first *m* most similar GIVs to that of the target TC	1–10 for 1, 2 . . . and 10, respectively
P8 Ensemble	Ensemble forecast scheme	1: Mean 2: Maximum 3: 90th percentile 4: Probability matching mean (PM) 5: Equal difference-weighted mean (ED-WM) 6: TSAI-weighted mean (TSAI-WM)
Total number of schemes: 6 × 20 × 3 × 6 × 5 × 4 × 5 × 10 × 6 = 12,960,000		

2.2.2 The new parameter values of the DSAEF_LTP model

The improvement of the DSAEF_LTP model with two newly added parameter values is tested in Fujian Province. The parameters and their values in the model are listed in Table 1. The first parameter is the similarity region (P2 in Table 1). Fifteen values of this parameter are obtained in the first version of the DSAEF_LTP model. That is, fifteen rectangular areas with diagonal points A and B can be chosen, and the TSAI is calculated in these rectangular areas. The TSAI is the area enclosed by the track of the historical TCs and the target TC in a specified similarity region. A is the TC position at 0, 12 or 24 h prior to the maximum prediction time, and C is the TC position at 0, 12, 24, 36 or 48 h prior to the start time of the forecast (i.e., the initial time). Jia et al. (2020) found that these rectangular areas are rather too small or too eastward or southward considering that the maximum diameter of a TC is about 2000 km in the Northwest Pacific, so five new values that represent five 2000 km^{-2} regions of this parameter are added.

The second parameter is the ensemble forecast scheme (P8 in Table 1). There are only two ensemble methods in the first version of the DSAEF_LTP model: mean and maximum. To address the high rates of misses and false alarms of these two methods respectively, Jia et al. (2022) added five new ensemble methods (i.e., the 90th percentile, fusion, probability matching mean, equal difference-weighted mean, and TSAI-weighted mean) and demonstrated that the overall performance of the 90th percentile is superior. Four new ensemble methods, excluding the fusion method presented by Jia et al. (2022), have been added in this paper. We did not consider this ensemble method as its prediction result for precipitation above 100 mm is the same as that of the maximum method. In this paper, the forecast performances of the four new ensemble schemes and the two original schemes are tested for TC precipitation over the Fujian Province.

2.2.3 Evaluation methods

In order to evaluate the forecast performance of the DSAEF_LTP model, the threat score (TS), false alarm rate (FAR), and missing alarm rate (MAR) are used (Wang et al., 2021). The TS is calculated as

$$TS = \frac{hits}{hits + misses + false\,alarms}, \tag{1}$$

whereby its value ranges from 0 to 1. The closer TS is to 1, the better the forecast performance. To evaluate the forecast performance at two thresholds above 100 mm and 250 mm, TSsum = TS100 + TS250 is selected as an evaluation index (where TS100 and TS250 are the TSs at two thresholds, above 100 mm and 250 mm respectively). Therefore, a larger TSsum indicates a better forecast performance of the DSAEF_LTP model at these two thresholds. For the other metrics,

$$\begin{aligned} FAR &= \frac{false\,alarms}{hits + misses + false\,alarms}, \\ MAR &= \frac{misses}{hits + misses}, \end{aligned} \tag{2}$$

where in the smaller the value of FAR and MAR, the better the forecast. Similarly, FAR100, MAR100, FAR250, and MAR250 are the MARs and FARs at the two thresholds above 100 mm and 250 mm, respectively.

3 Experiments

3.1 Samples

From 2004 to 2020, the historical TCs that caused a maximum daily precipitation exceeding 100 mm in Fujian Province are selected as experimental samples. After excluding some TCs with missing data, a total of 42 TCs are picked out, of which 30 TCs from 2004 to 2015 are chosen as training samples (Figure 2A), while 12 TCs from 2016 to 2020 are chosen as independent samples (Figure 2B).

3.2 Design

The forecasting procedures of the DSAEF_LTP model and its parameters were introduced in Section 2.2.1. Table 1 provides the values and physical meanings of these parameters. As each parameter has several different values, there is a large number of combinations of these values, and each combination is a forecast scheme. The simulation experiment for training samples is conducted to determine the best scheme according to highest TSsum, i.e., the highest prediction accuracy. Then, the forecast performance of this best scheme is tested in Fujian Province.

To examine the forecast performance after introducing the two new parameter values into the DSAEF_LTP model, four experiments are designed. The first experiment is conducted by the original DSAEF_LTP model that contains three physical factors, (i.e., TC track, landfall season, and intensity) in the GIVs of the model, without adding the new parameter values of similarity region and ensemble method, and the experiment is named DSAEF_A. The second experiment is the model with five new similarity region parameter values, here stated as DSAEF_B. The third experiment is the model with four new ensemble methods, named DSAEF_C. And the fourth experiment, DSAEF_D, is conducted with new values of these two parameters simultaneously.

The procedures for selecting the best scheme are as follows: First, calculate the TSsum for each forecast scheme when simulating the accumulated precipitation of a single TC. Due to the short impact period of some TCs, some parameter values of

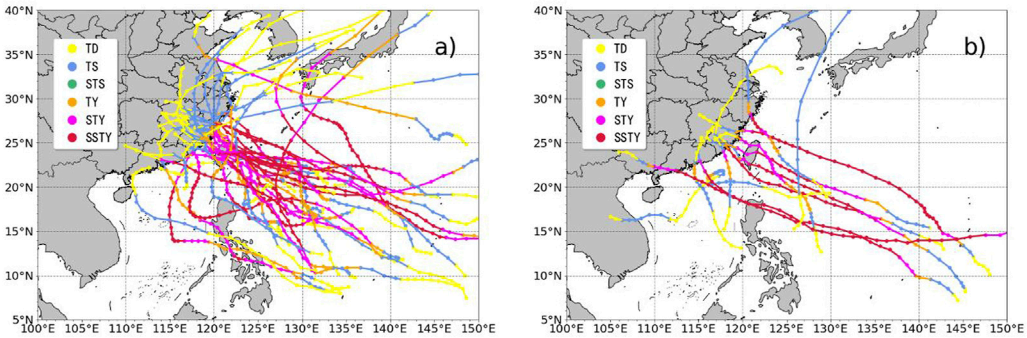

FIGURE 2
Tracks of **(A)** the 30 TCs used as training samples from 2004 to 2015 and **(B)** the 12 TCs used as independent samples from 2016 to 2020.

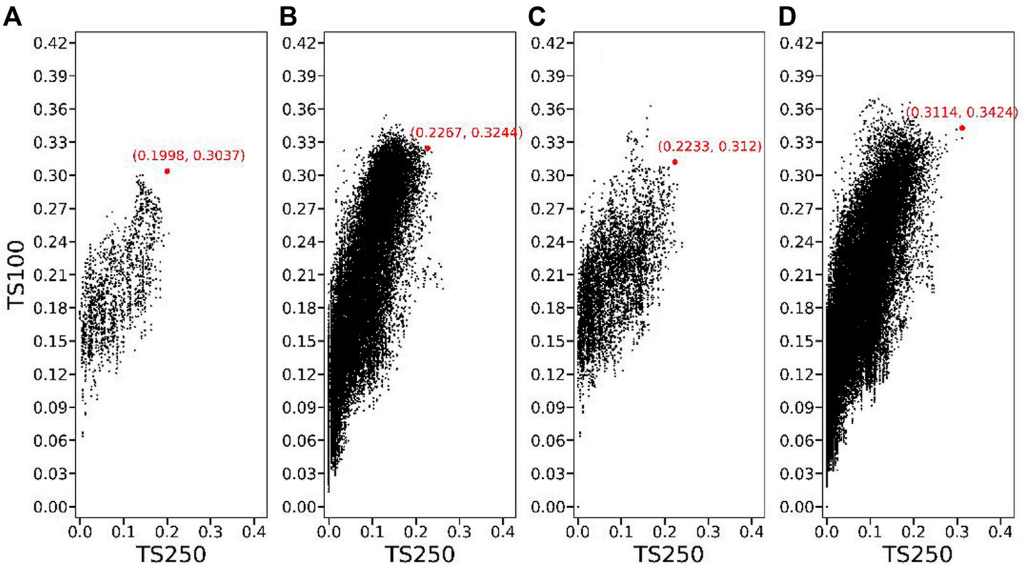

FIGURE 3
Threat scores of **(A)** DSAEF_A, **(B)** DSAEF_B, **(C)** DSAEF_C and **(D)** DSAEF_D in the accumulated precipitation simulation experiment for 30 training samples, in which each black dot represents a scheme and the red dot indicates the best scheme with the maximum TSsum (TSsum = TS250 + TS100).

the initial time and the similarity region cannot be used. Thus, when simulating the accumulated precipitation of a single TC, the total number of schemes may less than or equal to the number given in Table 1. The second step is to select the common scheme that can be used by all 30 TCs. In the third step, considering 100 mm and 250 mm are two important thresholds for operational forecasting of accumulated precipitation, the average values of TS250 and TS100 are calculated for each common scheme. The common scheme with the largest TSsum (the sum of TS250 and TS100) is considered as the best scheme, which will be applied to the TC precipitation forecast.

After the best schemes of the four experiments for the 30 training samples from 2004 to 2015 are determined, the four schemes are used to forecast the precipitation of 12 independent samples. Then, these forecast results are compared with the NWP models to further understand the forecasting skill of the best scheme for each configuration of experiments.

TABLE 2 Parameter values of the best scheme in the four experiments.

Parameter	DSAEF_A	DSAEF_B	DSAEF_C	DSAEF_D
P1 Initial time	2: 0000 UTC on Day 1	2: 0000 UTC on Day 1	4: 0000 UTC on Day 2	1: 1200 UTC on Day 1
P2 Similarity region	6: the 6th parameter of rectangular areas in Jia et al. (2020)	20: the 20th parameter of rectangular areas in Jia et al. (2020)	1: the 1st parameter of rectangular areas in Jia et al. (2020)	20: the 20th parameter of rectangular areas in Jia et al. (2020)
P3 Threshold of the segmentation ratio of a latitudinal extreme point	3: 0.3	2: 0.2	1: 0.1	2: 0.2
P4 Overlapping percentage threshold of two TC tracks	6: 0.4	4: 0.6	3: 0.7	6: 0.4
P5 Seasonal similarity	3: Jul–Sept	2: May–Nov	2: May–Nov	2: May–Nov
P6 Intensity similarity	4: maximum intensity on all rainy days	4: maximum intensity on all rainy days	4: maximum intensity on all rainy days	1: average intensity on the first rainy day
	1: all grades	2: the target TC intensity is the same grade or above the historical TC	1: all grades	4: only the same grade
P7 Number of analog TCs screened for the ensemble forecast	2: historical TCs with the two most similar GIVs to that of the target TC	5: historical TCs with the five most similar GIVs to that of the target TC	7: historical TCs with the seven most similar GIVs to that of the target TC	7: historical TCs with the seven most similar GIVs to that of the target TC
P8 Ensemble	2: Maximum	2: Maximum	3: 90th percentile	3: 90th percentile

4 Results

4.1 Simulation experiments

The black scatter points in Figure 3 show the TSs of the best scheme of the four simulation experiments for 30 training samples. Each black dot in the figure represents a scheme whose horizontal and vertical coordinates are the TS250 and TS100 of this scheme, respectively. The figure shows that there is a significant increase in the number of DSAEF_B schemes compared with the number of DSAEF_A schemes, and the distribution of TSsum is more widespread. The maximum TSsum of DSAEF_B is 0.5571, while the maximum TSsum of DSAEF_A is 0.5035, indicating that the forecasting capability of DSAEF_LTP improved after adding the new parameter values of the similarity region. In experiment DSAEF_C, the maximum TSsum increases to 0.5353 after adding new values of the ensemble method, indicating that a suitable ensemble method plays an important role in improving the forecasting capability of DSAEF_LTP. In experiment DSAEF_D, when the new similarity region and ensemble method are added simultaneously, the model's forecasting capability is significantly improved. Compared with DSAEF_A, the TS250 of DSAEF_D increases from 0.1998 to 0.3114, and the TS100 increases from 0.3037 to 0.3428, which is an increase of 55.8% and 12.8%, respectively. TSsum increases from 0.5035 to 0.6542, an increase of 29.9%.

The parameter values of the best scheme for the four experiments are given in Table 2. From Table 2, it can be seen that the parameters of the best scheme for the four experiments are very different, such as, the numbers of ensemble members (determined by P7) of DSAEF_A, B, C, D are 2, 5, 7, and 7, respectively. In the experiments with the addition of the new values of the similarity region (DSAEF_B and DSAEF_D), the new value of P2 is used in the best scheme. And the new ensemble method is also used in DSAEF_C and DSAEF_D. This indicates that the new values of similarity region and the ensemble scheme have a positive effect on the forecasting capability of the model.

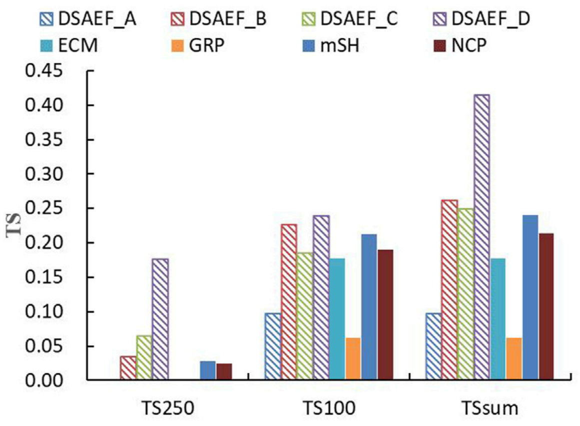

FIGURE 4
Comparison of the TS of the DSAEF_LTP model with four numerical models (ECM, GRP, NCP, mSH) in independent forecast experiments in Fujian Province.

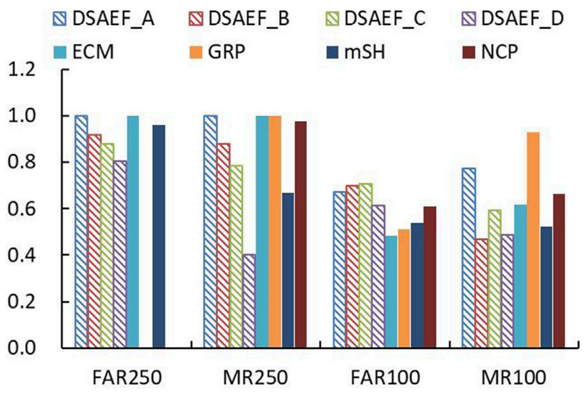

FIGURE 5
Comparison of the FAR and MAR of the DSAEF_LTP model with four numerical models (ECM, GRP, NCP, mSH) in independent forecast experiments in Fujian Province.

4.2 Forecast experiments

After obtaining the best scheme of the four experiments, as reported in the previous section, the four best schemes could be applied to the forecast experiments for 12 independent samples during 2016–2020, and their forecast performances were compared with the four NWP models (Figure 4). For the forecast of accumulated precipitation over 250 mm, the TS of both ECM and GRP is 0. The TS250 of the best schemes of the four models have advantages compared with the NWP models, demonstrating that DSAEF_LTP is good at forecasting precipitation over 250 mm, of which DSAEF_D performs the best, with a TS250 of 0.1767. For forecasts of accumulated precipitation ≥100 mm, DSAEF_D and DSAEF_B rank as the top two, with a TS100 of 0.2386 and 0.2268, respectively, which exceeds the best performer of the NWP models (mSH, with a TS100 of 0.2225). Except for DSAEF_A (original DSAEF_LTP model), whose TSsum (0.0974) is smaller than three of the NWP models (i.e., ECM, mSH and NCP), the TSsum of the best scheme of the other three improved DSAEF_LTP results exceeds those of the three NWP models. The TSsum of DSAEF_B, C and D is 0.2615, 0.2496 and 0.4153, respectively, and the TSsum of ECM, GRP, mSH, and NCP is 0.1769, 0.0622, 0.2403, and 0.2143. Among all the models, DSAEF_D ranks first, higher than DSAEF_A and higher than the best performer of the NWP models (mSH). From the forecast results above, regardless of whether adding the new values of ensemble method or similarity region or both, the forecast performance of the DSAEF_LTP model is improved when forecasting TC accumulated precipitation above 100 mm and 250 mm. The improved models (DSAEF_B to D) show advantages in predicting rainfall over 250 mm, and are comparable to the NWP models when predicting rainfall at magnitudes of 100 mm.

To further analyze the forecast skill of the DSAEF_LTP model, Figure 5 shows the FAR and MAR results of the four experiments compared with the four NWP models. It can be seen from the FAR250 and MAR250 results that, in terms of the forecast of accumulated precipitation ≥250 mm, the performances of the different NWP models are diametrically opposed. ECM and mSH have a FAR close to 1, indicating that their forecasted precipitation amounts are higher, which may relate to the physical characteristics of these models. The NCP model has a FAR of 0 for only one typhoon case (1617), and there are neither hits nor false alarms, so the result of the average FAR250 of the 12 TC samples is 0. GRP fails to forecast hits and false-alarm stations. For MAR250, a gradual decrease from DSAEF_A to D is shown, with the best being DSAEF_D with a score of 0.4048. The score for mSH is 0.6670, while the other three NWP models are closer to 1. That is, the forecast performance of DSAEF_D is the best. In the forecasting of accumulated precipitation ≥100 mm, the FAR of the NWP models ranges from 0.48 to 0.61, while that of DSAEF_A to D is 0.61–0.7. The NWP model scores all exceed that of DSAEF_LTP, and DSAEF_LTP does not perform as well as the NWP models in terms of FAR100. For MAR100, DSAEF_B and D perform better among all the DSAEF models, with values of 0.4704 and 0.4885, which is also better than the best NWP model (mSH) with a MAR100 of 0.5224. From the above analysis, as the magnitude of TC precipitation increases, the DSAEF_D model begins to show lower FAR and MAR. This reflects the advantages of DSAEF_D in extreme precipitation forecasting. The new values of similarity region and ensemble method can further improve the capability of this model in forecasting precipitation.

Figures 6A,B compare the forecast performances of the four configurations of the DSAEF_LTP model and the four NWP models for each LTC. The dashed line is the maximum single-station accumulated precipitation for each TC. In general, the larger the single-station maximum accumulated precipitation of a TC, the higher the TS value tends to be, both in terms of TS250 and TS100. For accumulated precipitation above 250 mm, only three TCs—TC1601, TC1614 and TC1617—caused more than 250 mm of precipitation in Fujian. Both the NWP models and the DSAEF_LTP models have no values on TS250 for the forecast of TC1601. In both TC1614 and TC1617, only one NWP model has forecasting ability on TS250 with a score less than 0.1, and the DSAEF_LTP models performed more prominently than the NWP models, with DSAEF_D scoring 0.33 for TC1614 and 0.55 for TC1617 on TS250, respectively. For accumulated precipitation above 100 mm, the advantages of the DSAEF_LTP models are not so obvious in the performance of TS100 as in TS250. Both the NWP models and the DSAEF_LTP models score 0 on TC 1822. Comparing the best performer of DSAEF_LTP models and NWP models, The forecasting ability of the NWP models are better than that of the DSAEF_LTP models for seven individual TC cases, and the remaining TC1619,

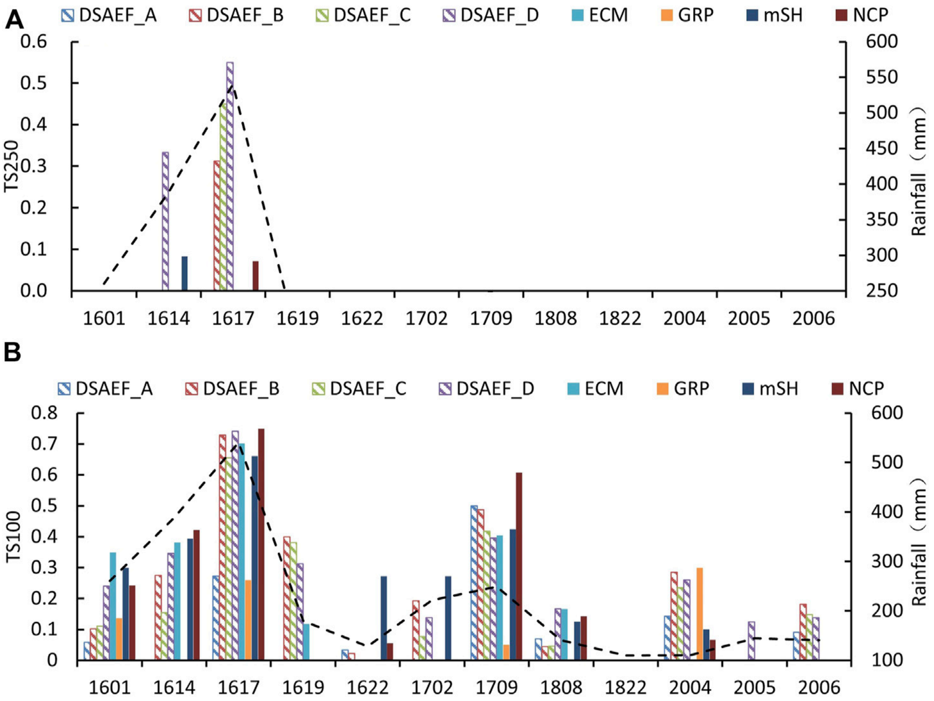

FIGURE 6
Comparison of the TS (histogram) in the four DSAEF_LTP model experiments and four NWP models (ECM, GRP, NCP, mSH) for each TC in independent forecast experiments and the maximum single-station accumulated precipitation (dashed line) for each TC accumulated precipitation **(A)** above 250 mm and **(B)** above 100 mm.

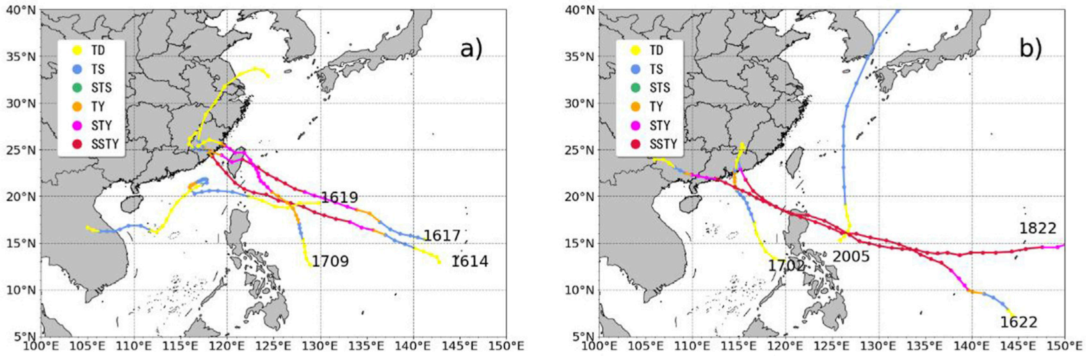

FIGURE 7
The TC tracks and intensity of **(A)** the top four TCs with higher TSsum and **(B)** the bottom four TCs with lower TSsum in independent forecast experiments simulated by the DSAEF_D model.

TC2005, and TC2006 are the ones where the DSAEF_LTP models outperforms the NWP models, and it can be seen that all the NWP models score 0 in the TS100 for TC2005 and TC 2006, which basically has no forecasting ability, while the DSAEF_LTP model has forecasting ability for them, reflecting the unique advantages of the DSAEF model. In order to analyze the differences in the forecast performance of the DSAEF_LTP model in forecasting different TC precipitation in Fujian, the top four TCs with higher TSsum and the bottom four TCs with lower TSsum in independent sample tests simulated by the DSAEF_D model are analyzed, respectively. Figure 7 shows the tracks and intensities of the top four and bottom four TCs. It can be clearly

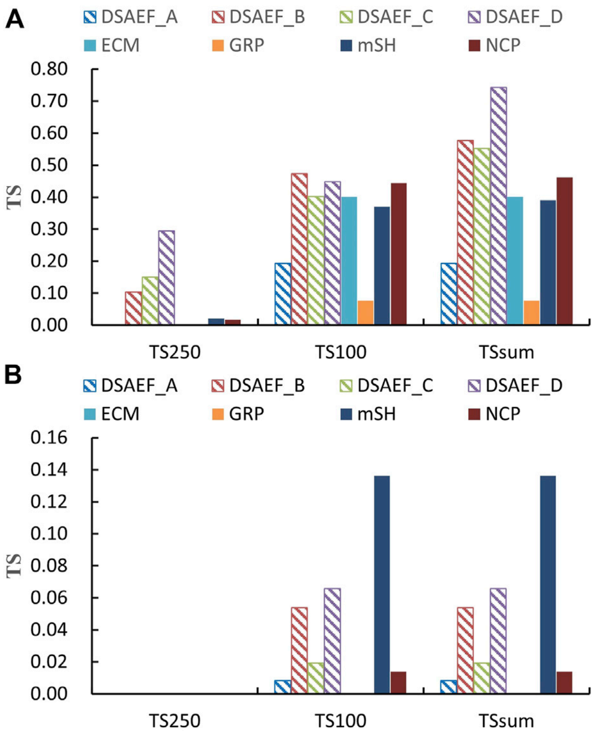

FIGURE 8
Comparison of the average TS of the DSAEF_LTP model with four numerical models (ECM, GRP, NCP, mSH) in independent forecast experiments in Fujian Province. **(A)** The top four TCs with higher TSsum,**(B)** the bottom four TCs with lower TSsum.

seen (Figure 7A) that, among the top four TC cases, two TCs make landfall in Taiwan first and then along the central coast of Fujian, one TC directly makes landfall along the southern coast of Fujian after wiping off from southern Taiwan, and the track of one TC is located in the northern South China Sea, where it hovers and circles before finally moving westward away from Fujian. As for the forecast performance of the bottom four TCs (Figure 7B), it can be seen that all four do not land directly in Fujian; three of them are active in the South China Sea to the south of Fujian and land in Guangdong, and the remaining TC moves northward in the Northwest Pacific to the east of Taiwan, which is far away from Fujian.

To better understand the characteristics of the DSAEF_LTP model and test whether DSAEF_LTP model has an advantage for NWP in the two subgroups of Figures 7, 8 compares the average TS of the DSAEF_LTP model with the NWP models for these two subgroups, i.e., the top four TCs with higher TSsum and the bottom four TCs with lower TSsum produced by the DSAEF_LTP models.

In terms of the four TCs with the best performance (i.e., TCs in Figure 7A) predicted by the DSAEF_LTP model, the improved DSAEF_LTP model generally outperforms the NWP models on the TS250 (Figure 8A), with the best DSAEF_D performance of 0.2944, while only mSH and NCP are greater than 0 among the four NWP models, and mSH only has the largest TS of 0.0208. The DSAEF_LTP model shows great advantages compared with NWP models at this precipitation level. When predicting the accumulated precipitation of ≥100 mm, the performance of DSAEF_LTP model and NWP model is closer, but the best performer of DSAEF_LTP model still has slight advantages over the best performer of NWP models. For TSsum, the DSAEF_D performs best among the DSAEF_LTP models with TSsum of 0.7432, which far exceeds the best performer NCP with TSsum of 0.4624.

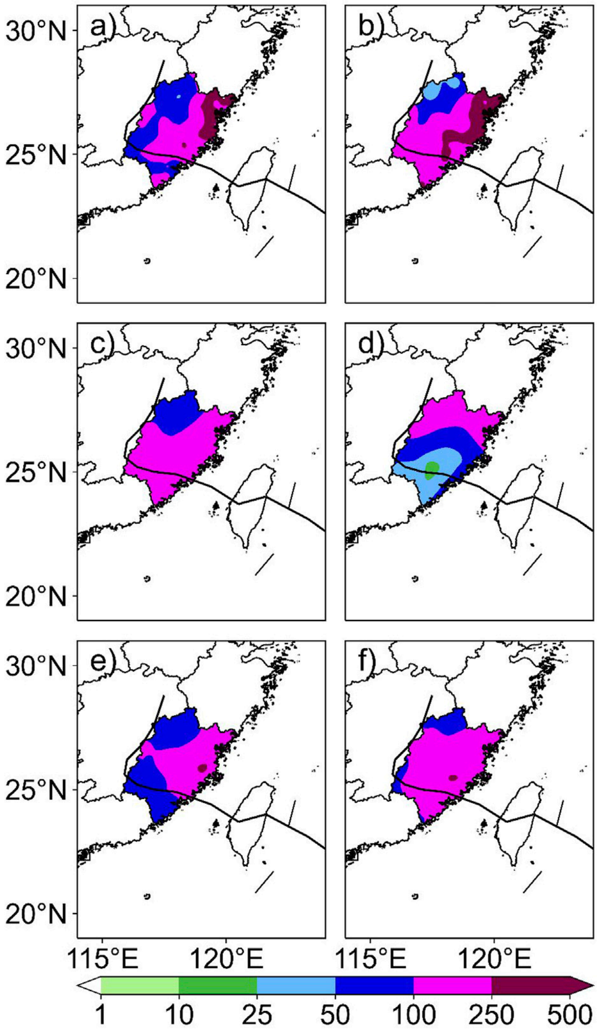

FIGURE 9
Accumulated precipitation distribution of TC1617 (Megi): **(A)** observed precipitation; **(B)** DSAEF_LTP model forecast; **(C)** ECM forecast; **(D)** GRP forecast; **(E)** mSH forecast; **(F)** NCP forecast. The black solid line is the observed track.

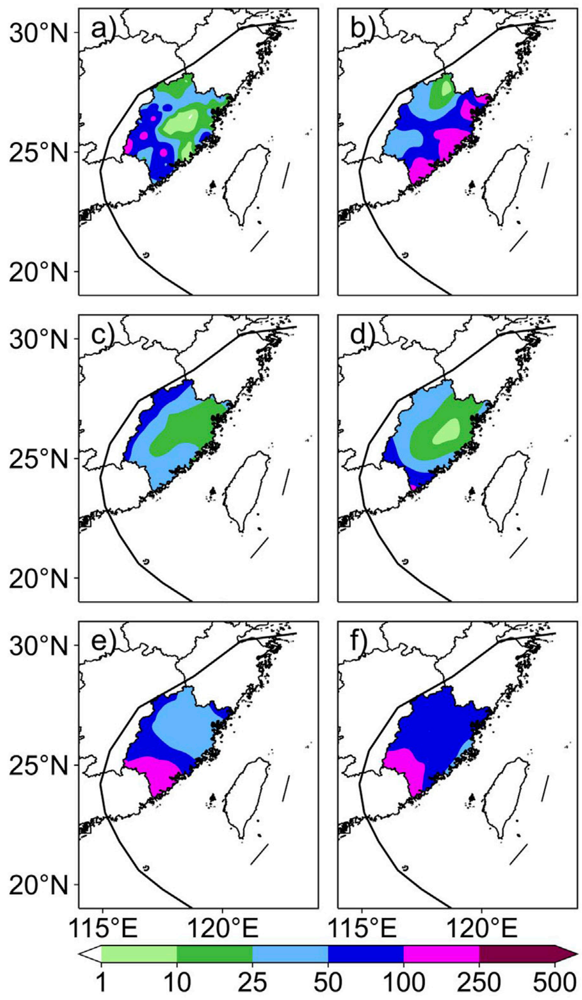

FIGURE 10
Accumulated precipitation distribution of TC1622 (Haima): **(A)** observed precipitation; **(B)** DSAEF_LTP model forecast; **(C)** ECM forecast; **(D)** GRP forecast; **(E)** mSH forecast; **(F)** NCP forecast. The black solid line is the observed track.

In terms of the four TCs with the worst performance (i.e., TCs in Figure 7B), both the DSAEF_LTP model and NWP models have generally low TS (Figure 8B), and on the TS250, no member of DSAEF_LTP model or NWP gets a score; on the TS100, the highest TS is mSH of 0.1364 and DSAEF_D ranks second with 0.0657. Therefore, it can be seen that the DSAEF_LTP model is comparable to NWP models, but there is still a big gap with mSH.

From the above description, it is obvious that the DSAEF_LTP model performs better for heavy rainfall produced by TCs that travel westward and make landfall in Fujian, and does not perform well for individual TC cases that are active in the South China Sea and cause heavy precipitation in Fujian. Therefore, it is necessary to strengthen the forecasting ability of the model for TCs in the South China Sea.

4.3 Analysis of representative cases

To demonstrate the characteristics of the improved DSEAF_LTP model, Figures 9, 10 show the precipitation distribution fields of two TCs (TC1617, with higher TSsum, and TC1622, with lower TSsum) produced by the improved DSAEF_LTP model with the new parameter values of similarity region and ensemble method added.

For TC1617 (Figure 9), DSAEF_D performs best in predicting the accumulated precipitation of ≥250 mm, and its precipitation patterns for northeastern Fujian agree well with observations, while the four NWP models cannot forecast heavy rainfall in northeastern Fujian Province at all. For the forecast of precipitation ≥100 mm, although the TS of DSAEF_D is the highest among the four experiments, however, it is still slightly worse than the NCP model. This is mainly caused by the false-alarming of heavy rainstorms in western and southern Fujian Province. Although the DSAEF_LTP model has imperfect forecasting effects in terms of fine-grained representation of TC heavy precipitation characteristics, the model-predicted heavy precipitation distribution can provide a good reference for forecasters and decision-makers in most cases.

For TC1622 (Figure 10), heavy rainfall ≥100 mm occurred in the south of Fujian. Only mSH and NCP successfully capture part of this heavy rainfall, and the forecast results of the other models, including DSAEF_D, ECM and GRP, have null TSs. For the DSAEF_LTP model, the heavy rainfall predicted by DSAEF_D is in the southeast of Fujian, which represents a relatively large deviation from the observed location, producing widespread false-alarm areas. Therefore, the DSAEF_LTP model needs to be further improved to reduce the FAR of its predictions.

It can be seen from the above analysis that DSAEF_D performs more stably and better than the other versions of the DSAEF_LTP model regardless of whether judging the performance according to the average value of TS, FAR or MAR of the independent sample TCs. Besides, compared with the other versions of the DSAEF_LTP model, DSAEF_D performs well for both of the precipitation thresholds focused upon in this work. Compared with the four NWP models, the TSsum of DSAEF_D is higher. Thus, applying DSAEF_D with the parameter values given in the fourth column in Table 2 in Fujian Province can provide reliable prediction results.

5 Summary and discussion

In this study, five new values of similarity region and four new ensemble methods are added in the DSAEF_LTP model.

Then, four experiments are conducted to identify the best scheme of the original and improved versions of the DSAEF_LTP model, and the best schemes of the four experiments are applied to TC precipitation prediction in Fujian Province. The forecasting performances of the DSAEF_LTP model are then compared with those of four NWP models. The main conclusions are as follows:

(1) The forecasting performance of the DSAEF_LTP model is significantly improved by adding the new values of similarity region or ensemble method. Also, the performance in Fujian Province is maximized when the values of these two parameters are both added (DSAEF_D), with the TSsum increasing from 0.0974 to 0.4153 relative to DSAEF_A. Analysis of two representative cases (TC1617 and TC1622) further demonstrates that the DSAEF_D model can successfully capture the heavy rainfall center in Fujian Province, while the model needs to be further improved to reduce the FAR.

(2) Compared with the TSs of the four NWP models, the DSAEF_LTP model versions (DSAEF_A to D) show advantages in predicting heavy rainfall at magnitude of ≥250 mm, and the improved models (DSAEF_B to D) are comparable to or better than the NWP models in predicting rainfall of ≥100 mm, of which the TS of DSAEF_D ranks first. On the whole, the forecasting performances of the improved models are better than those of the NWP models, and the TSsum of the best-performing DSAEF_LTP model (i.e., DSAEF_D) is higher than the best-performing NWP model (i.e., mSH).

(3) Analysis of the DSAEF_LTP model in Fujian Province shows that the model is better able to forecast TC extreme precipitation when the TC has made landfall in Fujian Province. Conversely, it is poor at forecasting the precipitation of TCs in the South China Sea that do not make landfall in Fujian or move northward in the Northwest Pacific far away from Fujian, meaning further improvement of the DSAEF_LTP model for Fujian Province is necessary.

After building and improving the DSAEF_LTP model, its application becomes a major issue. Previous studies have rarely focused on a small area, such as a single province, to choose the experimental TC samples, the best scheme, and then test the forecasting performance of the DSAEF_LTP model. This paper provides ideas for the operational application of the DSAEF_LTP model in different provinces. Adopting different schemes in different regions is an important method to improve the predictability of the DSAEF_LTP model.

Data availability statement

The original contributions presented in the study are included in the article/Supplementary Material, further inquiries can be directed to the corresponding author.

Author contributions

FR designed research. ZS conceptualized the analysis and wrote the manuscript. All authors were involved in helpful discussions and contributions to the manuscript.

Funding

This work was supported by the Natural Science Foundation of Fujian Province, China (Grant No. 2022J01445 and 2021J01464), the National Key R&D Program of China (Grant No. 2019YFC1510205), the Major Science and Technology Projects of Fujian Key Laboratory of Severe Weather (2022TF02), the Hainan Provincial Key R&D Program of China (SQ2019KJHZ0028), and the Jiangsu Collaborative Innovation Center for Climate Change.

Conflict of interest

The authors declare that the research was conducted in the absence of any commercial or financial relationships that could be construed as a potential conflict of interest.

Publisher’s note

References

Ams (2000). Policy statement: Hurricane research and forecasting. *Bull. Amer Meteor Soc.* 81 (6), 1341–1346.

Chen, L. S., and Meng, Z. Y. (2001). Progress of tropical cyclone research in China in the past decade(in Chinese). *Chin. J. Atmos. Sci.* 3, 420–432.

Ding, C., Ren, F., Liu, Y., Mcbride, J. L., and Feng, T. (2020). Improvement in the forecasting of heavy rainfall over south china in the DSAEF_LTP model by introducing the intensity of the tropical cyclone. *Weather and Forecasting* 35, 1–45. doi:10.1175/WAF-D-19-0247.1

Ebert, E. E., Turk, M., Kussion, S. J., Yang, J., Seybold, M., Keehn, P. R., et al. (2011). Ensemble tropical rainfall potential (eTRaP) forecasts. *Weather Forecast.* 26, 213–224. doi:10.1175/2010WAF2222443.1

Elsberry, R. L., and Tsai, H. C. (2014). Situation-dependent intensity skill metric and intensity spread guidance for Western North Pacific tropical cyclones. *Asia. Pac. J. Atmos. Sci.* 50 (3), 297–306. doi:10.1007/s13143-014-0018-5

Jia, L., Jia, Z., Ren, F., Ding, C., Wang, M., Feng, T., et al. (2020). Introducing TC intensity into the DSAEF_LTP model and simulating precipitation of super-typhoon Lekima (2019). *Q. J. R. Meteorol. Soc.* 146, 3965–3979. doi:10.1002/qj.3882

Jia, L., Ren, F., Ding, C., Jia, Z., Wang, M., Chen, Y., et al. (2022). Improvement of the ensemble methods in the dynamical-statistical-analog ensemble forecast model for landfalling typhoon precipitation. *J. Meteorological Soc. Jpn.* 100 (3), 2022–2592. doi:10.2151/jmsj.2022-029

Jia, Z., Ren, F., Zhang, D., Ding, C., Yang, M., Feng, T., et al. (2020). An application of the LTP_DSEF model to heavy precipitation forecasts of landfalling tropical cyclones over China in 2018. *Sci. China Earth Sci.* 63 (1), 27–36. doi:10.1007/s11430-019-9390-6

Kidder, S. Q., Kusselson, S. J., Knaff, J. A., Turk, M., Ferraro, R. R., and Kuligowski, R. J. (2005). The tropical rainfall potential (TRaP) technique. Part I: Description and examples. *Weather Forecast.* 20 (4), 456–464. doi:10.1175/WAF860.1

Lee, C. S., Huang, L. R., Shen, H. S., and Wang, S. T., A climatology model for forecasting typhoon rainfall in taiwan. *Nat. Hazards (Dordr).*, 2006, 37(1): 87–105, doi:10.1007/s11069-005-4658-8

Lei, X, Fong, C, Malano Vicente, B., and Che, I (2019). Overview on the progress of working group on meteorology of ESCAP/WMO typhoon committee in the recent 10 years. *Trop. cyclone Res. Rev.* 8 (2), 84–94. doi:10.1016/j.tcrr.2019.07.008

Li, B., and Zhao, S. X. (2009). Development of forecasting model of typhoon type rainstorm by using SMAT. *J. Meteorol. (in Chinese)* 35 (6), 3–12.

Liu, C. C. (2009). The influence of terrain on the tropical rainfall potential technique in taiwan. *Weather Forecast.* 24 (3), 785–799. doi:10.1175/2008WAF2222135.1

Lonfat, M., Rogers, R., Marchork, T., and Marks, F. D. (2007). A parametric model for predicting hurricane rainfall. *Mon. Weather Rev.* 135 (9), 3086–3097. doi:10.1175/MWR3433.1

Lu, X. Q., Yu, H., Ying, M., Zhao, B., Zhang, S., Lin, L., et al. (2021). western North pacific tropical cyclone database created by the China meteorological administration. *Adv. Atmos. Sci.* 38 (4), 690–699. doi:10.1007/s00376-020-0211-7

Marks, F. D., Kappler, G., and Demaria, M. Development of a tropical cyclone rainfall climatology and persistence (RCLIPER) model [R]. San Diego, CA, USA: Proceedings of the Preprints, 25th Conference on Hurricanes and Tropical Meteorology. June 2002, 327–328

Matsuura, T., Yumoto, M., and Iizuka, S. (2003). A mechanism of interdecadal variability of tropical cyclone activity over the Western North Pacific. *Clim. Dyn.* 21, 105–117. doi:10.1007/s00382-003-0327-3

Ren, F. M., Gleason, B., and Easterling, D. R. (2001). A technique for partitioning tropical cyclone precipitation. *J. Trop. Meteorology (in Chinese)* 17 (3), 308–313. doi:10.3969/j.issn.1004-4965.2001.03.015

Ren, F. M., Qiu, W. Y., Jiang, X. L., Wu, L. G., Xu, Y. L., and Duan, Y. H. (2018). An objective track similarity index and its preliminary application to predicting precipitation of landfalling tropical cyclones. *Weather Forecast.* 33, 1725–1742. doi:10.1175/WAF-D-18-0007.1

Ren, F. M., Wang, Y. M., Wang, X. L., and Li, W. (2007). Estimating tropical cyclone precipitation from station observations. *Adv. Atmos. Sci.* 24 (4), 700–711. doi:10.1007/s00376-007-0700-y

Ren, F., Ding, C., Zhang, D., Chen, D., Ren, H., and Qiu, W. (2020). A dynamical-statistical-analog ensemble forecast model: Theory and an application to heavy rainfall forecasts of landfalling tropical cyclones. *Mon. Weather Rev.* 148 (4), 1503–1517. doi:10.1175/mwr-d-19-0174.1

Ren, Fumin, and Xiang, Chunyi (2017). Review and prospect of researches on the pre liction of precipitation associated with landfalling tropical cyclones. *Journal of Marine Meteorology* 37 (4), 8–18. doi:10.19513/j.cnki.issn2096-3599.2017.04.002

Tsai, H. C., and Elsberry, R. L. (2017). Seven-Day intensity and intensity spread predictions for atlantic tropical cyclones. *Weather Forecast.* 32 (1), 141–147. doi:10.1175/WAF-D-16-0165.1

Tsai, H. C., and Elsberry, R. L. (2015). Seven-day intensity and intensity spread predictions for Western North Pacific tropical cyclones. *Asia. Pac. J. Atmos. Sci.* 51 (4), 331–342. doi:10.1007/s13143-015-0082-5

Tsai, H. C., and Elsberry, R. L. (2016). Skill of Western North Pacific tropical cyclone intensity forecast guidance relative to Weighted-Analog technique. *Asia. Pac. J. Atmos. Sci.* 52 (3), 281–290. doi:10.1007/s13143-016-0001-4

Wang, X. F., and Zhou, R. W., 2021.Performance verification of global precipitation forecast over Yalong River Basin in flood season (in Chinese).*Meteor Mon*, 47(10):1193–1205.

Ying, M., Zhang, W., Yu, H., Lu, X., Feng, J., Fan, Y., et al. (2014). An overview of the China meteorological administration tropical cyclone database. *J. Atmos. Ocean. Technol.* 31, 287–301. doi:10.1175/JTECH-D-12-00119.1

Zhang, F., Minamide, M., Nystrom, R. G., Chen, X., Lin, S., and Harris, L. M., (2019). Improving harvey forecasts with next-generation weather satellites: Advanced hurricane analysis and prediction with assimilation of GOES-R all-sky radiances. *Bull. Am. Meteorol. Soc.*100 (7), 1217–1222. doi:10.1175/BAMS-D-18-0149.1

Zhong, Y., Yu, H., Teng, W. P., and Chen, P. Y., (2009). A dynamic similitude scheme for tropical cyclone quantitative precipitation forecast (in Chinese). *J. Appl. Meteor. Sci.* 20 (1), 17–27. doi:10.7519/j.issn.1000-0526.2021.10.003

frontiers | Frontiers in Earth Science

TYPE Original Research
PUBLISHED 06 January 2023
DOI 10.3389/feart.2022.1021308

EDITED BY
Liguang Wu,
Fudan University, China

REVIEWED BY
Eric Hendricks,
National Center for Atmospheric Research (UCAR), United States
Qingyuan Liu,
Chinese Academy of Meteorological Sciences, China

*CORRESPONDENCE
Yan Li,
yanlee@nuist.edu.cn
Xianyan Chen,
chenxy@cma.gov.cn

SPECIALTY SECTION
This article was submitted to Atmospheric Science, a section of the journal Frontiers in Earth Science

RECEIVED 17 August 2022
ACCEPTED 15 September 2022
PUBLISHED 06 January 2023

CITATION
Jin R, Li Y, Chen X and Li M (2023), Characteristics of the upper-level outflow and its impact on the rapid intensification of Typhoon Roke (2011). *Front. Earth Sci.* 10:1021308.
doi: 10.3389/feart.2022.1021308

Characteristics of the upper-level outflow and its impact on the rapid intensification of Typhoon Roke (2011)

Ru Jin[1,2], Yan Li[1]*, Xianyan Chen[3]* and Meiying Li[4]

[1]Key Laboratory of Meteorological Disaster, Ministry of Education (KLME), Nanjing University of Information Science & Technology, Nanjing, China, [2]Zhejiang Institute of Meteorological Sciences, Hangzhou, China, [3]National Climate Center, China Meteorological Administration, Beijing, China, [4]Penglai Meteorological Bureau, Penglai, China

In this study, we investigate the structural characteristics of the upper-level outflow and its impact on the rapid intensification (RI) of Typhoon Roke (2011), which experienced an evident outflow transformation from equatorward to poleward during its RI period. The simulations by the Weather Research and Forecasting Model suggest that the upper-level outflow extends from 100 hPa to 150 hPa, with an upper-level warm core at around 150 hPa. The upper-level outflow is enhanced ahead of the typhoon intensification, which is closely related to the outflow-environment interaction. Further analyses indicate that at the early stage of Roke (2011) before the RI, the strong equatorward outflow and the updraft south of the typhoon center are enhanced, favoring the onset of RI. During the RI period, the strong divergent flow near the entrance of the southwesterly jet in front of the upper-level trough, induces the poleward outflow. The eddy flux convergence of angular momentum inward propagated to the typhoon center from a 1000-km radius further enhances the poleward outflow and leads to the development of the vertical motion north of the typhoon center. Then Roke (2011) intensifies rapidly. Simultaneously, the shallow weak positive potential vorticity (PV) anomaly south of the southwesterly jet increases the inner-core PV, favoring the sustained intensification of Roke (2011). After Roke (2011) reaches its peak intensity, its intensity decreases due to the increase of vertical wind shear and the approaching of the southwesterly jet. It is indicated that the interaction between the upper-level outflow and the upper-tropospheric trough has significant influence on the RI of TC.

KEYWORDS

tropical cyclone, the upper-level outflow, rapid intensification, outflow-environment interaction, upper-troposhere trough

1 Introduction

The characteristics and mechanisms of the intensity variation of tropical cyclones (TCs), especially the rapid intensification (RI), are one of the active areas in TC research (Wang and Zhou, 2008; Zhao et al., 2022a; Cai et al., 2022). Among the several factors affecting TC intensity variation, the upper-level outflow and its interaction with the upper-tropospheric environmental field have attracted more and more attention in recent years (Dai et al., 2017; Ryglicki et al., 2019; Li et al., 2020). The outflow can easily interact with the upper-tropospheric environmental flow due to the weak inertial stability (Holland and Merrill, 1984; Rappin et al., 2011) and the horizontal scale of the outflow can reach thousands of kilometers radially (Ditchek et al., 2017). Simultaneously, the outflow can affect TC intensity through dynamical and thermal processes. Therefore, the study on the characteristics of TC outflow and its influence on the intensity variation can help further understand the mechanisms of TC intensity variation, thus being of great significance to improving TC intensity prediction.

Most TC outflow layers are within 300 hPa to 100 hPa and show anticyclonic and divergent flow on the synoptic scale (Shi et al., 1990). Compared with the middle and lower layers, outflow layers are more asymmetric (Black and Anthes, 1971). Chen and Gray (1985) proposed three outflow patterns for intensifying TCs, namely single channel, double channel and no channel, and the change of outflow patterns is closely related to the upper-tropospheric environmental flow (Merrill, 1988a, b). Recently, with the improvement of detection methods (Komaromi and Doyle, 2017; Ohigashi et al., 2020; Ohigashi et al., 2021) and numerical simulation techniques (Dai et al., 2017; Montgomery et al., 2019), many advances have been achieved in the studies on the characteristics of TC outflow layers and their relationships with TC intensity variation. Using the dropsonde data from the NASA Hurricane and Severe Storm Sentinel (HS3) field campaign, Komaromi and Doyle (2017) found that the outflow extended from 300 hPa to 150 hPa and from 50-km to 200-km radius, with a region of low inertial stability and a shallow inflow layer above the maximum outflow layer. Both model simulations (Cohen et al., 2017) and observations (Cohen et al., 2019) suggested that the outflow layer may exhibit a low-pressure center surrounded by high pressure due to the strong outward-pointing centrifugal and pressure gradient forces that cannot be counterbalanced by the inward-pointing Coriolis force. Furthermore, Cohen and Paldor (2020) analyzed the Lagrangian trajectories of air parcels in the outflow layer and described the dynamics using an integrable, two degrees-of-freedom and angular momentum conserving Hamiltonian system with a single non-dimensional parameter. Several studies focused on the characteristics of low Richardson number in the outflow layer (Emanuel and Rotunno, 2011; Emanuel, 2012; Duran and Molinari, 2016). These studies hypothesized that the critical Richardson number stratifies the potential temperature profile, which leads to the change of outflow temperature with angular momentum to cause the change of TC intensity. However, Montgomery et al. (2019) evaluated the theory of TC intensification proposed by Emanuel (2012) using idealized, three-dimensional, convection-permitting numerical experiments, and the results showed that eddy processes in the outflow layer are more related to TC structure than the critical Richardson number. This finding is consistent with the results in Ditchek et al. (2017) which highlighted the larger dynamic effect of TC outflow layer on TC intensity than the thermodynamic effect.

Generally, TC outflow can influence the TC structure and intensity by interacting with the environmental field (Rappin et al., 2011; Li et al., 2017). Dai et al. (2017) pointed out that the interaction between TC outflow and mid-latitude jets can lead to the formation of the TC secondary eyewall. Moreover, the idealized numerical simulations in Dai et al. (2019) revealed that asymmetric rainbands are an essential source of outflow. However, the scholars are not unanimous on whether the outflow-environment interaction favors TC intensification. Some argued that the strong divergence in front of an upper-level trough, small-scale positive potential vorticity (PV) anomaly and eddy flux convergence (EFC) of angular momentum transported to TC inner-core could enhance TC outflow and develop the secondary circulation, thus intensifying TCs (Molinari and Vollaro, 1989; Hanley et al., 2001; Leroux et al., 2013). Additionally, Ryglicki et al. (2019) found that outflow can divert the environmental flow around TCs, reducing the vertical wind shear (VWS). Therefore, some TCs can still rapidly intensify with moderate VWS (Huang et al., 2022). However, Fischer et al. (2019) investigated the TC-trough interactions for both rapidly and non-rapidly intensifying TCs, and the results revealed that there is little relationship between the RI and EFC. Furthermore, upper-tropospheric systems such as upper-level cold low (UTCL) and mid-latitude jets approaching TCs often result in strong VWS, which can lead to mid-level ventilation, negatively affecting TC intensification (Merrill 1988b; Yan et al., 2021).

However, the mechanism of outflow affecting TC intensity variation is not yet clear. To explore the relationship between the outflow and intensity variation of TCs, we investigate the characteristics of outflow layers during the RI in this study and discuss their possible effects on TC intensity using numerical simulations. The outflow channel of Typhoon Roke (2011) had an evident change during the RI of the TC, which may be related to the outflow-environment interaction. Thus, we select Typhoon Roke (2011) as the study case in this research.

The remainder of this paper is organized as follows. Section 2 presents an overview of Typhoon Roke (2011). Section 3 shows model description and verification. Section 4 describes the characteristics of the upper-level outflow during the RI of Typhoon Roke (2011). Section 5 discusses the possible impacts of the upper-level outflow on the RI of Typhoon

Roke (2011). The main conclusions and discussion are presented in section 6.

2 Overview of Typhoon Roke (2011)

Roke (2011) was a super typhoon with a RI period and a noticeable change in the upper-level outflow channel. According to the best-track dataset from the Joint Typhoon Warning Center (JTWC), Typhoon Roke (2011) started to intensify rapidly at 1800 UTC 18 September and reached its peak at 0000 UTC 20 September, with the maximum wind speed of 59 m s^{-1} and the minimum central pressure of 937 hPa. Then, the RI ended at 0600 UTC 20 September. Based on Wang and Zhou (2008), the criteria for the RI are as follows: the maximum wind speed increases by at least five knots in the first 6 h, 10 knots in the first 12 h and 30 knots in 24 h. The RI period starts when the three criteria are first met simultaneously and ends 24 h later when they are no longer met together (Jiang and Ramirez, 2013).

Mid-to upper-level satellite-derived wind and the water vapor images collected from the Cooperative Institute for Meteorological Satellite Studies (CIMSS) Tropical Cyclones Group at the University of Wisconsin-Madison are used to reveal the evolution of the outflow channel of Typhoon Roke (2011) (Figure 1). 6 h before the onset of RI, there was no apparent outflow channel near the storm center, the cloud system was loose, and a long and narrow jet stream appeared around 10 latitudes north of Roke (2011) (Figure 1A). In the early stage of the RI, the outflow was mainly distributed to the east and south of the upper-level circulation of Roke (2011) (Figure 1B). With the approach of the mid-latitude southwesterly jet, the poleward outflow strengthened, and the equatorward outflow weakened gradually (Figure 1C). Meanwhile, the cloud system of Roke (2011) gradually became dense, and when Roke (2011) reached its peak intensity at 0000 UTC 20 September, the poleward outflow represented by the blue wind barbs was considerably stronger than that in the earlier stage with a mature eyewall in the satellite images (Figure 1D). Therefore, it is evident that the upper-level outflow pattern had a complex transformation with the strengthening of Roke (2011). Furthermore, the RI of Roke (2011) occurred at 26°N–28°N where the sea surface temperature (SST) was relatively low at about 26.5°C–27.5°C. Such an ocean surface cannot provide favorable thermal conditions for the development of Roke (2011). Thus, the leading factor of the intensification of Roke (2011) is the dynamic process of upper-level outflow.

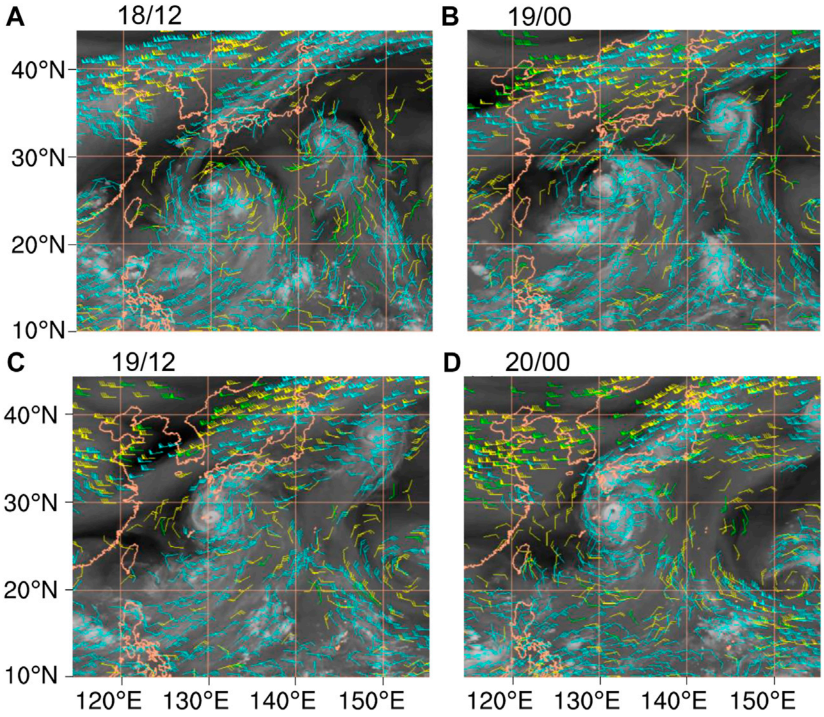

FIGURE 1
Mid-to upper-level satellite-derived wind (green: 351–500 hPa; yellow: 251–350 hPa; blue: 100–250 hPa) superimposed on the water vapor images for Typhoon Roke (2011) at **(A)** 1200 UTC 18 September, **(B)** 0000 UTC 19 September, **(C)** 1200 UTC 19 September and **(D)** 0000 UTC 20 September 2011.

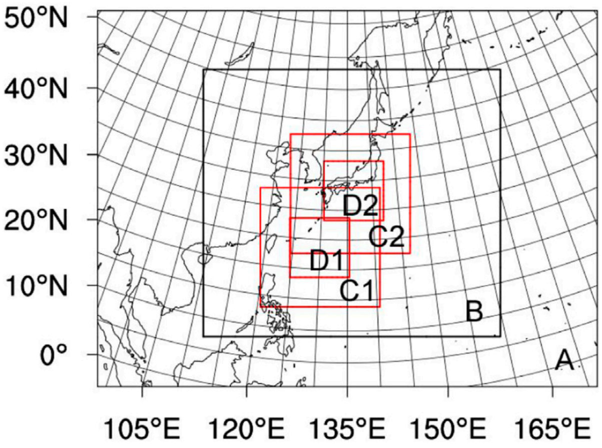

FIGURE 2
Model domain configuration. Domains A, B, C and D have horizontal resolutions of 54, 18, 6 and 2 km, respectively. Domain C and D are designed to follow the movement of the storm, with C1 (D1) and C2 (D2) denoting the initial and final position of the domain, respectively.

3 Model description and verification

3.1 Model description

Considering the limited observation areas of TC outflow and the underestimation of TC intensity in atmospheric reanalysis data (Schenkel and Hart, 2012; Li et al., 2020), the Advanced Research version of the Weather Research and Forecasting Model (WRF-ARW) version 3.4.1 (Skamarock et al., 2008) is used in this study. In this model, we set up four two-way interactive nested domains at horizontal resolutions (grid points) of 54 km (172 × 130), 18 km (307 × 277), 6 km (370 × 370) and 2 km (553 × 553), as shown in Figure 2. The simulations start at 0000 UTC 18 September 2011 and end at 0000 UTC 21 September 2011 in all four domains, with an integration period of 72 h, covering the RI process of Typhoon Roke (2011). The outer domains A and B are stationary, while the inner domains C and D move with the center of Roke (2011) at a 15-min interval, where C1 (D1) and C2 (D2) denote the initial and final positions of the domain C (D), respectively (Figure 2). The outermost domain A is sufficiently large to cover the region of the outflow-environment interaction. In the innermost domain D, the TC inner-core characteristics can be captured at a high resolution. The model initial and lateral boundary conditions in domain A are derived from the interpolation of the National Centers for Environmental Prediction Final Operational Global Analysis (FNL) data, which has spatio-temporal resolutions of 1° × 1° and 6 h. The NCEP FNL analysis is based on the Global Data Assimilation System (GDAS), which continuously collects observational data from the Global Telecommunications System (GTS) and other sources for many analyses. Although the atmospheric motion vectors (AMVs) were not ingested in the NCEP FNL analysis, it is still a good choice to use this data as the initial and boundary conditions in WRF simulations because more other observational data were assimilated into the NCEP FNL analysis. The sea surface temperature data is interpolated from the National Oceanic and Atmospheric Administration's Advanced Very High Resolution Radiometer data with a resolution of 0.25°. The 55 σ-vertical levels are applied in all domains, and the model top is set to 30 hPa (Chen et al., 2011). The vertical resolution is relatively high, especially in both the lower and upper tropospheres. For example, there are nine levels from 300 to 100 hPa, all at intervals below 1 km. The time interval of the model outputs is 1 hour.

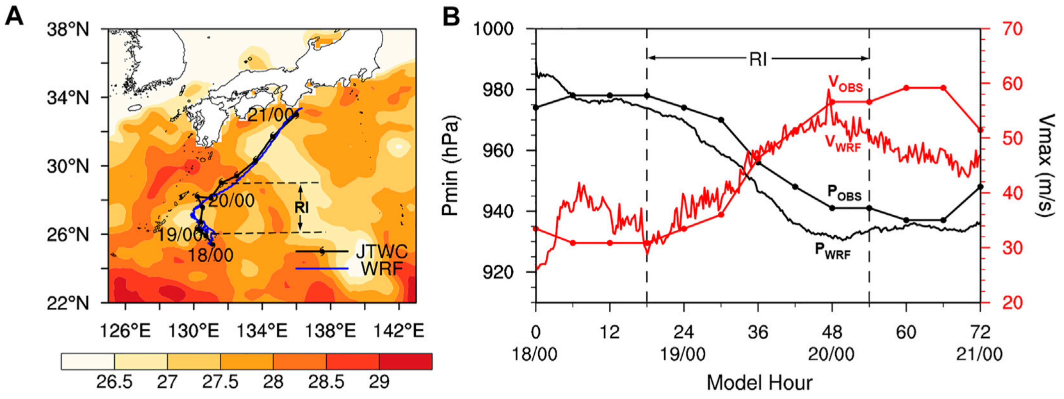

FIGURE 3
(A) Comparison of the track between the observations (black line with typhoon symbols) and simulations (blue line with typhoon symbols) superimposed on the sea surface temperature field (shaded areas, °C) at 0000 UTC 18 September 2011, and **(B)** time series of the maximum surface wind speed (red lines, m s^{-1}) and minimum central pressure (black lines, hPa) of the observations (OBS, dotted lines) and simulations (WRF, solid lines).

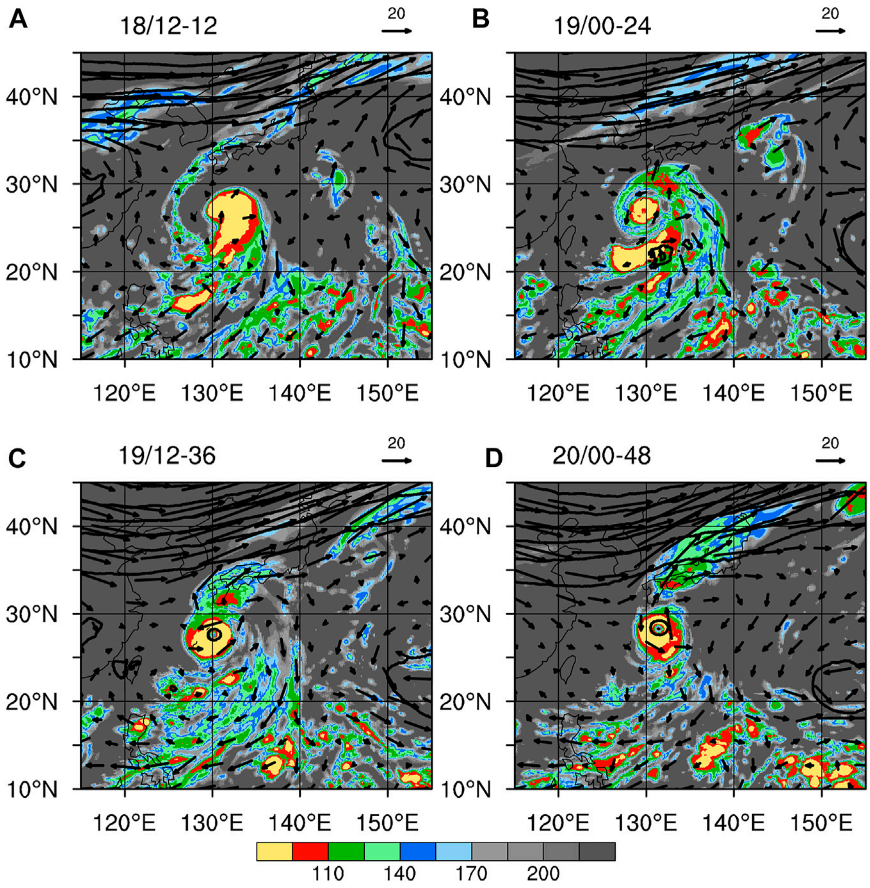

FIGURE 4
The flow (vectors, m s^{-1}), geopotential height (contours, gpm) at 200 hPa and outgoing long-wave radiation (shaded areas, W m^{-2}) for **(A)** 12-h integration (1200 UTC 18 September), **(B)** 24-h integration (0000 UTC 19 September), **(C)** 36-h integration (1200 UTC 19 September) and **(D)** 48-h integration (0000 UTC 20 September).

The physical parameterization schemes used in the model include the Betts-Miller-Janjic cumulus parameterization scheme (Betts, 1986), Yonsei University planetary boundary layer scheme (Hong et al., 2006), unified Noah land surface model scheme (Tewari et al., 2004), Rapid Radiative Transfer Model long-wave radiation scheme (Mlawer et al., 1997), Dudhia shortwave radiation scheme (Dudhia, 1989), and Thompson cloud microphysics scheme including six classes of hydrometeors (Thompson et al., 2004). Note that the Betts-Miller-Janjic cumulus parameterization scheme is only applicable to the domains A and B because it is no need to account for sub-grid-scale convection effects in the domains C and D (Molinari and Dudeck, 1992).

3.2 Model verification

To evaluate the reasonableness of the simulation results, we compare the 72-h simulated track and intensity of Typhoon Roke (2011) with the observations from the JTWC dataset. The results show that the simulated track of Typhoon Roke (2011) is basically consistent with the observations, showing a recurving track from northwestward to northeastward (Figure 3A).

The mean errors of the track in the whole simulation and RI periods are 44.9 km and 54.2 km, respectively. The mean errors of the maximum surface wind speed (V_{MAX}) and the minimum central pressure (P_{MIN}) during the RI period are 3.1 m s^{-1} and 8.5 hPa, respectively (Figure 3B). Therefore, the WRF can simulate well the intensity and RI rate of Typhoon Roke (2011) despite the certain differences in the TC intensity. Specifically, before the onset of RI at 1800 UTC 18 September (0–18 h of integration), the simulated V_{MAX} is obviously stronger than the observations, while the P_{MIN} is closer to the observations. During the RI period from 1800 UTC 18 September to 0000 UTC 20 September (18–48 h of integration), the simulated TC intensity and RI rate are almost the same as the observations. After Roke (2011) reaches its peak intensity at 0000 UTC 20 September, the

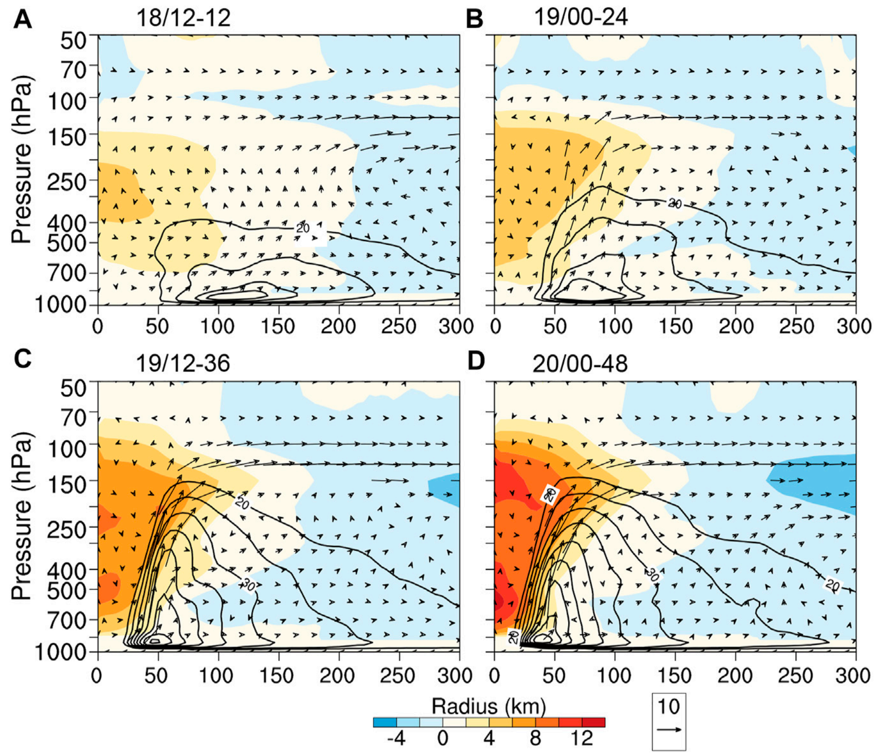

FIGURE 5
Radius-pressure plots of the azimuthally averaged potential temperature anomaly (shaded areas, K), tangential wind (contours, m s^{-1}) and radial-vertical wind velocity (vectors, m s^{-1}; vertical velocity multiplied by 10) for **(A)** 12-h integration (1200 UTC 18 September), **(B)** 24-h integration (0000 UTC 19 September), **(C)** 36-h integration (1200 UTC 19 September) and **(D)** 48-h integration (0000 UTC 20 September).

simulated intensity decreases, which is different from the observed intensity that remained constant and slowly intensified after the end of the RI. Overall, the WRF well simulates the track and intensity variation of Typhoon Roke (2011) during its RI period.

Moreover, the WRF successfully reproduces the upper-tropospheric large-scale environmental field and the upper-level outflow evolution during the intensification of Typhoon Roke (2011) (Figure 4). Specifically, the area of lower outgoing longwave radiation (OLR) which represents the strong convection is mainly distributed south of TC center before the RI (Figure 4A), consistent with the cloud system in Figure 1A. In the early stage of the RI, the low-value OLR area is distributed to the east and south of TC center (Figure 4B), which is similar to that in Figure 1B. In Figures 4C,D, the low-value OLR area north of TC center is greatly expanded, representing the strengthened poleward outflow. Overall, the OLR simulated by the WRF captures the cloud structure well compared with the observations (Figure 1). Simultaneously, the simulated flow and geopotential height fields at 200 hPa exhibit a circulation pattern similar to that in Figure 1. Crucially, the evolution characteristics of the TC outflow are well simulated at higher resolution, providing better conditions for the analyses in the following sections.

4 Characteristics of the upper-level outflow during the rapid intensification of Typhoon Roke (2011)

4.1 Vertical structure of Typhoon Roke (2011)

As shown in Figure 5, the evolution characteristics of the radial and vertical structure during the RI are presented. The warm cores are characterized by the anomalous potential temperature relative to the average temperature in domain D. Six hours before the RI (1200 UTC 18 September), the radius of the maximum tangential wind is around 100 km in the boundary layer, and the outflow appears within 100–200 hPa and at a 200-km radius. Note that the vertical velocity is small, and positive warm anomalies appear between 200 hPa and 400 hPa (Figure 5A). By comparison, the maximum tangential wind is concentrated to inner radius of 75 km, and the outflow markedly intensifies at 125 hPa and 100-km to 250-km radius 6 h after the onset of the RI (0000 UTC 19 September). Simultaneously, the upward motion near the storm center strengthens, and the positive warm anomaly of 4 K extends from 700 hPa to 150 hPa (Figure 5B). With the sustained intensification of

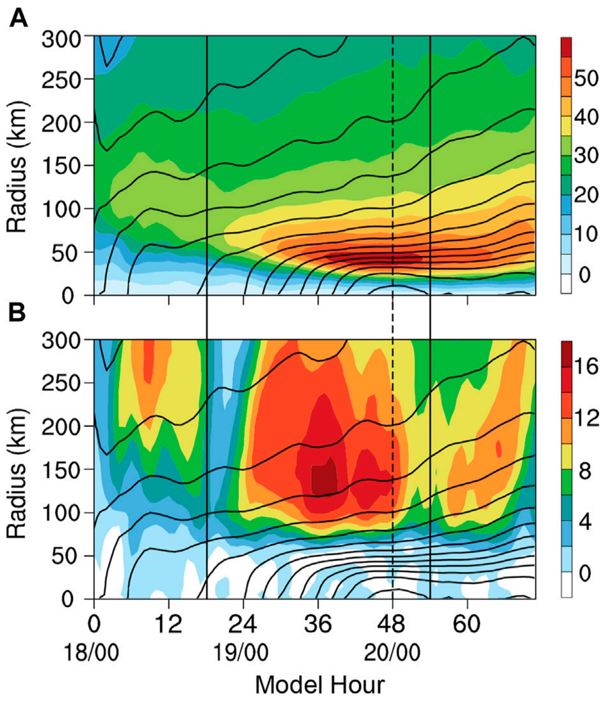

FIGURE 6
Time-radius plots of the azimuthally averaged **(A)** tangential wind (shaded areas, m s^{-1}) at 925 hPa and **(B)** radial wind at 125 hPa (shaded areas, m s^{-1}) and the sea level pressure (contours, hPa). The area between the two solid lines denotes the results in the observed RI period, while the dash lines represent the time when Typhoon Roke (2011) reaches its peak intensity in both simulations and observations.

Roke (2011), the lower-level tangential wind reaches its maximum within a 50-km radius, and the strong outflow peaks at 125 hPa, which can greatly enhance the secondary circulation (Figures 5C,D). Two warm cores arise at 1200 UTC 19 September at around 200 hPa and 500 hPa (Figure 5C), and the upper one peaks at 150 hPa when Roke (2011) reaches its peak intensity at 0000 UTC 20 September (Figure 5D). Overall, it is clear that the outflow is strengthened and thickened during the RI period of Roke (2011).

4.2 Horizontal structure of Typhoon Roke (2011)

Figure 6 presents the time-radius variation of tangential and radial wind with the sea level pressure. The results suggest that the maximum tangential wind at 925 hPa gradually strengthens and approaches the storm center, and then it reaches the peak from 1400 UTC 19 September (38-h integration) to 0400 UTC 20 September (52-h integration). The tangential wind strengthens with the sea level pressure, indicating that the cyclonic rotation increases with decreasing near-surface pressure (Figure 6A). Compared with the tangential wind in the boundary layer, the radial wind representing the wind field of outflow has a larger scale, with four maxima during the simulation (Figure 6B). Before the RI, the first maximum of radial wind speed appears within the radius of 250–300 km, consistent with the finding in Figure 5A. During the RI, the radial wind strengthens gradually and reaches its peak value of more than 16 m s^{-1} at 1200 UTC 19 September (36-h integration) within the radius of 100–150 km. Subsequently, the third maximum of radial speed appears. After the end of the RI, the radial wind strengthens slightly and reaches its fourth maximum. It can be concluded that the variation tendency of radial wind is relatively complex, indicating that the outflow is enhanced before the intensification of the storm, which can provide more favorable conditions for the RI of Roke (2011).

The TC circulation generally shows an asymmetric structure. Figure 7 presents the variation of the upper- and lower-level horizontal structure of Typhoon Roke (2011). Consistent with the results in Cohen et al. (2017, 2019), the 200-hPa wind field is visualized as a small-scale cyclonic flow within a 300-km radius surrounded by a larger-scale anticyclonic flow within an about 1000-km radius (Figures 7A–D). At 1200 UTC 18 September (12-h integration), an upper-level trough with shallow divergent flow appears in the northwest quadrant of the TC center (Figure 7A), where the convective activities are vigorous (Figure 7E). Moreover, the radar reflectivity shows that the asymmetric convection occurs in the east and south of the TC center (Figure 7E), indicating that the primary circulation of Roke (2011) is relatively far away from the upper-level trough. After that, the trough deepens obviously, and the convection is enhanced at 500 km north of the TC center, with the poleward outflow strengthening noticeably (Figure 7B). Simultaneously, the anticyclonic circulation becomes stronger, enhancing the strong convection corresponding to the upper-level outflow at 300 km north of the TC center (Figure 7F). At the following 1200 UTC 19 September and 0000 UTC 20 September, the jet stream and strong divergence in front of the trough approach the TC center gradually (Figures 7C,D), enabling the coupling of the divergent flow at the entrance of the southwesterly jet with the updraft of the TC circulation. Consequently, the poleward outflow is remarkably enhanced with extremely strong convective activities (Figures 7G,H). These analyses indicate that the outflow evolution of Typhoon Roke (2011) is closely related to the upper-tropospheric trough and the southwesterly jet. The dynamic mechanism of the outflow-environment interaction on the intensity variation is further analyzed in the next section.

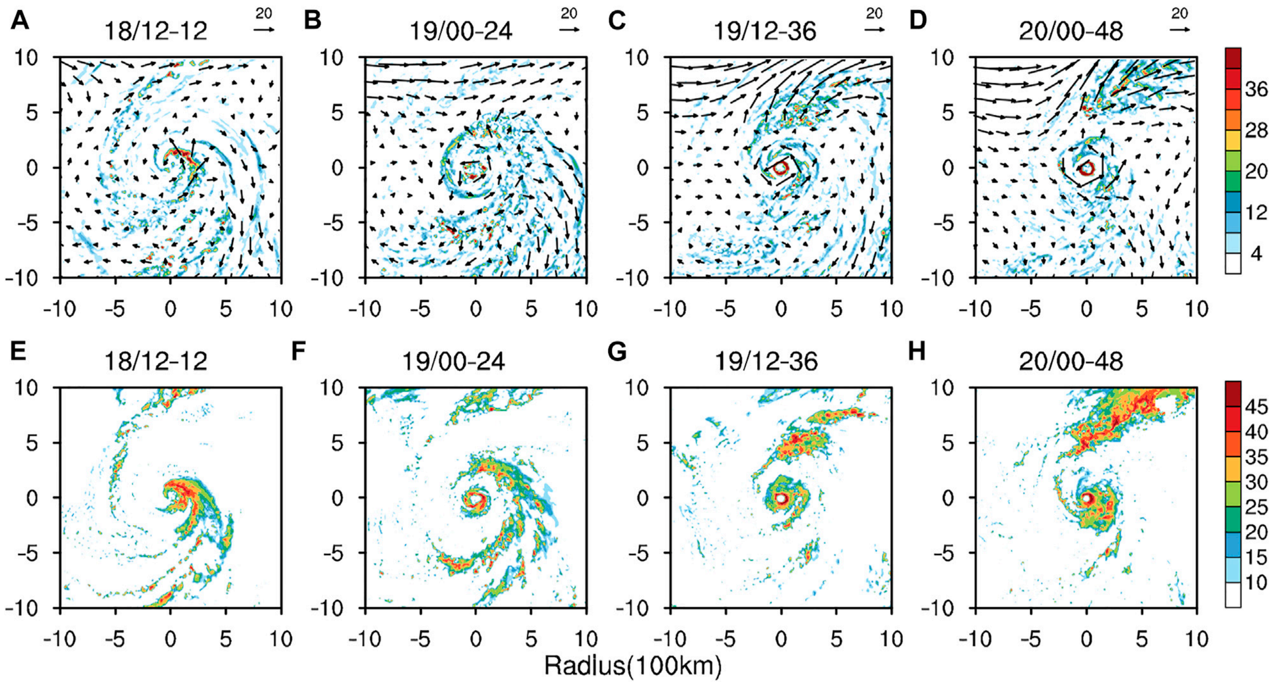

FIGURE 7
(A,B,C,D) The simulated 200-hPa wind field (vectors, m s^{-1}) and divergence (shaded areas, 10^{-5} s^{-1}) and **(E,F,G,H)** the radar reflectivity (dBZ) at 1-km height (around 850 hPa) at **(A,E)** 1200 UTC 18 September (12-h integration) **(B,F)** 0000 UTC 19 September (24-h integration) **(C,G)** 1200 UTC 19 September (36-h integration) and **(D,H)** 0000 UTC 20 September (48-h integration).

5 Impacts of the upper-level outflow on the rapid intensification of Typhoon Roke (2011)

5.1 Upper-tropospheric southwesterly jet and divergence

Typhoon Roke (2011) is a typical case with the outflow-environment interaction during its RI period. Accompanied by the enhancement of the convection and upper-level radial outflow north of the TC center (Figure 7), the sea level pressure decreases, and the surface wind speed increases rapidly (Figure 3). The divergent flow near the entrance of the southwesterly jet is remarkably strong, and the outward mass source needs to be compensated by the upward flow. Therefore, when the outflow and the upward motion are enhanced, the sea level pressure decreases and the TC intensifies. Figure 8 shows that the time-pressure variation of vertical velocity in the south and north of Typhoon Roke (2011) has evident differences because of the upper-level asymmetric structure and the outflow channel transforming from equatorward to poleward. From 1200 UTC 18 September to 0000 UTC 19 September, the relatively strong convection is enhanced within a radius of 400–500 km in the south of the TC center (Figures 7E,F), with strong upward motion in the entire troposphere from 850 hPa to 100 hPa, and then the vertical motion in the south decreases immediately (Figure 8A). Meanwhile, the vertical motion starts to strengthen in TC inner-core region within the radius of 60–80 km (Figure 8C), which indicates the intensification of the TC. The vertical motion in the annulus with a radius of 400–500 km in the north of the TC center gradually strengthens from the upper to lower levels, starting at around 1200 UTC 19 September and peaking at 0000 UTC 20 September (Figure 8B). Therefore, it can be concluded that the strong equatorward outflow enhances the updraft in the south of the TC center, providing favorable conditions for the onset of RI. Moreover, the strong divergence near the entrance of the approaching upper-tropospheric southwesterly jet can strengthen the poleward outflow and drive the strong upward motion in the north of the TC center, favoring the sustained intensification during the RI.

5.2 Eddy flux convergence and vertical wind shear

Several studies have focused on the eddy angular momentum convergence related to the upper-tropospheric synoptic systems,

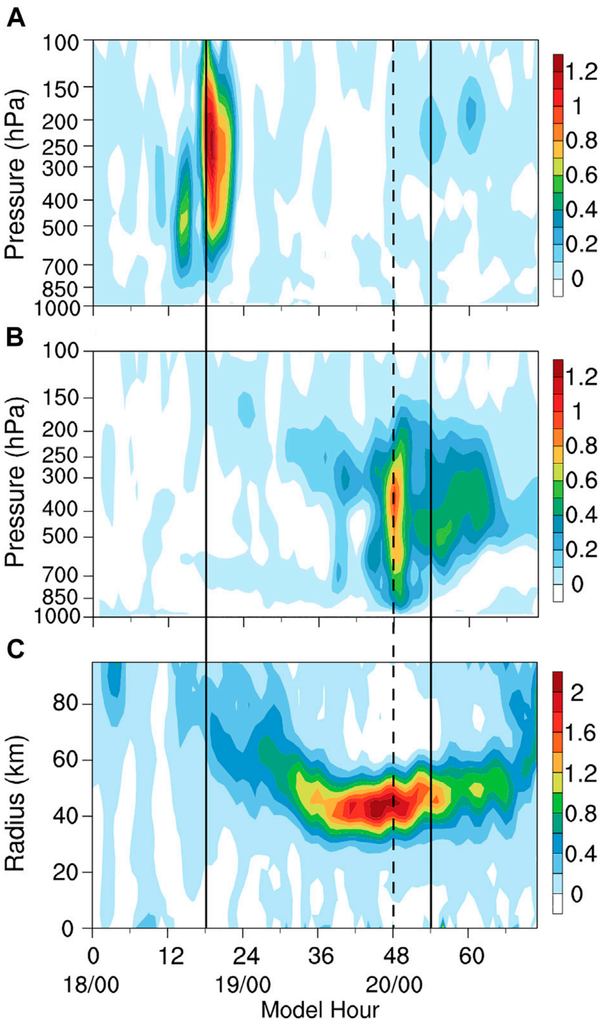

FIGURE 8
Time-pressure plots of the vertical velocity (m s^{-1}) averaged in the annulus with a radius of 400–500 km **(A)** south and **(B)** north of the TC center, and **(C)** the time-radius plot of the azimuthally averaged vertical velocity (m s^{-1}) at 500 hPa. The reference lines represent the same meaning as those in Figure 6.

which can enhance the angular momentum output in TC outflow layers and develop the secondary circulation (Molinari and Vollaro, 1989; Hanley et al., 2001). Therefore, the eddy flux convergence (EFC) of angular momentum can be used as an indicator of the interaction between the TC outflow and the environmental field. The EFC is defined based on Molinari and Vollaro (1989), as shown in Eq. 2.

$$EFC = -\frac{1}{r^2}\frac{\partial}{\partial r} r^2 \overline{U'_L V'_L} \qquad (2)$$

where r represents the radius from the TC center, U_L denotes the storm-relative radial wind and V_L denotes the storm-relative tangential wind. The overbar represents the azimuthal mean, and the prime denotes the deviation from the azimuthal mean.

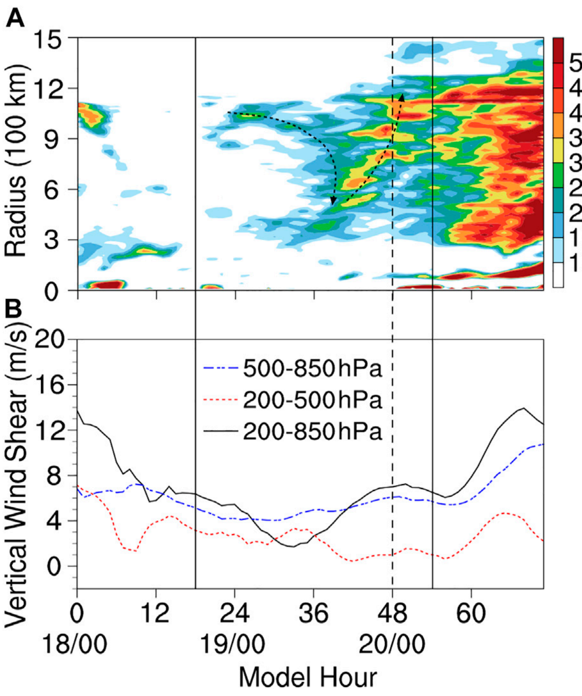

FIGURE 9
(A) The time-radius plot of the azimuthally averaged eddy flux convergence of angular momentum (m s^{-1} day^{-1}) at 200 hPa, and **(B)** time series of the vertical wind shear (m s^{-1}) in the 10° × 10° typhoon-centered region from 200 hPa to 850 hPa (black), 200 hPa to 500 hPa (red) and 500 hPa to 850 hPa (blue). The reference lines represent the same meaning as those in Figure 6.

As presented in Figure 9A, the temporal evolution of the azimuthally averaged EFC at 200 hPa with the radius from the TC center suggests that the EFC of greater than 10 m s^{-1} day^{-1} (the threshold value of the TC-environment interaction) propagates inward from the area with the 1000-km TC-centered radius, which starts at 0000 UTC19 September (24-h integration), indicating the starting time and location of the TC-environment interaction. Accompanied by the inward propagation of the EFC, the outflow strengthens (Figure 6B) and the upward motion is enhanced (Figure 8C). Moreover, during the RI period of Typhoon Roke (2011), the vertical wind shear (VWS) is relatively weak in different levels, especially in upper levels between 200 hPa and 500 hPa (Figure 9B). Specifically, the 200–850 hPa and 500–850 hPa VWS is less than 8 m s^{-1}, and the 200–500 hPa VWS (mid-to upper levels) is smaller than 4 m s^{-1} during the RI period. According to the result in Ryglicki et al. (2019), the strong divergent outflow can limit the VWS and favor the formation and maintenance of the two warm cores (Figure 5). However, the EFC continuously increases and propagates outward after 1200 UTC on September 19 (36-h integration), indicating the end of the

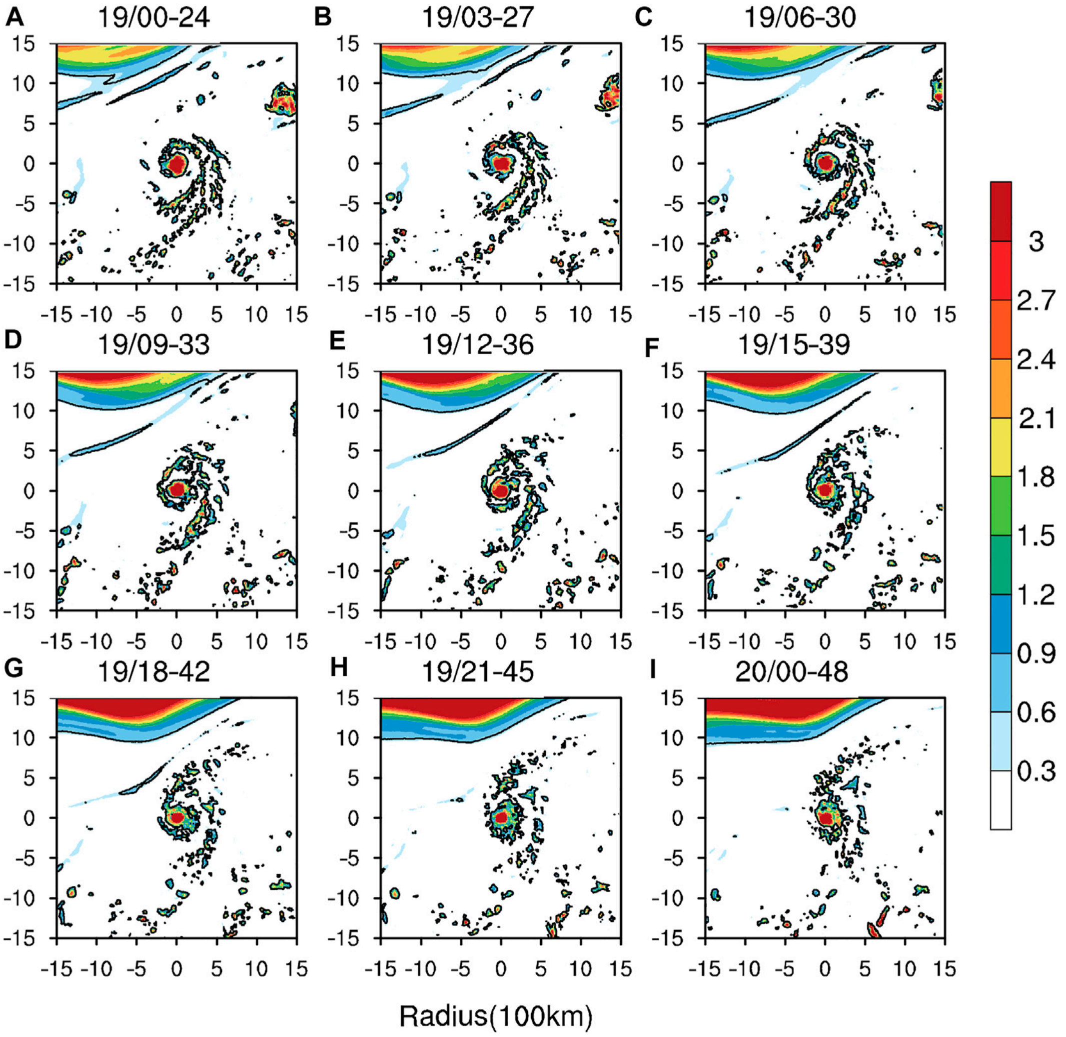

FIGURE 10
The 3-h potential vorticity anomaly (PVU) at the 350-K isentropic surface from 0000 UTC 19 September (24-h integration) to 0000 UTC 20 September (48-h integration). The contour represents the potential vorticity anomaly of 0.3 PVU.

RI. The remarkably enhanced VWS cannot insulate the ventilation influencing the warm cores, inhibiting the strengthening of Roke (2011) after 0600 UTC 20 September (54-h integration).

5.3 Potential vorticity

The PV is a comprehensive physical quantity which contains the information of both thermodynamic and dynamic states of the atmosphere. Unlike absolute vorticity, the PV is conserved in adiabatic frictionless flow. Thus, the evolution of the atmospheric perturbations can be traced by the PV anomaly (Hoskins et al., 1985). Numerous studies have used the Ertel PV to investigate the interaction between the TCs and upper-tropospheric circulation systems (Molinari and Vollaro, 1989; Molinari and Vollaro, 1989; Leroux et al., 2013; Perez-Reyes, 2016). The Ertel PV is defined as follows (Eq. 1)

$$PV = (f + \zeta_\theta)\left(-g\frac{\partial\theta}{\partial p}\right) \tag{1}$$

where and represent the absolute vorticity and the static stability on the isentropic surface, respectively. The unit of the Ertel PV is PVU (1 PVU = 10^{-6} m^2 K s^{-1} kg^{-1}).

Figure 10 presents the 3-h distribution and variation of the simulated PV anomaly in domain B at the 350-K isentropic surface (between 175 hPa and 225 hPa). The results indicate that the positive PV anomaly is mainly distributed around the TC center and the upper-tropospheric southwesterly jet area, where the perturbations are relatively strong. From 0000 UTC 19 September (24-h integration)

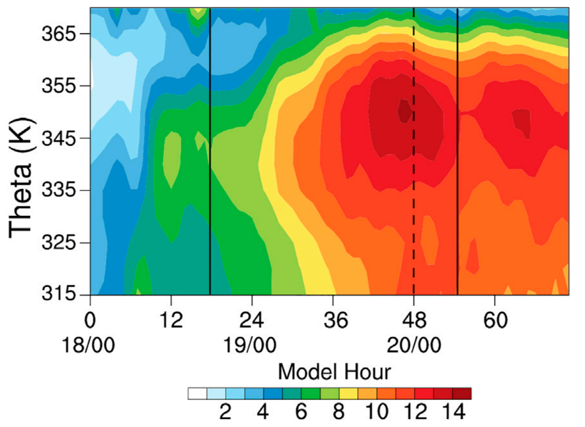

FIGURE 11
The time-theta plot of the potential vorticity (PVU) with isentropic surfaces in the 100 km × 100 km typhoon-centered region. The reference lines represent the same meaning as those in Figure 6.

to 1800 UTC 19 September (42-h integration), the shallow weak positive PV anomaly separated from south of the southwesterly jet gradually approaches the TC center, and the large-scale positive PV anomaly north of the TC center rises simultaneously. In the inner-core region, the PV increases from upper levels between 345-K and 355-K isentropic surfaces, transfers downward to lower levels and peaks at 0000 UTC 20 September (48-h integration), as shown in Figure 11. This result is consistent with the development of TC intensity. Therefore, the approaching southwesterly jet favors the enhancement and downward transmission of the upper-level positive PV, and it can increase the distance of isentropic surfaces in lower levels and decrease the atmospheric static stability (Hoskins et al., 1985). Due to the conservation property of PV on isentropic surfaces, the cyclonic vorticity in lower levels increases and the TC intensifies (Leroux et al., 2013).

6 Conclusion and discussion

Recently, the upper-level outflow has been recognized as an essential factor influencing TC intensification (Dai et al., 2017; Ryglicki et al., 2019; Li et al., 2020), but it remains a challenge to interpret the mechanism of its influence on TC intensity. In this study, Typhoon Roke (2011), with a clear outflow channel transformation from equatorward to poleward, is chosen to investigate this question. The results suggest that the track and intensity of Typhoon Roke (2011) during the RI period can be well reproduced by the WRF-ARW version 3.4.1. The high-resolution simulations for Typhoon Roke (2011) show the structure characteristics of the upper-level outflow and its impact on the RI of Roke (2011).

The upper-level characteristics of Typhoon Roke (2011) during the RI are as follows. The upper-level outflow expands from 100 hPa to 150 hPa, and constitutes the secondary circulation of the TC with an ascending branch of the vertical motion. Two warm cores are formed with the intensification of Typhoon Roke (2011), and the upper one appears at around 150 hPa. The upper-level outflow is enhanced ahead of the TC intensification, which is closely related to the upper-tropospheric trough and the southwesterly jet.

Further analyses indicate the possible impact of the outflow on the RI of Typhoon Roke (2011). Before the RI, the strong equatorward outflow and the upward motion are enhanced south of the TC center, favoring the onset of RI at the early stage of Roke (2011). During the RI period, there is strong divergent flow near the entrance of the southwesterly jet, and the EFC propagates inward from the area with the 1000-km typhoon-centered radius, enhancing the poleward outflow of Roke (2011). Moreover, the strong divergent flow restricts the VWS, protecting the warm cores from the ventilation. In this circulation situation, the updraft in the north of the TC center develops and Roke (2011) intensifies rapidly. Simultaneously, the shallow weak positive PV anomaly south of the southwesterly jet approaches the TC center, and the inner-core PV increases, favoring the sustained intensification of Roke (2011).

Unlike the results in previous studies focusing on the TC-environment interaction before the TC intensification (Molinari and Vollaro, 1989; Leroux et al., 2013), Typhoon Roke (2011) underwent the interaction of outflow and the southwesterly jet after the RI starts, which was conducive to the maintenance but not the onset of RI. The equatorward outflow enhanced at the earlier stage is probably due to the Fujiwara effect proposed in Sonca (2011) or the equatorial flow, which is to be demonstrated in future work.

In this research, the diagnostic analysis is carried out based on the simulations from the control experiment, and no sensitivity experiment is designed to confirm the impact of the upper-level outflow on the TC intensity. In the future, the sensitivity experiments will be conducted, such as changing the intensity of the upper-tropospheric synoptic systems and their distance from the TC, to explore and verify the mechanism of the outflow-environment interaction on TC intensity.

Data availability statement

The original contributions presented in the study are included in the article/supplementary material, further inquiries can be directed to the corresponding authors.

Author contributions

YL and XC designed research. RJ conceptualized the analysis and wrote the manuscript. All authors were involved in helpful discussions and contributions to the manuscript.

Funding

This work was jointly supported by National Key Research and Development Program of China (2017YFA0605004), and the National Natural Science Foundation of China (41775058). We acknowledge the High Performance Computing Center of Nanjing University of information science and technology for their support of this work.

The authors declare that this study received funding from the project of China Three Gorges Corporation (0704182). The funder was not involved in the study design, collection, analysis, interpretation of data, the writing of this article, or the decision to submit it for publication.

Conflict of interest

The authors declare that the research was conducted in the absence of any commercial or financial relationships that could be construed as a potential conflict of interest.

Publisher's note

References

Betts, A. K. (1986). A new convective adjustment scheme. Part I: Observational and theoretical basis. *Q. J. R. Meteorol. Soc.* 112, 677–691. doi:10.1002/qj.49711247307

Black, P. G., and Anthes, R. A. (1971). On the asymmetric structure of the tropical cyclone outflow layer. *J. Atmos. Sci.* 28, 1348–1366. doi:10.1175/1520-0469(1971)028<1348:otasot>2.0.co;2

Cai, Y., Han, X., Zhao, H., Klotzbach, P. J., Wu, L., Raga, G. B., et al. (2022). Enhanced predictability of rapidly intensifying tropical cyclones over the Western North Pacific associated with snow depth changes over the Tibetan Plateau. *J. Clim.* 35, 2093–2110. doi:10.1175/JCLI-D-21-0758.1

Chen, H., Zhang, D. L., Carton, J., and Atlas, R. (2011). On the rapid intensification of hurricane wilma (2005). Part I: Model prediction and structural changes. *Wea. Forecast.* 26, 885–901. doi:10.1175/WAF-D-11-00001.1

Chen, L. S., and Gray, W. M. (1985). Global view of the upper level outflow pattern associated with tropical cyclone intensity changes during FGGE. *Dept. Atmos. Sci. Pap.* 392, 126.

Cohen, Y., Durden, S. L., Harnik, N., and Heifetz, E. (2019). Relating observations of gradient non balance at the top of hurricanes with their warm core structures. *Geophys. Res. Lett.* 46, 11510–11519. doi:10.1029/2019GL084248

Cohen, Y., Harnik, N., Heifetz, E., Nolan, D. S., Tao, D., and Zhang, F. (2017). On the violation of gradient wind balance at the top of tropical cyclones. *Geophys. Res. Lett.* 44, 8017–8026. doi:10.1002/2017GL074552

Cohen, Y., and Paldor, N. (2020). Lagrangian trajectories at the outflow of tropical cyclones. *Q. J. R. Meteorol. Soc.* 147, 58–73. doi:10.1002/qj.3904

Dai, Y., Majumdar, S. J., and Nolan, D. S. (2017). Secondary eyewall formation in tropical cyclones by outflow-jet-interaction. *J. Atmos. Sci.* 74, 1941–1958. doi:10.1175/JAS-D-16-0322.1

Dai, Y., Majumdar, S. J., and Nolan, D. S. (2019). The outflow–rainband relationship induced by environmental flow around tropical cyclones. *J. Atmos. Sci.* 76, 1845–1863. doi:10.1175/JAS-D-18-0208.1

Ditchek, S. D., Molinari, J., and Vollaro, D. (2017). Tropical cyclone outflow-layer structure and balanced response to eddy forcings. *J. Atmos. Sci.* 74, 133–149. doi:10.1175/JAS-D-16-0117.1

Dudhia, J. (1989). Numerical study of convection observed during the winter monsoon experiment using a mesoscale two-dimensional model. *J. Atmos. Sci.* 46, 3077–3107. doi:10.1175/1520-0469(1989)046<3077:nsocod>2.0.co;2

Duran, P., and Molinari, J. (2016). Upper-tropospheric low richardson number in tropical cyclones: Sensitivity to cyclone intensity and the diurnal cycle. *J. Atmos. Sci.* 73, 545–554. doi:10.1175/JAS-D-15-0118.1

Emanuel, K., and Rotunno, R. (2011). Self-stratification of tropical cyclone outflow. Part I: Implications for storm structure. *J. Atmos. Sci.* 68, 2236–2249. doi:10.1175/JAS-D-10-05024.1

Emanuel, K. (2012). Self-stratification of tropical cyclone outflow. Part II: Implications for storm intensification. *J. Atmos. Sci.* 68, 988–996. doi:10.1175/JAS-D-11-0177.1

Fischer, M. S., Tang, B. H., and Corbosiero, K. L. (2019). A climatological analysis of tropical cyclone rapid intensification in environments of upper-tropospheric troughs. *Mon. Weather Rev.* 147, 3693–3719. doi:10.1175/MWR-D-19-0013.1

Hanley, D., Molinari, J., and Keyser, D. (2001). A composite study of the interactions between tropical cyclones and upper-tropospheric troughs. *Mon. Weather Rev.* 129, 2570–2584. doi:10.1175/1520-0493(2001)129<2570:acsoti>2.0.co;2

Holland, G., and Merrill, R. T. (1984). On the dynamics of tropical cyclone structural changes. *Q. J. R. Meteorol. Soc.* 110, 723–745. doi:10.1002/qj.49711046510

Hong, S. Y., Noh, Y., and Dudhia, J. (2006). A new vertical diffusion package with an explicit treatment of entrainment processes. *Mon. Weather Rev.* 134, 2318–2341. doi:10.1175/MWR3199.1

Hoskins, B. J., Mcintyre, M. E., and Robertson, A. W. (1985). On the use and significance of isentropic potential vorticity maps. *Q. J. R. Meteorol. Soc.* 111, 877–946. doi:10.1002/qj.49711147002

Huang, Q., Ge, X., and Bi, M. (2022). Simulation of rapid intensification of super typhoon Lekima (2019). Part II: The critical role of cloud-radiation interaction of asymmetric convection. *Front. Earth Sci.* 9, 1–14. doi:10.3389/feart.2021.832670

Jiang, H., and Ramirez, E. M. (2013). Necessary conditions for tropical cyclone rapid intensification as derived from 11 years of TRMM Data. *J. Clim.* 26, 6459–6470. doi:10.1175/JCLI-D-12-00432.1

Komaromi, W. A., and Doyle, J. D. (2017). Tropical cyclone outflow and warm core structure as revealed by HS3 dropsonde data. *Mon. Weather Rev.* 145, 1339–1359. doi:10.1175/MWR-D-16-0172.1

Leroux, M. D., Plu, M., Barbary, D., Roux, F., and Arbogast, P. (2013). Dynamical and physical processes leading to tropical cyclone intensification under upper-level trough forcing. *J. Atmos. Sci.* 70, 2547–2565. doi:10.1175/JAS-D-12-0293.1

Li, Y., Jin, R., and Gao, X. (2020). Outflow-jet interaction analysis of tropical cyclone Roke (2011) within different atmospheric reanalysis datasets. *Trans. Atmos. Sci.* 43, 525–536. (in Chinese). doi:10.13878/j.cnki.dqkxxb.20180302001

Li, Y., Zhou, H., Ge, X. Y., and Jin, R. (2017). Characteristics of the outflow layer of tropical cyclone rapid intensification in the Western North Pacific. *J. Trop. Meteor.* 33, 145–154. (in Chinese). doi:10.16032/j.issn.1004-4965.2017.02.001

Merrill, R. T. (1988a). Characteristics of the upper-tropospheric environmental flow around hurricanes. *J. Atmos. Sci.* 45, 1665–1677. doi:10.1175/1520-0469(1988)045<1665:cotute>2.0.co;2

Merrill, R. T. (1988b). Environmental influences on hurricane intensification. *J. Atmos. Sci.* 45, 1678–1687. doi:10.1175/1520-0469(1988)045<1678:eiohi>2.0.CO;2

Mlawer, E. J., Taubman, S. J., Brown, P. D., Iacono, M. J., and Clough, S. A. (1997). Radiative transfer for inhomogeneous atmospheres: RRTM, a validated correlated-k model for the longwave. *J. Geophys. Res.* 102, 16663–16682. doi:10.1029/97JD00237

Molinari, J., and Dudeck, M. (1992). Parameterization of convective precipitation in mesoscale numerical models: A critical review. *Mon. Wea. Rev.* 120, 326–344. doi:10.1175/1520-0493(1992)120<0326:pocpim>2.0.co;2

Molinari, J., and Vollaro, D. (1989). External influences on hurricane intensity. Part I: Outflow layer eddy angular momentum fluxes. *J. Atmos. Sci.* 46, 1093–1105. doi:10.1175/1520-0469(1989)046<1093:eiohip>2.0.co;2

Montgomery, M. T., Persing, J., and Smith, R. K. (2019). On the hypothesized outflow control of tropical cyclone intensification. *Q. J. R. Meteorol. Soc.* 145, 1309–1322. doi:10.1002/qj.3479

Rappin, E. D., Morgan, M. C., and Tripoli, G. J. (2011). The impact of outflow environment on tropical cyclone intensification and structure. *J. Atmos. Sci.* 68, 177–194. doi:10.1175/2009JAS2970.1

Ryglicki, D. R., Doyle, J. D., Hodyss, D., Cossuth, J. H., Jin, Y., Viner, K. C., et al. (2019). The unexpected rapid intensification of tropical cyclones in moderate vertical wind shear. Part III: Outflow-environment interaction. *Mon. Weather Rev.* 147, 2919–2940. doi:10.1175/MWR-D-18-0370.1

Schenkel, B. A., and Hart, R. E. (2012). An examination of tropical cyclone position, intensity, and intensity life cycle within atmospheric reanalysis datasets. *J. Clim.* 25, 3453–3475. doi:10.1175/2011JCLI4208.1

Shi, J. J., Chang, S. W. J., and Raman, S. (1990). A numerical study of the outflow layer of tropical cyclones. *Mon. Wea. Rev.* 118, 2042–2055. doi:10.1175/1520-0493(1990)118<2042:ansoto>2.0.CO;2

Skamarock, W. C., Klemp, J. B., Dudhia, J., David, O. G., and Jordan, G. P. (2008). *A description of the advanced research WRF version 3*. Boulder: NCAR Tech. Note NCAR/TN-475+STR. doi:10.5065/D68S4MVH

Tewari, M. F., Chen, W., Wang, J., Dudhia, M. A., LeMone, K., Mitchell, M., et al. (2004). "Implementation and verification of the unified Noah land surface model in the WRF model," in 20th Conf. on Weather Analysis and Forecasting/16th Conf. on Numerical Weather Prediction, Washington, 14 January, 2004 (Seattle, WA: Amer. Meteor. Soc.). Available at: https://ams.confex.com/ams/pdfpapers/69061.pdf.

Wang, B., and Zhou, X. (2008). Climate variation and prediction of rapid intensification in tropical cyclones in the Western North Pacific. *Meteorol. Atmos. Phys.* 99, 1–16. doi:10.1007/s00703-006-0238-z

Yan, Z., Ge, X., Wang, Z., Wu, C., and Peng, M. (2021). Understanding the impacts of upper-tropospheric cold low on typhoon Jongdari (2018) using piecewise potential vorticity inversion. *Mon. Weather Rev.* 149, 1499–1515. doi:10.1175/MWR-D-20-0271.1

Zhao, H., Zhao, K., Klotzbach, P. J., Wu, L., and Wang, C. (2022a). Interannual and interdecadal drivers of meridional migration of western north pacific tropical cyclone lifetime maximum intensity location. *J. Clim.* 35, 2709–2722. doi:10.1175/JCLI-D-21-0797.1

frontiers | Frontiers in Earth Science

TYPE Original Research
PUBLISHED 12 January 2023
DOI 10.3389/feart.2022.1093545

OPEN ACCESS

EDITED BY
Yuqing Wang,
University of Hawaii at Manoa,
United States

REVIEWED BY
Jianqi Sun,
Institute of Atmospheric Physics (CAS),
China
Si Gao,
Sun Yat-sen University, China
Jianhua Sun,
Institute of Atmospheric Physics China

*CORRESPONDENCE
Yi Zhang,
✉ yizhang@nju.edu.cn

SPECIALTY SECTION
This article was submitted
to Atmospheric Science,
a section of the journal
Frontiers in Earth Science

RECEIVED 09 November 2022
ACCEPTED 30 December 2022
PUBLISHED 12 January 2023

CITATION
Gao Y, Zhang Y, Lei L and Tang J (2023),
Multi-scale characteristics of an extreme
rain event in Shandong Province,
produced by Typhoon Lekima (2019).
Front. Earth Sci. 10:1093545.
doi: 10.3389/feart.2022.1093545

Multi-scale characteristics of an extreme rain event in Shandong Province, produced by Typhoon Lekima (2019)

Yue Gao[1], Yi Zhang[1]*, Lili Lei[1] and Jie Tang[2]

[1]Key Laboratory of Mesoscale Severe Weather, Ministry of Education, and School of Atmospheric Sciences, Nanjing University, Nanjing, China, [2]Shanghai Typhoon Institute, China Meteorological Administration, Shanghai, China

Super Typhoon Lekima (2019) is the fifth strongest typhoon to make landfall in mainland China since 1949. After its landfall, Typhoon Lekima moved northward along the coastline, resulting in an extreme rain event in Shandong Province that caused the highest precipitation in available meteorological records. A Weather Research and Forecasting (WRF) model simulation that properly produces the track and intensity of Typhoon Lekima and the spatio-temporal evolution of rainfall is used to analyze the multi-scale characteristics of the extreme rain event. The results show that different from the typhoon precipitation which occurred at low latitudes, the extreme rain event that occurred in mid-latitudes was influenced by the interactions of mid-latitude synoptic systems and typhoon circulation, especially with five mesoscale rainbands. The mid-latitude synoptic systems, mainly including the upper-tropospheric jet, the western North Pacific subtropical high, the mid-latitude trough, the low-level jets, and Typhoon Krosa (2019), allowed Typhoon Lekima to maintain its intensity after landfall and provided favorable kinematic, thermodynamic, and moisture conditions for the heavy rainfall in Shandong. Based on the evolution of the mesoscale rainbands, the extreme rain event can be divided into three stages. The first stage can be classified as distant rainfall, which was affected by two convective rainbands associated with boundary-layer processes. The second stage had the highest precipitation, featuring the formation of a frontal zone in Shandong, interacting with Typhoon Lekima. The third stage had weakened rainfall and was directly influenced by the spiral rainband of Typhoon Lekima.

KEYWORDS

Typhoon Lekima, heavy rainfall, frontogenesis, rainband, convergence line

1 Introduction

Tropical cyclones (TCs) are large cyclonic systems with organized deep convections and warm core structures, which are usually formed over tropical and subtropical oceans. TCs are called hurricanes in the Atlantic and typhoons in the Pacific. About 90 TCs form globally each year, of which about 30 occur in the western North Pacific, where the most frequent and, often, the strongest TCs occur (Peduzzi et al., 2012). On an average, about seven typhoons make landfall in China each year, and China is one of the countries in the world which experience the largest number of typhoons and the most severe impacts (Zhang et al., 2009).

Disasters of typhoons are mainly caused by strong winds, heavy rainfall, and storm surges. Among them, heavy rainfall is the most severe one, which could cause mudslides, landslides, and many other related geological disasters (Jonkman et al., 2009). Meanwhile, heavy rainfall also occurs frequently, resulting in serious casualty and property loss in China (Meng et al., 2002; Zhang et al., 2013). In addition, there is an increasing trend for TC intensity in the 21st century due to global warming (Knutson et al., 2010; Emanuel, 2013), and the region of TC occurrence tends to expand with wider mid- and high-latitude areas (Kossin et al., 2014; Studholme and Gulev, 2018; Guo and Tan, 2022; Studholme et al., 2022). Thus, northern China in mid-latitudes becomes more vulnerable due to typhoons' heavy rainfall, which requires special attention.

A favorable large-scale environment is necessary for typhoons' heavy rainfall in mid-latitudes (Yu et al., 2020). A low-level jet, generally existing between a typhoon and the western Pacific subtropical high (WPSH), transports large amounts of warm and moist air northward from the tropic which then accumulate in the rainfall area. This process provides abundant water vapor and energy for precipitation and also leads to an unstable atmospheric condition (Wang et al., 2009; Byun and Lee, 2012; Schumacher and Galarneau, 2012). In the upper level, there is often an upper-tropospheric jet. The divergence in its equatorward entrance region contributes to the enhancement of quasi-geostrophic upward motion, and the rapid removal of latent heat from condensation over the rainfall area allows instability to be re-established (Galarneau et al., 2010; Bosart et al., 2012; Moore et al., 2013). Similarly, there is generally a mid-latitude westerly trough in the middle level. When a typhoon is located in front of the trough, the upper-level divergence will enhance the positive vorticity advection below (Ritchie and Elsberry, 2007; Leroux et al., 2016). When a typhoon is superimposed upon the trough, typhoon intensity and peripheral shear, which are both favorable to the maintenance of typhoons' heavy rainfall, tend to increase under positive potential vorticity disturbance (Klein et al., 2000; Hanley et al., 2001; Zhou et al., 2022).

In a suitable large-scale environment, mesoscale fronts are favored to form, providing baroclinic energy for convectional organization in the rainfall area (Colle, 2003; Gao et al., 2009; Torn, 2010). The convergence of southward cold air behind the westerly trough and warm air transported northward from northeast of the typhoon can produce a frontal area in the middle level. Baek et al. (2014) showed that the warm air carried by Typhoon Rusa (2002) interacted with the cold air behind the trough to trigger frontogenesis in the middle troposphere, resulting in heavy rainfall over the Korean Peninsula. Between the strong, warm, and moist low-level jet and the mid-latitude cold and dry air, large thermal and moisture gradients can form, which contribute to the frontal area at the low level. Heavy rainfall caused by Hurricane Erin (2007) in the United States was associated with a warm frontogenesis in the lower troposphere (Schumacher et al., 2011). Frontal regions over the outer periphery of typhoons can enhance convections with increased vorticity through the growth of temperature gradients, promoting the development of a typhoon and associated rainfall (Han and Wu, 2008).

Moreover, mesoscale spiral rainbands of typhoon can directly influence heavy rainfall. Houze (2010) proposed three types of spiral rainbands based on the appearance: principal rainbands, secondary rainbands, and distant rainbands. Spiral rainbands can also be divided into inner and outer rainbands. Inner rainbands are mainly dominated by the vortex dynamic process, while outer rainbands with a looser organization of convections are dominated by the vortex's dynamic process and the environment (Willoughby et al., 1984; Wang, 2008; Li and Wang, 2012). When approaching the mid-latitude westerly zone, the asymmetry of typhoon rainbands increases due to stronger environmental vertical wind shear, and precipitation is more likely to occur downshear left (Corbosiero and Molinari, 2003; Chen et al., 2006). For example, the south–north-oriented spiral rainband of northward-moving Typhoon Nina (1975) after landfall led to rainfall intensification in the southern Henan Province (Yang et al., 2017); the heavy precipitation near Shanghai during the landfall of Typhoon Fitow (2013) was associated with two spiral rainbands in its north (Bao et al., 2015).

Most previous studies of typhoon rainfall in China have focused on regions near the southeast coast and Taiwan (Chen et al., 2010; Lee et al., 2010; Li and Zhou, 2015). But the studies on typhoons and their associated rainfall in northern China provinces such as Shandong are limited, although under climate change, northern China would face heavier rainfall from typhoons. Moreover, the majority of previous studies focus on synoptic-scale analysis, yet there is a lack of detailed mesoscale studies, especially based on numerical simulations. Super Typhoon Lekima (2019) dramatically affected Shandong with an extreme rain event and record-breaking precipitation (He et al., 2020). It is the perfect case for understanding the multi-scale characteristics of an extreme rain event in Shandong, which could provide valuable knowledge for understanding the mechanisms of typhoon rainfall in mid-latitudes. The investigation of the extreme rain event caused by Typhoon Lekima has also provided guidance for precipitation prediction with similar processes, which is of great theoretical and practical importance for disaster risk management in China. Thus, in this study, we simulate the extreme rain event in the Shandong Province produced by Typhoon Lekima and analyze the characteristics of the multi-scale influence system during the rainfall process in detail.

The paper is organized as follows. Section 2 describes the data and configurations of numerical simulations. A brief description of Typhoon Lekima and the heavy rainfall in Shandong is provided in Section 3. Section 4 evaluates the numerical simulation and discusses the extreme rain event, mainly in three stages. The main factors influencing the track and intensity of Typhoon Lekima and the favorable conditions for precipitation are analyzed in Section 5. Section 6 examines the direct influence systems in different stages of the extreme rain event. Section 7 gives the conclusions.

2 Data and model configurations

Observations for Typhoon Lekima were obtained from the tropical cyclone best track dataset compiled by the Tropical Cyclone Information Center of the China Meteorological Administration (http://tcdata.typhoon.org.cn). It contains the storm's central latitude and longitude, maximum 2-min average near-center 10-m wind speed, minimum central sea level pressure, etc. for every 3 h (Ying et al., 2014). The observed precipitation was collected from the Multi-source Merged Precipitation Analysis System (CMPAS)-hourly V2.1 dataset, which combines the automatic weather station and Climate Precipitation Centre Morphing (CMORPH) precipitation over China with a horizontal resolution of .1° (http://data.cma.cn). The observed composite radar reflectivity is available every 6 min from the National Meteorological Center (http://www.nmc.cn).

In order to reproduce Lekima's northward movement along the land edge, and the location of the rainbands near Shandong Province, the three-dimensional, fully compressible, non-hydrostatic mesoscale

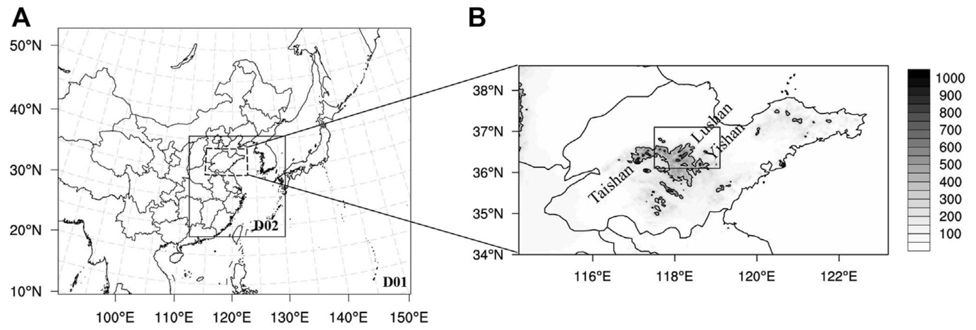

FIGURE 1
(A) Domains for numerical simulations, where outer domain D01 and inner domain D02 have 12- and 2.4-km horizontal grid spacings, respectively; **(B)** Zoomed terrain height (shaded; unit: m) of the black dashed box in **(A)** near Shandong Province with the main mountains. Black contours in **(B)** show the terrain heights of 300 m and 600 m. The black solid box in **(B)** indicates the heavy rainfall area as in Figure 2.

numerical model, Advanced Research Weather Research and Forecasting Model (ARW-WRF) version 4.2 (Skamarock et al., 2019), is used. A combinational scheme of FNL (Final) re-analysis data as the initial conditions and ERA5 re-analysis data as the lateral boundary conditions is adopted. The National Centers for Environmental Prediction (NCEP) FNL global re-analysis has a horizontal resolution of .25° and a temporal resolution of 6 h. This product can properly characterize Lekima's initial intensity so it is used as the initial condition. Lateral boundary conditions are produced from the European Centre for Medium-Range Weather Forecasts' (ECMWF) latest ERA5 climate re-analysis. It has a horizontal resolution of .25° and an enhanced temporal resolution of 1 h, which allows for a detailed description of a large-scale background field. The simulation was initialized at 0600 UTC 9 August 2019 and integrated for 54 h until 1200 UTC 11 August.

As shown by Figure 1A, 2 one-way nested domains are used. Outer domain 1 (D01) has 565 × 426 grid points with a 12-km horizontal grid spacing, and inner domain 2 (D02) has 770 × 805 grid points with a 2.4-km horizontal grid spacing. The outer domain covers most of East Asia and the western North Pacific for analyzing the large-scale circulation, while the inner domain covers the typhoon activity region during the integration period and Shandong Province for analyzing the structure of Typhoon Lekima and mesoscale precipitation systems. There are 56 vertical levels, and they are stretched with gradually decreasing vertical resolution as the height increases, with the finest vertical resolution (approximately 70 m) in the boundary layer and the coarsest one (about 1 km) near the top of the model at 10 hPa. The terrain feature around Shandong Province is shown in Figure 1B.

The model physics parameterization are chosen as follows: the Weather Research and Forecasting (WRF) single-moment six-class (WSM 6) microphysics scheme (Hong and Lim, 2006), the rapid radiative transfer model for general circulation (RRTMG) longwave and shortwave radiation scheme (Iacono et al., 2008), the Yonsei University (YSU) boundary layer scheme (Hong et al., 2006), and the Noah land surface model (Chen and Dudhia, 2001). The Kain–Fritsch cumulus parameterization scheme (Kain, 2004) and moisture-advection-modulated trigger function (Ma and Tan, 2009) are only used for subgrid-scale deep convection in D01.

3 Overview of Typhoon Lekima (2019) and the associated extreme rain event

Lekima, the ninth typhoon over western North Pacific in 2019, was formed east of the Philippines. It featured strong intensity at landfall and long duration over land with strong winds and rainfall, which caused a severe disaster and drew widespread concern (He et al., 2020). Lekima became a tropical depression around 1800 UTC 3 August 2019 and then moved to the northwest and intensified rapidly into a tropical storm around 1200 UTC 4 August; it became a severe storm around 1800 UTC 5 August, became a typhoon around 1800 UTC 6 August, and then a severe typhoon around 1200 UTC 7 August, with the supply of water vapor and energy from the wide and warm ocean surface. Lekima finally became a super typhoon around 1800 UTC 7 August and made the first landfall in Wenling, Zhejiang Province, around 1800 UTC 9 August with a maximum sustained near-surface wind speed of 52 m/s and a minimum central sea level pressure of 930 hPa. By then, it became the fifth strongest super typhoon to make landfall in mainland China since 1949. After its first landfall, Lekima decayed rapidly to typhoon intensity and subsequently moved northward toward the Yellow Sea and made the second landfall in Qingdao, Shandong Province, around 1200 UTC 11 August, with a maximum sustained near-surface wind speed of 23 m/s and a minimum central sea level pressure of 982 hPa. After its second landfall, Lekima continued to move northward through the Shandong Peninsula, hovered near Laizhou Bay for about 1 day, and eventually moved northeast into the Bo Sea, decaying into a tropical depression. The China Metrological Administration stopped numbering it at 0600 UTC 13 August 2019.

The extreme rain event in Shandong mainly occurred from 0000 UTC 10 August to 1200 UTC 11 August 2019 before Lekima's landfall in Shandong, with maximum accumulated precipitation exceeding 400 mm. The precipitation center was located in central Shandong Province including the western part of Weifang, the southern part of Dongying, and the central part of Zibo, denoted by the black solid box (36. 1°–37. 1°N, 117. 5°–119. 1°E) in Figure 2, which is defined as "heavy rainfall area" in this study. According to Figure 1B, the heavy rainfall area denoted by the black solid box is located in the mountainous area of central Shandong near Taishan Mountain, Lushan Mountain, and Yishan Mountain, so the orographic lifting caused by convergence in front of the mountains might contribute to the enhancement and spatial distribution of precipitation (Lin et al., 2002; Wu et al., 2002; Yang et al., 2008).

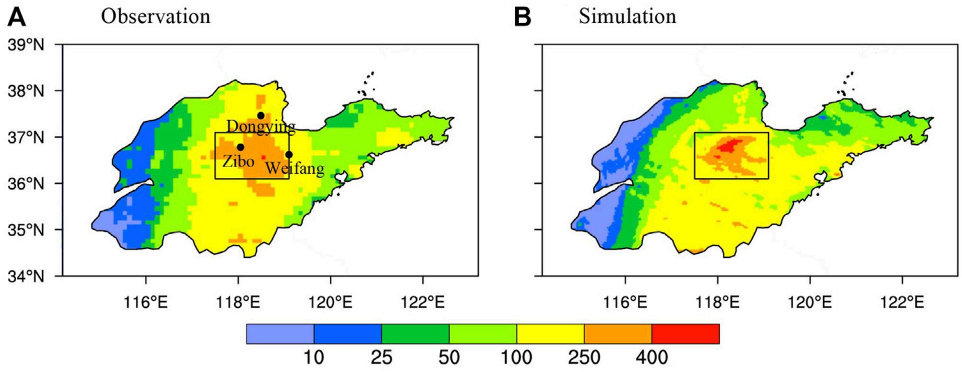

FIGURE 2
Accumulated precipitation (unit: mm) of **(A)** observation and **(B)** simulation for Shandong Province from 0000 UTC 10 August to 1200 UTC 11 August 2019. The rectangle zone (36. 1°–37. 1°N, 117. 5°–119. 1°E) indicated by the black solid box is used to perform the area-averaged time series in Figure 6.

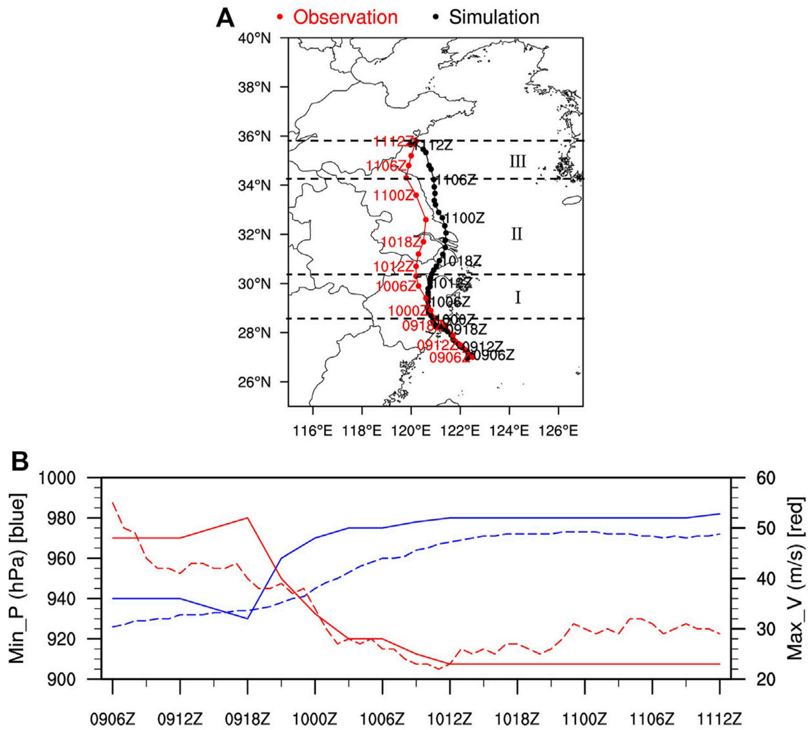

FIGURE 3
Observed and simulated tracks and intensities of Lekima from 0600 UTC 9 August to 1200 UTC 11 August 2019. **(A)** Observed track from the best track dataset (red line with filled circles denoting Lekima's location every 3 h) and the simulated track from WRF (black line with filled circles denoting Lekima's location every 1 h). Dashed lines and I, II, and III denote the three stages of the extreme rain event in Figure 4; **(B)** time series of the observed (solid line) and simulated (dashed line) maximum sustained 10-m wind speed (red line; unit: m/s) and minimum central sea level pressure (blue line; unit: hPa).

4 Verification of numerical simulation and stages of the extreme rain event

In this section, the WRF simulation is verified relative to observations, with a focus on the reproduction of the evolution of Typhoon Lekima after landfall. The track, intensity, and the spatio-temporal evolution of the extreme rain event in Shandong Province from 0000 UTC 10 August to 1200 UTC 11 August 2019 are evaluated.

Figure 3 shows Lekima's track and intensity from observation and simulations. The simulated typhoon center is determined by the minimum sea level pressure in D02. The simulated typhoon moves slower than the observation after landfall, leading to an approximate 3-h lag since 0000 UTC 10 August (Figure 3A). Compared with the

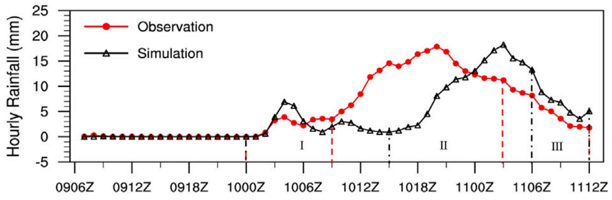

FIGURE 4
Evolution of hourly rainfall (unit: mm) averaged over the heavy rainfall area (black solid box in Figure 2) from 0600 UTC 9 August to 1200 UTC 11 August 2019 for observation (red line with circles) and simulation (black line with triangles). The three stages of the extreme rain event from observation (simulation) are separated by dashed (dash-dotted) lines, and I, II, and III denote the three stages.

observed track from the best track dataset, the simulated typhoon reproduced the northward track along the coastal line with a slightly eastward (within 150 km) north of 30° N well. Because the simulated WPSH's eastward retreat process is consistent with that of the observation and the simulated typhoon's moving speed is slower than that of the observation, the simulated TC track appears to deviate eastward under the steering of WPSH circulation which moved eastward earlier.

Figure 3B compares the maximum sustained 10-m wind speed and the minimum central sea level pressure from the observations and simulations. The intensity of Lekima is also well simulated with a decay after the first landfall in Zhejiang around 1800 UTC 9 August, despite the underestimated decaying rate. The simulated typhoon intensity is also stronger than those of the observed quantities, which might be due to the closer distance to the coastline and more sufficient water vapor supply due to the eastward track bias. The observed and simulated typhoon intensities do not decay significantly when passing through Shandong.

Accumulated precipitation from 0000 UTC 10 August to 1200 UTC 11 August 2019 in Shandong Province from D02 simulation is compared to the observed precipitation (Figure 2). The WRF simulation captures the spatial pattern of the heavy rainfall, with the maximum over 400 mm in central Shandong, but slightly underestimates the range of rainfall over 250 mm. Figure 4 shows the evolution of the observed and simulated hourly rainfall average over the heavy rainfall area (black solid box in Figure 2). Both hourly rainfalls show similar magnitudes and temporal evolutions, except for a time lag in the simulated one that is probably related to the southward track bias. Considering the evolution of precipitation and influence systems, the extreme rain event in Shandong can be divided into three stages. The three stages for observations and simulations are shown by the dashed and dotted lines in Figure 4, respectively, with notations of I, II, and III. The locations of Lekima during the three stages are shown in Figure 3A. During stage I, the typhoon's center was located in Zhejiang Province, about 800 km away from Shandong Province; thus, Lekima did not directly affect Shandong at this time, and the rainfall was weak. Lekima moved northward to Jiangsu Province along the coastline during stage II, and its outer rainband started to affect Shandong directly, producing the strongest precipitation. During stage III, Lekima was located on the Yellow Sea and continued to move north. The rainfall in Shandong Province caused by the typhoon gradually decreased.

Since the typhoon position and movement of rainbands from the landfall typhoon greatly affected the spatial distribution of typhoon precipitation, the performance of the WRF model for simulating the rainband characteristics was further examined. Figures 5A–C show observed composite radar reflectivity during the three stages, while (D)–(F) show the corresponding simulation results when the typhoon center is located close to that of the observation. It can be seen that the shapes and locations of the simulated and observed rainbands in each stage are in good agreement. Multiple southwest–northeast-oriented rainbands affected Shandong for a long time, resulting in the extreme rain event.

During stage I of the extreme rain event, Shandong Province is affected by both rainband 1 (denoted as RB1) and rainband 2 (denoted as RB2). Both rainbands are about 800 km away from the typhoon center in a southwest–northeast linear structure, with RB1 located in the north and RB2 in the south (Figures 5A, D). Rainband 3 (denoted as RB3) and rainband 4 (denoted as RB4) in the northwest of Lekima are located south of Shandong Province, which have no influence on Shandong during the stage I. As Lekima moves northward, RB1 and RB2 propagate northwestward to northern Shandong and weaken, and the extreme rain event enters stage II. Shandong is mainly affected by RB3 and RB4 that are about 600 km away from the typhoon center (Figures 5B, E). RB3 is located north of RB4. The spiral rainband 5 (denoted as RB5), about 200 km north of the typhoon center, has not influenced Shandong Province during stage II. But as Lekima moves further north, RB3 and RB4 propagate to the northwest, and RB5 starts to affect central Shandong, entering stage III of the extreme rain event (Figures 5C, F). Along with the movement of Lekima into mid-latitudes, the structure of RB5 dissipates gradually.

The aforementioned analysis shows that the WRF simulation was a good reproduction of the track, intensity change of Typhoon Lekima, and the impacts on the Shandong Province when the typhoon propagated northward. The location of the precipitation center, evolution of rainfall, and distribution of main rainbands have all been reasonably reproduced. Thus, the simulation can be used to obtain detailed diagnostics to understand the multi-scale characteristics of this extreme rain event in Shandong produced by the northward-moving Typhoon Lekima. The large-scale environment and mesoscale systems contributed to the extreme rain event, which will be analyzed in subsequent sections.

5 Large-scale environment

As can be seen in the previous section, Typhoon Lekima moves northward along the coastline after landfall. The typhoon intensity does not decay significantly when influencing Shandong and the minimum central sea level pressure is maintained at about 980 hPa. In this section, from the perspective of a large-scale environment, the main systems that influence the typhoon's track and intensity and favorable conditions for the extreme rain event at each stage are analyzed.

5.1 Synoptic systems

The extreme rain event in Shandong Province occurred under a favorable configuration of synoptic systems, which are stable through

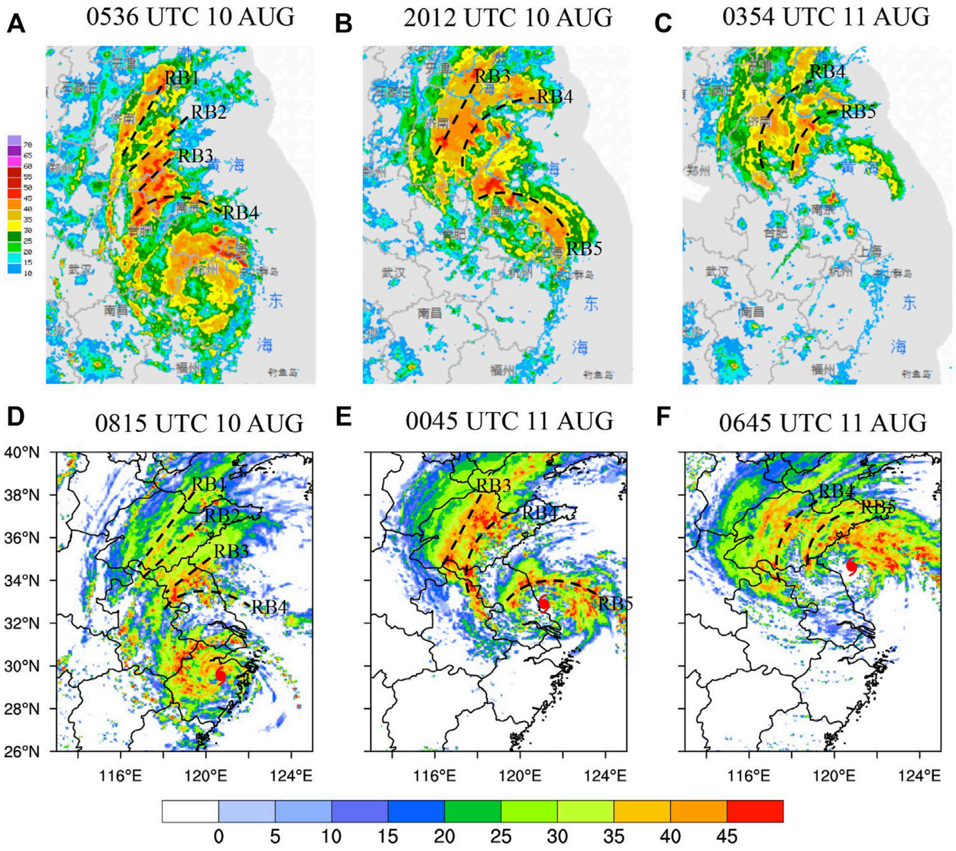

FIGURE 5
Observed **(A–C)** and simulated **(D–F)** composite radar reflectivities (unit: dBZ). Observation: **(A)** 0536 UTC 10 August 2019, **(B)** 2012 UTC 10 August 2019, **(C)** 0354 UTC 11 August 2019; simulation: **(D)** 0815 UTC 10 August 2019, **(E)** 0045 UTC 11 August 2019, and **(F)** 0645 UTC 11 August 2019. Black dashed lines denote the positions of rainbands, and typhoon symbols indicate the locations of Lekima's center.

the event and provide persistent impacts. The analyses here use the D01 simulation.

At the upper-level of 200 hPa (Figures 6A, B), there is an upper-tropospheric westerly jet of wind speed over 30 m/s, intensified to over 60 m/s at 0300 UTC 11 August 2019. It gradually evolves from north–south to east–west orientation, with a tendency of northward propagation. There are divergences of non-geostrophic winds in the equatorward entrance region of the upper-tropospheric jet. Lekima is located in the equatorward entrance region of the upper-tropospheric jet during the extreme rain event, and the anti-cyclonic divergent wind field at the upper-level over Lekima prohibits its fast decay. On the other hand, upper-tropospheric southerly outflows from Lekima extend poleward to enhance the southwesterly upper-tropospheric jet in front of the trough.

At the mid-level of 500 hPa (Figures 6C, D), the large-scale environment in eastern Asia is characterized by two ridges and one trough. The mid-latitude westerly trough is located in northern China, the western ridge is located over the Tibetan Plateau, and the eastern ridge is located over the Korean Peninsula, superimposed on the WPSH. There is another typhoon, Typhoon Krosa, at Lekima's southeast. It tends to push the WPSH northward and eastward and limits the strength of the WPSH. Steered by southerlies on the western flank of the WPSH, Lekima keeps moving northward, close to the coastline and slowly enough to influence Shandong for a long time. One of the unique features about Typhoon Lekima is its proximity to the coastline after landfall (Ding et al., 2020), which allows it to receive more water vapor from the oceans and maintain its intensity. Lekima moves into the westerly trough as it propagates northward, and the positive potential vorticity disturbance in the trough area can help Lekima maintain its intensity as well.

At the level of 850 hPa (Figures 6E, F), abundant moisture from the ocean in the East and the South China Sea is transported to Lekima by a southeasterly low-level jet between the typhoon and the WPSH and a southwesterly low-level jet in its southeast of the typhoon. The horizontal water vapor flux is over 30 kg/(hPa·m·s), which helps maintain Lekima's intensity (Wu et al., 2015) and provides a sufficient source of water vapor for heavy rainfall. The maintenance of typhoon intensity can also sustain the southeasterly low-level jet through a pressure gradient between Lekima and the WPSH. The cyclonic circulation of Typhoon Krosa in Lekima's southeast drains water vapor from the western North Pacific in its east and the tropical oceans in its south, and transports the water vapor to Lekima by easterlies on the southern flank of the WPSH, which enhances the southeasterly low-level jet and helps maintain typhoon intensity. Previous studies have also shown that in cases of binary typhoons, the western typhoons receive warm and moist air from the eastern ones (Wang et al., 2021a).

Vertical wind shear with appropriate magnitudes could be beneficial to the maintenance of the intensity and structure of

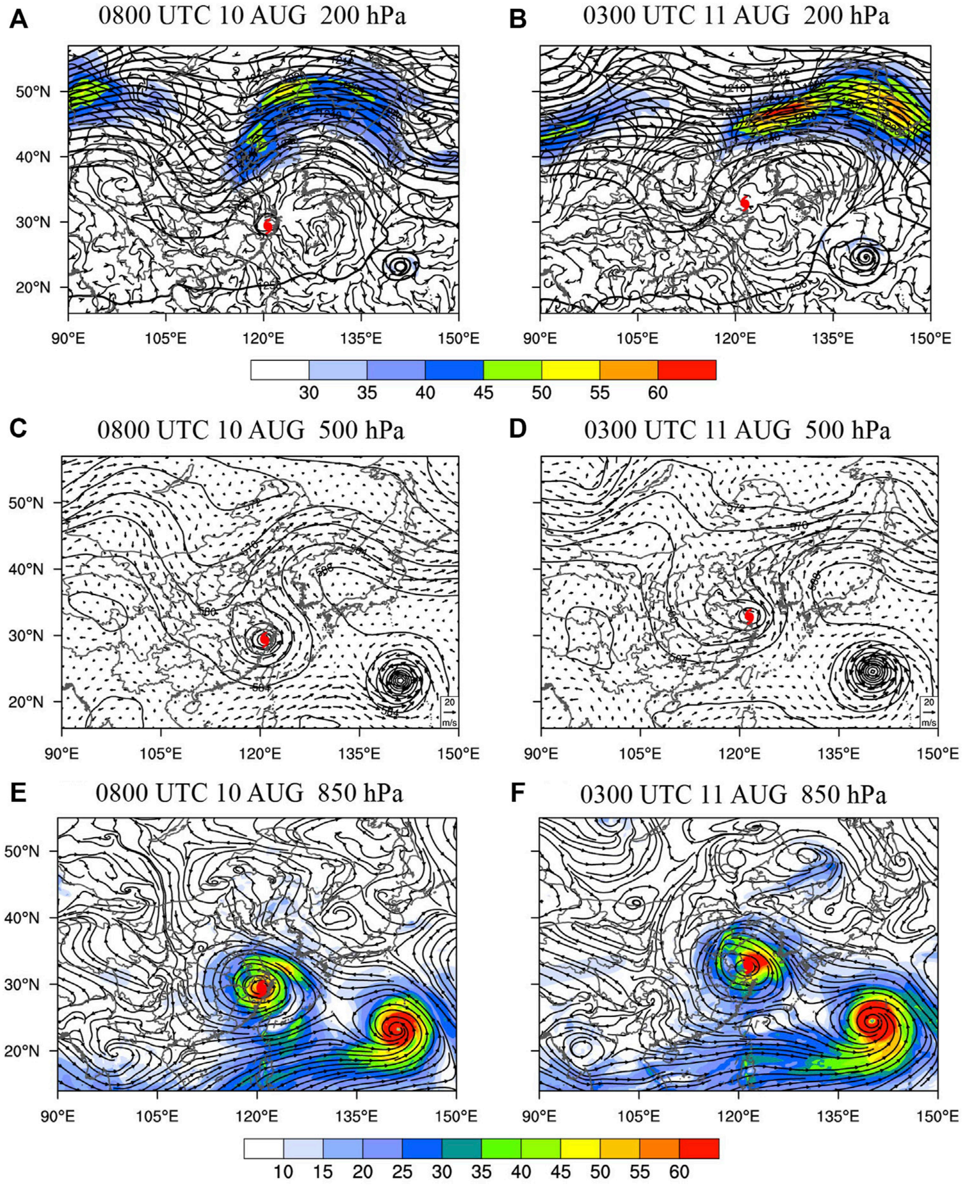

FIGURE 6
For 0800 UTC 10 August 2019, **(A)** the 200-hPa geopotential height (contours; unit: dagpm), horizontal wind speed (shaded; unit: m/s), and horizontal non-geostrophic winds (streamlines); **(C)** the 500-hPa geopotential height (contours; unit: dagpm) and horizontal winds (vectors, unit vector represents 20 m/s); and **(E)** the 850-hPa horizontal winds (streamlines) and horizontal water vapor flux (shaded; unit: kg/(hPa·m·s)) from the D01 simulation. **(B)**, **(D)**, **(F)** as in **(A)**, **(C)**, **(E)**, but at 0300 UTC 11 August. Typhoon symbols indicate the locations of Lekima's center.

landfall typhoons and, thus, to the production of rainfall (Yang et al., 2017). There is a significant negative correlation between the typhoon intensity change and the vertical wind shear resulting from three thermodynamic effects (upper-level ventilation, mid-level ventilation, and low-level ventilation) (Wang, 2012) and dynamical effects by eddy-induced angular momentum mixing across the radius of the maximum wind (Xu and Wang, 2013). Through statistical analysis based on TCs in the western North Pacific, it is found that when the deep-layer shear (difference of the mean horizontal wind vectors within a radius of 500 km from typhoon center between 300 and 1,000 hPa) is less than 11 m/s and the low-level shear (difference between 850 and 1,000 hPa) is less than 3.5 m/s, so the typhoon does not decay easily (Wang et al., 2015). During the heavy rain event in Shandong, the deep-layer shear is basically below 11 m/s and still below 16 m/s even with an increase after 0000 UTC 11 August, led by the mid-latitude westerly trough; the low-level shear is smaller than 3 m/s (Figure 7).

Wang et al. (2015) also point out that when the translational speed of typhoons exceeds 12 m/s, it is detrimental to the typhoon's intensity. This is often explained as a result of the development of a strong asymmetric structure in fast-moving storms (Uhlhorn et al., 2014). The speed of Lekima is slow and does not exceed 12 m/s during the whole process. As a result, the environmental background is favorable for Lekima to maintain its intensity after landfall without decaying rapidly.

Based on the aforementioned analysis, the WPSH is pushed northward and eastward by Typhoon Krosa in Lekima's

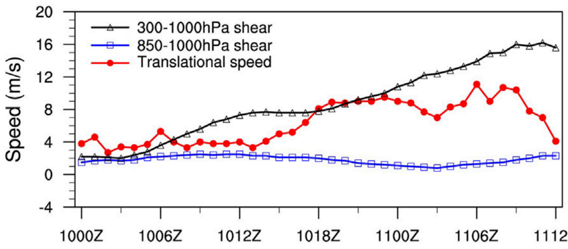

FIGURE 7
Time series of deep-layer vertical wind shear between 300 and 1,000 hPa (black line with triangles), low-level shear between 850 and 1,000 hPa (blue line with squares) within a radius of 500 km from the typhoon center, and translational speed of Lekima (red line with filled circles) from 0000 UTC 10 August to 1200 UTC 11 August, 2019, from the D02 simulation (unit: m/s).

southeast, and Lekima moves north along the coastline, steered by southerlies on the western flank of the WPSH during the extreme rain event. The proximity to the coastline enables Lekima to receive sufficient water vapor from oceans by low-level jets.

5.2 Environmental conditions over the most intense rainfall area

Kinematic and thermodynamic processes and moisture are important for heavy rainfall. Considering the configuration of synoptic systems in Figure 6, the favorable conditions for the most intense precipitation center in Shandong Province are analyzed for different stages, based on the time–height series of related physical quantities averaged near the rainfall center (black solid box in Figure 2), as shown by Figure 8.

The time–height series of area-averaged horizontal divergence and vertical velocity (Figure 8A) indicates that the divergence zone in the equatorward entrance region evolves from controlling southern Shandong to the entire Shandong Province, as the upper-tropospheric jet propagates northward. The heavy rainfall area is controlled by the divergence exceeding 500 hPa with an enhanced trend due to the jet intensification,

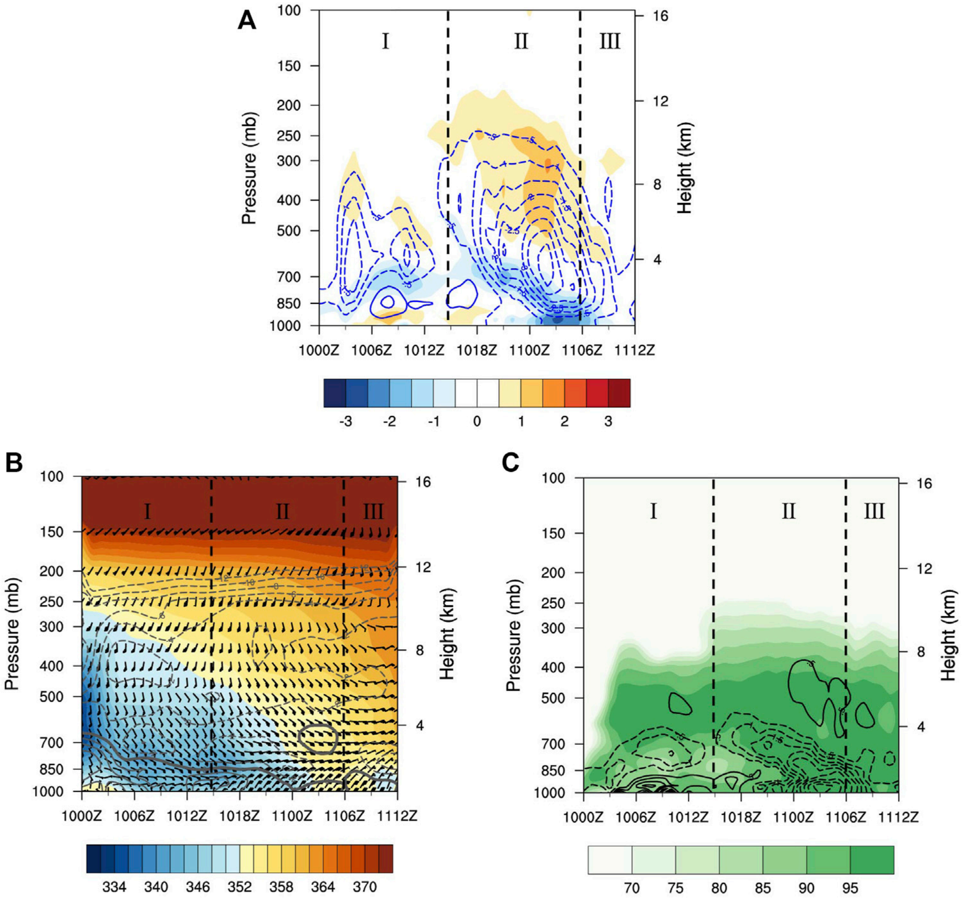

FIGURE 8
Time−height series of area-averaged **(A)** horizontal divergence (shaded; unit: 10^{-4} s^{-1}) and vertical velocity (contours, positive values are in solid contours, negative values are in dashed contours; unit: Pa/s); **(B)** equivalent potential temperature (shaded; unit: K), equivalent potential temperature change with height (contours, positive values are in solid contours, negative values are in dashed contours, zero values are in bold contours; unit: 10^{-2} K/hPa), and horizontal winds (barbs); **(C)** relative humidity (shaded; unit: %) and divergence of the horizontal water vapor flux (contours, positive values are in solid contours, negative values are in dashed contours; unit: 10^{-4} kg/(hPa·m^2·s)) over the heavy rainfall area (black solid box in Figure 2) from 0000 UTC 10 August to 1200 UTC 11 August 2019 from the D02 simulation. I, II, and III denote the three stages of the extreme rain event.

and the associated dynamical forcing for ascent flows contributes to the development of heavy rainfall. The low-level convergence and the corresponding updraft are twice enhanced at 0300 UTC 10 August and 0900 UTC 10 August 2019 during stage I, possibly affected by RB1 and RB2, respectively. The convergent layer is located between 700–500 hPa at the beginning of stage II, with weak divergence and downdraft at a low level. Low-level convergence becomes significant in the heavy rainfall area later in stage II, and the updraft reaches the maximum velocity over 4 Pa/s. During stage III, the upward motion weakens.

Figure 8B shows equivalent potential temperature and horizontal winds, and areas with solid contours denote unstable zones. Central Shandong is controlled by the mid-latitude westerly trough at the beginning of stage I, with cold and dry air located between 700–500 hPa. A potentially unstable stratification exists below 700 hPa, where equivalent potential temperature decreases with height. The cold and dry air sinks down as the southern part of the trough merges into the typhoon circulation and eventually becomes a cold pad with warm air lift-up. There is an unstable region appearing near 700 hPa later in stage II (after 1100 UTC), which is just near the strongest uplift center. The appearance of this unstable region may be due to the heat dissipation by enhanced the divergence above the ascending center. The low level of the heavy rainfall area is controlled by southeasterlies between the typhoon and the WPSH at its northeast during stage I while turning to northeasterlies during stage II, starting to be directly influenced by typhoon circulation in the northwest. Winds over the heavy rainfall area turn clockwise with height, which suggests the presence of warm advection in the troposphere when Lekima approaches. As a result, equivalent potential temperature increases with time, providing thermodynamic forcing for the ascent flows of the heavy rainfall.

Figure 8C shows relative humidity and divergence of horizontal water vapor flux. The southeasterly low-level jet on the northeast side of typhoon propagates to the north as Lekima moves northward, conveying water vapor to Shandong in the northwest. At the same time, the horizontal wind field in Lekima's north, composed of easterlies and northerlies, facilitates the convergence of water vapor in central Shandong. Maximum relative humidity exceeds 95% during all three stages that is nearly saturated, and thus, sufficient source of water vapor is provided for heavy rainfall. A saturated layer with relative humidity above 95% is located in middle level near 600 hPa during stage I. The saturated layer becomes the thickest, in stage II, due to a thicker layer of water vapor convergence, extending from 1,000 hPa to about 400 hPa.

In conclusion, the strong pressure gradient between Lekima and the WPSH in the northeast of Lekima is caused by the maintenance of typhoon intensity. Both the strong pressure gradient and the easterly airflow transported by Typhoon Krosa contribute to the enhancement of southeasterly low-level jet on the northeast side of Lekima, which conveys large amounts of water vapor to Shandong Province. The warm advection brought to Shandong by the approaching Lekima and the dynamical forcing for ascent flows in the equatorward entrance region of upper-tropospheric jet provide favorable background conditions for the heavy rainfall as well.

6 Mesoscale rainbands affecting the heavy rainfall area

Under favorable large-scale environments, the location and intensity of the heavy rainfall are mainly determined by the positions and intensities of the mesoscale systems, and the accumulated precipitation is affected by duration of the influencing mesoscale systems. According to the composite radar reflectivity in Figure 5, five mesoscale rainbands (RB1, RB2, RB3, RB4, and RB5) in the north quadrant of Lekima affect Shandong successively, which directly influence the heavy rainfall. The generation, evolution, and structure of the five main mesoscale rainbands in different stages of the extreme rain event are examined here.

6.1 Stage I (0000 UTC 10 August to 1500 UTC 10 August 2019)

Figures 9A,B zoom into the area of interest near Shandong Province and provide composite radar reflectivity during stage I of the extreme rain event. The main rainbands affecting the heavy rainfall area in stage I are RB1 and RB2, and this subsection focuses on their generation mechanisms. At the beginning of stage I, there is a convergence of westerlies in front of the westerly trough and southerlies on the western flank of the WPSH at 500 hPa, and a rainband forms in front of the trough, northwest of Shandong under favorable dynamical forcing for ascent (Figure 9A). RB1 forms in central Shandong between the rainband in front of the trough and Lekima. After Lekima propagates northward, RB2 begins to develop in the southeast of RB1, and RB1 weakens due to the cut-off of warm and moist flows from the southeast by RB2 (Figure 9B).

Considering that the terrain height near Shandong Province is basically below 600 m (Figure 1B), the distribution of related physical quantities at 600 m can reflect a relatively realistic boundary layer condition. Figures 9C, D show horizontal cross-sections of equivalent potential temperature and horizontal winds at the height of 600 m at the same time as in Figures 9A, B. A southwest–northeast-oriented cold pool exists in the boundary layer beneath the rainband in front of trough, denoted by the blue-shaded area in Figure 9C. Cold pools result from the evaporation cooling of precipitation, and the penetrative downdraft transports cold and dry air from the middle troposphere into the boundary layer (Barnes and Garstang 1982). The large thermal and moisture gradients between the cold pool caused by rainbands in front of the trough and the surrounding non-precipitation areas generate divergent outflows. The cold outflows pointing to the south converge with the warm, moist southeasterlies transported northward from Lekima's northeast, forming a boundary layer convergence line in central Shandong and contributing to the generation and intensification of linear convective rainband RB1 (denoted by red solid contours in Figure 9C). After RB1 moves northwestward, cold outflows appear in the boundary layer beneath it and converge with warm, moist southeasterlies from the south, producing another linear convective rainband RB2 parallel to RB1 in its southeast (Figure 9D). RB2 also propagates to the northwest and influences Shandong Province later.

The rainfall in Shandong during stage I can be classified as distant rainfall, affected by convective rainbands RB1 and RB2, respectively. The two convective rainbands are far from the main body of Lekima and are indirectly influenced by typhoon circulation. RB1 and RB2 are

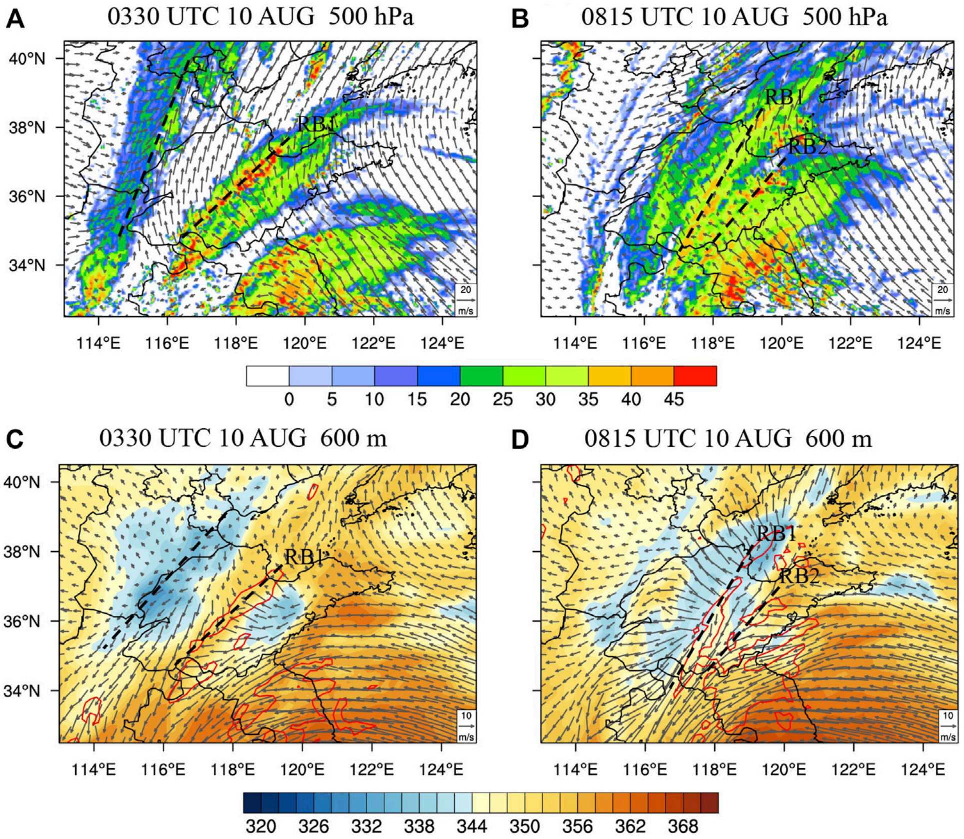

FIGURE 9
For 0330 UTC 10 August 2019, **(A)** composite reflectivity (shaded; unit: dBZ) and 500-hPa horizontal winds (vectors, unit vector represents 20 m/s); **(C)** 600-m-equivalent potential temperature (shaded; unit: K), horizontal winds (vectors, unit vector represents 10 m/s), and 32-dBZ composite reflectivity (red contours) from the D02 simulation. **(B)** and **(D)** as in **(A)** and **(C)**, but at 0815 UTC 10 August. Black dashed lines indicate the positions of the rainbands.

both triggered and organized by the boundary-layer convergence line that is formed from the convergence of the outflows to the south of the cold pool, while the cold pool is generated by previous precipitation in the northwest and the warm, moist southeasterlies transported northward from the northeast side of Lekima. The mechanism of the generation of convective systems, as the new rainband generated in the southeast of the old rainband, is called "Band Training." It has also been mentioned in studies of rainfall caused by the Mei-Yu front (Luo et al., 2014; Wang et al., 2021b).

6.2 Stage II (1500 UTC 10 August, to 0600 UTC 11 August, 2019)

During stage II, RB1 and RB2 propagate northwestward and weaken, while RB3 and RB4 in Lekima's northwest propagate into central Shandong successively, producing the strongest precipitation (Figure 10). RB3 is positioned at the radially outward side of Lekima with reflectivity basically below 45 dBZ, while RB4 is positioned at the radially inward side of Lekima consisting of individual convective cells with a reflectivity over 45 dBZ. RB3 and RB4 are located in areas with strong gradients of equivalent potential temperature. In order to understand their developing mechanisms, five vertical cross sections are taken along the AB direction perpendicular to the rainbands (Figures 10A, C), and the average characteristics along the five vertical profiles are studied. A (B) is on the radially inward (outward) side of Lekima in the southeast (northwest).

Figure 11 shows the average of five vertical cross-sections of reflectivity, vertical velocity, equivalent potential temperature, and winds. A frontal zone tilting with height from side A to side B with a strong gradient of equivalent potential temperature can be seen in Figure 11B. The dry and cold air invades from an altitude of nearly 3 km from the "B" side and sinks afterward, while the warm and moist air lifts up from the "A" side along the front from the boundary layer. The collision of warm and cold air triggers the frontal convection systems, which is further organized into RB3 and RB4. RB3 is triggered near the level of 700 hPa, and RB4 is triggered near 850 hPa due to the different heights of the collision of warm and cold air. The reflectivity and the penetrative updraft of RB4 are stronger compared to that of RB3 (Figure 11A).

Heavy rainfall produced by a frontal zone due to the interaction between typhoon and mid-latitude systems is a unique physical process in northward-moving typhoons. How does the front in the northwest of Lekima develop? Miller (1948) proposed a frontogenesis function to quantitatively show the Lagrangian change rate of the magnitude of the horizontal equivalent potential temperature gradient in the frontal zone, which is adopted here. Following Miller (1948), the frontogenesis function (denoted as F) can be split into four terms:

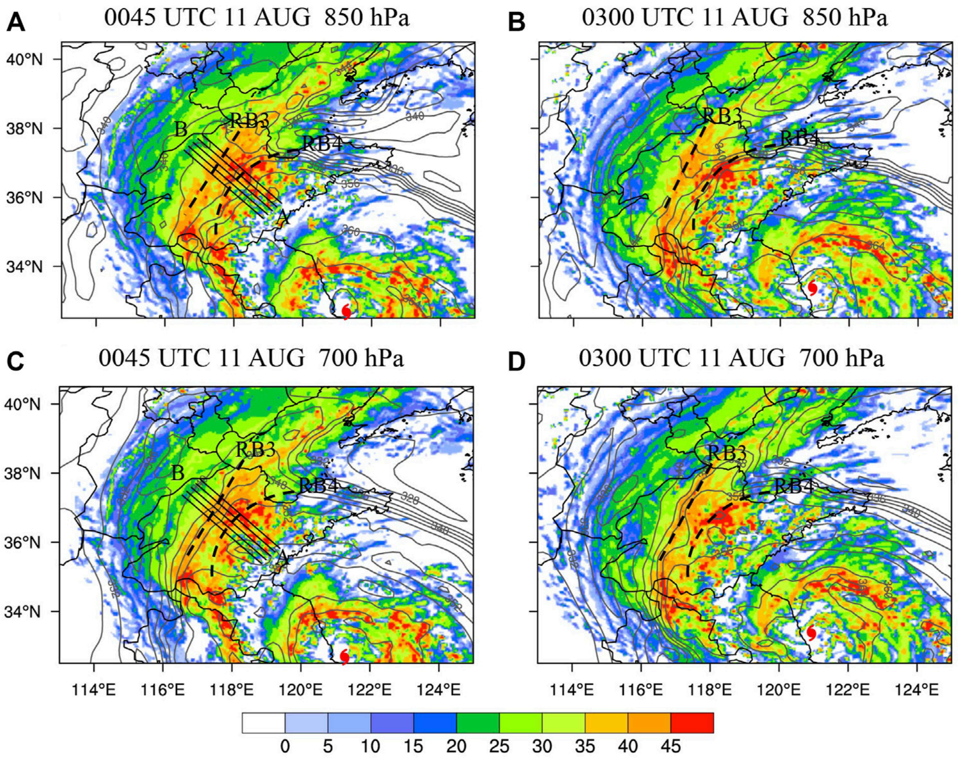

FIGURE 10
Composite reflectivity (shaded; unit: dBZ) and 850-hPa equivalent potential temperature (contours; unit: K) from the D02 simulation at **(A)** 0045 UTC 11 August; **(B)** 0300 UTC 11 August 2019. **(C)** and **(D)** as in **(A)** and **(B)** but at 700 hPa. Black solid lines indicate the positions of the vertical cross sections taken in Figure 11, black dashed lines indicate the positions of the rainbands, and typhoon symbols denote the locations of Lekima's center.

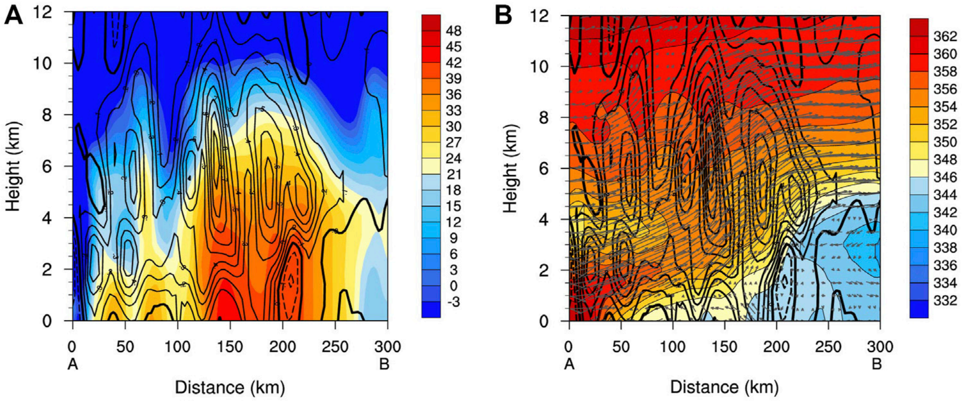

FIGURE 11
The average of five vertical cross-sections along AB in Figures 10A, C of the vertical velocity (contours with interval of .1, positive values are in solid contours, negative values are in dashed contours, zero values are in bold contours; unit: m/s) with **(A)** reflectivity (shaded; unit: dBZ); **(B)** equivalent potential temperature (shaded; unit: K) and winds (vectors) from the D02 simulation. X-axis coordinate is the horizontal distance from A (unit: km), and y-axis coordinate is the height (unit: km).

$$F = \frac{d}{dt}|\nabla_h\theta_{se}| = F_1 + F_2 + F_3 + F_4 \tag{1}$$

$$F_1 = -\frac{1}{|\nabla_h\theta_{se}|}\left\{\frac{1}{2}\left[\left(\frac{\partial\theta_{se}}{\partial x}\right)^2 - \left(\frac{\partial\theta_{se}}{\partial y}\right)^2\right]\left(\frac{\partial u}{\partial x} - \frac{\partial v}{\partial y}\right) + \frac{\partial\theta_{se}}{\partial x}\frac{\partial\theta_{se}}{\partial y}\left(\frac{\partial v}{\partial x} + \frac{\partial u}{\partial y}\right)\right\} \tag{2}$$

$$F_2 = -\frac{1}{2|\nabla_h\theta_{se}|}\left[\left(\frac{\partial\theta_{se}}{\partial x}\right)^2 + \left(\frac{\partial\theta_{se}}{\partial y}\right)^2\right]\left(\frac{\partial u}{\partial x} + \frac{\partial v}{\partial y}\right) \tag{3}$$

$$F_3 = -\frac{1}{|\nabla_h\theta_{se}|}\left(\frac{\partial\theta_{se}}{\partial x}\frac{\partial\omega}{\partial x} + \frac{\partial\theta_{se}}{\partial y}\frac{\partial\omega}{\partial y}\right)\frac{\partial\theta_{se}}{\partial p} \tag{4}$$

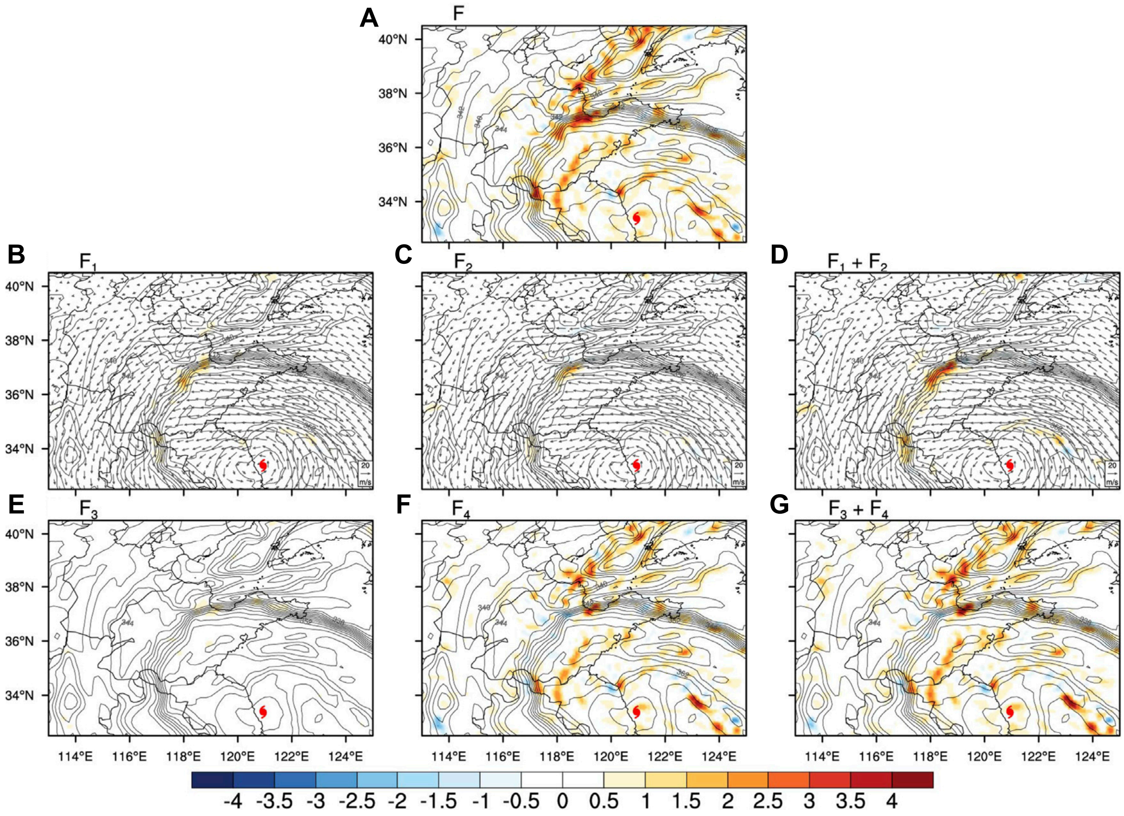

FIGURE 12
For 0300 UTC 11 August 2019, the 850-hPa equivalent potential temperature (gray contours; unit: K) with **(A)** frontogenesis function (F) (shaded; unit: 10^{-7} K/s); **(B)** deformation term (F_1) (shaded; unit: 10^{-7} K/s), **(C)** divergence term (F_2) (shaded; unit: 10^{-7} K/s), **(D)** $F_1 + F_2$ (shaded; unit: 10^{-7} K/s) and horizontal winds (vectors, unit vector represents 20 m/s); **(E)** tilting term (F_3) (shaded; unit: 10^{-7} K/s), **(F)** diabatic term (F_4) (shaded; unit: 10^{-7} K/s), and **(G)** $F_3 + F_4$ (shaded; units: 10^{-7} K/s) from the D02 simulation. Typhoon symbols denote the locations of Lekima's center.

$$F_4 = \frac{1}{|\nabla_h \theta_{se}|}\left[\frac{\partial\theta_{se}}{\partial x}\frac{\partial}{\partial x}\left(\frac{d\theta_{se}}{dt}\right)+\frac{\partial\theta_{se}}{\partial y}\frac{\partial}{\partial y}\left(\frac{d\theta_{se}}{dt}\right)\right] \qquad (5)$$

where θ_{se} is equivalent potential temperature, and F_1, F_2, F_3, and F_4 are deformation term, divergence term, tilting term, and diabatic term, respectively. $F > 0$ indicates frontogenesis with enhanced horizontal equivalent potential temperature gradient; while $F < 0$ indicates frontolysis with reduced horizontal equivalent potential temperature gradient.

There is frontogenesis with $F > 0$ at 850 hPa in the frontal area (Figure 12A). The four terms on the right-hand side of Eq. 1 are computed separately. The deformation term (F_1) is positive due to the advection of cold, dry air by northerlies in the northwest and advection of warm, moist air by easterlies in the southeast (Figure 12B). The divergence term (F_2) is also positive due to the convergence of the northerlies and easterlies (Figure 12C). Both F_1 and F_2 contribute to the frontogenesis (Figure 12D). The tilting term (F_3) has small magnitudes (Figure 12E), while the diabatic term (F_4) has large positive values but does not overlap with the frontal area (Figure 12F). Thus, F_3 and F_4 make little contributions to the frontogenesis (Figure 12G). Consistent results at 700 hPa are also obtained (figures are not shown). These analyses of the frontogenesis function are similar to those of Novak et al. (2004). Since the frontogenesis is mainly caused by deformation and divergence terms in the horizontal direction, the horizontal wind field composed of southeasterlies and northeasterlies in Lekima's north plays a crucial role in the development of the frontal zone in the northwest of Lekima.

Therefore, as Lekima propagates northward, its peripheral circulation directly affects Shandong Province during stage II. The horizontal wind field in Lekima's north, composed of southeasterlies and northeasterlies, leads to frontogenesis in the frontal zone between cold, dry continental air in the northwest and warm, moist oceanic air near the typhoon in the northwest of Lekima. The front tilts toward the northwest with height, and the frontal convective systems are organized into two convective rainbands RB3 and RB4. The heaviest precipitation occurs in Shandong under the influence of RB3 and RB4. It is worth mentioning that the extra-tropical transition of Typhoon Lekima is identified by the cyclonic phase space (CPS) method (Hart 2003) in this study, and it is found that although the baroclinicity of the precipitation area is enhanced and the frontal rainband appears at this stage, the typhoon does not appear to be in transition at this time.

6.3 Stage III (0600 UTC 11 August to 1200 UTC 11 August 2019)

As Lekima moves further north, the extreme rain event enters stage III. RB3 and RB4 continue moving toward northwest and out of the heavy rainfall area, while central Shandong is mainly controlled by RB5. RB5 is about 200 km north of the typhoon center and can be classified as the

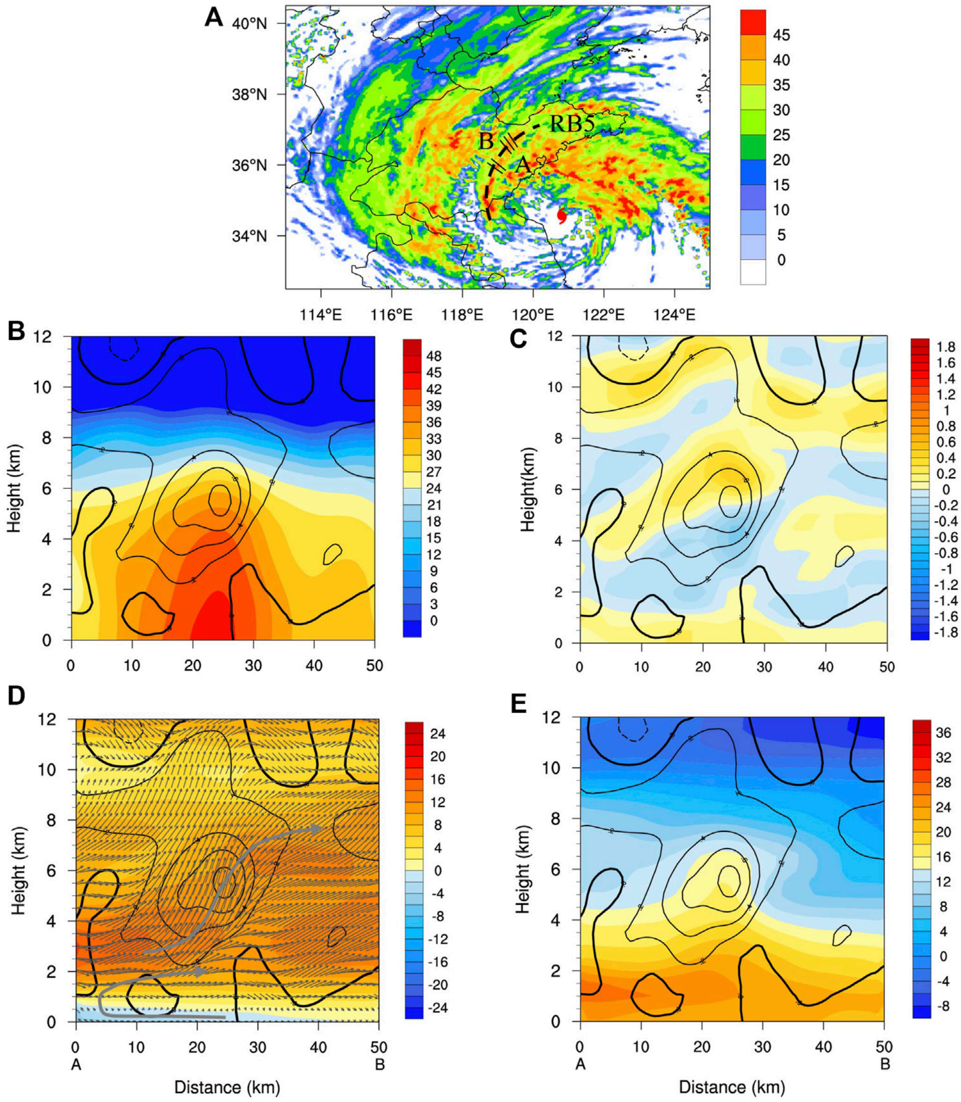

FIGURE 13
(A) Composite reflectivity (shaded; unit: dBZ) at 0645 UTC 11 August 2019; the black dashed line indicates the position of the rainband, the typhoon symbol denotes the location of Lekima's center, and black solid lines indicate the positions of radius–height cross-sections taken in **(B–E)**. The average of five radius–height cross-sections of vertical velocity (contours with interval of .2, positive values are in solid contours, negative values are in dashed contours, zero values are in bold contours; unit: m/s) with **(B)** reflectivity (shaded; unit: dBZ); **(C)** horizontal divergence (shading; 10^{-3} s^{-1}); **(D)** radial velocity (shaded; unit: m/s) and winds (vectors); and **(E)** tangential velocity (shaded; unit: m/s) from D02 simulation, x-axis coordinate is the horizontal distance from A (unit: km), and y-axis coordinate is the height (unit: km).

principal rainband (Houze, 2010). As a result, the precipitation during this stage is mainly due to the direct influence of the typhoon spiral rainband. Considering that Lekima has moved northward into mid-latitudes by this time and is now influenced by mid-latitude systems, how does the rainband structure change? We further analyze the vertical structure of RB5 and compare it with the typical structure of typhoon principal rainband proposed by Hence and Houze (2008).

Five radius–height cross-sections toward the typhoon center with a distance of 50 km are taken at convective cells embedded in RB5 with composite reflectivity greater than 40 dBZ (Figure 13A). A (B) denotes the radially inward (outward) side of Lekima. Figures 13B–E show the averaged radius–height cross-sections of reflectivity, vertical velocity, horizontal divergence, radial velocity, and tangential velocity.

Convective cells in RB5 slightly tilt radially outward (the side of B) with height (Figure 13B). The vertical circulation of RB5 is characterized by a low-level overturning flow and a middle-level rising radial outflow from the side of typhoon center and lifted near the convective cell (Figure 13D). The radial inflow is located only below 1 km and turns upward near the side of A, while the radial outflow layer is above 1 km. A strong outflow from the side of A exists between the height of 2–4 km and leads to the convergence center in Figure 13C, blocked by the convective cell developing upward. In conjunction with the convergence, upward motions occur above 1.5 km near the convection center with the maximum near z = 6 km, while the layer below 1.5 km is dominated by weak subsidence due to divergence. According to tangential velocity (Figure 13E), there is a secondary horizontal wind maximum (SHWM) with the maximum wind speed over 26 m/s near z = 1.5 km. In comparison with the structure of the principal rainband of Hence and Houze (2008) (their Figure 13), RB5 shows similar characteristics of radial inflow in the lower level, rising radial outflow in the upper level, and the presence of SHWM near the top of boundary layer. However, here, the height of SHWM and radial inflow is lower in RB5, and weak subsidence exists at a low level.

Thus, as Lekima moves further north, rainfall in Shandong is directly produced by the spiral rainband RB5 during stage III. Lekima has moved into mid-latitudes by this time, experiencing structural changes. As a result, the kinematic structure of RB5 differs from that of a typical typhoon's principal rainband in terms of vertical flow fields and height of the radial inflow and SHWM.

7 Summary and discussion

The mechanisms and forecasts of landfalling typhoon precipitation are challenging scientific problems. Lekima, the ninth typhoon in the western North Pacific in 2019, is the fifth strongest super typhoon to make landfall in mainland China since 1949. Lekima moved northward after a landfall, resulting in an extreme rain event in Shandong Province from 0000 UTC 10 August to 1200 UTC 11 August 2019, with maximum accumulated precipitation in central Shandong exceeding 400 mm, becoming the process with highest precipitation since meteorological records were kept in Shandong. This extreme rain event is a typical process under the interaction of mid-latitude systems and typhoon circulation. This study uses the mesoscale numerical WRF model (version 4.2) with two fixed grids at 12- and 2.4-km horizontal spacing for simulation, which was a good reproduction of the track, intensity of Typhoon Lekima, distribution of the main rainbands, and the spatio-temporal evolution of rainfall in Shandong. On this basis, we use the simulation to explore multi-scale characteristics of this extreme rain event in terms of favorable large-scale environments and mesoscale rainbands.

Synoptic systems in middle and low latitudes are stable during the process. The main system at the upper level is an upper-tropospheric westerly jet with wind speeds over 30 m/s. At the middle level, other than the WPSH, there exists a mid-latitude westerly trough, and Shandong is located in front of the trough. A southeasterly low-level jet and a southwesterly low-level jet can be seen at the low level. In addition, there is another Typhoon Krosa in the western North Pacific in Lekima's southeast. In the aforementioned background, Lekima maintains its intensity for a long time after landfall. The relatively slow translation speed and weak vertical wind shear can also help Lekima maintain its intensity. Under the influence of the large-scale environmental field formed by the typhoon and the westerly trough system, it provides favorable dynamic, thermal, and water vapor conditions for the heavy precipitation area.

During the torrential rainfall, five mesoscale rainbands in Lekima's north affect Shandong successively, which directly influence the heavy rainfall. Considering the evolution of precipitation and mesoscale rainbands, the extreme rain event in Shandong can be divided into three stages. Stage I can be classified as distant rainfall, and two linear convective rainbands affect Shandong successively, both of which are triggered by the boundary-layer convergence line. The boundary-layer convergence line is formed by the interaction between the cold pool outflow caused by the precipitation of the westerly trough and the warm and humid airflow transported by the typhoon. The precipitation in stage II is the strongest. There exists a frontal zone in central Shandong between warm, moist air carried by Lekima and cold, dry air behind the trough in the northwest. The front tilts toward the northwest with height, and warm, moist air transported by southeasterly low-level jet on the southeast side is lifted up along the front to form precipitation. According to the frontogenesis function, deformation and convergence in the horizontal wind field, composed of southeasterlies and northeasterlies in Lekima's north, plays a crucial role in frontogenesis. During stage III, Shandong is directly influenced by the principal rainband. However, this rainband shows a kinematic structure different from that of a typical typhoon principal rainband due to Lekima's structural change and weaker typhoon intensity after moving into mid-latitudes.

The precipitation of landfalling typhoon is affected by multiple physical processes, multi-scale systems, and is related to the internal processes in the typhoon, the interaction between typhoon and the environment, and the underlying surface. This research discusses the influences of the environment and typhoon rainband on heavy rainfall in Shandong after Lekima's landfall. Considering that the precipitation center is located in the mountainous area of central Shandong, we have also conducted a numerical experiment exploring the effects of mountainous terrains on the intensity and spatial distribution of this extreme rain event in Shandong Province. The results show that the topography in central Shandong mainly affects the location of the precipitation center, while the impact on precipitation intensity is not significant, which is not discussed in this paper due to the limitation of pages. The internal dynamic processes in a typhoon play important roles in the propagation and development of typhoon rainbands, but the influence of internal dynamical processes such as vortex Rossby waves on the formation of rainbands is not considered because the typhoon is far away from Shandong Province in precipitation stage I. However, during the second and third stages, how the internal dynamic processes in typhoon changes and how they influence the movement and development of rainbands when Lekima interacts with the mid-latitude systems require further study.

Data availability statement

The raw data supporting the conclusion of this article will be made available by the authors, without undue reservation.

Author contributions

YZ conceptualized this study. YG executed numerical experiments, analyzed the data, and wrote the manuscript. LL gave comments on the numerical experiment. YZ, LL, and JT provided revision advice for the submitted version of the manuscript.

Funding

This work was sponsored by the National Natural Science Foundation of China under Grants 42192555, 41775057.

Conflict of interest

The authors declare that the research was conducted in the absence of any commercial or financial relationships that could be construed as a potential conflict of interest.

Publisher's note

References

Baek, E. H., Lim, G. H., Kim, J. H., and Kug, J. S. (2014). Antecedent mid-tropospheric frontogenesis caused by the interaction between a tropical cyclone and midlatitude trough: A case study of typhoon Rusa (2002). *Theor. Appl. Climatol.* 118 (1-2), 9–24. doi:10.1007/s00704-013-1045-3

Bao, X. W., Davidson, N. E., Yu, H., Hankinson, M. C. N., Sun, Z. A., Rikus, L. J., et al. (2015). Diagnostics for an extreme rain event near Shanghai during the landfall of typhoon Fitow (2013). *Mon. Wea. Rev.* 143 (9), 3377–3405. doi:10.1175/MWR-D-14-00241.1

Barnes, G. M., and Garstang, M. (1982). Subcloud layer energetics of precipitating convection. *Mon. Wea. Rev.* 110 (2), 102–117. doi:10.1175/1520-0493(1982)110<0102:sleopc>2.0.co;2

Bosart, L. F., Cordeira, J. M., Galarneau, T. J., Moore, B. J., and Archambault, H. M. (2012). An analysis of multiple predecessor rain events ahead of tropical cyclones ike and lowell: 10-15 september 2008. *Mon. Wea. Rev.* 140 (4), 1081–1107. doi:10.1175/MWR-D-11-00163.1

Byun, K. Y., and Lee, T. Y. (2012). Remote effects of tropical cyclones on heavy rainfall over the Korean Peninsula - statistical and composite analysis. *Tellus A Dyn. Meteorol. Oceanogr.* 64, 14983. doi:10.3402/tellusa.v64i0.14983

Chen, F., and Dudhia, J. (2001). Coupling an advanced land surface–hydrology model with the penn state–ncar Mm5 modeling system. Part I: Model implementation and sensitivity. *Mon. Wea. Rev.* 1292 (4), 569–585. doi:10.1175/1520-0493(2001)129<0569:caalsh>2.0.co;2

Chen, J. M., Li, T., and Shih, C. F. (2010). Tropical cyclone- and monsoon-induced rainfall variability in taiwan. *J. Clim.* 23 (15), 4107–4120. doi:10.1175/2010JCLI3355.1

Chen, S. Y. S., Knaff, J. A., and Marks, F. D. (2006). Effects of vertical wind shear and storm motion on tropical cyclone rainfall asymmetries deduced from trmm. *Mon. Wea. Rev.* 134 (11), 3190–3208. doi:10.1175/MWR3245.1

Colle, B. A. (2003). Numerical simulations of the extratropical transition of floyd (1999): Structural evolution and responsible mechanisms for the heavy rainfall over the northeast United States. *Mon. Wea. Rev.* 131 (12), 2905–2926. doi:10.1175/1520-0493(2003)131<2905:nsotet>2.0.co;2

Corbosiero, K. L., and Molinari, J. (2003). The relationship between storm motion, vertical wind shear, and convective asymmetries in tropical cyclones. *J. Atmos. Sci.* 602 (2), 366–376. doi:10.1175/1520-0469(2003)060<0366:trbsmv>2.0.co;2

Ding, Y. F., Liu, J. P., Chen, S. Z., Cheng, X., and Zheng, Z. J. (2020). Uniqueness of Lekima compared to tropical cyclones landed in the East coast of China during 1979-2019. *Acta Oceanol. Sin.* 39 (8), 121–124. doi:10.1007/s13131-020-1639-4

Emanuel, K. A. (2013). Downscaling Cmip5 climate models shows increased tropical cyclone activity over the 21st century. *Proc. Natl. Acad. Sci.* 110(30), 12219–12224. doi:10.1073/pnas.1301293110

Galarneau, T. J., Bosart, L. F., and Schumacher, R. S. (2010). Predecessor rain events ahead of tropical cyclones. *Mon. Wea. Rev.* 138 (8), 3272–3297. doi:10.1175/2010mwr3243.1

Gao, S., Meng, Z., Zhang, F., and Bosart, L. F. (2009). Observational analysis of heavy rainfall mechanisms associated with severe tropical storm bilis (2006) after its landfall. *Mon. Wea. Rev.* 137 (6), 1881–1897. doi:10.1175/2008mwr2669.1

Guo, Y.-P., and Tan, Z.-M. (2022). Influence of track change on the inconsistent poleward migration of typhoon activity. *J. Geophys. Res. Atmos.* 127, e2022JD036640. doi:10.1029/2022JD036640

Han, Y., and Wu, R. S. (2008). The effect of cold air intrusion on the development of tropical cyclone. *Chin. J. Geophys.* 51 (5), 931–943. *(in Chinese)*. doi:10.1002/cjg2.1288

Hanley, D., Molinari, J., and Keyser, D. (2001). A composite study of the interactions between tropical cyclones and upper-tropospheric troughs. *Mon. Wea. Rev.* 1292 (10), 2570–2584. doi:10.1175/1520-0493(2001)129<2570:acsoti>2.0.co;2

Hart, R. E. (2003). A cyclone phase space derived from thermal wind and thermal asymmetry. *Mon. Wea. Rev.* 131 (4), 585–616. doi:10.1175/1520-0493(2003)131<0585:acpsdf>2.0.co;2

He, L., Chen, S., and Guo, Y. (2020). Observation characteristics and synoptic mechanisms of typhoon Lekima extreme rainfall in 2019. *J. Appl. Meteorol. Sci.* 31 (5), 513–526.

Hence, D. A., and Houze, R. A. (2008). Kinematic structure of convective-scale elements in the rainbands of hurricanes katrina and rita (2005). *J. Geophys. Res.* 113 (D15), D15108. doi:10.1029/2007JD009429

Hong, S. Y., and Lim, J. O. J. (2006). The wrf single-moment 6-class microphysics scheme (Wsm6). *Asia-Pac. J. Atmos. Sci.* 42.

Hong, S. Y., Noh, Y., and Dudhia, J. (2006). A new vertical diffusion package with an explicit treatment of entrainment processes. *Mon. Wea. Rev.* 134 (9), 2318–2341. doi:10.1175/MWR3199.1

Houze, R. A. (2010). Clouds in tropical cyclones. *Mon. Wea. Rev.* 138 (2), 293–344. doi:10.1175/2009mwr2989.1

Iacono, M. J., Delamere, J. S., Mlawer, E. J., Shephard, M. W., Clough, S. A., and Collins, W. D. (2008). Radiative forcing by long-lived greenhouse gases: Calculations with the aer radiative transfer models. *J. Geophys. Res.* 113 (D13), D13103. doi:10.1029/2008JD009944

Jonkman, S. N., Maaskant, B., Boyd, E., and Levitan, M. L. (2009). Loss of life caused by the flooding of new orleans after hurricane katrina: Analysis of the relationship between flood characteristics and mortality. *Risk Anal.* 29 (5), 676–698. doi:10.1111/j.1539-6924.2008.01190.x

Kain, J. S. (2004). The kain-fritsch convective parameterization: An update. *J. Appl. Meteorol.* 43 (1), 170–181. doi:10.1175/1520-0450(2004)043<0170:tkcpau>2.0.co;2

Klein, P. M., Harr, P. A., and Elsberry, R. L. (2000). Extratropical transition of Western north pacific tropical cyclones: An overview and conceptual model of the transformation stage. *Wea. Forecast* 15 (4), 373–395. doi:10.1175/1520-0434(2000)015<0373:etownp>2.0.co;2

Knutson, T. R., McBride, J. L., Chan, J., Emanuel, K., Holland, G., Landsea, C., et al. (2010). Tropical cyclones and climate change. *Nat. Geosci.* 3 (3), 157–163. doi:10.1038/ngeo779

Kossin, J. P., Emanuel, K. A., and Vecchi, G. A. (2014). The poleward migration of the location of tropical cyclone maximum intensity. *Nat.* 509(7500), 349-352, doi:10.1038/nature13278

Lee, M. H., Ho, C. H., and Kim, J. H. (2010). Influence of tropical cyclone landfalls on spatiotemporal variations in typhoon season rainfall over south China. *Adv. Atmos. Sci.* 27 (2), 443–454. doi:10.1007/s00376-009-9106-3

Leroux, M.-D., Plu, M., and Roux, F. (2016). On the sensitivity of tropical cyclone intensification under upper-level trough forcing. *Mon. Wea. Rev.* 144 (3), 1179–1202. doi:10.1175/mwr-d-15-0224.1

Li, Q. Q., and Wang, Y. Q. (2012). A comparison of inner and outer spiral rainbands in a numerically simulated tropical cyclone. *Mon. Wea. Rev.* 140 (9), 2782–2805. doi:10.1175/MWR-D-11-00237.1

Li, R. C. Y., and Zhou, W. (2015). Interdecadal changes in summertime tropical cyclone precipitation over southeast China during 1960-2009. *J. Clim.* 28 (4), 1494–1509. doi:10.1175/JCLI-D-14-00246.1

Lin, Y.-L., Ensley, D. B., Chiao, S., and Huang, C.-Y. (2002). Orographic influences on rainfall and track deflection associated with the passage of a tropical cyclone. *Mon. Wea. Rev.* 1302 (12), 2929–2950. doi:10.1175/1520-0493(2002)130<2929:oiorat>2.0.co;2

Luo, Y. L., Gong, Y., and Zhang, D. L. (2014). Initiation and organizational modes of an extreme-rain-producing mesoscale convective system along a mei-yu front in east China. *Mon. Wea. Rev.* 142 (1), 203–221. doi:10.1175/MWR-D-13-00111.1

Ma, L. M., and Tan, Z. M. (2009). Improving the behavior of the cumulus parameterization for tropical cyclone prediction: Convection trigger. *Atmos. Res.* 92 (2), 190–211. doi:10.1016/j.atmosres.2008.09.022

Meng, Z. Y., Chen, L. S., and Xu, X. D. (2002). Recent progress on tropical cyclone research in China. *Adv. Atmos. Sci.* 19 (1), 103–110. doi:10.1007/s00376-002-0037-5

Miller, J. E. (1948). On the concept of frontogenesis. *J. Meteor.* 5 (4), 169–171. doi:10.1175/1520-0469(1948)005<0169:otcof>2.0.co;2

Moore, B. J., Bosart, L. F., Keyser, D., and Jurewicz, M. L. (2013). Synoptic-scale environments of predecessor rain events occurring east of the rocky mountains in association with atlantic basin tropical cyclones. *Mon. Wea. Rev.* 141 (3), 1022–1047. doi:10.1175/mwr-d-12-00178.1

Novak, D. R., Bosart, L. F., Keyser, D., and Waldstreicher, J. S. (2004). An observational study of cold season-banded precipitation in northeast us cyclones. *Wea. Forecast* 19 (6), 993–1010. doi:10.1175/815.1

Peduzzi, P., Chatenoux, B., Dao, H., De Bono, A., Herold, C., Kossin, J., et al. (2012). Global trends in tropical cyclone risk. *Nat. Clim. Change* 2 (4), 289–294. doi:10.1038/NCLIMATE1410

Ritchie, E. A., and Elsberry, R. L. (2007). Simulations of the extratropical transition of tropical cyclones: Phasing between the upper-level trough and tropical cyclones. *Mon. Wea. Rev.* 135 (3), 862–876. doi:10.1175/mwr3303.1

Schumacher, R. S., Galarneau, T. J., and Bosart, L. F. (2011). Distant effects of a recurving tropical cyclone on rainfall in a midlatitude convective system: A high-impact predecessor rain event. *Mon. Wea. Rev.* 139 (2), 650–667. doi:10.1175/2010MWR3453.1

Schumacher, R. S., and Galarneau, T. J. (2012). Moisture transport into midlatitudes ahead of recurving tropical cyclones and its relevance in two predecessor rain events. *Mon. Wea. Rev.* 140 (6), 1810–1827. doi:10.1175/mwr-d-11-00307.1

Skamarock, W. C., Klemp, J. B., Dudhia, J., Gill, D. O., Liu, Z., Berner, J., et al. (2019). *A description of the advanced research WRF model version 4*. Boulder, CO: NCAR.

Studholme, J., Fedorov, A. V., Gulev, S. K., Emanuel, K., and Hodges, K. (2022). Poleward expansion of tropical cyclone latitudes in warming climates. *Nat. Geosci.* 15(1), 14-28, doi:10.1038/s41561-021-00859-1

Studholme, J., and Gulev, S. (2018). Concurrent changes to hadley circulation and the meridional distribution of tropical cyclones. *J. Clim.* 31 (11), 4367–4389. doi:10.1175/JCLI-D-17-0852.1

Torn, R. D. (2010). Diagnosis of the downstream ridging associated with extratropical transition using short-term ensemble forecasts. *J. Atmos. Sci.* 67 (3), 817–833. doi:10.1175/2009jas3093.1

Uhlhorn, E. W., Klotz, B. W., Vukicevic, T., Reasor, P. D., and Rogers, R. F. (2014). Observed hurricane wind speed asymmetries and relationships to motion and environmental shear. *Mon. Wea. Rev.* 142, 1290–1311. doi:10.1175/MWR-D-13-00249.1

Wang, M. Y., Ren, F. M., Xie, Y. J., Li, G. P., Yang, M. J., and Feng, T. (2021a). Characteristics and causes of extreme rainfall induced by binary tropical cyclones over China. *Asia-Pac. J. Atmos. Sci.* 57 (2), 311–320. doi:10.1007/s13143-020-00201-6

Wang, Q. W., Zhang, Y., Zhu, K. F., Tan, Z. M., and Xue, M. (2021b). A case study of the initiation of parallel convective lines back-building from the South side of a mei-yu front over complex terrain. *Adv. Atmos. Sci.* 38 (5), 717–736. doi:10.1007/s00376-020-0216-2

Wang, Y. Q. (2008). Rapid filamentation zone in a numerically simulated tropical cyclone. *J. Atmos. Sci.* 65 (4), 1158–1181. doi:10.1175/2007JAS2426.1

Wang, Y. Q., Wang, Y. Q., and Fudeyasu, H. (2009). The role of typhoon songda (2004) in producing distantly located heavy rainfall in Japan. *Mon. Wea. Rev.* 137 (11), 3699–3716. doi:10.1175/2009MWR2933.1

Wang, Y., Rao, Y., Tan, Z.-M., and Schönemann, D. (2015). A statistical analysis of the effects of vertical wind shear on tropical cyclone intensity change over the Western north pacific. *Mon. Wea. Rev.* 143 (9), 3434–3453. doi:10.1175/mwr-d-15-0049.1

Wang, Y. (2012). Recent research progress on tropical cyclone structure and intensity. *Trop. Cyclone Res. Rev.* 1, 254–275. doi:10.6057/2012TCRR02.05

Willoughby, H. E., Marks, F. D., and Feinberg, R. J. (1984). Stationary and moving convective bands in hurricanes. *J. Atmos. Sci.* 41 (22), 3189–3211. doi:10.1175/1520-0469(1984)041<3189:samcbi>2.0.co;2

Wu, C.-C., Yen, T.-H., Kuo, Y.-H., and Wang, W. (2002). Rainfall simulation associated with typhoon herb (1996) near taiwan. Part I: The topographic effect. *Wea. Forecast* 17 (5), 1001–1015. doi:10.1175/1520-0434(2003)017<1001:rsawth>2.0.co;2

Wu, L., Su, H., Fovell, R. G., Dunkerton, T. J., Wang, Z., and Kahn, B. H. (2015). Impact of environmental moisture on tropical cyclone intensification. *Atmos. Chem. Phys.* 15 (24), 14041–14053. doi:10.5194/acp-15-14041-2015

Xu, Y.-M., and Wang, Y. (2013). On the initial development of asymmetric vertical motion and horizontal relative flow in a mature tropical cyclone embedded in environmental vertical shear. *J. Atmos. Sci.* 70, 3471–3491. doi:10.1175/JAS-D-12-0335.1

Yang, L., Liu, M. F., Smith, J. A., and Tian, F. Q. (2017). Typhoon Nina and the August 1975 flood over central China. *J. Hydrometeorol.* 18 (2), 451–472. doi:10.1175/JHM-D-16-0152.1

Yang, M.-J., Zhang, D.-L., and Huang, H.-L. (2008). A modeling study of typhoon nari (2001) at landfall. Part I: Topographic effects. *J. Atmos. Sci.* 65 (10), 3095–3115. doi:10.1175/2008jas2453.1

Ying, M., Zhang, W., Yu, H., Lu, X. Q., Feng, J. X., Fan, Y. X., et al. (2014). An overview of the China meteorological administration tropical cyclone database. *J. Atmos. Ocean. Technol.* 31 (2), 287–301. doi:10.1175/JTECH-D-12-00119.1

Yu, J., Gao, S., Zhang, L., Shen, X., and Guo, L. (2020). Analysis of a remote rainstorm in the yangtze river delta region caused by typhoon mangkhut (2018). *J. Mar. Sci. Eng.* 8 (5), 345. doi:10.3390/jmse8050345

Zhang, J. Y., Wu, L. G., Ren, F. M., and Cui, X. P. (2013). Changes in tropical cyclone rainfall in China. *J. Meteorol. Soc. Jpn.* 91 (5), 585–595. doi:10.2151/jmsj.2013-502

Zhang, Q. A., Wu, L. G., and Liu, Q. F. (2009). Tropical cyclone damages in China 1983-2006. *Bull. Am. Meteorol. Soc.* 90(4), 489-496, doi:10.1175/2008BAMS2631.1

Zhou, X. L., Xie, Q., and Yang, L. (2022). Long-wave trough and ridge controlling of the water vapor transport to the tibet plateau by the tropical cyclones in the Bay of bengal in may. *Clim. Dyn.* 58 (3-4), 711–728. doi:10.1007/s00382-021-05930-6

frontiers | Frontiers in Earth Science

TYPE Original Research
PUBLISHED 12 January 2023
DOI 10.3389/feart.2022.1056882

OPEN ACCESS

EDITED BY
Liguang Wu,
Fudan University, China

REVIEWED BY
Xiaogang Huang,
National University of Defense Technology, China
Yubin Li,
Nanjing University of Information Science and Technology, China
Zhanhong Ma,
National University of Defense Technology, China

*CORRESPONDENCE
Yubin Yu,
yuyb@cma.gov.cn

SPECIALTY SECTION
This article was submitted to Atmospheric Science, a section of the journal Frontiers in Earth Science

RECEIVED 29 September 2022
ACCEPTED 31 October 2022
PUBLISHED 12 January 2023

CITATION
Wang H, Yu Y, Xu H, Zhao D and Liang J (2023), A numerical study on the effects of a midlatitude upper-level trough on the track and intensity of Typhoon Bavi (2020).
Front. Earth Sci. 10:1056882.
doi: 10.3389/feart.2022.1056882

A numerical study on the effects of a midlatitude upper-level trough on the track and intensity of Typhoon Bavi (2020)

Hui Wang[1], Yubin Yu[1,2]*, Hongxiong Xu[1], Dajun Zhao[1] and Jia Liang[1,3]

[1]State Key Laboratory of Severe Weather, Chinese Academy of Meteorological Sciences, Beijing, China, [2]China Meteorological Administration Training Centre, Beijing, China, [3]School of Atmospheric Sciences, Nanjing University of Information Science and Technology, Nanjing, China

The complex interactions between a tropical cyclone (TC) and the midlatitude upper-level trough or cutoff low (sometimes called a cold-core vortex) can lead to an unusual track, such as sudden turning motion, and intensity change of the tropical cyclone, often leading to large forecast errors. In this study, the track and intensity changes of Typhoon Bavi (2020) under the influence of the upper-level trough and the detached cutoff low from its base are investigated based on numerical experiments using the advanced Weather Research and Forecasting (WRF) model. Bavi formed over the western North Pacific between Taiwan and Okinawa Islands on 23 August 2020. Under the influence of an upper-level trough to the north, Bavi initially moved northeastward. As the trough propagated eastward, a cutoff low was detached from the base of the trough on the next day. The downward penetration of the upper-level cutoff low led to a sudden northwestward turning motion of Bavi when it intensified to a severe typhoon and then moved almost due north and made landfall over North Korea. These changes and processes are well captured in a control numerical experiment. In a sensitivity experiment with the mid-latitude upper-level trough removed in the initial conditions, the tropical cyclone moved primarily north-northeastward after 1-day simulation without the sudden northwestward turning. This track change led to an earlier landfall of the storm over South Korea and, thus, an earlier weakening than in the control experiment, which is termed as the indirect effect on the storm intensity due to the change in the tropical cyclone track. The results also show that eddy angular momentum flux convergence associated with the upper-level trough contributed little to the simulated tropical cyclone intensification, while the environmental vertical wind shear is key to the intensity change of Bavi.

KEYWORDS

midlatitude upper-level trough, typhoon, track and intensity, numerical study, vertical wind shear (VWS)

1 Introduction

Skillful prediction of tropical cyclone (TC) sudden track change and intensity remains one of the great challenges for both research and operational communities. Although the improvements in TC track and intensity forecasts are envisioned over the past few decades, large track and intensity errors still occur in some situations (Wang and Wu, 2004). Particularly, large errors are often related to the unusual sudden change in TC motion and rapid intensification (Elsberry et al., 2013). In addition, the multiscale interactions between the TC and its environmental weather and climate systems make the forecasts of TC track and intensity changes more difficult (Xin et al., 2021).

TCs over the western North Pacific (WNP) often interact with the large-scale weather systems. In addition to the low-level systems, the upper-level synoptic systems, such as the nearby upper-level westerly trough and the associated cutoff low, often have significant impacts on TC track, intensity, and structure. Such effects have been given considerable attention in the literature (Holliday and Thompson, 1979; Hanley et al., 2001; Li et al., 2012; Leroux et al., 2013; Leroux et al., 2016; Wei et al., 2016; Fischer et al., 2019; Yan et al., 2021). Specifically, the upper-level outflow channel of a TC may be modified by the upper-level westerly trough, and the upper-level cutoff low may affect TC motion and intensity through downward penetration.

An upper-level westerly trough often induces TC recurvature, a typical track over the WNP. In those cases, a TC moves northwestward and turns northeastward in the Northern Hemisphere (Riehl and Shafer, 1944; George and Gray, 1976; JTWC, 1988; Dobos and Elsberry, 1993; O'Shay and Krishnamurti, 2004; Zhang et al., 2013). Favorable conditions for TCs to recurve in the WNP include the southward penetration of a midlatitude upper-level westerly trough and the eastward retreat of the WNP subtropical high (Riehl and Shafer, 1944; George and Gray, 1976; Holland and Merrill, 1984; Elsberry, 1990; Evans et al., 1991). Yu and Kwon (2005) noticed the recurvature tracks of typhoons Olga (1999) and Prapiroon (2000) under the influence of the midlatitude trough, although they mainly focused on the TC intensity change. Wu et al. (2009) found that the steering effect of the midlatitude trough is one of the dominant factors that led to the recurvature of Typhoon Shanshan (2006). By evaluating the structure and evolution of the total energy singular vectors, Kim and Jung (2009) revealed the dominant role of the midlatitude trough in the track recurvature of Typhoon Usagi (2007). Other studies have mainly focused on the TC intensity change when the TC interacts with an upper-level trough. Leroux et al. (2016) provided a comprehensive map summarizing processes that may lead to TC intensity change under the influence of the upper-level forcing (see their Figure 1). Among those effects, it is still hard to distinguish whether the upper-level trough is "good" or "bad" for the development of a TC.

The TC–trough interaction can induce a favorable environment for TC intensification. First, the upper-level outflow of a TC can be enhanced by the inward eddy angular momentum flux, which can lead to the strengthening of the secondary circulation and eyewall convection, and thus favorable for TC intensification (Sadler, 1975; Holland and Merrill, 1984; Merrill, 1988a, Merrill, 1988b; Molinari and Vollaro, 1989; Molinari and Vollaro, 1990; Molinari et al., 1995; Rodgers et al., 1991; Shi et al., 1997; Bosart et al., 2000; Titley and Elsberry, 2000). The upper-level potential vorticity (PV) associated with the midlatitude trough can serve as a

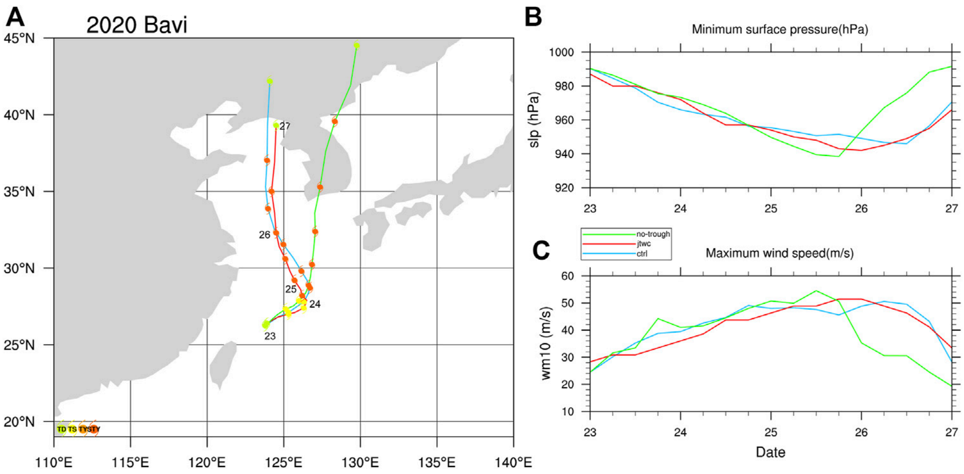

FIGURE 1
(A) Track of Typhoon Bavi (2010) with every 6-h position indicated by solid circles with different colors for different categories in storm intensity, **(B)** the storm's central sea level pressure (hPa), and **(C)** the maximum sustained 10-m wind speed (m s^{-1}) from 0000 UTC 23 August to 0000 UTC 27 August 2020 based on the JTWC best track data (red) and from both CTRL (blue) and No-trough (green) experiments.

dynamical forcing and also destabilizes the atmospheric vertical column, enhancing convection and the secondary circulation and, thus, the intensification of TC (Hoskins, 1990; Montgomery and Farrel, 1993; Molinari et al., 1995, 1998; Hanley et al., 2001). In addition, the upper-level trough is often accompanied by the upper-level westerly jet. The right entrance of the jet can trigger upward motion, which can enhance the outflow and eyewall convection when a TC moves into the region (Hoskins et al., 1985; Rodgers et al., 1991; Shi et al., 1997; Hanley et al., 2001; Komaromi and Doyle, 2018). Some other studies also found that the TC–trough interaction can trigger the secondary eyewall formation in TCs and lead to TC intensity change (Leoux et al., 2013; Leoux et al., 2016; Komaromi and Doyle, 2018). The TC–trough interaction may be unfavorable for TC intensification or lead to TC weakening. An approaching trough may bring strong vertical wind shear (VWS) that is unfavorable for TC intensification (Lewis and Jorgensen, 1978; Hanley et al., 2001). The cold and dry air intrusion may reduce the entropy gradient between the environment and the TC core and weaken the TC (Zhang et al., 2016).

The TC–trough interaction can be sensitive to the strength and depth of the trough and the initial structure of the TC (Kimball and Evans, 2002). Leroux et al. (2016) showed that the PV configuration associated with the upper-level trough increases the upper-level divergence while preventing strong VWS to affect TC Dora (2007). They found that TC intensification under the upper-level forcing is greater for stronger TCs and is favorable when the TC and the trough is at an appropriate distance. Based on idealized simulations, Komaromi and Doyle (2018) found that when the center of a TC is within 0.2–0.3 times the wavelength of a trough in the zonal direction and 0.8–1.2 times the amplitude of the trough in the meridional direction, the strong TC–trough interaction favors the occurrence of the TC intensification. From the climatological study of TCs in the North Atlantic during 1989–2016, Fischer et al. (2019) found that rapid intensifying TCs frequently occurred under the influence of the upper-level trough with shorter zonal wavelengths, especially at the base of the trough and greater upstream TC–trough displacement.

A number of studies have identified the eddy angular momentum flux convergence (EFC) as a parameter indicating the occurrence of TC–trough interaction (Molinari and Vollaro, 1990; Yu and Kwon, 2005; Komaromi and Doyle, 2018), but some other studies found that large EFC might not be a favorable factor for TC development (Titley and Elsberry 2000; Peirano et al., 2016). DeMaria et al. (1993) examined the EFC during the 1989–1991 hurricane seasons over the North Atlantic and found that TCs intensified just after the period of enhanced EFC. They defined the TC–trough interaction as any time when the EFC exceeded 10 m s^{-1} d^{-1} within 1,500 km of the TC center. When interacting with a trough, a TC over warm water is more likely to intensify than weaken in the composite study of TCs in the North Atlantic during 1985–1996 (Hanley et al., 2001). They adopted DeMaria's 1993 criterion of the TC–trough interaction but added a temporal threshold, namely, the enhanced EFC must have lasted for two consecutive 12-h periods. Based on TCs over the North Atlantic during 1979–2014, Peirano et al. (2016) revisited the TC–trough interaction and found that troughs have a negative effect on TC intensification, and the EFC is a poor predictor of TC intensity change compared to the associated environmental VWS.

Large TC track forecast errors are often related to sudden turning motion or recurvature of TCs (George and Gray, 1976; Peak and Elsberry, 1986; Holland and Wang, 1995; Elsberry et al., 2013). In the WNP, most of TCs that experienced sudden turning motion are influenced by changes in large-scale circulations or synoptic interactions (George and Gray, 1976; Hodanish and Gray, 1993; Liu and Chan, 2003; Fudeyasu et al., 2006). The equatorial penetration of a midlatitude westerly trough or/and the associated cutoff low often provides favorable synoptic conditions for sudden turning motion or recurvature of a TC (Lander, 1996). Some previous statistical studies have indicated that part of the intensity forecast errors are related to errors in the predicted TC track, or equivalently skillful intensity forecasts may benefit from the improved track forecasts (DeMaria, 2010; Du et al., 2013; Kieu et al., 2021).

Most of the previous studies on the TC–trough interaction are based on global reanalysis data or real-case simulations to investigate the impact of TC–trough interaction on TC intensification as mentioned previously. However, few studies have focused on the sensitivity of the TC track to the upper-level trough or cutoff low, subsequently affecting the TC intensity change. In this study, Typhoon Bavi (2020) was chosen as a case study to illustrate how the upper-level trough affected the TC track and the associated intensity change. Bavi was selected because there were large differences in its track and intensity among the deterministic forecasts by different operational forecasting systems (Zhou et al., 2022). Notably, Bavi's track was more difficult to predict than its intensity. Our study focuses on the dynamic processes that contributed to the northwestward track turning of Bavi, and the consequence of the track change under the influence of the midlatitude upper-level trough and the associated cutoff low based on numerical sensitivity experiments. Bavi experienced two sharp turning motions during its lifetime. One is the turning toward the northeast on August 23 and then the sudden northwestward turn on the next day. We will show that the interaction between the TC and the upper-level trough (and the associated cutoff low) played key roles in leading to the sudden track change but had little direct effect on the intensity. We will address the following two questions: what are the synoptic features or mechanisms that caused the special track of Bavi? Is the midlatitude upper-level trough "favorable" or "unfavorable" for the intensification of Bavi? The rest of the paper is organized as follows. Section 2 describes the data, model, and experimental design. An overview of Typhoon Bavi is given in Section 3. The simulation results are analyzed in Section 4. The robustness of the results is discussed with additional experiments in Section 5. Main conclusions are drawn in the last section.

2 Data, model, and experimental design

The fifth generation of the European Centre for Medium-Range Weather Forecasting (ECMWF) atmospheric reanalysis (ERA5) dataset was used to describe the synoptic conditions. The ERA5 dataset was chosen because of its high horizontal resolution (0.25° x 0.25°) and has shown improved representation of the location and intensity of TCs (Hersbach et al., 2020). The best track data are obtained from the Joint Typhoon Warning Center (JTWC), which include the 6-hourly TC position (longitude and latitude), maximum sustained near-surface wind speed, and minimum sea level pressure.

The numerical simulations presented in this study were performed using version 4.3.3 of the Advanced Research Weather Research and Forecasting Model (ARW-WRF; Skamarock et al., 2019), with three 2-way interactive nested meshes with horizontal grid spacings of 27, 9, and 3 km, respectively. The three meshes have sizes of 320 × 320, 310 × 310, and 478 × 358 grid points, respectively. The outermost mesh is fixed, and the two nested inner meshes automatically move following the model TC during the model integration so that the model TC is always located near the mesh centers. The model has 60 vertical levels extending from the surface to the model top at 50 hPa. The model’s physics include the Thompson cloud microphysics scheme (Thompson et al., 2008), Yonsei University planetary boundary layer (PBL) scheme (YSU, Hong et al., 2006), Rapid Radiative Transfer Model (RRTM; Mlawer et al., 1997) for longwave radiation calculation and the Dudhia scheme (Dudhia, 1989) for shortwave radiation calculation, Noah land surface scheme (Ek et al., 2003) for land surface processes, and Kain–Fritsch scheme (Kain, 2004) applied for the outermost model domain.

The model initial and lateral boundary conditions and daily SST dataset were obtained from the National Centers for Environment Prediction (NCEP) Global Forecast System (GFS) Final Analysis (FNL). The spectral nudging method was applied to the outermost domain to preserve the large-scale flow with wavelengths longer than 1,000 km throughout the model simulations (Wang et al., 2013). In the control experiment (CTRL), the upper-level trough to the north of the TC vortex was initially present as in the FNL analysis. In the sensitivity experiment (No-trough), the upper-level trough above 500 hPa, which is located to the north of Bavi, was removed in the initial fields by a smoothing algorithm (cubical smoothing algorithm with five-point approximation) such that the upper-level westerly trough was effectively filtered out in the initial conditions. As a result, a comparison of the simulations between CTRL and No-trough can help reveal the influences of the upper-level trough and its associated cutoff low on the track and intensity evolution of Typhoon Bavi.

3 An overview of the observed and simulated Typhoon Bavi (2020)

On 19 August 2020, a broad area of low pressure about a couple of hundred miles northeast of the Philippines archipelago developed. The system rapidly organized on the next day and became a tropical depression on August 21 and was subsequently named Bavi by the JTWC. Bavi gradually strengthened between Taiwan and Okinawa over the WNP and subsequently moved northward and further strengthened into a tropical storm on 22 August. Bavi experienced a brief rapid intensification followed by a slow intensification from 23 August (Figures 1B,C) and moved east-northeastward (Figure 1A). It suddenly turned northwestward and was upgraded to a typhoon by the next day. Bavi further intensified to a severe typhoon on 25 August, turned to the north, and reached its peak intensity on 26 August. Soon afterward, as Bavi continued moving northward, it weakened rapidly. Finally, it made landfall over North Korea and became an extratropical cyclone.

Figure 2 depicts the evolution of the 200-hPa PV and wind fields from 0000 UTC 23 to 1200 UTC 25 August from the ERA5 analyses. On 23 August, there was a northeast-southwest-oriented westerly trough located north of 30°N between 120°–135°E, which was accompanied by strong cyclonic PV anomalies (Figure 2A). Bavi was located near the base of the trough axis to the north. This configuration indicates the possible TC–trough interaction. The westerly trough propagated eastward and later a cutoff low appeared and was detached from the base of the trough at 1200°UTC 24 (Figure 2D). The cutoff low was maintained at around 135°E and 30°N, with the maximum PV of 6°PVU and to the east of the TC near the time when Bavi turned northwestward. As Bavi continued moving northward under the influence of the new-coming westerly trough, the cutoff low dissipated.

The CTRL experiment simulated the track of Bavi reasonably well compared with the JTWC best track, except for some small errors during the turning period and the extratropical transition stage (Figure 1A). Both CTRL and No-trough simulated the northeastward movement on the first day but considerable differences between the two experiments appeared after one and half day of simulations. The simulated Bavi in CTRL turned suddenly northwestward after one-and-half-day simulation, while that in No-trough turned nearly north-northeastward. The large track differences between CTRL and No-trough indicate that the TC–trough interaction contributed to the unusual motion of Bavi.

The simulated Bavi shows similar intensity evolution in CTRL and No-trough in terms of the central sea level pressure and the maximum sustained near-surface wind speed and compared reasonably well with those shown in the JTWC best track data (Figures 1B,C). The rapid weakening of the storm in No-trough occurred earlier than in CTRL mainly because the storm made landfall over South Korea instead of the west of North Korea. This suggests that the upper-level trough had little direct effect on the simulated storm intensity when the storm was not affected by

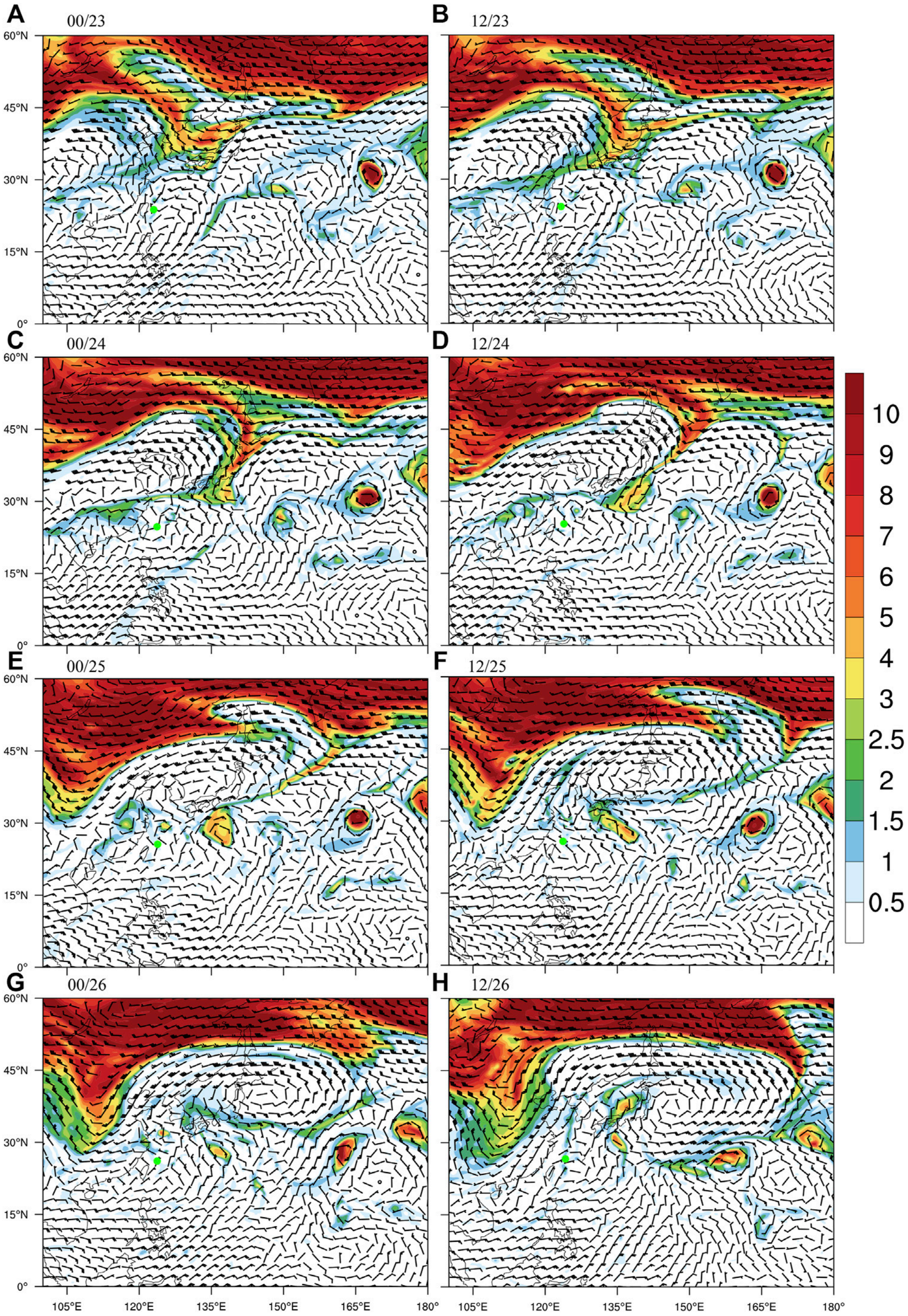

FIGURE 2
200-hPa wind barbs (m s^{-1}) and potential vorticity (shaded, PVU) based on ERA5 reanalysis data for Typhoon Bavi with 12-h intervals. The green dot indicates the TC center from the JTWC best track data.

landfall. Large difference in intensity at the later stage was mainly due to the indirect effect associated with the changes in the simulated storm track. Such an indirect effect, however, has not been discussed in previous studies.

Figure 3 shows the 200-hPa PV, wind, and geopotential height fields simulated in CTRL and No-trough. The simulated large-scale fields in the CTRL (Figures 3A–D) show little deviation from those in the FNL analysis throughout the

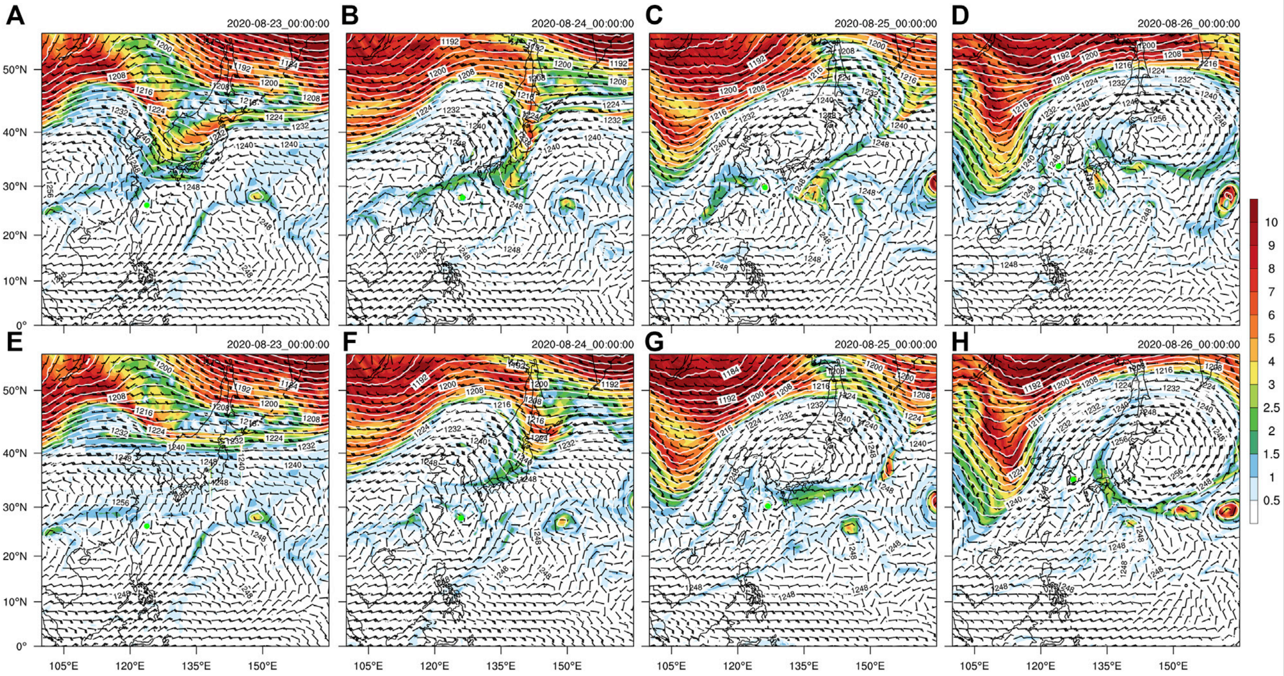

FIGURE 3
Simulated PV (shaded, PVU), wind vectors, and geopotential height (contour, m) at 200 hPa. The upper panels are for CTRL experiment and the lower panels are for No-trough experiment, respectively.

simulation. In the No-trough experiment (Figures 3E–H), because the trough originally located north to Bavi was removed at the initial time, the cutoff low detached from the base of the westerly trough was absent during the simulation. The weak westerly trough appeared to the north of the TC after 1-day simulation was due to the eastward propagation of the PV maximum and westerly trough to the north of 43°N at the initial time. Almost no TC–trough interaction occurred in this case because the weak trough was about 2,000 km northeast of the TC center by the end of the simulation. Note that in the simulation, the northern boundary of the smoothing area to remove the westerly trough at the initial time was chosen to be 43 N, but the results are similar if the northern boundary is moved further northward (not shown).

4 Effect of the upper-level trough on the track and intensity of the simulated Bavi

4.1 Relationship between the tropical cyclone track change and the steering flow

The TC track change is often related to changes in the large-scale environmental steering flow. The steering flow is often defined as the averaged wind vector between 300 and 850 hPa or at the nearly nondivergent level around 500 hPa (Wang and Elsberry, 1998). In this study, we calculated the steering flow as a wind vector averaged within a radius of 500 km from the TC center between 900 and 200 hPa. As we can see from Figure 4, the motion of the TC follows the steering flow well in the two experiments. The steering flow shows a strong northward component after one-and-half-day simulations in both experiments. The direction change of the zonal component of the steering flow is responsible for the sudden northwestward change of the track in CTRL, while the zonal component of the steering flow is always positive with a small magnitude in No-trough, indicating the slowly north-northeastward movement of the TC.

The TC movement is mainly steered by the asymmetric flow across the TC center. Figure 5 shows the evolution of the asymmetric wind fields at 500 hPa within 500 km from the TC center at 0000 UTC 24, 1200 UTC 24, 0000 UTC 25, and 0000 UTC 26, respectively, in CTRL and in No-trough. The calculated asymmetric flow is consistent with the TC motion, and the track change is largely caused by the change in the steering flow. The TC structure is nearly axisymmetric with weak asymmetric wind on the first day (Figure 5A), leading to the slowdown of the northeastward motion. In the next 12 h (Figure 5B), relatively strong northeasterly winds occurred in the northeastern quadrant of the TC, showing the interaction

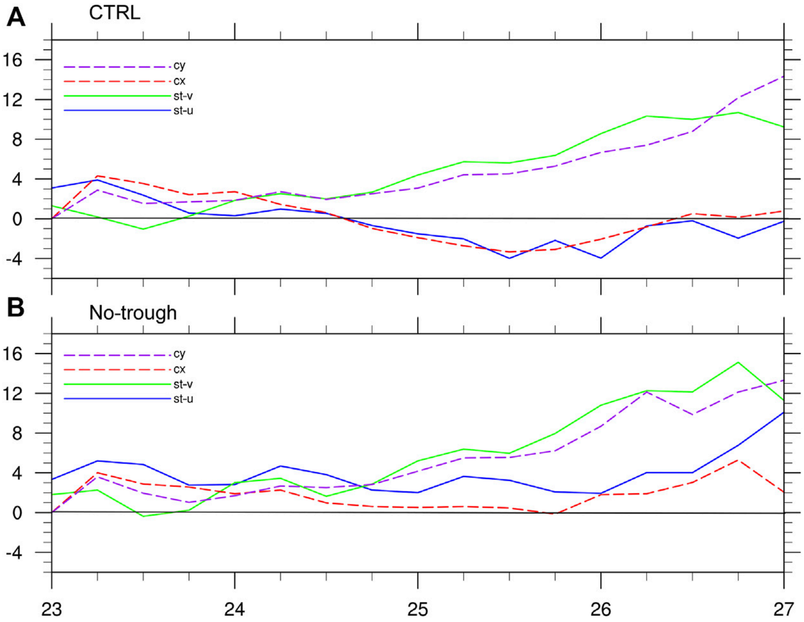

FIGURE 4
Time series of the zonal and meridional components (cx, cy; m s^{-1}) of TC translation speed estimated with difference of the TC center positions and steering flow (st-u, st-v; m s^{-1}) in the CTRL **(A)** and in No-trough experiments.

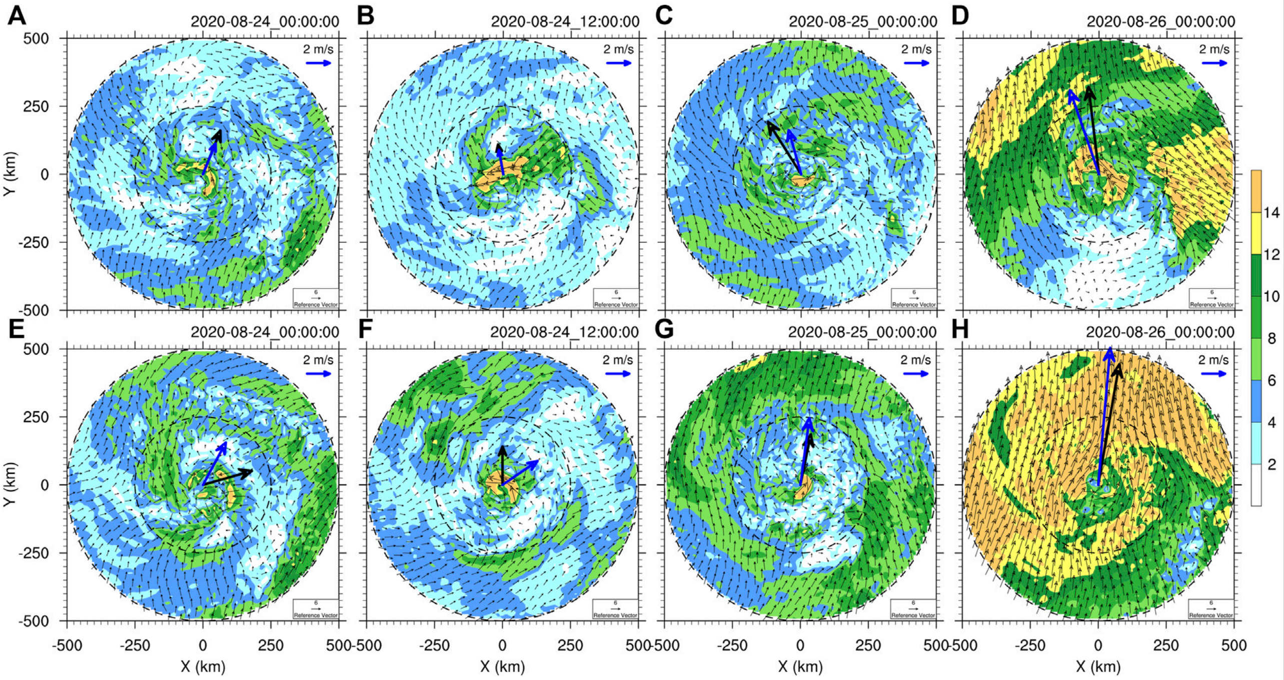

FIGURE 5
Simulated 500-hPa asymmetric winds (vectors, m s^{-1}) and speeds greater than 2 m s^{-1} (shaded) in the 9-km domain in both CTRL (upper panels) and No-trough (lower panels). Black and blue thick arrows indicate the TC motion vector and the averaged asymmetric wind vector within 500 km from the TC center. Black dotted circles are 250 and 500 km away from the TC centers.

with the upper-level cutoff low. The southerly winds are prevalent in the northwestern quadrant of the TC, in agreement with the sudden northwestward turning motion of the TC. Weak southerly winds occur southwest of the TC center, while weak easterly winds appear east of the TC center, corresponding to the continuous northwestward motion of the TC during 1200 UTC 24 and 0000 UTC 25, (Figure 5C). By the next day (Figure 5D), the acceleration of motion speed is due to the gradually enhanced southerly winds in both the eastern and northwestern quadrants of the TC.

The asymmetric flow pattern in No-trough is greatly different from that in CTRL. At 0000 UTC 24 August (Figure 5E), strong southerly flow is dominant in the southeastern quadrant of the TC inner core, causing the northeastward turning of the TC track. In the next 12 h (Figure 5F), the TC structure becomes quasi-axisymmetric with relatively weak asymmetric winds, the TC continues moving northeastward. The TC accelerates due to the enhanced southerly winds outside the inner core since 0000 UTC 25 August (Figure 5G). During 0000 UTC 25–0000 UTC 26 August (Figure 5H), strong southerly winds rapidly spread in both the inner and outer core regions, leading to the faster north-northeastward movement of the TC. The direction of the TC motion corresponds well with the mean asymmetric wind vector at 500 hPa. This demonstrates that the middle-level asymmetric wind pattern can well indicate the TC motion.

4.2 Vertical penetration effect of the upper-level systems

The steering flow and the asymmetric winds over the TC core are largely controlled by the large-scale circulation that the storm is embedded. In the Bavi case, part of the steering flow is related to the vertical penetration effect of the upper-level synoptic system, namely, the cutoff low detached from the base of the westerly trough to the north as mentioned above. During the turning motion of the TC from 23 to 24 August, the upper-level PV streamer propagated along with the northwesterly winds down to the base of the trough. Then, a cutoff low characterized by cyclonic PV maximum and cyclonic circulation was detached from the base of the upper-level trough from 1200 UTC 24 August. To examine the interaction between the TC and the upper-level cutoff low, the orbiting tracks of the two systems are shown in Figure 6A. The interaction began when the two systems were oriented in the southwest-northeast direction. From 24 to 26 August, the separation distance between the TC and the upper-level cutoff low was around 1,000–1,200 km, which is within the critical distance of about 1,500 km defined by Patla et al. (2009). In the study by Patla et al. (2009), the upper-level system is a tropical upper-tropospheric trough (TUTT) cell, while here, the upper-level system is the cutoff low detached from the base of the westerly trough as an independent circulation system.

The upper-level cutoff low had a maximum PV of 5–6 PVU with a diameter of about 1,200 km based on the 200 hPa 0.5 PVU isoline. The cutoff low was located to the northeast of the TC center initially and then orbited anticyclonically with time because of the effect of the anticyclonic circulation in the outflow of Bavi from 0000 UTC 24 to 0012 UTC 24 August. Later, the directions of the TC and the upper-level cutoff low suddenly changed, with the TC moving from north-northeastward to northwestward and the upper-level cutoff low moving from southeastward to southwestward. During this period, the upper-level cutoff low increasingly affected the TC motion through vertical penetration and was responsible for the sudden northwestward turning motion of the TC. This is different from the track guidance for the influence of a TUTT cell on TC motion given by Patla et al. (2009). In their conceptual model, the TC moves toward the northeast if the upper-level TUTT cell is located to the northeast of the TC center. In No-trough with the cutoff low greatly suppressed, the TC kept moving north-northeastward, indicating that the upper-level cutoff low contributed to the northwestward motion of Typhoon Bavi during 24 and 25 August.

To further demonstrate the downward penetration effect of the upper-level system on the northwestward motion of Bavi, we estimated the Rossby penetration depth, which is defined as $D = I \times L_R / N$, where L_R is the horizontal scale of the upper-level system, I is the inertial stability, and N is Brunt–Väisälä frequency. The horizontal scale of the upper-level cutoff low (trough) is defined as the outermost radius of the 0.5 PVU isoline of PV anomaly. The inertial stability at 200 hPa is calculated by using the tangential winds and relative vorticity radially averaged within the L_R. N is also calculated within the L_R at 200 hPa. For simplicity, D is shown as the lowest level to which the upper-level system can penetrate. There are two kinds of interactions during the track turning and the intensification of Typhoon Bavi (Figure 6B). During 23–24 August, the winds from the upper-level westerly tough can penetrate downward to around a 4-km height, indicating that the upper-level trough and the TC interacted with each other and the winds above 4 km were influenced by the upper-level trough. On the next day, the upper-level trough continuously propagated eastward with its base detached to form a cutoff low. The PV anomalies of the upper-level trough can penetrate down to about a 5.5-km height but become less penetrative from 1800 UTC 24 to 1800 UTC 25 August, indicating that the upper-level trough had a decreasing impact on the TC motion. However, the penetration depth increased again afterward because of the influence of the new-coming westerly trough from the west.

With the development of the upper-level cutoff low, the penetration depth increased with time. The largest penetration depth occurred on 1800 UTC 24 August, which corresponds to the direction change of the TC motion, indicating that the TC

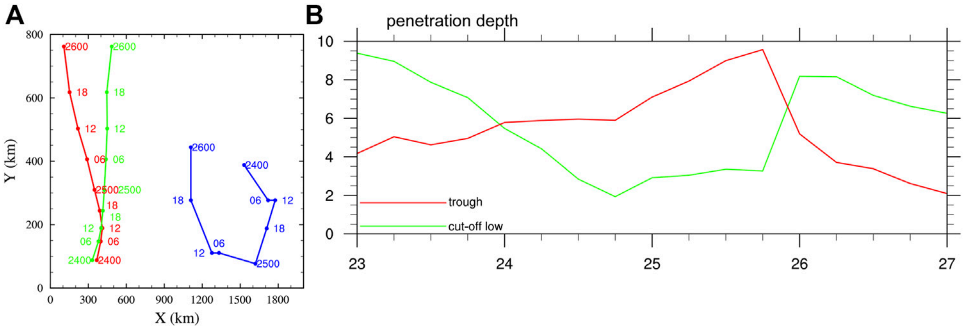

FIGURE 6
(A) Tracks of the TC and the cutoff low. The red (green) curve represents the track in CTRL (No-trough), and the blue curve denotes the track of the cutoff low and **(B)** the time evolution of the lowest level at which the upper-level trough and cutoff low can penetrate (km).

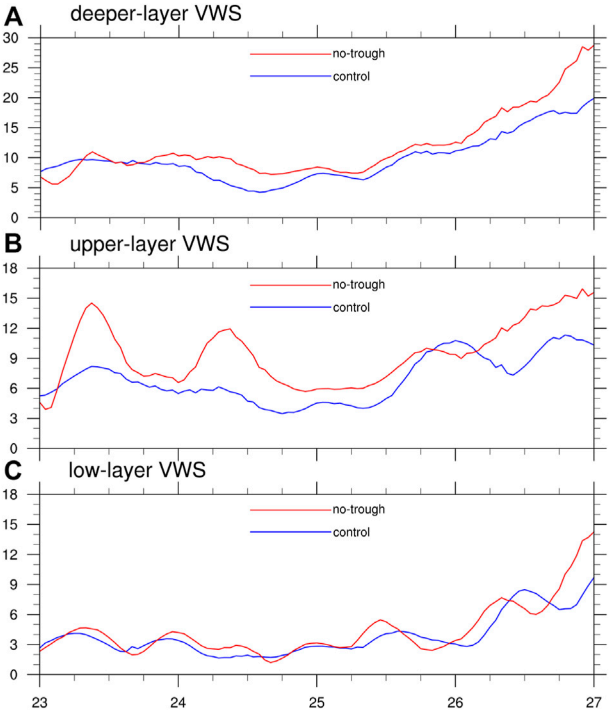

FIGURE 7
Time series of the deep-layer shear **(A)** between 200 and 850 hPa (m s^{-1}), upper-layer shear **(B)** between 200 and 500 hPa (m s^{-1}), and low-layer shear **(C)** between 500 and 850 hPa (m s^{-1}) in CTRL (blue) and No-trough (red), respectively.

motion was influenced by the cutoff low. As the separation distance between the TC and the cutoff low increased, the effect of the upper-level cutoff low on the TC motion became negligible from 1800 UTC 25 August. The results, thus, strongly suggest that the Rossby penetration depth can help quantitatively evaluate the effects of the synoptical system on TC motion. In the case of Typhoon Bavi, both the upper-level trough and the associated cutoff low interacted with the TC at different stages of the TC development. Such interaction at different vertical levels contributed to the change in the steering flow and, thus, the TC motion.

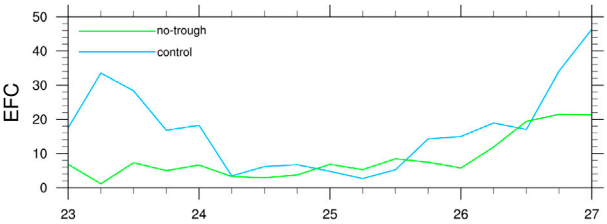

FIGURE 8
Time series of the EFC (m s^{-1} day^{-1}) averaged over the annulus between the radii of 300–600 km at 200 hPa.

4.3 Effects of vertical wind shear and eddy angular momentum flux convergence on intensity change of Bavi

Previous studies have demonstrated that the trough-related VWS in the TC environment can affect TC intensity change (Hanley et al., 2001; Peirano et al., 2016). The environmental VWS is commonly measured as the vector difference in the horizontal winds averaged over an area within a given radius (e.g., within a radius of 500 km from the TC center with the TC circulation removed) between 200 and 850 hPa (Emanuel, 2000; Zehr, 2003; Paterson et al., 2005). To investigate the effect of the environmental VWS associated with the upper-level circulation systems on the TC intensity change, we calculated the deep-layer shear between 200 and 850 hPa, upper-layer shear between

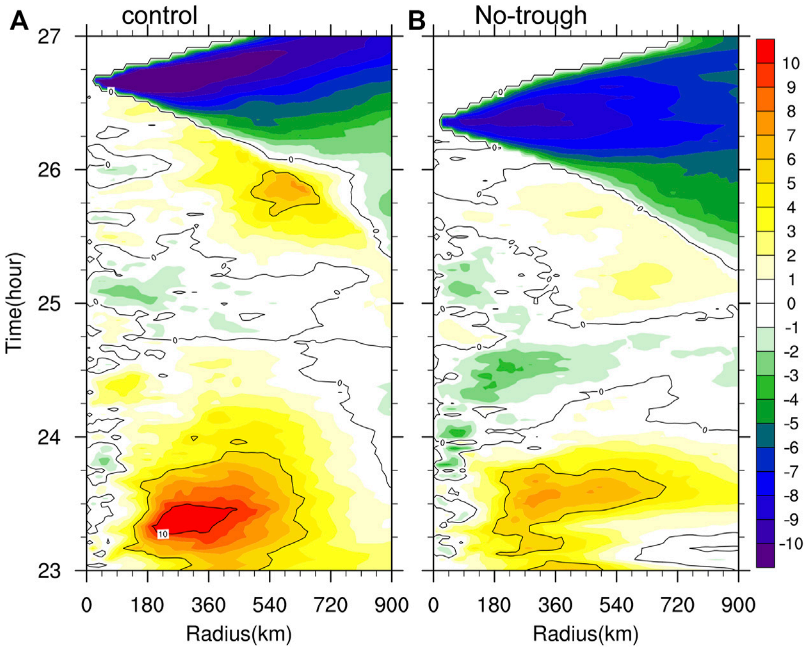

FIGURE 9
Radius–time plots of 200-hPa azimuthal-mean radial wind (m s^{-1}) in CTRL **(A)** and No-trough **(B)**, respectively.

200 and 500 hPa, and low-layer shear between 500 and 850 hPa with the results shown in Figure 7.

In CTRL, there were moderate deep-layer shear (between 4.5 and 11 m s^{-1}; Rios-Berrios and Torn, 2017) and upper-layer shear during the first 60 h of the simulation, consistent with the intensification period of the TC. Both the deep-layer shear and upper-layer shear then decreased gradually until 1000 UTC 24 August except that a transient large shear value appeared at 0000 UTC 25 August but increased rapidly when the new-coming upper-level trough approached the TC. The low-layer shear exhibited steady evolution before the TC reached its maximum intensity at 0000UTC 26 August and then increased with time quickly. There existed a lagged correlation between the low-layer shear and the deep-layer shear. In No-trough, both the deep-layer shear and the upper-layer shear were greater than 6 m s^{-1} for most of the time during the TC intensification period except that two transient large values of around 15 m s^{-1} and 10 m s^{-1} appeared at 0800 UTC 23 and 0800 UTC 24 August. The deep-layer shear and the upper-layer shear began to increase after 1000 UTC 25 August and reached their maximum values by the end of the simulation. The low-layer shear was weak during the TC intensification period and began to increase after the TC reached its peak intensity, consistent with the evolution in CTRL. There also existed a lagged correction between the deep/upper-layer shear and the low-layer shear as well as the TC intensity. In both experiments, the TC intensity is highly correlated with the low-layer shear, which is consistent with some statistical results for TCs over the WNP (Shu et al., 2013; Wang et al., 2015). Note that the deep-layer shear and the upper-layer shear are largely correlated with the 200-hPa wind. The magnitude of deep-layer shear and upper-layer shear are relatively smaller in CTRL than in No-trough due to the westerly trough to the north in the former being replaced by the westerly jet in the latter. These results suggest that the upper-layer shear may have a relatively weaker effect on TC intensity change than the low-layer shear for TCs interacting with the midlatitude westerly systems (Elsberry and Jeffries, 1996; Wang et al., 2015; Finocchio et al., 2016).

In addition to the environmental VWS, the EFC is often used to quantitatively characterize the TC–trough interaction through both the magnitude and duration (e.g., Molinari and Vollaro, 1989). From the perspective of balanced response, the upper-level trough can be viewed as a momentum source, which can spin-up the TC outflow and increase the upper-level divergence and eyewall ascending model, leading to the falling of the central pressure and the increase in surface wind. The TC–trough interaction is assumed to occur when the EFC averaged within 300–600 km of the TC center at 200 hPa is greater than 10 (m s^{-1}) day^{-1} (DeMaria et al., 1993; Hanley et al., 2001). The value of the EFC was greater than 10 (m s^{-1}) day^{-1} in the first day of the simulation in CTRL (Figure 8), indicating that the trough was within 300–600 km radii of the TC center. Namely, the southwesterlies ahead of the upper-level trough did reach the inner radii of the TC, leading to the convergence of the

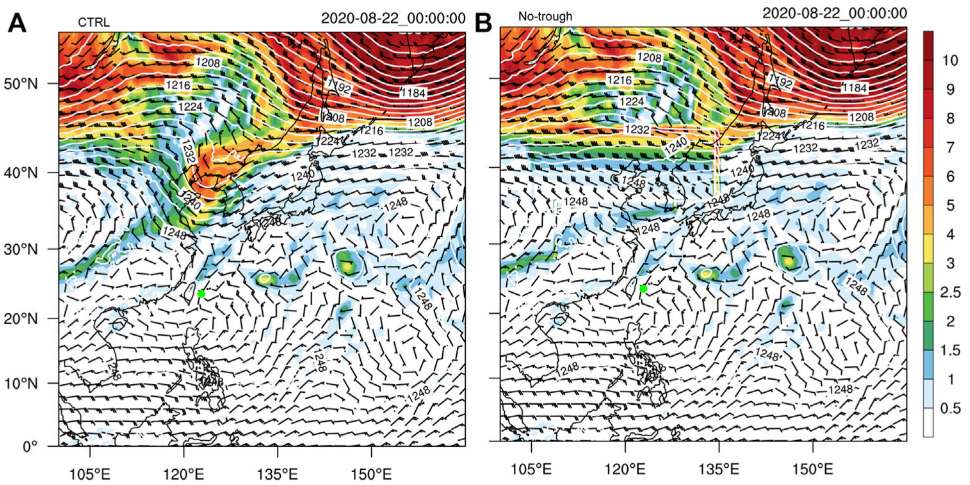

FIGURE 10
Simulated PV (shaded, PVU), wind vectors, and geopotential height (contour, m) at 200 hPa at the initial time of 0000 UTC 22 August in CTRL **(A)** and No-trough **(B)**, respectively.

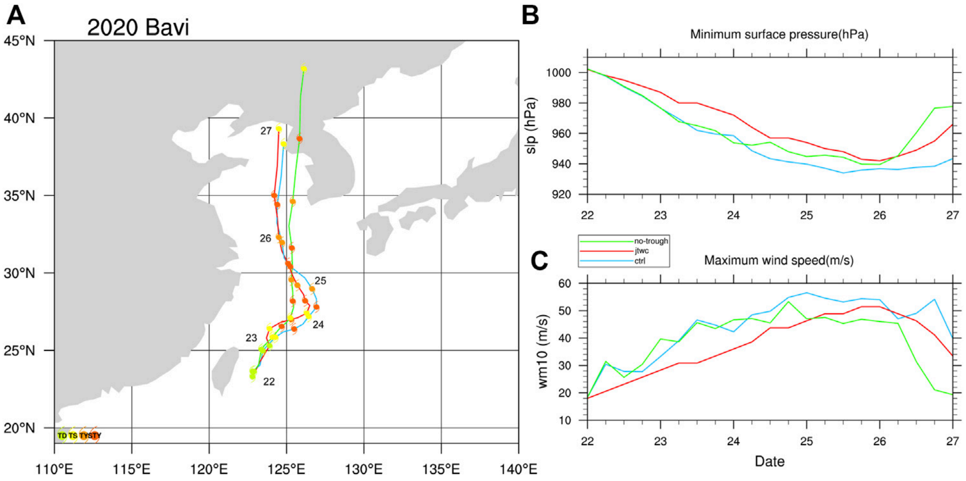

FIGURE 11
(A) Track of Typhoon Bavi (2010) with every 6-h position indicated by solid circles with different colors for different categories in storm intensity, **(B)** the storm's central sea level pressure (hPa), and **(C)** the maximum sustained 10-m wind speed (m s^{-1}) from 0000 UTC 22 to 0000 UTC 27 August 2020 based on the JTWC best track data (red) and from CTRL (blue) and No-trough (green).

eddy angular momentum at the upper levels and thus the spin-up of the outflow. The EFC was not persistently large during the intensification period from 24 to 26 August when the westerly trough moved eastward, and the cutoff low was detached from the trough base and began to interact with Bavi. The interaction between the TC and cutoff low was associated with weak EFC and did not satisfy the criteria for the TC–trough interaction given in previous studies (Molinari and Vollaro, 1989; DeMaria et al., 1993; Hanley et al., 2001).

Although previous studies found that large EFC related to the upper-level trough is favorable for TC intensification, our results imply that the enhanced EFC used as a precursor for TC intensity change may depend on the type of the TC–trough interactions (Fischer et al., 2019). The TC continued to intensify after the TC interacted with the cutoff low. Note that when the TC reached its peak intensity, the EFC began to increase again. The enhanced EFC at the end of the simulation indicates the strengthened TC–trough interaction due to the new-coming trough. However, this new

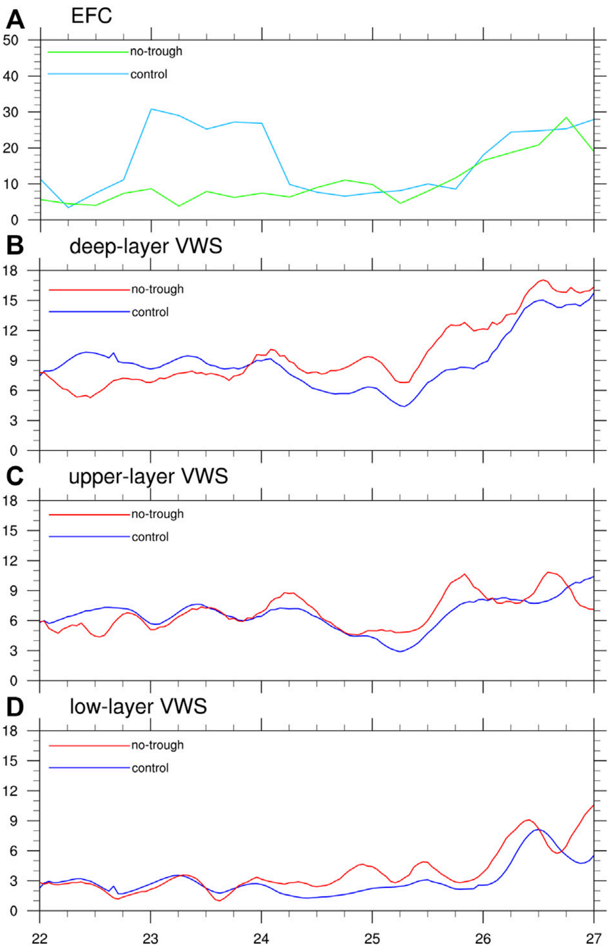

FIGURE 12
Time series of **(A)** the EFC (m s^{-1} day^{-1}) calculated at 200 hPa averaged over the 300–600 km annulus and the deep-layer shear **(B)** between 200 and 850 hPa (m s^{-1}), upper-layer shear **(C)** between 200 and 500 hPa (m s^{-1}), and low-layer shear **(D)** between 500 and 850 hPa (m s^{-1}) in CTRL (blue) and No-trough (red), respectively.

trough seemed to be a “bad-trough” and unfavorable for TC intensification. In No-trough, the EFC in the inner radii of the TC was almost unchanged in the 4-day simulation until 0600 UTC 26 August, showing quite small EFC forcing at the inner radii of the TC. This is consistent with the removal of the upper-level trough and subsequently, the absence of the upper-level cutoff low.

In addition, we noticed that the trough-induced large EFC that occurred on the first day of the simulation in CTRL could directly affect the outflow. The outflow in CTRL (Figure 9A) was much stronger than that in No-trough (Figure 9B). The enhanced outflow could strengthen the secondary circulation and thus the storm intensification. However, although the EFC differed greatly in the two experiments, the TC intensity evolution was comparable. This suggests that the TC–trough interaction might play a secondary role in the intensity change of Typhoon Bavi. The intensity change may be influenced more predominantly by the environmental VWS than the EFC in this case, which is consistent with the composite study by Peirano et al. (2016).

5 Discussion with additional sensitivity experiments

The results discussed in Section 4 are based on one initial time. To see the robustness of the finding, similar experiments were conducted with the model initialized 24 h earlier. The upper-level westerly trough was orientated in the northeast-southwest direction and located north of 30°N between 115 and 130°E (Figure 10A). The PV maximum associated with the trough was concentrated near the trough line. At this time, Typhoon Bavi was located to the southeast of the trough line, which remained as the trough moved eastward. In No-trough, the aforementioned westerly trough was removed (Figure 10) as done in the No-trough experiment discussed in Section 4.

The simulated TC track and intensity in CTRL are similar to the observed (Figure 11). The TC began to move northeastward and then turned toward to the east-northeast as it interacted with the upper-level westerly trough. The sudden direction change occurred at 1200 UTC 24 August when the TC was influenced by the cutoff low, leading to the northwestward turning motion of the TC. The approach of the new-coming westerly trough caused the TC to accelerate northward eventually. In No-trough with the westerly trough initially removed, the TC moved northeastward after 2-day simulation and then turned northward with a faster translation speed than that in CTRL. The intensity in both experiments showed little difference in the first 4-day simulations. Significant differences appeared in the last day of the simulation, which was primarily due to the difference in the simulated TC track. This is an indirect effect of the upper-level trough on TC intensity. The direct effect of the upper-level trough on the TC is on the storm track in this case.

An examination of the EFC (Figure 12A) confirms that the first TC–trough interaction occurred from 1800 UTC 23 to 0600 UTC 24 August and the second occurred from 0000 UTC 26 August, consistent with the result in the simulation initialized 24-h later discussed in Section 4. The steady evolution of the moderate VWS (Figures 12B–D) favored the TC intensification but the increased deep-layer shear associated with the new-coming upper-level westerly trough became unfavorable for TC intensification after 1000 UTC 25 August. Note that the VWS magnitude in the two experiments shows little difference. This further confirms that the VWS is the main control of TC intensification during the TC–trough interaction, consistent with the results discussed in Section 4 and also the findings by Peirano et al. (2016).

The aforementioned results together with those in Section 4 strongly suggest that the TC–trough interaction is complicated and more attention should be given to the relative importance of favorable and unfavorable aspects of the interaction. In addition to the direct effect, attention needs to be paid to the indirect effect as well. The TC–trough interaction directly led to the track change in the Typhoon Bavi case, while the effect on TC intensity was insignificant until the TC reached its peak intensity. Large intensity difference occurred by the end of the simulations largely due to the track difference. This effect is termed as the indirect effect of the TC–trough interaction in this study, which has not been emphasized in previous studies.

6 Conclusion

In this study, the effects of a midlatitude upper-level westerly trough on the track and intensity of Typhoon Bavi (2020) over the WNP has been investigated through numerical experiments using the advanced WRF model. Typhoon Bavi formed over the WNP on 23 August 2020 and moved northeastward between Taiwan and Okinawa Islands under the influence of the upper-level westerly trough. As the upper-level trough to the north of the TC center propagated eastward, a cutoff low formed as a detached circulation from the base of the westerly trough on the next day. The enhanced circulation of the cutoff low increased the vertical penetration depth, imposing a considerable effect on the motion of Bavi and leading to a sudden northwestward turning motion. Bavi intensified to a severe typhoon and moved almost due north under the influence of the upper-level cutoff low and finally made landfall over North Korea.

The aforementioned processes were well captured in a control numerical experiment and further confirmed with an experiment in which the upper-level westerly trough was removed in the initial conditions. Namely, in the experiment No-trough with the upper-level westerly trough above 500 hPa removed by a smoothing algorithm, the TC moved primarily north-northeastward after 1-day simulation without the sudden northwestward turning. We also showed that the interactions between the TC and the upper-level trough or the cutoff low were dominated by the downward penetration and steering effects on Bavi's motion, while the effect of the environmental VWS associated with the upper-level systems showed little differences between the two experiments, implying that the VWS might play a secondary role in causing the different motion of the storm in the two experiments.

Although the EFC was shown to have an influence on the TC outflow through enhancing the TC outflow, the TC intensity showed little difference in the two experiments, while the EFC showed large different evolutions. This demonstrates that the TC–trough interaction is complicated, and the EFC is not always a good indicator of TC intensification, while the related VWS is the main control, at least in the Bavi case. Although the moderate deep-layer shear and upper-layer shear are favorable for the intensification of Bavi, the low-layer shear is also important to the intensity change of Typhoon Bavi. In the Bavi case, the increase in deep-layer shear and upper-layer shear occurred prior to the increase in the low-layer shear, and the increase in the low-layer shear corresponded well with the weakening of the TC in the late stage of the simulations.

The results from this study also show that the upper-level systems (including the westerly trough and the subsequent cutoff low) affect the TC motion through the downward penetration and modifying the steering flow. Such a downward penetration effect played a secondary role in affecting the TC intensification because the TC intensity change showed similar evolution before landfall in the experiments with and without the upper-level westerly trough. The difference in TC intensity in the later stage was mainly an indirect effect of the earlier landfall due to the change in the TC track. It should be pointed out that the interaction between a TC and the upper-level trough or cutoff low is complicated and could be quite sensitive to the relative location of the two systems. Komaromi and Doyle (2018) conducted idealized simulations to understand the TC–trough interactions, but they did not include the westerly jet environment. This study can be extended by conducting semi-idealized simulations with the upper-level trough of different strength and size and at different relative locations from the TC, which will be further conducted in a follow-up study.

Data availability statement

The original contributions presented in the study are included in the article/Supplementary Material; further inquiries can be directed to the corresponding author.

Author contributions

HW designed the study. HW, HX, DZ and JL analyzed the datasets and generated figures. HW and YY wrote the manuscript with contributions from Yuqing Wang.

Funding

This study was supported by the National Natural Science Foundation of China under grants 42175008, 42192554, and 41730960; National Key R&D Program of China under grant 2017YFC1501602 and 2022YFC3004200; Basic Research Fund of Chinese Academy of Meteorological Sciences (2020Y015); and Open Grants of the State Key Laboratory of Severe Weather (2021LASW-A14).

Conflict of interest

The authors declare that the research was conducted in the absence of any commercial or financial relationships that could be construed as a potential conflict of interest.

Publisher's note

References

Bosart, L. F., Bracken, W. E., Molinari, J., Velden, C. S., and Black, P. G. (2000). Environmental influences on the rapid intensification of hurricane opal (1995) over the gulf of Mexico. *Mon. Weather Rev.* 128, 322–352. doi:10.1175/1520-0493(2000)128<0322:eiotri>2.0.co;2

DeMaria, M., Kaplan, J., and Baik, J. (1993). Upper-level eddy angular momentum fluxes and tropical cyclone intensity change. *J. Atmos. Sci.* 50 (8), 1133–1147. doi:10.1175/1520-0469(1993)050<1133:uleamf>2.0.co;2

DeMaria, M. (2010). "Tropical cyclone intensity change predictability estimates using a statistical-dynamical model," in *29th conf. On hurricanes and tropical meteorology* (Tucson, AZ: Amer. Meteor. Soc.). AvaliableAt: https://ams.confex.com/ams/29Hurricanes/techprogram/paper_167916.htm.

Dobos, P. H., and Elsberry, R. L. (1993). Forecasting tropical cyclone recurvature. Part I: Evaluation of existing methods. *Mon. Wea. Rev.* 121, 1273–1278. doi:10.1175/1520-0493(1993)121<1273:ftcrpi>2.0.co;2

Du, T. D., Ngo-Duc, T., Hoang, M. T., and Kieu, C. Q. (2013). A study of connection between tropical cyclone track and intensity errors in the WRF model. *Meteor. Atmos. Phys.* 122, 55–64. doi:10.1007/s00703-013-0278-0

Dudhia, J. (1989). Numerical study of convection observed during the winter monsoon experiment using a mesoscale two-dimensional model. *J. Atmos. Sci.* 46, 3077–3107. doi:10.1175/1520-0469(1989)046<3077:nsocod>2.0.co;2

Ek, M. B., Mitchell, K. E., Lin, Y., Rogers, E., Grunmann, P., Koren, V., et al. (2003). Implementation of Noah land surface model advances in the national centers for environmental prediction operational mesoscale eta model. *J. Geophys. Res.* 108, 2002JD003296. doi:10.1029/2002JD003296

Elsberry, L. E., Chen, L.-S., Davidson, J., Rogers, R., Wang, Y., and Wu, L. (2013). Advances in understanding and forecasting rapidly changing phenomena in tropical cyclones. *Trop. Cyclone Res. Rev.* 2, 13–24. doi:10.6057/2013TCRR01.02

Elsberry, R. L. (1990). International experiments to study tropical cyclones in the Western North Pacific. *Bull. Amer. Meteor. Soc.* 71, 1305–1316. doi:10.1175/1520-0477(1990)071<1305:ietstc>2.0.co;2

Elsberry, R. L., and Jeffries, R. (1996). Vertical wind shear influences on tropical cyclone formation and intensification during TCM-92 and TCM-93. *Mon. Wea. Rev.* 124, 1374–1387. doi:10.1175/1520-0493(1996)124<1374:vwsiot>2.0.co;2

Emanuel, K. A. (2000). A statistical analysis of tropical cyclone intensity. *Mon. Wea. Rev.* 128, 1139–1152. doi:10.1175/1520-0493(2000)128<1139:asaotc>2.0.co;2

Evans, J. L., Holland, G. J., and Elsberry, R. L. (1991). Interactions between a barotropic vortex and an idealized subtropical ridge. Part I: Vortex motion. *J. Atmos. Sci.* 48, 301–314. doi:10.1175/1520-0469(1991)048<0301:ibabva>2.0.co;2

Finocchio, P. M., Majumdar, S. J., Nolan, D. S., and Iskandarani, M. (2016). Idealized tropical cyclone responses to the height and depth of environmental vertical wind shear. *Mon. Weather Rev.* 144, 2155–2175. doi:10.1175/MWR-D-15-0320.1

Fischer, M. S., Tang, B. H., and Corbosiero, K. L. (2019). A climatological analysis of tropical cyclone rapid intensification in environments of upper-tropospheric troughs. *Mon. Weather Rev.* 147 (10), 3693–3719. doi:10.1175/MWR-D-19-0013.1

Fudeyasu, H., Iizuka, S., and Matsuura, T. (2006). Impact of ENSO on landfall characteristics of tropical cyclones over the Western North Pacific during the summer monsoon season. *Geophys. Res. Lett.* 33, L21815. doi:10.1029/2006GL027449

George, J. E., and Gray, W. M. (1976). Tropical cyclone motion and surrounding parameter relationships. *J. Appl. Meteor.* 15 (12), 1252–1264. doi:10.1175/1520-0450(1976)015<1252:tcmasp>2.0.co;2

Hanley, D. E., Molinari, J., and Keyser, D. (2001). A composite study of the interactions between tropical cyclones and upper-tropospheric troughs. *Mon. Wea. Rev.* 129, 2570–2584. doi:10.1175/1520-0493(2001)129<2570:acsoti>2.0.co;2

Hersbach, H., Bell, B., Berrisford, P., Hirahara, S., Horanyi, A., Munoz-Sabater, J., et al. (2020). The ERA 5 global reanalysis. *Q. J. R. Meteorol. Soc.* 146, 1999–2049. doi:10.1002/qj.3803

Hodanish, S., and Gray, W. M. (1993). An observational analysis of tropical cyclone recurvature. *Mon. Wea. Rev.* 121, 2665–2689. doi:10.1175/1520-0493(1993)121<2665:aoaotc>2.0.co;2

Holland, G. J., and Merrill, R. T. (1984). On the dynamics of tropical cyclone structural changes. *Q. J. R. Meteorol. Soc.* 110, 723–745. doi:10.1002/qj.49711046510

Holland, G. J., and Wang, Y. (1995). Baroclinic dynamics of simulated tropical cyclone recurvature. *J. Atmos. Sci.* 52, 410–426. doi:10.1175/1520-0469(1995)052<0410:bdostc>2.0.co;2

Holliday, C. R., and Thompson, A. H. (1979). Climatological characteristics of rapidly intensifying typhoons. *Mon. Wea. Rev.* 107 (8), 1022–1034. doi:10.1175/1520-0493(1979)107<1022:ccorit>2.0.co;2

Hong, S., Noh, Y., and Dudhia, J. (2006). A new vertical diffusion package with an explicit treatment of entrainment processes. *Mon. Weather Rev.* 134 (9), 2318–2341. doi:10.1175/MWR3199.1

Hoskins, B. J., Mclntyre, M. E., and Robertson, A. W. (1985). On the use and significance of isentropic potential-vorticity maps. *Q. J. R. Meteorol. Soc.* 111, 877–946. doi:10.1002/qj.49711147002

Hoskins, B. J. (1990). Theory of extratropical cyclones. *Amer. Meteor. Soc.* 64, 63–80. doi:10.1007/978-1-944970-33-8_5

JTWC (1988). *1988 annual tropical cyclone report*. Guam, USA: Joint Typhoon Weather Center, 216. Available At: http://www.usno.navy.mil/NOOC/nmfc-ph/RSS/jtwc/atcr/1988atcr.pdf.

Kain, J. S. (2004). The Kain–Fritsch convective parameterization: An update. *J. Appl. Meteor.* 43, 170–181. doi:10.1175/1520-0450(2004)043<0170:tkcpau>2.0.co;2

Kieu, C., Evans, C., Jin, Y., Doyle, J. D., Jin, H., and Moskaitis, J. (2021). Track dependence of tropical cyclone intensity forecast errors in the COAMPS-TC model. *Weather Forecast.* 36 (2), 469–485. doi:10.1175/WAF-D-20-0085.1

Kim, H. M., and Jung, B. (2009). Singular vector structure and evolution of a recurving tropical cyclone. *Mon. Weather Rev.* 137 (2), 505–524. doi:10.1175/2008MWR2643.1

Kimball, S. K., and Evans, J. L. (2002). Idealized numerical simulations of hurricane–trough interaction. *Mon. Wea. Rev.* 130, 2210–2227. doi:10.1175/1520-0493(2002)130<2210:insoht>2.0.co;2

Komaromi, W. A., and Doyle, J. D. (2018). On the dynamics of tropical cyclone and trough interactions. *J. Atmos. Sci.* 75, 2687–2709. doi:10.1175/JAS-D-17-0272.1

Lander, M. (1996). Specific tropical cyclone track types and unusual tropical cyclone motions associated with a reverse-oriented monsoon trough in the Western North Pacific. *Weather Forecast.* 11, 170–186. doi:10.1175/1520-0434(1996)011<0170:stctta>2.0.co;2

Leroux, M. D., Plu, M., Barbary, D., Roux, F., and Arbogast, P. (2013). Dynamical and physical processes leading to tropical cyclone intensification under upper-level trough forcing. *J. Atmos. Sci.* 70, 2547–2565. doi:10.1175/JAS-D-12-0293.1

Leroux, M. D., Plu, M., and Roux, F. (2016). On the sensitivity of tropical cyclone intensification under upper-level trough forcing. *Mon. Weather Rev.* 144, 1179–1202. doi:10.1175/mwr-d-15-0224.1

Lewis, B. M., and Jorgensen, D. P. (1978). Study of the dissipation of hurricane gertrude (1974). *Mon. Wea. Rev.* 106 (9), 1288–1306. doi:10.1175/1520-0493(1978)106<1288:sotdoh>2.0.co;2

Li, Y., Guo, L., Ying, Y., and Hu, S. (2012). Impacts of upper-levelcold vortex on the rapid change of intensity and motion of Typhoon Meranti (2010). *J. Trop. Meteor.* 18, 207–219. doi:10.3969/j.issn.1006-8775.2012.02.010

Liu, K. S., and Chan, J. C. L. (2003). Climatological characteristics and seasonal forecasting of tropical cyclones making landfall along the south China coast. *Mon. Weather Rev.* 131, 1650–1662. doi:10.1175//2554.1

Merrill, R. T. (1988b). Characteristics of the upper-tropospheric environmental flow around hurricanes. *J. Atmos. Sci.* 45, 1665–1677. doi:10.1175/1520-0469(1988)045<1665:cotute>2.0.co;2

Merrill, R. T. (1988a). Environmental influences on hurricane intensification. *J. Atmos. Sci.* 45, 1678–1687. doi:10.1175/1520-0469(1988)045<1678:eiohi>2.0.co;2

Mlawer, E. J., Taubman, S. J., Brown, P. D., Iacono, M. J., and Clough, S. A. (1997). Radiative transfer for inhomogeneous atmospheres: RRTM, a validated correlated-k model for the longwave. *J. Geophys. Res.* 102, 16663–16682. doi:10.1029/97JD00237

Molinari, J., Skubis, S., Vollaro, D., Alsheimer, F., and Willoughby, H. E. (1998). Potential vorticity analysis of tropical cyclone intensification. *J. Atmos. Sci.* 55, 2632–2644. doi:10.1175/1520-0469(1998)055<2632:pvaotc>2.0.co;2

Molinari, J., Skubis, S., and Vollaro, D. (1995). External influences on hurricane intensity. Part III: Potential vorticity structure. *J. Atmos. Sci.* 52, 3593–3606. doi:10.1175/1520-0469(1995)052<3593:eiohip>2.0.co;2

Molinari, J., and Vollaro, D. (1989). External influences on hurricane intensity. Part I: Outflow layer eddy angular momentum fluxes. *J. Atmos. Sci.* 46, 1093–1105. doi:10.1175/1520-0469(1989)046<1093:eiohip>2.0.co;2

Molinari, J., and Vollaro, D. (1990). External influences on hurricane intensity. Part II: Vertical structure and response of the hurricane vortex. *J. Atmos. Sci.* 47, 1902–1918. doi:10.1175/1520-0469(1990)047<1902:eiohip>2.0.co;2

Montgomery, M. T., and Farrell, B. F. (1993). Tropical cyclone formation. *J. Atmos. Sci.* 50, 285–310. doi:10.1175/1520-0469(1993)050<0285:tcf>2.0.co;2

O'Shay, A. J., and Krishnamurti, T. N. (2004). An examination of a model's components during tropical cyclone recurvature. *Mon. Wea. Rev.* 132, 1143–1166. doi:10.1175/1520-0493(2004)132<1143:aeoamc>2.0.co;2

Paterson, L. A., Hanstrum, B. N., Davidson, N. E., and Weber, H. C. (2005). Influence of environmental vertical wind shear on the intensity of hurricane-strength tropical cyclones in the Australian region. *Mon. Weather Rev.* 133, 3644–3660. doi:10.1175/MWR3041.1

Patla, J. E., Stevens, D., and Barnes, G. M. (2009). A conceptual model for the influence of TUTT cells on tropical cyclone motion in the Northwest Pacific Ocean. *Weather Forecast.* 24 (5), 1215–1235. doi:10.1175/2009WAF2222181.1

Peak, J. E., and Elsberry, R. L. (1986). Prediction of tropical cyclone turning and acceleration using empirical orthogonal function representations. *Mon. Wea. Rev.* 114, 156–164. doi:10.1175/1520-0493(1986)114<0156:potcta>2.0.co;2

Peirano, C. M., Corbosiero, K. L., and Tang, B. H. (2016). Revisiting trough interactions and tropical cyclone intensity change. *Geophys. Res. Lett.* 43, 5509–5515. doi:10.1002/2016GL069040

Riehl, H., and Shafer, R. J. (1944). The recurvature of tropical storms. *J. Meteor.* 1, 42–54. doi:10.1175/1520-0469(1944)001<0001:trots>2.0.co;2

Rios-Berrios, R., and Torn, R. D. (2017). Climatological analysis of tropical cyclone intensity changes under moderate vertical wind shear. *Mon. Weather Rev.* 145, 1717–1738. doi:10.1175/MWR-D-16-0350.1

Rodgers, E. B., Chang, S. W., Stout, J., Steranka, J., and Shi, J. J. (1991). Satellite observations of variations in tropical cyclone convection caused by upper-tropospheric troughs. *J. Appl. Meteor.* 30, 1163–1184. doi:10.1175/1520-0450(1991)030<1163:soovit>2.0.co;2

Sadler, J. C. (1975). The monsoon circulation and cloudiness over the GATE area. *Mon. Wea. Rev.* 103, 369–387. doi:10.1175/1520-0493(1975)103<0369:tmcaco>2.0.co;2

Shi, J. J., Chang, S., and Raman, S. (1997). Interaction between Hurricane Florence (1988) and an upper-tropospheric westerly trough. *J. Atmos. Sci.* 54, 1231–1247. doi:10.1175/1520-0469(1997)054<1231:ibhfaa>2.0.co;2

Shu, S., Wang, Y., and Bai, L. (2013). Insight into the role of lower-layer vertical wind shear in tropical cyclone intensification over the Western North Pacific. *Acta Meteorol. Sin.* 27, 356–363. doi:10.1007/s13351-013-0310-9

Skamarock, W. C., Klemp, J. B., Dudhia, J., Gill, D. O., Barker, D. M., Wang, W., et al. (2019). *A description of the Advanced Research WRF Model version 4. NCAR Tech. Note NCAR/TN-556+STR*, 145. doi:10.5065/1dfh-6P97

Thompson, G., Field, P. R., Rasmussen, R. M., and Hall, W. D. (2008). Explicit forecasts of winter precipitation using an improved bulk microphysics scheme. Part II: Implementation of a new snow parameterization. *Mon. Weather Rev.* 136 (12), 5095–5115. doi:10.1175/2008MWR2387.1

Titley, D. W., and Elsberry, R. L. (2000). Large intensity changes in tropical cyclones: A case study of super typhoon flo during TCM-90. *Mon. Wea. Rev.* 128, 3556–3573. doi:10.1175/1520-0493(2000)128<3556:licitc>2.0.co;2

Wang, B., Elsberry, R. L., and Wang, Y. (1998). Dynamics in tropical cyclone motion: A review. *Chin. J. Atmos. Sci.* 22, 416–434.

Wang, H., Wang, Y., and Xu, H.-M. (2013). Improving simulation of a tropical cyclone using dynamical initialization and largescale spectral nudging: A case study of typhoon megi (2010). *Acta Meteorol. Sin.* 27, 455–475. doi:10.1007/s13351-013-0418-y

Wang, Y., Rao, Y., Tan, Z.-M., and Schonemann, D. (2015). A statistical analysis of the effects of vertical wind shear on tropical cyclone intensity change over the Western North Pacific. *Mon. Weather Rev.* 143, 3434–3453. doi:10.1175/MWR-D-15-0049.1

Wang, Y., and Wu, C.-C. (2004). Current understanding of tropical cyclone structure and intensity changes-A review. *Meteorol. Atmos. Phys.* 87, 257–278. doi:10.1007/s00703-003-0055-6

Wei, N., Li, Y., Zhang, D. L., Mai, Z., and Yang, S. Q. (2016). A statistical analysis of the relationship between upper-tropospheric cold low and tropical cyclone track and intensity change over the Western North Pacific. *Mon. Wea. Rev.* 144, 1805–1822. doi:10.1175/MWR-D-15-0370.1

Wu, C., Chen, S., Chen, J., Chou, K., and Lin, P. (2009). Interaction of Typhoon Shanshan (2006) with the midlatitude trough from both adjoint-derived sensitivity steering vector and potential vorticity perspectives. *Mon. Weather Rev.* 137 (3), 852–862. doi:10.1175/2008mwr2585.1

Xin, J.-J., Yu, H., and Chen, P.-Y. (2021). Evaluation of tropical cyclone intensity forecasts from five global ensemble prediction systems during 2015-2019. *J. Trop. Meteor.* 27 (3), 218–231. doi:10.46267/j.1006-8775.2021.020

Yan, Z., Ge, X., Wang, Z., Wu, C., and Peng, M. (2021). Understanding the impacts of upper-tropospheric cold low on typhoon jongdari (2018) using piecewise potential vorticity inversion. *Mon. Weather Rev.* 149 (5), 1499–1515. doi:10.1175/MWR-D-20-0271.1

Yu, H., and Kwon, H. J. (2005). Effect of TC–trough interaction on the intensity change of two typhoons. *Weather Forecast.* 20 (2), 199–211. doi:10.1175/WAF836.1

Zehr, R. M. (2003). Environmental vertical wind shear with Hurricane Bertha (1996). *Weather Forecast.* 18, 345–356. doi:10.1175/1520-0434(2003)018<0345:evwswh>2.0.co;2

Zhang, G., Wang, Z., Dunkerton, T. J., Peng, M. S., and Magnusdottir, G. (2016). Extratropical impacts on Atlantic tropical cyclone activity. *J. Atmos. Sci.* 73, 1401–1418. doi:10.1175/JAS-D-15-0154.1

Zhang, W., Leung, Y., and Chan, J. C. L. (2013). The analysis of tropical cyclone tracks in the western north pacific through data mining. Part II: Tropical cyclone landfall. *J. Appl. Meteorol. Climatol.* 52 (6), 1417–1432. doi:10.1175/JAMC-D-12-046.1

Zhou, G. B., Liu, L., and Dong, L. (2022). The analysis of characteristics and forecast difficulties of TCs in Western North Pacific in 2020. *Meteorol. Mon.* 48 (4), 504–515. doi:10.7519/j.issn.1000-0526.2021.112401

frontiers | Frontiers in Earth Science

TYPE Original Research
PUBLISHED 13 January 2023
DOI 10.3389/feart.2022.1024979

OPEN ACCESS

EDITED BY
Liguang Wu,
Fudan University, China

REVIEWED BY
Qinglan Li,
Shenzhen Institutes of Advanced Technology (CAS), China
Zifeng Yu,
China Meteorological Administration, China
Wei Tian,
Nanjing University of Information Science and Technology, China

*CORRESPONDENCE
Bin Mu,
binmu@tongji.edu.cn

SPECIALTY SECTION
This article was submitted to Atmospheric Science, a section of the journal Frontiers in Earth Science

RECEIVED 22 August 2022
ACCEPTED 10 November 2022
PUBLISHED 13 January 2023

CITATION
Yuan S, You Q, Mu B, Qin B and Xu J (2023), Estimating the tropical cyclone wind structure using physics-incorporated networks.
Front. Earth Sci. 10:1024979.
doi: 10.3389/feart.2022.1024979

Estimating the tropical cyclone wind structure using physics-incorporated networks

Shijin Yuan[1], Qianhu You[1], Bin Mu[1]*, Bo Qin[1] and Jing Xu[2]

[1]School of Software Engineering, Tongji University, Shanghai, China, [2]State Key Laboratory of Severe Weather, Chinese Academy of Meteorological Sciences, China Meteorological Administration, Beijing, China

Satellite-based remote sensing technology plays a significant role in identifying tropical cyclones (TCs), and most of the current research focuses on intensity estimation. However, analyzing the wind structure of TCs, which is directly related to the danger they bring, remains a challenge. By adding prior knowledge of TCs into the model, we propose a physics-incorporated network based on multi-task learning to estimate wind radii and intensity, whose layers can automatically extract rotation-invariant features related to the TC core from multichannel satellite imageries. In addition, we build a more comprehensive dataset, including global Statistical Hurricane Intensity Prediction Scheme (SHIPS) predictors, to tackle the structure task. We compare our model with existing methods, and it shows that our model gets better results in estimating 50-knot and 64-knot wind radii and achieves a 4.87-knot root-mean-squared error (RMSE) of intensity. By predicting probability density functions, our model quantifies the uncertainty of the result. The experimental results show that the incorporation of rotation equivariance into the layers can enhance TC structure estimation. By considering the feature importance of multi-source predictors, we find that our model pays attention to key predictors related to the TC structure. Specifically, the tangential wind speed at 500 km from the TC center and the radius of the 5-knot wind both greatly reduce the error of the estimated parameters. Finally, two case studies show that the proposed model performs well most of the time during TCs' rapid intensification. However, when TCs' system is not well organized, estimating the wind structure is challenging.

KEYWORDS

tropical cyclone wind structure, physics-incorporated network, multi-task learning, rotation-invariant features, multi-source predictors

1 Introduction

TCs combined with high winds and heavy rainfall are considered extreme weather phenomena that cause significant damage to coastal areas around the world, and the potential damage level of a TC is determined by its surface wind field (Maclay et al., 2008). Estimating TC near-surface winds accurately helps operational centers make better forecasts. The radius of maximum winds (RMW) and different maximum radial extents of wind speed thresholds, like 34-, 50-, and 64-kt (R34, R50, and R64), are used by operational centers to represent the wind field. U.S. TC warning centers include these parameters in input files (i.e., "TC vitals" files) for assimilation to improve TC-focused numerical weather prediction (Knaff et al., 2021).

The most direct way to obtain TC winds is using spaceborne active radars such as scatterometers (Figa-Saldaña et al., 2002; Stiles et al., 2014), but it is not possible to get an expected frequency because they are usually located on polar-orbiting satellites that only scan the same TC twice a day. To meet operational needs, we can use geostationary satellites, which typically collect data every 15 minutes. Infrared imageries that observe cloud features from geostationary satellites have been used to locate the TC center and identify cloud band distribution by the conventional Dvorak method (Dvorak, 1975). Knaff et al. (2014b) demonstrated that features extracted from infrared imageries are related to structural parameters such as wind radii. With the advent of higher resolution instruments, infrared imageries are more widely used to estimate the TC structure, especially by statistical methods (Dolling et al., 2016; Reul et al., 2017).

However, traditional statistical methods do not make effective use of data. Following the success of deep learning in the field of computer vision, Pradhan et al. (2018) first applied deep convolutional neural networks (CNN) to estimate the intensity of TCs and obtained better results than the optimal model at that time. The current consensus is that incorporating prior knowledge can efficiently enhance prediction skills. Chen B. et al. (2018) blended multiple TC intensity estimations, thus reducing the variance of results caused by rotation. Chen et al. (2021) also obtained better performance on the TC structure task by using convolutional kernels on polar coordinates compared with Cartesian coordinates. By incorporating the knowledge of meteorology, such as the rotation invariance of TCs, these models achieve better results. In this study, we further incorporate the rotation invariance of TCs into the model structure using rotation-equivariant layers, which can output permuted features with rotated input.

Besides optimizing the model structure, data is a crucial component of deep learning. In addition to satellite imageries, we can infuse auxiliary information to improve the model's performance (Chen B.-F. et al., 2019). Zhuo and Tan (2021) showed that the inclusion of TC fullness can help the model improve TC structure estimation. There are many available auxiliary variables related to the TC structure. Knaff et al. (2014b) showed that the radius of a 5-kt wind can represent TC size variations. Environmental variables are also critical for analyzing the TC structure since the ocean and the atmosphere exchange a lot of energy when TCs are active. For example, the central pressure deficit increases with increasing intensity, size, and the Coriolis parameter (Chavas et al., 2017). A decrease in the sea surface temperature (SST) under a TC's eye has a significant impact on the TC intensity (Schade, 2000). To incorporate the previously mentioned and additional variables into the model, we build a dataset by collecting large-scale SHIPS predictors from multiple sources.

As mentioned previously, we propose the physics-incorporated network to tackle the TC structure task by extracting rotation-invariant features and combining multiple sources of auxiliary information. To show the efficacy of our methods, we conduct comparison experiments, the structure ablation study, the predictor sensitivity study, and the case study. First, we evaluate the model's performance under an operational setting and obtain 39.90, 21.35, 11.80, and 24.86 km mean absolute error (MAE) on R34, R50, R64, and RMW. The RMSE of the model on intensity reaches an error of 4.87 kt. To make more informed predictions, Softmax is used as the activation layer to predict probability density functions. We can select bins with high confidence to further enhance the credibility of the results. Second, we compare models with and without rotation-equivariant layers, which shows that rotation-equivariant layers can further extract rotation-invariant features from infrared imageries on the TC structure task. Third, we conduct experiments about predictors to get more insight from the model. By incorporating these predictors, our model surpasses the baseline in estimating the wind radii of TCs by 18.5%, 18.2%, 18.6%, 20.2%, and 55.7% for R34, R50, R64, RMW, and intensity, respectively. Then, we calculate feature attributions on estimated parameters and find that it takes into account important predictors associated with the TC structure. Among the 120 predictors we use, the model focuses on predictors related to the TC size derived from infrared imageries. Finally, we select two TCs to analyze our model.

This study is organized as follows. Section 2 describes the structure of our model and the composition of the dataset. Section 3 discusses experiments and results, including comparison experiments, the structure ablation study, the predictor sensitivity study, and the case study. Section 4 concludes our study.

2 Methods

2.1 Physics-incorporated network

2.1.1 Network architecture

We develop the physics-incorporated network, as shown in Figure 1, to estimate wind radii and intensity. The input to our model consists of two parts: satellite imageries and predictors. First, we use a deep residual network as the backbone to extract features from images. Second, the predictors are concatenated as the input of fully connected layers. In computer vision, much work has confirmed the effectiveness of convolutional neural networks with residuals (He et al., 2016; Chen H. et al., 2019; He et al., 2020). Shortcut connections in the residual network help the first few layers get updates efficiently, and the vanishing

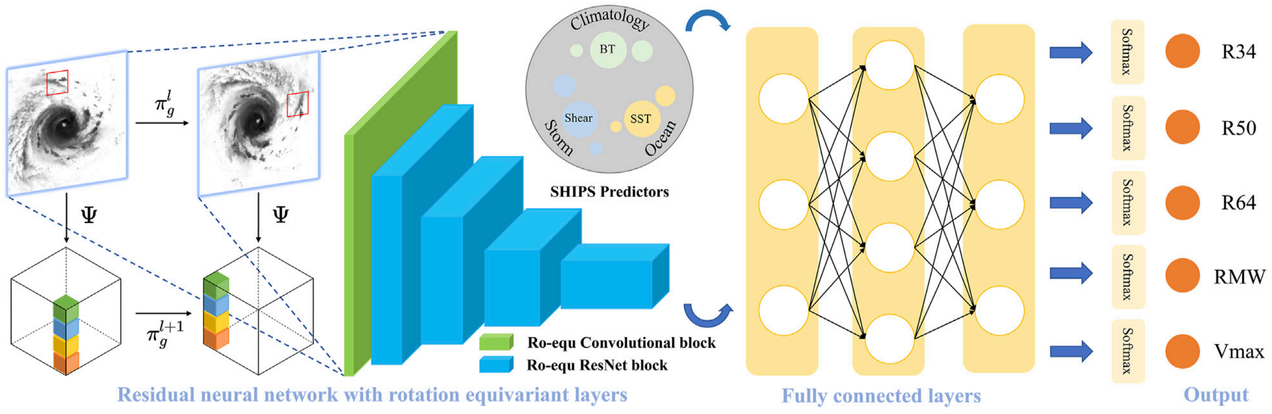

FIGURE 1
Overview of the physics-incorporated network. Residual neural network with rotation-equivariant (Ro-equ) layers extracts rotation invariance features from satellite imageries. Then, the extracted features and SHIPS predictors are combined in one tensor to be the input of fully connected layers in terms of feature representations. The last layer of the model applies softmax to output probabilistic results. Finally, we calculate the expectation to get the final estimation value.

gradient problem no longer happens. We endeavor to improve model performance by incorporating the physical knowledge of TCs into the model. It is known that a TC can be seen as a tropical mesoscale convective system with rotation invariance. The rotation-invariant feature is important for identifying arbitrary-oriented objects. Feeding a rotated image to a regular CNN is not the same as rotating feature maps of the original image. Group equivariant convolutional neural networks extend the equivariance of convolutional neural networks from translation to rotation (Cohen and Welling, 2016), and more experiments (Worrall et al., 2017) demonstrate the validity. Given a transformation group G and a function Φ: $X \to Y$, equivariance can be expressed as follows:

$$\Phi\left[T_g^X(x)\right] = T_g^Y[\Phi(x)] \quad \forall (x,g) \in (X,G), \tag{1}$$

where T_g indicates a group action in the space. The translation equivariant of CNNs can be expressed as follows:

$$[[T_t f]*\psi](x) = [T_t[f*\psi]](x), \tag{2}$$

where T_t denotes an action of the translation group $(\mathbb{R}^2, +)$, and we apply it to K-dimension feature maps f: $\mathbb{Z}^2 \to \mathbb{R}^K$. The convolution filter can be represented as ψ: $\mathbb{Z}^2 \to \mathbb{R}^K$, and $*$ indicates convolution operation. Rotation-equivariant layers are based on the cyclic group C_N containing discrete rotations by angles multiple of $\frac{2\pi}{N}$. The rotation-equivariant convolution can be defined as follows:

$$\left[[T_g f]*\psi\right](g) = \left[T_g[f*\psi]\right](g), \tag{3}$$

where G is a semidirect product of the translation group and the rotation group. Our model stacks rotation-equivariant layers with a higher degree of weight sharing. The extracted features and multi-source predictors are concatenated as the input of fully connected layers. At last, the output of the fully connected layers is separated into five parts on average before feeding to the last layer.

2.1.2 Loss function and metrics

The optimization objective of our model contains five components: R34, R50, R64, RMW, and intensity. Manually adjusting the loss coefficient for each task not only wastes computational resources but also makes it difficult to trade off each task. We use dynamic weight averaging (DWA) (Liu et al., 2019) to learn the adaptive weights λ_k for each task k, where w_k represents the relative descending rate between epochs as follows:

$$\lambda_k(t) := \frac{K\exp\left(w_k(t-1)/T\right)}{\sum_i \exp\left(w_i(t-1)/T\right)},\ w_k(t-1) = \frac{\mathcal{L}_k(t-1)}{\mathcal{L}_k(t-2)}, \tag{4}$$

where $\mathcal{L}_k(t)$ is calculated as the average loss value in epoch t over iterations. For $t = 1, 2$, $w_k(t)$ is initialized as 1. T adjusts the softness of task weighting, and it is set to 2. The sum of task weighting is equal to the number of tasks. Compared with other methods (Chen Z. et al., 2018), DWA is easy to implement since it does not require internal gradient calculation. However, assessing the uncertainty of estimations is difficult for regression tasks. One way to estimate uncertainty is by producing probabilistic output. To enable our model to output probabilistic results, we convert the output value into 100 bins of equal width, and the last activation layer is replaced with Softmax (Clare et al., 2021), which predicts the probability density of the categories of targets. In this way, we collect notably more information from our network predictions. To obtain the final results, we calculate the expectation of the probability values using the following equation:

$$\mathbb{E}[X] = \sum_{i=1}^{100} x_i \mathbb{P}(X = x_i). \tag{5}$$

We choose MAE as the metric for wind radii tasks because of its robustness to anomaly data and MSE as the metric for the intensity task.

2.2 Tropical cyclone wind dataset

Currently, most of the datasets related to TC winds use satellite data. It is worth noting that they do not consider auxiliary information, including environmental variables. Knaff et al. (2017) developed a global statistical–dynamical TC wind radii forecast scheme using a subset of SHIPS predictors. We can further make use of these predictors on the TC structure task. As far as we know, there is no available dataset containing these variables. Therefore, we build the Tropical Cyclone Wind Dataset (TCWD), which includes multi-source variables and satellite imageries, to further explore the TC structure.

TCWD collects Statistical Hurricane Intensity Prediction Scheme (SHIPS) predictors related to climatology, persistence, the atmosphere, and the ocean (DeMaria et al., 2005). These predictors are used to predict the rapid intensification of TCs (Kaplan et al., 2015; Xu et al., 2021). With a large number of variables being added to the predictors, we can use deep neural networks to learn complex nonlinear relationships. Predictors related to brightness temperature (BT) are derived from GOES infrared imageries, which provide information about the structure of the deep convection near the TC center. Several predictors are obtained from the GOES Channel 4 (10.7 μm) imagery. The Channel 4 BT were azimuthally averaged on a 4-km, TC-centered radial grid. The BT standard deviations from the azimuthal average were also calculated at each radius. Storm environment predictors are derived from numerical models such as the global forecasting system (GFS), which include zonal and meridional wind, shear, vorticity, and divergence. The zonal component of motion distinguishes between TCs in easterly and westerly basic currents. The divergence measures synoptic-scale forcing. The climatological SST and the climatological depth of the 20 °C isotherms are derived from the 2005–2010 mean of the Navy Coupled Ocean Data Assimilation analyses. Oceanic predictors along the path of the TCs include oceanic heat content derived from Navy Coupled Ocean Data Assimilation (NCODA) analyses.

The SHIPS development version dataset includes reanalysis data for over 100 predictors, most of which are applicable every 6 hours, but only 20% of which are actually applied to operational forecasts. Unlike the reanalysis data, the operational data are only applicable when National Hurricane Center (NHC) forecasts are available, and the Joint Typhoon Warning Center (JTWC) maintains operational data for other regions. The operational data tend to have larger errors than the reanalysis data. The TCWD contains all available predictors from the operational version of the SHIPS dataset at the time step of 0 h. The data are interpolated every 3 hours.

The satellite imageries consist of four channels, as shown in Figure 2. We collect infrared (IR) imageries, water vapor (WV), and visible (VIS) from GridSat (Knapp et al., 2011), and the passive microwave rain rate (PMW) from CMORPH (Xie et al., 2017). The imageries are externally cut rectangles with the center of the TCs as the center of the circle. For each imagery, there are 161 × 161 pixels, and the resolution is 7/100° lat/lon. The actual distance between two pixels is about 7.7 km. We replace the missing data with zero because it does not affect convolution operations.

The wind radii and intensity labels come from JTWC and the Tropical Cyclone Extended Best Track Dataset (EBTRK) (Demuth et al., 2006). We interpolated the labels every 3 h to get more samples and applied a nonzero-azimuthal average to get the wind radii labels since they are recorded for each quadrant (NE, SE, SW, and NW).

TCWD contains 90486 samples from 1614 TCs, of which 55,218 samples contain SHIPS predictors. The training set contains 67,454 samples from 2004 to 2016. A total of 10,824 samples from 2017 to 2019 are selected as the validation set, and 12,198 samples from 2018 to 2020 are selected as the test set. Table 1 shows the sample number of SHIPS predictors that are available. The TCWD is a benchmark dataset for the structure analysis of TCs.

3 Experiments and result

3.1 Training and testing

We use the Adam optimizer (Kingma and Ba, 2015) to train the network, and the learning rate is set to 0.001. Every ten epochs, we reduce the learning rate by half. When the model shows no improvement after 20 epochs, we will stop training. To make the experiments consistent, we train and test our models on the data that contains SHIPS predictors. To simulate operational predictions, only IR and WV channels are used because the PMW channel has a delay. We exclude the VIS channel because the VIS channel is unstable at night. The input is filled with zero when the predictors are not available.

3.2 Comparison experiments

In this section, we compare the performance of our model with other TC structure estimate methods. The final model,

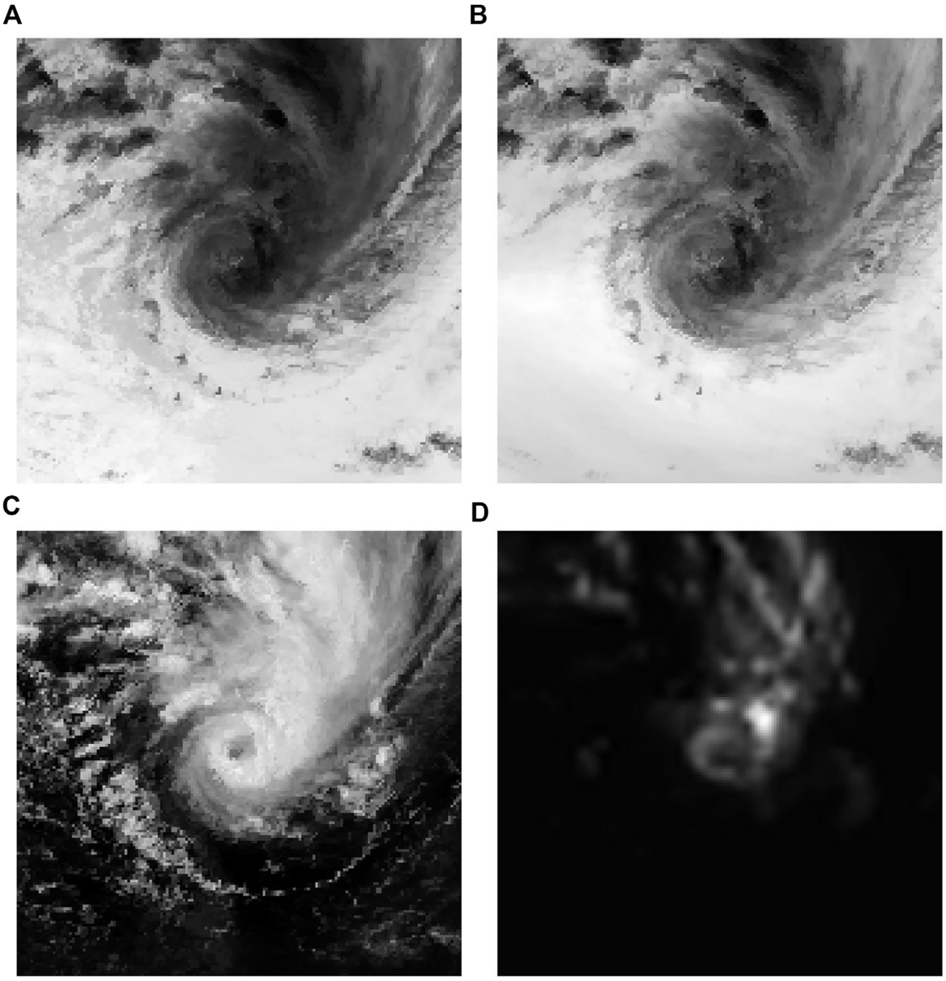

FIGURE 2
Four channels of a TC from TCWD. **(A)** Infrared. **(B)** Water vapor. **(C)** Visible. **(D)** Passive microwave rain rate.

TABLE 1 Tropical cyclone wind dataset description.

	R34 sample	R50 sample	R64 sample	RMW sample	Intensity sample
Training	32810	19950	12159	40551	48212
Validation	2291	1361	824	2835	2995
Test	3055	1808	1029	3762	4021

combined with rotation equivariance and SHIPS predictors, produces MAEs of 39.90, 21.35, 11.80, and 24.86 km for R34, R50, R64, and RMW, respectively, which is better than those of Knaff et al. (2016) and close to the deviation angle variance technique (Dolling et al., 2016). To compare with other deep learning methods, we collect satellite imageries from the same source. However, there are still inconsistencies between datasets, such as the year of the sample. A subjective comparison suggests that the errors of all estimated parameters are lower than those reported by Knaff et al. (2016) and Chen et al. (2021). The RMSE of the model on intensity reaches an error of 4.87 kt, which is currently the best model for estimating the intensity to the best of our knowledge. Compared with DeepTCNet (Zhuo and Tan, 2021), our model yields better results on R50, R64, and intensity. There are some gaps between our model and DeepTCNet in estimating R34 and RMW because the DeepTCNet takes TC

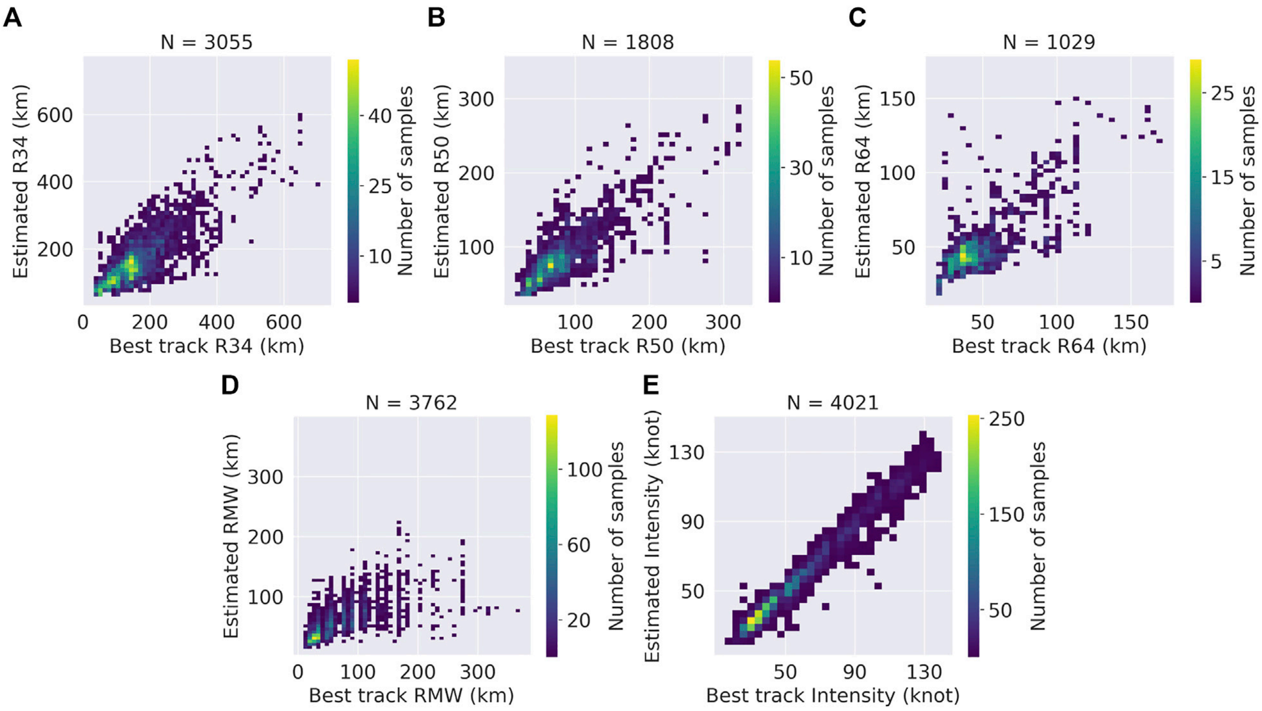

FIGURE 3
Scatter plot of the degree of fit and dispersion for estimated R34 **(A)**, R50 **(B)**, R64 **(C)**, RMW **(D)**, and intensity **(E)**. The model is evaluated on the test set for TCs in 2018 and 2020.

fullness calculated from TC vitals (namely, R34 and RMW) as the input. It is difficult for the DeepTCNet to achieve the corresponding performance in a real-time setting. To evaluate the performance of our model for each estimated parameters, a scatter plot and a box diagram are used. The vertical axis represents the estimated values of our model, while the horizontal axis represents the labels from the best track. From Figure 3, it is seen that the estimated TC wind radii are consistent with the best track data. However, the model underestimates TCs with high RMW due to the strongly convecting inner core. On the other hand, since these parameters in the best tracks are not subjected to vigorous post-storm review (Knaff et al., 2021), the result of our model is reasonable. In particular, Figure 4 shows that the estimated intensity is almost in line with the best track data. Although our model tends to underestimate the intensity of TCs, we can conclude that our model is robust and generalizes well. Because we need to estimate multiple variables, we use DWA to calculate the loss. We train a ResNet to estimate wind structure with different loss coefficients in Table 3. Compared with manually setting the loss coefficient, DWA achieves the smallest normalized error. Finally, we evaluate the probabilistic results from the model. Since we use the Softmax layer, we can also get the probability of each interval, which is equally divided by the minimum and maximum values of the label. Figure 5 shows that it is difficult to take the bin with the predicted highest probability, that is, top 1, as the correct bin. But when we take the top five bins, the chances of getting the correct result are greatly

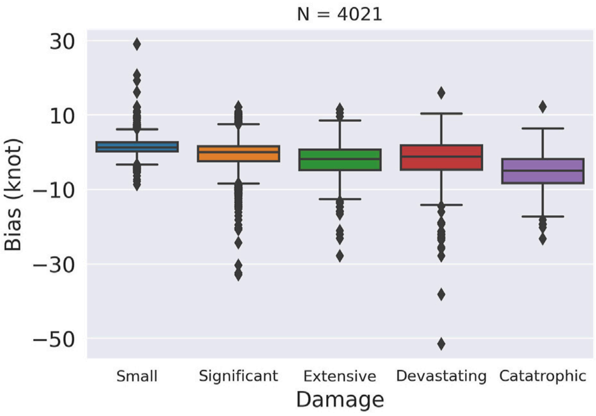

FIGURE 4
Box diagram of the bias plot for TCs by different scales of damage. The model is evaluated on the test set for TCs in 2018 and 2020. Although a small number of anomalous points can be observed, the majority of estimation results are within the 10-knot bias, which is sufficiently accurate.

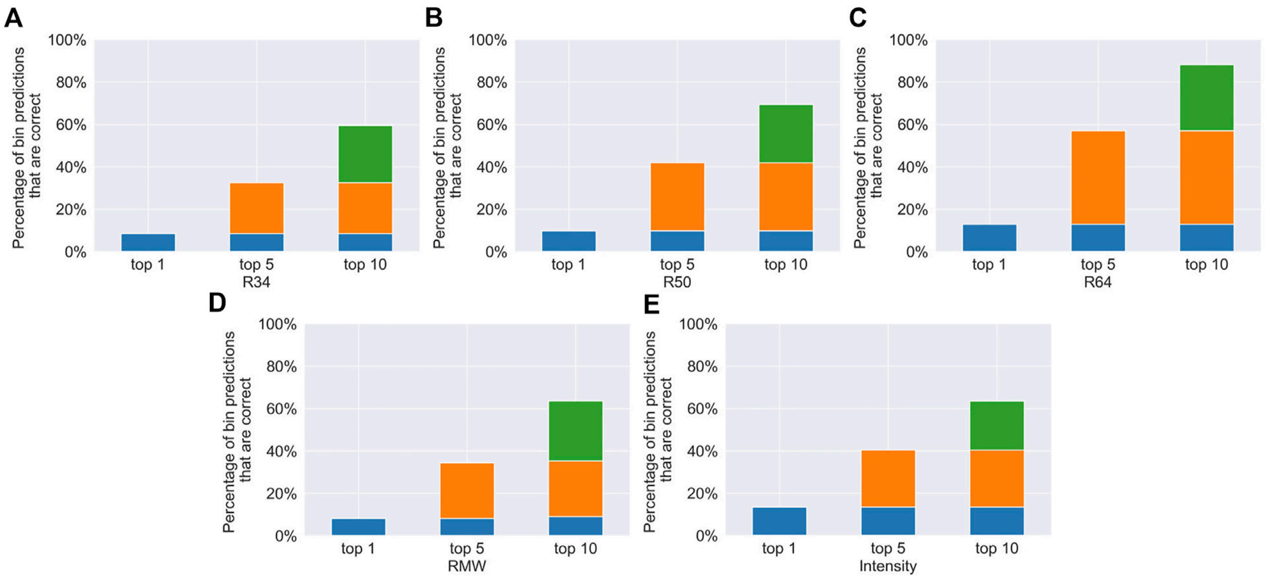

FIGURE 5
Percentage of all samples on the test set for TCs in 2018 and 2020 where one of the top *k* most likely bins predicted by our model is the observed bin for R34 **(A)**, R50 **(B)**, R64 **(C)**, RMW **(D)**, and intensity **(E)**, respectively. The *k* is set to 1, 5, and 10. Different colors are used to indicate the gap between columns.

increased. Moreover, about 60% of the test samples are correctly classified in the top 10 bins. Given that there are 100 bins, the probabilistic results are valuable in weather forecasting. In terms of probabilistic results, our model excels at estimating R64 and R50.

3.3 Structure ablation study

This part performs ablation studies based on satellite data and predictors by adding rotation-equivariant layers to demonstrate the efficacy of the model structure. As shown in Table 2, the incorporation of the rotation equivariance property improves the errors of wind radii and intensity by 3.1% and 3.0%, on average, compared with ResNet without the rotation-equivariant layers (baseline). We also compare models with the inclusion of SHIPS predictors, and the rotation equivariance layers reduce the error of wind radii and intensity by 1.3% and 5.0%, on average. This proves that our model can extract more features independent of rotation by assuming that the TC is fairly axis-symmetric with respect to the center.

However, it should be noted that the errors for best track wind radii could be as high as 40% decades ago, differing by year and observation. The errors in the best track intensity have been estimated to be more than 10% (Landsea and Franklin, 2013). In recent years, TC warning centers have made efforts to reanalyze the estimations. Moreover, as the quality of observations improves, the error will become smaller. To mitigate the TC-related damage, it is necessary to further improve the wind structure estimations.

3.4 Predictor sensitivity study

We find that the model incorporating SHIPS predictors surpasses the baseline in estimating the wind radii of TCs by 18.5%, 18.2%, 18.6%, 20.2%, and 55.7% for R34, R50, R64, RMW, and intensity, respectively. Due to limited knowledge, it is difficult to manually identify the importance of predictors. If a feature is important, then it should be crucial for the output and have a high value. So a baseline approach for computing the contribution degree is to multiply the input with the gradient with respect to the input (Shrikumar et al., 2017). However, this method violates the axiom of sensitivity, which can be solved by approximating the product of the gradient integral and the input x_i as follows (Sundararajan et al., 2017):

$$\text{IntegratedGrads}\left(x_i\right) = \left(x_i - x_i'\right)\int_0^1 \frac{\partial F\left(x' + \alpha\left(x - x'\right)\right)}{\partial x_i} d\alpha. \tag{6}$$

We get the top 10 most important predictors and contribution degree to each parameter, as shown in Table 4, by normalizing them across all the inputs for each feature (the 120 final predictors used in this study are listed in Supplementary Table S1). Obviously, our model pays attention to IR-related

TABLE 2 Comparison of our models with other methods.

Model	Input Channel		MAE (km)			RMSE (kt)
		R34	R50	RMW	R64	Intensity
Knaff et al. (2016)	IR	68.5	37.0	22.2	-	-
Dolling et al. (2016)	IR	38.5	23.2	13.5	-	-
Chen et al. (2021)	IR, WV, and PMW	50.58	-	-	-	10.43
Zhuo and Tan (2021)	IR	**31.82**	21.83	13.51	**13.51**	8.7
ResNet (Baseline)	IR and WV	49.87	26.29	14.93	31.19	11.59
+ Ro-equ layers	IR and WV	48.54	25.61	13.94	31.05	11.24
+ SHIPS predictors	IR and WV	40.64	21.49	12.14	24.87	5.13
Final model	IR and WV	39.90	**21.35**	**11.80**	24.86	**4.87**

These bold values represent the optimal values for each column.

TABLE 3 Dynamic weight averaging contrastive experiment.

Loss coefficient	R34 loss	R50 loss	R64 loss	RMW loss	Intensity loss	Normalized loss
DWA	53.565	**29.808**	**17.747**	28.563	11.206	**20.459**
0.2:0.2:0.2:0.2:0.2	53.304	32.021	18.667	29.344	11.452	21.082
0.6:0.1:0.1:0.1:0.1	52.405	31.801	18.743	28.645	11.983	21.117
0.1:0.6:0.1:0.1:0.1	**52.057**	31.184	18.824	28.362	11.821	20.889
0.1:0.1:0.6:0.1:0.1	52.934	30.900	18.270	28.425	11.491	20.705
0.1:0.1:0.1:0.6:0.1	52.290	32.066	18.998	**27.698**	11.225	20.554
0.1:0.1:0.1:0.1:0.6	56.230	32.583	19.043	28.026	**10.659**	20.889

These bold values represent the optimal values for each column.

TABLE 4 Top 10 most important predictors and contribution degree to estimated parameters.

Rank	R34		R50		R64		RMW		Intensity	
1	IR00_v20	0.069	IR00_v20	0.116	IRM3_v20	0.061	IR00_v19	0.060	IRM1_v20	0.066
2	IRM1_v19	0.063	IRM1_v20	0.098	IRM1_v20	0.051	IRM1_v20	0.057	IR00_v19	0.065
3	IRM1_v20	0.061	IRM3_v20	0.088	IR00_v20	0.051	IR00_v20	0.056	IRM1_v19	0.061
4	IRM3_v20	0.059	IRM1_v19	0.055	IRM1_v19	0.043	IR00_v18	0.054	IR00_v18	0.057
5	IR00_v19	0.058	IRM1_v18	0.052	PENC	0.043	IRM1_v19	0.053	IR00_v20	0.056
6	IRM1_v18	0.057	IR00_v19	0.051	IRM3_v19	0.040	IRM1_v18	0.047	IRM1_v18	0.055
7	IR00_v18	0.057	IR00_v18	0.051	IRM1_v18	0.039	IRM3_v19	0.047	IRM3_v19	0.054
8	IRM3_v19	0.053	IRM3_v19	0.050	IRM3_v18	0.038	IRM3_v18	0.046	IRM3_v18	0.053
9	IRM3_v18	0.052	IRM3_v18	0.043	T250	0.036	IRM3_v20	0.039	IRM3_v20	0.050
10	PENC	0.030	PENC	0.025	IR00_v18	0.030	CSST	0.030	IRM3_v6	0.025

For IR-based variables, IR00 represents the variables at the current time. IRM1 and IRM3 mean 1.5 and 3 h before current time, respectively. The postfix is used to distinguish different variables.

IR00_v18 (V500) is an IR-based estimate of the tangential wind speed at 500 km from the TC center.

IR00_v19 (R5) is an IR-based estimate of the radius (km) of the 5-knot wind.

IR00_v20 is a scaling factor for R5 based on climatological values based just on intensity.

PENC is the azimuthally averaged surface pressure at the outer edge of the vortex.

T250 is 200–800 km area average 250 hPa temperature (°C × 10).

CSST is climatological SST.

TABLE 5 Top five most important predictors and contribution degree to estimated parameters except TC size estimation variables.

Rank	R34		R50		R64		RMW		Intensity	
1	PENC	0.030	PENC	0.025	PENC	0.043	CSST	0.030	IRM3_v6	0.025
2	Z000	0.030	TWXC	0.018	T250	0.036	T250	0.025	IRM3_v11	0.020
3	PENV	0.029	TWAC	0.018	TWXC	0.028	IRM3_v6	0.021	IRM3_v16	0.020
4	CD20	0.019	PENV	0.013	COHC	0.024	IR00_v11	0.017	IRM3_v10	0.019
5	IRM3_v11	0.019	T150	0.013	DELV	0.019	IR00_v6	0.015	IR00_v11	0.018

For IR-based variables, IR00 represents the variables at the current time. IRM1 and IRM3 mean 1.5 and 3 h before current time, respectively. The postfix is used to distinguish different variables.
PENC is the azimuthally averaged surface pressure at the outer edge of the vortex.
Z000 is 1000-hPa height deviation (m) from the U.S. standard atmosphere.
PENV is 200–800-km average surface pressure [(hPa −1000) × 10].
CD20 is climatological depth (m) of 20°C isotherms from 2005 to 2010 NCODA analyses.
IR00_v10/IR00_v11 is percentage area r = 50–200 km of the GOES Channel 4 BT < (−50)/(−60)°C.
TWXC is the maximum 850-hPa symmetric tangential wind at 850 hPa from NCEP analysis (ms^{-1} × 10).
TWAC is 0–600-km average symmetric tangential wind at 850 hPa from NCEP analysis (ms^{-1} × 10).
T150/T250 is a 200–800 km area average 150/250 hPa temperature (°C × 10).
COHC is the climatological depth (m) of ocean heat content ($kJ\ cm^{-2}$) isotherm from 2005 to 2010 NCODA analyses.
DELV is the last 12-h intensity change (kt).
CSST is climatological SST.
IR00_v6 is the percentage area r = 50–200 km of GOES Channel 4 BT < − 10°C.
IR00_v16 is the average brightness temperature from 20- to 120-km radius (°C × 10).

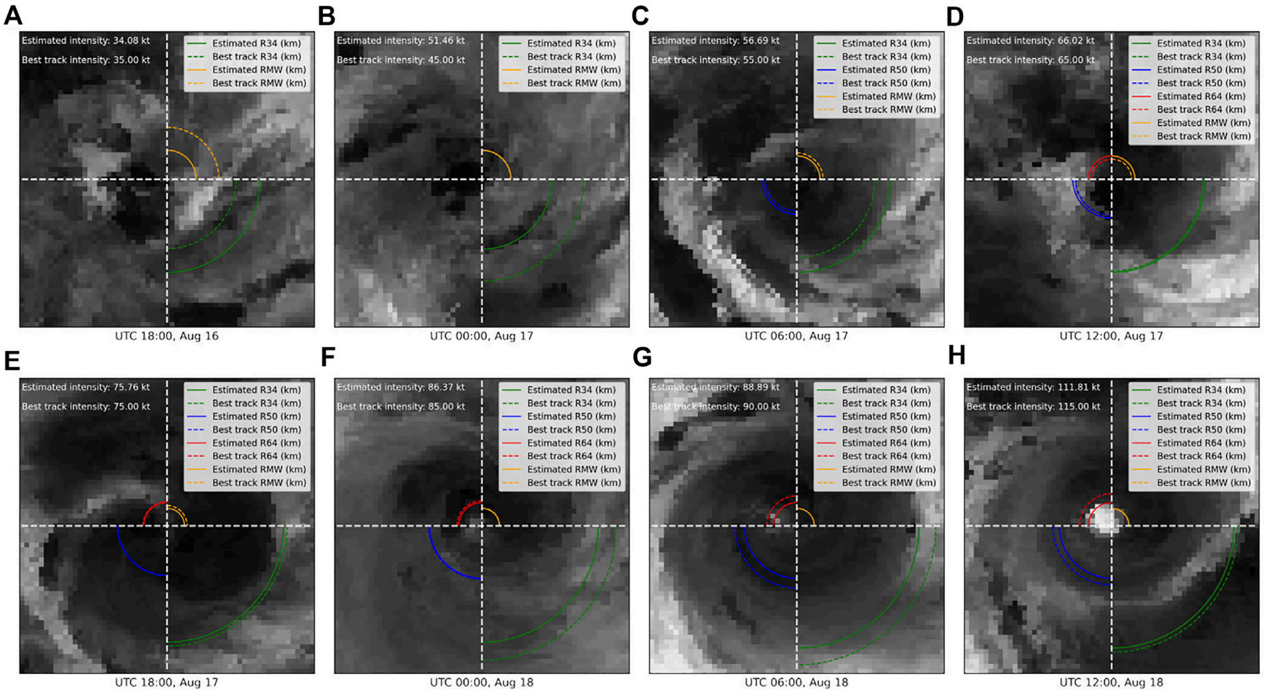

FIGURE 6
Plots of estimated R34, R50, R64, RMW, and intensity of Hurricane Genevieve throughout its intensification.

predictors, which are extracted from Geostationary Operational Environmental Satellite (GOES) data. V500, R5, and the scaling factor are TC size estimation variables that rank in top 3. V500 is regressed by the sine of the latitude, and the first three normalized principle components (PCs) are azimuthally averaged radial profiles of IR brightness temperatures. R5 is the radius where the TC wind field is indistinguishable from the background flow in a climatological environment. Knaff et al.

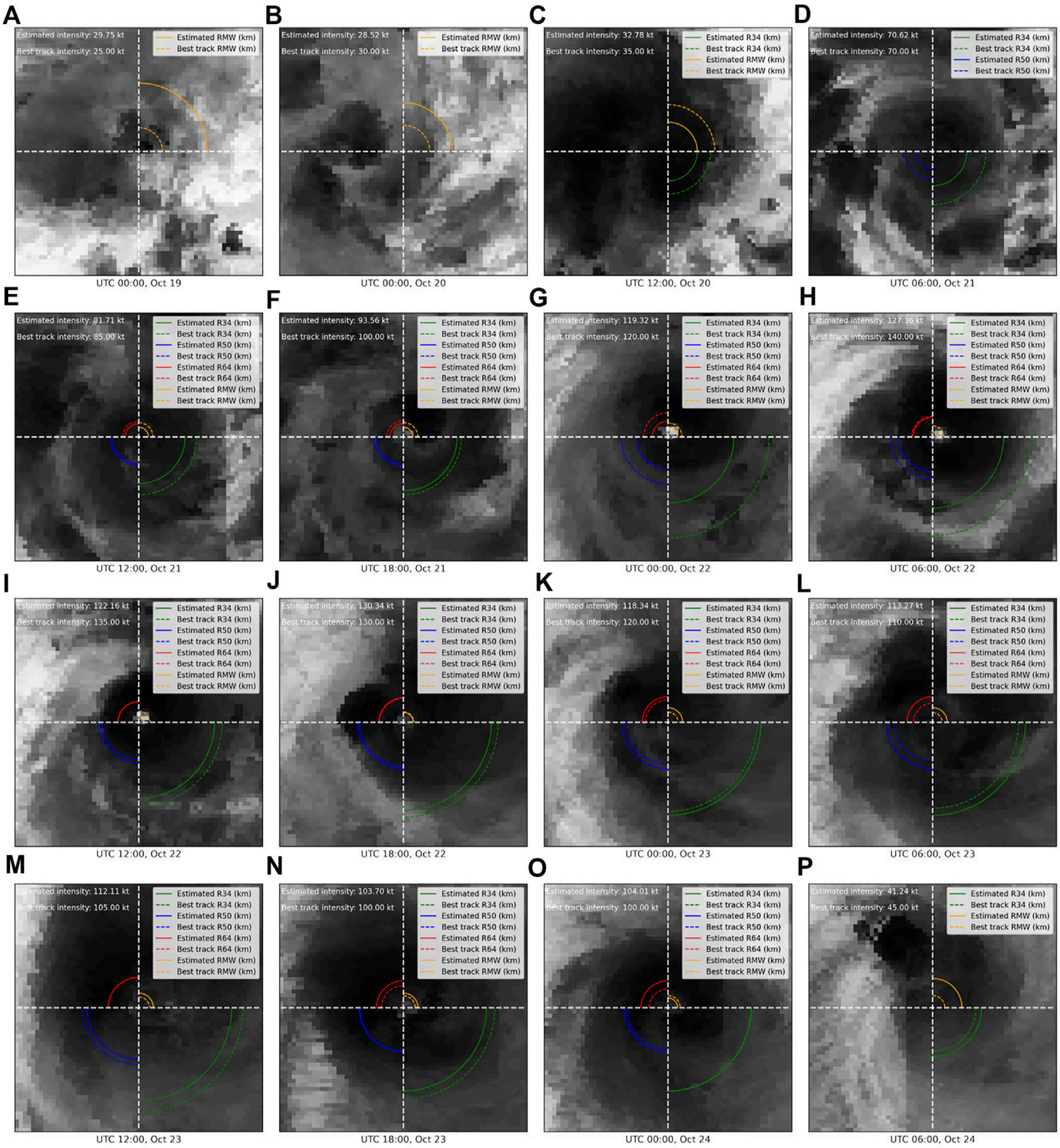

FIGURE 7
Plots of estimated R34, R50, R64, RMW, and intensity of Hurricane Willa throughout its lifespan.

(2014b) showed that R5, V500, and intensity can explain the R34 variance in linear regression. The radial scaling factor F_{R5} is created by dividing the observed R5 by $R5_c$ as follows:

$$R5_c = 7.653 + \left(\frac{V_m}{11.651}\right) - \left(\frac{V_m}{59.067}\right)^2, \quad (7)$$

$$F_{R5} = \frac{R5}{R5_c}, \quad (8)$$

where $R5_c$ has units of the degree latitude based on the intensity V_m. The scaling factor affects the spatial distribution of brightness temperatures, which is directly related to wind radii (Knaff et al., 2014a).

In addition to these TC size estimation variables, we also list other top five important predictors and contribution degrees in Table 5. In these predictors, PENC, Z000, and PENV are all variables related to pressure. For example, PENC describes the azimuthally averaged surface pressure at the outer edge of the vortex. The relationship between the radial distributions of the pressure and azimuthal wind can be approximated as follows (Chavas et al., 2017):

$$-\frac{1}{\rho}\frac{\partial P}{\partial r}+\frac{v^2}{r}+fv=0, \tag{9}$$

where p is air pressure, r is the radius from the TC center, v is the azimuthal wind, ρ is the air density, and f is the Coriolis parameter evaluated at the latitude of the TC center. CSST is also important to estimate RMW because SST may play a role in increasing the TC wind field (Maclay et al., 2008). TWXC and TWAC are tangential wind-related predictors that describe the quality of the TC cyclonic structure. As ocean heat content controls the energy supply of TCs, CD20 and COHC are both useful predictors (Wada and Usui, 2007). Other important predictors include brightness-related variables from infrared imageries that describe the strength of convection and the cloud structure. These predictors can also improve prediction skills in terms of the degree of contribution.

3.5 Case study

Additionally, we select two TCs and plot our predictions and labels to show concrete results.

Hurricane Genevieve was one of the most powerful and long-lived hurricanes in 2020, which caused more than $50 million in economic losses in Mexico. Genevieve became a hurricane by August 17, and it started to rapidly intensify the following day. By UTC 12:00 on August 18, Genevieve reached its peak intensity, with maximum sustained winds of 115 kt. As shown in Figure 6, our model gives a closer estimate of the wind structure most of the time. However, it would be challenging to predict the wind structure when the system is disordered.

Another case is Hurricane Willa, which is shown in Figure 7, which killed nine people and caused $825 million in damage after its landfall in Mexico. To begin with, a new low-pressure trough, an elongated region of low atmospheric pressure, developed to the west of the original low on October 19. At UTC 00:00 on October 20, the system developed into a tropical depression while being located approximately 425 km south of Manzanillo, Mexico. Around UTC 12:00, the system's tight inner core strengthened into a tropical storm. The system was chaotic as we saw on the satellite imageries until this moment, which was hard to be estimated. Willa soon started to rapidly intensify. Environmental conditions allowed Willa to strengthen into a hurricane around UTC 06:00 on October 21. The eye of Willa became well-defined on satellite imageries by UTC 18:00. It can be seen that the estimation results of our model are relatively close to the best track during this process, where the largest error is R34. Continuing to rapidly intensify, Willa reached the peak intensity with maximum sustained winds of 140 kt at approximately UTC 06:00 on October 22. The system weakened and made landfall at UTC 01:20 on October 24. Following the landfall, Willa rapidly weakened, degenerating into a tropical storm by UTC 06:00, which became chaotic on satellite imageries. Six hours later, Willa dissipated over northeastern Mexico. In general, our model has a good performance in the rapid intensification of Hurricane Willa. The estimation of wind radii is a challenge for our model when the eye of TCs is not clear.

4 Conclusion

In this study, we develop a physics-incorporated network to estimate the TC wind structure. Our method boosts performance on both the model and data sides. On one hand, rotation-equivariant layers enhance the performance because of the rotation invariance of TCs. On the other hand, multi-source predictors related to the TC structure augment the performance from the perspective of features. We apply dynamic weight averaging to achieve a balance among multi-tasks in a simple way. By splitting the range of labels into 100 bins on an average, we provide more informed estimations to quantify the uncertainty of network outputs. Specifically, the correct bin is one of the top 10 most likely for around 60% of the data points of the estimated parameters. We compare our model with other methods on the TC structure task. The structure ablation study is performed to examine the efficacy of rotation-equivariant layers. We also conduct predictor sensitivity studies to mine the relationship between models and predictors. Hurricane Genevieve and Hurricane Willa are used as examples to show our prediction.

Our model obtains 39.90, 21.35, 11.80, and 24.86 km MAEs on R34, R50, R64, and RMW under an operational setting. It also reaches an error in the intensity of 4.87 kt, which surpasses other models. In the current experimental settings, we find that the incorporation of rotation-equivariant layers reduces wind radii and intensity errors compared with the baseline. In addition, with the incorporation of predictors, we find the results are improved by 18.8% and 55.7% for wind radii and intensity estimation, on average. The predictors are ranked by calculating feature attribution that describes the degree of importance to the output. The result shows that our model focuses on key predictors, including V500, R5, and the scaling factor. We also find environmental variables such as surface pressure and SST to be helpful. Our model gets close results to the wind structure of Hurricane Genevieve and Hurricane Willa during rapid intensification in the case study. However, the performance of the model needs to be improved when the system is unstable. It is worth noting that there are still unavoidable errors in the labels we use, especially in wind radii, which will be improved with more frequent post-season analysis.

In general, the physics-incorporated network is well-designed for estimating the tropical cyclone wind structure and can be applied to operational settings. Although observations like scatterometers can directly detect the TC wind field, our method can play a role in the rapid intensification of TCs at a high frequency because early awareness of these disasters results in saving many lives. With the emergence of more high-quality observations, estimation could be more accurate in the future by incorporating auxiliary information. Currently, although this study only discussed the symmetric wind radii estimation, we provide the dataset with asymmetric features such as wind shear when considering the TC wind field's asymmetries.

Data availability statement

The datasets presented in this study can be found in online repositories. The names of the repository/repositories and accession number(s) can be found at: Tropical Cyclone Wind Dataset Qianhu, 2022.

Author contributions

All authors designed the experiments and carried them out. QY developed the model code and performed the simulations. QY and SY prepared the manuscript with contributions from all co-authors.

Funding

This study is supported in part by the Meteorological Joint Funds of the National Natural Science Foundation of China under Grant U2142211, in part by the Key Project Fund of Shanghai 2020 "Science and Technology Innovation Action Plan" for Social Development under Grant 20dz1200702, in part by the National Key Research and Development Program of China under Grant 2020YFA0608000, in part by the National Natural Science Foundation of China under Grant 42075141, 41875057, 41730960, and in part by the first batch of Model Interdisciplinary Joint Research Projects of Tongji University in 2021 under Grant YB-21-202110.

Acknowledgments

The authors thank Dr. Mark DeMaria for his generous help to the data.

Conflict of interest

The authors declare that the research was conducted in the absence of any commercial or financial relationships that could be construed as a potential conflict of interest.

Publisher's note

Supplementary material

The Supplementary Material for this article can be found online at: https://www.frontiersin.org/articles/10.3389/feart.2022.1024979/full#supplementary-material

References

Chavas, D. R., Reed, K. A., and Knaff, J. A. (2017). Physical understanding of the tropical cyclone wind-pressure relationship. *Nat. Commun.* 8, 1360. doi:10.1038/s41467-017-01546-9

Chen, B.-F., Chen, B., Lin, H.-T., and Elsberry, R. L. (2019a). Estimating tropical cyclone intensity by satellite imagery utilizing convolutional neural networks. *Weather Forecast.* 34, 447–465. doi:10.1175/WAF-D-18-0136.1

Chen, B., Chen, B.-F., and Hsiao, C. M. (2021). CNN profiler on polar coordinate images for tropical cyclone structure analysis. *Proc. AAAI Conf. Artif. Intell.* 35, 991–998. doi:10.1609/aaai.v35i2.16183

Chen, B., Chen, B.-F., and Lin, H.-T. (2018a). "Rotation-blended CNNs on a new open dataset for tropical cyclone image-to-intensity regression," in *Proceedings of the 24th ACM SIGKDD international conference on knowledge discovery data mining*. (New York, NY: KDD), 18, 90–99. doi:10.1145/3219819.3219926

Chen, H., Mo, Z., Yang, Z., and Wang, X. (2019b). "Theoretical investigation of generalization bound for residual networks," in *Proceedings of the twenty-eighth international Joint conference on artificial intelligence*. (Macao, China: International Joint Conferences on Artificial Intelligence Organization), 2081–2087. IJCAI-19. doi:10.24963/ijcai.2019/288

Chen, Z., Badrinarayanan, V., Lee, C.-Y., and Rabinovich, A. (2018b). "GradNorm: Gradient normalization for adaptive loss balancing in deep multitask networks," in *Proceedings of the 35th international conference on machine learning*. Editors J. Dy and A. Krause (Stockholm, Sweden: PMLR), 794–803.

Clare, M. C., Jamil, O., and Morcrette, C. J. (2021). Combining distribution-based neural networks to predict weather forecast probabilities. *Q. J. R. Meteorol. Soc.* 147, 4337–4357. doi:10.1002/qj.4180

Cohen, T., and Welling, M. (2016). "Group equivariant convolutional networks," in *Proceedings of the 33rd international conference on machine learning*. Editors M. F. Balcan and K. Q. Weinberger (New York, New York, USA: PMLR), 48, 2990–2999.

DeMaria, M., Mainelli, M., Shay, L. K., Knaff, J. A., and Kaplan, J. (2005). Further improvements to the statistical hurricane intensity prediction scheme (SHIPS). *Weather Forecast.* 20, 531–543. doi:10.1175/WAF862.1

Demuth, J. L., DeMaria, M., and Knaff, J. A. (2006). Improvement of advanced microwave sounding unit tropical cyclone intensity and size estimation algorithms. *J. Appl. Meteorol. Climatol.* 45, 1573–1581. doi:10.1175/JAM2429.1

Dolling, K., Ritchie, E. A., and Tyo, J. S. (2016). The use of the deviation angle variance technique on geostationary satellite imagery to estimate tropical cyclone size parameters. *Weather Forecast.* 31, 1625–1642. doi:10.1175/WAF-D-16-0056.1

Dvorak, V. F. (1975). Tropical cyclone intensity analysis and forecasting from satellite imagery. *Mon. Weather Rev.* 103, 420–430. doi:10.1175/1520-0493(1975)103¡0420:TCIAAF¿2.0.CO;2

Figa-Saldaña, J., Wilson, J. J., Attema, E., Gelsthorpe, R., Drinkwater, M. R., and Stoffelen, A. (2002). The advanced scatterometer (ascat) on the meteorological operational (MetOp) platform: A follow on for European wind scatterometers. *Can. J. Remote Sens.* 28, 404–412. doi:10.5589/m02-035

He, F., Liu, T., and Tao, D. (2020). Why ResNet works? Residuals generalize. *IEEE Trans. Neural Netw. Learn. Syst.* 31, 5349–5362. doi:10.1109/TNNLS.2020.2966319

He, K., Zhang, X., Ren, S., and Sun, J. (2016). "Deep residual learning for image recognition," in *2016 IEEE conference on computer vision and pattern recognition (CVPR)*, 770–778. doi:10.1109/CVPR.2016.90

Kaplan, J., Rozoff, C. M., DeMaria, M., Sampson, C. R., Kossin, J. P., Velden, C. S., et al. (2015). Evaluating environmental impacts on tropical cyclone rapid intensification predictability utilizing statistical models. *Weather Forecast.* 30, 1374–1396. doi:10.1175/WAF-D-15-0032.1

Kingma, D. P., and Ba, J. (2015). "Adam: A method for stochastic optimization," in *3rd international conference on learning representations*. ICLR 2015.

Knaff, J. A., DeMaria, M., Longmore, S. P., and DeMaria, R. T. (2014a). *Improving tropical cyclone guidance tools by accounting for variations in size.* San Diego, CA: Environmental Science.

Knaff, J. A., Longmore, S. P., and Molenar, D. A. (2014b). An objective satellite-based tropical cyclone size climatology. *J. Clim.* 27, 455–476. doi:10.1175/JCLI-D-13-00096.1

Knaff, J. A., Sampson, C. R., and Chirokova, G. (2017). A global statistical–dynamical tropical cyclone wind radii forecast scheme. *Weather Forecast.* 32, 629–644. doi:10.1175/WAF-D-16-0168.1

Knaff, J. A., Sampson, C. R., Kucas, M. E., Slocum, C. J., Brennan, M. J., Meissner, T., et al. (2021). Estimating tropical cyclone surface winds: Current status, emerging technologies, historical evolution, and a look to the future. *Trop. Cyclone Res. Rev.* 10, 125–150. doi:10.1016/j.tcrr.2021.09.002

Knaff, J. A., Slocum, C. J., Musgrave, K. D., Sampson, C. R., and Strahl, B. R. (2016). Using routinely available information to estimate tropical cyclone wind structure. *Mon. Weather Rev.* 144, 1233–1247. doi:10.1175/MWR-D-15-0267.1

Knapp, K. R., Ansari, S., Bain, C. L., Bourassa, M. A., Dickinson, M. J., Funk, C., et al. (2011). Globally gridded satellite observations for climate studies. *Bull. Am. Meteorol. Soc.* 92, 893–907. doi:10.1175/2011BAMS3039.1

Landsea, C. W., and Franklin, J. L. (2013). Atlantic hurricane database uncertainty and presentation of a new database format. *Mon. Weather Rev.* 141, 3576–3592. doi:10.1175/MWR-D-12-00254.1

Liu, S., Johns, E., and Davison, A. J. (2019). "End-to-end multi-task learning with attention," in *2019 IEEE/CVF conference on computer vision and pattern recognition* (Long Beach, CA: CVPR), 1871–1880. doi:10.1109/CVPR.2019.00197

Maclay, K. S., DeMaria, M., and Haar, T. H. V. (2008). Tropical cyclone inner-core kinetic energy evolution. *Mon. Weather Rev.* 136, 4882–4898. doi:10.1175/2008MWR2268.1

Pradhan, R., Aygun, R. S., Maskey, M., Ramachandran, R., and Cecil, D. J. (2018). Tropical cyclone intensity estimation using a deep convolutional neural network. *IEEE Trans. Image Process.* 27, 692–702. doi:10.1109/TIP.2017.2766358

Qianhu, Y. (2022). Tropical Cyclone Wind Dataset. *Estimating Tropical Cyclone Wind Structure Using Physics Incorporated Network*. doi:10.5281/zenodo.6992187

Reul, N., Chapron, B., Zabolotskikh, E., Donlon, C., Mouche, A., Tenerelli, J., et al. (2017). A new generation of tropical cyclone size measurements from space. *Bull. Am. Meteorol. Soc.* 98, 2367–2385. doi:10.1175/BAMS-D-15-00291.1

Schade, L. R. (2000). Tropical cyclone intensity and sea surface temperature. *J. Atmos. Sci.* 57, 3122–3130. doi:10.1175/1520-0469(2000)057¡3122:TCIASS¿2.0.CO;2

Shrikumar, A., Greenside, P., and Kundaje, A. (2017). "Learning important features through propagating activation differences," in *Proceedings of the 34th international conference on machine learning*. Editors D. Precup and Y. W. Teh (PMLR. (Sydney, Australia: Proceedings of Machine Learning Research), 70, 3145–3153.

Stiles, B. W., Danielson, R. E., Poulsen, W. L., Brennan, M. J., Hristova-Veleva, S., Shen, T.-P., et al. (2014). Optimized tropical cyclone winds from QuikSCAT: A neural network approach. *IEEE Trans. Geosci. Remote Sens.* 52, 7418–7434. doi:10.1109/TGRS.2014.2312333

Sundararajan, M., Taly, A., and Yan, Q. (2017). "Axiomatic attribution for deep networks," in *Proc. 34th Int. Conf. Mach. Learn*. Editors D. Precup and Y. W. Teh (Sydney, Australia: Proceedings of Machine Learning Research), 70, 3319–3328.

Wada, A., and Usui, N. (2007). Importance of tropical cyclone heat potential for tropical cyclone intensity and intensification in the Western North Pacific. *J. Oceanogr.* 63, 427–447. doi:10.1007/s10872-007-0039-0

Worrall, D. E., Garbin, S. J., Turmukhambetov, D., and Brostow, G. J. (2017). "Harmonic networks: Deep translation and rotation equivariance," in *2017 IEEE conference on computer vision and pattern recognition (CVPR)*, 7168–7177. doi:10.1109/CVPR.2017.758

Xie, P., Joyce, R., Wu, S., Yoo, S.-H., Yarosh, Y., Sun, F., et al. (2017). Reprocessed, bias-corrected CMORPH global high-resolution precipitation estimates from 1998. *J. Hydrometeorol.* 18, 1617–1641. doi:10.1175/JHM-D-16-0168.1

Xu, W., Balaguru, K., August, A., Lalo, N., Hodas, N., DeMaria, M., et al. (2021). Deep learning experiments for tropical cyclone intensity forecasts. *Weather Forecast.* 36, 1453–1470. doi:10.1175/WAF-D-20-0104.1

Zhuo, J.-Y., and Tan, Z.-M. (2021). Physics-augmented deep learning to improve tropical cyclone intensity and size estimation from satellite imagery. *Mon. Weather Rev.* 149, 2097–2113. doi:10.1175/MWR-D-20-0333.1

frontiers | Frontiers in Earth Science

TYPE Original Research
PUBLISHED 17 January 2023
DOI 10.3389/feart.2022.1058734

EDITED BY
Liguang Wu,
Fudan University, China

REVIEWED BY
Qingyuan Liu,
Chinese Academy of Meteorological Sciences, China
Jia Liang,
Nanjing University of Information Science and Technology, China

*CORRESPONDENCE
Shengming Tang,
tangsm@typhoon.org.cn

SPECIALTY SECTION
This article was submitted to Atmospheric Science, a section of the journal Frontiers in Earth Science

RECEIVED 30 September 2022
ACCEPTED 31 October 2022
PUBLISHED 17 January 2023

CITATION
Li T, Qu H, Tang S, Tang J, Yan J, Lin L, Li Y and Yang Y (2023), Investigation of wind characteristics of typhoon boundary layer through field experiments and CFD simulations.
Front. Earth Sci. 10:1058734.
doi: 10.3389/feart.2022.1058734

Investigation of wind characteristics of typhoon boundary layer through field experiments and CFD simulations

Tiantian Li[1], Hongya Qu[2], Shengming Tang[1,3]*, Jie Tang[1], Jiaming Yan[1], Limin Lin[1], YongPing Li[1] and Yuhua Yang[1]

[1]Shanghai Typhoon Institute of China Meteorological Administration, Shanghai, China, [2]Department of Bridge Engineering, Tongji University, Shanghai, China, [3]Fujian Key Laboratory of Severe Weather, Fujian Institute of Meteorological Sciences, Fuzhou, China

High-resolution observations of typhoon boundary layer above 100 m are rare as traditional wind towers are generally below 100 m, which limits the study of typhoon boundary layer and engineering applications such as wind-resistant design of tall buildings and wind turbines in typhoon-prone regions. In this study, boundary layer winds of super typhoon Lekima (2019) are observed, simulated and analyzed. Together with traditional wind tower, Doppler wind lidar is utilized for observations of typhoon boundary layer in order to obtain measured data above 100 m. Besides, Computational Fluid Dynamics (CFD) simulation based on Large Eddy Simulation (LES) method is conducted to further investigate the impact of complex terrain on the near-surface wind characteristics. The results show that the power law fits the mean wind speed profile well below 100 m. However, before and after the typhoon lands, a local reverse or low-level jet occurs in the mean wind speed profile at the height of 100–300 m, which cannot be depicted by the power law. Meanwhile, the turbulence intensity increases with height and experiences larger fluctuations. In addition, there is a significant negative correlation between the ground elevation and power exponents of the fitted mean wind speed profiles. This study provides useful information to better understand wind characteristics of the typhoon boundary layer.

KEYWORDS

Boundary layer, wind characteristics, computational fluid dynamics, field experiment, typhoon, complex terrain

Introduction

Typhoons are devastating natural hazards that have huge social, economic and environmental influences on the earth. An average of 43 deaths and US$ 78 million in damage every day are caused by typhoons (WMO, 2022). They include a number of different hazards, such as extreme winds, heavy precipitation, large storm surges, and their secondary disasters, and extreme winds are commonly considered as one of major hazard factors (Zhang et al., 2009; Chen et al., 2019; Li et al., 2021; Wang et al., 2022). Typhoon-induced extreme winds mainly occur in coastal and nearshore regions, which not only pose threats to agriculture, fisheries, and transportation industries, but also bring security risks to engineering facilities such as high-rise buildings, cross-sea bridges, power transmission lines, and wind farms. In recent years, the rapid development of urbanization process prompts the developments of transportation and power networks and the emergence of large-scale wind turbines and high-rise buildings. Such structures are inherently vulnerable to the hit of typhoons, and therefore wind characteristics of typhoons are of great concern and gain more and more attention.

As a complex weather system, field experiments are commonly performed to reveal wind characteristics of typhoons since they are effective and reliable. Regarding the observations of typhoon boundary layer, meteorological stations and wind towers are mostly used to measure and analyze characteristics of the wind field through instruments such as anemometers. Law et al. (2006) presented wind characteristics of Typhoon Dujuan as measured by a 50-m-high wind tower. Cao et al. (2009) reported wind characteristics of a strong typhoon (Typhoon Maemi 2003) based on measurements of nine vane and seven sonic anemometers at a height of about 15 m. Masters et al. (2010) described the mean flow and turbulence characteristics of three hurricanes from data collected at two elevations (5 and 10 m) by nine mobile instrumented towers deployed at coastal locations. Song et al. (2012) investigated wind characteristics of Typhoon Hagupit through field experiments by a 100-m-high offshore wind tower, which was equipped with an ultrasonic anemometer and a number of cup anemometers at heights between 10 and 100 m. Li et al. (2018) analyzed wind characteristics concerned in engineering applications based on field measurements by a 100-m-high wind tower in typhoon Hagupit (2008). Fang et al. (2019) discussed gust characteristics of 10 typhoons based on 14 sets of records observed by 4 meteorological stations equipped with 3-cup mechanical anemometers and the observation heights ranged from 10 m to 120 m. Zhou et al. (2022) estimated the dissipative heating in three landfalling typhoons according to wind observations from a multilevel wind tower with the heights between 56 m and 111 m. Based on previous studies, it is promising that wind towers equipped with anemometers are regarded as the most reliable and direct approach to investigate wind characteristics of typhoon boundary layer. However, almost all previous tower-based studies of wind characteristics of typhoons utilized records from towers lower than 120 m, because taller wind towers are rather rare due to high economic costs and difficult erection and maintenance. A few studies have employed the 356-m-high Shenzhen wind tower for investigation of wind characteristics of typhoons (He et al., 2020; Luo et al., 2020; He et al., 2022). However, relevant high-resolution observations above 100 m are still lacking.

More advanced remote sensing instruments have been deployed in observations of typhoon boundary layer, consisting of wind profile radar (WPR), GPS radiosonde (GPS sonde), and Doppler wind lidar (DWL). Powell et al. (2003) and Ming et al. (2014) studied mean wind speed of typhoon boundary layer based on GPS sonde data and it was found that wind speed profiles within 200 m of the near-surface layer still conform to the logarithmic law. Liao et al. (2017) analyzed radial direction and tangential wind characteristics of typhoon Usagi based on a combined usage of WPR and GPS sonde. Tsai et al. (2019) observed and analyzed mean wind speed profiles in different stages of the passage of two typhoons over Taiwan with the help of ground-based DWL up to a height of 240 m. Zhao et al. (2020) investigated turbulence characteristics of typhoon boundary layer based on atmospheric data (observation heights concentrated between 500 and 700 m) collected during six reconnaissance flights through five typhoons. Shi et al. (2021) investigated turbulent kinetic energy and typhoon boundary layer height of typhoon Lekima using joint observations from multiple DWLs. The development of remote sensing techniques and their application in meteorology enable and enrich observations of typhoon boundary layer to higher altitude, facilitating studies of wind characteristics of typhoons at comparable heights with large wind turbines or high-rise buildings (over 200 m).

Besides field experiments, numerical simulations provide an alternative way to investigate typhoon boundary layer. For example, the commonly used Computational Fluid Dynamics (CFD) approach in the field of aerodynamics has been increasingly applied to the meteorological modelling in recent years. Nakayama et al. (2012) conducted building-resolving large eddy simulations (LESs) of boundary layer flows over urban areas under typhoon conditions, and LES successfully represented the observed wind fluctuations and significant decelerations of wind speeds within the urban canopy layer. Li et al. (2014) simulated a fine-scale three-dimensional wind field over mountains during the landfall of Typhoon Molave. It is claimed that CFD simulations could reasonably describe the three-dimensional wind structure over complex terrain under strong wind conditions and describe the terrain effects on the wind field. Li et al. (2019, 2020) reproduced the strong wind field around an engineering structure induced by tornadoes using LES, and the flow structures of different types of tornadoes could be regenerated with high fidelity. Yang et al. (2022) performed CFD simulations of small-scale wind fields with complex terrain to establish wind speed and terrain correction algorithm for modelling large-scale wind field of typhoons, and it was found that the accuracy improved by 17% compared to the model that ignored the influence of terrain conditions. From previous studies, CFD simulation is advantageous in characterizing complex geometric shapes (Blocken et al., 2015), and therefore it is capable and suitable to simulate realistic fine-scale wind fields of typhoon boundary layer under complex terrain conditions.

Although continuous efforts and great achievements have been made from previous studies, high-resolution observations and further understanding of wind characteristics of typhoon boundary layer at comparable heights with large wind turbines or high-rise buildings (over 200 m) are still limited. To address this issue, on top of traditional wind tower observations, the remote sensing instrument of DWL is adopted in current study to provide observational data above 100 m. CFD simulation is also conducted to aid the investigation of wind characteristics of typhoon boundary layer considering complex terrain conditions. The main goal of current study is to further understand wind characteristics of typhoon boundary layer, especially between 0 and 300 m, facilitating the wind-resistant design of tall civil structures in typhoon-prone regions, and providing references for boundary layer parameterization schemes used in numerical models of typhoons. The remainder of this paper is organized as follows. *Field Experiments of Super Typhoon Lekima (2019) Section* introduces super typhoon Lekima (2019) and associated field experiments, including wind tower and DWL observations. *Experimental Results and Discussion Section* performs observational analysis and discusses the mean and turbulent wind characteristics of Lekima between 0 and 300 m. *CFD simulations and discussion Section* describes CFD simulations and further discusses wind characteristics of typhoon boundary layer. *Conclusion Section* summarizes main findings and makes concluding remarks.

Field experiments of super typhoon Lekima (2019)

Overview of super typhoon Lekima

Super typhoon Lekima is the ninth named tropical cyclone of the 2019 Pacific typhoon season. It was named on August 4, intensified to typhoon at 05:00 CST (China Standard Time: CST = UTC +08:00) on the 7th, and then peaked as a super typhoon at 23:00 CST the same day. Lekima made landfall on the coast of Chengnan of Zhejiang Province (China) at 01:45 CST on August 10. At the time of landing, maximum wind speed near center was 52 m/s (wind force was 16 on the Beaufort Wind Scale), and the minimum central pressure was 930 hPa. After making landfall, Lekima began to weaken rapidly and moved to the north. Then, Lekima traveled through Zhejiang and Jiangsu provinces and moved into the western waters of the Yellow Sea. At 20:50 CST on the 11th, Lekima landed again on the coast of Huangdao District, Qingdao City, Shandong Province (China), with the maximum wind force of 9 (23 m/s), and the minimum pressure of 980 hPa. Then it passed through the Shandong Peninsula and moved into the Bohai Sea. It weakened subsequently and was declared to have dissipated on the 13th. Figures 1, 2 present the best track of Lekima, as well as the evolution of intensity and central pressure over time. The data are obtained from best-track database officially released by the China Meteorological Administration (Ying et al., 2014; Lu et al., 2021). Lekima reached the maximum wind speed and lowest central pressure at around 20:00 CST on August 8. After that, the wind speed decreased and the pressure increased significantly as the typhoon landed.

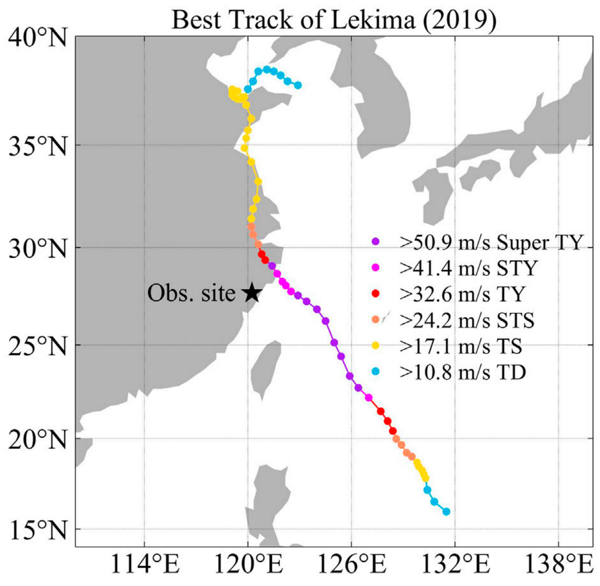

FIGURE 1
Best track of Super typhoon Lekima (2019). Different colors represent different intensities. Super TY: super typhoon, STY: severe typhoon, TY: typhoon, STS: severe tropical storm, TS: tropical storm, and TD: tropical depression. Black star indicates the location of the field experiment.

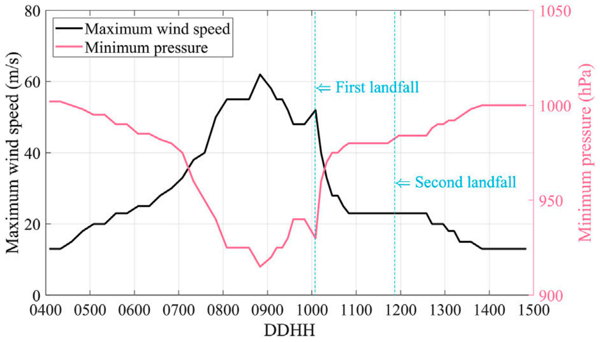

FIGURE 2
Time evolution of the intensity and central pressure of Lekima. Horizontal axis is time in the format of day and hour in August. Vertical axis on the left represents maximum wind speed (unit: m/s), and vertical axis on the right represents minimum pressure (unit: hPa).

FIGURE 3
East China Typhoon Field Science Experiment Base located in Sansha of Fujian Province as indicated by the black star in Figure 1.

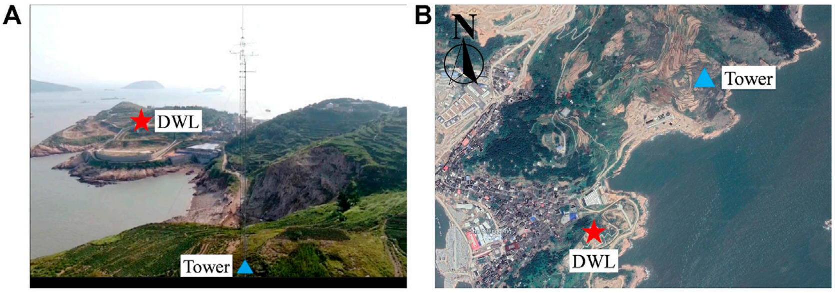

FIGURE 4
Relative positions of wind tower and DWL: **(A)** Photo of observation sites; **(B)** Top view of observation sites from map.

Field experiments

To further investigate and understand wind characteristics of typhoon boundary layer, field experiments were performed at East China Typhoon Field Science Experiment Base (Figure 3), which is located in Sansha of Fujian Province as indicated by the black star in Figure 1 (STI, 2022). The closest distance between the observational site and the typhoon center is 181 km based on the best-track data, which is much larger than the radius of maximum wind obtained from Joint Typhoon Warning Center (JTWC, 2022). Therefore, characteristics of wind field outside of the typhoon eyewall are represented by the observations.

The field experiments include wind tower test equipped with ultrasonic anemometers and DWL test, and their relative positions are shown in Figure 4. The wind tower observation site is located in the north of the DWL observation site, and the distance between these two is 620 m. As shown in Figure 5A, the wind tower is located on a vegetated hillside at an altitude of 44 m. The south and east sides of the tower are close to the sea, and it is 170 m and 100 m away from the coastline on the south and east sides, respectively. The tower is surrounded by hills to the north and west. The tower is equipped with ultrasonic anemometers at four different heights, i.e., 10 m, 30 m, 50 m, and 70 m. The ultrasonic anemometer is WindMaster PRO manufactured by British Gill Company (Figure 6A), which is a precision anemometer offering three-axis wind measurement data and widely used in boundary layer turbulence observation and wind engineering measurements. Operating temperature of this instrument is −40°C to +70°C, the requirement of humidity is <5% to 100%RH, and the allowed precipitation is up to 300 mm/h. The instrument monitors wind speeds of 0–65 m/s with the resolution of 0.01 m/s. It also provides wind direction measurements of 0–360° with the resolution of 0.1°, as well as sonic temperature of −40°C to +70°C with the resolution of

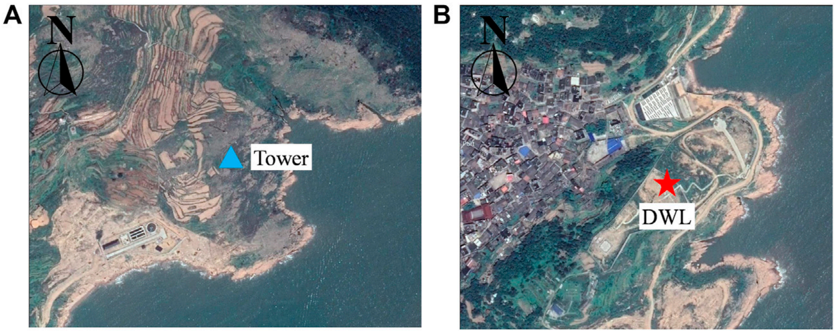

FIGURE 5
Terrain conditions at observation sites: **(A)** Wind tower; **(B)** DWL.

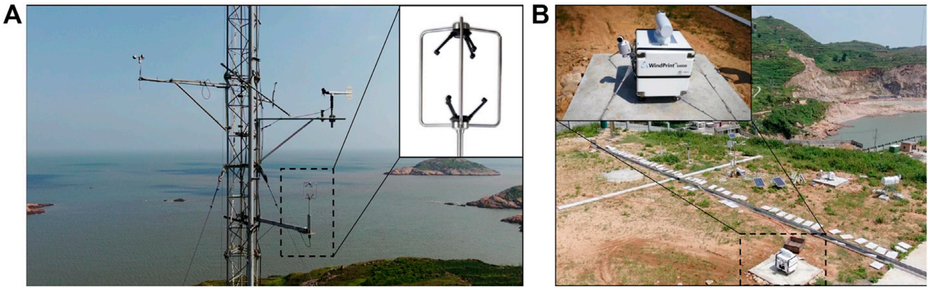

FIGURE 6
Measurement instruments: **(A)** Ultrasonic anemometer deployed on the wind tower; **(B)** WindPrint S4000 3D scanning DWL.

0.01°C. The observation test was conducted from 00:00 on August 9 to 00:00 on August 11, with data output rate of 20 Hz.

Figure 5B shows that the DWL is deployed on a relatively flat site, and the surface is covered with sparse and low grass and shrubs. The altitude of the DWL is 33 m. Its northern and southern sides are close to the sea, and the closest distance to the coastline is 50 m. The deployed DWL is a WindPrint S4000 3D scanning lidar (Figure 6B), which is manufactured by Qingdao Huahang Environmental Technology Co., Ltd. Its scanning cone angle is 60° in DBS (Doppler beam swing) five-beam mode, and its maximum detection distance can reach 4 km. The measurement range of wind speed is 0–75 m/s with the resolution of 0.1 m/s, and the measurement range of wind direction is 0–360° with the resolution of less than 3°. The observation period of the DWL is the same as that of the wind tower, but it has lower internal sampling rate (data output interval: 4 s).

Experimental results and discussion

Before analyzing the experimental results, abnormal data are removed by checking spikes, dropouts, and absolute limits (Hojstrup, 1993; Vickers and Mahrt, 1997; Tang et al., 2022). Signal-to-noise ratio is also checked for DWL data (Tang et al., 2020; Tang et al., 2022). Both wind tower and DWL data are divided into 10-min datasets for data analysis. Therefore, each dataset of wind tower contains 12,000 data points and 150 for DWL data.

Mean wind speed and direction

Figure 7 presents time evolution of 10-min mean wind speed and direction obtained from wind tower measurements and those from DWL measurements. The tower data include four layers of readings from 10 m to 70 m. The maximum measurement height of the DWL can reach 4 km, which is more than enough to cover the height of interest (77.9 m–402.7 m). From Figure 7A, the mean wind speed generally increases as the height increases, and the wind speed gradient is relatively larger before landing than that after landing. Wind speed weakens at the time of landing, and then increases again, reaching a peak at around 06:00 CST on the 10th. The peak wind speed is due to the speed-up effects of

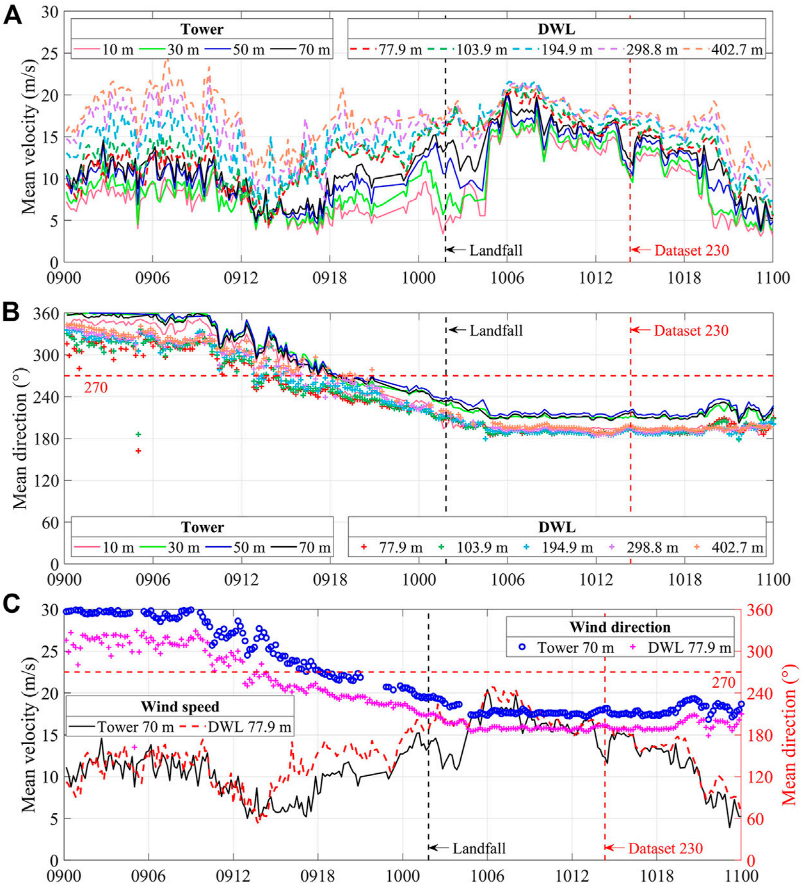

FIGURE 7
Time evolution of 10-min mean: **(A)** Wind speed (unit: m/s); **(B)** Wind direction (unit: °); **(C)** Comparison between wind tower (70 m) and DWL (77.9 m), with vertical axis on the left representing wind speed (unit: m/s) and that on the right representing wind direction (unit: °).

the local mountainous terrain. Specifically, after 05:00 CST on the 10th, the center of Lekima passes through a northeast-southwest ridge with an altitude of up to 1.0 km, resulting in compressed wind on the windward side of the hill and hence increased wind speed. After reaching peak speed at 06: 00 CST, the mean wind speed gradually decreases. From Figure 7B, the wind blows from the north to the south before landing, and changes to west wind at around 18: 00 CST on the 9th. Then, the wind becomes southwesterly and southerly at the time of landing, which is kept unchanged even after the landing. Along the vertical direction, wind directions at 30–70 m are close to each other, while the wind direction at 10 m shifts 20° counterclockwise. Compared to the wind direction at 10 m, wind directions above 70 m shift a little counterclockwise before landing and are close to that at 10 m after landing.

Wind tower data at the height of 70 m and DWL data at 77.9 m are compared in Figure 7C to examine the agreement between these two measurements. Since the tower base is around 10 m higher than that of the DWL, it can be considered that the two observations are performed at the same height. From Figure 7C, general trend and magnitude of wind speeds measured by both instruments are almost the same except for the time period before and after the landing of typhoon, during which wind tower measured wind speed is lower. At that time, prevailing winds start to blow from the west and southwest, and upstream terrain conditions of the wind tower is hilly with an altitude of more than 100 m, while it is residential areas and gentle slopes for the DWL with an altitude of about 40 m. Since hilly terrain with higher altitude exerts stronger shielding effects on the wind field, the associated downstream wind speed is much lower. Therefore, the wind speed measured by the wind tower is lower. Regarding to the wind direction, although the trends of wind tower and DWL data are consistent, the wind direction monitored by the DWL shifts around 30° counterclockwise due to local terrains.

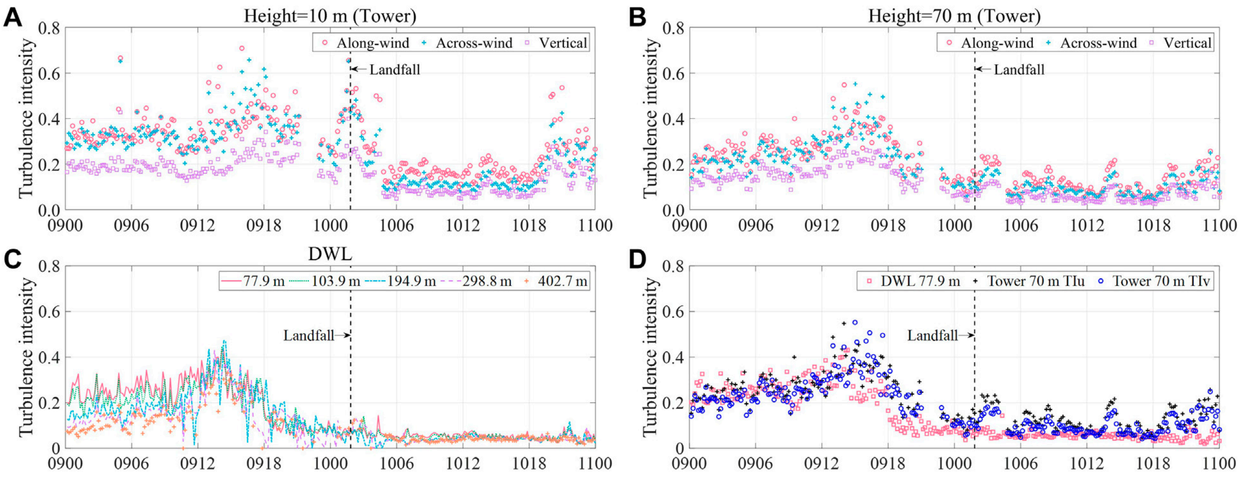

FIGURE 8
Time evolution of turbulence intensity: **(A)** Tower data at the height of 10 m; **(B)** Tower data at the height of 70 m; **(C)** DWL data at five heights (77.9 m, 103.9 m, 194.9 m, 298.8 m, and 402.7 m); **(D)** Comparison between wind tower (70 m) and DWL (77.9 m).

Turbulence intensity

Besides the mean wind, unsteady random motions are also encountered in air flow of typhoon boundary layer, which is referred to as turbulence. Turbulence can be visualized as consisting of eddies (irregular swirls of air motion), which are of many different sizes superimposed onto each other (Stull, 1988). Turbulence intensity is commonly used to characterize turbulence level of the air flow. It is defined as the ratio of standard deviation of the turbulent velocity fluctuations to the mean wind velocity.

Figure 8 presents the time evolution of turbulence intensity at different heights. Time histories of three components of wind velocity are provided for wind tower data, and three-axis turbulence intensities are thus calculated. For DWL data, only horizontal total wind speed is provided, and therefore the total horizontal turbulence intensity is calculated. Although components of wind speed can be back calculated by total wind speed and wind direction, the time resolution of data is found to be degraded. Therefore, original data is used for the calculation of turbulence intensity to guarantee its time resolution. From Figures 8A–C, turbulence intensity generally decreases with the increase of height. At the time of landfall, turbulence intensity tends to increase due to wind speed reduction, which is more obvious at the heights of 10 m and 70 m. After the landfall, the development of turbulence intensity is relatively stable. Figures 8A,B indicate that the magnitudes of turbulence intensity in the along-wind direction and across-wind direction are equivalent before landfall, and the along-wind turbulence intensity becomes higher after landfall; both are higher than the vertical turbulence intensity.

Figure 8D shows the comparison of turbulence intensity between wind tower data at the height of 70 m and DWL data at 77.9 m. From 00:00 to 15:00 CST on August 9, turbulence intensities measured by both instruments are comparable. Then, turbulence intensity begins to decrease and DWL measured data are lower than wind tower data. This phenomenon is consistent with the time evolution of wind speed as illustrated in Figure 7C, because lower wind speed is mainly associated with higher turbulence intensity due to their inversely proportional relationship. On the other hand, the 100-m-high hill may cause boundary layer separation and vortex shedding on its leeward side, leading to increased wind fluctuations in its wake region where the wind tower is located and therefore higher turbulence intensity is observed.

Profiles of wind speed and turbulence intensity

Since the maximum measurement height of the wind tower is limited to 70 m, DWL data are used to investigate profiles of wind speed and turbulence intensity below the height of 300 m. The power law as given in Eq. 1 is employed to fit the wind speed and turbulence intensity profiles.

$$u(z) = u_{10}\left(\frac{z}{10}\right)^{\alpha} \tag{1a}$$

$$I(z) = I_{10}\left(\frac{10}{z}\right)^{\alpha} \tag{1b}$$

where $u(z)$ and $I(z)$ are the wind speed and turbulence intensity at the elevation z; z is the elevation above the ground; u_{10} and I_{10} are the wind speed and turbulence intensity at the height of 10 m; and α is the power exponent of wind speed profile, and the same α is applied for turbulence intensity profile (GB50009, 2012).

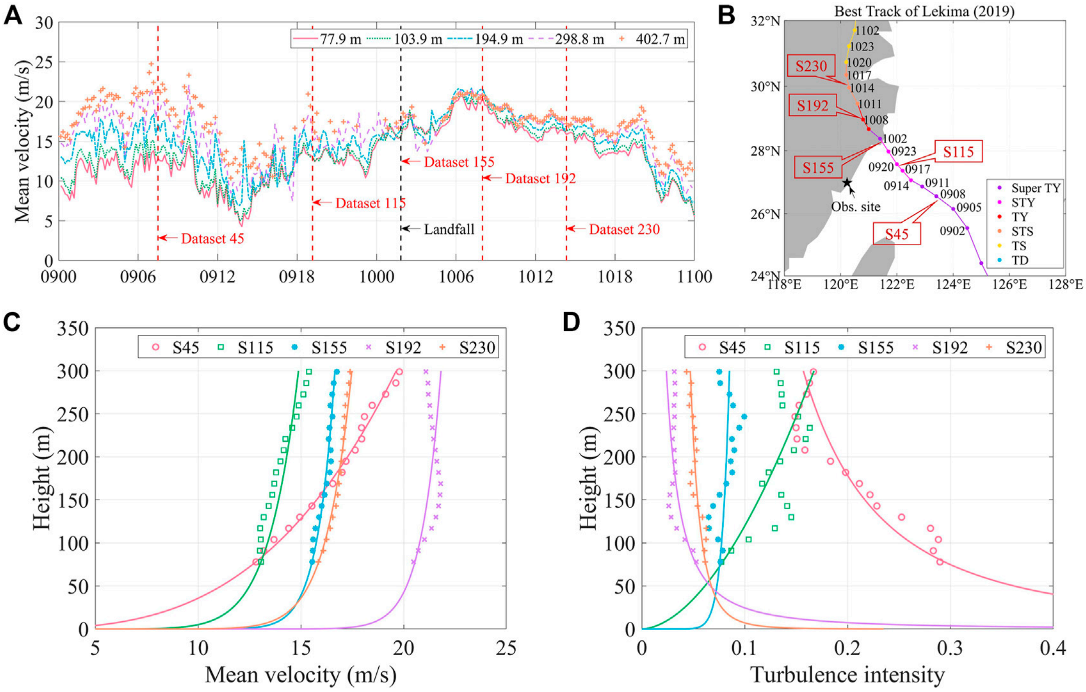

FIGURE 9
Wind speed profile determined based on DWL data: **(A)** Indication of selected time instants for wind speed profile extraction, with horizontal axis representing time in the format of day and hour and vertical axis representing mean wind speed (unit: m/s); **(B)** Indication of selected time instants on Lekima's best track; **(C)** Power-law fit for wind speed profile; **(D)** Power-law fit for turbulence intensity profile.

Because u_{10} and I_{10} are not available from DWL measurements, they are first back calculated from recorded data. Then, Eq. 1a is applied to fit the wind speed profile and the power exponent α is determined. A total of five time instants are selected for the investigation of wind speed profiles, which are illustrated in Figures 9A,B. The final fitted power-law profiles are presented in Figures 9C,D.

Dataset S45 represents the 10-min period from 07:20 to 07:30 CST on August 9, during which Lekima is categorized as a super typhoon that has not made landfall. The center of Lekima is 331 km away from the DWL. The gradient of mean wind speed is relatively large, and the speed increases by about 7 m/s within the range between 77.9–298.8 m. The power law is used to match with the observations and fit the wind speed profile, with the power exponent α of 0.317 and the coefficient of determination R^2 of 0.99. Dataset S115 belongs to the 10-min period from 19:00 to 19:10 CST on the 9th, during which Lekima degrades to a severe typhoon and is about to make landfall. The typhoon center is 190 km away from the DWL. The exponent of fitted power law is 0.097, and R^2 is 0.81. Although a small local reverse of wind speed profile occurs at the height of 120 m, the power law can basically depict the wind speed profile well. Dataset S155 is associated with the time instant of Lekima landfall as a super typhoon. The DWL is 191 km away from the typhoon center. The power exponent is 0.051 and R^2 is 0.93 for the fitted power-law profile. Wind speed gradient is relatively small, and the speed only increases by 1–2 m/s within the range between 77.9–298.8 m. The fitted power law agrees with DWL data fairly well. Dataset S192 is from the time instant at 08:00 CST on the 10th after Lekima landfall, with the intensity of typhoon. The DWL is 227 km away from the typhoon center. The R^2 of the fitted power law is -0.45 due to the presence of a low-level jet. Peak velocity is reached at the height of 160 m. The power law is not able to match with the DWL data. Dataset S230 indicates the 10-min period from 14:10 to 14:20 on the 10th, which is after Lekima landfall when it is degraded to severe tropical storm. The DWL is 335 km away from the typhoon center. The R^2 of the fitted power-law profile of mean wind speed is 0.96, and the power exponent is 0.072, implying that the power law can well describe the mean wind speed profile.

Eq. 1b is applied to fit the profile of turbulence intensity, and the comparison between fitted curve and observations is given in Figure 9D. Datasets S45, S192, and S230 follow the trend that turbulence intensity decreases with height. However, turbulence intensities of datasets S115 and S155 increase as the height increases. Typically, one or more local reverses are observed for turbulence intensity profiles. Turbulence intensities of

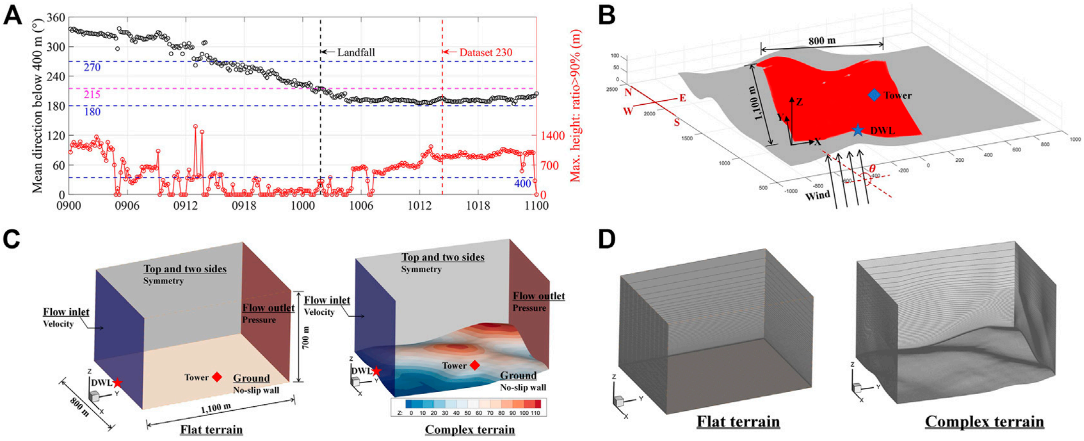

FIGURE 10
Setup of CFD simulation: **(A)** Time evolution of mean wind direction below 400 m (vertical axis on the left) and the maximum height associated with data quality ratio exceeding 90% (vertical axis on the right); **(B)** Schematic diagram of computational domain, and the grey color represents the larger region of 2 km × 2 km territory with grids along latitude and longitude, and the red color represents the determined computational domain; **(C)** Schematic diagram of numerical models with boundary conditions for both flat and complex terrains; **(D)** Schematic diagram of numerical grids for the two models.

datasets S115 and S155 experience much larger fluctuations than the remaining, when the typhoon approaches and passes. Also, their R^2 for power-law fit are the lowest (smaller than 0.3). Therefore, the power law is incapable of characterizing the shape of turbulence intensity profiles.

CFD simulations and discussion

On top of observational analysis, CFD approach is deployed to simulate the boundary layer of Lekima at Sansha observatory. This section first introduces the setup of CFD simulation of the wind field related to Lekima, then numerical results are validated against wind tower data, and analysis of wind characteristics below 300 m is finally given.

Setup of CFD simulations

Simulated time period and numerical model

Although Lekima lasted for several days, only a certain time period is numerically simulated, which is selected based on two aspects. First, it is assumed that only horizontal wind speed is applied as the velocity input of the CFD simulation for simplification. Therefore, the computational domain is determined according to the wind direction, in order to make flow direction of the domain follow the horizontal wind direction. Figure 10A presents time evolution of mean wind direction below 400 m. Because the wind tower is located at the north of the DWL, the wind direction is required to be in the range between 190° and 270°, so that the wind tower is positioned downstream of the DWL in the computational domain, which can then be served as the benchmark for the validation of CFD simulation. The optimum wind direction is 215° where the wind tower is directly in the downstream of the DWL. Second, the maximum height associated with the data quality ratio exceeding 90% is required to be greater than 400 m to ensure reasonable and reliable observations for the establishment of velocity input. Based on the above considerations, the dataset 230, representing the 10-min period from 14:10 to 14:20 CST on August 10, is selected for CFD simulation. In this dataset, the mean wind direction below 400 m is 195.7°, and the maximum height corresponding to data quality ratio exceeding 90% is 883.3 m.

According to the wind direction of 195.7°, the determined computational domain is presented in red in Figure 10B. Flow direction of the computational domain (positive direction of Y-axis) is along the wind direction. The width and length of the computation domain are 800 m and 1,100 m, respectively. To determine the computational domain, a much larger region of 2 km × 2 km is first introduced with grids along latitude and longitude, which is illustrated in grey of Figure 10B. Digital elevation data are derived from NASADEM (2020). Then, the computational domain is determined based on coordinate transformation according to the wind direction of 195.7°, which is the angle θ in Figure 10B.

On top of the computational domain, the final CFD simulation model is established as shown in Figure 10C, with the height of 700 m in Z direction. The numerical model with a flat terrain is used to validate the boundary conditions at flow inlet, and that with a complex terrain is used to simulate the wind field of typhoon boundary layer. For both numerical models, the same boundary conditions are applied. Velocity inlet and pressure outlet boundary conditions are applied at flow inlet and outlet. The input at the velocity inlet is determined according to DWL measurements. Symmetry-type wall boundary conditions are applied to the top and two sides of the numerical model where a zero flux of all quantities is assumed. No-slip wall boundary condition is applied to the ground where the fluid sticks to the wall. For turbulence modelling with complex terrain, LES as a scale-resolving simulation model is applied. LES directly resolves large scales of motion, and the smaller scales are ignored by filtering the Navier-Stokes equations. The governing equations for LES is given in Eq. 2.

$$\frac{\partial \bar{u}_i}{\partial t}+\frac{\partial \bar{u}_i\bar{u}_j}{\partial x_j}=-\frac{1}{\rho}\frac{\partial \bar{p}}{\partial x_i}+\nu\frac{\partial^2 \bar{u}_i}{\partial x_j\partial x_j}+\frac{\partial \bar{\tau}_{ij}}{\partial x_j};\ \bar{\tau}_{ij}=\bar{u}_i\bar{u}_j-\overline{u_iu_j} \tag{2a}$$

$$\frac{\partial \bar{u}_i}{\partial x_i}=0 \tag{2b}$$

where ρ is the density of air; t is time; ν is the kinematic viscosity; $\bar{u}_i$ and $\bar{u}_j$ are filtered velocities, $i = 1, 2$, and 3, and $j = 1, 2$, and 3; x_i and x_j are the Cartesian coordinates in three dimensions; $\bar{p}$ is filtered pressure. $\bar{\tau}_{ij}$ is referred to as the subgrid-scale stresses, which are unknown and require additional modelling. Dynamic Smagorinsky-Lilly model is selected as the subgrid-scale model in current study. To solve the governing equations, the segregated solver, semi-implicit method for pressure linked equation-consistent (SIMPLEC), is selected. Second order discretization is used for pressure, bounded central differencing discretization scheme is used for momentum equations, and bounded second order implicit for transient formulation is used.

Numerical models with both flat and complex terrains are discretized into structured mesh (Figure 10D). The grids near the ground are refined in order to accurately capture large velocity gradient. Grid height of the first layer is 0.02 m. Taking the wind speed at the height of 10 m as the reference wind speed and 10 m as the characteristic length, the Reynolds number is estimated to be in the order of 10^6, and Y+ value is estimated to be 350. The total number of numerical grids for both models is 2.35 million.

Determination of velocity input

As mentioned in *Simulated Time Period and Numerical Model Section*, the velocity input at flow inlet is determined based on DWL data. The time history of DWL measured wind speed associated with dataset 230 is presented in Figure 11A. Because the sampling rate of the DWL is low (about 4 s), time histories of wind speed and direction only exhibit minor fluctuations. In general, wind speed fluctuates between 14 m/s and 20 m/s, and wind direction varies between 185° and 205° below the height of 400 m. To maintain the equilibrium of wind field from inlet to outlet, the equilibrium inflow boundary condition (EIBC) based on Reynolds-averaged Navier-Stokes (RANS) equations (Yang et al., 2009; Zheng et al., 2012) is applied before the running of LES. RANS is another approach to analyze turbulent flows, in which Navier-Stokes equations are averaged over all scales of motion, and only the mean flow is resolved. EIBC is favorable because it considers the applied turbulent kinetic energy to vary with height, which is conventionally assumed to be a constant along height (Richards and Hoxey, 1993). Eq. 3 shows the equations used in EIBC.

$$u(z)=\frac{u_*}{\kappa}\ln\left(\frac{z+z_0}{z_0}\right) \tag{3a}$$

$$\varepsilon(z)=C_\mu^{1/2}k(z)\frac{\partial u}{\partial z} \tag{3b}$$

$$k(z)=\sqrt{2C_1\cdot\ln(z+z_0)+C_2} \tag{3c}$$

$$\omega(z)=\frac{\varepsilon(z)}{C_\mu k(z)} \tag{3d}$$

where $u(z)$ is wind speed profile; $\varepsilon(z)$ is the profile of turbulent dissipation rate; $k(z)$ is the profile of turbulent kinetic energy; $\omega(z)$ is the profile of specific dissipation rate, which is also used to represent the dissipation of turbulent kinetic energy and similar to turbulent dissipation rate; u_* is fiction velocity; z_0 is surface roughness length; κ is von Kármán's constant, taken as 0.4; C_μ is model constant, taken as 0.09; C_1 and C_2 are constants.

Equations 3a,c are used to fit profiles of mean wind speed and turbulent kinetic energy from dataset 230 in order to obtain the velocity input. The finalized input for flow inlet is presented in Figure 11B along with observations, and the associated equations are:

$$u(z)=\frac{0.4205}{\kappa}\ln\left(\frac{z+0.08}{0.08}\right) \tag{4a}$$

$$\varepsilon(z)=\sqrt{C_\mu}k(z)\frac{u_*}{\kappa(z+z_0)} \tag{4b}$$

$$k(z)=\sqrt{-0.9858\cdot\ln(z+z_0)+6.555} \tag{4c}$$

$$\omega(z)=\frac{u_*}{\sqrt{C_\mu}\kappa(z+z_0)} \tag{4d}$$

Verification of CFD simulations

The EIBC is first validated through numerical simulation associated with the flat terrain (Figure 10C) through RANS. It should be noted that only RANS simulation is conducted for this validation, since it is derived on the basis of RANS. In order to reduce the effects of terrain on the wind field, flat terrain is utilized in the numerical model. As shown in Figure 12A, a total of twenty-one wind speed profiles are extracted from the numerical simulation, and they are very close to each other. In comparison to the velocity input at flow inlet (Eq. 4), the maximum mean error is 0.9 m/s and the maximum root-mean-square error is 0.06 m/s. Therefore, EIBC is effective and valid, and the profile of mean wind speed can be maintained from inlet to outlet.

Secondly, LES is validated using the numerical model with complex terrain (Figure 10C), and wind tower data are used as

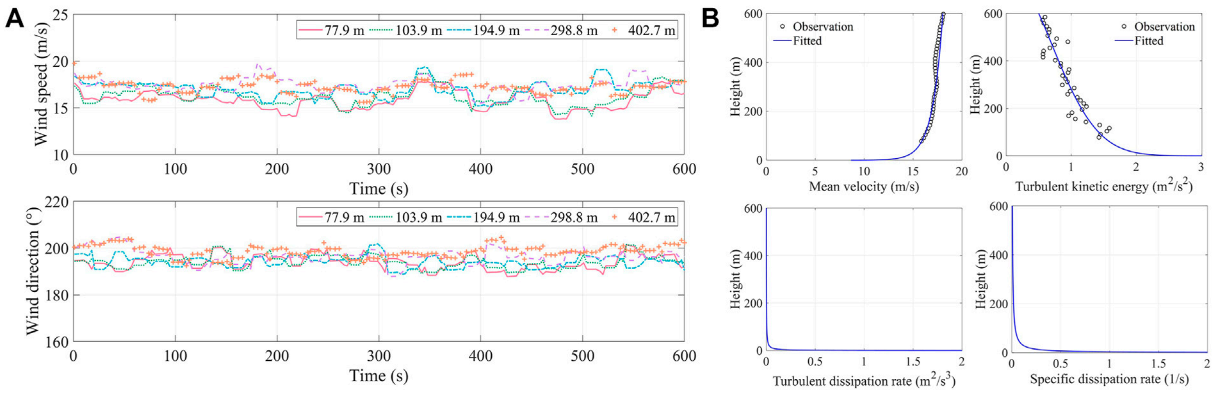

FIGURE 11
(A) Time histories of wind speed (unit: m/s) and wind direction (unit: °) from dataset 230 measured by DWL at five heights, and the horizontal axis is time in seconds; **(B)** Velocity input at flow inlet in CFD simulations, including mean speed profile (unit: m/s), turbulent kinetic energy profile (unit: m^2/s^2), turbulent dissipation rate profile (unit: m^2/s^3), and specific dissipation rate (unit: 1/s).

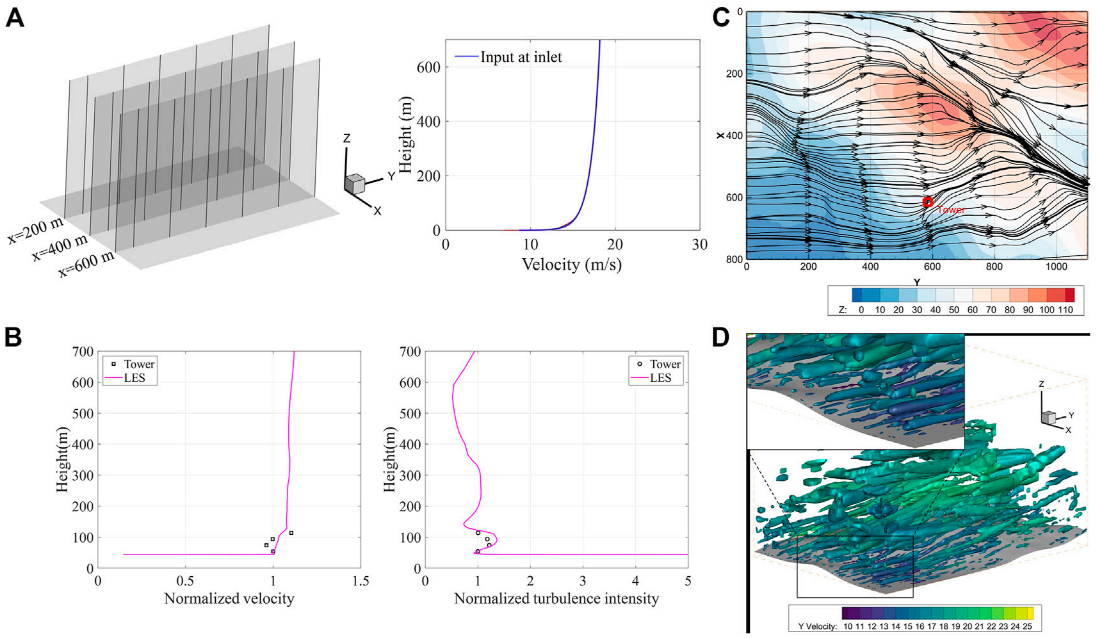

FIGURE 12
Verification of CFD simulations: **(A)** Equilibrium inflow boundary conditions: **(B)** Comparison of wind speed and turbulence intensity between numerical results (LES) and wind tower measurements; **(C)** Mean surface streamline of the wind field and ground elevation (shaded, unit: m), and vertical axis (X) represents across-wind direction in meters, and horizontal axis (Y) represents flow direction in meters; **(D)** Instantaneous vortex structure of the wind field colored by Y velocity (unit: m/s).

the benchmark. Figure 12B presents the comparison of wind speed profile and turbulence intensity profile between numerical results and wind tower data (dataset 230).

Wind speed profile associated with LES generally increases with height. However, its gradient is smaller than that of observations, and the local reverse occurring in observations is not captured. The reason is that wind direction changes a lot among different heights for wind tower measurements, e.g., wind direction difference between the heights of 10 m and 30 m is up to 20°. Such large variation of wind direction leads to the reverse of wind speed profile at the height of 30 m and large wind speed gradient. However, in the numerical simulation, constant wind

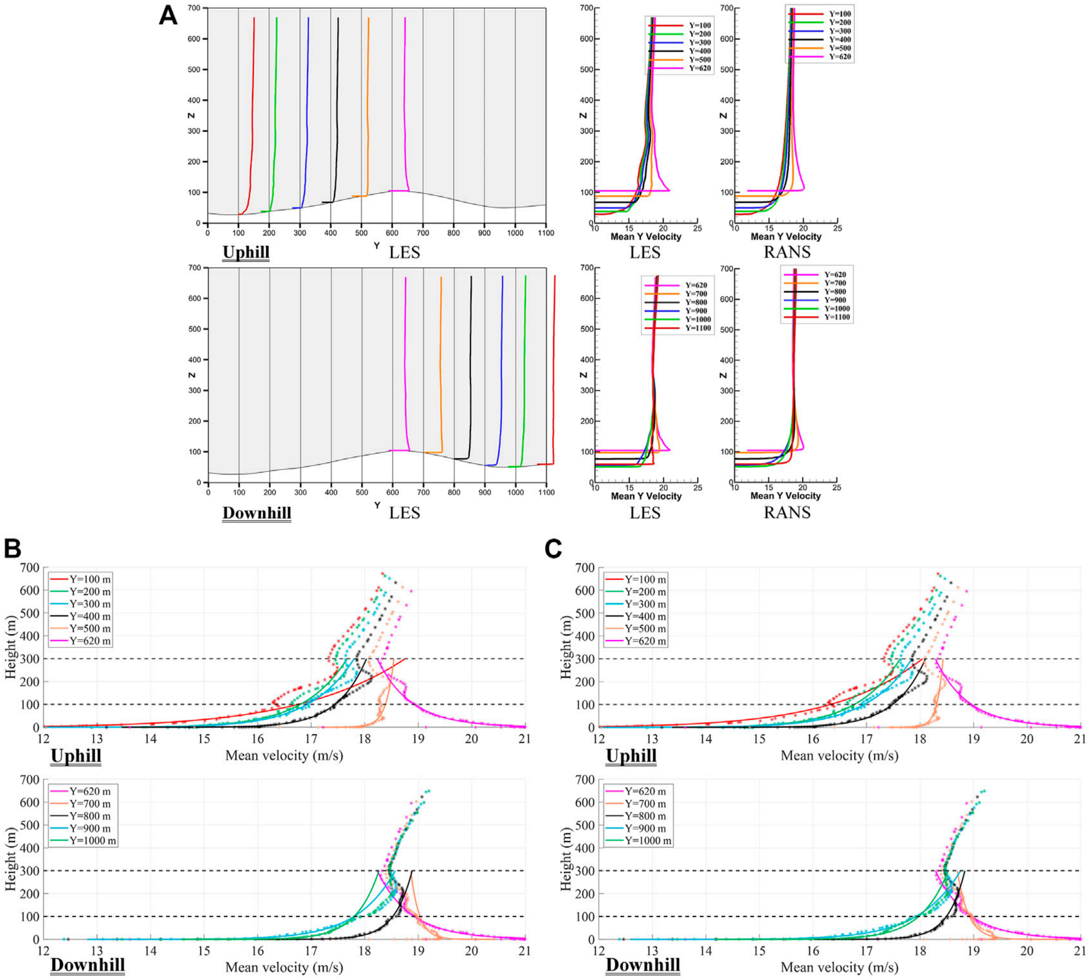

FIGURE 13
Mean wind speed profiles when X=320 m and Y=100–620 m (uphill) or Y=620–1100 m (downhill): **(A)** Numerical results with absolute coordinates. For subfigures on the left, vertical axis (Z) represents height in meters, and horizontal axis (Y) represents flow direction in meters. For the four subfigures on the right, vertical axis (Z) represents height in meters, and horizontal axis represents mean wind speed; **(B)** Numerical results (dotted star curves) and fitted power-law profiles (solid curves) between 0 and 100 m with coordinates relative to ground; **(C)** Numerical results (dotted star curves) and fitted power-law profiles (solid curves) between 0 and 300 m with coordinates relative to ground.

direction along height is assumed at flow inlet, ignoring its variation in the vertical direction. Therefore, the simulated wind speed profile differs from the observations regarding the wind speed gradient and the local reverse. The simulated turbulence intensity profile is generally consistent with wind tower data, but with slightly larger magnitude, which corresponds to smaller magnitude of simulated wind speed.

Figure 12C shows the mean surface streamline of the wind field and the ground elevation. According to the shaded ground elevation, there is a small hill with an altitude of 105 m in the middle upper region. West winds prevail on the windward side of the hill and northwesterly winds are formed on the leeward side. At the location where the wind tower stands (red square in Figure 12C), the simulated mean wind direction is about 225°. The mean wind direction determined based on dataset 230 from wind tower data varies in the range of 197°–221°, indicating an error of 1.8%–14.2%.

The simulated instantaneous vortex structure colored by Y velocity is illustrated in Figure 12D. Vortices mainly develop along the flow direction. The scale of vortex near the ground is small due to the influence of terrain and surface friction. Away from the ground, the vortex grows with the height. In summary, the results associated with LES are reasonably consistent with wind tower data and the wind field of typhoon boundary layer can be reproduced by LES. Then, the numerical results are adopted to further understand wind characteristics of typhoon boundary layer below 300 m.

Analysis of wind characteristics

By averaging the instantaneous results from LES, mean wind speed profiles are obtained and presented in Figure 13A in absolute coordinates. Since the apex of the hill in the upper middle region (Figure 12C) is located at X=320 m and Y=620 m, Figure 13A mainly illustrates wind speed profiles on the vertical Y-Z plane where X=320 m to investigate the effects of hilly terrain on wind speed profiles. For uphill winds, six wind speed profiles located at Y=100, 200, 300, 400, 500, and 620 m are extracted. For downhill winds, another six wind speed profiles located at Y=620, 700, 800, 900, 1000, and 1100 m are extracted. For wind speed profiles in the uphill direction, wind speed increases gradually as the ground elevation increases. Along vertical direction, all wind speed profiles obey the law that wind speed increases with height except for the wind speed profile at the apex of the hill (Y=620 m) where a completely reversed and almost monotonically decreasing profile is observed. In the downhill direction, wind speed gradually decreases with the decrease of ground elevation. The reversed wind speed profile is also observed at Y=700 m. Due to local terrain and surface friction, gradient of wind speed is much larger below the height of 300 m while it tends to be stable above 300 m. The same numerical model is also simulated by RANS approach for comparison. Since RANS approach only resolves mean flow, the obtained wind speed profiles are smoother and more consistent with the ideal power law. Because turbulent characteristics of wind field are generated by LES through directly solving large scales of motion, local fluctuations of wind speed profile are observed for LES results, especially below 300 m.

The power law as listed in Eq. 1 is applied to fit the wind speed profiles from LES. Wind speeds below the height of 100 m are first fitted. Comparison between the fitted curve and numerical results is shown in Figure 13B. It should be noted coordinates relative to ground are used for the regression of the power law. From Figure 13B, except for the wind speed profiles at Y=500 m and 700 m, wind speed profiles obtained from LES generally conform to the power-law profile, and fitted curves match the measured data well; the R^2 of fitted curves are all greater than 0.96, the maximum mean error is 0.19 m/s and the maximum root-mean-square error is 0.23 m/s. The errors of fitted power-law profile for wind speeds at Y=500 m and 700 m are relatively larger, because both regions are located in the transition zone where the wind speed profile changes from monotonically increasing to monotonically decreasing. Therefore, wind speed profile is more oscillating and fluctuating, which cannot be characterized by the power law that leads to larger deviations. In general, wind speed profiles below the height of 100 m in the uphill and downhill directions obey the law that wind speed increases with height, which can be well depicted by the power law. At the apex of the hill, reverse wind speed profile is observed and the power law with negative exponent can be applied. For the transition zone close to the apex of the hill, the power law can only characterize the development trend of the wind speed profile, neglecting local fluctuations.

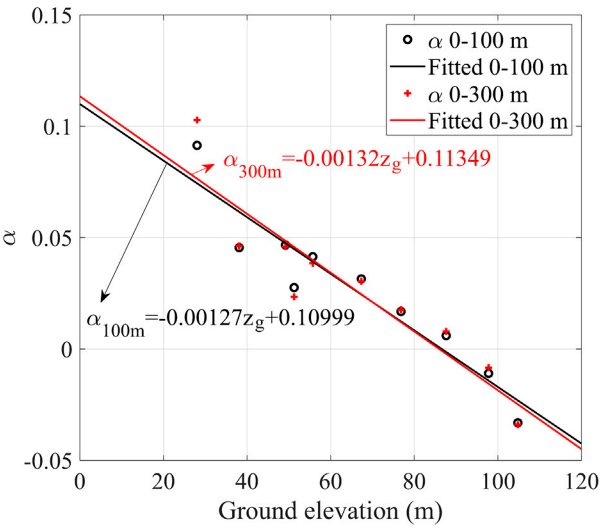

FIGURE 14
Linear relation between power exponents (vertical axis) and ground elevation (horizontal axis). Black solid line represents the fitted relation curve for power exponents obtained from power-law profiles between 0 and 100 m, and black circle represents associated power exponents. Red solid line represents the fitted relation curve for power exponents obtained from power-law profiles between 0 and 300 m, and red plus sign represents associated power exponents.

The power-law fit for wind speed profiles above 100 m is presented in Figure 13C. Here, wind speeds between 0 and 300 m are used for the power-law fit. From Figure 13C, wind speed profiles no longer follow the monotonically increasing or decreasing law. Local reverses occur at the heights between 110 and 130 m and low-level jets occur at 180–250 m in the uphill direction and at the apex. In the downhill direction, low-level jet normally occurs at the height of 220 m. If the absolute coordinates are applied (Figure 13A), the height where reverse and low-level jet occur is more consistent. Generally, reverse occurs at the height of 125 m, and low-level jet occurs at the height of 290 m in the uphill direction and at the apex. The low-level jet occurs at the height of 270 m in the downhill direction. Due to the above-mentioned inversion and jet, the power law cannot describe mean wind speed profiles above 100 m well. Comparing to parameters from power-law fit based on wind speed data below 100 m, the R^2 decreases by 0.11, the mean error increases by 0.08 m/s, and the root-mean-square error increases by 0.07 m/s.

Power exponents of the fitted wind speed profiles between 0–100 m and 0–300 m are correlated to the ground elevation, and linear relation is found, which are calibrated and presented in Eq. 5 and Figure 14.

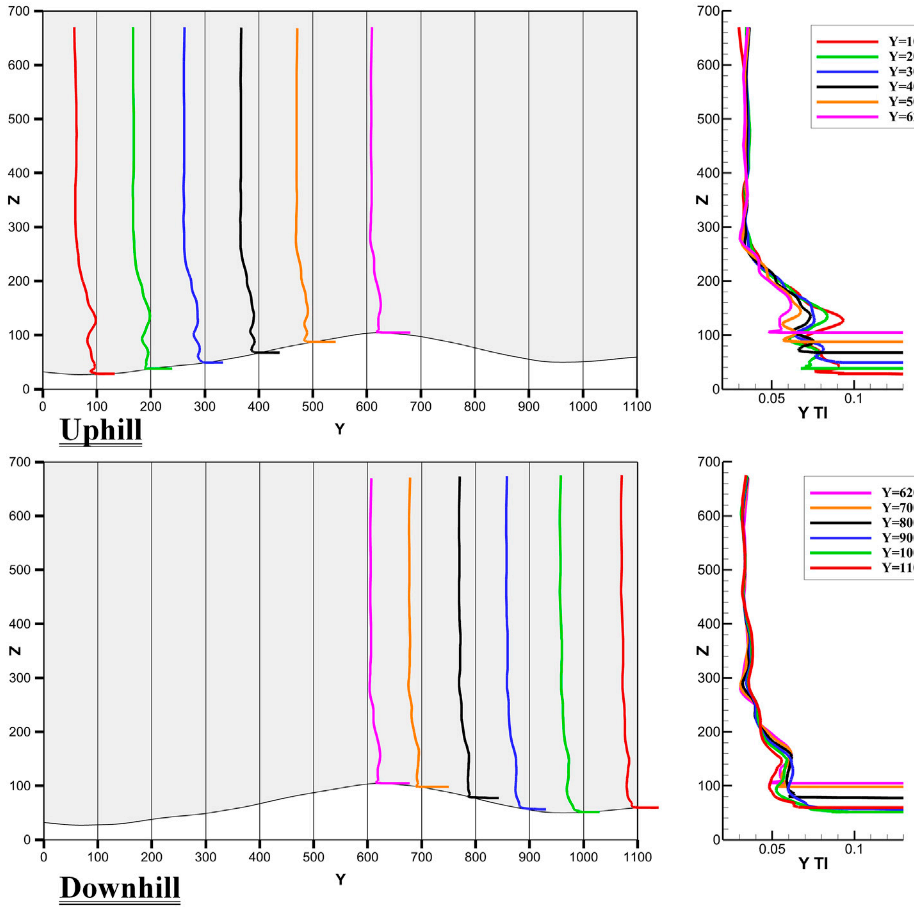

FIGURE 15
Simulated turbulence intensity profiles when X=320 m and Y=100–620 m (uphill) or Y=620–1100 m (downhill). For subfigures on the left, vertical axis (Z) represents height in meters, and horizontal axis (Y) represents flow direction in meters. For subfigures on the right, vertical axis (Z) represents height in meters, and horizontal axis represents turbulence intensity.

$$\alpha_{100\mathrm{m}} = -0.00127 z_g + 0.10999 \tag{5a}$$

$$\alpha_{300\mathrm{m}} = -0.00132 z_g + 0.11349 \tag{5b}$$

where z_g is the ground elevation (m); $\alpha_{100\mathrm{m}}$ is the power exponent of the fitted wind speed profile below the height of 100 m; and $\alpha_{300\mathrm{m}}$ is the power exponent of the fitted wind speed profile below the height of 300 m.

From Figure 14, power exponents decrease with the increase of ground elevation and even become negative, which corresponds to completely reversed or partially reversed wind speed profiles. Power exponents $\alpha_{100\mathrm{m}}$ and $\alpha_{300\mathrm{m}}$ slightly differ from each other. Specifically, $\alpha_{300\mathrm{m}}$ is larger than $\alpha_{100\mathrm{m}}$ when the ground elevation is lower than 80 m. $\alpha_{300\mathrm{m}}$ is smaller than $\alpha_{100\mathrm{m}}$ when the ground elevation is greater than 80 m.

Figure 15 presents simulated profiles of turbulence intensity. Large variations are observed below the height of 300 m, while the profiles remain almost unchanged above 300 m. For all profiles of turbulence intensity, two local reverses are exhibited, while one is more obvious than the other. In the uphill direction, the dominant local reverse normally occurs at around 120 m and it occurs at around 160 m for the downhill case. Besides, local reverse of turbulence intensity profile typically becomes more significant when ground elevation decreases.

Conclusion

This study investigates wind characteristics of atmospheric boundary layer during super typhoon Lekima (2019) by the combination of observational analysis (wind tower equipped with ultrasonic anemometers and DWL) and CFD simulations. The research focuses on the exploration of mean wind speed and turbulence intensity profiles within 300 m (special attention is paid to the height between 100 and 300 m) under the condition of complex terrain. Main conclusions are summarized as follows:

- Measurements by wind tower and DWL are compared, and both data are generally consistent with each other. However, due to change of wind direction caused by the approaching of typhoon, upstream conditions of both instruments gradually differ from each other. The measured wind characteristics start to deviate. Therefore, it is necessary to consider wind direction and upstream terrain conditions when analyzing wind characteristics of typhoon boundary layer.
- DWL measurements show that mean wind speed profile in the range of 100–300 m cannot be fully described by the power law at different typhoon stages. When typhoon center is far away from the DWL (around 330 km), the power law can well describe the wind speed profile with R^2 greater than 0.96. When typhoon is close to the DWL, local reverse and low-level jet are observed for wind speed profile, which cannot be characterized by the power law. Turbulence intensity does not completely decrease with height. When the wind field of typhoon passes the DWL, turbulence intensity increases with height and experiences larger fluctuations.
- Based on CFD simulations, mean wind speed below 100 m is fitted for uphill, downhill, hill apex, and transition zone. Power law is able to describe uphill and downhill cases with positive exponent and apex case with negative exponent, while it is less effective for transition zone with local fluctuations. When the height is increased to 100–300 m, local reverse or low-level jet are observed. The R^2 of power-law fitted curve is thus reduced by 0.11 compared to that of the power-law fit below 100 m. Simulated turbulence intensity profiles experience local reverses, and degree of reverse is decreased with terrain elevation.
- Ground elevation and power exponents of fitted wind speed profiles are successfully correlated with linear relation: power exponents decrease with the increase of ground elevation. However, power exponent becomes negative when ground elevation is greater than 90 m, which corresponds to the apex of the hill.

The above findings are useful to better understand wind characteristics of typhoon boundary layer concentrated between 100 and 300 m. In the future, it is suggested to apply wind direction varying with height in the CFD simulation in order to generate more realistic wind field of typhoons. Also, it is suggested to provide suitable analytical profiles to fit wind speed and turbulence intensity profiles, facilitating wind-resistant design of civil structures in typhoon-prone regions and numerical modelling of typhoons.

Data availability statement

The raw data supporting the conclusion of this article will be made available by the authors, without undue reservation.

Author contributions

TL and ST conducted the study and wrote the manuscript. HQ performed the data analysis and manuscript reviewing and editing. JT, JY, and LL conducted the experimental tests and reviewed the manuscript. YL and YY provided critical feedback on the research.

Funding

This work was supported by the National Key R&D Program of China (No. 2018YFB1501104); National Natural Science Foundation of China (Nos. 42005144, U2142206, 52008316, 41805088); China Postdoctoral Science Foundation (No. 2020M681443); Shanghai Post-doctoral Excellence Program (No. 2020518); Basic Research Fund of Shanghai Typhoon Institute (No. 2022JB01); and Fujian Key Laboratory of Severe Weather Open Foundation (2021TFS02).

Conflict of interest

The authors declare that the research was conducted in the absence of any commercial or financial relationships that could be construed as a potential conflict of interest.

The handling editor (LW) declared a past co-authorship with the author (LL).

Publisher's note

References

Blocken, B., van der Hout, A., Dekker, J., and Weiler, O. (2015). CFD simulation of wind flow over natural complex terrain: Case study with validation by field measurements for Ria de Ferrol, Galicia, Spain. *J. Wind Eng. Ind. Aerodyn.* 147, 43–57. doi:10.1016/j.jweia.2015.09.007

Cao, S., Tamura, Y., Kikuchi, N., Saito, M., Nakayama, I., and Matsuzaki, Y. (2009). Wind characteristics of a strong typhoon. *J. Wind Eng. Ind. Aerodyn.* 97 (1), 11–21. doi:10.1016/j.jweia.2008.10.002

Chen, P., Yu, H., Xu, M., Lei, X., and Zeng, F. (2019). A simplified index to assess the combined impact of tropical cyclone precipitation and wind on China. *Front. Earth Sci.* 13 (4), 672–681. doi:10.1007/s11707-019-0793-5

Fang, G., Zhao, L., Cao, S., Ge, Y., and Li, K. (2019). Gust characteristics of near-ground typhoon winds. *J. Wind Eng. Ind. Aerodyn.* 188, 323–337. doi:10.1016/j.jweia.2019.03.008

GB50009 (2012). *Lode code for the design of building structures*. Beijing: China Architecture Publishing & Media Co., Ltd.

He, J. Y., He, Y. C., Li, Q. S., Chan, P. W., Zhang, L., Yang, H. L., et al. (2020). Observational study of wind characteristics, wind speed and turbulence profiles during Super Typhoon Mangkhut. *J. Wind Eng. Ind. Aerodyn.* 206, 104362. doi:10.1016/j.jweia.2020.104362

He, J. Y., Chan, P. W., Li, Q. S., Li, L., Zhang, L., and Yang, H. L. (2022). Observations of wind and turbulence structures of Super Typhoons Hato and Mangkhut over land from a 356 m high meteorological tower. *Atmos. Res.* 265, 105910. doi:10.1016/j.atmosres.2021.105910

Hojstrup, J. (1993). A statistical data screening procedure. *Meas. Sci. Technol.* 4 (2), 153–157. doi:10.1088/0957-0233/4/2/003

JTWC (Joint Typhoon Warning Center) (2022). *Best track archive*. Available at: https://www.metoc.navy.mil/jtwc/jtwc.html?best-tracks (Accessed September 1, 2022).

Law, S. S., Bu, J. Q., Zhu, X. Q., and Chan, S. L. (2006). Wind characteristics of Typhoon Dujuan as measured at a 50m guyed mast. *Wind Struct.* 9 (5), 387–396. doi:10.12989/was.2006.9.5.387

Li, L., Chan, P. W., Hu, F., Zhang, L. J., and Liu, Y. X. (2014). Numerical simulation on the wind field structure of a mountainous area beside South China Sea during the landfall of typhoon Molave. *J. Trop. Meteorol.* 20 (1), 66–73.

Li, L., Xiao, Y., Zhou, H., Xing, F., and Song, L. (2018). Turbulent wind characteristics in typhoon Hagupit based on field measurements. *Int. J. Distrib. Sens. Netw.* 14 (10), 155014771880593. doi:10.1177/1550147718805934

Li, T., Yan, G., Yuan, F., and Chen, G. (2019). Dynamic structural responses of long-span dome structures induced by tornadoes. *J. Wind Eng. Ind. Aerodyn.* 190, 293–308. doi:10.1016/j.jweia.2019.05.010

Li, T., Yan, G., Feng, R., and Mao, X. (2020). Investigation of the flow structure of single-and dual-celled tornadoes and their wind effects on a dome structure. *Eng. Struct.* 209, 109999. doi:10.1016/j.engstruct.2019.109999

Li, Y., Zhao, S., and Wang, G. (2021). Spatiotemporal variations in meteorological disasters and vulnerability in China during 2001-2020. *Front. Earth Sci.* 9, 1194. doi:10.3389/feart.2021.789523

Liao, F., Deng, H., Gao, Z., and Chan, P. W. (2017). The research on boundary layer evolution characteristics of Typhoon Usagi based on observations by wind profilers. *Acta Oceanol. Sin.* 36 (9), 39–44. doi:10.1007/s13131-017-1109-9

Lu, X., Yu, H., Ying, M., Zhao, B., Zhang, S., Lin, L., et al. (2021). Western north pacific tropical cyclone database created by the China meteorological administration. *Adv. Atmos. Sci.* 38 (4), 690–699. doi:10.1007/s00376-020-0211-7

Luo, Y. P., Fu, J. Y., Li, Q. S., Chan, P. W., and He, Y. C. (2020). Observation of Typhoon Hato based on the 356-m high meteorological gradient tower at Shenzhen. *J. Wind Eng. Ind. Aerodyn.* 207, 104408. doi:10.1016/j.jweia.2020.104408

Masters, F. J., Tieleman, H. W., and Balderrama, J. A. (2010). Surface wind measurements in three Gulf Coast hurricanes of 2005. *J. Wind Eng. Ind. Aerodyn.* 98 (10-11), 533–547. doi:10.1016/j.jweia.2010.04.003

Ming, J., Zhang, J. A., Rogers, R. F., Marks, F. D., Wang, Y., and Cai, N. (2014). Multiplatform observations of boundary layer structure in the outer rainbands of landfalling typhoons. *J. Geophys. Res. Atmos.* 119 (13), 7799–7814. doi:10.1002/2014jd021637

Nakayama, H., Takemi, T., and Nagai, H. (2012). Large-eddy simulation of urban boundary-layer flows by generating turbulent inflows from mesoscale meteorological simulations. *Atmos. Sci. Lett.* 13, 180–186. doi:10.1002/asl.377

NASADEM (2020). *Release of NASADEM data products*. Available at: https://lpdaac.usgs.gov/news/release-nasadem-data-products/(Accessed September 1, 2022).

Powell, M. D., Vickery, P. J., and Reinhold, T. A. (2003). Reduced drag coefficient for high wind speeds in tropical cyclones. *Nature* 422 (6929), 279–283. doi:10.1038/nature01481

Richards, P. J., and Hoxey, R. P. (1993). Appropriate boundary conditions for computational wind engineering models using the k-ϵ turbulence model. *J. Wind Eng. Ind. Aerodyn.* 46, 145–153. doi:10.1016/0167-6105(93)90124-7

Shi, W., Tang, J., Chen, Y., Chen, N., Liu, Q., and Liu, T. (2021). Study of the boundary layer structure of a landfalling typhoon based on the observation from multiple ground-based Doppler wind lidars. *Remote Sens. (Basel).* 13, 4810. doi:10.3390/rs13234810

Song, L., Li, Q. S., Chen, W., Qin, P., Huang, H., and He, Y. C. (2012). Wind characteristics of a strong typhoon in marine surface boundary layer. *Wind Struct. Int. J.* 15 (1), 1–15. doi:10.12989/was.2012.15.1.001

STI (Shanghai Typhoon Institute) (2022). *Opening ceremony of east China typhoon field science experiment base of China meteorological administration*. (in Chinese). Available at: https://www.sti.org.cn/gongzuodongtai/2071.html (Accessed September 1, 2022).

Stull, R. B. (1988). *An introduction to boundary layer meteorology*. Berlin: Springer Science & Business Media.

Tang, S., Guo, Y., Wang, X., Tang, J., Li, T., Zhao, B., et al. (2020). Validation of Doppler wind lidar during super typhoon Lekima (2019). *Front. Earth Sci.* 16, 75–89. doi:10.1007/s11707-020-0838-9

Tang, S., Li, T., Guo, Y., Zhu, R., and Qu, H. (2022). Correction of various environmental influences on Doppler wind lidar based on multiple linear regression model. *Renew. Energy* 184, 933–947. doi:10.1016/j.renene.2021.12.018

Tsai, Y. S., Miau, J. J., Yu, C. M., and Chang, W. T. (2019). Lidar observations of the typhoon boundary layer within the outer rainbands. *Bound. Layer. Meteorol.* 171 (2), 237–255. doi:10.1007/s10546-019-00427-6

Vickers, D., and Mahrt, L. (1997). Quality control and flux sampling problems for tower and aircraft data. *J. Atmos. Ocean. Technol.* 14 (3), 512–526. doi:10.1175/1520-0426(1997)014<0512:qcafsp>2.0.co;2

Wang, Y., Yin, Y., and Song, L. (2022). Risk assessment of typhoon disaster chains in the guangdong-Hong Kong-Macau greater bay area, China. *Front. Earth Sci.* 10, 839733. doi:10.3389/feart.2022.839733

WMO (World Meteorological Organization) (2022). *Tropical cyclones*. Available at: https://public.wmo.int/en/our-mandate/focus-areas/natural-hazards-and-disaster-risk-reduction/tropical-cyclones (Accessed September 1, 2022).

Yang, Y., Gu, M., Chen, S., and Jin, X. (2009). New inflow boundary conditions for modelling the neutral equilibrium atmospheric boundary layer in computational wind engineering. *J. Wind Eng. Ind. Aerodyn.* 97 (2), 88–95. doi:10.1016/j.jweia.2008.12.001

Yang, Y., Dong, L., Li, J., Li, W., Sheng, D., and Zhang, H. (2022). A refined model of a typhoon near-surface wind field based on CFD. *Nat. Hazards* 114, 389–404. doi:10.1007/s11069-022-05394-9

Ying, M., Zhang, W., Yu, H., Lu, X., Feng, J., Fan, Y., et al. (2014). An overview of the China Meteorological Administration tropical cyclone database. *J. Atmos. Ocean. Technol.* 31 (2), 287–301. doi:10.1175/jtech-d-12-00119.1

Zhang, Q., Wu, L., and Liu, Q. (2009). Tropical cyclone damages in China 1983–2006. *Bull. Am. Meteorol. Soc.* 90 (4), 489–496. doi:10.1175/2008bams2631.1

Zhao, Z., Chan, P. W., Wu, N., Zhang, J. A., and Hon, K. K. (2020). Aircraft observations of turbulence characteristics in the tropical cyclone boundary layer. *Bound. Layer. Meteorol.* 174 (3), 493–511. doi:10.1007/s10546-019-00487-8

Zheng, D. Q., Zhang, A. S., and Gu, M. (2012). Improvement of inflow boundary condition in large eddy simulation of flow around tall building. *Eng. Appl. Comput. Fluid Mech.* 6 (4), 633–647. doi:10.1080/19942060.2012.11015448

Zhou, K., Li, Q., and Tang, J. (2022). Estimation of dissipative heating properties above the internal boundary layer in landfalling typhoons using multi-layer tower observations. *Front. Earth Sci.* 10, 833994. doi:10.3389/feart.2022.833994

Frontiers in
Earth Science

Investigates the processes operating within the major spheres of our planet

Advances our understanding across the earth sciences, providing a theoretical background for better use of our planet's resources and equipping us to face major environmental challenges.

Discover the latest Research Topics

See more →

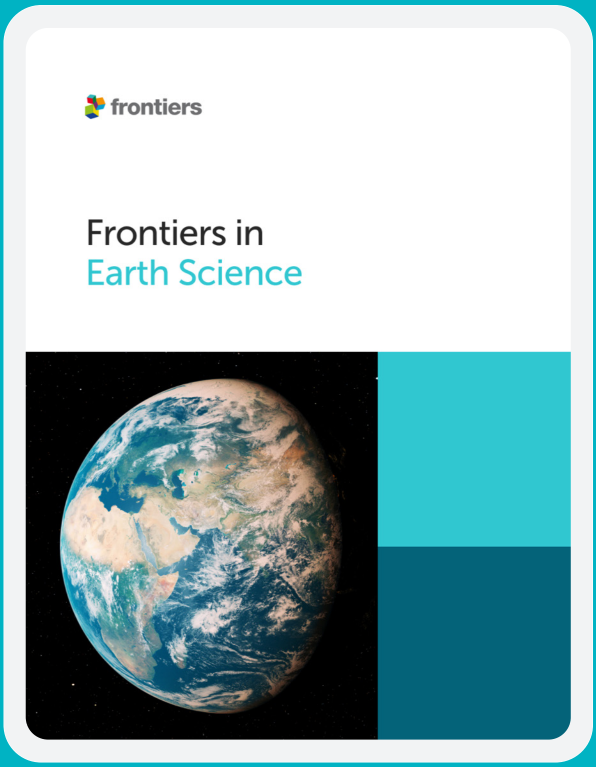

frontiers

Frontiers in
Earth Science

Frontiers

Avenue du Tribunal-Fédéral 34
1005 Lausanne, Switzerland
frontiersin.org

Contact us

+41 (0)21 510 17 00
frontiersin.org/about/contact